UNITED STATES DEPARTMENT OF THE INTERIOR

GEOLOGICAL SURVEY

Geotechnical Framework Study of the northern Bering Sea, Alaska

by

Monty A. Hampton

and

William J. Winters

OPEN-FILE REPORT

83-404

TABLE OF CONTENTS

INTRODUCTION

Geologic studies in the northern Bering Sea (Fig. 1) have identified several features and processes that can have significant impact on offshore industrial operations (Thor and Nelson, 1980; Larsen and others, 1980). Faulting, thermogenic and biogenic gas charging, sediment liquefaction, ice gouging, current scouring, and bedform migration have been identified as potential hazards (Fig. 2). The occurrence of specific conditions depends partly on local geologic history, especially with regard to the types of sediment that have accumulated. Also important are modern environmental forces, which in the northern Bering Sea include severe storms, strong geostrophic ocean currents, and movement of seasonal ice.

This report presents the results of a two-year geotechnical framework study, designed to determine representative values of sediment mechanical (geotechnical) properties and to use these values in an assessment of soil response to engineering and natural loading. Geotechnical data have been gathered previously and applied to the analysis of particular problems in the area (Olsen and others, 1980; Clukey and others, 1980). The framework study is a quantitative supplement to the other geologic and geotechnical studies and provides engineering data that can be used from a regional perspective in preliminary evaluations for siting offshore operations.

An important aspect of this study is that geotechnical properties were measured in situ, as well as in the laboratory. The in situ tests consist of pushing a cone-tipped rod into the seabed and measuring the resistance to penetration, from which correlations to sediment properties are made. Laboratory techniques involve deformation testing of sediment core samples. An advantage of in situ testing is that it measures properties of sediment in

the natural, undisturbed state. Sediment cores can suffer significant disturbance before they are tested in the laboratory. This is particularly true for the silty and sandy sediment types in the northern Bering Sea that were cored using vibratory methods (Koutsoftas and others, 1976). The natural stress state is difficult to reproduce in the laboratory, and original sediment fabric can be broken down during and after coring operations. Laboratory testing of disturbed core samples can measure physical properties that are different from those of sediment in the natural state. However, present equipment allows examination of a wider range of properties with laboratory testing than with in situ testing. This study offers an excellent opportunity to compare the two methods.

GEOLOGIC SETTING.

The northern Bering Sea comprises a broad, shallow epicontinental shelf that extends about 200,000 km^2 between Alaska and Siberia (Fig. 1). Two major physiographic subdivisions are Norton Sound (water depth < 30 m) and Chirikov Basin (water depth < 60 m). The entire region was emergent during Pleistocene low stands of sea level. Glaciers encroached on western and northern portions. An extensive tundra vegetation developed on the remainder of the shelf, except where rivers carved channels that led to large submarine canyons. Shoreline transgression at the close of Pleistocene time initiated marine sedimentation, first in the deeper parts of Chirikov Basin and finally across shallow Norton Sound (Nelson, 1980a). The Yukon River migrated north to its present position from the vicinity of Cape Romanzov about 2500 years ago (Dupré and Thompson, 1979). During sealevel stillstands, coastal shoals were formed near Port Clarence and Nome (Nelson and others, 1980).

The distribution of unconsolidated sediment types therefore reflects glacial, subaerial, and marine processes (Nelson, 1980a). In Chirikov Basin the sequence is in most places less than a few meters thick and consists of coarse glacial till and outwash, limnic peaty mud, transgressive gravel to medium sand, and inner-shelf fine sand. This sediment is Pleistocene age, and individual units are patchy in their distribution. Strong northward geostrophic flow has bypassed Holocene sediment and deposited it in the southern Chukchi Sea (Nelson and Creager, 1977).

Peaty mud with incised fluvial deposits cover bedrock in Norton Sound. Transgressive sand has been found only in the central sound and in a trough in the northern sound. Yukon River silt with interbedded storm-sand layers is the dominant sediment type. It covers nearly all of the seafloor in Norton Sound and has accumulated up to 14 m thickness. The sediment type grades to silt and mud in the eastern sound.

METHODS

Field methods: A geotechnical cruise in the northern Bering Sea was conducted August 3-18, 1981 aboard the NOAA ship DISCOVERER. Sites were occupied that represent a broad range of geologic environments, many where special engineering problems might be encountered (Figs. 2 and 3; Table 1). In Chirikov Basin, only the shoreline shoals near Port Clarence were visited. The rest of the stations were in Norton Sound at locations of biogenic gas-charged sediment (2 stations), a thermogenic gas seep, muddy sediment, and a range of Yukon prodelta sediment types (5 stations).

Geotechnical data were obtained with in situ testing equipment and from laboratory testing of sediment cores. The in situ device is a static cone

penetrometer, the XSP-40, that belongs to the Naval Civil Engineering Laboratory (Fig. 4; Beard and Lee, 1982). The instrument measures resistance to penetration of a 3.56-cm diameter cone that can be driven into the seabed a maximum depth of 6 m. Frictional resistance along the side of a sleeve above the cone is also measured. The instrument is housed on a tall frame supported on four broad-based, retractable legs. Total weight is about 4.5 metric tons, which determines the maximum force that can be measured. The cone and sleeve are attached to the end of a rod that is driven by a double chain. In operation the instrument is lowered to the seafloor, and penetration at a rate of 1 m/min is actuated by an onboard switch to the 1-horsepower drive motor. Cone and sleeve resistance are plotted continuously versus penetration depth on a chart recorder; tilt angle is also monitored. A test is terminated either when the maximum penetration depth is achieved or when the tilt meters indicate that the instrument has lifted from the seafloor (i.e., the maximum reaction force has been reached). The push rod and cone are retracted from the seabed by reversing the drive motor.

Core samples were taken with a large vibracorer (Fig. 5). This device is housed on a frame similar to that of the XSP-40. Cores are retrieved in plastic liners, 8 cm inside diameter, and maximum core length is 6 m. The core barrel is driven into the seabed by a pneumatic hammer mounted at the top of the barrel. Penetration rate of the core barrel was recorded during sampling operations (Table 2). Two cores were taken at each station. Both were cut into 1-m-long sections, and the ends were capped. One core was split lengthwise onboard ship, described geologically and subsampled at regular intervals for grain size, water content, grain specific gravity and carbon content determinations. When fine-grained cohesive sediment was encountered,

strength was measured with a motorized vane shear device, and subsamples were taken for determination of plasticity (Atterberg limits). The sections of the other core were wrapped in cheesecloth, covered with microcrystalline wax, and stored upright in a refrigerator. This core was used for geotechnical testing in the shorebased laboratory.

Shipboard operations at each station were as follows. A seismic-reflection line was run over each station, using 12 kHz, 3.5 kHz, and 600 joule minisparker systems. Navigation used Loran C with satellite updates. The ship was anchored at each station, the XSP-40 was deployed from an outboard storage position using the ship's deep-sea winch and large crane, and a cone penetration test (CPT) was run. More than one test was run at each station. Some successive tests were run after lifting the XSP-40 a small distance off the seafloor and setting it down again at essentially the same location. Other tests were rerun after the ship was allowed to drift a short distance, in order to study local variability of penetration resistance.

After all the penetrometer stations were occupied, the vibracorer was exchanged with the XSP-40 in the outboard storage position, and several stations were re-occupied. After anchoring, two vibracores were taken at these stations.

Vibracores had been taken in previous years for geological study at all but one of the stations we did not re-occupy, so most sites discussed in this paper have companion vibracores and cone penetration tests. Vibracores for laboratory geotechnical testing are not available for all stations, however.

The XSP-40 and the vibracorer were not both deployed at a single anchorage because the large size of the instruments made frequent interchange to the deployment position unfeasible. The XSP-40 was used first at all

stations while the vibracorer was stored on deck. Then, stations were re-occupied, and cores were taken. Relocation of the stations had a positional error of from 180 to 1647 m, so the CPT and vibracores were not from exactly the same place (Table 1B).

Laboratory methods:

In the shipboard lab, vane shear tests were made with a standard motorized apparatus, using a 1.27-cm diameter by 1.27-cm long vane and a rotation rate of 90°/min. Peak undisturbed and remolded strengths were measured at regular intervals down split cores (Table 4). In the shorebased lab, Atterberg limits were determined according to standard procedures (Lambe, 1951, p. 22-28), but with water content corrected for a salt concentration of 35 ppt. Grain sizes were measured by sieve, pipette and hydrometer methods (Carver, 1971; Lambe, 1951) (Tables 3 and 4, Appendix A). A LECO model WR-12 carbon determinator with an acid digestor and an induction furnace was used to measure organic carbon and carbonate content. An air comparison pycnometer aided in the calculation of grain density (Table 4).

Consolidation tests to measure sub-failure deformation properties of sediment were run by two different methods. Seven tests were performed on standard front-loading oedometers in a stress-controlled mode (Lambe, 1951), whereas 15 tests were run in triaxial loading cells at constant rate of strain (Wissa and others, 1971).

Static strength tests were run in triaxial loading cells on cylindrical samples approximately 3.6-cm diameter and 7.6-cm long. Tests were performed under undrained conditions with pore pressure measurements (Bishop and Henkel, 1964). Most samples were consolidated isotropically prior to testing, but some were consolidated anisotropically.

Cyclically loaded triaxial tests were also run, with the axial stress on samples varied sinusoidally at 0.1 H_z. Both compression and tension were applied at a predetermined percentage of the confining (consolidation) stress.

A total of 23 static and 38 cyclically loaded triaxial tests were conducted according to the scheme presented in Table 5. Some test specimens were consolidated to the in situ level before axial loading to failure was initiated. Others were consolidated to at least four times the maximum past stress for plastic sediment, in order to minimize the effects of disturbance (Ladd and Foott, 1974). Consolidation was isotropic in most tests but anisotropic in some. A condition of overconsolidation was induced in some test samples, whereby a high consolidation stress state was followed by rebounding to a lower consolidation stress before axial loads were applied. The ratio of the higher consolidation stress to the lower, rebounded stress defines the overconsolidation ratio (OCR).

Derived test parameters: The in situ penetration tests and laboratory tests described above are standard civil engineering procedures for evaluating the behavior of soil. Typical applications are the design of foundations, excavations, and artificial fills. The parameters that are derived from geotechnical test data can be used in geologic analyses as well, to determine the triggering forces for submarine sediment slides, for example.

Three sediment properties commonly deduced from cone penetration records are 1) stratigraphic variation 2) sediment type, and 3) relative density. Stratigraphic variation is a qualitative evaluation based on the shape of the cone pressure versus depth curve (Fig. 6, Appendix B). A smooth curve indicates uniform stratigraphy, whereas abrupt changes in slope reflect

stratigraphic interfaces between different sediment types. Of particular importance to engineering applications are major increases in slope of the curve, possibly beyond vertical, which identify soft strata beneath more firm material (Fig. 6).

Several attempts have been made to estimate sediment type from penetrometer data (Begemann, 1965; Schmertmann, 1978a; Martin and Douglas, 1981). The common technique is to delineate distinct fields of sediment types on plots of friction ratio (sleeve friction stress/cone pressure, expressed as a percent) versus cone pressure (Fig. 7). Successful correlations have been made, but they are somewhat limited to the local area from which the data were collected. Substantial engineering information about soil behavior can be deduced from a general knowledge of sediment type, and once a correlation has been established within an area, the expense and effort of collecting core samples can be reduced or eliminated.

Relative density refers to the magnitude of the natural density state relative to maximum and minimum density states. A relative density of 100% means that a sediment exists naturally in its densest possible state, and a relative density of 0% indicates the least dense state. Schmertmann (1978b) derived an empirical correlation between cone pressure, vertical effective stress (a measure of the buoyant weight of the sediment column at a particular depth below the surface), and relative density:

$$D_r = 0.34 \ln [(q_c/(12.31 \sigma'^{10.71}_{vo}))] \times 100$$

where D_r = relative density in percent

q_c = cone pressure in kg/cm^2

σ'_{vo} = effective vertical (overburden) stress

This correlation was derived from laboratory testing of normally consolidated sand, and its application to field situations may be imprecise (Appendix C).

As discussed by Schmertmann (1978a), measurements of cone pressure are influenced by the proximity of an interface between materials of different physical properties. In particular, as the cone enters the seabed, it must penetrate up to about 8 cone diameters (28 cm in our case) before the failure surface around the cone tip is fully developed and cone pressure readings truly reflect sediment physical properties. A similar argument applies to friction sleeve readings, and also to interfaces between sediment strata. As applied to the present study, the cone-pressure and friction-ratio curves (Appendix B) have only qualitative significance at depths less that about 0.28 m in the seabed; stratigraphic variation can be detected from irregularities in the shape of the curve, but measurement of relative density and identification of sediment type are inaccurate.

Laboratory consolidation tests are used to predict the amount and rate of consolidation of sediment in response to sustained loads, as well as to deduce the stress history of the sediment. Test results are plotted as void ratio (e = volume of voids/volume of solids) versus the logarithm of effective vertical stress (σ'_v) (Table 6, Appendix D). The curve typically has a straight line segment, termed the "virgin compression curve", in the range of high consolidation pressures. The slope of this line is the compression index (C_c), which indicates the amount of consolidation for a tenfold increase in load. The maximum past pressure (σ'_{vm}) is the greatest effective overburden stress that the sediment has ever been exposed to and is determined from the e-log σ_v' curve by a simple graphical construction (Casagrande, 1936). The ratio of σ'_{vm} to the effective overburden stress at the time of

sampling (σ'_{vo}) is the overconsolidation ratio (OCR), which describes the stress history, for example in terms of the amount of unloading that may have occurred by erosion. The rate of consolidation is determined for each load increment of an oedometer test, and is denoted by the coefficient of consolidation (c_v).

Sediment properties derived from static triaxial strength tests can be used to predict failure conditions of sedimentary deposits. The primary measured property is undrained shear strength ($S_u = q_{max}$) (Table 7, Fig. 8, Appendix E). It is the maximum sustainable shear stress within a sample that experiences no pore water drainage after consolidation to a predetermined stress level (σ'_c). S_u acts along a plane inclined at 45° to the axial load. The arcsine of S_u divided by the effective normal stress across this plane is the effective friction angle (ϕ'), whose magnitude is an indication of the strength of the sediment under slow (drained) loading conditions. In comparison, the ratio S_u/σ'_c gives an indication of the strength during rapid (undrained) loading conditions. The difference between drained and undrained strength behavior depends on the pore water pressure generated in response to the tendency for volume change when the sediment is axially loaded. If a sediment has a high tendency for volume change, the difference in strength between rapid and slow loading can be substantial.

Cyclically loaded triaxial strength tests are performed in order to study the strength properties of sedimentary deposits under the repeated application of loads, such as by earthquakes or waves. Tests are run at a predetertmined cyclic stress level ($\tau_{cyc\ ave\ max}/\sigma'_c$), which is the average maximum cyclically applied shear stress ($\tau_{cyc\ ave\ max}$) divided by the consolidation stress (σ'_c) (Table 8, Figs. 9-11, Appendix F). Pore water pressure and

strain accumulate with repeated application of $\tau_{cyc\ ave\ max}$. At some point, the pore water pressure approaches the confining stress, strain increases at a faster rate, and the sediment fails. In our tests, failure was chosen when 5% strain was reached.

RESULTS

Yukon prodelta: The Yukon River delta protrudes into Norton Sound from the south coast (Fig. 1). The prodelta - the outer, low-gradient, submerged area - extends over 100 km offshore and marks the distal zone of deltaic sedimentation. Sediment from the Yukon River is deposited mostly from suspension on the prodelta and is reworked by large storm waves and strong geostrophic currents (Dupré and Thompson, 1979; Nelson 1980b). Much of the fine-grained fraction from the Yukon River is eventually transported north to the Chukchi Sea (Nelson and Creager, 1977; Cacchione and Drake, 1979). The material left behind on the prodelta is predominantly silt and very fine sand (McManus and others, 1977). Graded storm-sand layers (mean grain size = 0.250 mm, bedding thickness 10-20 cm) make up 50-100% of the deposits near shore; in distal areas 60-75 km from the source, they are finer (mean size = 0.125 mm), thinner (1-2 cm), and make up 35% of the section (Nelson, 1980b).

We occupied five penetrometer stations on the prodelta (667, 668, 669, 670, 674) and collected vibracores near three of these (685 near 670, 686 near 669, and 687 near 674) (Fig. 1, Table 1). Cores were collected near the two other sites on previous cruises (78-22 near 668, 78-24 near 667) (Fig. 1, Table 1).

Sediment cores on the prodelta are mixtures of non-plastic sand and silt, with clay content commonly less than 10% (Table 4 Figs. 12-16). The cores

have similar textures and compositions, and these change relatively little with depth, except at station 686 there is a general downward fining of grain size. Thin shell layers occur sparsely. Burrow mottles and a carbon-rich layer appear in core 686. The Alpine vibracorer penetrated at a slower rate and to a shallower depth west of the delta (station 686) than to the northeast (stations 685 and 687) (Table 2).

Maximum XSP-40 penetration depth is shallow for the two stations west of the delta (668, 669), greater at the next two stations to the northeast (667, 670) and intermediate at the farthest northeast station (674) (Figs. 12-16). Replicate tests are similar at each site (Appendix B). Cone pressure increases abruptly and relatively smoothly at the first two stations, whereas it is more gradual and somewhat erratic at the others. The cores show only minor stratigraphic variation with depth, which is consistent with the shape of the penetrometer curves.

Plots of friction ratio versus cone pressure for stations on the prodelta where penetration exceeded 0.28 m (stations 669, 670, and 674) are inconsistent in terms of the sediment types they imply when compared to samples recovered in cores. Silt-rich muddy sediment, with major amounts of sand at stations 669 and 670 and minor amount of sand at station 674, constitutes the core samples. The penetrometer data indicate a wider range of sediment types: clay and mud at station 669, silt and sandy silt at station 670 (the closest correlation between cores and penetrometer data), and silt to sand at station 674 (Fig. 17). As clearly pointed out by Martin and Douglas (1981), a sediment classification scheme developed from penetrometer data is area-dependent and refers to sediment <u>behavior</u> types; that is, sediment types classified according to physical properties and not necessarily according to

texture. Perhaps the variation in sediment behavior types on the prodelta reflects more than grain size. Organic carbon is one compositional variable that would be an obvious suspect, but values are uniformly low at all 3 stations.

Relative density is high at the two southwest stations (668 and 669); typical values in excess of 100% were calculated with Schmertmann's equation (Appendix C). These numbers are unrealistic, of course, because the upper limit of relative density is 100%. The calculations probably indicate that the sediment is overconsolidated; that is, its state of consolidation is greater than would be produced by the existing overburden stress (Beard and Lee, 1982). Schmertmann's equation assumes normal consolidation. Although the calculations give unrealistically high values for relative density, they at least imply a dense sediment state shallow in the seabed at these sites. In contrast, the two stations farther to the northeast (667, 670) have comparatively low calculated relative densities, whereas intermediate values were calculated for station 674.

Laboratory test results show that low values of compression index (C_c = 0.03 - 0.25) are present west and north of the delta (stations 685, 686 and 687), and they vary erratically down-core (Table 6). The results agree relatively well with material from other study areas (Fig. 18) (Lambe and Whitman, 1969, p. 321). Sediment in the western prodelta appears the most overconsolidated (station 686), station 685 in the north is the least overconsolidated, and sediment in the northeast (station 687) is in between, however OCR values typically decrease with subbottom depth at all locations (Table 6).

Triaxial tests demonstrate that sediment at the various sites behaves differently under static loading (Table 7). West of the delta (station 686) the material has the highest friction angle (ϕ' = 42°) and a high S_u/σ'_c ratio (1.38), whereas to the northeast (station 687) a low friction angle (38.3°) and S_u/σ'_c ratio (0.83) are present. North of the delta (station 685) sediment down-core responded differently to testing (tests 95, 103 and 120 in Fig. 8e), ϕ' varied from 36.8° to 38.1° and the S_u/σ'_c ratio from 0.91 to 1.39. Contractive behavior occurred in all areas at high consolidation stresses (the S- shaped curves in the q versus p' plots in Figs. 8e - 8g), whereas dilatant behavior developed at lower stresses (σ'_c < 100 kPa). Dilatant undrained behavior produces stronger sediment than contractive behavior would at the same consolidation stress. Some tests at each station produced peaked stress-strain curves that are indicative of sensitive behavior (Figs. 8e - 8g).

Liquefaction, caused by repeated loading of waves or earthquakes, transforms sediment from a solid into a liquefied state as a consequence of increased pore pressure and reduced effective stress (Committee on Soil Dynamics of the Geotechnical Engineering Division, 1978). Liquefaction does not imply that ground failure will occur; however, many sediment movements have been attributed to the process. North and west of the delta (stations 685 and 686) the sediment type is within the limits for observed liquefaction, whereas in the northeast (station 687) the one detailed grain size distribution was close to but not fully in the range (Table 3, Fig. 19 and Appendix A). Susceptibility to liquefaction in cyclic triaxial tests is indicated by a low cyclic shear stress ratio ($\tau_{cyc\ ave\ max}/\sigma'_c$) (Table 8, Fig. 9). Cyclic test results of sediment from the northern prodelta (station 685)

plotted lowest on Figure 9, followed by material from the northeast (station 687), and west (station 686). A plot of laboratory cyclic triaxial stress ratio versus in situ cone penetration test (CPT) relative density for nearby sediment illustrates that loose sediment is more likely to liquefy (because it builds up pore pressure more readily) than dense material (Fig. 20).

Analyses, incorporating laboratory cyclic triaxial test and CPT results, determined the minimum seafloor earthquake acceleration (a_{max}) and the smallest sustained storm wave height (H) necessary to cause liquefaction at particular stations (Table 9, Appendix G). Liquefaction potential varies markedly on the prodelta. Sediment at the northern station (685) requires an a_{max} from 0.09 g to 0.14 g and a wave height from 9 to over 13 meters, depending on the analysis, to induce liquefaction. At the northeast station (687) a_{max} ranges from 0.11 g to 0.27 g and wave heights over 13 meters are required to cause instability. The range in earthquake acceleration is 0.15 g to 0.35 g, at station 686 in the western prodelta, with waves over 13 meters necessary to cause liquefaction (Table 9).

Thermogenic gas seep: Thermogenically derived gas is actively seeping from the seafloor in Norton Sound about 40 km south of Nome (Fig. 2). Anomalously high concentration of hydrocarbon gas in the water column originally pointed to the existence of the seep (Holmes and Cline, 1979). Subsequent seismic-reflection profiling identified an area of about 50 km^2 where reflector pull-downs and terminations (acoustic anomalies) occur in the sediment column (Holmes and Cline, 1979). Bubbles escaping from the seafloor have been observed with underwater television and high frequency seismic-reflection profilers over this area (Nelson and others, 1978).

Geochemical analyses of sediment cores show that the gas is composed of about 98% CO_2 (Kvenvolden and others, 1979). The remainder is hydrocarbons with high relative abundance of homologues heavier than methane, which indicates that the gas is derived from a deep, thermogenic source (Nelson and others, 1978; Kvenvolden and others, 1979). The gas has accumulated in a zone a few hundred meters thick; and the top of the zone is 50 to 200 m beneath the seafloor. Gas is believed to percolate upward from this zone along faults (Holmes and Cline, 1979).

We ran a network of seismic lines that allowed us to map the extent of the seep (Fig. 21). It covers approximately 4 km^2 and is elongate in a northwest direction, parallel to the trend of major faults (Johnson and Holmes, 1978). We deployed the penetrometer four times within the seep area, at station 675 (Fig. 3, Table 1). Between successive deployments the ship was allowed to drift so that some areal coverage of the seep was achieved. One vibracore station was occupied within the seep area. For comparison, two penetrometer stations were occupied outside, but near, the seep, as was one vibracore station.

The vibracore within the seep area is a silty sand with minor biogenic mottling (Fig. 22). At intervals down the core are zones of voids that apparently mark levels of bubble-phase gas. Some, but not all, grain-size measurements from these zones show more silt (less sand) than at other levels, but no other distinctive features are evident.

Confirmation that this core was gas-charged was obtained after it was cut into meter-long sections. End caps on the sections bulged markedly, which indicates that active degassing was occurring.

The penetrometer records from within the seep area all show erratic variation of cone pressure (Fig. 22, Appendix B). But, a tangent to the maximum values shows a fairly uniform increase in cone pressure with depth, and narrow intervals of low resistance are superimposed upon this general trend.

The vibracore outside the seep area has similar lithology to the one from within (silty sand), except for the top few centimeters (mud to sandy mud) (Fig. 22). Other physical and compositional properties also are similar, except that the zones of voids do not occur in the core from outside the seep. The vibracorer penetrated to a shallower depth and usually at a slower rate outside the seep (Table 2). The penetrometer record west of the seep (station 677) shows shallow total penetration with a fairly uniform increase in cone pressure and high relative density (Fig. 23, Appendices B and C). The penetrometer records east of the seep, at station 671, are more erratic (Appendix B). Most show a general increase in cone pressure with intervals of minor decrease.

The erratic nature of the cone pressure versus depth curves within the seep area probably reflects the presence of bubble-phase gas, distributed nonuniformly with depth. The narrow intervals of low cone pressure could correspond to the zones of voids in the sediment core. The reason for vertical variation in gas content is uncertain; there is some indication that gas concentration occurs at locations of finer grain size (Fig. 22). Pressurized cores taken from the Mississippi Delta show analogous vertical variations in gas content (Denk and others, 1981).

Evidence for areal nonuniformity in gas distribution also exists. Fathometer records across the seep show variations in cloudiness of the water

column that extend down to the seafloor (Fig. 24). This may indicate that gas is seeping strongly from some local areas (piping) and weakly or not at all from others. In some sectors, the variation is so strong as to warrant mapping the gas seepage as "patchy" (Fig. 21).

Olsen and others (1980) report low gas concentrations in two of three cores taken from the seep area. This also implies areal variation in gas-charging.

To the west of the seep, conditions are similar to those on the western prodelta (Fig. 23). The sediment apparently is not gas-charged and has uniformly high penetration resistance and calulated relative densities, at least to the shallow depths we were able to test (Table 2, Appendix C). Seismic-reflection records do not show anomalous acoustic returns that would indicate gas-charging, and the vibracore contained no zones of voids nor did it show any signs of degassing.

Intervals of low cone pressure in penetrometer records east of the mapped seep perhaps are indicative of gas-charging, but further study is necessary for confirmation. This station was originally planned to be within the mapped seep area, but strong winds and currents caused the ship to drag anchor, and we drifted away from the seep by the time conditions settled. Therefore, we have no seismic-reflection records over this site, and time did not permit collection of a sediment core. The low cone pressure intervals are not as pronounced as at station 675, which remains an unresolved question pertaining to records at this site.

Sediment type as inferred from friction-ratio plots are shown for station 675 (within the gas seep) and station 677 (west of the gas seep) in Figures 25 and 26, respectively. Most data points center around the silt-sand category,

but with much scatter. The cores appear to be more uniform and contain less fine material than indicated by the penetrometer data.

Compression index (C_c) ranges from 0.04 to 0.09 inside (station 683), and from 0.07 to 0.12 outside (station 684) the gas seep (Table 6). Evidently, from the low values, consolidation tests were not performed in stratigraphic intervals that had been expanded due to gas-charging within the seep. Overconsolidation ratios decrease with subbottom depth outside the gas seep, whereas an anomalously low value (OCR = 2) was determined within gas-seep sediment. The C_c value for that test appears to be low in relation to other test data (Table 6, Fig. 18). Whether gas charging, and resultant de-gassing, affected the consolidation behavior is unclear. The other test values plot closer to Lambe and Whitman's curve (Fig. 18).

Behavior under static loading is similar for sediment inside and west of the gas seep, perhaps indicating that the gas is not uniformly distributed within the area, i.e., the triaxial tests performed on sediment from the gas-seep area were located in a non-gas-charged stratum. Friction angles are: 38.8° inside (station 683), 38.0° outside (station 684) the gas-prone region. Ratios of S_u/σ'_c are also similar: 3.05 inside and 3.31 outside (Table 7). Remarkably analogous shear behavior was recorded, including peaked stress-strain curves (Figs. 8c and 8d). Contractive behavior at high consolidation stresses was less pronounced at stations 683 and 684 than from prodelta material (stations 685, 686 and 687). That behavior, coupled with the high S_u/σ'_c values, indicates that overconsolidation effects may have influenced the test results.

Detailed grain size distributions indicate that similar liquefiable sediment types exist within and outside the seep (Table 3, Fig. 19, Appendix

A). De-gassed sections of core could not be trimmed for cyclic testing, however sediment west of the thermogenic gas seep (station 684) showed cyclic triaxial behavior approximately midway between the other station's results (Table 8, Fig. 9). Liquefaction analyses show that an earthquake acceleration between 0.20 g and 0.32 g or wave heights greater than 13 meters are necessary to cause instability at station 684, whereas the analysis based on CPT data indicates a higher liquefaction potential within (station 675) and east (station 671) of the seep (a_{max} = 0.07 - 0.12 g) (Table 9).

Areas of biogenic gas:

Seismic-reflection profiles that exhibit anomalous acoustic returns from the sediment column have been collected over most of Norton Sound and eastern Chirikov Basin, and it has been estimated that over 7000 km^2 of seafloor is underlain by gas-charged sediment (Holmes and Thor, 1982). We occupied two sites (Fig. 3, Table 1) where cores that contain high concentrations of biogenically derived gas have previously been collected and where acoustic anomalies exist (Kvenvolden and others, 1980). The biogenic gas is believed to originate at shallow depths in the seabed as a byproduct of microbial breakdown of peat deposits. It is composed mostly of methane.

One biogenic gas site is about 10 km north of the thermogenic gas seep (Fig. 3). A vibracore at station 682 consists of interbedded sandy silt, silty sand, and mud (silt-clay) (Appendix A, Fig. 27). The conspicuous interval with high organic carbon content, high water content, and low bulk density from about 1 to 4.5m is a peat layer. Plant fragments and a distinctive brownish tint typify this interval in split core sections. The core smelled of hydrogen sulfide but did not show signs of degassing.

The vibracorer penetrated deeply and with the most rapid penetration rate (Table 2). The XSP-40 deployments at this site (station 676) achieved the deepest penetration of all tests (Fig. 27, Appendix B). The records show variable cone pressure with depth, but the tangent to maximum pressures trends nearly vertical (constant value). Calculated relative densities typically are low (Appendix C).

The implication of the penetrometer tests is that the sediment is weak; it does not become stronger with depth as most sedimentary deposits do. Vane shear measurements of this cohesive material support this conclusion (Fig. 27). The cause of this behavior is probably a consequence of the relatively high levels of water or organic carbon. It cannot be directly attributed to bubble-phase gas, because no evidence for its presence was detected in this core. However, high levels of methane-rich gas were measured in a vibracore previously collected 3 km from our core (Kvenvolden and others, 1980). It has concentrations of organic carbon in excess of 2% in a peat layer over 1-m thick beginning at about 1-m depth. Low penetration resistance (deduced from vibracore penetration rate) was encountered to a depth of about 3 m (Olsen and others, 1980). Although the data are scant, the low penetration resistance seems to correlate better with high water and organic carbon contents than with high biogenic gas levels.

The other biogenic gas site is in eastern Norton Sound, about 35 km south of Cape Darby (Fig. 3, Table 1). A penetrometer station (673) was occupied approximately 0.7 km from where a 155-cm-long vibracore (76-125) was previously taken (Fig. 28). The vibracore grades from silty sand to sandy silt and has physical and chemical properties that show similarity to other Yukon River-derived deposits in Norton Sound. In particular, the organic carbon

level is less than 2% and water content is 20-40%. However, high levels of biogenic gas were measured (Kvenvolden and others, 1980). Olsen and others (1980) report an abrupt increase of vibracore penetration resistance with depth at this station. Our penetrometer records show a similar trend (Fig. 28, Appendix B); total penetration depth is small, cone pressure increases sharply, and calculated relative density is high (Appendix C).

The vibracore penetration-rate data at both biogenic-gas sites suggest the same conclusion: gas, if it is present, does not significantly decrease penetration resistance. Perhaps the in situ gas pressure is not high enough at these sites to significantly decrease the effective stress between grains (as it apparently is at the thermogenic gas site), although bubble-phase gas may well exist at the penetrometer stations.

The penetrometer data at station 676 south of Nome indicate a range of sediment behavior types mostly from sandy silt to silty clay, which is roughly the textural range recovered in the core at nearby staion 682 (Fig. 29). This correspondence might be coincidence, to judge from plots of other penetrometer data that have similarly large ranges of sediment behavior types where cores indicate a relatively uniform sediment type.

The sediment within the peat zone (station 682) is by far the most compressible of all the tested material (C_c = 0.53-0.69) (Table 6). The C_c values plot in the high compressibility range in good agreement with results of soils from western United States and Colombia (Fig. 18). The one test performed below the organic layer shows a low compressibility (C_c = 0.06) that is consistent with other northern Bering Sea sediment (Table 6), but with a lower $C_c/(1 + e_o)$ ratio than most of the other tests (Fig. 18). Overconsolidation ratios are somewhat lower (OCR = 4 - 8) than in other regions (Table 6).

The sediment above the organic zone in core 682 has a higher strenth ratio (S_u/σ'_c = 0.78 versus 0.46), but a lower friction angle (ϕ = 35.2° versus 40.2°) than the peat (Table 7). Similar static loading behavior is exhibited by both the organic and non-organic sediment in this core. Contractive behavior occurs at high consolidation stresses; however, the slightly contractive response at low confining stresses, is atypical for northern Bering Sea material. Sensitive (peaked) stress-strain behavior is also less pronounced than at other Norton Sound sites.

The peaty sediment is slightly finer grained than other liquefiable sediment (Table 3, Fig. 19, Appendix A), but repeated loading reduces its strength, nevertheless. Cyclic stress ratios for the organic material plot in the low range in relation to the other stations (Table 8, Fig. 9). The minimum earthquake acceleration necessary to induce liquefaction is 0.07 g to 0.22 g, and waves 9 meters high would liquefy normally consolidated sediment; however, waves 13 meters high would not liquefy overconsolidated material (Table 9). Earthquake accelerations (a_{max} = 0.11-0.14g), based on CPT data, necessary to cause liquefaction at the eastern Norton Sound biogenic gas site (station 673) are within the range for station 682.

Eastern Norton Sound:

Eastern Norton Sound is protected from high wave energy that is imparted to the seafloor farther west, and a relatively tranquil sedimentary environment exists (Howard and Nelson, 1982). A vibracore collected in 1976 (station 76-133, Fig. 3) contains silty sediment with minor amounts of sand and clay (Fig. 30). Relative to other sediment cores in Norton Sound, water contents are high, and bulk densities are low. The few measurements of

organic carbon show low levels. Several other cores in the eastern sound have similar features (Nelson and Howard, 1980).

Our penetrometer test near the vibracore station experienced low cone pressure throughout most of its extent, evidently reflecting the high water content (Fig. 30, Appendix B). The values of cone pressure and relative density are similar to the low values at the biogenic gas site south of Nome, where water contents and organic carbon levels are high (Fig. 27, Appendix B).

Penetrometer data predict sediment behavior types that correlate well with the core sample. Most data points fall in the silt and silty clay categories (Fig. 31).

Ridge and swale topography

Ridge and swale topography exists near Port Clarence in Chirikov Basin (Fig. 32). The ridges are in 10-40m water depth and are 15-30 km long, 3-7 km wide, and 10-15m high. They are believed to be ancient shoreline shoals, analogous to present-day subaerial Port Clarence spit, deposited upon truncated Tertiary bedrock during the Holocene transgression (Nelson and others, 1980). Strong currents have prevented burial of these features by Holocene deposits, and sediment on the ridges is being reworked into a series of migrating sand waves (Field and others, 1981).

Vibracores from a ridge and an ajacent swale exhibit strikingly different compositions (Figs. 33 and 34). The core from the ridge is well sorted sand with scattered shells. Muddy sand occurs at the top of the swale core, with some peat layers and lenses. Below this, the sediment is varied but generally contains more mud, except for the lowest 50 cm, and gravel (to cobble size) appears in increasing quantity. Water and organic carbon contents are in the

normal range for Norton Sound sediment (Table 4). Shallow depth with a relatively slow penetration rate was achieved by the vibracorer on the ridge (station 680), whereas the penetration rate and depth were much greater in the trough (station 681) (Table 2).

The penetrometer records from the ridge and swale are also distinctly different. The test on the ridge shows a uniform increase of cone resistance, and shallow penetration (Fig. 33, Appendix B), similar to the silt and sand deposits elsewhere except that the calculated relative densities are less (Appendix C). The test in the swale achieved greater penetration depth and recorded a relatively low gradient and substantial variation of cone pressure with depth (Fig. 34, Appendix B).

The data at these sites demonstrate a large variation in sediment type and physical properties over a small distance. The sediment on the ridge is relatively dense. The sediment in the swale is relatively weak, which evidently reflects its greater percentage of silt and clay. Interestingly, water and organic carbon contents are not as high as at other locations where penetration resistance is low (Figs. 27 and 30). Sediment in the swale beneath the level of the penetrometer test probably becomes stronger due to the decrease in silt and clay and the appearance of gravel.

The penetrometer tests at station 679 on the ridge yield consistently low friction ratios, which implies sandy material as was recovered in the core sample (Fig. 35). The two tests in the trough at station 678 show different results. The test with less scatter indicates silty to sandy material. This correlates fairly well with the cone (Fig. 36).

The consolidation characteristics (C_c = 0.07-0.11, OCR = 21-6) of the sediment in the trough (station 681) are typical of northern Bering Sea

material (Table 6, Fig. 18). Static loading behavior is also similar to other tests; the strength ratio S_u/σ'_c is 1.23 and the friction angle is 37.3° for slightly overconsolidated sediment (OCR = 2). Dilatant properties exist at low confining stresses, and analogous to the sediment at the biogenic gas area (station 682), peaked stress-strain behavior is limited (Fig. 8a).

The grain size distributions of sediment within the ridge and swale areas are similar to material that has previously undergone liquefaction (Table 3, Fig. 19, Appendix A). Cyclic triaxial tests on trough sediment (station 681) show low resistance to liquefaction (Table 8, Fig. 9). Analyses indicate that a 0.10 g to 0.37 g earthquake acceleration will liquefy trough sediment (Table 9). Earthquake accelerations (a_{max} = 0.10-0.13 g) based on CPT data suggest that some sediment on the ridge (station 679) has the same liquefaction susceptibility as trough material (station 678). Sustained wave heights greater than 13 m are required to liquefy both ridge and swale sediment (Table 9).

DISCUSSION

The northern Bering Sea encompasses a diverse suite of geologic environments that contain sedimentary deposits with distinct physical properties. The aim of this geotechnical framework study is to characterize the deformational behavior of sediment in each environment and to explain the behavior in terms of geology.

Two types of geotechnical testing were employed. Each has its own advantages and limitations with regard to accurately defining the deformational behavior of northern Bering Sea sediment. Cone penetrometer tests were used to measure sediment properties in situ, in a nearly undisturbed state. However, most sediment in the northern Bering Sea is

highly resistant to penetration, and tests were possible only to small depths beneath the seafloor. Moreover, the penetrometer can only be used to infer a few physical properties, and no sediment sample is recovered. Laboratory testing of sediment cores, on the other hand, enables inferences to be made about a wide range of static and dynamic loading parameters. But, sediment samples are disturbed during coring operations, which can only be partly compensated for with special laboratory techniques.

Yukon prodelta: The variation in sediment physical properties on the Yukon prodelta might be related to the degree of exposure to large storm waves that approach dominantly from the southwest. Exposure to wave-induced stresses should decrease around the prodelta to the northeast because of topographic shielding and frictional dissipation. The penetration resistance appears to roughly correlate with the level of wave-energy exposure. This correlation could be the result of sediment liquefaction during exposure to major storm waves (see Clukey and others, 1980) followed by reconsolidation to a greater density state during quiet periods. It could also result from preloading by soft Yukon River silt during quiet periods and removal of this soft surface material during passage of major storms (Nelson, 1980b; Cacchione and Drake, 1979). At station 686, the sediment is incompressible and has a high friction angle (ϕ'), stress ratio (S_u/σ_c'), and penetration resistance, all of which indicate high strength and relative density. In fact, relative densities well in excess of 100% were calculated at that site, indicating a state of overconsolidation at shallow subbottom depths and consequent strong, dilatant behavior.

The western prodelta sediment has a low wave-induced liquefaction suseptibility (Table 9), despite having one of the highest concentrations of

wave energy in the northern Bering Sea. The material probably is reworked and densified often enough that a substantial thickness of loose, liquefiable sediment cannot accumulate.

Relative density and strength decrease between station 686 and station 685 to the northeast. Of the 5 stations on the prodelta, the sediment at station 685 is the loosest, weakest, and least consolidated. Although it is the most suseptible to liquefaction, failure due to storm-wave loading seems unlikely because of its shielded location. Infrequent, large storm waves from the north could cause failure if the sediment was normally consolidated and if pore pressure was not dissipated (Table 9), but these conditions are unlikely.

Station 687 north on the prodelta is denser than at station 685 to the southeast, in spite of being more shielded from storm waves. Forces caused by intense ice-gouging on the northern prodelta may act to locally densify and strengthen the sediment (Thor and Nelson, 1980).

It is worthwhile to note that the wave and ice forces that have acted to stabilize sediment on the prodelta can be significant agents of erosion and also can have significant impact directly on engineering structures. Therefore, they are potential hazards.

The effects of earthquakes on prodelta sediment stability must be considered. Seismic activity in western Alaska, particularly on the Seward Peninsula, is moderate (Biswas and Gedney, 1979), but earthquakes above magnitude 4.0 with epicenters under Norton Sound are unlikely (Biswas, University of Alaska, oral communication, 1982). Therefore, liquefaction in response to earthquakes in southwest Norton Sound is unlikely.

Thermogenic gas seep: The occurrence of thermogenic gas 40 km south of Nome is vertically and areally discontinuous, as shown by the uneven distribution of gas bubbles in sediment cores and seismic-reflection profiles. Laboratory tests on lithologically similar cores collected within and west of the seep show high sensitivity, low compressibility, and a state of overconsolidation for both. Only sections that were undisturbed by gas bubbles were tested in the core from within the seep. Penetrometer tests suggest that the bubble-rich intervals are weak and relatively suseptible to liquefaction. Exposure to storm waves does not appear severe enough to induce liquefaction, however a M6.75 earthquake located in the vicinity of Nome could cause liquefaction within and east of the seep (Table 9). The occurrence of that event is improbable. Analysis of penetrometer data suggests that liquefaction is unlikely at the station west (684) of the seep.

Areas of biogenic gas: Two stations were occupied within extensive areas of biogenic gas-charged sediment in Norton Sound. Station 682, approximately 10 km north of the thermogenic gas seep has a 3.5-m thick peat layer with high percentages of water and organic carbon. The peat is weak and is the most compressible material sampled in the northern Bering Sea. The low strength correlates better with high water and organic carbon contents than with gas content. Possibly, the gas pressure is not high enough to significantly decrease the effective stress within the sediment. Sensitivity and degree of overconsolidation are less at this site compared to others, indicating that although the sediment is weak, the strength will not rapidly decrease after shear.

Liquefaction analysis indicates that an M6.75 earthquake located in the south-western Seward Peninsula could cause sediment failure, but as previously mentioned a seismic event of that magnitude is unlikely.

Physical properties of sediment at the other biogenic-gas station (673) are somewhat different from those at station 682. Penetrometer records indicate high sediment density, for which there is no obvious explanation in terms of exposure to environmental forces. Liquefaction analysis predicts that susceptibility is less than at station 682, but a M6.75 earthquake located approximately 63 km from the site could induce failure.

More testing within areas of biogenic gas is necessary to determine the variability of gas-changing, as well as the range of physical properties and deformational behavior.

Eastern Norton Sound: Although local variations exist, the silty sediment core in eastern Norton Sound has high water content, perhaps because of an open sedimentary fabric produced in this relatively tranquil environment. An earthquake of magnitude 6.75 at an approximate distance of 107 km theoretically could cause liquefaction at station 672 (Table 9). Because an M6.5 earthquake occurred in 1950, approximately 30 km inland from the northeastern coast of Norton Sound, sediment in the vicinity of station 672 appears to be more suseptible to liquefaction than at any other station.

Ridge and swale topography: Large variation in physical properties over small lateral distance characterize sediment at stations on a ridge and in a swale near Port Clarence. The ridge material is a dense, uniform sand, whereas the swale sediment is a less-dense, muddy sand with gravel at depth.

Laboratory tests imply that static engineering behavior of sediment in the swale is similar to the loose prodelta sediment at station 685, except that sensitivity is not as pronounced. As at most other stations, earthquake-induced liquefaction is improbable. Although unlikely, the ridge material is more prone to liquefy from wave action, because at the shallower water depth energy is more readily imparted to it, than the trough.

CONCLUSIONS

Sediment cover in the northern Bering Sea is thin, typically less than 10 m, and physical properties of the widespread silt and sand indicate generally favorable engineering behavior. Local conditions such as high gas concentration pose special concerns in some areas.

Environmental forces from waves, currents, and ice can be severe, and they can have direct impact on engineering structures or they can erode sediment that is meant to serve as a base for foundations. Expectable levels of environmental forces do not appear to be high enough to cause large scale failure of sediment, however.

ACKNOWLEDGMENT

This study was jointly funded by the U.S. Geological Survey and the Bureau of Land Management through interagency agreement with the National Oceanic and Atmospheric Administration, under which a multi-year program responding to needs of petroleum development of the Alaskan continental shelf is managed by the Outer Continental Shelf Environmental Assessment Program (OCSEAP) office.

REFERENCES

Arctic Environmental Information and Data Center, 1977, Climatic Atlas of the Outer Continental Shelf Waters and Coastal Regions of Alaska, Vol. II: Bering Sea. Anchorage, University of Alaska, 443p.

Beard, R.M., and Lee, H.J., 1982, A 40-foot static core penetrometer. Proceedings 14th Offshore Technology Conference, p. 69-818.

Begemann, H.K., 1965, The friction jacket core as an aid in determining the soil profile. Proceedings 6th International Conference on Soil Mechanics and Foundation Engineering, v. 1, p. 17-20.

Bishop, A.W., and Henkel, D.J., 1964, The Measurement of Soil Properties in the Triaxial Test. London, Edward Arnold, Ltd (Publishers), 227p.

Biswas, H.N., and Gedney, L., 1979, Seismotectonic studies of northern and western Alaska. In: Outer Continental Shelf Environmental Assessment Program, Environmental Assessment of the Alaskan Continental Shelf Annual Reports of Principal Investigators For the Year Ending March 1979, vol. X. Hazards Data Management, Boulder, p. 155-208.

Cacchione, D.A., and Drake, D.E., 1979, Sediment transport in Norton Sound, Alaska: Regional patterns and GEOPROBE system measurements. U.S. Geological Survey Open-File Report 79-1555, 88 p.

Carver, R.E., 1971, Procedures in Sedimentary Petrology. New York, John Wiley and Sons, Inc., 653p.

Casagrande, A., 1936, The determination of the pre-consolidation load and its practical significance. Proceedings First International Conference on Soil Mechanics and Foundation Engineering, V. III, Cambridge, Massachusetts, p. 60-64.

Clukey, E.C., Cacchione, D.A., and Nelson, C.H., 1980, Liquefaction potential of the Yukon prodelta, Bering Sea. Proceedings 12th Offshore Technology Conference, p. 315-325.

Committee on Soil Dynamics of the Geotechnical Engineering Division, 1978, Definition of terms related to liquefaction. Journal Geotechnical Engineering Division, ASCE, September, p. 1197-1200.

Denk, E.W., Dunlap, W.A., Bryant, W.R., Milberger, L.J., Whellan, T.J., III, 1981, A pressurized core barrel for sampling gas-charged marine sediments. Proceedings 13th Offshore Technology Conference, p. 43-52.

Dupré, W.R., and Thompson, R., 1979, The Yukon Delta: A model for deltaic sediment in an ice-dominated environment. Proceedings 11th Offshore Technology Conference, p. 657-664.

Field, M.E., Nelson, C.H., Cacchione, D.A., and Drake, D.E., 1981, Sand waves on an epicontinental shelf: northern Bering Sea. Marine Geology, v. 42, p. 233-258.

Finn, W.D., 1972, Soil dynamics liquefaction of sands. Proceedings International Conference on Microzonation for Safer Construction Research and Application, v. 1, Seattle, p, 87-111.

Holmes, M.L., and Cline, J.D., 1979, Geologic setting and source depth of the Norton Basin gas seep. Jour. Petroleum Technology, October, p. 1241-1248.

Holmes, M.L., and Thor, D.R., 1982, Distribution of gas-charged sediment in Norton Sound and Chirikov Basin. Geologie en Mijnbouw, v. 61, p. 79-90.

Howard, J.D., and Nelson, C.H., 1980, Sedimentary structures on a delta-influenced shallow shelf, Norton Sound, Alaska. In: Larsen, M.C., Nelson, C.H., and Thor, D.R. (eds.), Geological, Geochemical, and Geotechnical Observations on the Bering Shelf, Alaska. U.S. Geological Survey Open-File Report 80-979, 19 p.

Johnson, J.L., and Holmes, M.L., 1978, Report on surface and subsurface faulting in Norton Sound and northeastern Chirikov Basin, Alaska. In: Larsen, M.C., Nelson, C.H., and Thor, D.R. (eds.), Geological, Geochemical, and Geotechnical Observations on the Bering Shelf, Alaska U.S. Geological Survey Open-File Report 80-979, 25 p.

Kishida, H., 1969, A note on the liquefaction of hydraulic fill during the Tokachi-Oki earthquake. Second Seminar on Soil Behavior and Ground Response During Earthquakes, University of California, Berkeley, Aug.

Koutsoftas, D.C., Fischer, J.A., Dette, J.T., and Singh, H., 1976, Evaluation of the vibracorer as a tool for underwater geotechnical explorations. Proceedings 8th Offshore Technology Conference, p. 107-121.

Kvenvolden, K.A., Nelson, C.H., Thor, D.R., Larsen, M.C., Redden, G.D., Rapp, J.B., and Des Marais, D.J., 1979, Biogenic and thermogenic gas in gas-charged sediment of Norton Sound, Alaska. Proceedings 11th Offshore Technology Conference, p. 479-486.

Kvenvolden, K.A., Redden, G.D., Thor, D.R., and Nelson, C.H., 1980, Hydrocarbon gases in near-surface sediment of northern Bering Sea (Norton Sound and Chirikov Basin). In: Larsen, M.C., Nelson, C.H., and Thor, D.R. (eds.), Geological, Geochemical, and Geotechnical Observations on the Bering Shelf, Alaska. U.S. Geological Survey Open-File Report 80-979, 28 p.

Ladd, C.C., and Foott, R., 1974, New design procedure for stability of soft clays. Journal Geotechnical Engineering Division, ASCE, July, p. 763-786.

Lambe, T.W., 1951, Soil Testing for Engineers. New York, John Wiley and Sons, Inc., 165 p.

Lambe, T.W., and Whitman, R.V., 1969, Soil Mechanics. New York, John Wiley and Sons, Inc., 553 p.

Larsen, M.C., Nelson, C.H., and Thor, D.R. (eds.) 1980, Geological, geochemical, and geothechnical observations on the Bering Shelf, Alaska. U.S. Geological Survey Open-File Report 80-979, 492 p.

Lee, K.L., and Fitton, J.A., 1968, [1969], Factors affecting the cyclic loading strength of soil. In: Vibration Effects of Earthquakes on Soils and Foundations, ASTM Special Technical Pub. 450, p. 71-95.

Martin, F.R., and Douglas, B.J., 1981, Evaluation of the core penetrometer for liquefaction hazard assessment. U.S. Geological Survey Open-File Report 81-284, 185 p.

Mayne, P.W., and Kulhawy, F.H., 1982, K_o-OCR relationships in soil. Journal Geotechnical Engineering Division, ASCE, June, p. 851-872.

McCormick, J.M., and Thiruvathukal, J.V., 1976, Elements of Oceanography. Philadelphia, W.B. Saunders Company, 346 p.

Nelson, C.H., and Creager, J.S., 1977, Displacement of Yukon-derived sediment from Bering Sea to Chukchi Sea during the Holocene. Geology, v. 5, p. 141-146.

Nelson, C.H., Dupré, W.R., Field, M.E., and Howard, J.D., 1980, Linear sand bodies in the Bering Sea epicontinental shelf. In: Larsen, M.C., Nelson, C.H., and Thor, D.R. (eds.), Geological, Geochemical, and Geotechnical Observations on the Bering Shelf, Alaska. U.S. Geological Survey Open-File Report 80-979, 28 p.

Nelson, C.H., Kvenvolden, C.H., and Clukey, E.C., 1978, Thermogenic gases in near-surface sediments of Norton Sound, Alaska. Proceedings 10th Offshore Technology Conference, p. 2623-2633.

Nelson, C.H., 1980a, Late Pleistocen-Holocene transgressive sedimentation in deltaic and non-deltaic areas of the Bering continental shelf. In: Larsen, M.C., Nelson, C.H., and Thor, D.R. (eds.), Geological, Geochemical, and Geotechnical Observations on the Bering Shelf, Alaska. U.S. Geological Survey Open-File Report 80-979, 30 p.

Nelson, C.H., 1980b, Graded storm sand layers offshore from the Yukon delta, Alaska. In: Larsen, M.C., Nelson, C.H., and Thor, D.R. (eds.), Geological, Geochemical, and Geotechnical Observations on the Bering Shelf, Alaska. U.S. Geological Survey Open-File Report 80-979, 21 p.

Olsen, H.W., Clukey, E.C., and Nelson, C.H., 1980, Geotechnical characteristics of bottom sediments in the northern Bering Sea. In: Larsen, M.C., Nelson, C.H., and Thor, D.R. (eds.), Geological, Geochemical, and Geotechnical Observations on the Bering Shelf, Alaska. U.S. Geological Survey Open-File Report 80-979, 32 p.

Schmertmann, J.H., 1976, Predicting the Q_c/N ratio. Final report D-636, Engineering and industrial experiment station, Dept. of Civil Engineering, University of Florida, Gainesville, October. (Cited in: Martin, G.R., and Douglas, B.J., 1981).

Schmertmann, J.H., 1978a, Guidelines for core penetration test performance and design. U.S. Department of Transportation, FWHA-TS-78-209, 145 p.

Schmertmann, J.H., 1978b, Study of feasibility of using Wissa-type piezometer probe to identify liquefaction potential of saturated fine sands. U.S. Army Waterways Experiment Station Technical Report S-78-2, 73 p.

Seed, H.B., and Idriss, I.M., Evaluation of liquefaction potential using field performance data. Journal Geotechnical Engineering Division, ASCE, in press.

Seed, H.B., and Idriss, I.M., 1971, Simplified procedure for evaluating soil liquefaction potential. Journal Geotechnical Engineering Division, ASCE, September, p. 1249-1273.

Seed, H.B., and Rahman, M.S., 1978, Wave-induced pore pressure in relation to ocean floor stability of cohesionless soils. Marine Geotechnology, Vol. 3, No. 2, p. 123-150.

Seed, H.B., 1979, Soil liquefaction and cyclic mobility evaluation for level ground during earthquakes. Journal Geotechnical Engineering Division, ASCE, February, p. 201-255.

Thor, D.R., and Nelson, C.H., 1980, A summary of interacting, surficial geologic processes and potential geologic hazards in the Norton Basin, northern Bering Sea. Jour. Petroleum Technology, March, p.355-362.

Wiegel, R.L., 1964, Oceanographical Engineering. Prentice-Hall, Inc., Englewood Cliffs, NJ. (Cited in: Seed, H.B., and Rahman, M.S., 1978)

Wissa, A.E., Christian, J.T., Davis, E.H., and Heiberg, S., 1971, Consolidation at constant rate of strain. Journal Soil Mechanics and Foundations Division, ASCE, October, p. 1393-1413.

Woodward-Clyde Consultants, 1978, Offshore Alaska Seismic Exposure Study, v. 2, Attenuation, Prepared for the Alaska Subarctic Offshore Committee, San Francisco, 256p.

NOMENCLATURE AND LITHOLOGIC SYMBOLS

A_f - The coefficient of pore pressure response at failure during a triaxial test (change in pore pressure at failure/change in deviator stress).

AVG MAX q - The average single amplitude cyclic compressive stress applied to a cyclic triaxial test sample.

AVG MIN q - The average single amplitude cyclic tensile stress applied to a cyclic triaxial test sample.

a_{max} - The maximum earthquake induced acceleration at the ground surface.

C_c - The compression index, defined as the slope of the linear part of a consolidation curve plotted on a graph of void ratio vs. log of effective stress.

CE - The prefix for a constant rate of strain (CRS) consolidation test number.

C_N - A factor applied to the blow count to correct for influence of overburden pressure (reference value is 1 ton/sq ft).

C_u - Uniformity coefficient = D_{60}/D_{10}.

cm - Centimeter.

c_m - A coefficient that relates unidirectional cyclic shear test results to multidirectional shaking in situ.

c_r - A coefficient that modifies the cyclic triaxial stress ratio to a corresponding cyclic simple shear stress ratio that is more representative of field conditions.

C_r - Rebound index, determined from a consolidation test.

c_v - The coefficient of consolidation, a sediment property that reflects the rate at which consolidation will occur.

$C_{v\ ave}$ - The average of all coefficients of consolidation except rebound values determined from an oedometer test.

D - Prefix for a cyclic triaxial test number.

D - Maximum distance to an earthquake fault from which a particular ground acceleration would occur.

D_L - Subbottom depth to which liquefaction may occur due to a particular sustained average storm wave.

D_r - Relative density, natural density state relative to maximum and minimum density states.

D_{60} - Diameter at which 60% of the soil is finer.

D_{50} - Diameter at which 50% of the soil is finer.

D_{10} - Diameter at which 10% of the soil is finer.

d - Still water depth.

Damping - A dynamic sediment property calculated from a cyclic triaxial test. It represents the amount of energy lost per cycle as a percentage of the energy introduced.

DELU - Same as Delta u.

Delta u - The change in excess porewater pressure from the beginning of a shear test.

Dev Stress - The deviator stress or difference between the major and minor principal effective stresses $(\sigma'_1 - \sigma'_3)$.

E - The modulus of elasticity.

e - The void ratio.

e_o - Initial void ratio in a consolidation test, in situ void ratio.

g - Acceleration due to gravity (9.8 m/sec^2).

H - Sustained average storm wave height.

h - Subbottom depth at which a shear stress is determined.

K_o - Coefficient of earth pressure at rest in situ, horizontal effective stress/vertical effective stress.

km - Kilometer.

kPa - KiloPascal, kN/m^2.

L - Sustained average storm wave length.

M - Earthquake magnitude.

m - Meter.

mm - Millimeter.

N - Blow count, the number of blows required to drive a sampling spoon 1 ft during a standard penetration test.

N_c - Blow count corrected to an overburden pressure of 1 ton/sq ft.

NP - Non-plastic.

OCR - Overconsolidation ratio ($\sigma'_{vm}/\sigma'_{vo}$).

OE - Prefix for oedometer test numbers.

p' - The average normal effective stress acting on a sample at some point in a triaxial shear test $\frac{\sigma_1' + \sigma_3'}{2}$.

q - The peak shear stress acting on a sample at some point in a triaxial shear test $\frac{\sigma'_1 - \sigma'_3}{2}$.

q_c - Cone pressure, determined during a cone penetration test.

q_{max} - Maximum value of q reached during a static triaxial test, equal to S_u.

r_d - Stress coefficient to reduce horizontal shear stresses, induced by an earthquake, from a rigid to a deformable body.

SIG 1_c' - The major (or vertical) principal stress applied to a triaxial test sample prior to shear.

SIG 3_c' - The minor (or horizontal) principal stress applied to a triaxial test sample prior to shear.

STATIC q_f - Strength of a static triaxial test sample, however in Appendix E it typically refers to the test consolidation stress.

S_u - Undrained shear strength, determined from a static triaxial test.

T - Sustained average storm wave period.

TC - Prefix for a cyclic triaxial test number.

TE - Prefix for a static triaxial test number.

TR - Trace.

w - Water content expressed as a percent of dry weight.

w sheared - Water content of a sheared triaxial test sample.

Z - Subbottom depth at which a shear stress is determined.

° - Symbol for angular degrees.

% - Percent.

γ - The total unit weight of a sediment.

γ' - The buoyant (submerged) unit weight of a sediment.

γ_w - The unit weight of saltwater (10.05 kN/m^3).

μm - Micrometer.

σ'_1 - The major (or vertical) principal effective stress applied at any point in a triaxial test.

σ'_3 - The minor (or horizontal) principal effective stress applied at any point in a triaxial test.

σ'_c - The consolidation stress exerted on a triaxial test sample.

$\sigma'_v = \sigma'_{vo}$ - The in situ vertical effective stress exerted by the weight of overburden.

σ'_{vm} - The maximum vertical effective stress that a sediment has ever experienced.

ϕ' - The friction angle of a sediment expressed in terms of effective stresses.

τ_{ave} - Average horizontal shear stress at a subbottom depth induced by an earthquake.

τ_c - Horizontal shear stress at a subbottom depth caused by storm waves.

$\tau_{cyc\ ave\ max}$ - The maximum average single amplitude cyclic stress applied to a cyclic triaxial test sample.

τ_h - Horizontal shear stress at a subbottom depth induced by an earthquake.

τ_{max} - Same as AVG MAX q.

τ_{min} - Same as AVG MIN q.

LITHOLOGIC SYMBOLS.

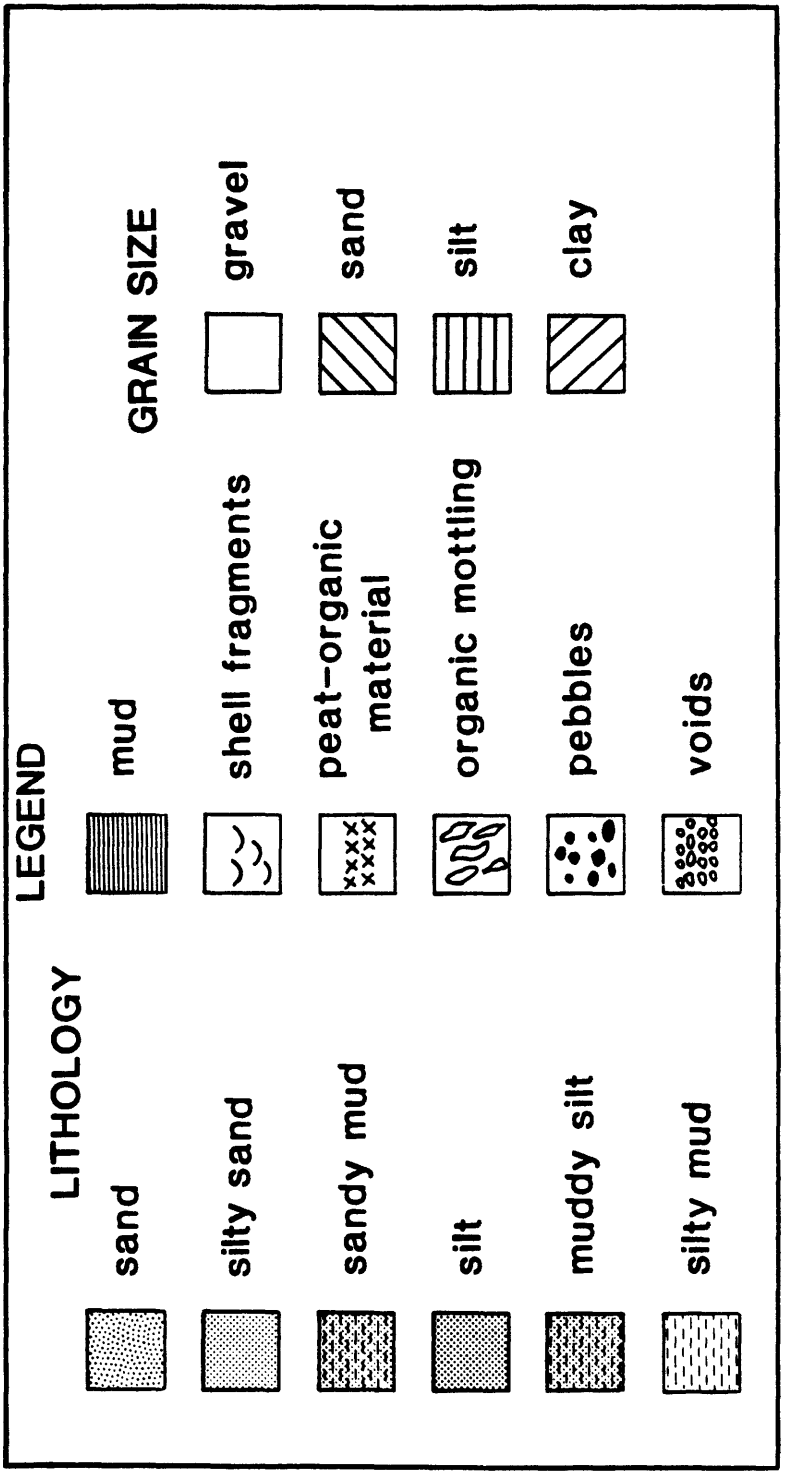

Table 1. Stations.

A. XSP-40 penetrometer

Station	Attempt	Latitude (N)	Longitude (W)	Water depth (m)	Geologic environment	Penetration Depth (m)	Distance from first penetrometer test (m)
667	1	63°28.60'	165°19.18'	18	Yukon prodelta	2.43	-
668	1	63°20.13'	165°49.90'	23	Yukon prodelta	0.49	-
	2	63°20.13'	165°49.91'	23		0.56	13
	3	63°20.02'	165°49.95'	23		0.55	148
	4	63°20.02'	165°49.94'	23		0.61	142
669	1	62°57.87'	165°41.71'	19	Yukon prodelta	0.48	-
	2	62°57.86'	165°41.70'	19		0.46	29
670	1	63°41.77'	165°18.69'	18	Yukon prodelta	1.43	-
	3	63°41.69'	165°18.67'	18		1.33	145
	4	63°41.67'	165°18.69'	18		1.64	169
671	1	64°05.58'	165°29.25'	19	east of thermogenic gas seep	1.34	-

Table 1. Stations (cont'd).

Station	Attempt	Latitude (N)	Longitude (W)	Water depth (m)	Geologic environment	Penetration Depth (m)	Distance from first penetrometer test (m)
671 (cont)	2	64°05.58'	165°29.24'			1.12	20
	3	64°05.64'	165°29.18'			0.78	146
	4	64°05.64'	165°29.19'			0.80	136
	5	64°05.66'	165°29.03'			1.03	384
	6	64°05.66'	165°29.01'			1.48	412
	7	64°05.66'	165°26.78'			0.94	4037
	8	64°05.65'	165°26.72'			1.02	4134
672	1	64°06.08'	161°36.19'	18	eastern Norton Sound	2.94	-
	2	64°06.08'	161°36.20'			2.71	10
673	1	64°00.46'	162°24.62'	18	biogenic gas	0.51	-
	2	64°00.46'	162°24.61'			0.42	10
	3	64°00.33'	162°24.59'			0.41	222
	4	64°00.33'	162°24.59'			0.46	222

Table 1. Stations (cont'd).

Station	Attempt	Latitude (N)	Longitude (W)	Water depth (m)	Geologic environment	Penetration Depth (m)	Distance from first penetrometer test (m)
674	1	63°49.68'	164°21.19'	18	Yukon prodelta	0.92	-
	2	63°49.68'	164°21.17'			0.82	40
675	1	64°05.31'	165°30.54'	19	thermogenic gas seep	2.20	-
	2	64°05.30'	165°30.57'			1.15	53
	3	64°05.40'	165°30.87'			1.93	558
	4	64°05.57'	165°30.79'			1.17	589
676	1	64°11.45'	165°34.36'	20	biogenic gas	3.66	-
	2	64°11.45'	165°34.33'			3.67	49
677	1	64°05.70'	165°31.71'	20	west of thermogenic gas seep	0.90	-
	2	64°05.70'	165°31.75'			0.89	69

Table 1B.

Station	Attempt	Latitude (N)	Longitude (W)	Water depth (m)	Geologic environment	Use of core	Core length (m)	Distance from nearest penetration test (m)
680	1	65°05.94'	167°37.38'	21	ridge	geological	2.72	1107
681	2	65°07.06'	167°32.81'	30	swale	geotechnical	5.72	465
	3	65°07.27'	167°33.34'			geological	5.49	615
682	1	64°11.41'	165°33.85'	20	biogenic gas	geotechnical	5.17	782
	2	64°11.44'	165°33.58'			geological	5.16	1219
683	1	64°05.24'	165°30.33'	20	thermogenic gas seep	geotechnical	6.10	362
	2	64°05.23'	165°30.46'			geological	4.50	180
684	1	64°05.92'	165°32.73'	20	west of thermo-genic gas seep	geotechnical	2.60	1636
	2	64°05.95'	165°32.74'			geological	2.61	1647
685	1	63°41.74'	165°18.15'	18	Yukon prodelta	geological	3.26	895
	2	63°41.76'	165°18.12'			geotechnical	4.85	944

Table 1. Stations (cont'd).

Station	Attempt	Latitude (N)	Longitude (W)	Water depth (m)	Geologic environment	Penetration Depth (m)	Distance from first penetrometer test (m)
678	1	65°06.97'	167°33.09'	32	swale	2.12	-
	2	65°06.97'	167°33.09'			2.28	0
679	1	65°06.55'	167°37.73'	20	ridge	1.09	-
	2	65°06.54'	167°37.73'			1.48	19

Table 1B (cont'd).

Station	Attempt	Latitude (N)	Longitude (W)	Water depth (m)	Geologic environment	Use of core	Core length (m)	Distance from nearest penetration test (m)
686	1	62°58.03'	165°41.51'	18	Yukon prodelta	geotechnical	3.88	426
	2	62°58.16'	165°41.42'			geological	3.88	699
687	1	63°49.95'	164°21.64'	18	Yukon prodelta	geotechnical	5.50	865
	3	63°49.93'	164°21.64'			geological	5.50	850
76-125	1	64°00.04'	162°24.92'	18	biogenic gas	geological	1.55	717
76-133	1	64°05.62'	161°36.78'	18	eastern Norton Sound	geological	1.70	1206
78-22	1	63°20.86'	165°50.14'	23	Yukon prodelta	geological	2.81	1152
78-24	1	63°28.53'	165°20.13'	18	Yukon prodelta	geological	4.95	1586

Table 2. Vibracorer penetration rates (in meters/min).

DEPTH (m) \ CORE	680A3	681A2	681A3	682A1	682A2	683A1	683A2	684A1	684A2	685A1	685A2	686A1	686A2	687A1	687A3
0.2	1.5	22.9	22.9	45.7	36.6	61.0	26.1	20.3	45.7	45.7	45.7	18.3	36.6	61.0	45.7
0.5	4.6	6.8	5.9	30.5	18.3	6.1	6.3	8.7	5.4	91.4	12.2	1.2	1.6	15.2	12.2
0.8	3.0	9.6	8.3	10.2	8.7	5.5	2.8	2.1	2.4	10.8	6.3	0.7	0.7	1.5	0.6
1.1	2.1	8.7	10.2	9.1	5.7	4.6	2.6	1.5	2.6	7.6	5.5	1.7	0.8	1.1	2.2
1.4	1.6	6.5	6.8	18.3	9.6	4.5	1.1	0.8	1.0	4.6	4.6	1.3	1.1	1.6	2.0
1.7	0.9	3.8	3.3	30.5	10.2	2.6	0.4	2.3	0.3	5.7	3.0	0.6	0.5	1.5	2.0
2.0		2.3	2.4	22.9	8.3	1.5	0.5	0.2	0.3	1.4	0.9	0.5	0.5	1.6	1.8
2.3		1.8	2.4	18.3	8.7	1.8	0.2	0.3	0.2	0.6	0.5	0.7	0.7	0.9	1.1
2.6		1.1	1.4	16.6	8.3	2.2	0.5	0.3		0.5	0.3	0.8	1.0	1.0	1.4
2.9		0.8	0.9	14.1	8.0	2.8	0.5	0.3		0.2	0.1	1.0	0.8	1.1	1.2
3.2		0.6	1.2	11.4	8.0	2.3	0.6	0.1		0.3	0.2	0.7	0.6	1.2	1.3
3.5		0.6	1.2	11.4	7.6	1.5	0.5			0.2	0.3	0.5		1.1	1.0
3.8		0.4	1.1	8.0	6.1	1.4	0.4				0.4	0.4		1.0	0.7
4.1		0.3	0.5	0.6	5.2	1.5					0.4			0.8	0.7
4.4		0.2	0.1		4.9	1.1					0.5			0.6	0.7
4.7					4.9	0.6					0.2			0.4	0.5
5.0					4.3	0.4								0.3	0.4
5.3					3.5	0.4								0.3	0.5
5.6					2.3	0.3								0.2	0.4

Table 3. Detailed grain size summary.

CORE	DEPTH (m)	TEST	D_{60} (μm)	D_{50} (μm)	D_{10} (μm)	$C_u = \frac{D_{60}}{D_{10}}$	LEE & FITTON (1968)	KISHIDA (1969)	BOTH RANGES (1)
680A3	0.30		273	261	175	1.6	*	*	
	0.82		255	250	180	1.4	*	*	
	1.52		245	237	161	1.5	*	*	
	2.22		225	212	156	1.4	*	*	
681A2	1.46	D 100,101	40	33	4.7	8.5			
681A3	0.20		225	197	20	11.2		*	
	0.40		270	245	110	2.4		*	
	0.84		141	126	40	3.5	*	*	
	1.40		107	95	12.3	8.7		*	
	2.20		120	114	19.5	6.2		*	
	2.84		41	23.5	2.0	20.5			
682A1	0.97	TC 38,39	80	68	9.2	8.7		*	
	1.09	TE 76,77	39	26	4.2	9.3			
	1.78	TE 98,99	16	12.4	1.4	11.4			
	1.89	TC 76,77	45	34	4	11.0			
683A1	1.05		62	60	10.1	6.1			*
	4.25	TE 109,110	62	60	21	3.0			*

TABLE 3. Detailed grain size summary (cont'd).

CORE	DEPTH (m)	TEST	D_{60} (μm)	D_{50} (μm)	D_{10} (μm)	$C_u = \frac{D_{60}}{D_{10}}$	Lee & Fitton (1968)	KISHIDA (1969)	BOTH RANGES (1)
684A1	0.66	TC 90,91	62	56	9.4	6.6			*
685A2	0.44	TC 80,81	54	49	11.8	4.6			*
	1.05	TC 62,74	60	54	9.6	6.2			*
686A1	0.45	TC 96,97	105	84	11.5	9.1		*	
687A1	0.49	TC 94,95	34	30	4.7	7.2			

* Grain size distribution curve falls within the zone of liquefaction suseptibility (Figure 19).

(1) Part of grain size distribution curve falls within the zone designated by both Lee and Fitton (1968) and Kishida (1969).

Table 4. Index properties and vane shear strength.

CORE	DEPTH IN CORE(m)	GRAIN SIZE (%) GRAVEL	SAND	SILT	CLAY	WATER CONTENT (%)	BULK DENSITY (gm/cm^3)	GRAIN DENSITY (gm/cm^3)	ORGANIC CARBON (%)	$CaCO_3$ (%)	VANE SHEAR STRENGTH (kPa) INTACT	REMOLDED	SENSITIVITY	ATTERBERG LIMITS LIQUID LIMIT	PLASTIC LIMIT	PLASTICITY INDEX	LIQUIDITY INDEX
665G1	0.02	0.0	20.2	75.8	4.0				0.43	1.35							
	0.10	0.0	26.9	62.4	10.7	40.5	1.86	2.76	0.61	1.26						NP	
	0.20					41.1	1.78	2.56									
672G1	0.02					89.4	1.38	2.01									
	0.35					112.5	1.46	2.78			4.9 *	2.6 *	1.9				
672G3	0.02					93.3	1.53	2.80			2.6 *	0.6 *	4.6				
680A3	0.02	0.0	98.1	0.9	1.0				0.12	0.61							
	0.36	0.0	98.8	0.9	0.3	20.9	2.09	2.66	0.09	0.74						NP	
	0.60					21.1	2.17	2.64									
	0.82	0.0	97.6	1.8	0.6	16.7	2.16	2.65	0.07	0.84						NP	
	1.12					16.8	2.12	2.58									
	1.32					18.7	2.12	2.65									
	1.52	0.0	99.2	0.2	0.6	19.5	2.11	2.66	0.08	0.95						NP	
	1.82					18.9	2.11	2.64									
	2.02					19.4	1.60	1.80									
	2.22	0.0	98.4	0.4	1.2	21.1	2.06	2.61	0.08	0.98						NP	
	2.57					22.9	1.64	1.91									
681A2	0.02					24.8	2.01	2.63									
	0.76					50.2	1.71	2.56									
	1.77					21.1	2.03	2.57									
	2.75					23.2	2.10	2.78			21.8 *	3.5 *	6.2				
	3.74					23.0	2.12	2.80			61.8 *	4.2 *	14.5				
	4.74					23.4	2.14	2.88			28.1 *	3.5 *	8.0				

Table 4. Index properties and vane shear strength (cont'd).

CORE	DEPTH IN CORE(m)	GRAIN SIZE (%) GRAVEL	SAND	SILT	CLAY	WATER CONTENT (%)	BULK DENSITY (gm/cm^3)	GRAIN DENSITY (gm/cm^3)	ORGANIC CARBON (%)	$CaCO_3$ (%)	VANE SHEAR STRENGTH (kPa) INTACT	REMOLDED	SENSITIVITY	ATTERBERG LIMITS LIQUID LIMIT	PLASTIC LIMIT	PLASTICITY INDEX	LIQUIDITY INDEX
681A3	0.02	0.0	76.9	15.4	7.7				0.49	1.57							
	0.10					25.7	1.99	2.62									
	0.20	0.0	83.8	10.6	5.6	20.3	2.10	2.67	0.31	1.47						NP	
	0.30					24.4	1.98	2.57									
	0.40	14.9	75.6	6.4	3.1	19.1	1.77	2.66	0.39	2.41						NP	
	0.61					26.8	1.98	2.64									
	0.84	0.0	87.7	9.0	3.3	28.9	1.97	2.68	1.70	1.08						NP	
	1.00					30.2	1.96	2.71									
	1.20					16.6	2.21	2.73									
	1.40	0.0	64.3	27.1	8.6	18.9	2.16	2.74	0.56	3.64						NP	
	1.80					19.7	2.14	2.73									
	1.98					15.2	2.20	2.67									
	2.20	1.0	77.1	10.8	11.1	18.4	2.15	2.69	0.41	1.63						NP	
	2.40					17.8	2.18	2.73									
	2.60					26.0	2.02	2.71									
	2.84	0.0	26.3	51.1	22.6	35.0	1.90	2.70	1.00	4.48	34.8	7.5	4.7	33	24	9	1.22
	3.00	1.1	75.7	16.1	7.1	19.7	1.57	1.76	0.47	2.19						NP	
	3.20					20.6	2.13	2.74									
	3.37					36.3	1.99	3.01			38.0	11.2	3.4				
	3.57	0.0	15.0	57.6	27.4	41.7	1.90	2.96	0.95	2.12	38.6	9.0	4.3	50	32	18	0.54
	3.81					32.8	1.97	2.82			39.2	11.2	3.5				
	3.99					28.1	2.03	2.79			41.7	9.3	4.5				
	4.16	1.4	35.1	37.7	25.8	21.0	2.13	2.76	0.90	1.96	61.0	18.0	3.4	30	20	10	0.10
	4.35					23.0	2.08	2.73			62.8	14.9	4.2				
	4.55					25.7	2.07	2.80			34.8	9.3	3.7				
	4.75	22.6	46.3	22.0	9.1	16.8	2.24	2.79	0.60	5.01						NP	
	4.95					14.7	2.26	2.74									
	5.15					12.8	2.30	2.74									
	5.35	28.7	54.5	11.8	5.0	10.5	2.36	2.73	0.68	5.71						NP	

Table 4. Index properties and vane shear strength (cont'd).

CORE	DEPTH IN CORE (m)	GRAIN SIZE (%) GRAVEL	SAND	SILT	CLAY	WATER CONTENT (%)	BULK DENSITY (gm/cm^3)	GRAIN DENSITY (gm/cm^3)	ORGANIC CARBON (%)	$CaCO_3$ (%)	VANE SHEAR STRENGTH (kPa) INTACT	REMOLDED	SENSITIVITY	ATTERBERG LIMITS LIQUID LIMIT	PLASTIC LIMIT	PLASTICITY INDEX	LIQUIDITY INDEX
682A1	1.17					73.5	1.56	2.52			35.1	6.3	5.5				
	2.16					75.9	1.55	2.54			8.8	0.7	12.5				
	3.15					67.3	1.60	2.58			21.4	7.7	2.8				
	4.14					33.8	1.90	2.66			3.9	0.7	5.5				
682A2	0.02	0.0	22.7	67.0	10.3				0.85	1.09							
	0.19	0.0	18.7	68.7	12.6	39.9	1.87	2.78	0.74	1.29	11.6	1.8	6.4			NP	
	0.41					29.0	1.97	2.68			5.8	1.1	5.5				
	0.66					28.9	1.97	2.69			16.5	2.1	7.7				
	0.80	0.0	52.5	41.0	6.5	27.1	2.01	2.73	0.65	0.93	29.6	3.5	8.4			NP	
	1.00					69.8	1.57	2.51			23.0	4.9	4.7				
	1.05					78.2	1.52	2.42			22.8	7.1	3.2				
	1.18										27.2 *	6.3 *	4.3				
	1.40	0.0	56.3	33.1	10.6	62.7	1.62	2.56	3.81	1.27	35.6	9.9	3.6	65	43	22	0.90
	1.60					62.9	1.62	2.57			34.6	10.9	3.2				
	1.80					69.9	1.58	2.53			34.0	11.4	3.0				
	2.00	0.0	3.0	63.2	27.8	61.5	1.64	2.59	4.71	0.99	27.9	9.0	3.1	68	42	26	0.75
	2.20	0.0	17.4	52.8	29.8	63.4	1.62	2.56	4.02	1.28	19.2	6.9	2.8	73	43	30	0.68
	2.40					89.6	1.48	2.40			23.0	9.3	2.5				
	2.60					89.6	1.48	2.47			24.5	8.2	3.0				
	2.80	0.0	4.3	51.7	44.0	95.4	1.27	1.66	5.22	1.32	22.8	8.5	2.7	97	58	39	0.96
	3.00					77.2	1.49	2.29			23.1	9.1	2.6				
	3.26	0.0	21.8	42.9	29.3	62.9	1.63	2.59	4.12	0.69	28.1	9.5	3.0	73	43	30	0.66
	3.40					83.7	1.53	2.62			23.0	9.0	2.6				
	3.65					69.4	1.59	2.59			35.3	10.5	3.4				
	3.80	0.0	4.4	58.2	37.4	75.2	1.55	2.53	6.47	0.73	41.4	14.6	2.8	101	49	52	0.50
	4.00										35.1	14.7	2.4				
	4.24	0.0	57.5	31.7	10.8	49.3	1.71	2.54	3.37	0.87	20.9	9.3	2.2			NP	
	4.40										16.9	6.6	2.6				
	4.60	TR	69.3	25.1	5.6	36.1	1.88	2.68	1.90	0.58	14.8	5.8	2.5			NP	
	4.80					37.9	1.84	2.64									
	5.00	0.0	83.7	14.3	0.0	23.1	2.05	2.67	0.32	0.54						NP	

Table 4. Index properties and vane shear strength (cont'd).

CORE	DEPTH IN CORE (m)	GRAIN SIZE (%) GRAVEL	SAND	SILT	CLAY	WATER CONTENT (%)	BULK DENSITY (gm/cm^3)	GRAIN DENSITY (gm/cm^3)	ORGANIC CARBON (%)	$CaCO_3$ (%)	VANE SHEAR STRENGTH (kPa) INTACT	REMOLDED	SENSITIVITY	ATTERBERG LIMITS LIQUID LIMIT	PLASTIC LIMIT	PLASTICITY INDEX	LIQUIDITY INDEX
683A1	0.85					20.5	2.13	2.74									
	2.91					27.6	1.99	2.69									
	3.90					26.6	1.98	2.63									
	4.90					27.2	2.03	2.77									
683A2	0.02	0.0	36.0	57.4	6.6				0.45	0.66							
	0.10	0.0	54.4	40.0	5.6	27.1	2.02	2.73	0.51	0.49						NP	
	0.30					26.7	1.98	2.64									
	0.50					21.8	2.08	2.69									
	0.74	0.2	72.0	23.8	4.0	19.6	2.16	2.75	0.25	0.76						NP	
	0.88					20.1	2.08	2.62									
	1.14	0.0	38.4	46.1	15.5	51.0	1.73	2.66	0.45	0.48						NP	
	1.34					25.0	1.99	2.61									
	1.52					23.7	2.22	3.06									
	1.70	0.0	61.8	35.3	2.9	25.4	2.02	2.68	0.35	0.60						NP	
	1.90	0.0	75.7	22.3	2.0	23.7	2.03	2.65	0.21	0.47						NP	
	2.10	0.0	85.7	12.6	1.7	24.2	2.02	2.64	0.08	0.76						NP	
	2.30					23.6	2.05	2.69									
	2.50	3.9	86.1	8.8	1.2	22.9	2.05	2.66	0.23	0.41						NP	
	2.70					27.5	2.01	2.74									
	2.90					27.2	2.17	3.12									
	3.10	0.0	34.6	62.5	2.9	27.1	1.99	2.68	0.27	0.31						NP	
	3.30					25.1	2.04	2.71									
	3.50					26.4	2.00	2.66									
	3.67					27.6	1.98	2.67									
	3.87	0.0	39.0	57.8	3.2	27.6	1.96	2.62	0.22	0.65						NP	
	4.07					27.4	1.98	2.65									
	4.27	0.0	42.0	54.6	3.4	26.3	1.99	2.65	0.28	0.43						NP	
684A1	1.55					19.4	2.14	2.72									
	2.55					27.5	1.99	2.68			2.0 *	0.7 *	2.7				

Table 4. Index properties and vane shear strength (cont'd).

CORE	DEPTH IN CORE (m)	GRAIN SIZE (%) GRAVEL	SAND	SILT	CLAY	WATER CONTENT (%)	BULK DENSITY (gm/cm^3)	GRAIN DENSITY (gm/cm^3)	ORGANIC CARBON (%)	$CaCO_3$ (%)	VANE SHEAR STRENGTH (kPa) INTACT	REMOLDED	SENSITIVITY	ATTERBERG LIMITS LIQUID LIMIT	PLASTIC LIMIT	PLASTICITY INDEX	LIQUIDITY INDEX
684A2	0.02	0.0	15.2	70.2	14.6				0.92	1.57							
	0.27	0.0	25.5	61.9	12.6	55.2	1.70	2.68	0.86	1.03						NP	
	0.57					26.2	2.03	2.74									
	0.71					23.3	2.08	2.74									
	0.91	0.0	76.3	17.5	6.2	22.9	2.07	2.71	0.39	0.84						NP	
	1.31					21.9	2.08	2.68									
	1.71	0.0	72.3	24.1	3.6	24.6	2.05	2.73	0.30	1.05						NP	
	1.91					24.8	2.03	2.69									
	2.11	0.0	62.8	20.5	2.7	25.5	1.97	2.57	0.31	0.60						NP	
	2.51	0.0	65.8	36.1	3.1	24.1	2.01	2.62	0.26	0.89						NP	
685A1	0.02	0.0	38.6	47.3	14.1	41.3	1.84	2.75	0.95	1.64						NP	
	0.26	0.0	45.3	47.3	7.4	37.1	1.87	2.69	0.72	1.23	5.7	1.4	4.1			NP	
	0.40					60.5	1.37	1.72			4.9	1.8	2.7				
	0.60	0.0	46.7	45.1	8.2	32.1	1.93	2.70	0.98	1.12	14.0	4.7	3.0			NP	
	0.80					61.0	1.45	1.93			16.5	6.5	2.5				
	1.00					28.1	1.99	2.71									
	1.20	0.0	61.5	32.9	5.6	26.9	1.74	2.14	0.42	0.88						NP	
	1.29					30.6	1.64	2.01									
	1.40					31.2	1.68	2.10									
	1.60	0.0	51.5	41.9	6.6	23.2	2.09	2.76	0.42	1.40						NP	
	1.80					22.8	2.10	2.75									
	2.00					23.1	2.10	2.76									
	2.20	0.0	61.5	32.4	6.1	21.9	2.11	2.75	0.45	0.99						NP	
	2.28					27.4	2.02	2.76									
	2.40					23.1	1.80	2.18									
	2.60	0.0	50.8	42.7	6.5	23.9	2.08	2.76	0.44	1.38						NP	
	2.80					22.8	2.10	2.76									
	3.00	0.0	43.3	50.9	5.8	23.4	2.08	2.73	0.44	1.17						NP	
	3.20					23.0	2.08	2.73									

Table 4. Index properties and vane shear strength (cont'd).

CORE	DEPTH IN CORE (m)	GRAIN SIZE (%) GRAVEL	SAND	SILT	CLAY	WATER CONTENT (%)	BULK DENSITY (gm/cm^3)	GRAIN DENSITY (gm/cm^3)	ORGANIC CARBON (%)	$CaCO_3$ (%)	VANE SHEAR STRENGTH (kPa) INTACT	REMOLDED	SENSITIVITY	ATTERBERG LIMITS LIQUID LIMIT	PLASTIC LIMIT	PLASTICITY INDEX	LIQUIDITY INDEX
685A2	0.85					31.8	1.95	2.73									
	1.85					23.7	2.09	2.77									
	2.85					22.2	2.10	2.73									
	3.85					25.7	2.04	2.74									
686A1	1.35					57.4	1.34	1.63			50.9 *	13.2 *	3.9				
	2.36					29.8	1.98	2.74			131.2 *	37.7 *	3.5				
686A2	0.02	0.0	74.0	19.8	6.2				0.55	0.88							
	0.20	0.0	64.6	24.9	10.5	27.5	1.88	2.44	0.57	1.68						NP	
	0.40					20.9	2.10	2.68									
	0.60					21.8	2.09	2.71									
	0.80	0.0	60.3	33.4	6.3	22.2	2.09	2.71	0.41	1.54						NP	
	1.00					27.3	2.00	2.71									
	1.20	0.0	69.6	26.1	0.3	35.4	1.88	2.68	1.09	1.34						NP	
	1.40					28.5	1.97	2.67									
	1.60	0.0	30.7	58.2	11.1	29.4	1.97	2.71	1.42	1.87						NP	
	1.80					28.5	1.99	2.73									
	2.02	0.0	49.9	47.2	2.9	26.4	2.02	2.71	0.35	1.46						NP	
	2.20					30.3	1.95	2.68									
	2.40	3.1	56.5	40.4		48.3	1.78	2.76	3.58	4.17				68	48	20	0.02
	2.60					29.3	1.97	2.71									
	2.76	0.0	9.4	70.6	20.0	32.9	1.93	2.73	1.63	2.72						NP	
687A1	1.91					30.8	1.97	2.80			99.5 *	32.4 *	3.1				
	2.91					38.8	1.83	2.71			50.3 *	16.8 *	3.0				
	3.91					27.8	1.94	2.62			92.3 *	16.8 *	5.5				

Table 4. Index properties and vane shear strength (cont'd).

CORE	DEPTH IN CORE (m)	GRAIN SIZE (%) GRAVEL	SAND	SILT	CLAY	WATER CONTENT (%)	BULK DENSITY (gm/cm^3)	GRAIN DENSITY (gm/cm^3)	ORGANIC CARBON (%)	$CaCO_3$ (%)	VANE SHEAR STRENGTH (kPa) INTACT	REMOLDED	SENSITIVITY	ATTERBERG LIMITS LIQUID LIMIT	PLASTIC LIMIT	PLASTICITY INDEX	LIQUIDITY INDEX
687A3	0.02	0.0	25.4	61.6	13.0				0.86	1.41							
	0.40										18.9						
	0.45					55.9	1.67	2.68									
	0.60										60.5	12.6	4.8				
	0.70	0.0	12.1	82.3	9.6	26.6	2.01	2.69	0.66	1.20						NP	
	0.80										102.1	63.0	1.6				
	1.00										39.1	36.6	1.1				
	1.10					32.0	1.90	2.62									
	1.20										124.8	89.5	1.4				
	1.30	0.0	10.0	80.6	9.4	26.9	2.00	2.68	0.78	1.61						NP	
	1.40										151.3	93.3	1.6				
	1.60										155.1	34.0	4.6				
	1.70					33.7	1.91	2.69									
	1.80										132.4	18.9	7.0				
	1.90					37.5	1.86	2.69									
	2.00										116.0	65.6	1.8				
	2.10					25.5	2.00	2.65									
	2.20										156.3	88.3	1.8				
	2.30					30.8	1.97	2.75									
	2.40										131.1	100.9	1.3				
	2.55					33.1	1.94	2.75									
	2.60										45.4	16.4	2.8				
	2.75	0.0	1.5	87.6	10.9	31.5	1.93	2.68	0.68	1.55							
	2.80										107.2	30.3	3.5				
	2.95					29.9	1.97	2.72									
	3.00										104.6	22.7	4.6				
	3.15	0.0	4.6	82.1	13.3	36.9	1.87	2.68	0.89	1.80				53	35	18	0.11
	3.20										83.2	42.9	1.9				
	3.35					35.6	1.89	2.70									
	3.40										63.0	26.5	2.4				

Table 4. Index properties and vane shear strength (cont'd).

CORE	DEPTH IN CORE (m)	GRAIN SIZE (%) GRAVEL	SAND	SILT	CLAY	WATER CONTENT (%)	BULK DENSITY (gm/cm^3)	GRAIN DENSITY (gm/cm^3)	ORGANIC CARBON (%)	$CaCO_3$ (%)	VANE SHEAR STRENGTH (kPa) INTACT	REMOLDED	SENSITIVITY	ATTERBERG LIMITS LIQUID LIMIT	PLASTIC LIMIT	PLASTICITY INDEX	LIQUIDITY INDEX
687A3	3.60					27.0	2.04	2.78									
(cont)	3.65										84.5	25.2	3.4				
	3.80	0.0	11.9	77.2	10.9	28.3	1.98	2.70	0.84	1.32						NP	
	3.85										131.1	40.3	3.2				
	4.00					26.0	2.02	2.71									
	4.05										138.7	34.0	4.1				
	4.20	0.0	9.6	83.7	6.7	27.9	1.97	2.65	0.76	1.83						NP	
	4.25										100.9	5.0	20.0				
	4.62										191.6	65.6	2.9				
	4.66					25.1	2.19	3.12									
	4.70										175.3	83.2	2.1				
	4.85	0.0	14.4	74.3	11.3				0.68	1.93						NP	
	4.90										148.8	66.8	2.2				
	5.05					28.4	2.00	2.79									
	5.10										114.7	36.6	3.1				
	5.20	0.0	2.2	73.1	24.7	47.2	1.78	2.80	1.51	1.67						NP	
	5.35										76.9	27.7	2.8				
	5.45					40.7	1.86	2.86									

NOTE: NP = Non-plastic
TR = Trace
* = Vane inserted parallel to core axis

Table 5. Triaxial test types.

STATIC TESTS	DESCRIPTION	NUMBER OF TESTS PERFORMED
T-2	Isotropically consolidated to the in situ vertical stress with undrained shear.	1
T-3	Isotropic normally consolidated (OCR=1) undrained shear.	11
T-4	Isotropic overconsolidated (OCR ~ 6) undrained shear.	8
T-7	Anisotropic normally consolidated (OCR = 1) undrained shear.	1
T-8	Isotropic overconsolidated (OCR ~ 3) undrained shear.	2
CYCLIC TESTS		
T-5	Isotropic normally consolidated (OCR = 1) undrained shear with a high cyclic shear stress ratio ($\tau_{cyc\ ave\ max}/\sigma_c$).	13
T-6	Isotropic normally consolidated (OCR = 1) undrained shear with a low cyclic shear stress ratio.	15
T-9	Isotropic overconsolidated (OCR ~ 6) undrained shear with a high cyclic shear stress ratio.	3
T-10	Isotropic overconsolidated (OCR ~ 6) undrained shear with a low cyclic shear stress ratio.	3
T-11	Isotropically consolidated to the in situ vertical stress with undrained shear and a high cyclic shear stress ratio.	1
T-12	Isotropically consolidated to the in situ vertical stress with undrained shear and a low cyclic shear stress ratio.	1
T-13	Isotropically consolidated to the in situ vertical stress. Cyclic shear stresses were increased and drainage was allowed between burst cycles to simulate storm wave events and densification due to pore pressure dissipation.	1
T-14	Anisotropically consolidated to the in situ vertical stress. Cyclic shear stresses were increased and drainage was allowed between burst cycles to simulate storm wave events and densification due to pore pressure dissipation.	1

Table 6. Consolidation test results.

CORE	DEPTH (m)	TEST No.	σ'_{vo} (kPa)	σ'_{vm} (kPa)	C_c	C_r	c_v(ave)x10^{-2} (cm^2/sec)	OCR	w (%)	e_o	$\frac{C_c}{1 + e_o}$
681A2	2.13	OE36	24	500	0.11	0.002	2.0	21	21.6	0.520	0.07
	5.53	OE38	66	410	0.07	0.003	0.6	6	13.9	0.382	0.05
682A1	1.47	OE34	8	64	0.53	0.065	0.3	8	65.3	1.886	0.18
	2.91	OE35	16	70	0.69	0.072	0.3	4	75.1	1.991	0.23
	4.61	CE19	28	190	0.06	-	-	7	33.6	0.967	0.03
683A1	1.50	CE34	13	20	0.04	-	-	2	28.6	0.809	0.02
	2.55	CE35	22	660	0.09	-	-	30	30.0	0.967	0.05
	4.47	CE43	38	280	0.08	-	-	7	25.6	0.636	0.05
684A1	0.37	CE37	4	250	0.08	-	-	61	28.5	0.724	0.05
	1.07	CE47	11	200	0.12	-	-	18	21.0	0.625	0.07
	2.37	CE49	24	170	0.07	-	-	7	23.5	0.605	0.04
685A2	0.77	OE39	5	105	0.25	0.018	0.9	20	40.0	1.165	0.12
	1.53	CE20	12	190	0.10	-	-	16	27.0	0.671	0.06
	1.81	CE21	19	260	0.03	-	-	14	21.7	0.551	0.02
686A1	0.28	CE39	3	300	0.09	-	-	100	26.7	0.678	0.05
	0.77	CE41	8	425	0.08	-	-	53	29.0	0.740	0.05
	1.83	CE40	18	1100	0.05	-	-	61	24.3	0.600	0.03
	2.86	CE42	28	280	0.24	-	-	10	37.3	1.044	0.12
687A1	0.67	OE42	6	490	0.11	0.007	1.9	77	29.0	0.748	0.06
	1.07	CE48	10	300	0.22	-	-	30	33.4	0.881	0.12
	2.20	OE43	21	320	0.14	0.010	1.1	15	31.0	0.774	0.08
	3.63	CE44	33	470	0.14	-	-	14	29.0	0.854	0.08

Table 7. Static triaxial test results.

CORE	DEPTH (m)	TEST NO. (TE)	TEST TYPE	w (%)	w SHEARED (%)	σ'_c (kPa)	A_f	INDUCED OCR	STRAIN AT FAILURE (%)	q AT FAILURE (kPa)	p' AT FAILURE (kPa)	$\frac{q_{max}}{\sigma'_c}$ (1)	ϕ' (degrees) (2)
681A2	1.36	107	T-8	34.7	30.6	151.0	0.07	2.0	11.9	186.0	312.3	1.23	<37.3
	1.36	108	T-4	32.1	28.7	40.7	-0.19	7.4	17.3	149.0	247.2	3.66	<40.4
682A1	1.12	76	T-3	29.7	25.5	236.7	0.25	1.0	13.1	183.9	327.7	0.78	35.2
	1.12	77	T-7	40.4	32.3	242.3	0.19	1.0	10.2	124.5	197.5	0.51	39.2
	1.26	85	T-4	71.2	54.0	44.1	0.03	5.5	17.4	82.9	121.4	1.88	<43.4
	1.26	86	T-8	69.3	50.9	77.9	0.18	3.0	19.2	89.5	135.3	1.15	<41.4
	1.78	98	T-3	78.4	52.5	201.3	0.81	1.0	17.6	93.2	144.3	0.46	40.2
	1.78	99	T-4	77.8	59.0	27.3	0.04	8.3	14.6	63.6	85.5	2.33	<48.9
683A1	4.26	109	T-3	25.5	25.5	289.7	-0.13	1.0	9.9	882.4	1409.2	3.05	38.8
	4.26	110	T-4	26.0	25.0	47.4	-0.30	6.3	8.6	634.3	1064.5	13.38	<37.8
684A1	0.95	105	T-3	21.4	21.4	293.0	-0.17	1.0	7.2	969.8	1591.1	3.31	38.0
	0.95	106	T-4	21.0	21.0	48.1	-0.35	6.2	8.5	675.3	1116.4	14.04	<37.7
685A2	0.55	103	T-3	29.9	26.6	303.8	0.01	1.0	10.7	423.4	719.0	1.39	38.1
	0.55	104	T-4	29.8	26.9	38.3	-0.32	7.5	14.6	281.3	499.7	7.34	<37.8
	1.35	119	T-2	30.2	29.3	20.9	-0.212	(?)	11.65	77.54	131.33	3.71	<42.1
	1.35	120	T-3	29.8	26.7	292.0	0.159	1.0	17.62	266.20	473.60	0.91	36.8
	2.36	94	T-3	23.6	23.6	101.5	-0.20	1.0	9.2	427.6	703.3	4.21	38.8
	2.46	95	T-3	23.5	21.9	343.2	-0.16	1.0	8.4	1189.5	1916.5	3.47	39.0
686A1	1.75	100	T-3	-	25.6	304.2	0.01	1.0	9.4	419.9	716.7	1.38	42.0
	1.75	101	T-4	-	24.9	47.7	-0.26	6.2	8.8	372.9	616.1	7.82	<38.2
687A1	0.60	102	T-4	27.9	27.7	45.1	-0.28	6.5	9.6	409.7	686.3	9.08	<39.9
	1.15	96	T-3	34.3	32.3	299.6	0.26	1.0	20.0	248.5	419.0	0.83	38.3
	1.15	97	T-3	33.9	32.9	94.4	0.03	1.0	12.9	147.6	232.4	1.56	42.1

(1) $q_{max}/\sigma'_c = s_u/\sigma'_c$ may be influenced by overconsolidation in some cores (even at high consolidation stresses).

(2) ϕ' = arcsine (q/p') for (q/p') with the highest σ'_1/σ'_3 ratio; ϕ' is valid only for T-3 and T-7 tests at high consolidation stresses.

Table 8. Cyclic triaxial test results.

CORE	DEPTH (m)	TEST NO. (TC)	TEST TYPE	w (%)	w SHEARED (%)	σ'_c (kPa)	INDUCED OCR	τ_{max}/σ'_c (%)	τ_{min}/σ'_c (%)	CYCLES TO 5% STRAIN	CYCLES TO 10% STRAIN	CYCLES TO 20% STRAIN	COMMENTS
681A2	1.46	100	T-5	31.4	26.1	294.5	1.0	47.9	-39.2	4 C	15 C	35 C	M.B.
	1.46	101	T-6	26.7	21.6	298.4	1.0	36.3	-34.0	9 T	28 T	47 T	
	1.56	127	T-6	25.3	21.4	300.4	1.0	22.4	-18.7	571C	722C	765C	
	1.56	128	T-5	24.4	20.7	55.3	1.0	66.7	-60.9	196C	272C	460C	CSR
682A1	0.80	44	T-6	29.8	24.1	241.8	1.0	27.2	-23.5	91 C	130 C	214 C	
	0.80	45	T-6	30.5	25.5	239.4	1.0	18.1	-8.8	216 C	320 C	413 C	
	0.90	40	T-6	24.3	21.6	240.4	1.0	39.5	-36.1	3 T	5 T	5 T	NECKING
	0.90	41	T-6	26.8	26.1	241.8	1.0	38.2	-44.6	4 T	12 T	15 T	
	1.00	38	T-5	24.0	-	238.4	1.0	53.4	-55.0	1 T	3 T	-	M.B.
	1.00	39	T-6	24.0	-	237.3	1.0	35.5	-52.1	2 T	7 T	17 T	M.B.
	1.38	78	T-10	69.5	52.6	37.8	6.3	98.1	-82.3	105 T	193 C	242 C	
	1.38	79	T-9	69.6	53.0	39.8	6.0	151.5	-131.2	4 C	10 C	20 C	
	1.90	76	T-6	76.9	49.1	238.0	1.0	28.3	-22.4	339 C	390 C	440 C	CSR
	1.90	77	T-5	69.1	44.8	239.1	1.0	47.3	-45.5	4 T	7 T	12 T	
684A1	0.66	90	T-6	23.6	21.0	296.6	1.0	54.1	-36.5	11 T	60 T	62 T	
	0.66	91	T-5	26.0	21.4	297.2	1.0	94.8	-79.6	1 T	4 T	13 T	
685A2	0.33	111	T-5	39.9	31.3	292.6	1.0	47.6	-41.8	2 T	5 T	6 T	
	0.33	112	T-6	39.8	29.8	298.0	1.0	26.4	-22.8	107 C	152 C	163 T	
	0.44	80	T-6	37.0	27.5	289.8	1.0	19.5	-16.1	427 T	591 C	653 T	
	0.44	81	T-5	47.2	35.9	297.4	1.0	46.7	-39.5	2 T	4 T	5 T	
	0.65	82	T-10	31.0	26.0	46.7	6.4	108.8	-96.4	13 T	61 T	122 T	
	0.65	83	T-9	31.1	26.3	49.7	6.0	171.0	-161.2	2 T	10 T	18 T	
	0.95	D113	T-12	31.5	28.8	16.4	1.0	112.0	112.0	192 T	885 T	980 T	(1)
	0.95	D120	T-11	28.6	25.9	17.0/8.7	1.0	171.0	-122.0	-	35 C	150 C	(2)
	1.05	62	T-5	28.6	25.8	17.4	1.0	81.6	-86.2	180 C	389 C	800 C	CSR
	1.05	74	T-6	26.1	25.3	20.8	1.0	32.7	-29.8	1200	1600	1800	CSR
	2.06	50	T-5	23.0	21.8	301.0	1.0	51.4	-40.0	40 T	-	-	M.B.
	2.06	51	T-5	26.4	25.4	294.1	1.0	66.2	-50.1	14 T	-	-	M.B.
686A1	0.20	88	T-9	25.2	21.3	53.4	5.7	101.5	-100.2	13 T	48 T	53 T	
	0.20	89	T-10	27.4	21.8	50.0	6.0	68.2	-63.6	113 C	211 C	356 C	
	0.35	84	T-6	20.6	-	296.7	1.0	54.4	-44.5	22 T	-	-	M.B.
	0.35	85	T-5	21.3	-	298.9	1.0	76.8	-65.7	4 T	-	-	M.B.
	0.45	96	T-6	22.2	20.6	295.5	1.0	61.6	-51.9	96 C	-	-	M.B.
	0.45	97	T-5	-	-	298.1	1.0	103.0	-57.5	2 T	-	-	M.B.
	0.56	109	T-6	-	-	293.6	1.0	54.2	-46.2	420 T	423 T	426 T	M.B.
	0.56	110	T-5	-	-	297.1	1.0	93.1	-76.9	11 T	25 T	40 T	M.B.
687A1	0.49	95	T-5	33.6	29.4	298.7	1.0	64.3	-57.8	2 T	5 T	6 T	
	0.49	94	T-6	40.6	34.0	296.7	1.0	26.7	-22.5	330 C	402 T	414 T	

C = Compressive strain; M.B. = Membrane broke during cycling;

T = Tensile strain; CSR = Changed stress ratio (results are questionable);

(1) Isotropic consolidation, drainage between bursts, τ/σ'_c = 6; 12; 25; 56; 112%

(2) Anisotropic consolidation, drainage between bursts, τ/σ'_c = 37, 4; 49, 0; 73, -24; 98, -49; 122, -73; 171, -122%

Table 9. Liquefaction susceptibility based on laboratory cyclic triaxial and cone penetration tests.

AREA/STATION	ANALYSIS 1				ANALYSIS 2				ANALYSIS 3	ANALYSIS 3a(2)	ANALYSIS 4
	M = 5.25		M = 6.75		M = 5.25		M = 6.75		OCR = 1	OCR = 6	
	a_{max} (g)	D (1) (km)	a_{max} (g)	D (1) (km)	a_{max} (g)	D (1) (km)	a_{max} (g)	D (1) (km)	H (m)	H (m)	H (m)
PRODELTA											
674-687	0.27	9	0.21	33	0.14	19	0.11	63	>13	-	11
670-685	0.14	19	0.11	63	0.11	24	0.09	76	9	>13	8
667	-	-	-	-	-	-	-	-	-	-	-
668	-	-	-	-	0.21	12	0.16	44	-	-	>13
669-686	0.35	6	0.26	26	0.19	13	0.15	47	>13	>13	>13
E. THERMO. GAS											
671	-	-	-	-	0.10	26	0.07	94	-	-	8
THERMO. GAS											
675-683	-	-	-	-	0.12	22	0.09	76	-	-	9
W. THERMO. GAS											
677-684	0.32	7	0.26	26	0.26	9	0.20	35	>13	-	>13
BIOGENIC GAS											
676-682	0.22	11	0.18	39	0.10	26	0.07	94	9	>13	6
E. NORTON SOUND											
673	-	-	-	-	0.14	19	0.11	63	-	-	-
E. NORTON SOUND											
672	-	-	-	-	0.07	36	0.06	107	-	-	-
RIDGE											
679-680	-	-	-	-	0.13	20	0.10	69	-	-	>13
SWALE											
678-681	0.37	5	0.25	27	0.13	20	0.10	69	>13	-	>13

Analysis 1 determined the minimum ground surface earthquake acceleration (a_{max}) required to cause liquefaction in deep subbottom sediment based on laboratory cyclic triaxial test data.

Analysis 2 determined the minimum ground surface earthquake acceleration (a_{max}) required to cause liquefaction in shallow subbottom sediment based on cone penetration test data.

Analysis 3 determined the smallest sustained storm wave height (H) required to cause liquefaction in normally consolidated sediment based on laboratory cyclic triaxial test data.

Analysis 3a determined the smallest sustained storm wave height (H) required to cause liquefaction in overconsolidated (OCR = 6) sediment based on laboratory cyclic triaxial test data.

Analysis 4 determined the smallest sustained storm wave height (H) (valid only as a comparison of relative liquefaction susceptibility between stations) required to cause liquefaction based on cone penetration test data. This analysis compared the stress ratio caused by storm waves to the stress ratio required to cause liquefaction induced by a M = 5.25 earthquake. The values of wave height (H) do not represent actual conditions, but are presented solely for comparing liquefaction susceptibility between stations.

(1) Distance to fault (D) necessary to cause the specified ground surface acceleration was determined from Woodward-Clyde Consultants (1978).

(2) Because the northern Bering Sea sediment is typically overconsolidated near the seafloor, this analysis is probably more appropriate than Analysis 3.

LIST OF FIGURES

17c. Sediment type determined from cone penetration test 674X1 (Yukon prodelta - "protected" - near station 687).

18. Compression index (C_c) determined from consolidation tests related to the initial void ratio (e_o) vs water content (w).

19. Zones of grain size distributions of liquefiable soil (from Finn, 1972).

20. Cyclic stress ratio determined from cyclic triaxial tests vs the relative density of nearby sediment determined from cone penetration tests.

21. Map of the thermogenic gas seep.

22. Lithology, index properties and cone pressure vs subbottom depth for stations 683 and 675 (thermogenic gas seep).

23. Lithology, index properties and cone pressure vs subbottom depth for stations 684 and 677 (adjacent to thermogenic gas seep).

24. Fathometer record of thermogenic gas seep.

25. Sediment type determined from cone penetration test 675X1 (thermogenic gas seep - near station 683).

26. Sediment type determined from cone penetration test 677X2 (west of thermogenic gas seep-near station 684).

27. Lithology, index properties and cone pressure vs subbottom depth for stations 682 and 676 (biogenic gas seep, south of Nome).

28. Lithology, index properties and cone pressure vs subbottom depth for stations 673 and 76-125 (biogenic gas seep, south of Cape Darby).

29. Sediment type determined from cone penetration test 676X2 (biogenic gas seep, south of Nome - near station 682).

30. Lithology, index properties and cone pressure vs subbottom depth for stations 672 and 76-133 (easternmost Norton Sound).

31. Sediment type determined from cone penetration test 672X2 (easternmost Norton Sound).

32. Bathymetric map of ridge and swale area.

33. Lithology, index properties and cone pressure vs subbottom depth for stations 680 and 679 (sand ridge crest).

34. Lithology, index properties and cone pressure vs subbottom depth for stations 681 and 678 (swale).

35. Sediment type determined from cone penetration test 679X1 (sand ridge crest - near station 680).

36. Sediment type determined from cone penetration test 678X1 (swale - near station 681).

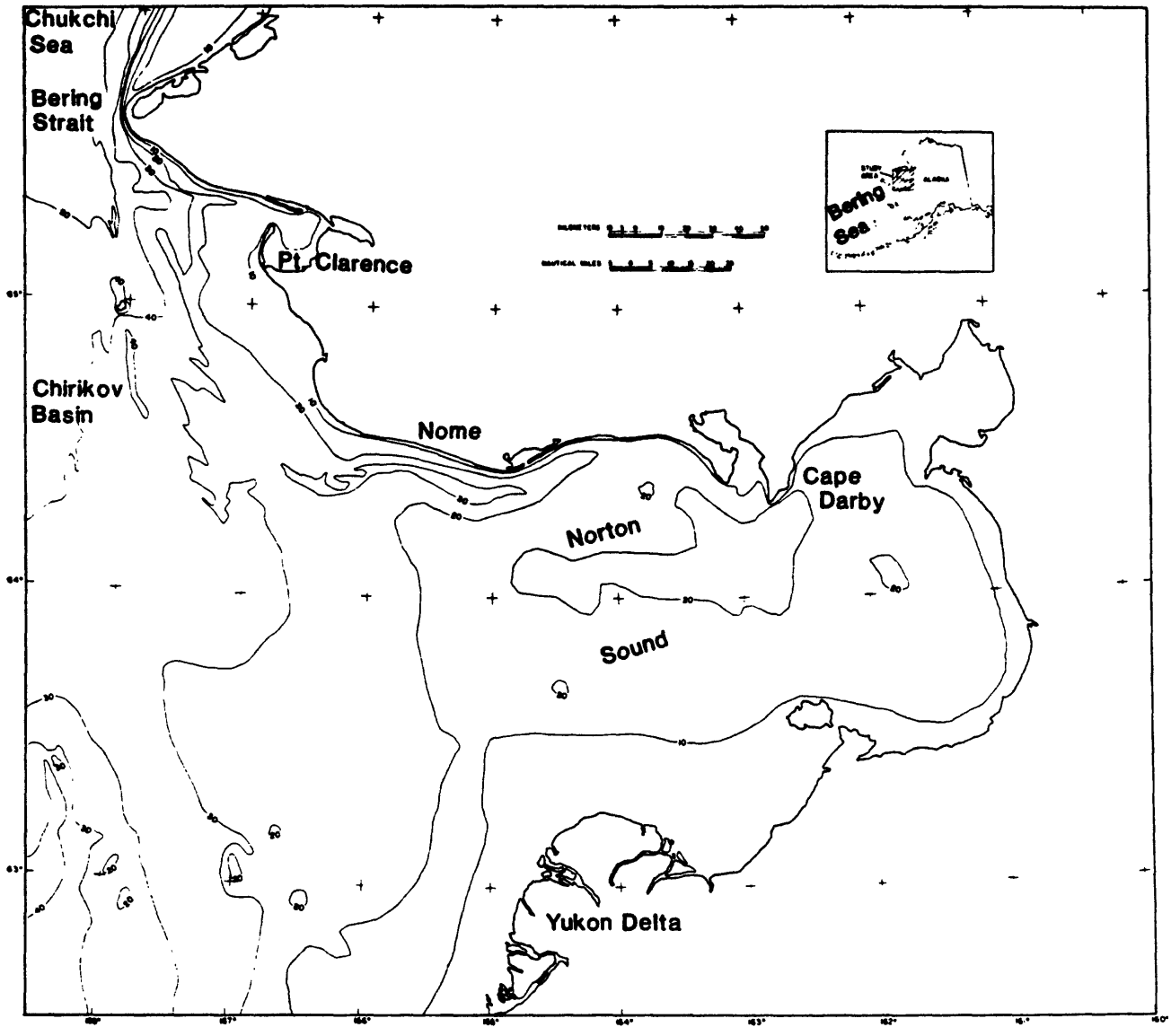

Fig. 1. Location map of the study area in the northern Bering Sea.

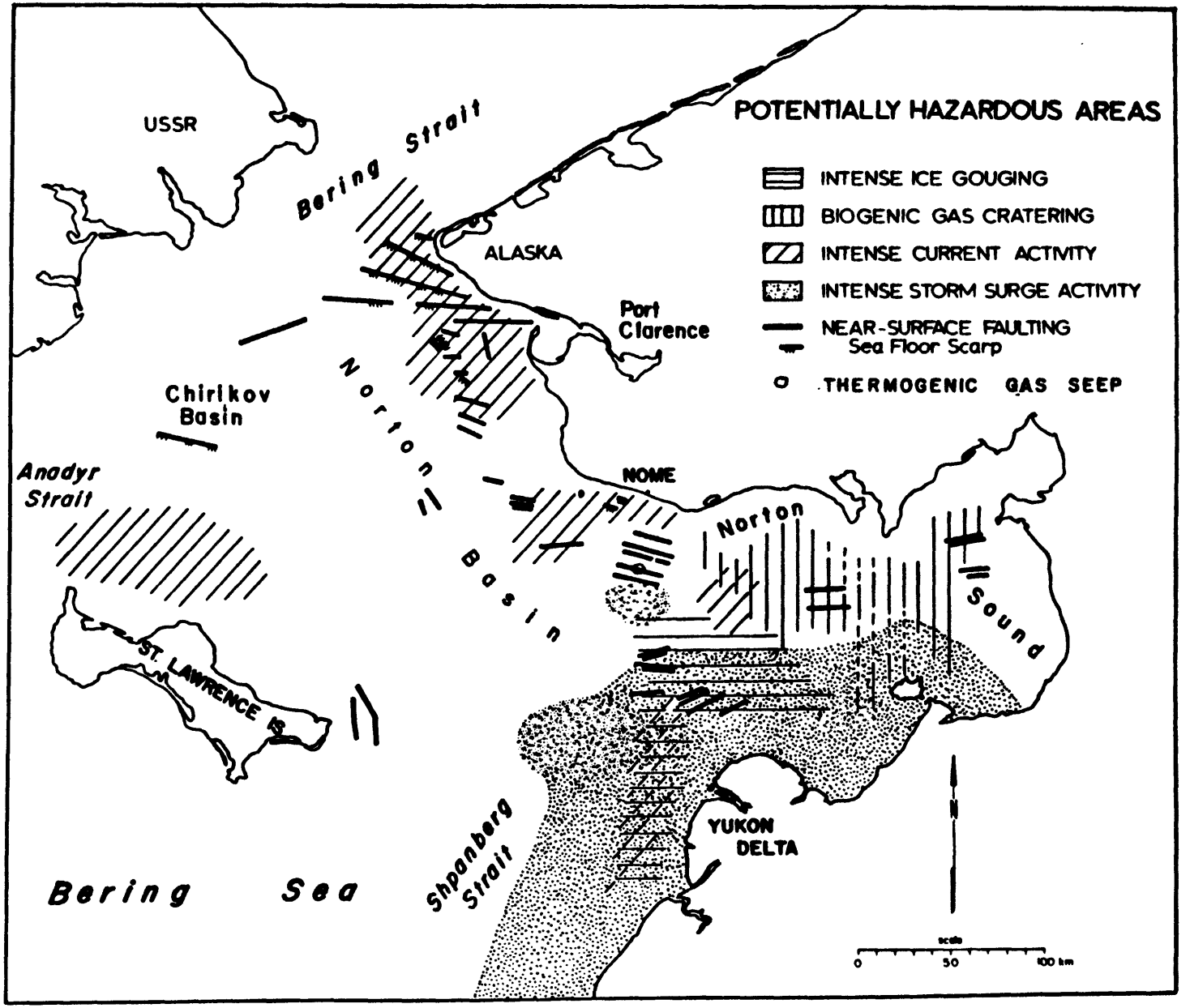

Fig. 2. Geo-hazard locations in the northern Bering Sea (from Larsen and

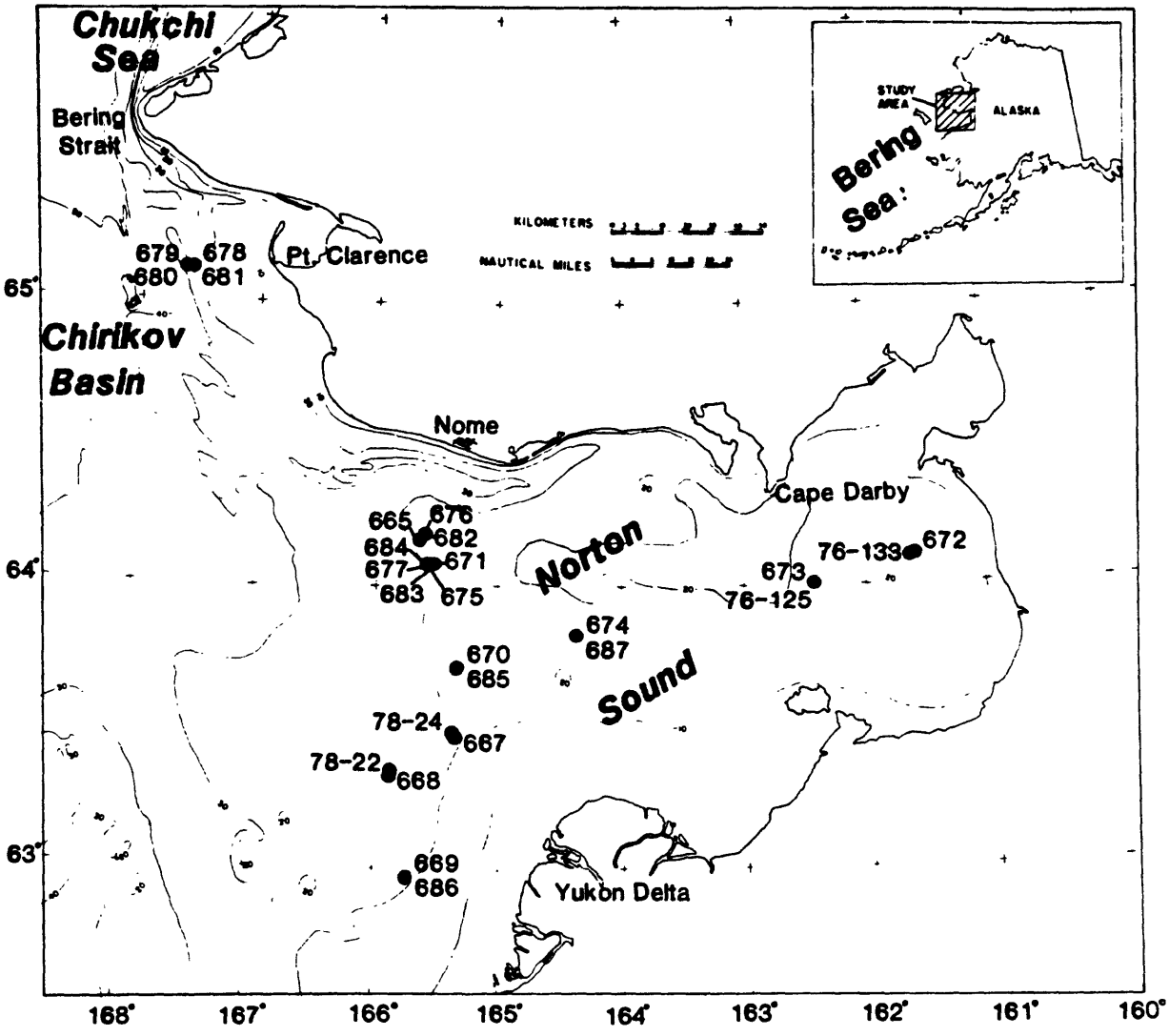

Fig. 3. Station location map.

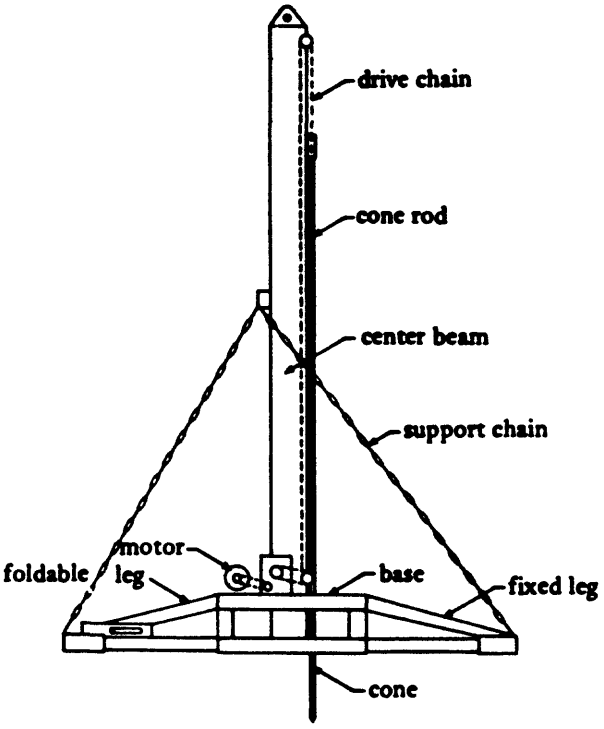

Fig. 4. XSP - 40 penetrometer (from Beard and Lee, 1982).

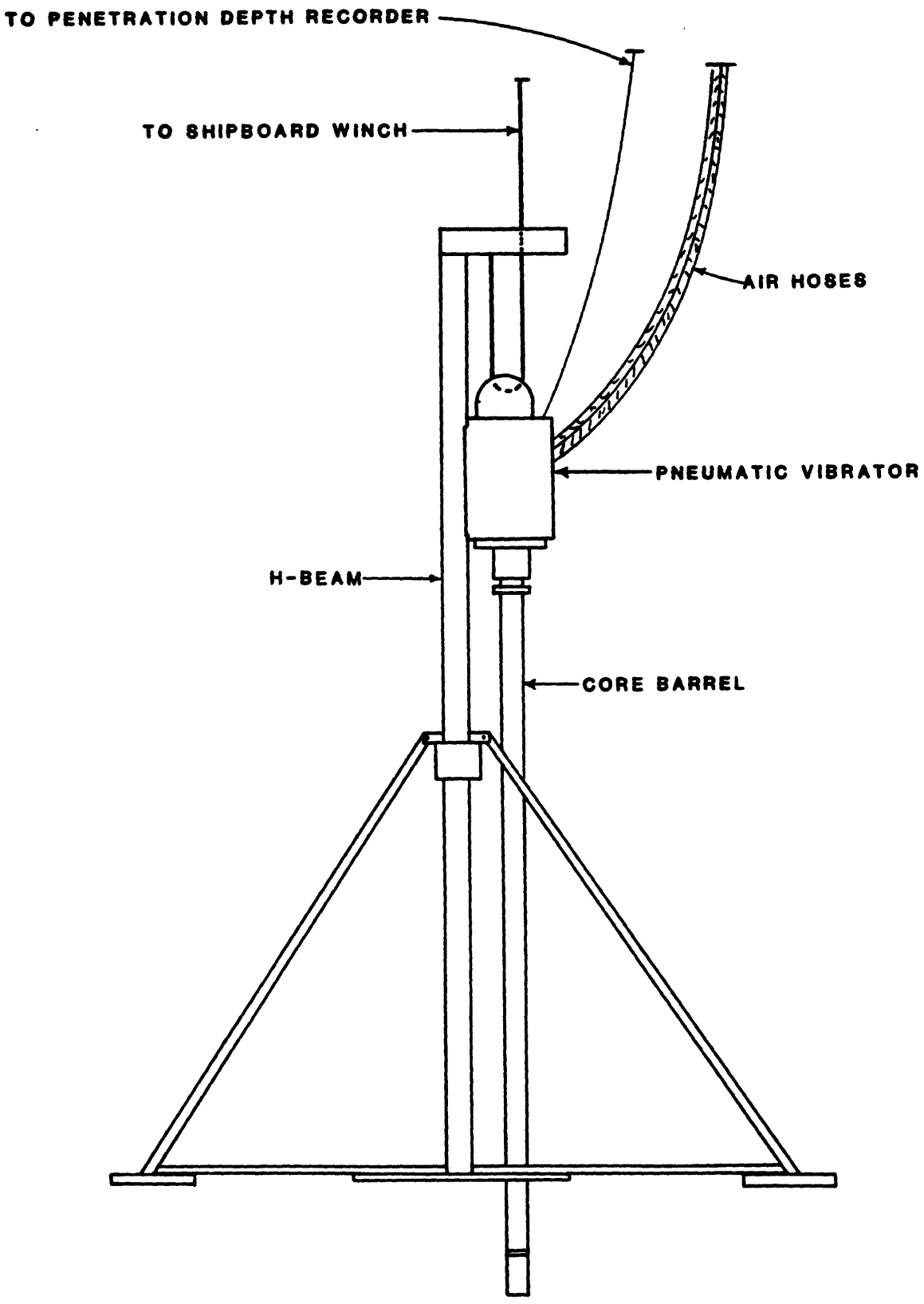

Fig. 5 Pneumatic vibracorer.

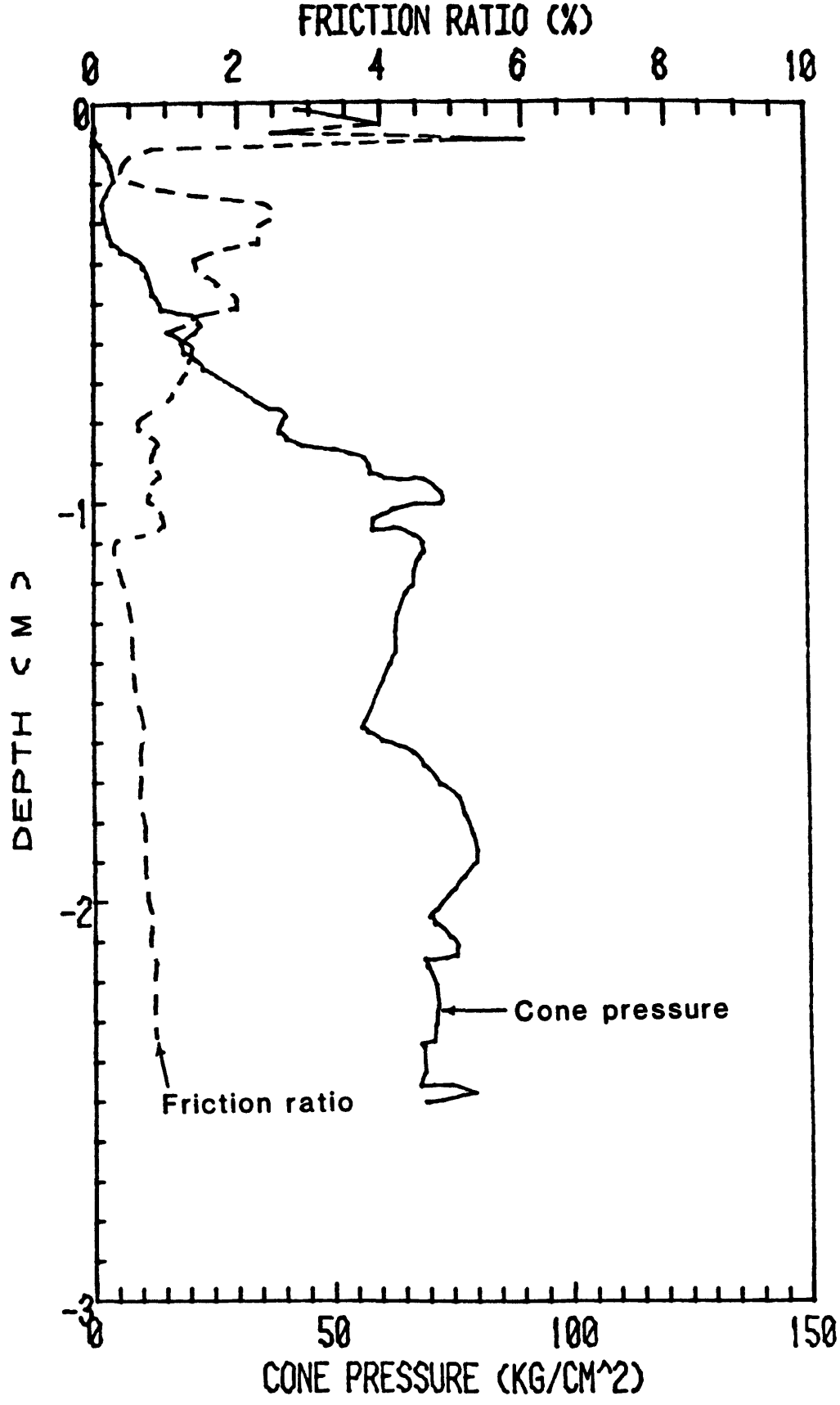

Fig. 6 Typical cone penetration test record illustrating cone pressure and friction ratio vs subbottom depth.

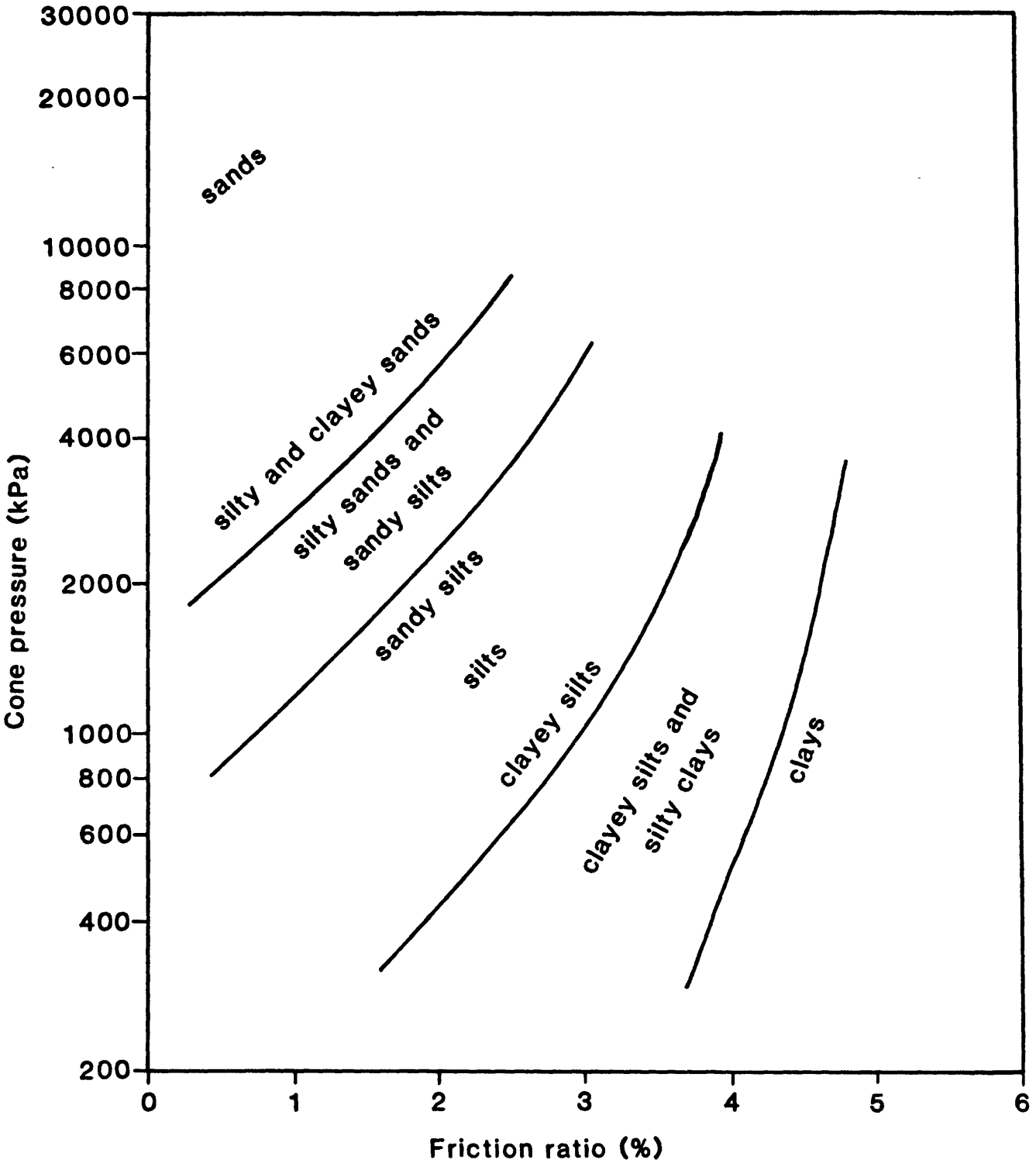

Fig. 7 Sediment type plotted as a function of CPT cone pressure vs friction ratio.

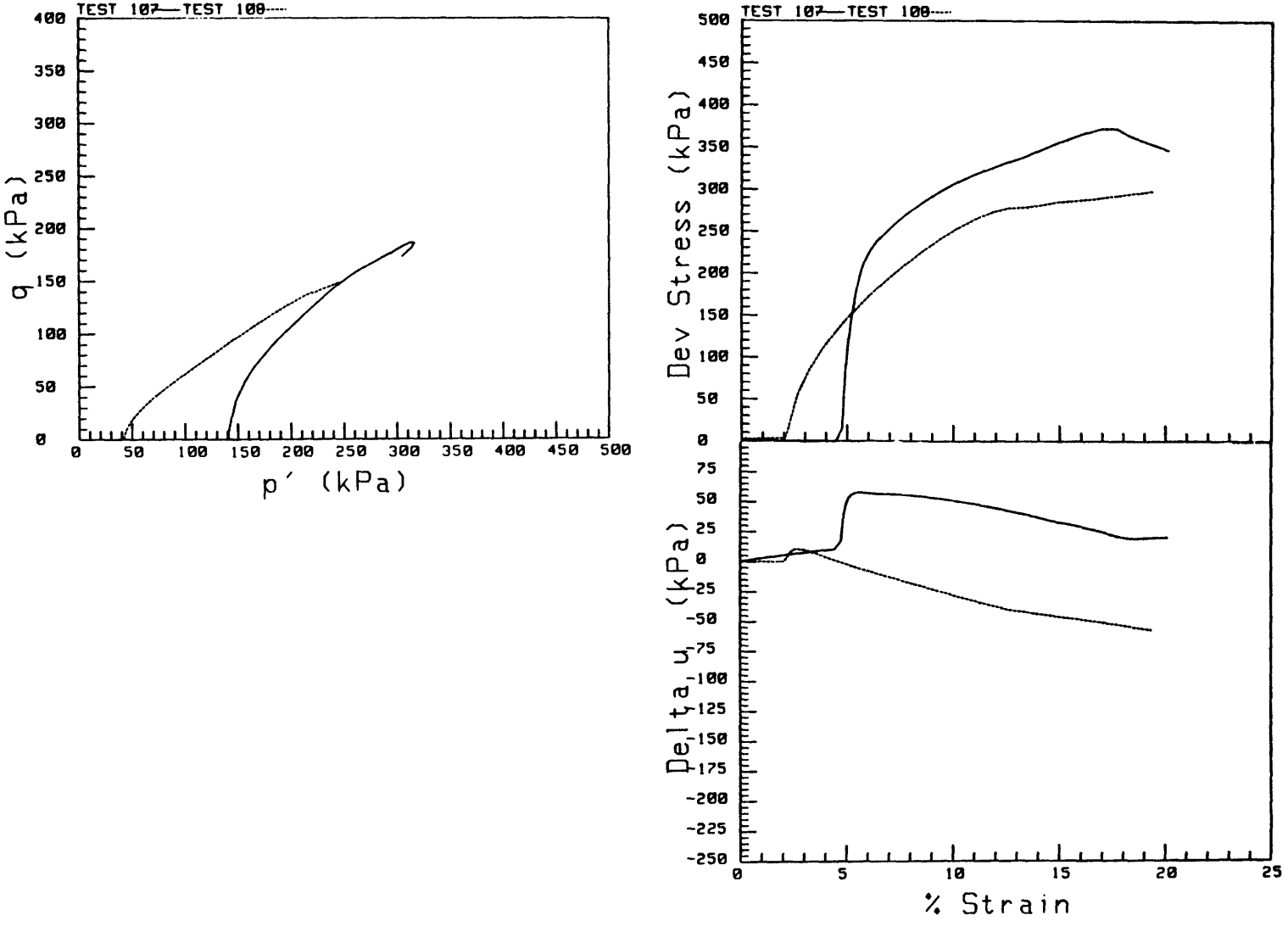

Fig. 8a. Multiple static triaxial test results (core 681 A2).

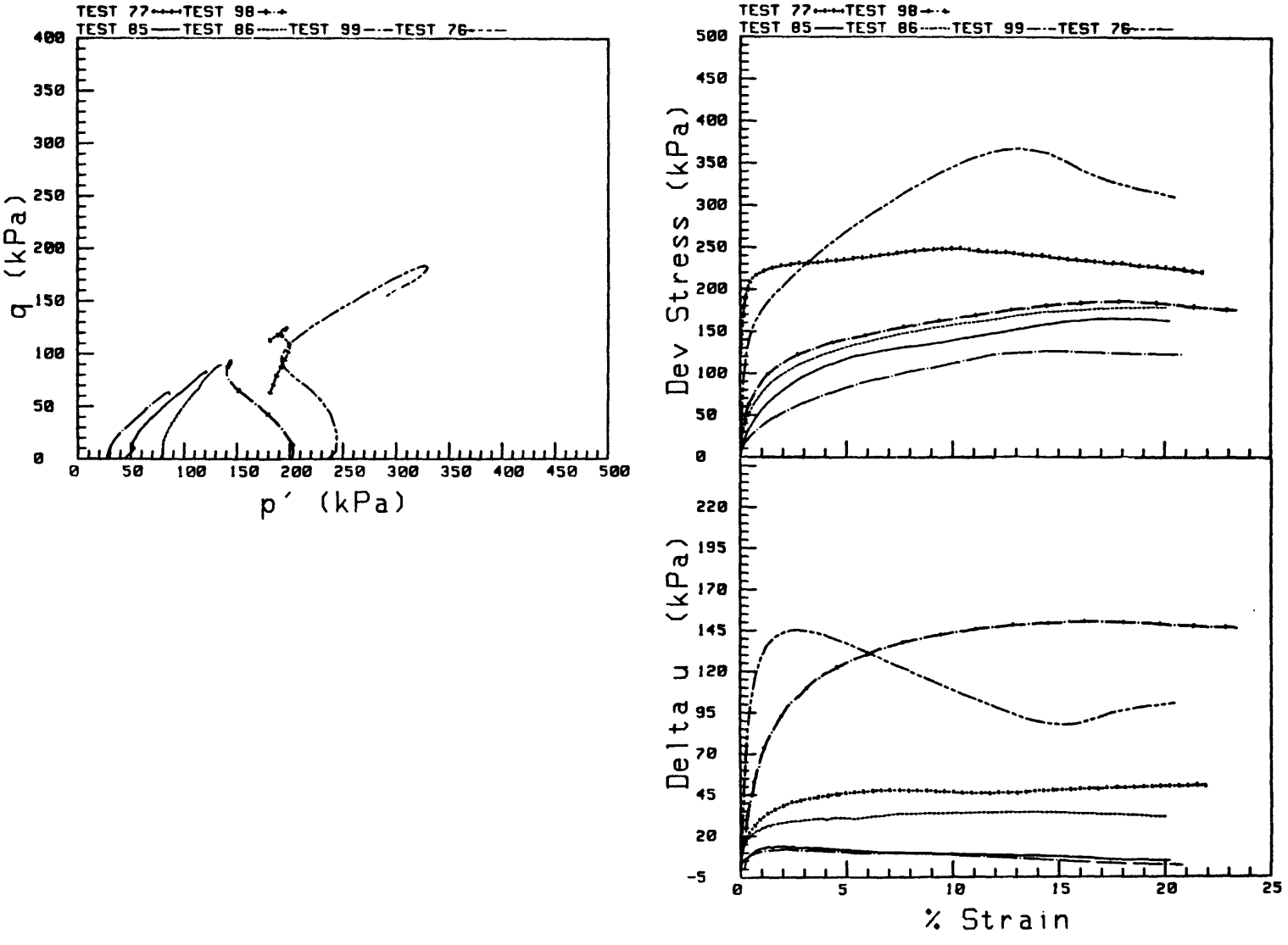

Fig. 8b. Multiple static triaxial test results (core 682 A1).

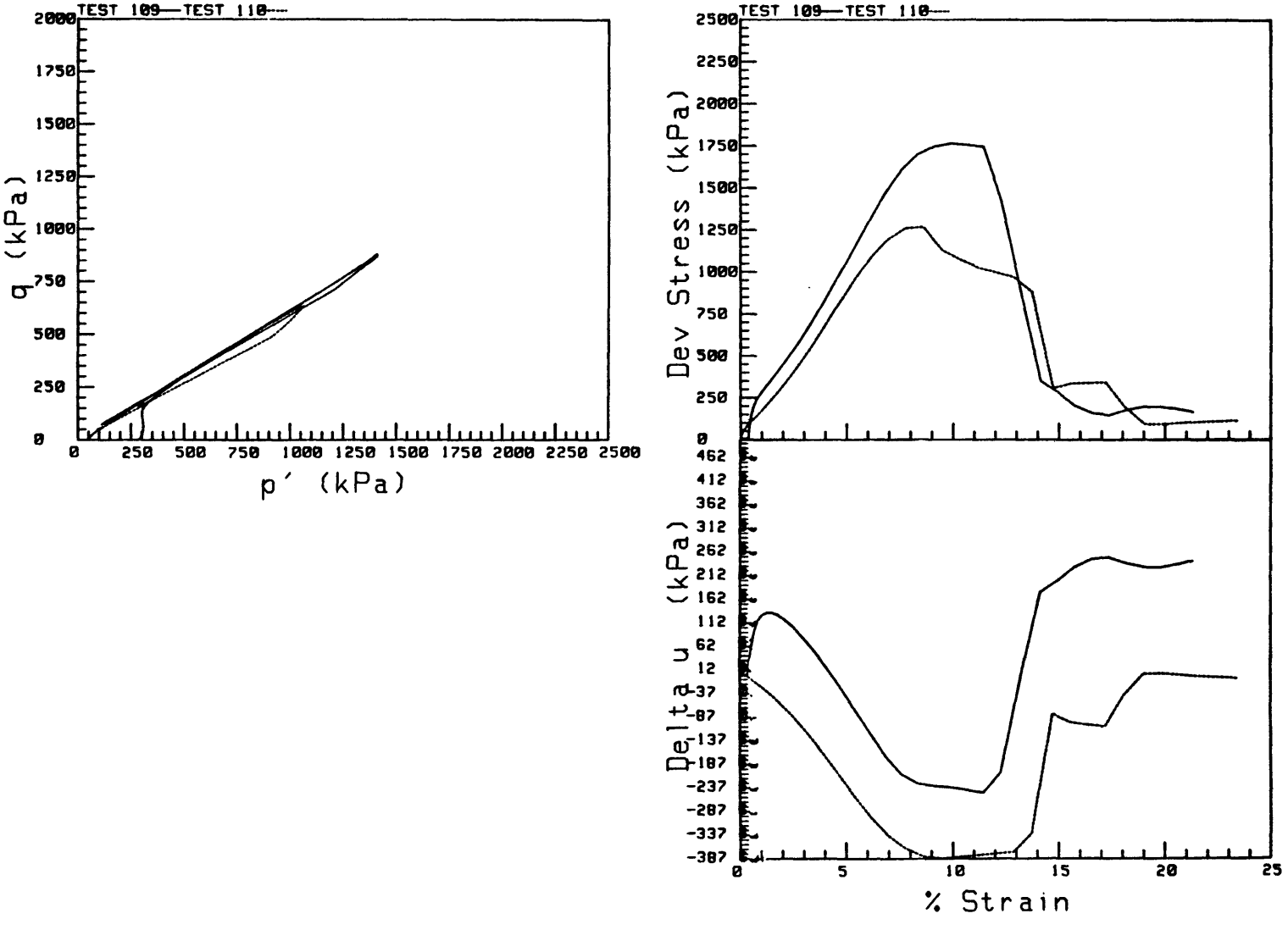

Fig. 8c. Multiple static triaxial test results (core 683 A1).

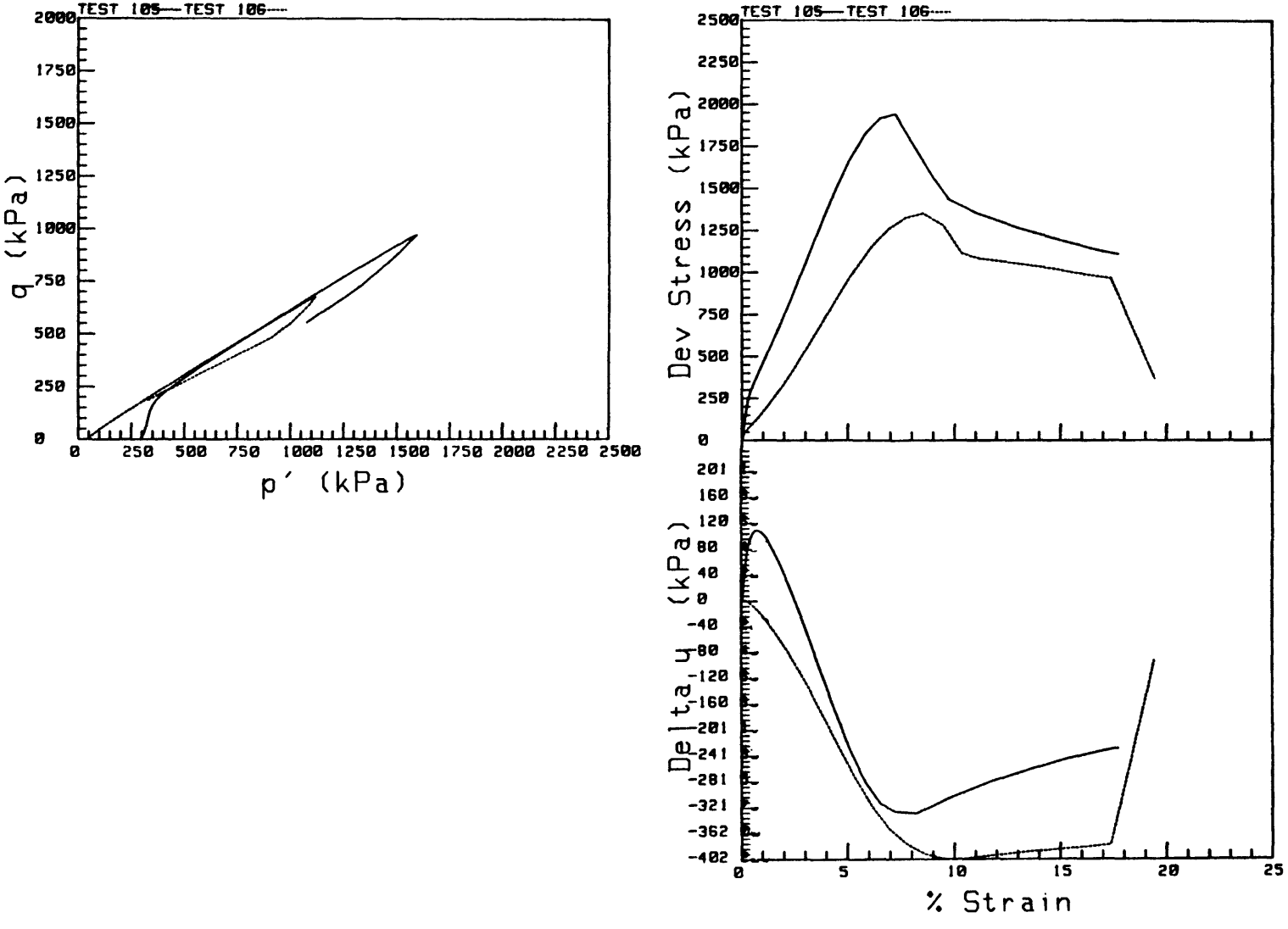

Fig. 8d. Multiple static triaxial test results (core 684 A1).

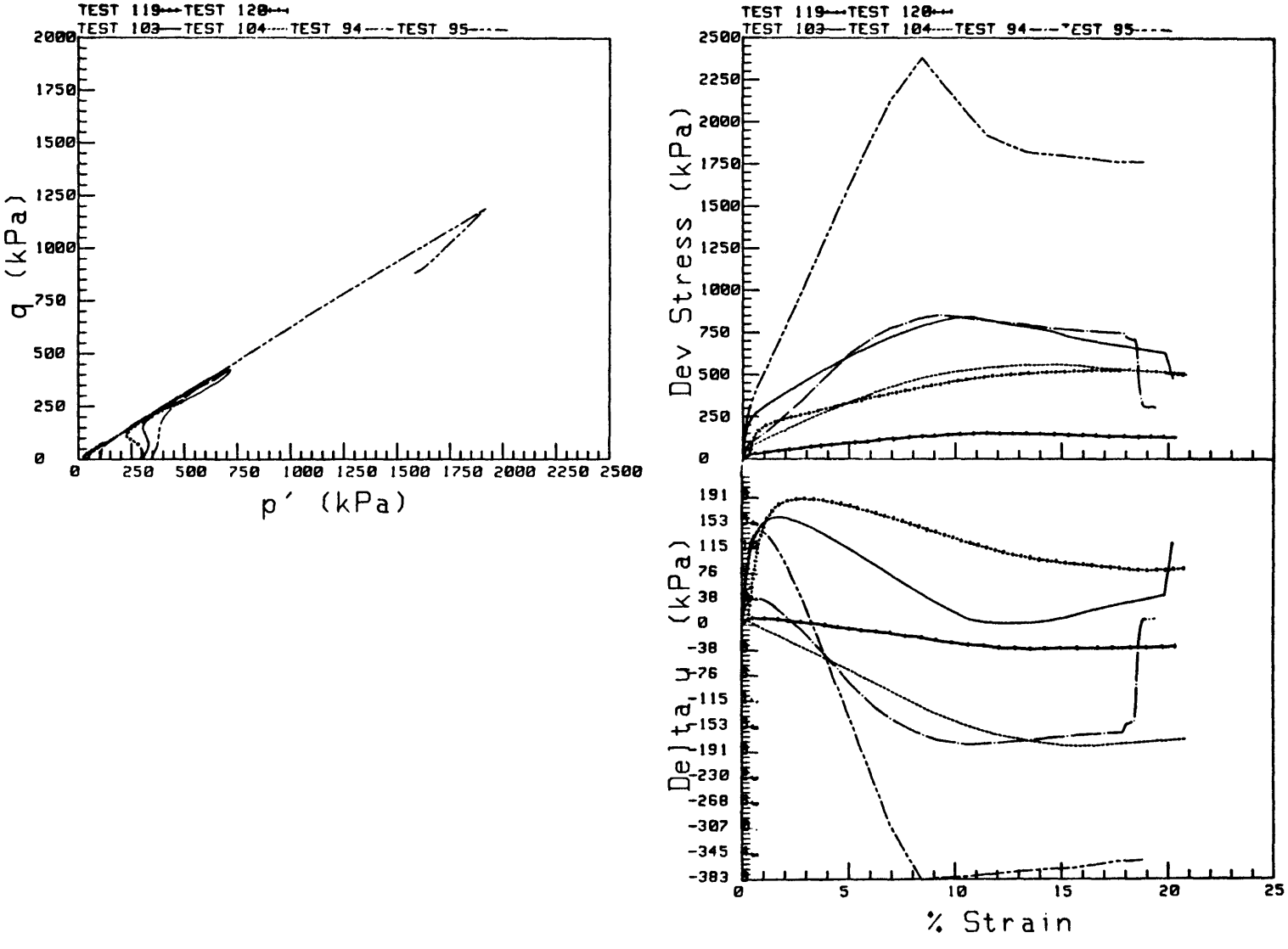

Fig. 8e. Multiple static triaxial test results (core 685 A2).

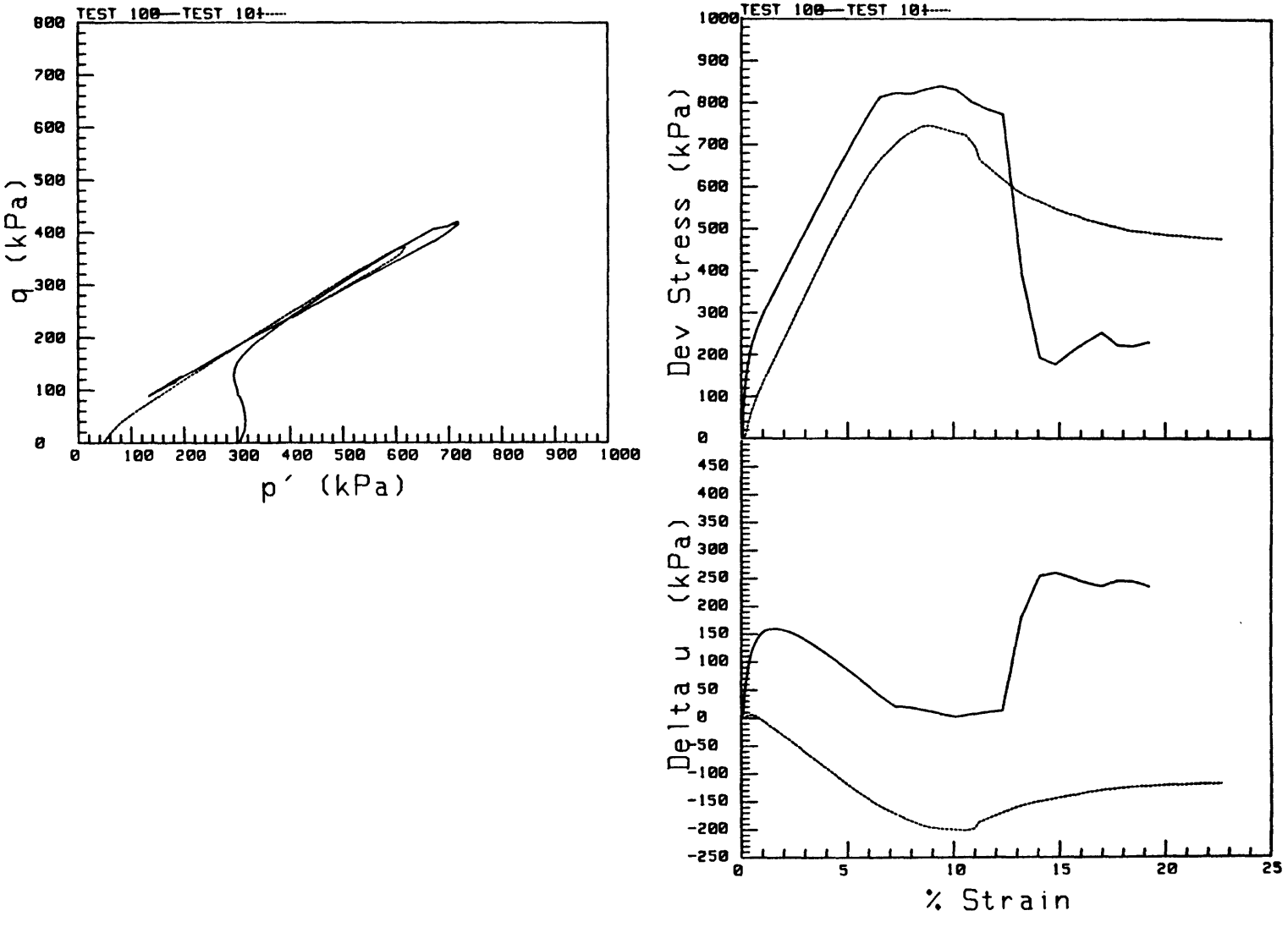

Fig. 8f. Multiple static triaxial test results (core 686 A1).

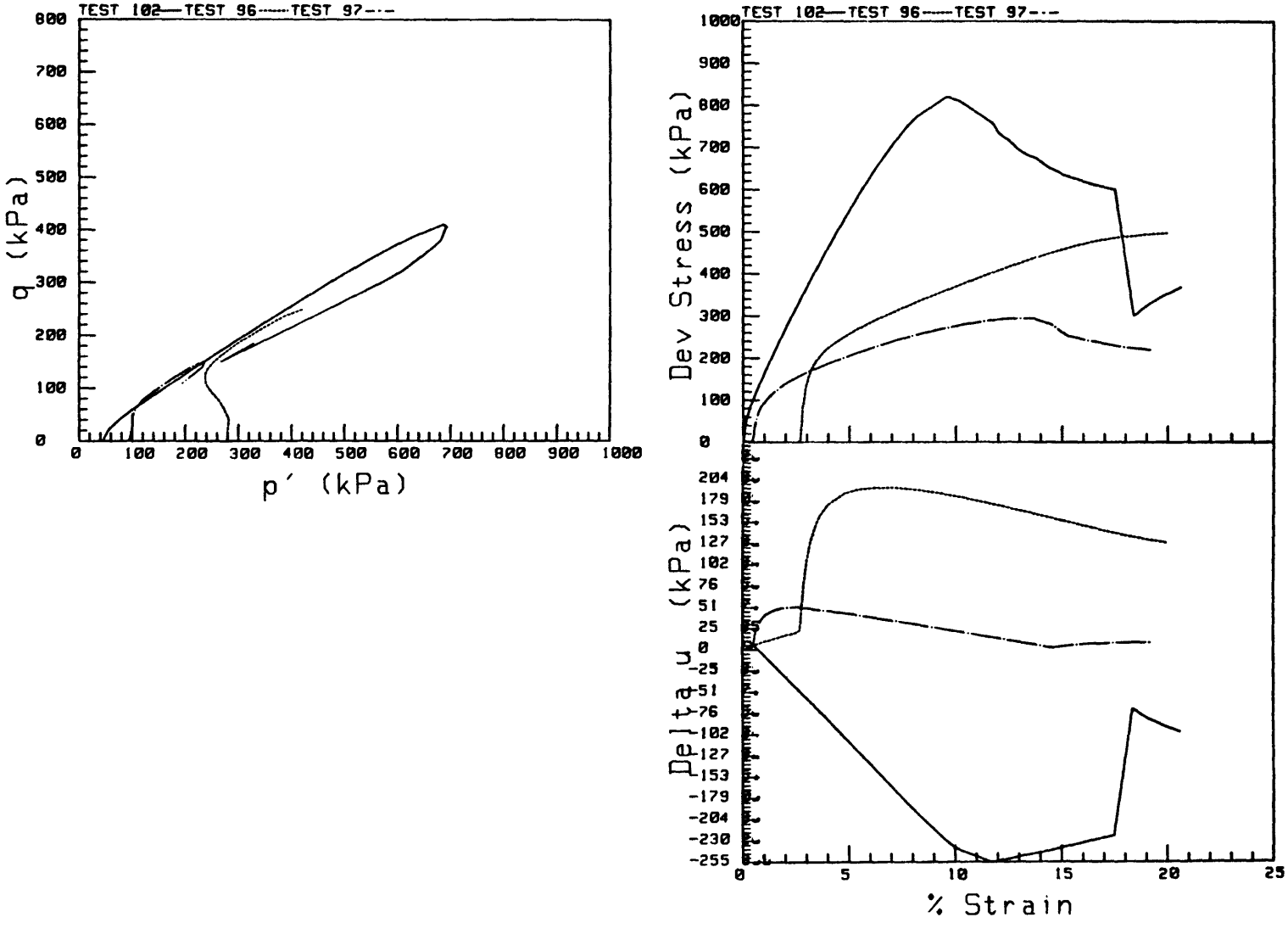

Fig. 8g. Multiple static triaxial test results (core 687 A1).

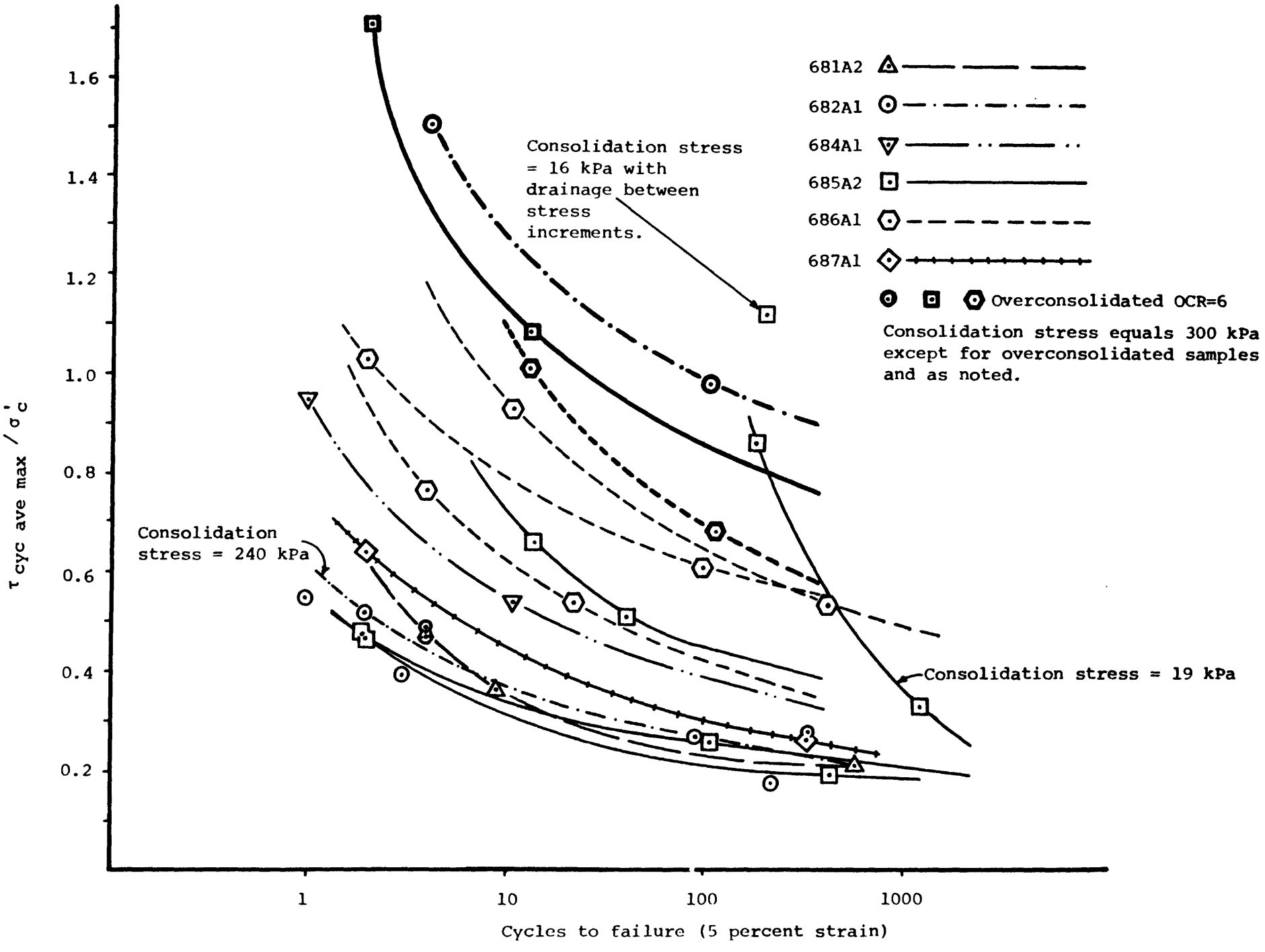

Fig. 9. Cyclic stress ratio vs number of cycles to reach 5% strain in cyclic triaxial tests.

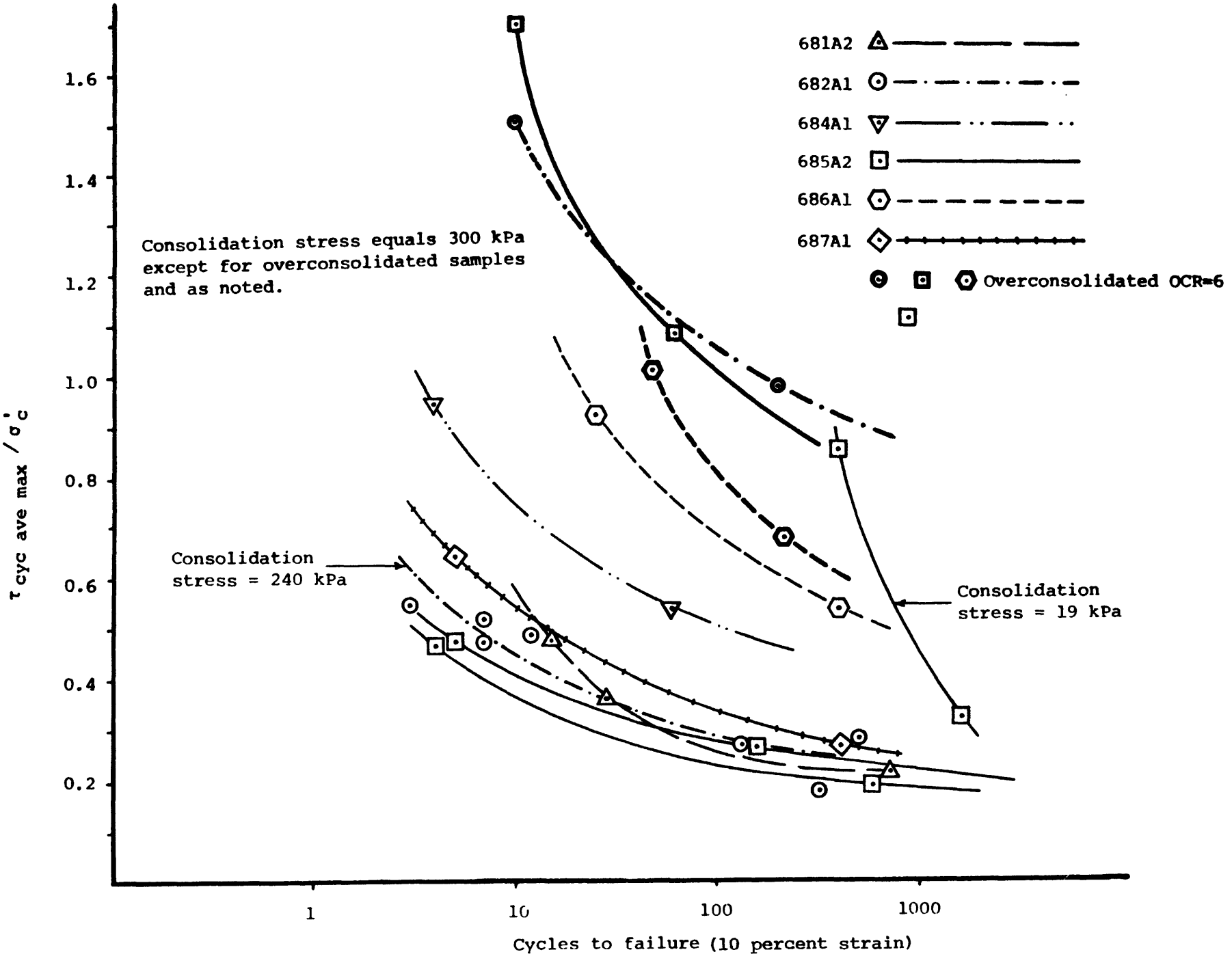

Fig. 10. Cyclic stress ratio vs number of cycles to reach 10% strain in cyclic triaxial tests.

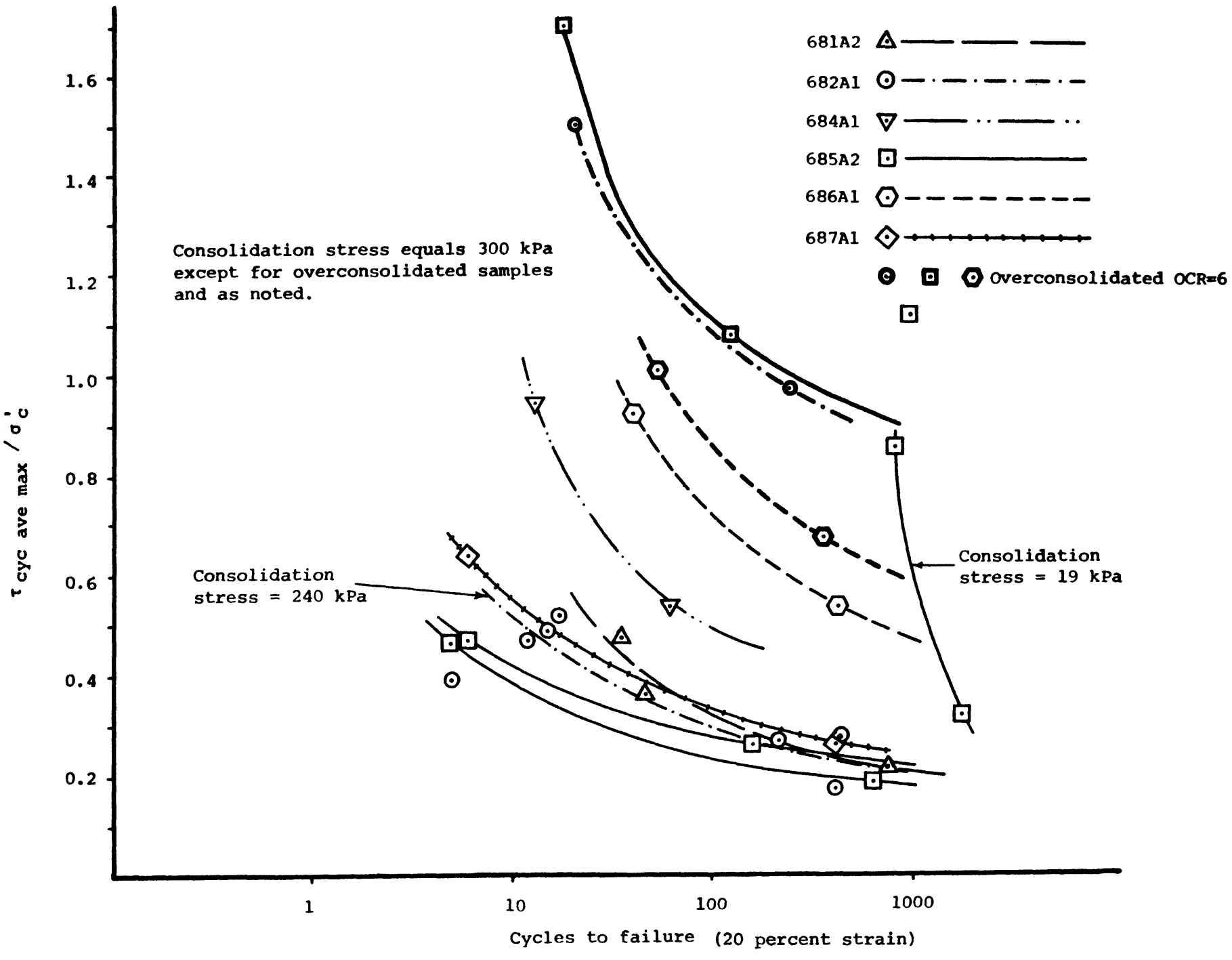

Fig. 11. Cyclic stress ratio vs number of cycles to reach 20% strain in cyclic triaxial tests.

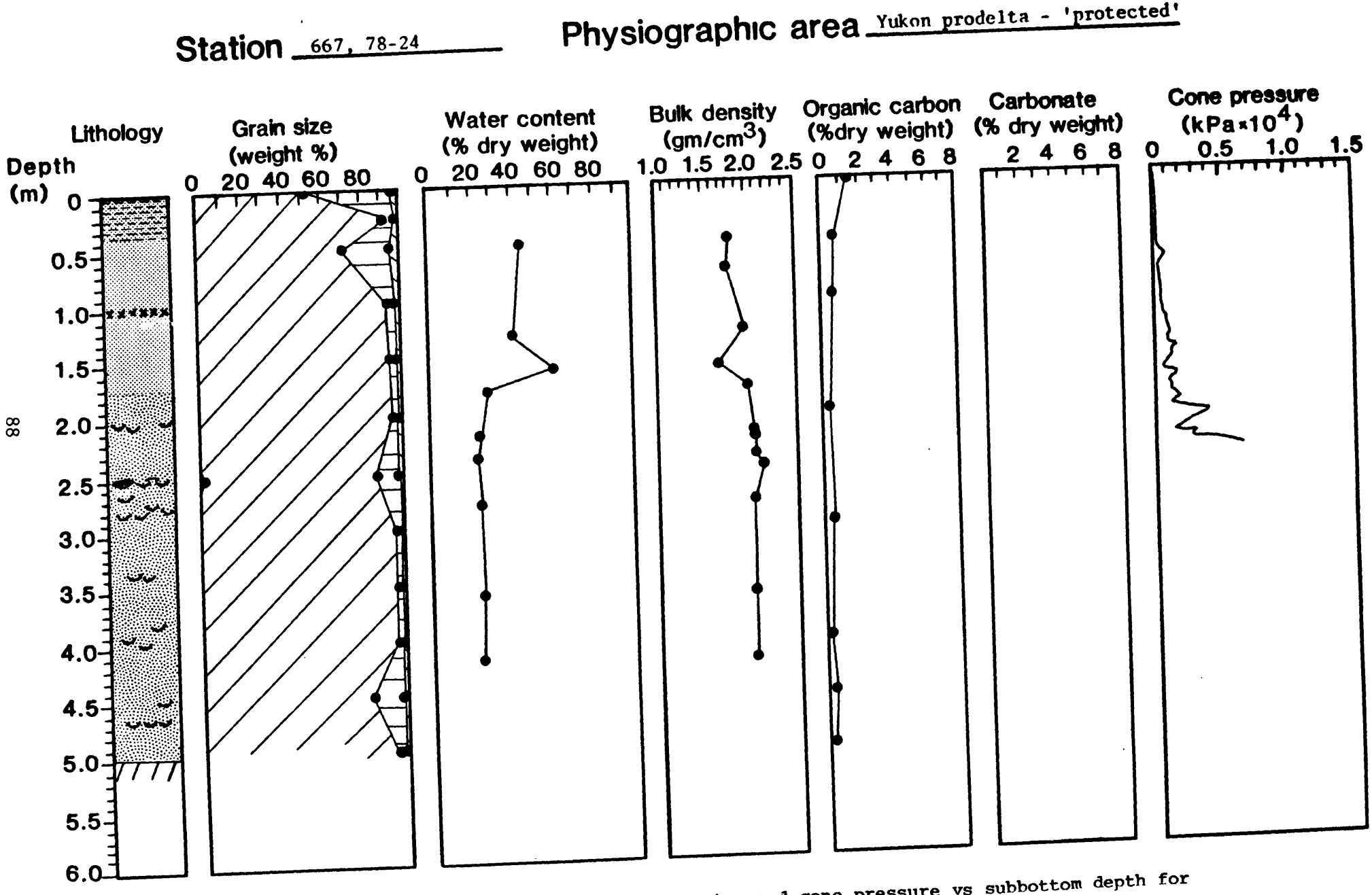

Fig. 12. Lithology, index properties and cone pressure vs subbottom depth for stations 667 and 78-24 (Yukon prodelta - "protected").

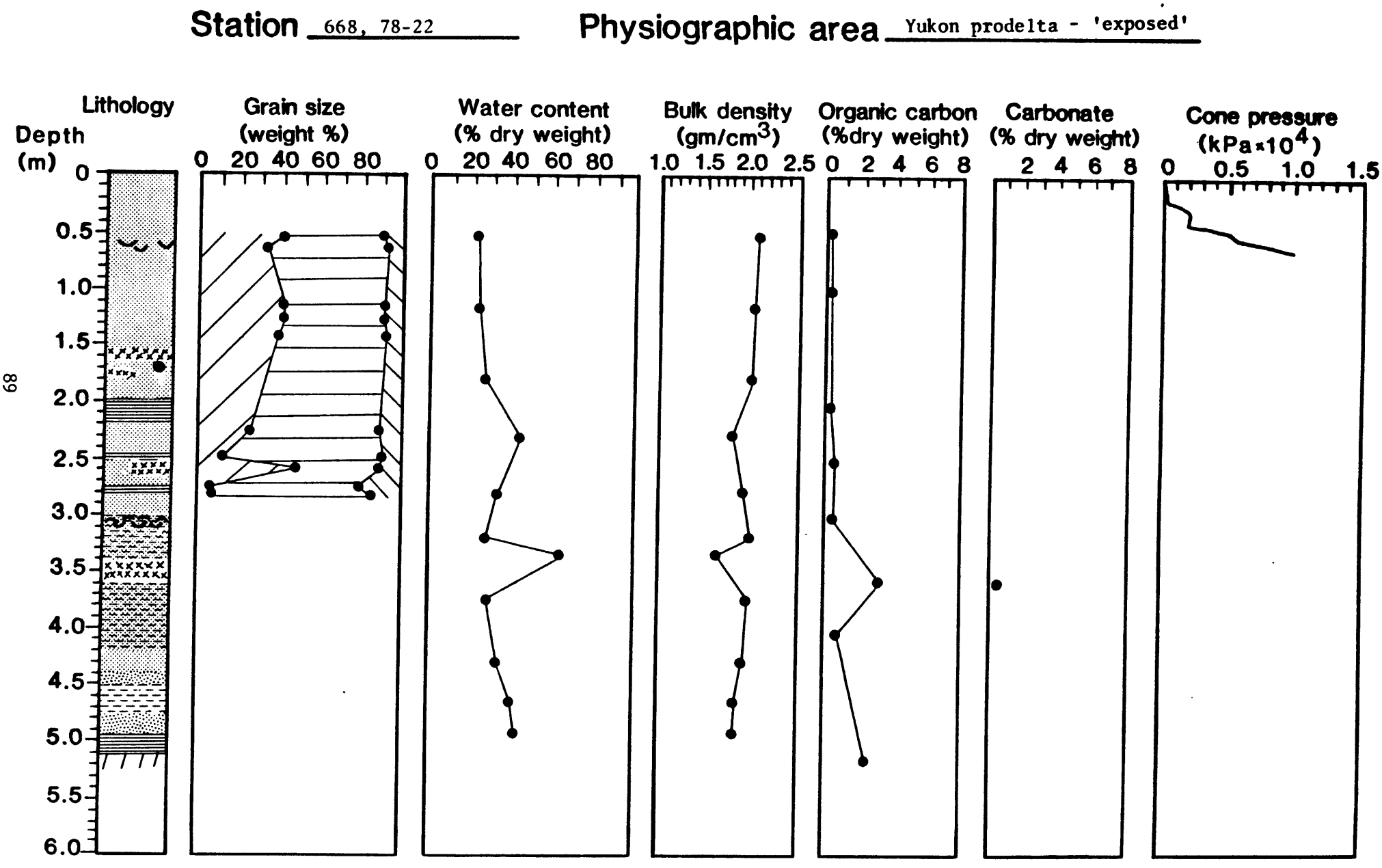

Fig. 13. Lithology, index properties and cone pressure vs subbottom depth for stations 668 and 78-22 (Yukon prodelta - "exposed").

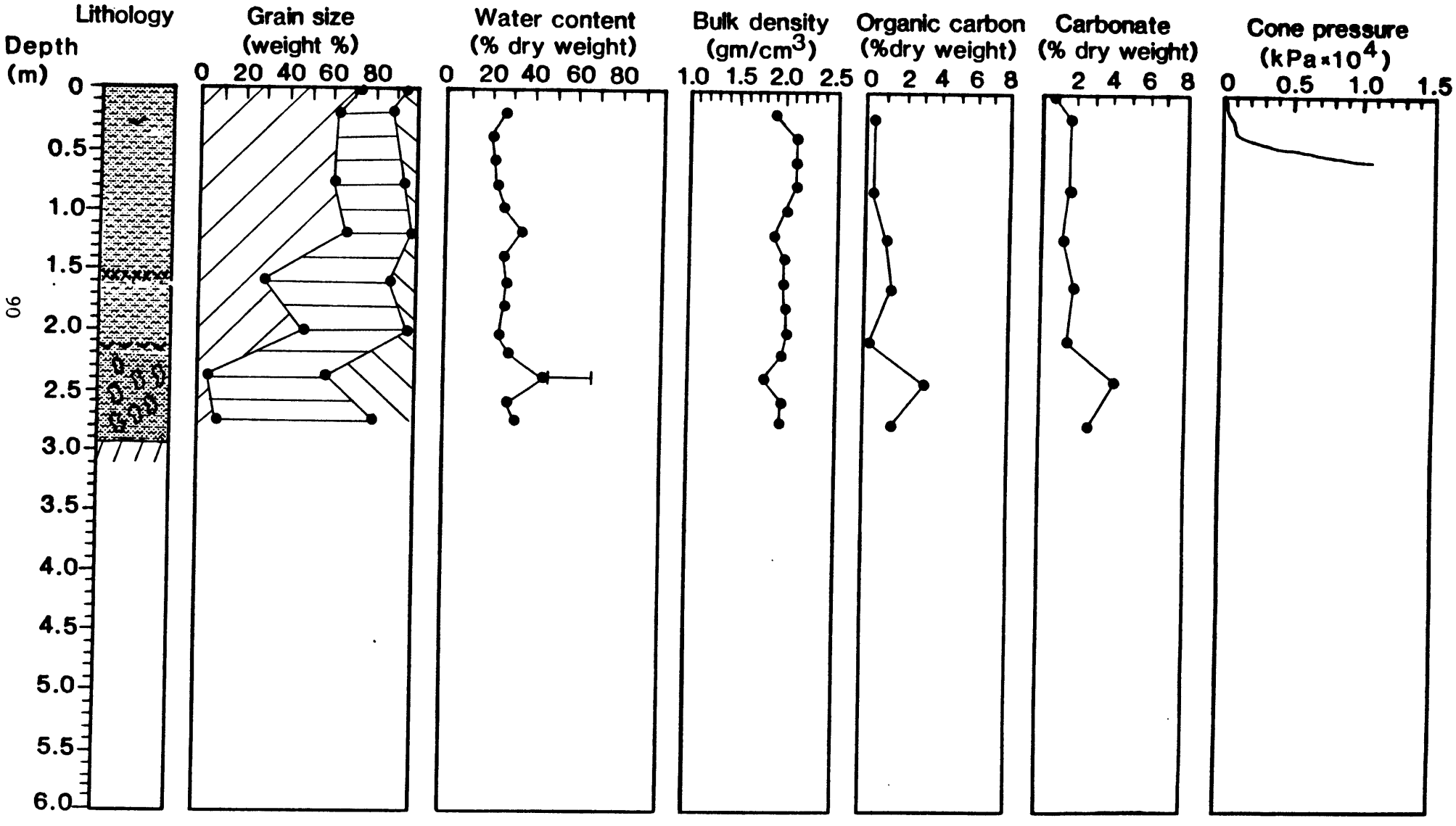

Fig. 14. Lithology, index properties and cone pressure vs subbottom depth for stations 686 and 669 (Yukon prodelta - "exposed").

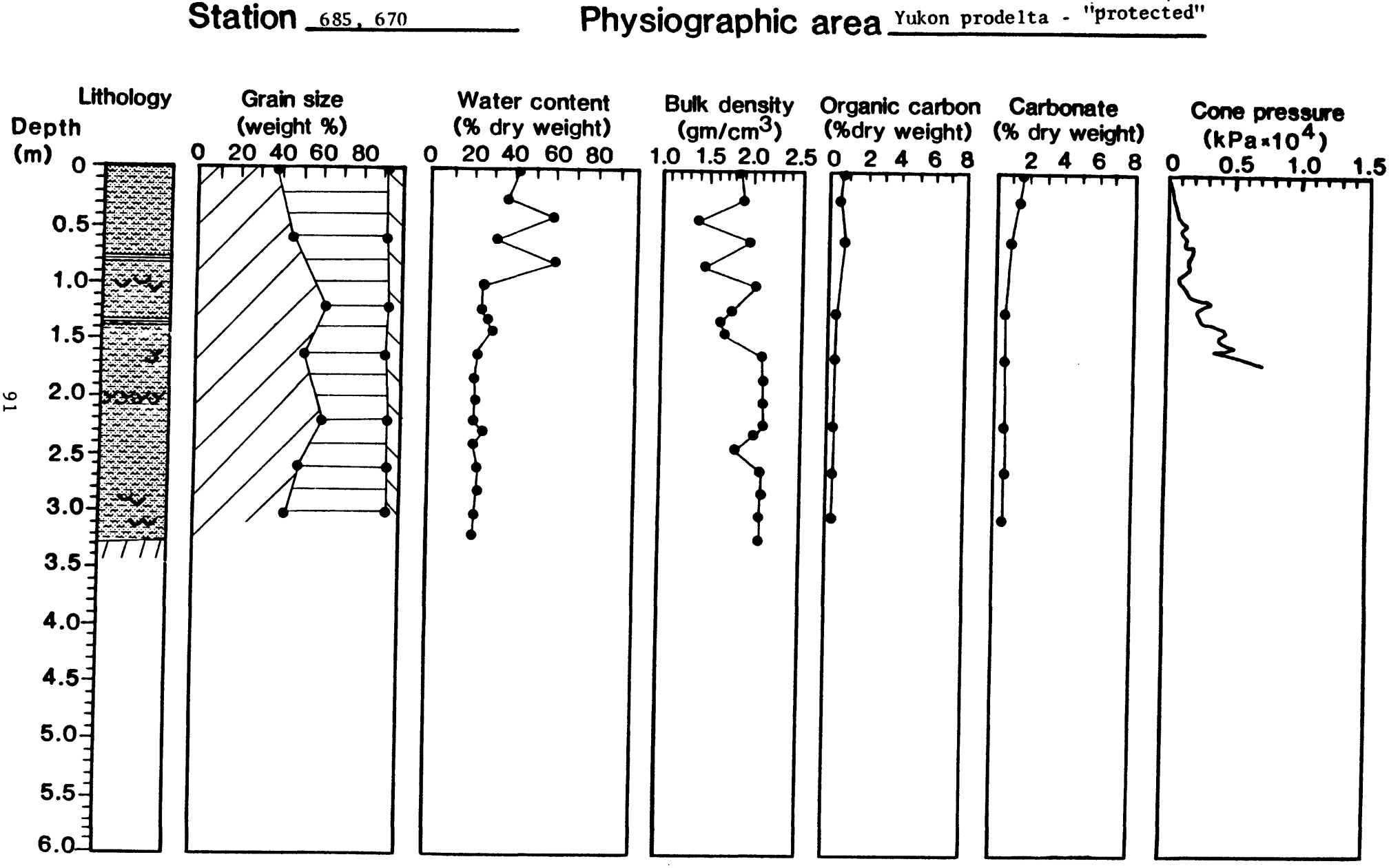

Fig. 15. Lithology, index properties and cone pressure vs subbottom depth for stations 685 and 670 (Yukon prodelta - "protected").

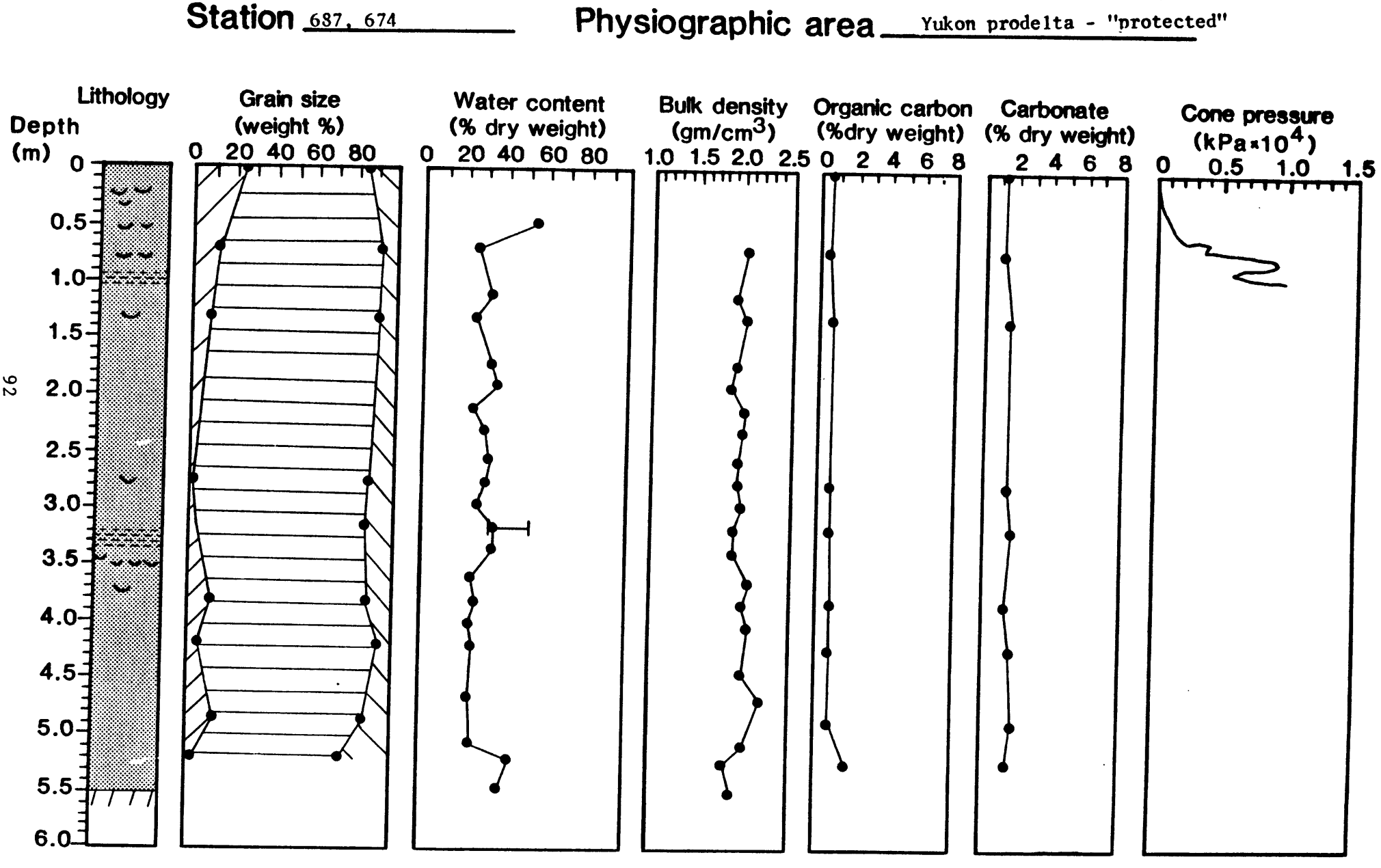

Fig. 16. Lithology, index properties and cone pressure vs subbottom depth for stations 687 and 674 (Yukon prodelta - "protected").

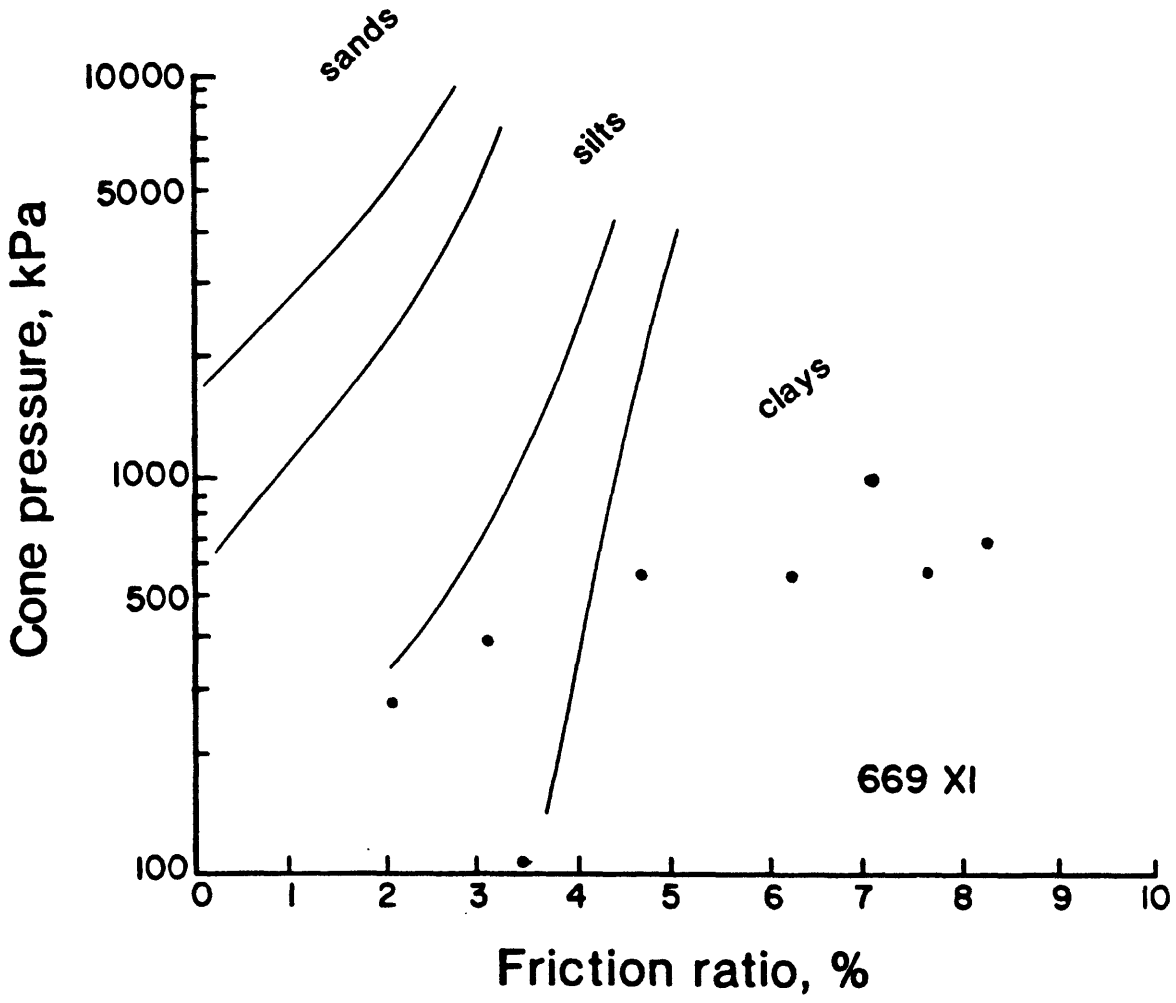

Fig. 17a. Sediment type determined from cone penetration test 669X1 (Yukon prodelta - "exposed" - near station 686).

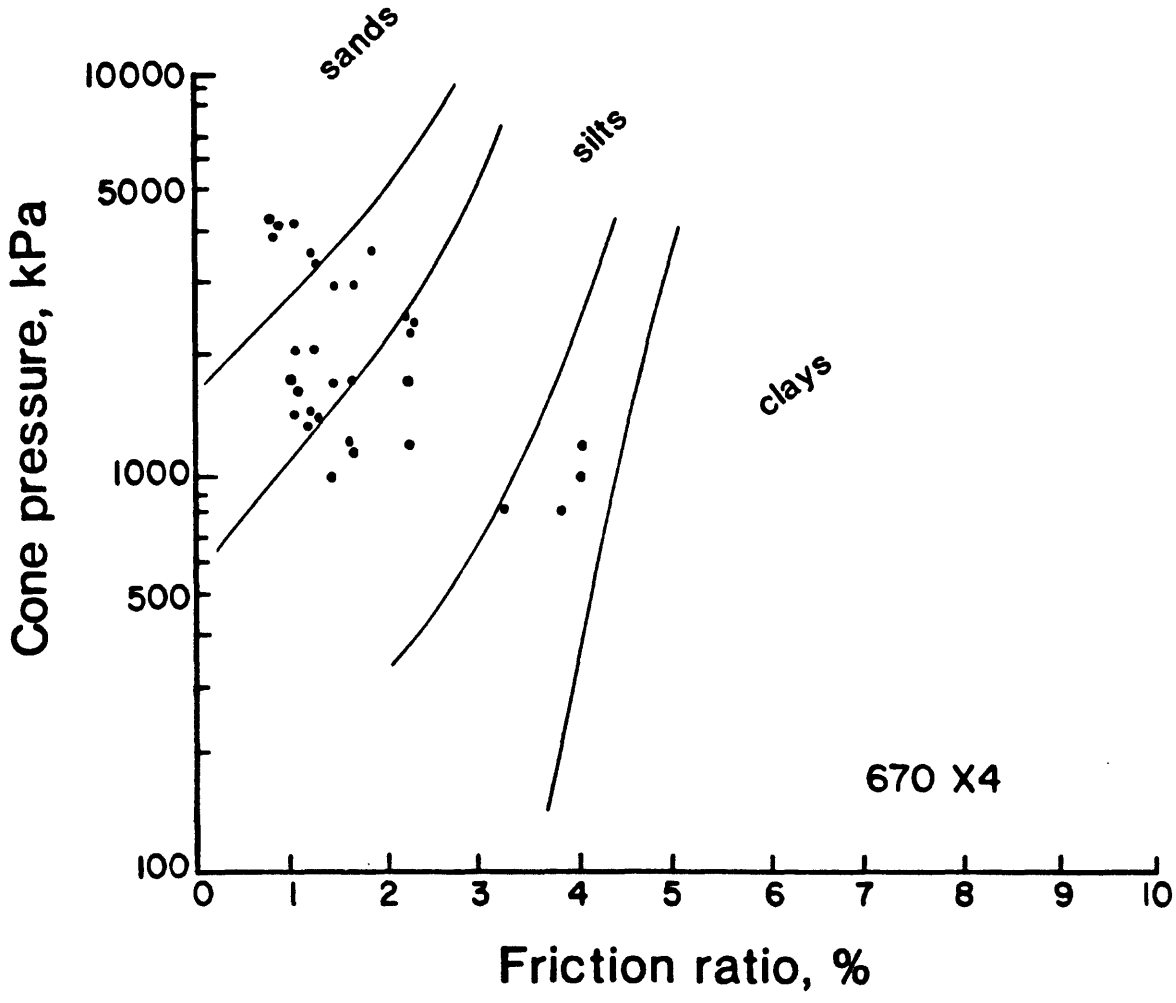

Fig. 17b. Sediment type determined from cone penetration test 670X4 (Yukon prodelta - "protected" - near station 685).

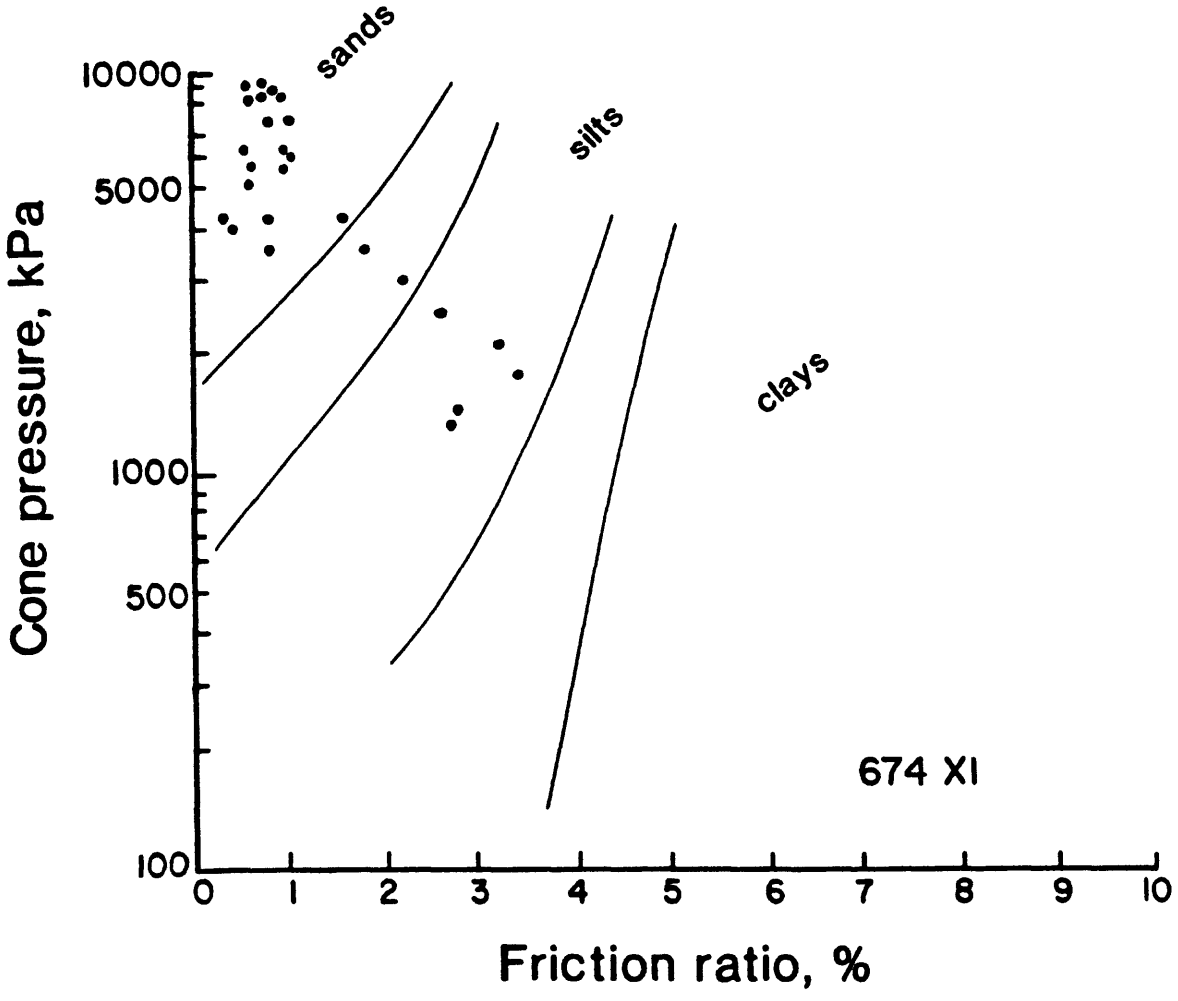

Fig. 17c. Sediment type determined from cone penetration test 674X1 (Yukon prodelta - "protected" - near station 687).

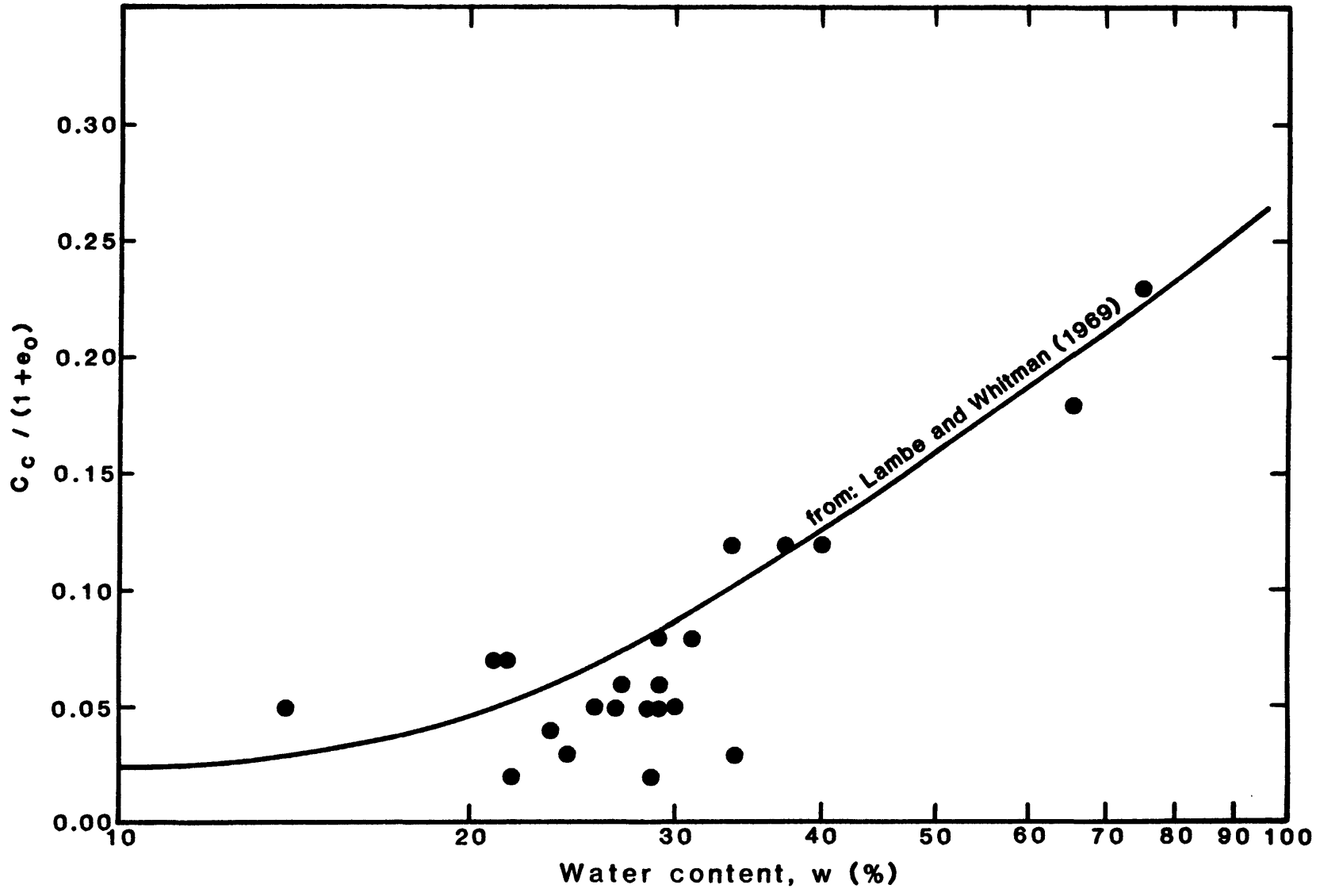

Fig. 18. Compression index (C_c) determined from consolidation tests related to the initial void ratio (e_o) vs water content (w).

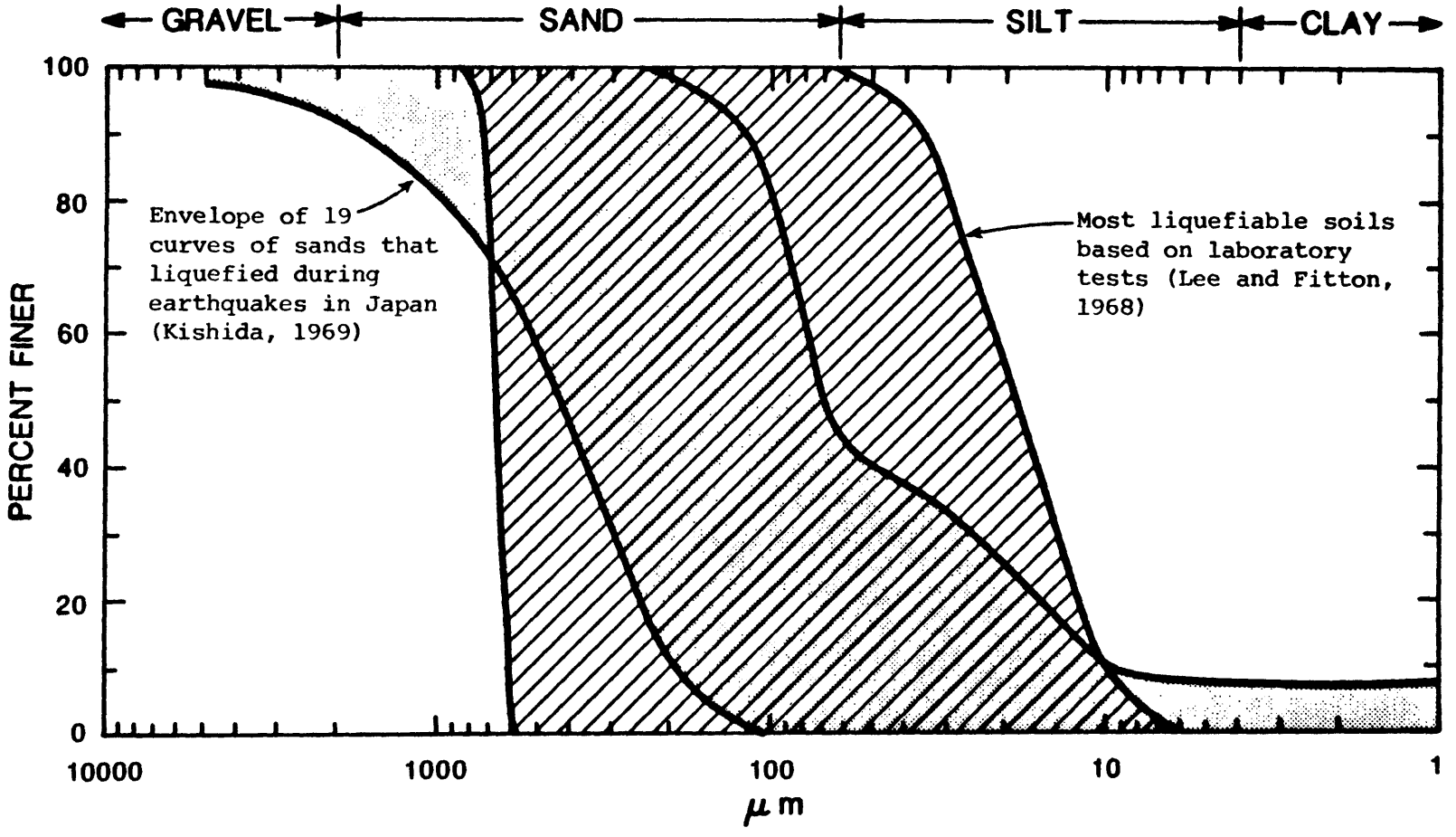

Fig. 19. Zones of grain size distributions of liquefiable soil (from Finn, 1972).

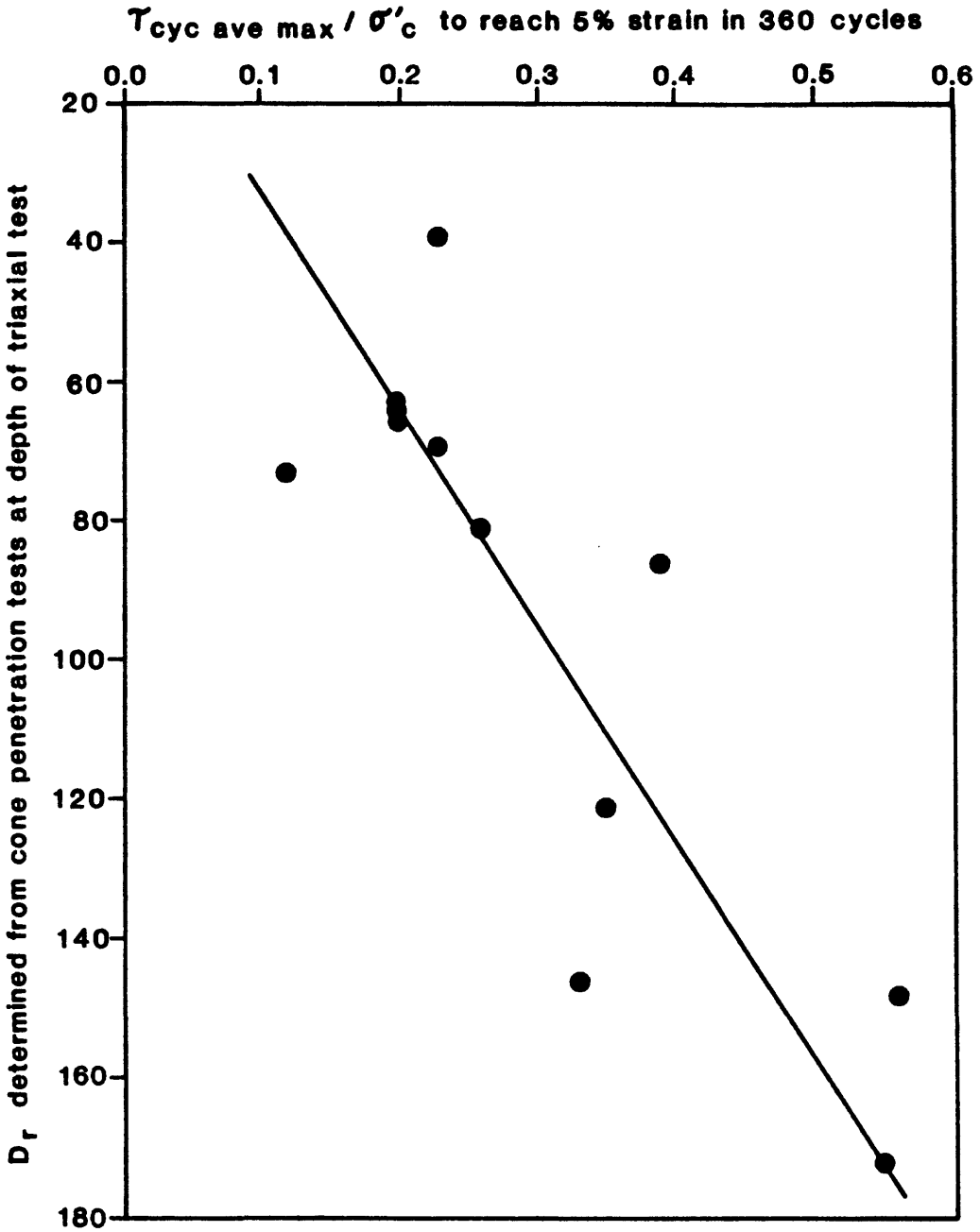

Fig. 20. Cyclic stress ratio determined from cyclic triaxial tests vs the relative density of nearby sediment determined from cone penetration tests.

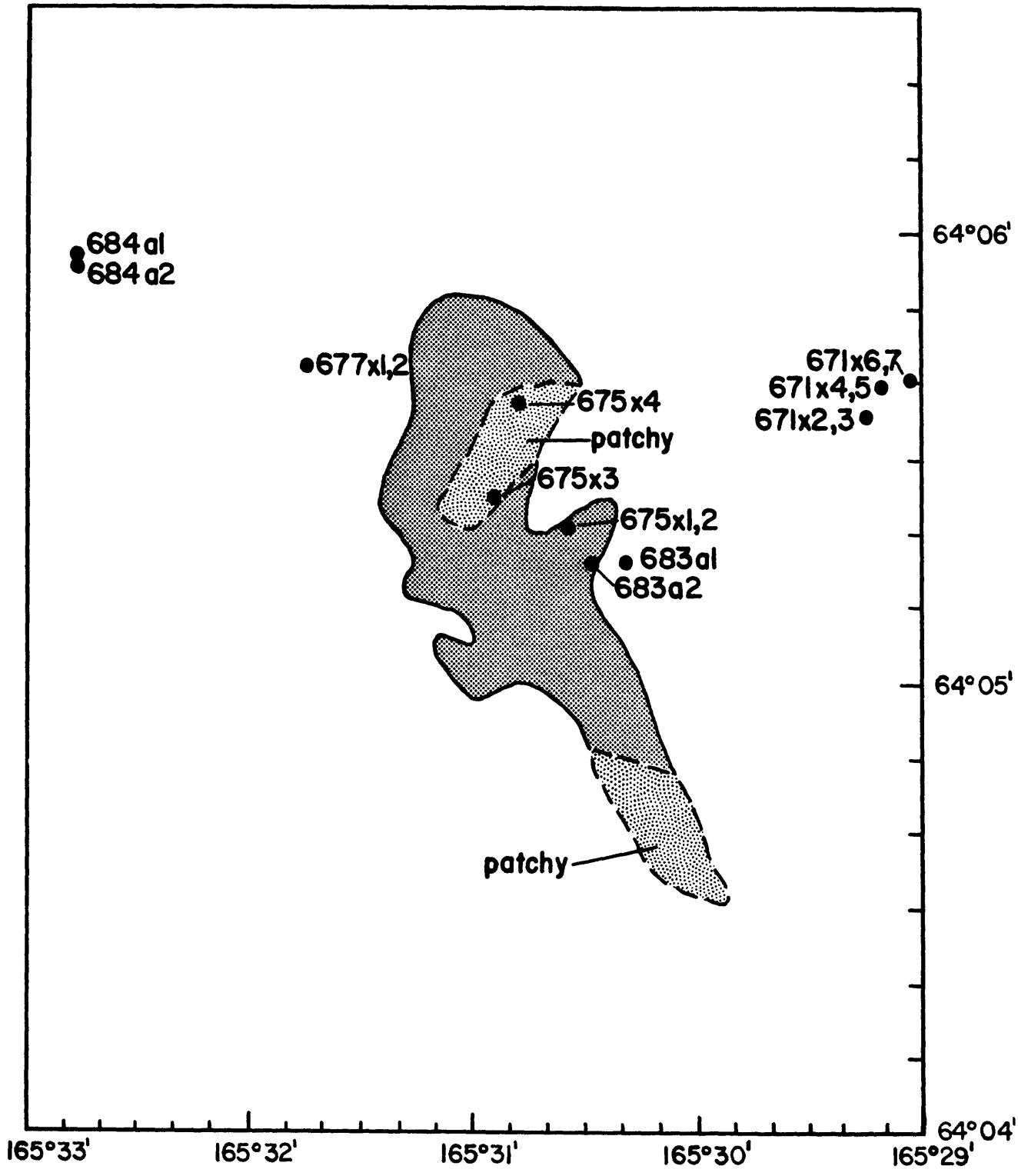

Fig. 21. Map of thermogenic gas seep.

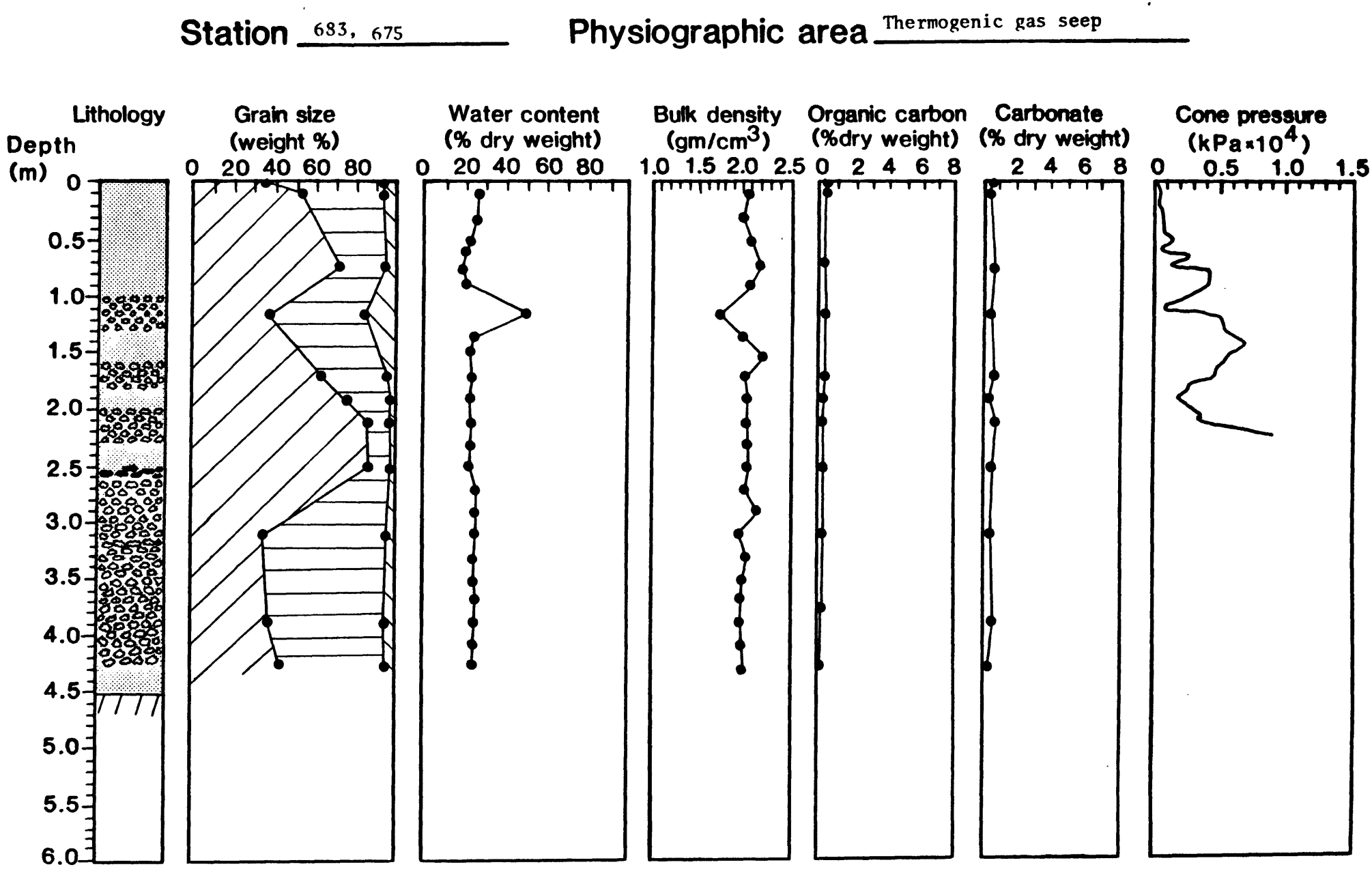

Fig. 22. Lithology, index properties and cone pressure vs subbottom depth for stations 683 and 675 (thermogenic gas seep).

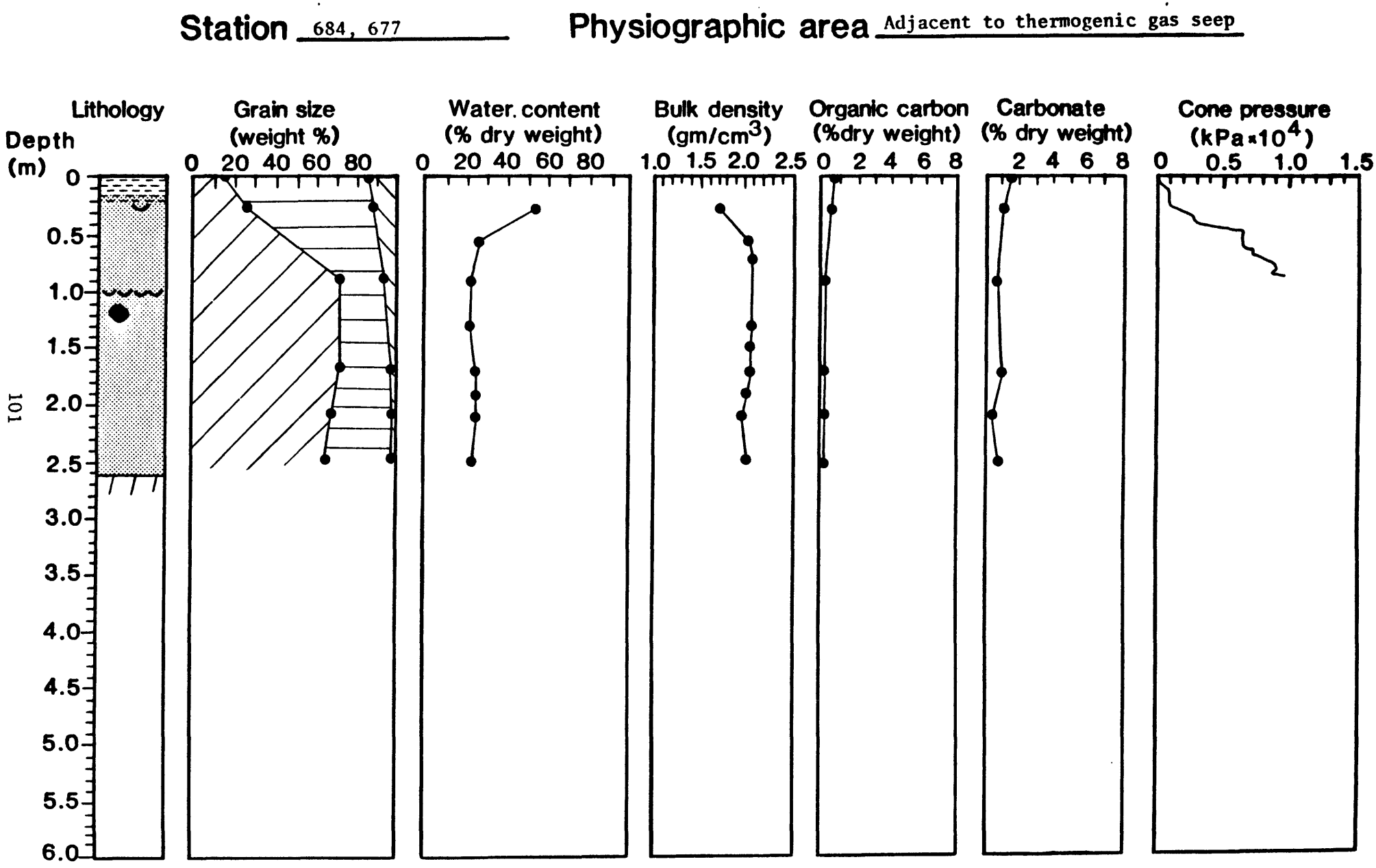

Fig. 23. Lithology, index properties and cone pressure vs subbottom depth for stations 684 and 677 (adjacent to thermogenic gas seep).

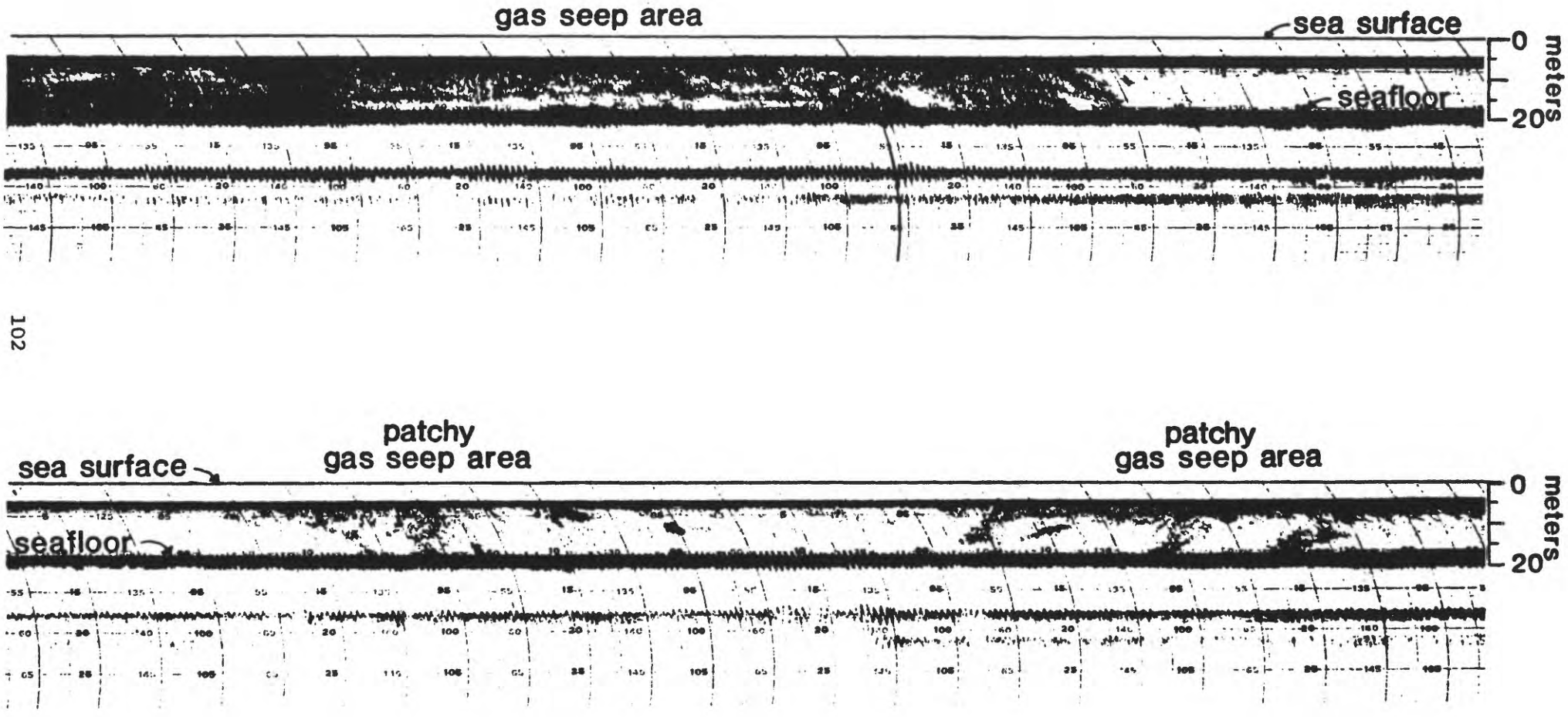

Fig. 24. Fathometer record of thermogenic gas seep.

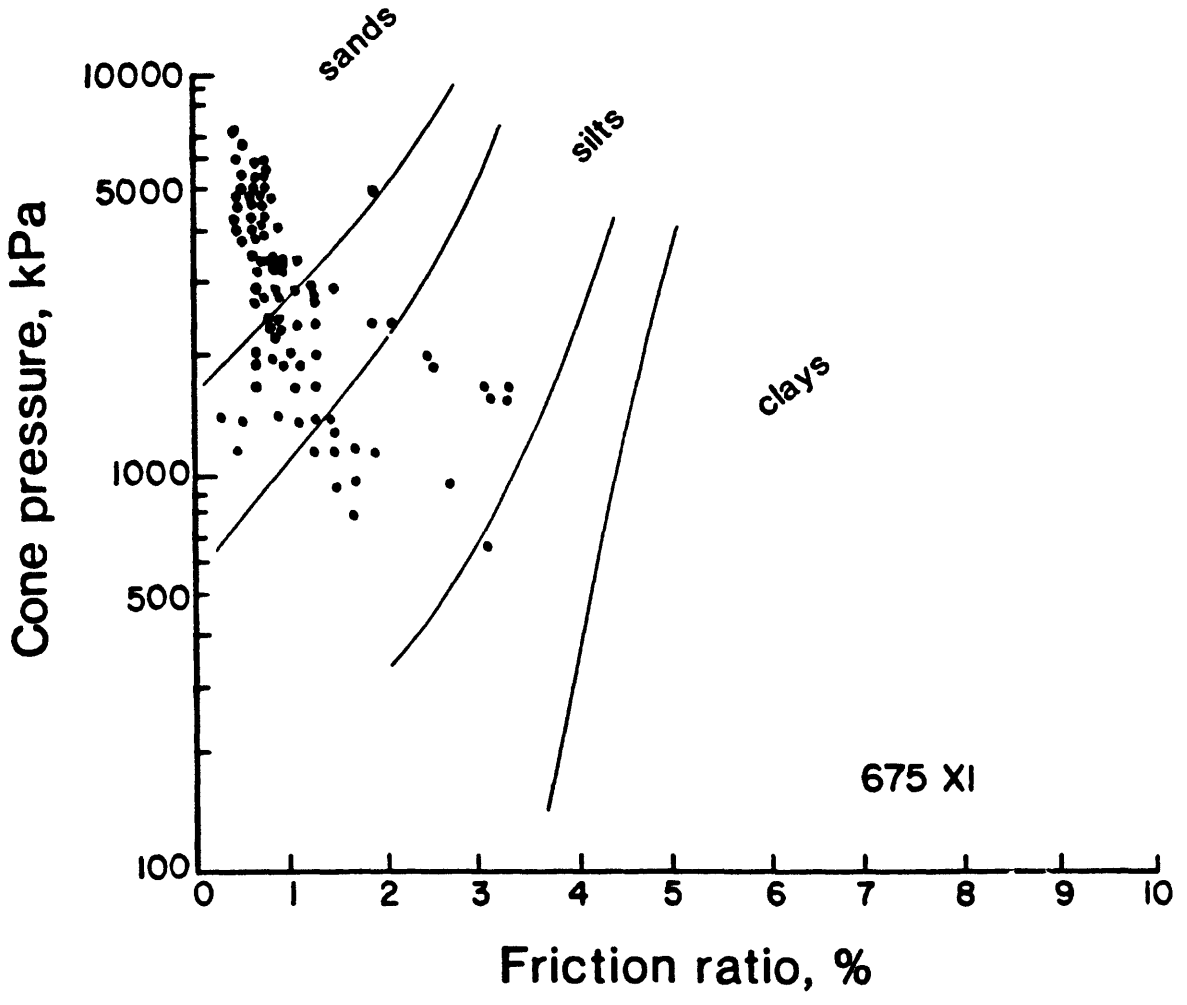

Fig. 25. Sediment type determined from cone penetration test 675X1 (thermogenic gas seep - near station 683).

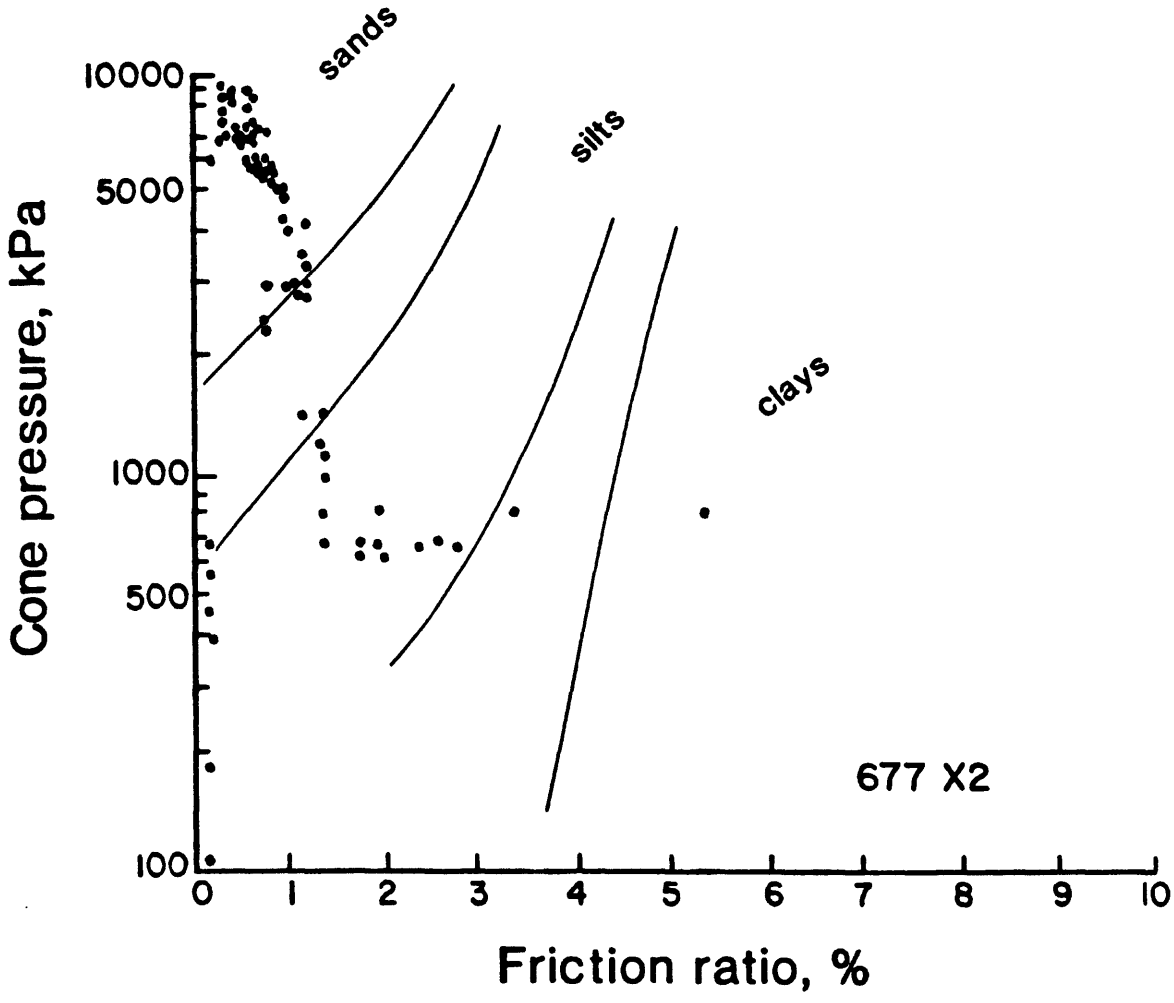

Fig. 26. Sediment type determined from cone penetration test 677X2 (west of thermogenic gas seep-near station 684).

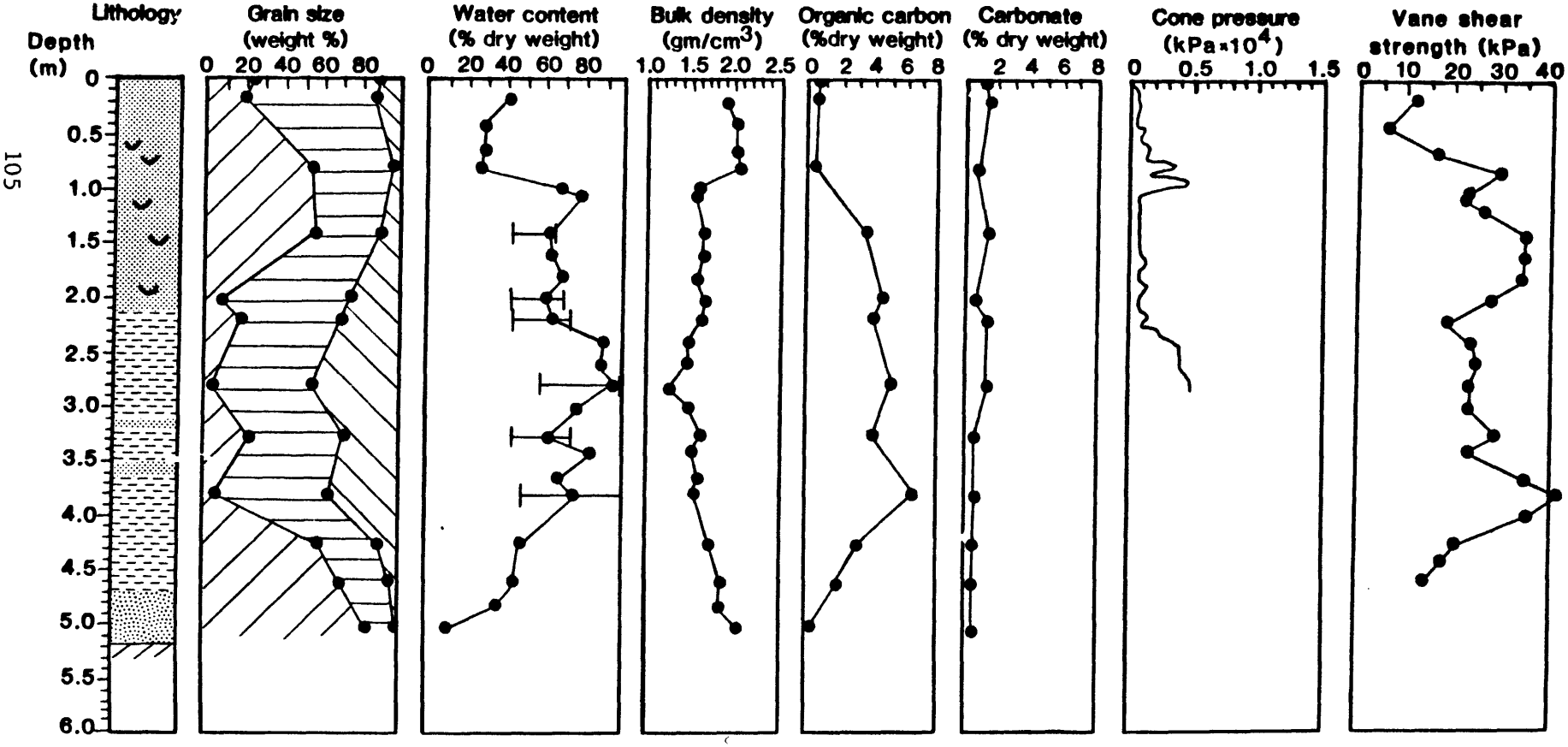

Fig. 27. Lithology, index properties and cone pressure vs subbottom depth for stations 682 and 676 (biogenic gas seep, south of Nome).

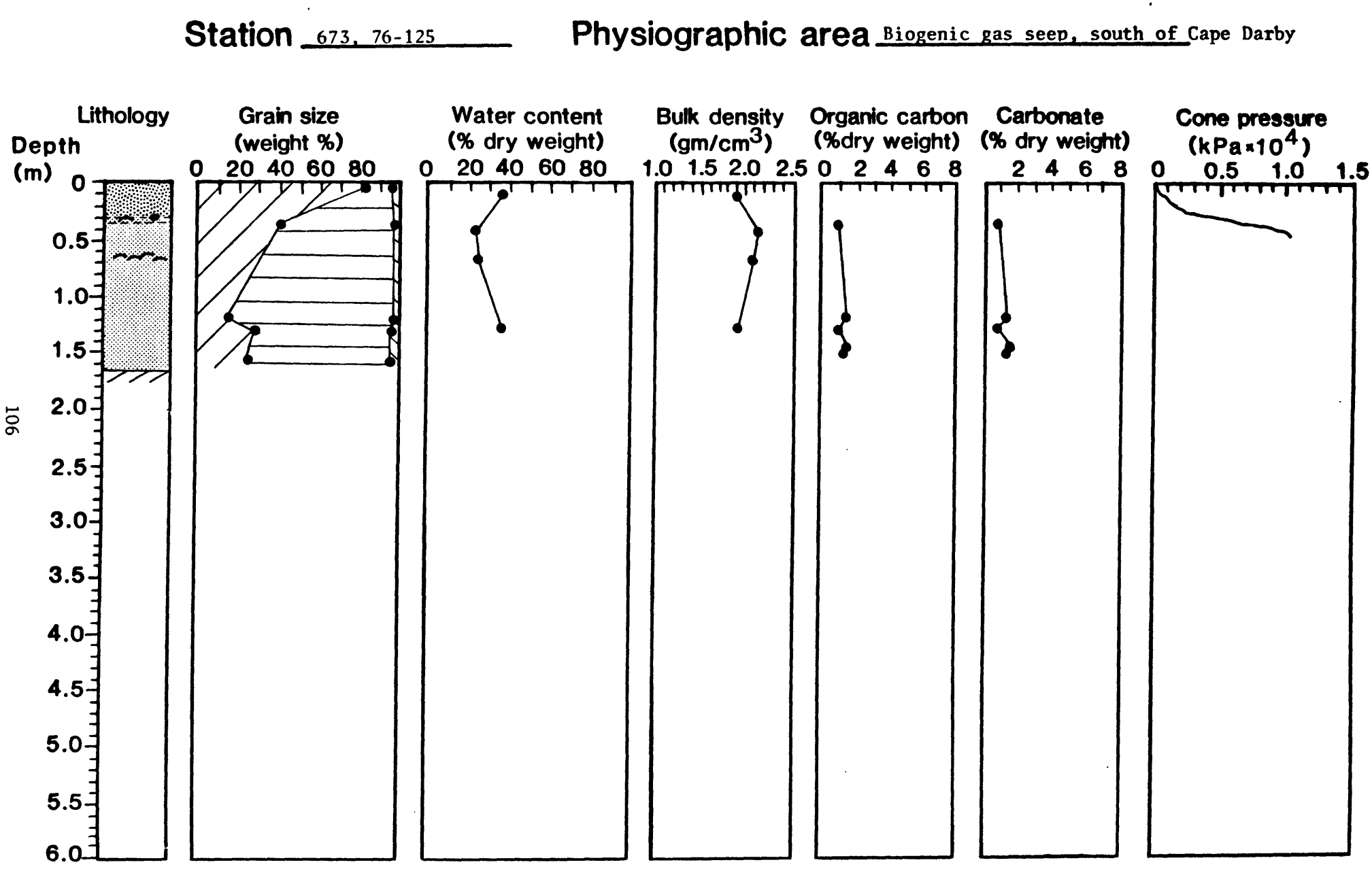

Fig. 28. Lithology, index properties and cone pressure vs subbottom depth for stations 673 and 76-125 (biogenic gas seep, south of Cape Darby).

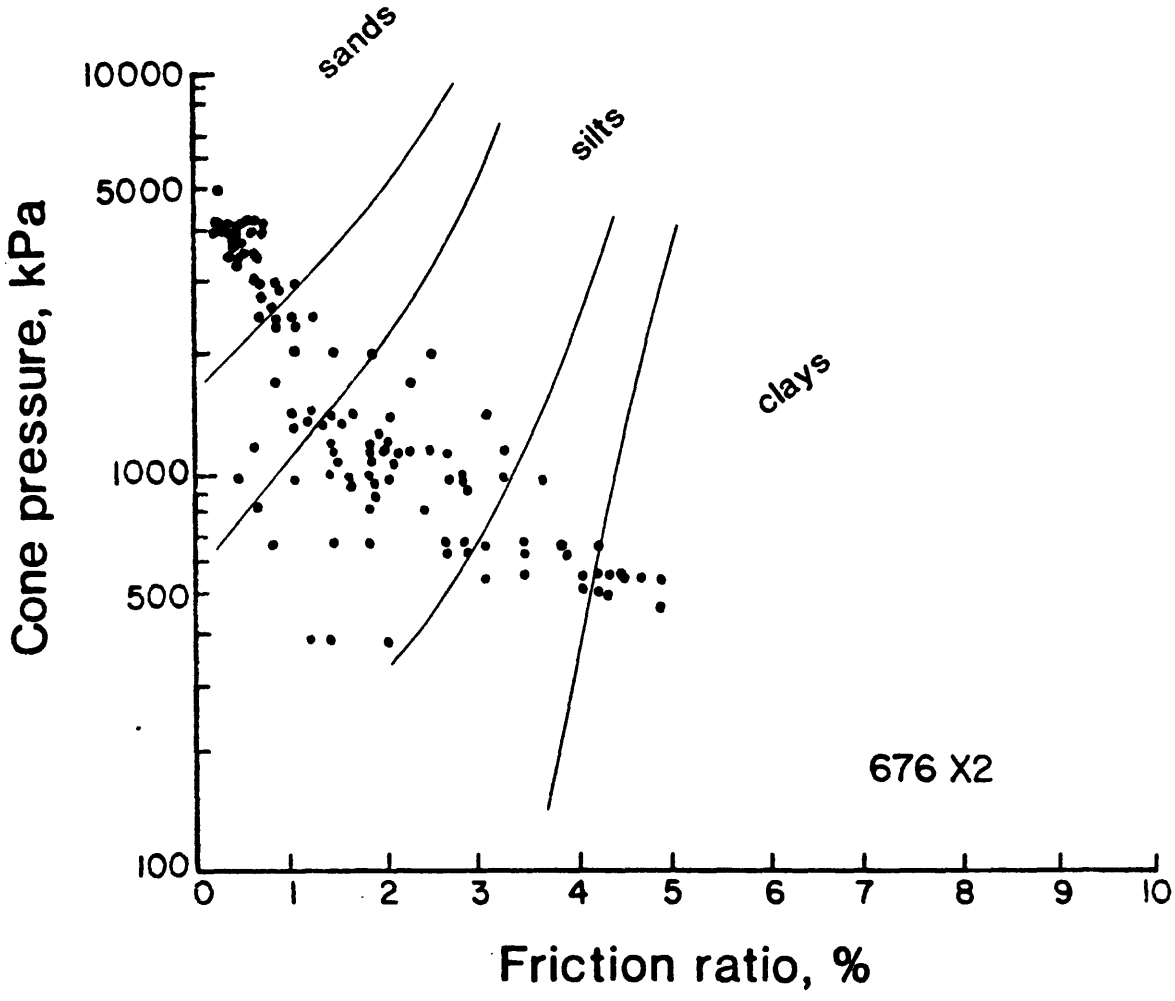

Fig. 29. Sediment type determined from cone penetration test 676X2 (biogenic gas seep, south of Nome - near station 682).

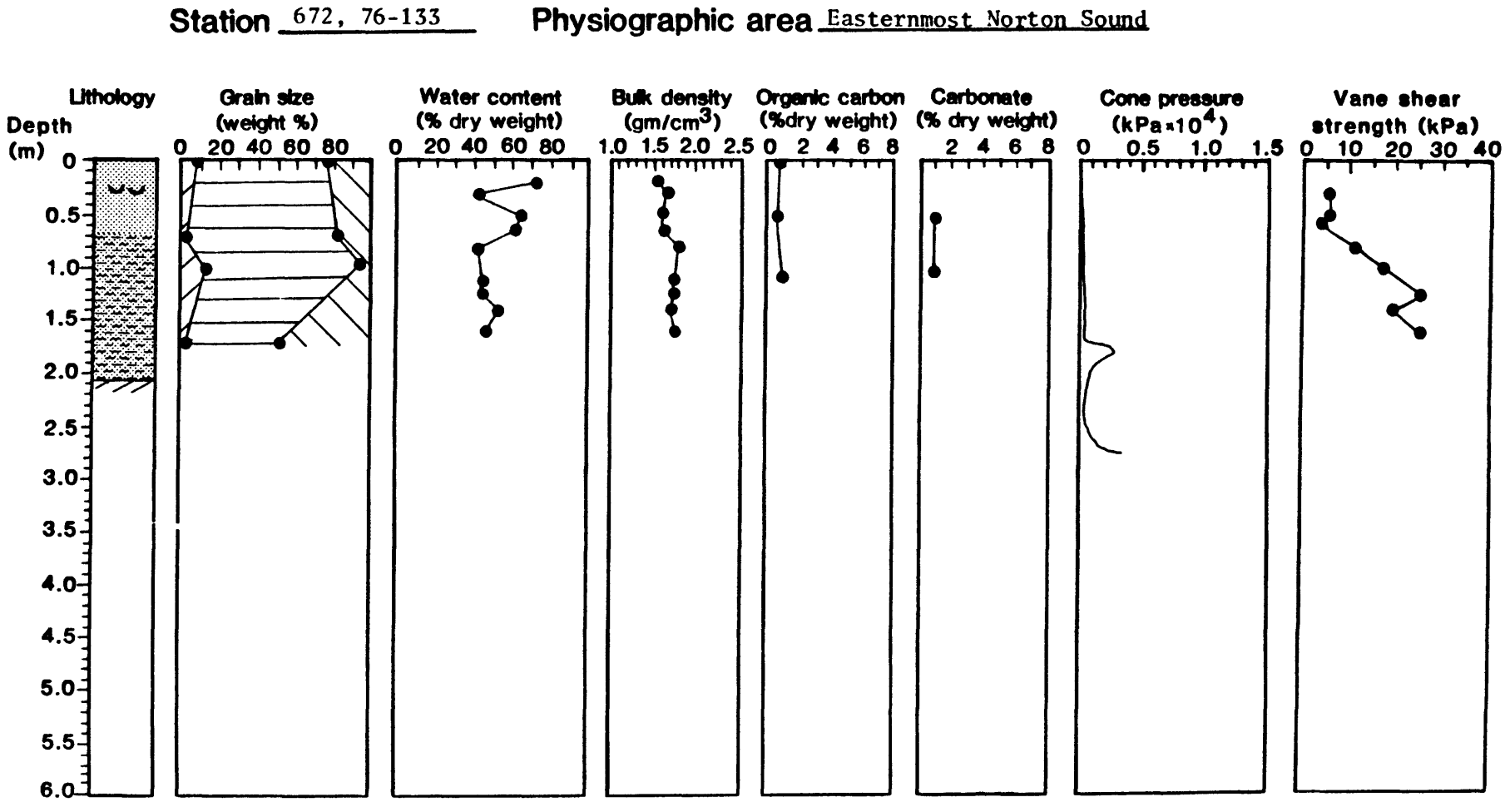

Fig. 30. Lithology, index properties and cone pressure vs subbottom depth for stations 672 and 76-133 (easternmost Norton Sound).

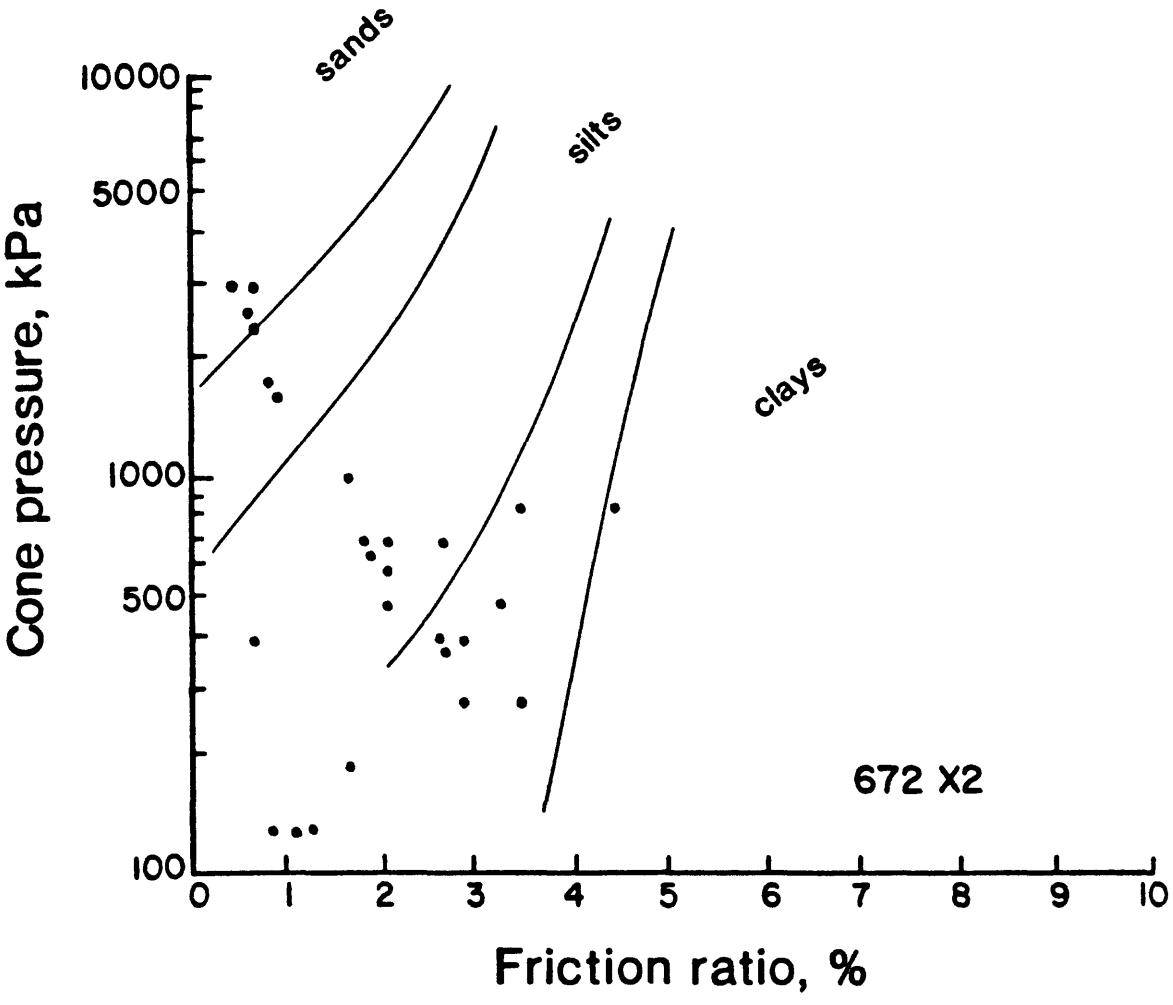

Fig. 31. Sediment type determined from cone penetration test 672X2 (easternmost Norton Sound).

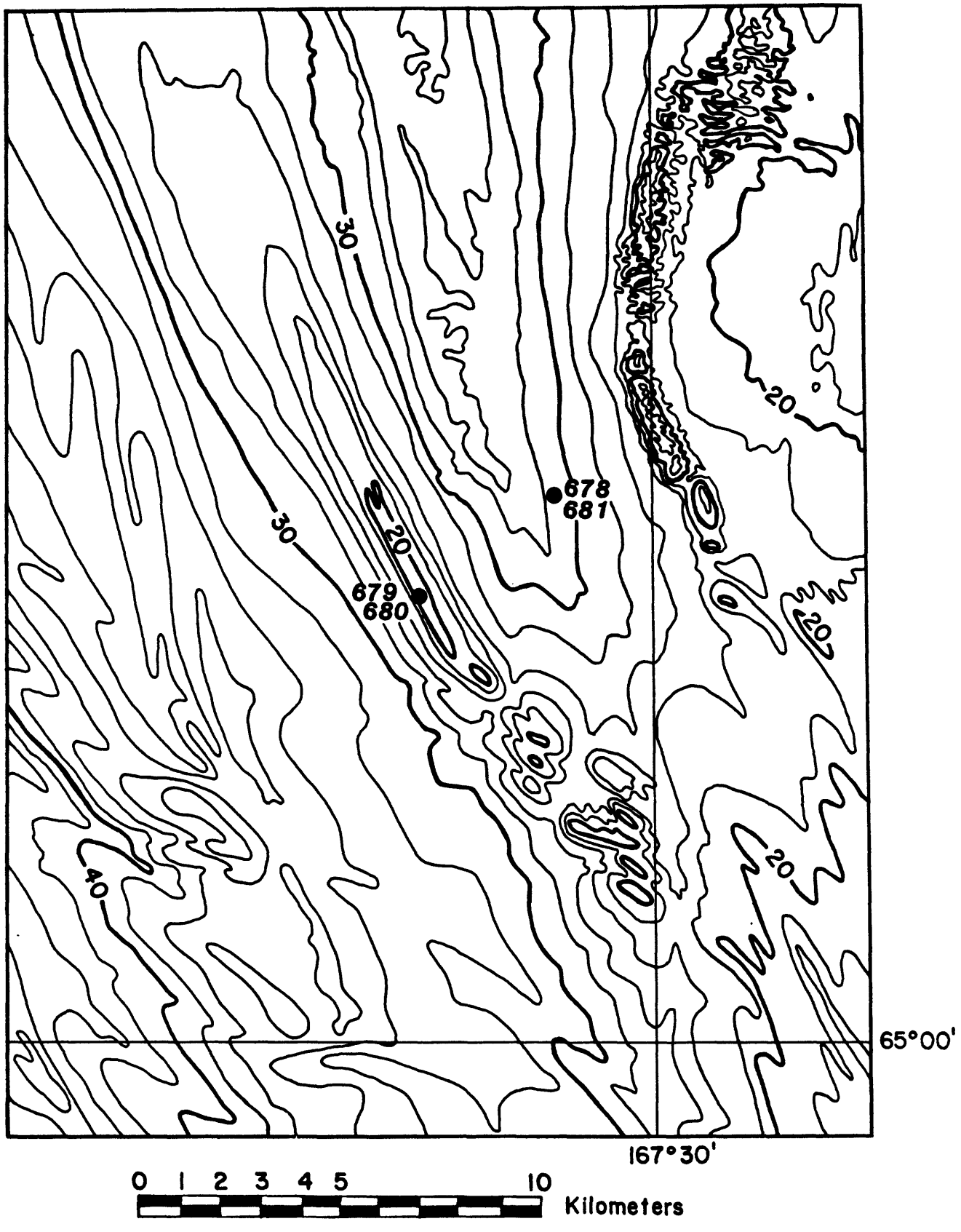

Fig. 32. Bathymetric map of ridge and swale area.

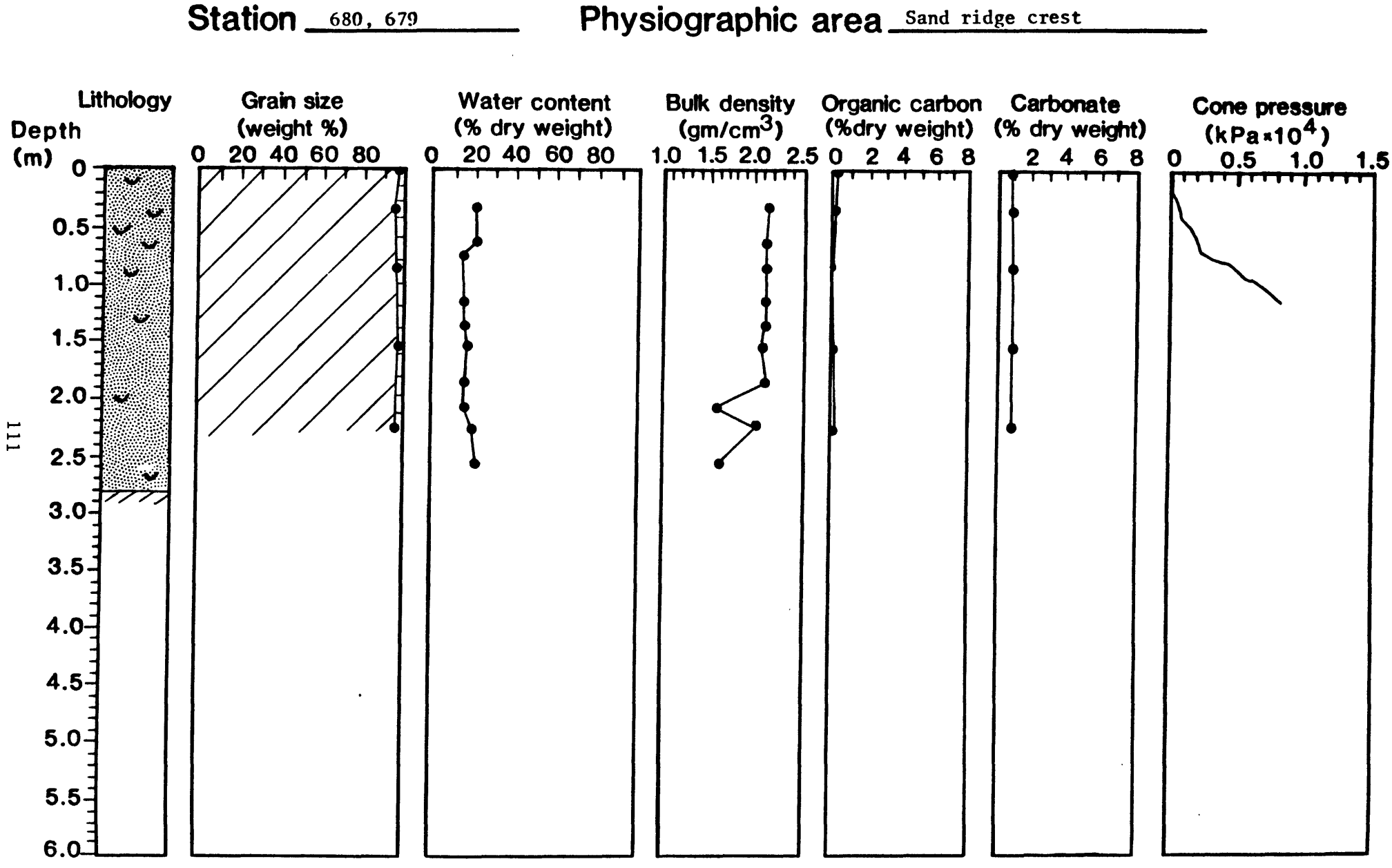

Fig. 33. Lithology, index properties and cone pressure vs subbottom depth for stations 680 and 679 (sand ridge crest).

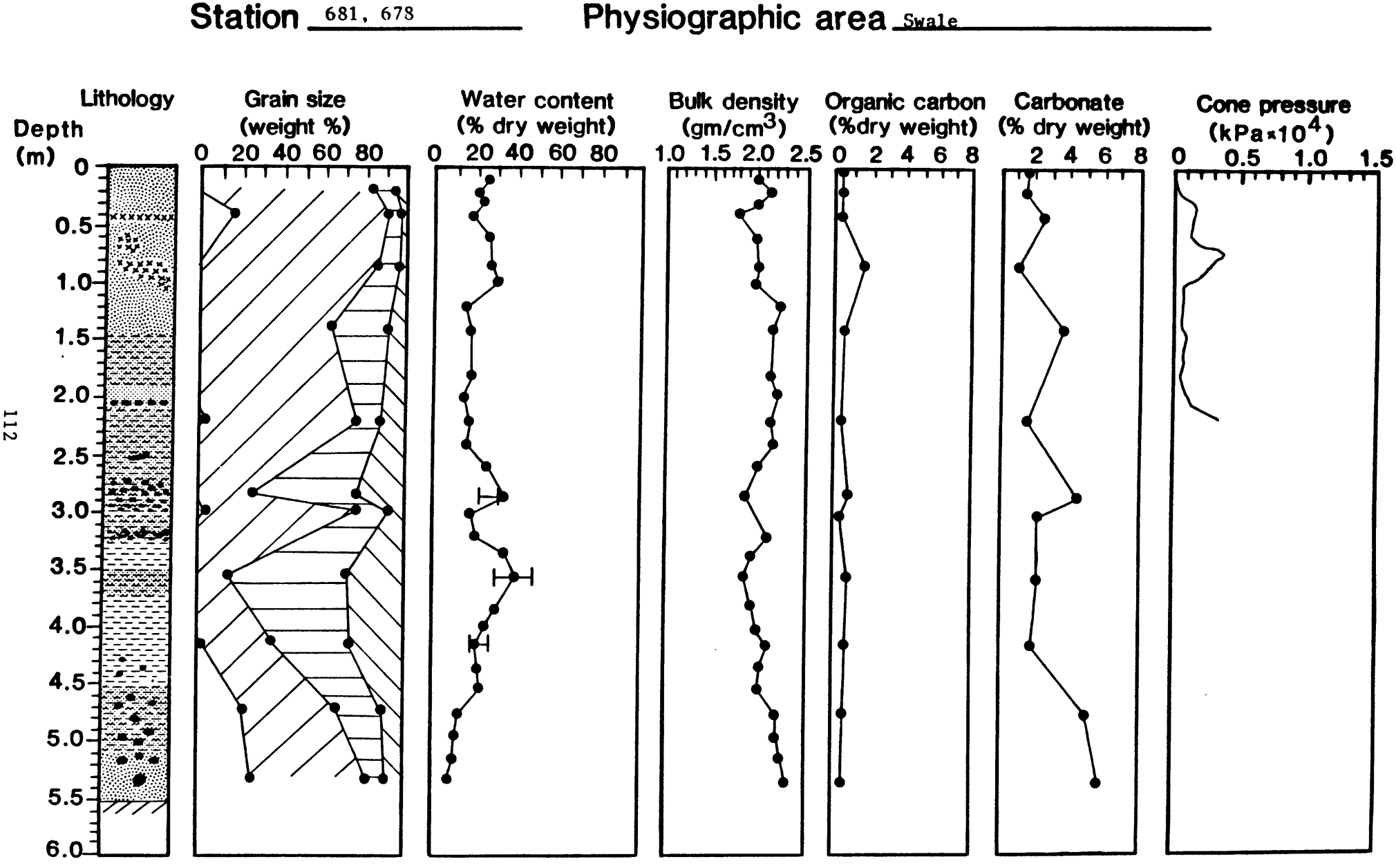

Fig. 34. Lithology, index properties and cone pressure vs subbottom depth for stations 681 and 678 (swale).

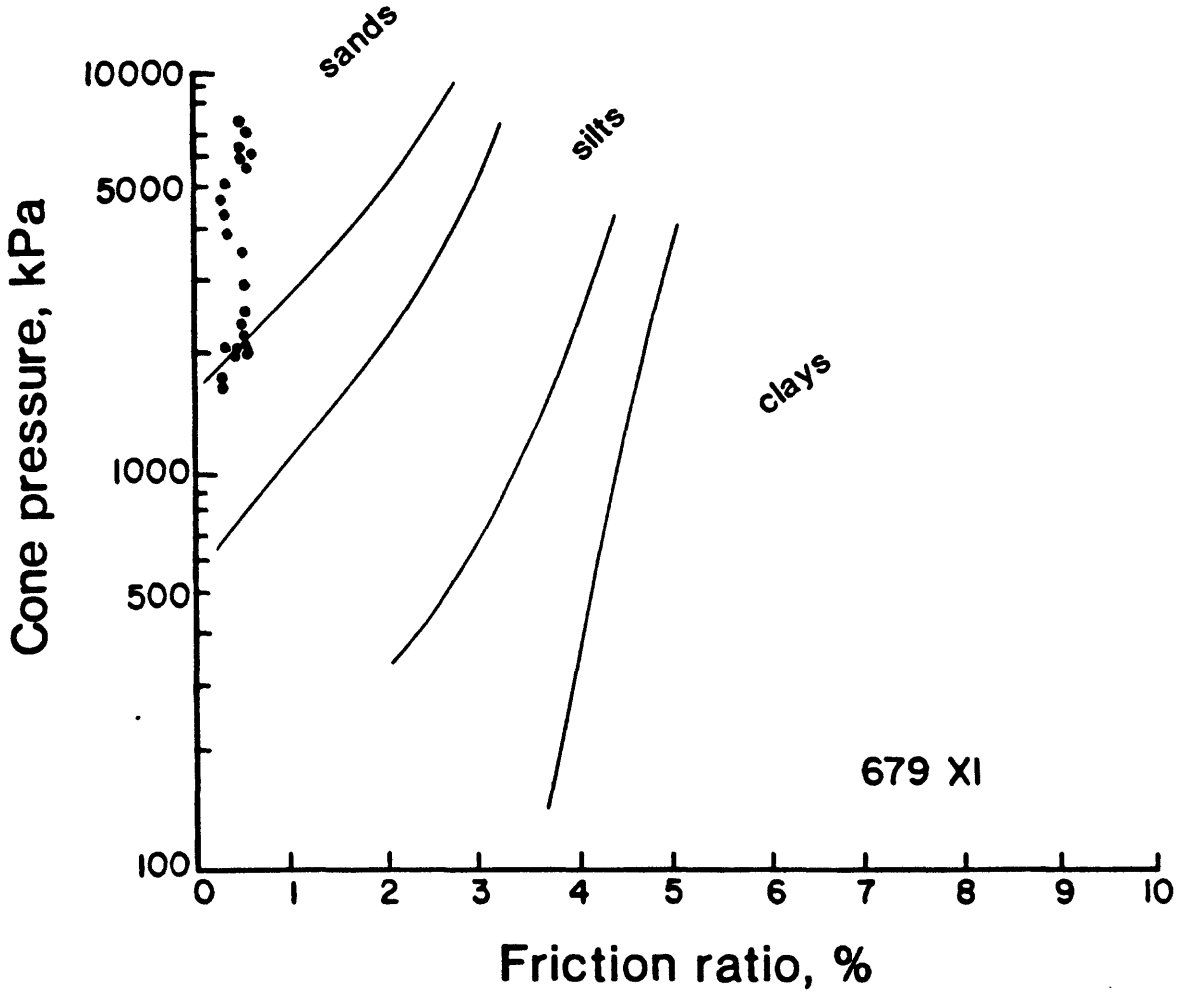

Fig. 35. Sediment type determined from cone penetration test 679X1 (sand ridge crest - near station 680).

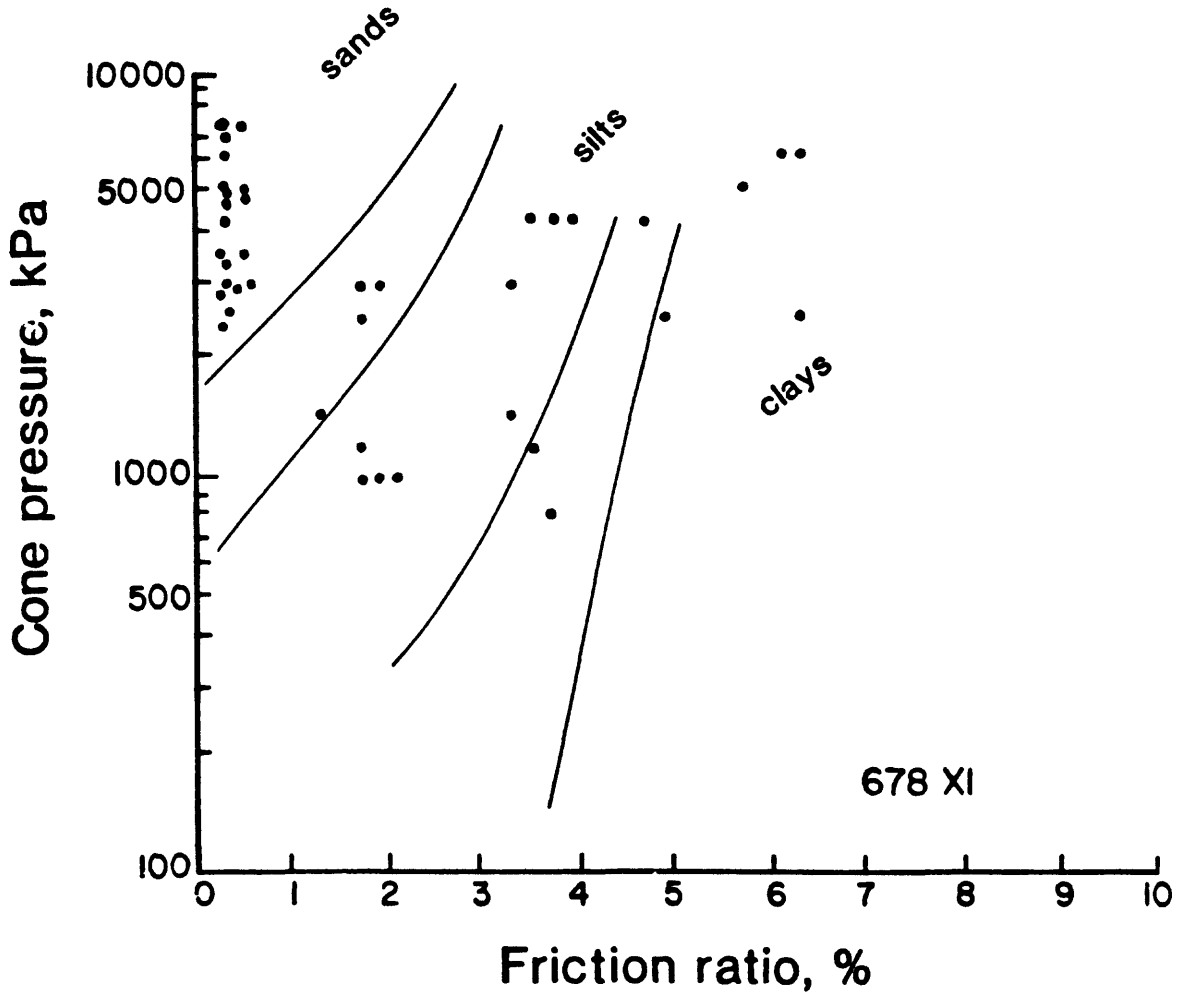

Fig. 36. Sediment type determined from cone penetration test 678X1 (swale - near station 681).

Appendix A. Grain size distribution curves.

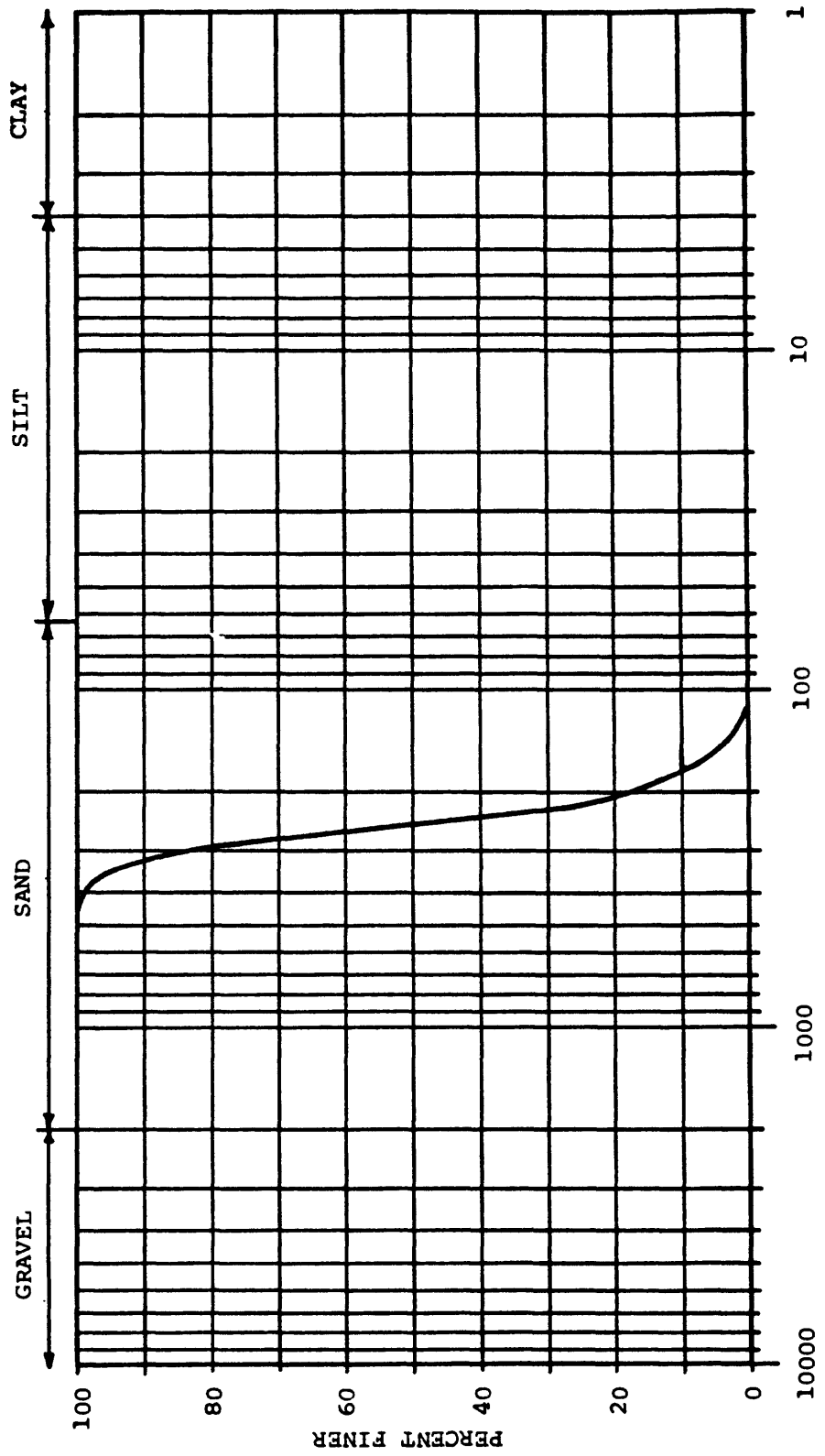

Core: 680A3, Depth: 0.30 m

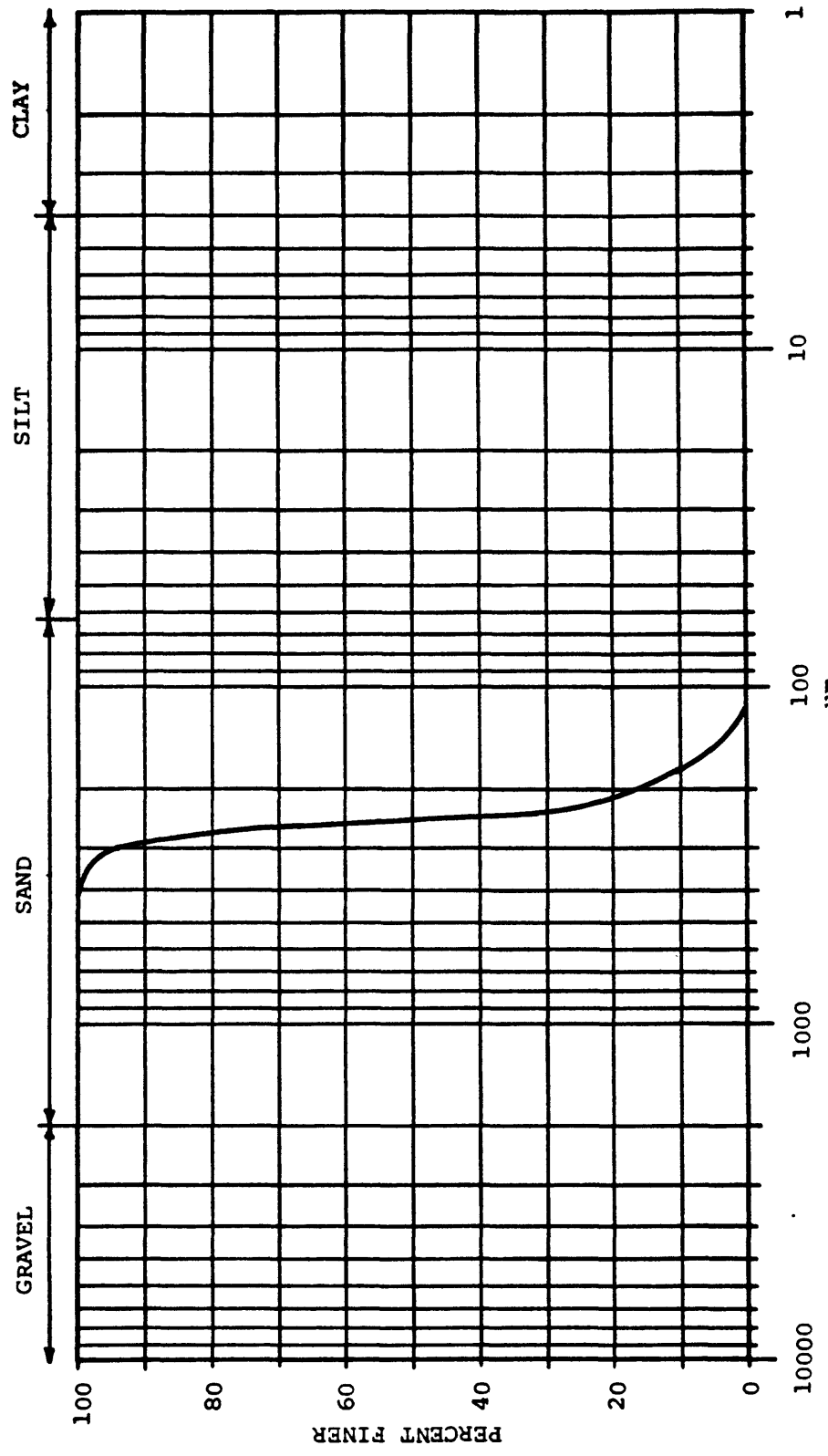

Core: 680A3, Depth: 0.82 m

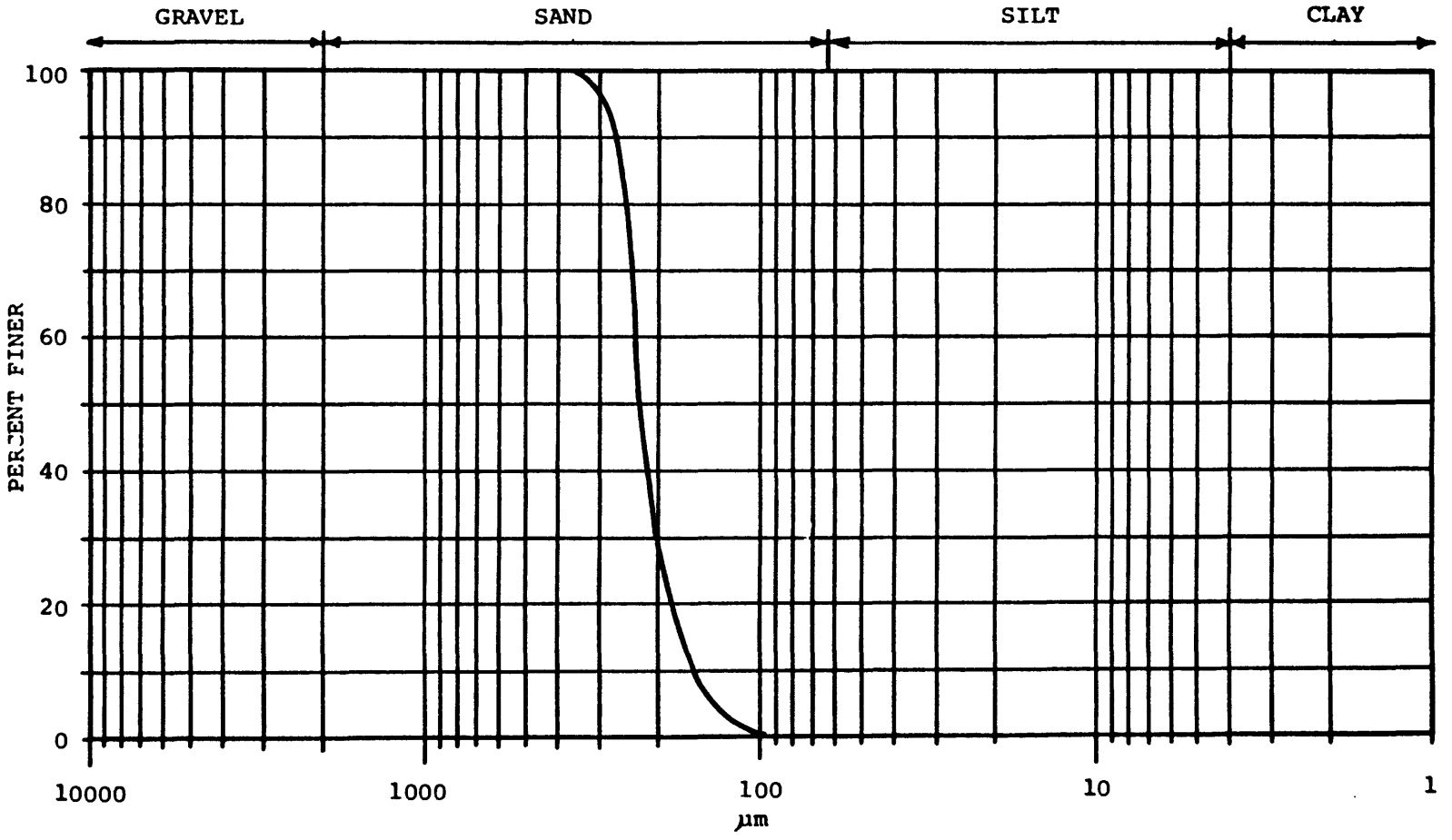

Core: 680A3, Depth: 1.52 m

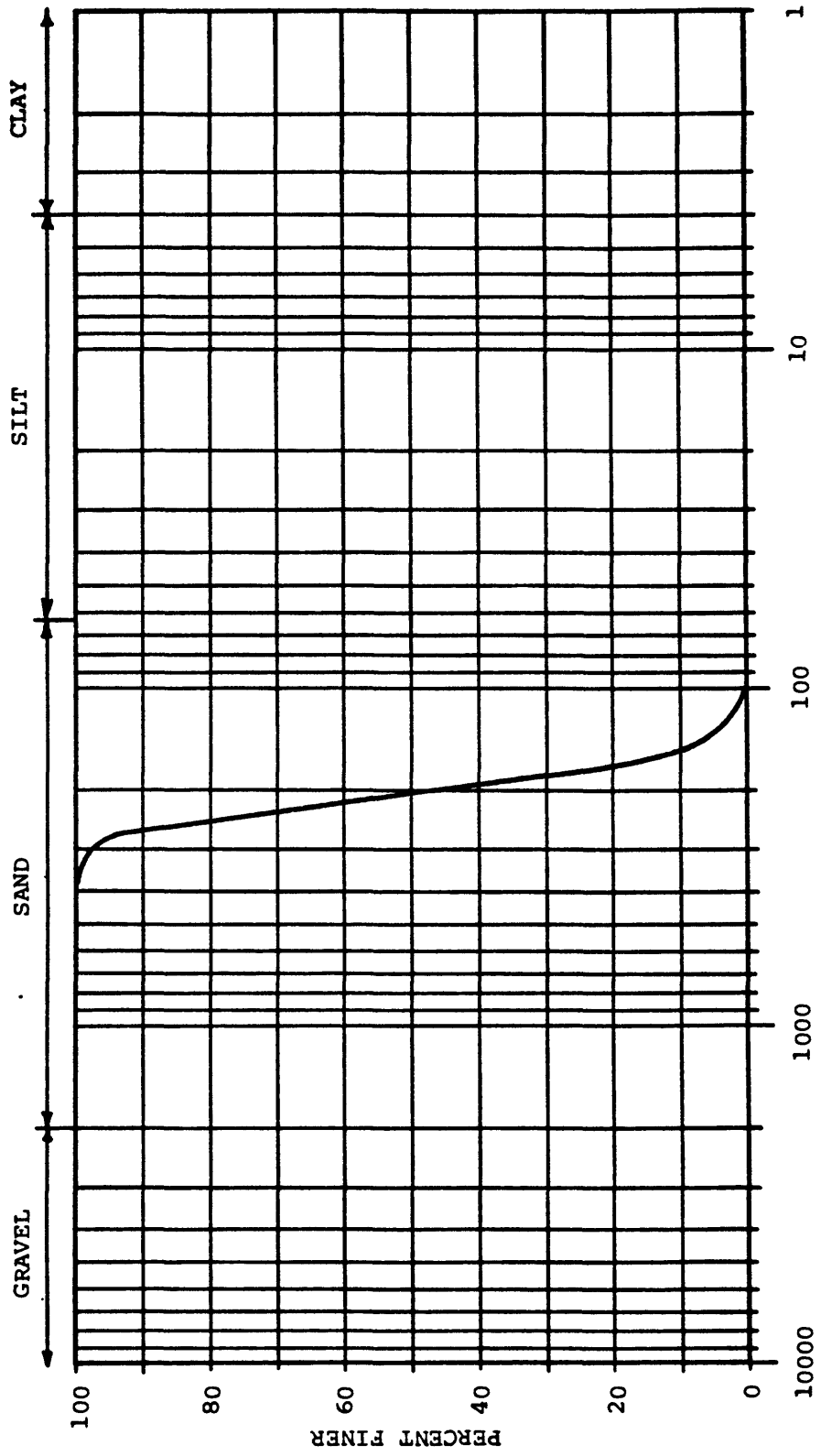

Core: 680A3, Depth: 2.22 m

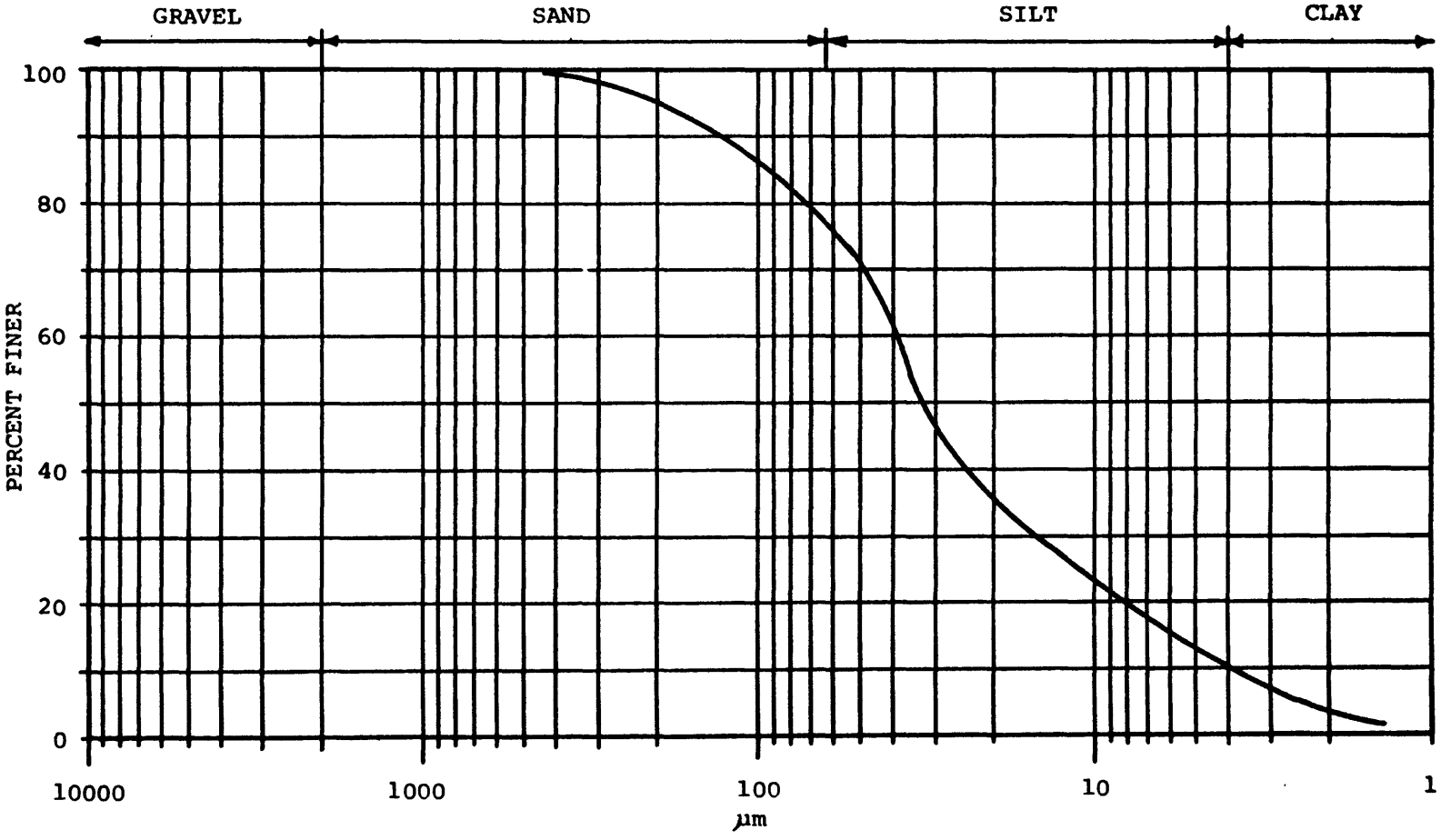

Core: 681A2, Depth: 1.46 m, Sampled from tests D 100, D 101

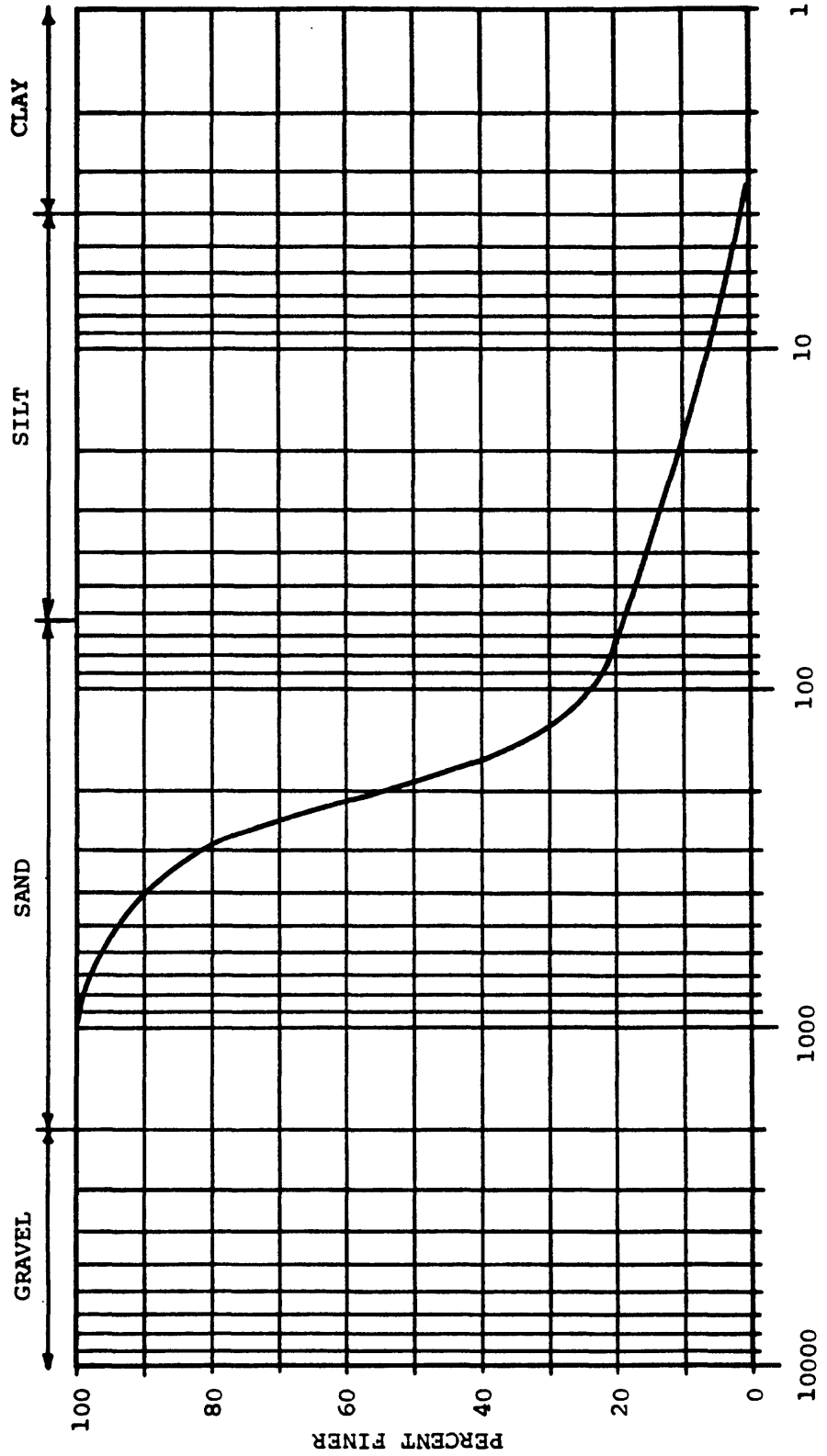

Core: 681A3, Depth: 0.20 m

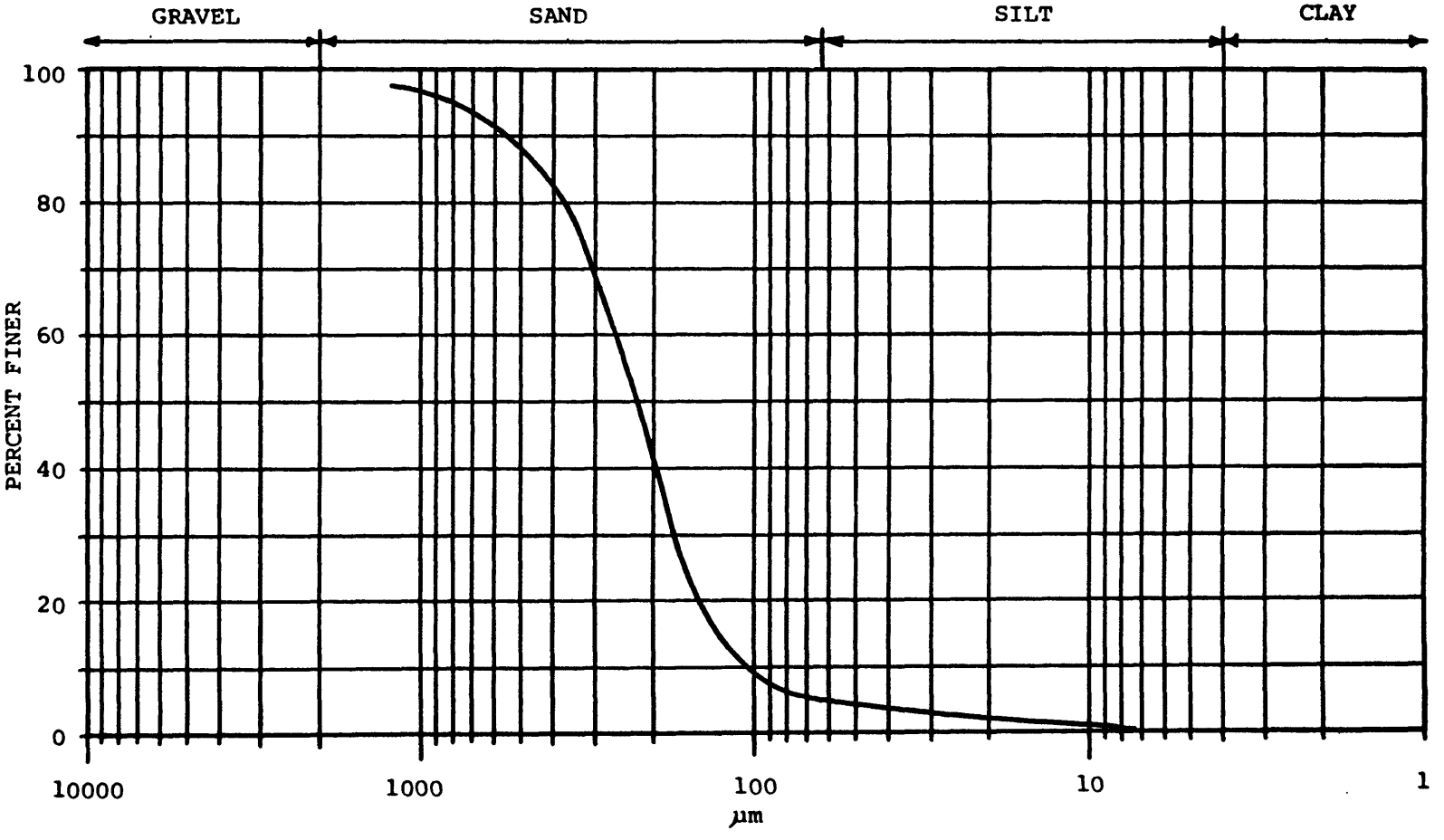

Core: 681A3, Depth: 0.40 m

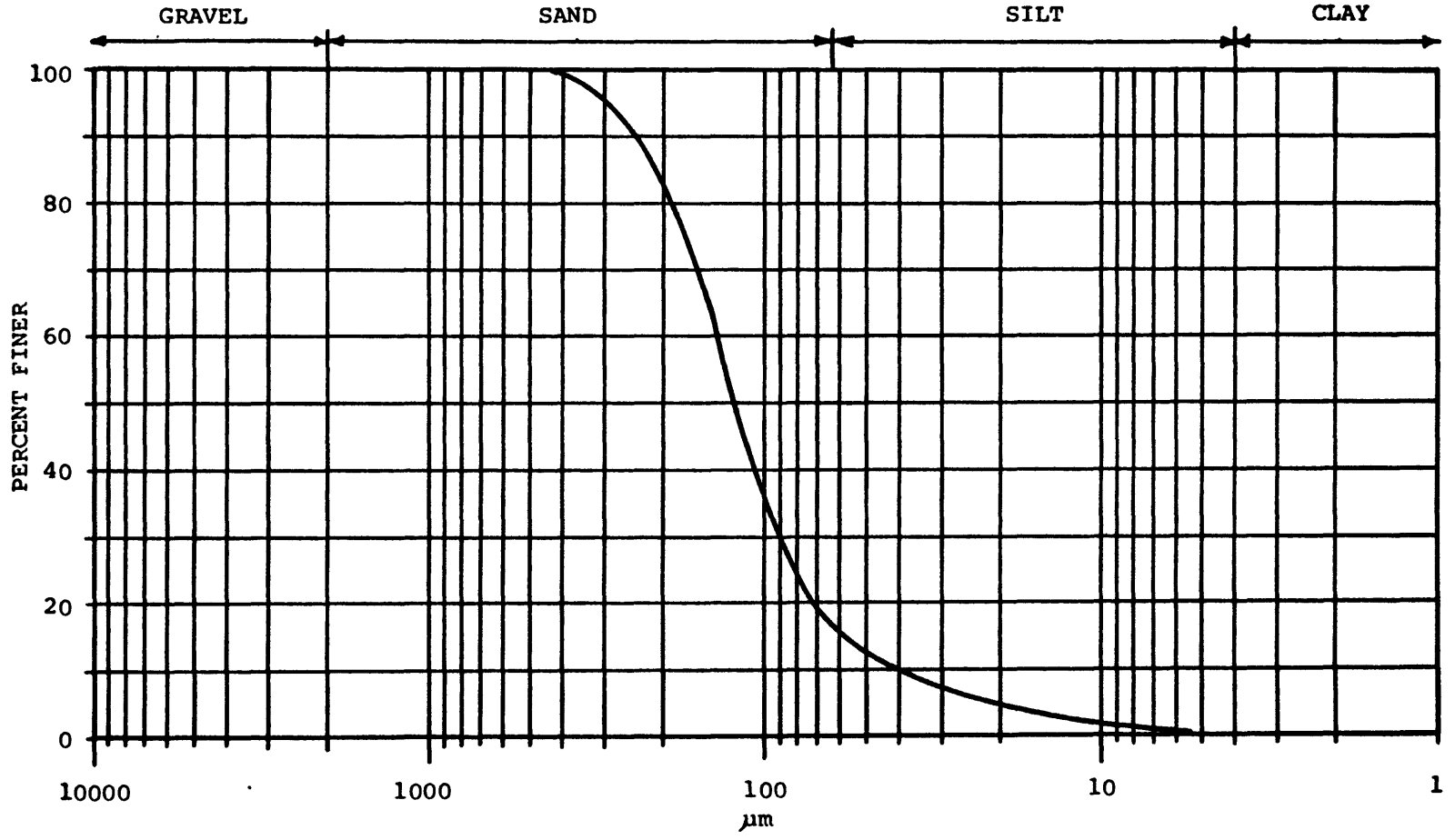

Core: 681A3, Depth: 0.84 m

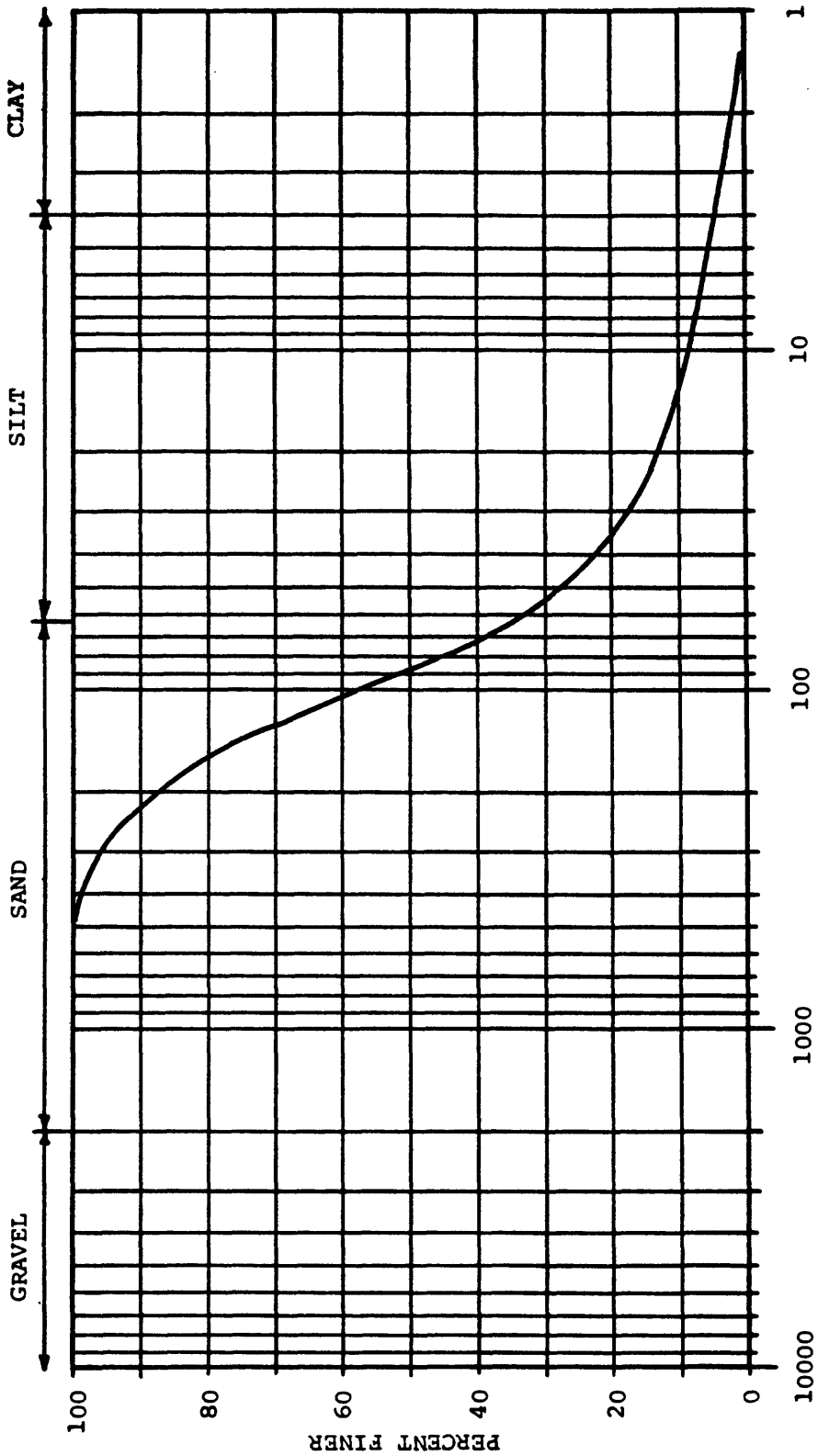

Core: 681A3, Depth: 1.40 m

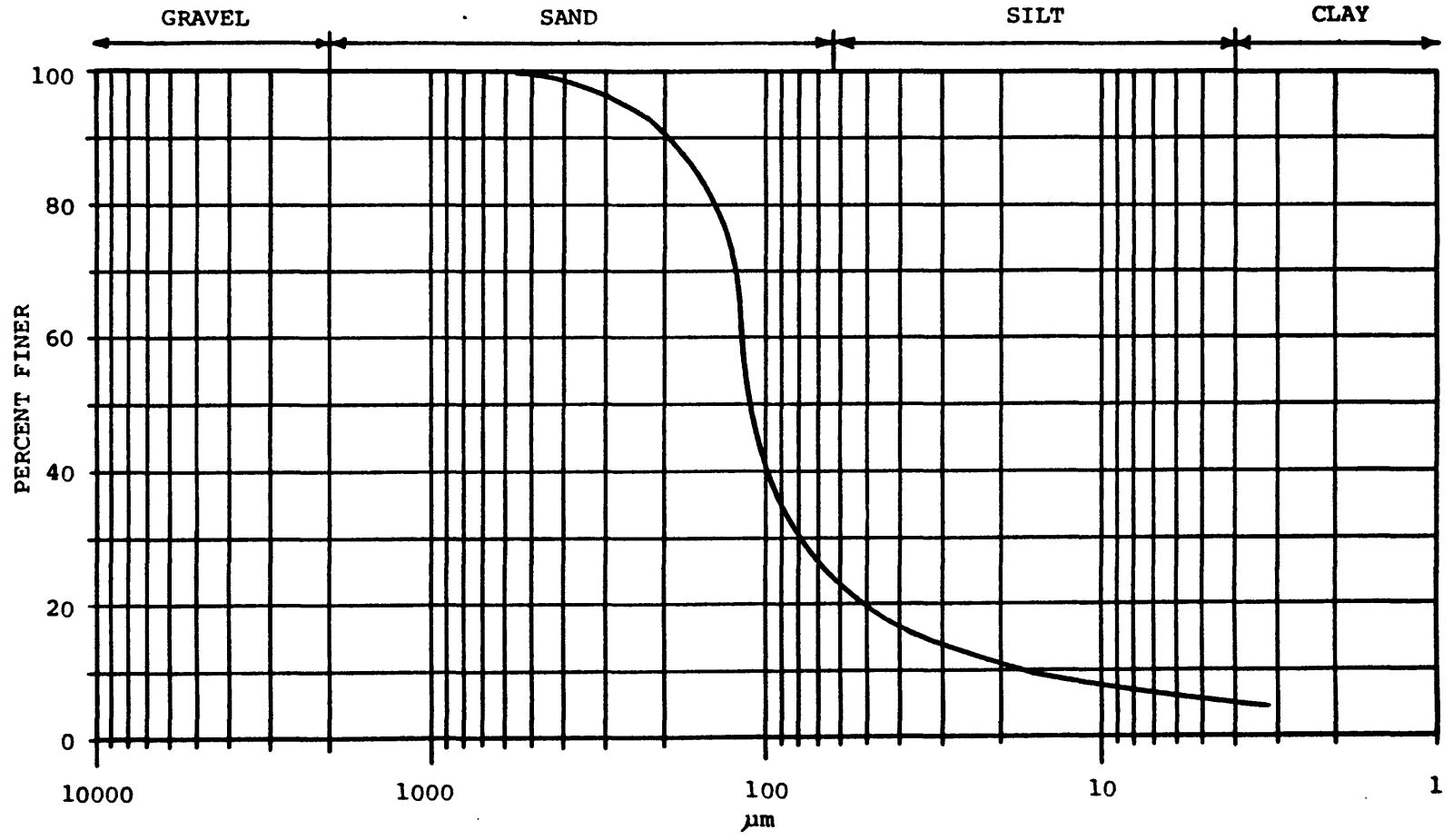

Core: 681A3, Depth: 2.20 m

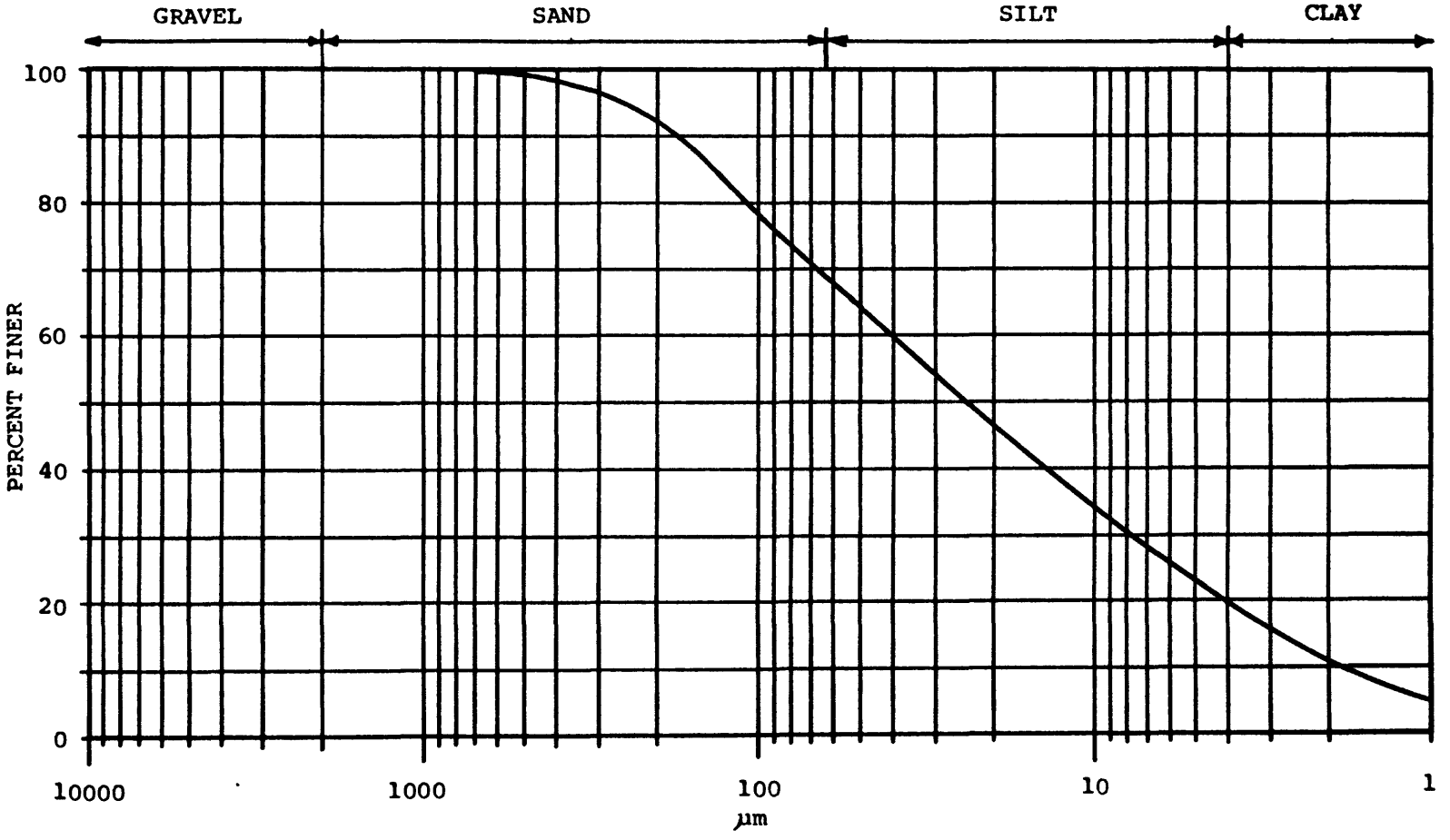

Core: 681A3, Depth: 2.84 m

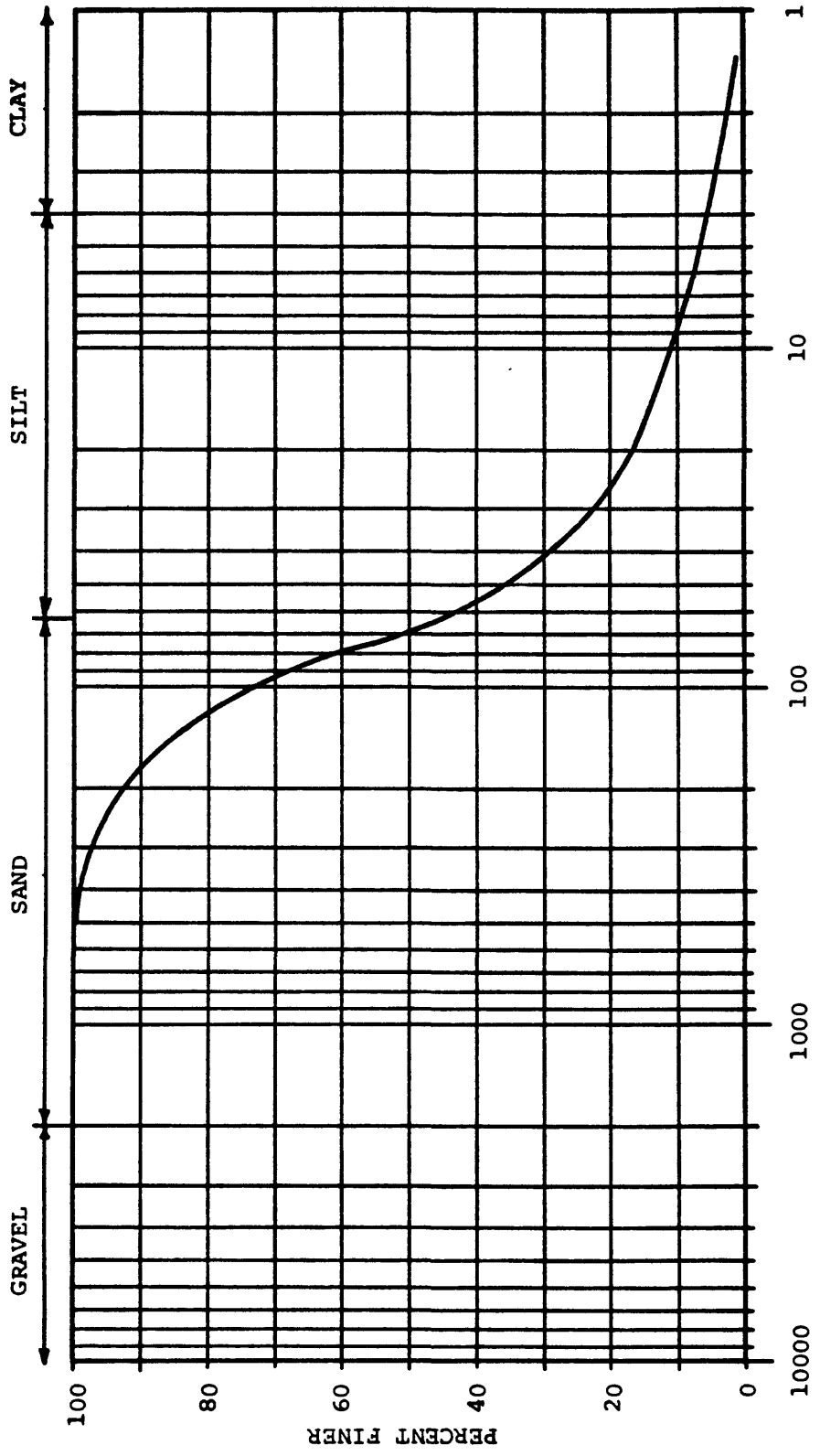

Core: 682A1, Depth: 0.97 m, Sampled from tests TC 38, TC 39

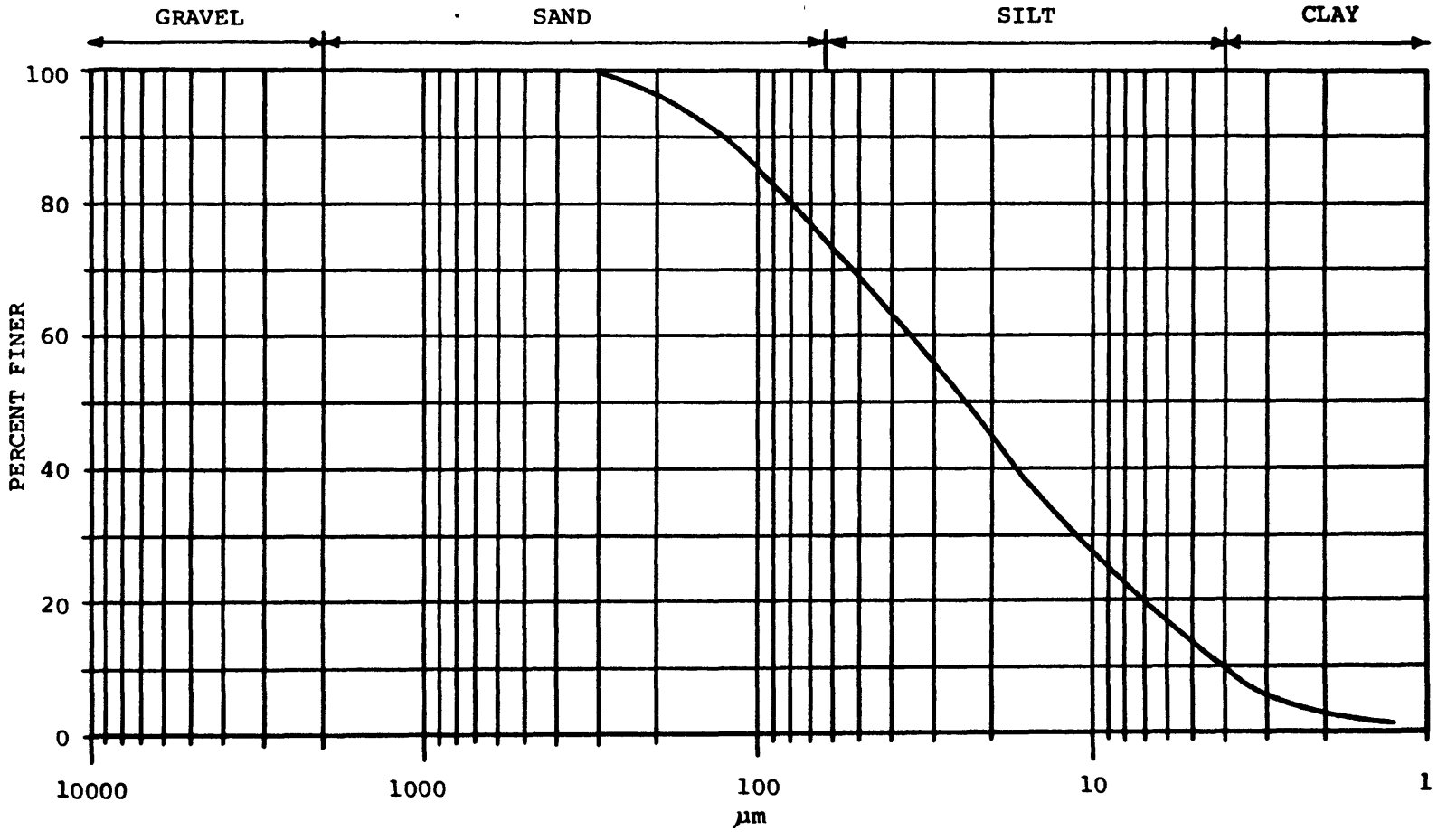

Core: 682A1, Depth: 1.09 m, Sampled from tests TE 76, TE 77

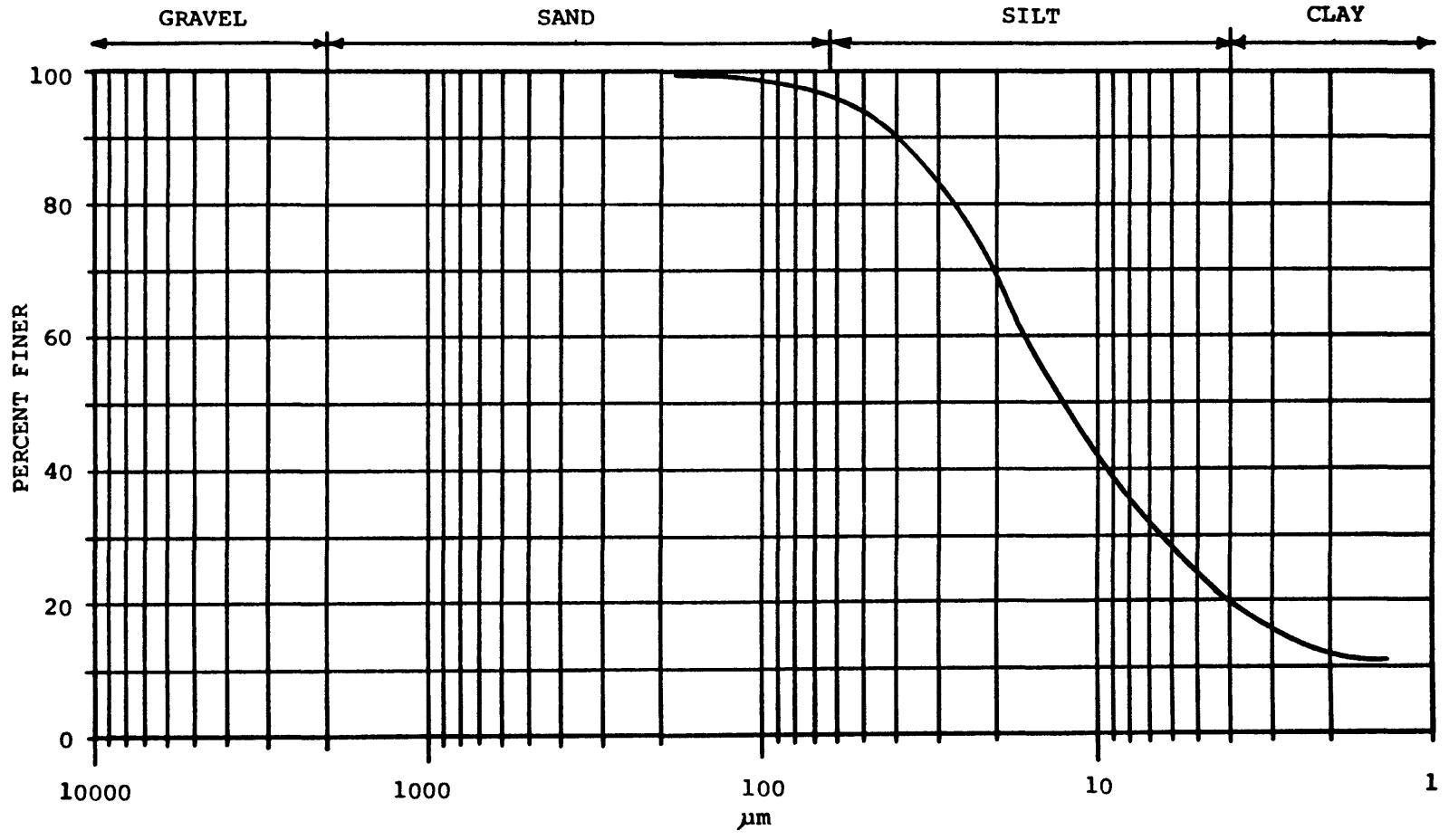

Core: 682A1, Depth: 1.78 m, Sampled from tests TE 98, TE99

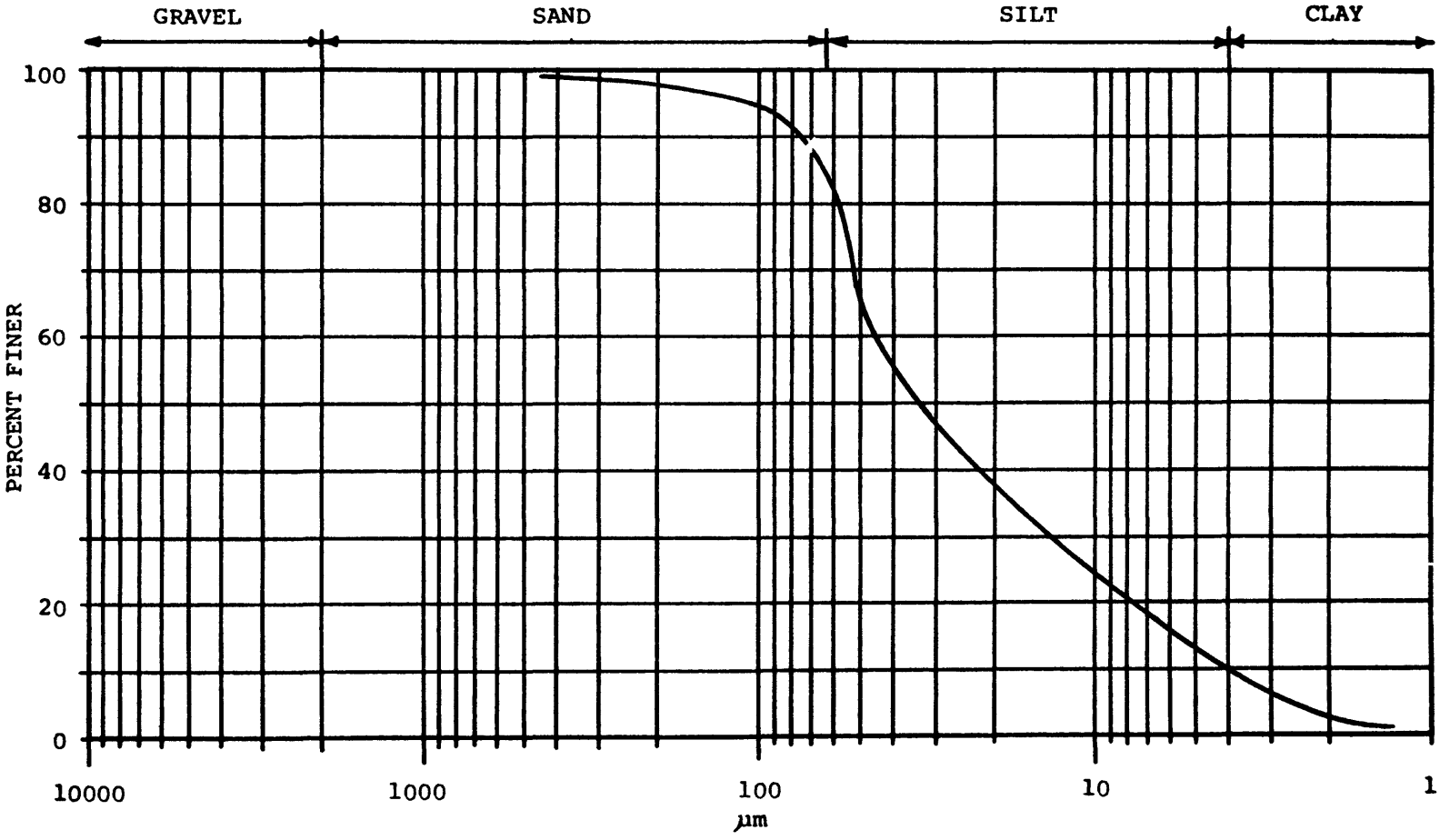

Core: 682A1, Depth: 1.89 m, Sampled from tests TC 76, TC 77

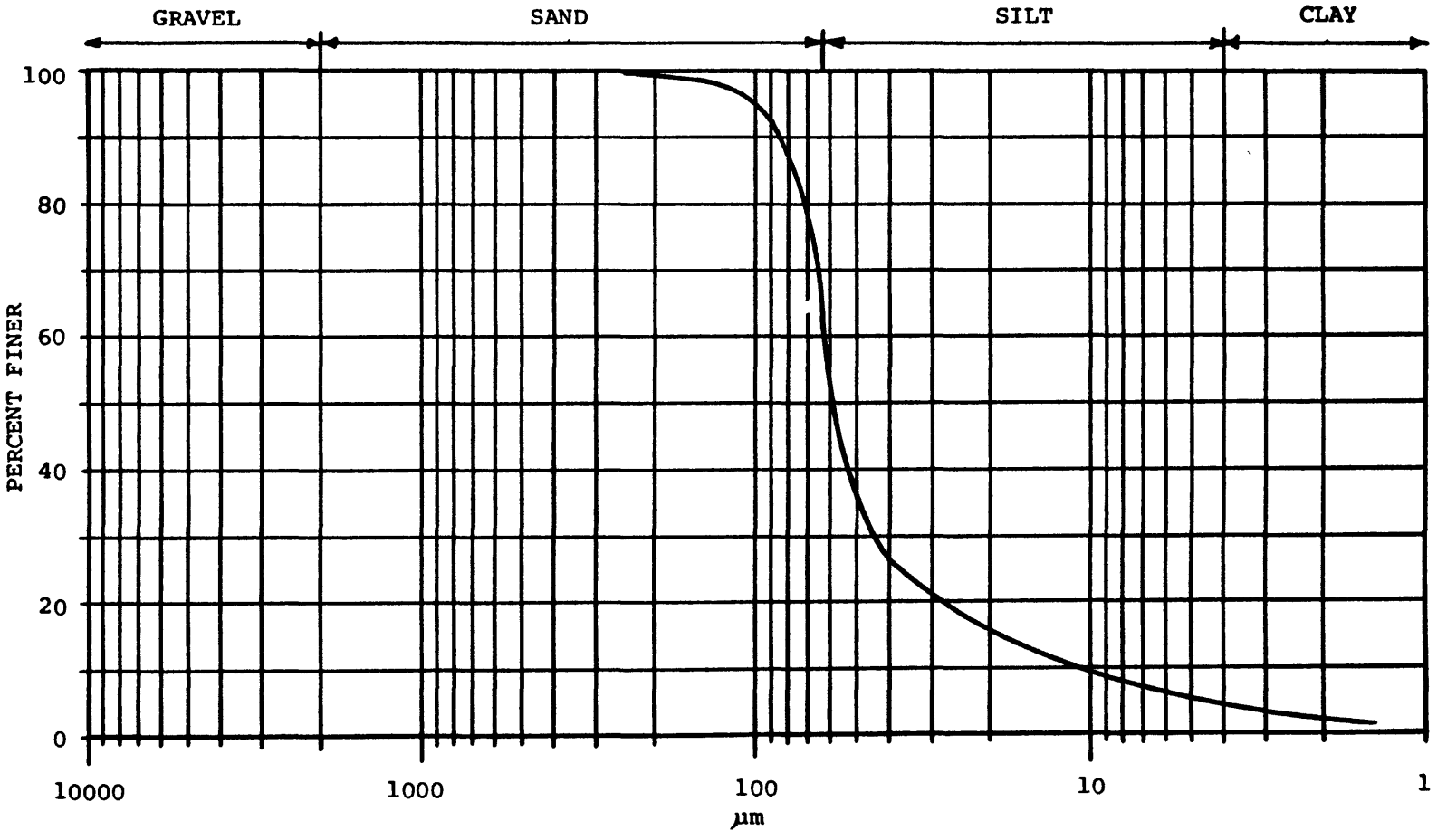

Core: 683A1, Depth: 1.05 m

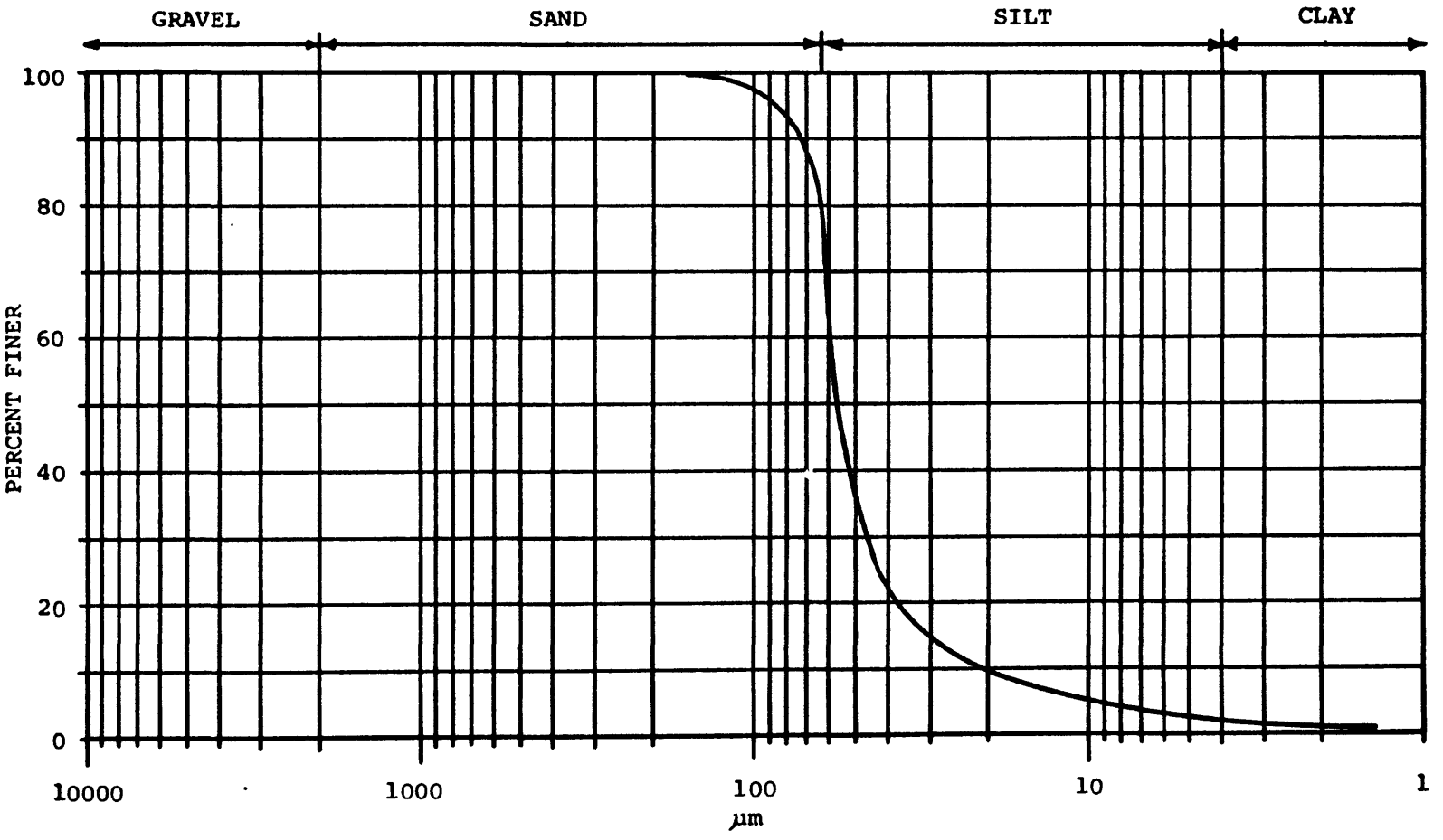

Core: 683A1, Depth: 4.25 m, Sampled from tests TE 109, TE110

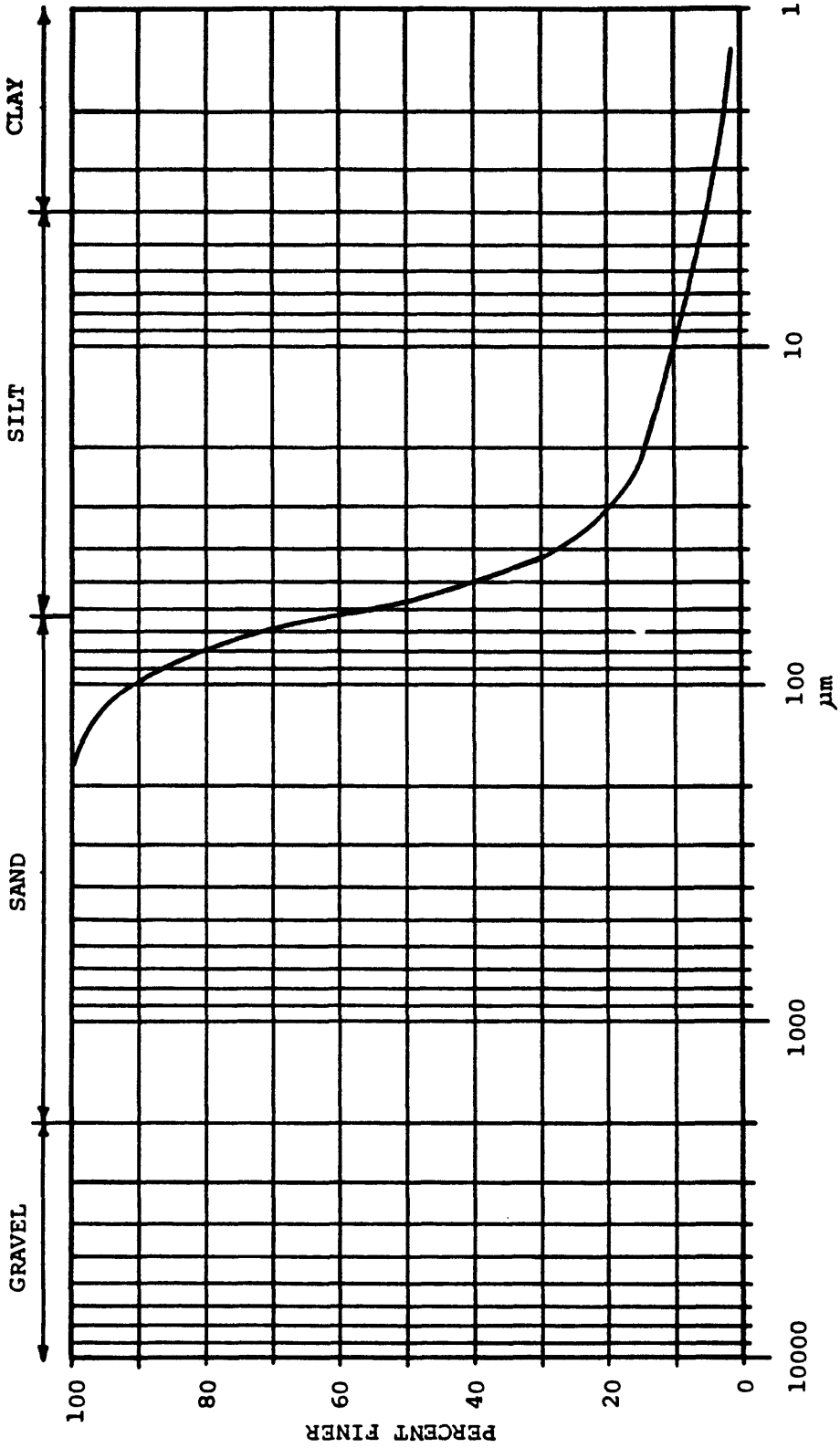

Core: 684Al, Depth: 0.66 m, Sampled from tests TC 90, TC 91

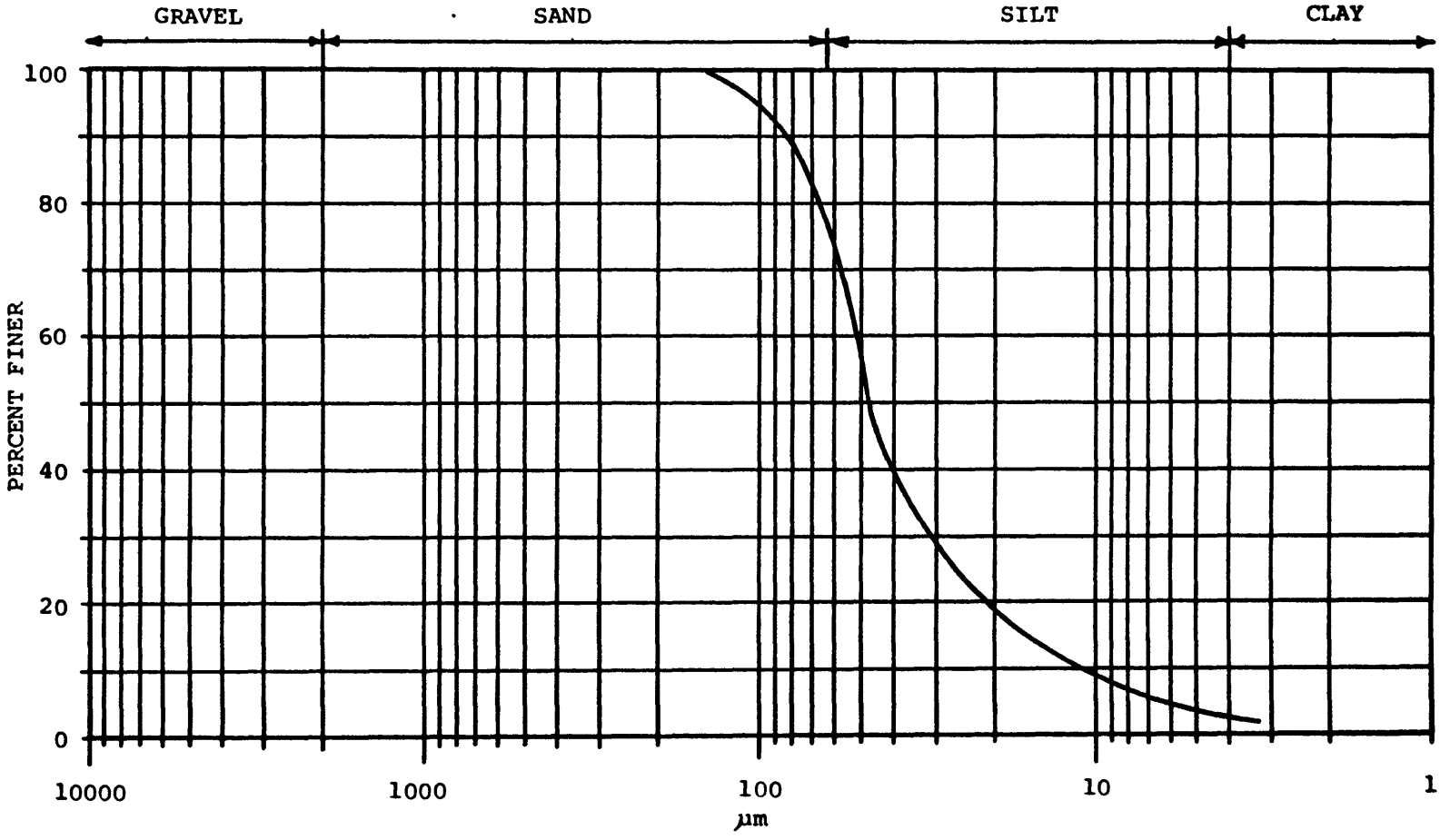

Core: 685A2, Depth: 0.44 m, Sampled from tests TC 80, TC 81

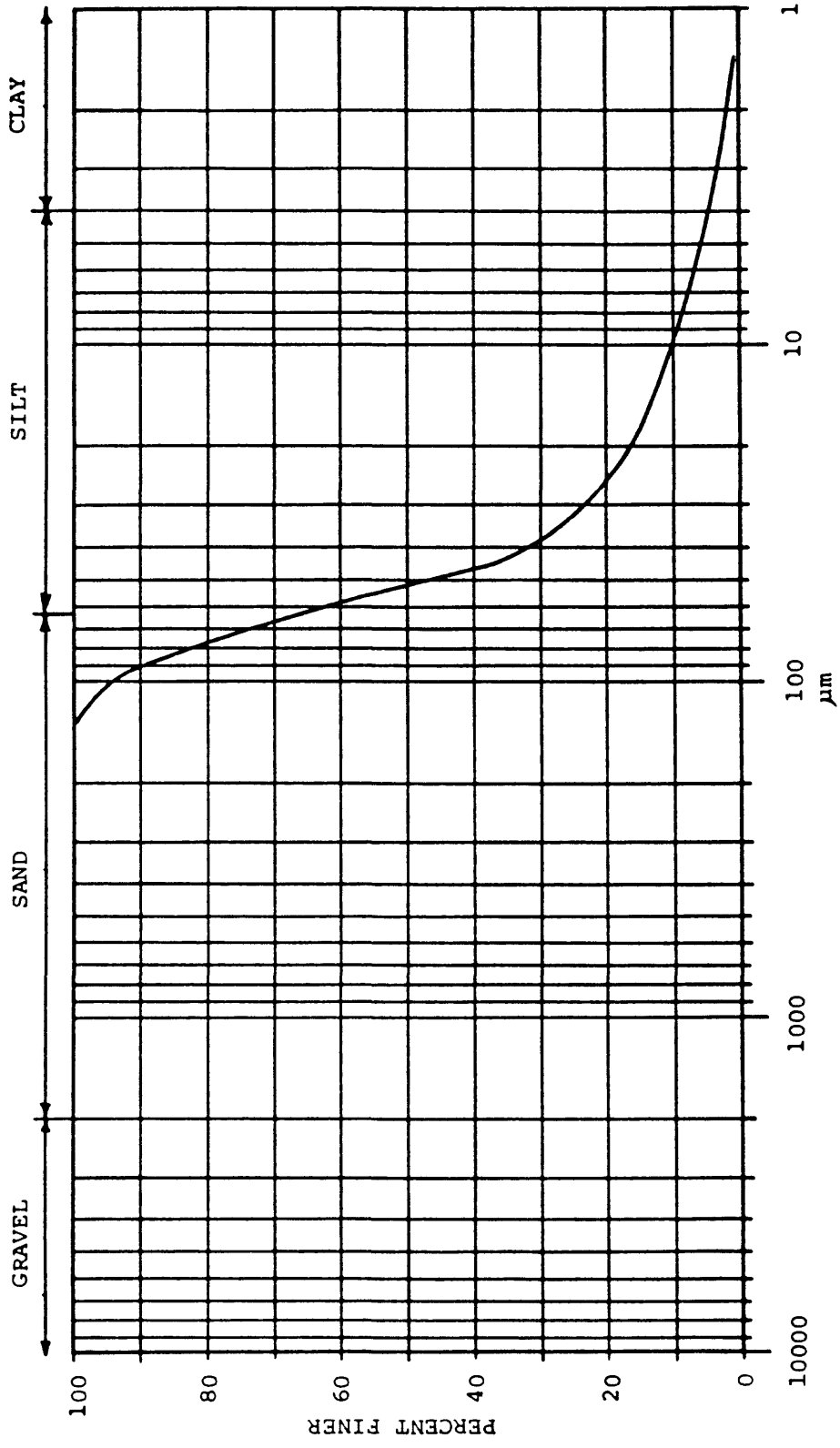

Core: 685A2, Depth: 1.05 m, Sampled from tests TC 62, TC 74

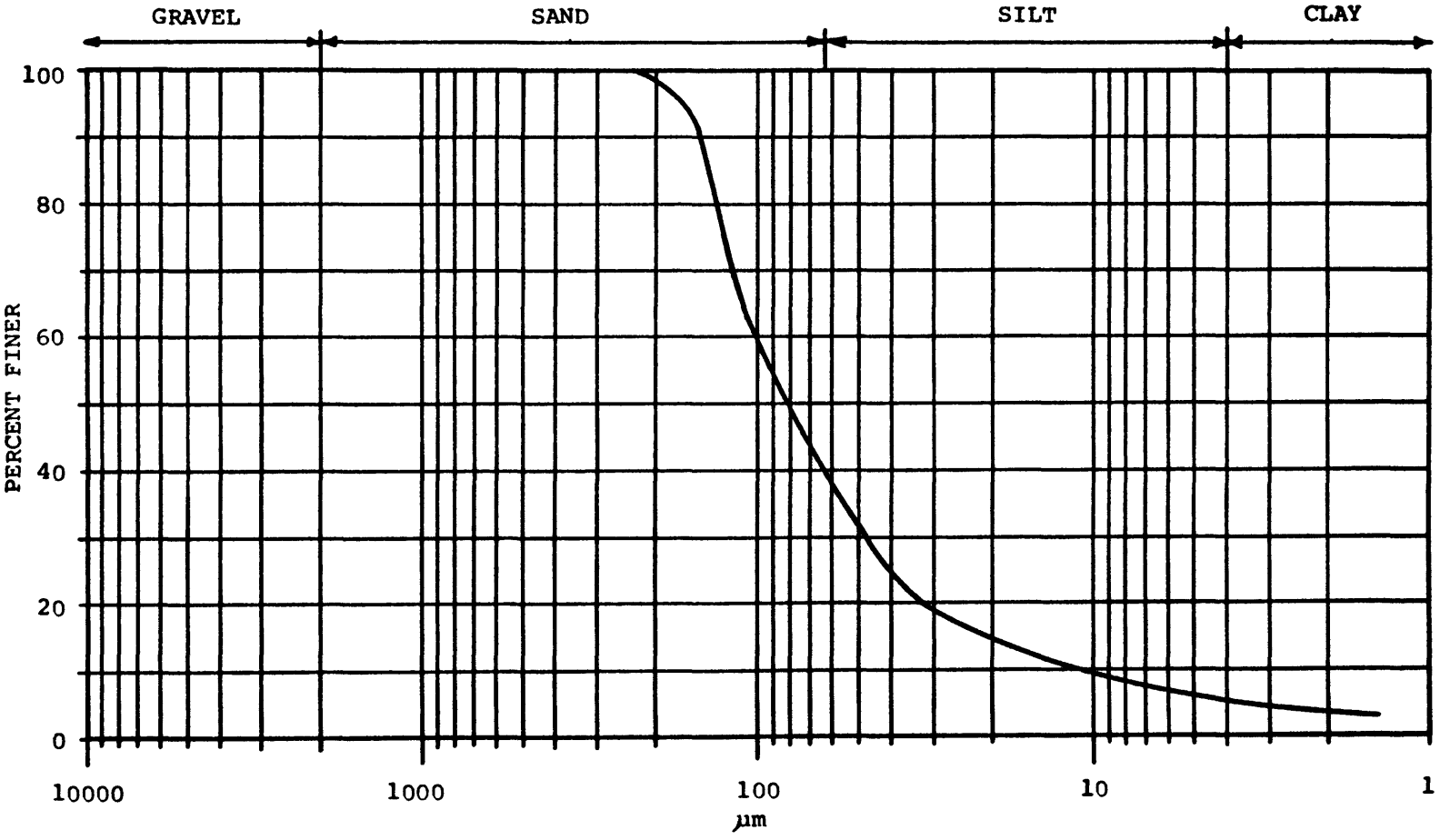

Core: 686A1, Depth: 0.45 m, Sampled from tests TC 96, TC 97

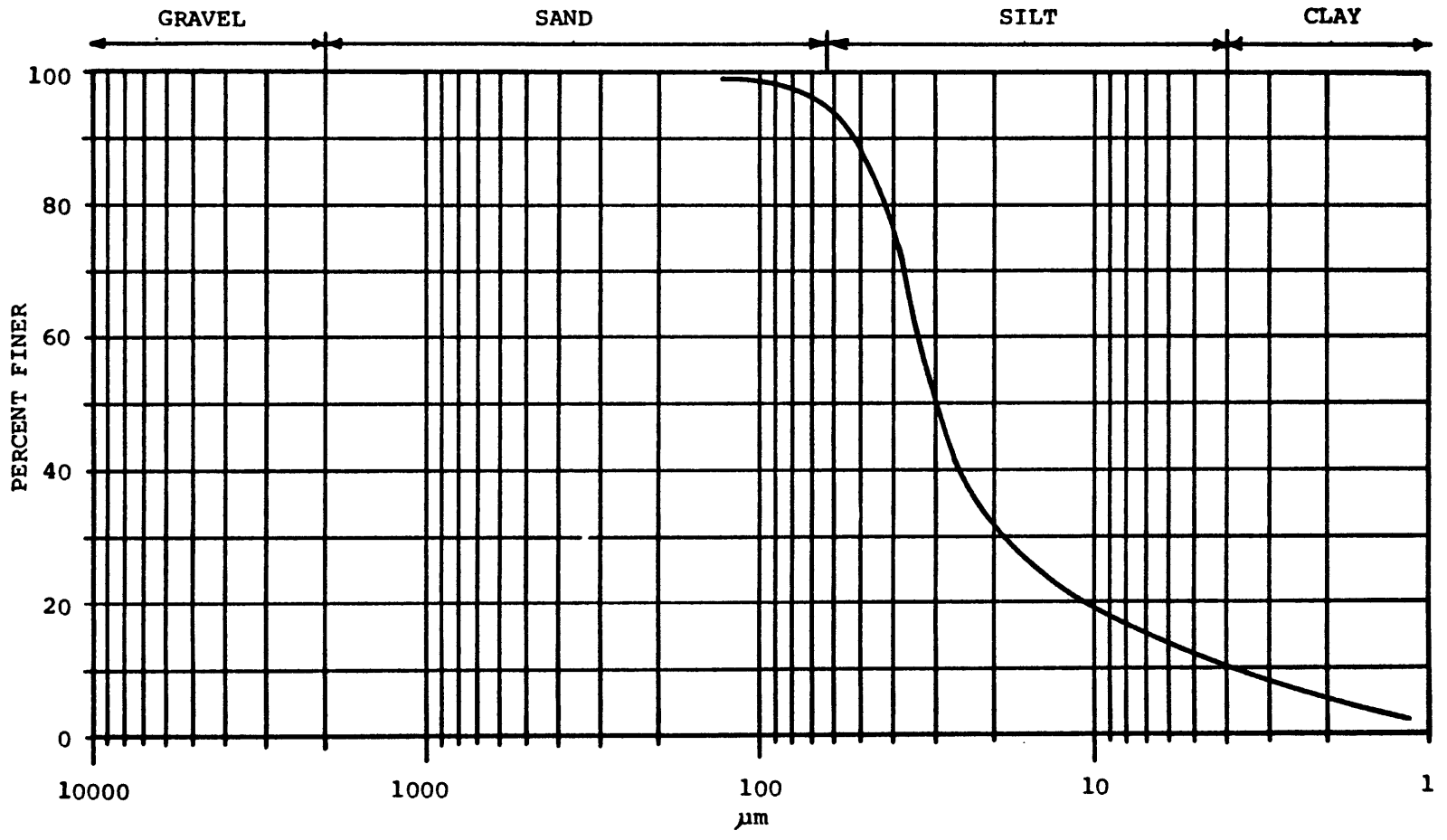

Core: 687A1, Depth: 0.49 m, Sampled from tests TC 94, TC 95

Appendix B. Cone penetration test plots.

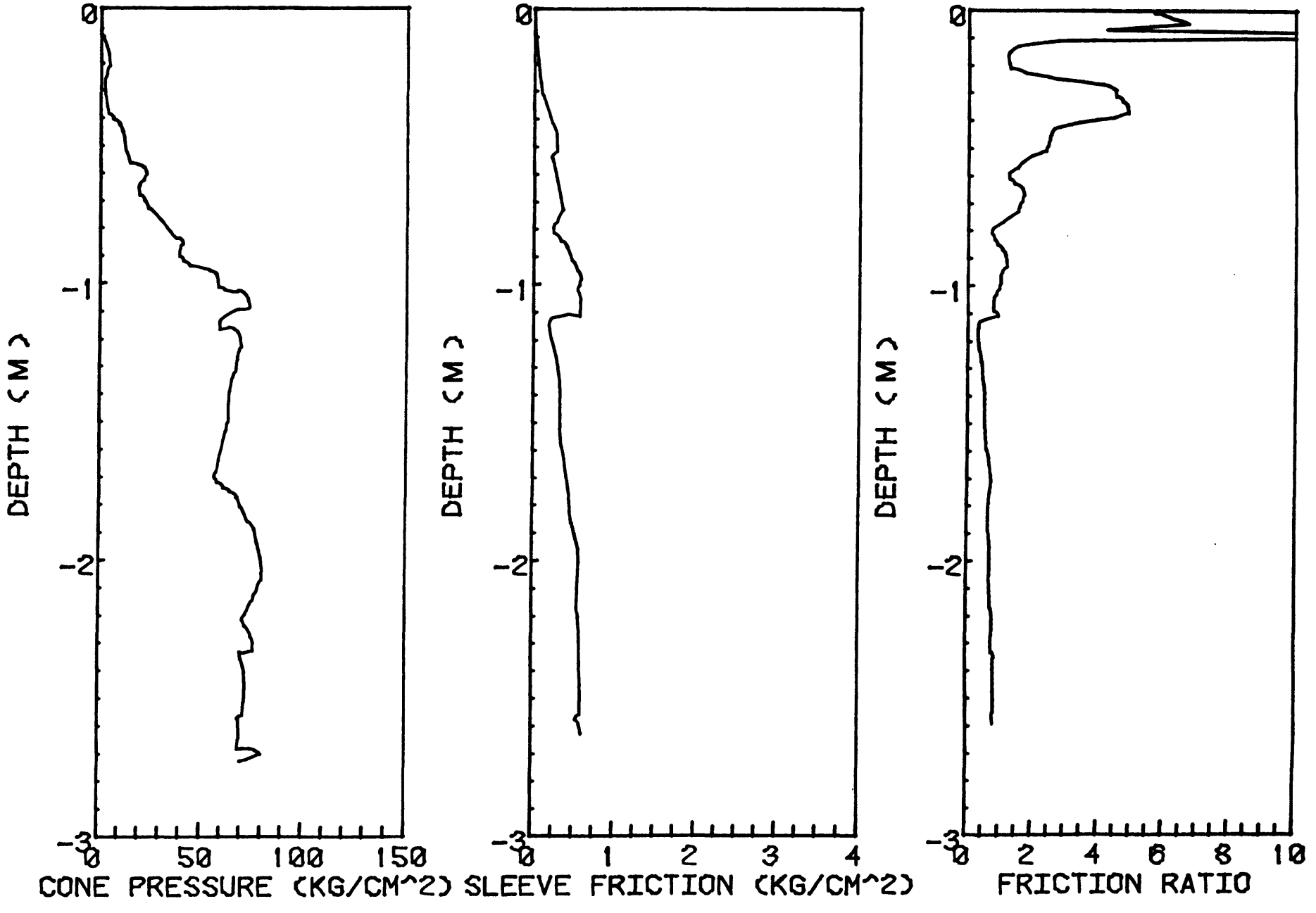

FIG. 665X1. NON-GAS ZONE S. OF NOME. ALASKA. 8/7/81

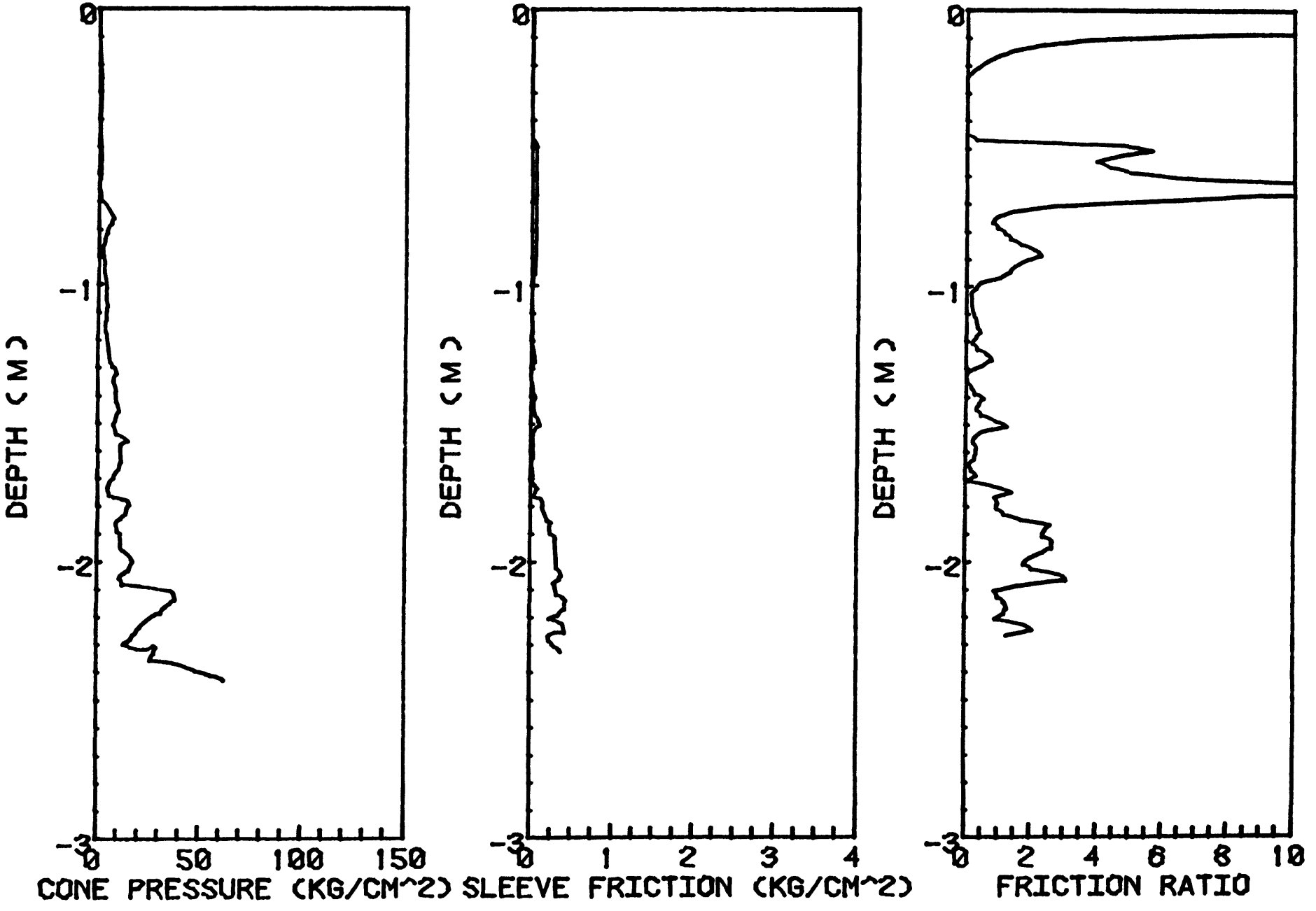

FIG. 667X1. N. S. YUKON DELTA - PROTECTED. ALASKA. 8/8/81

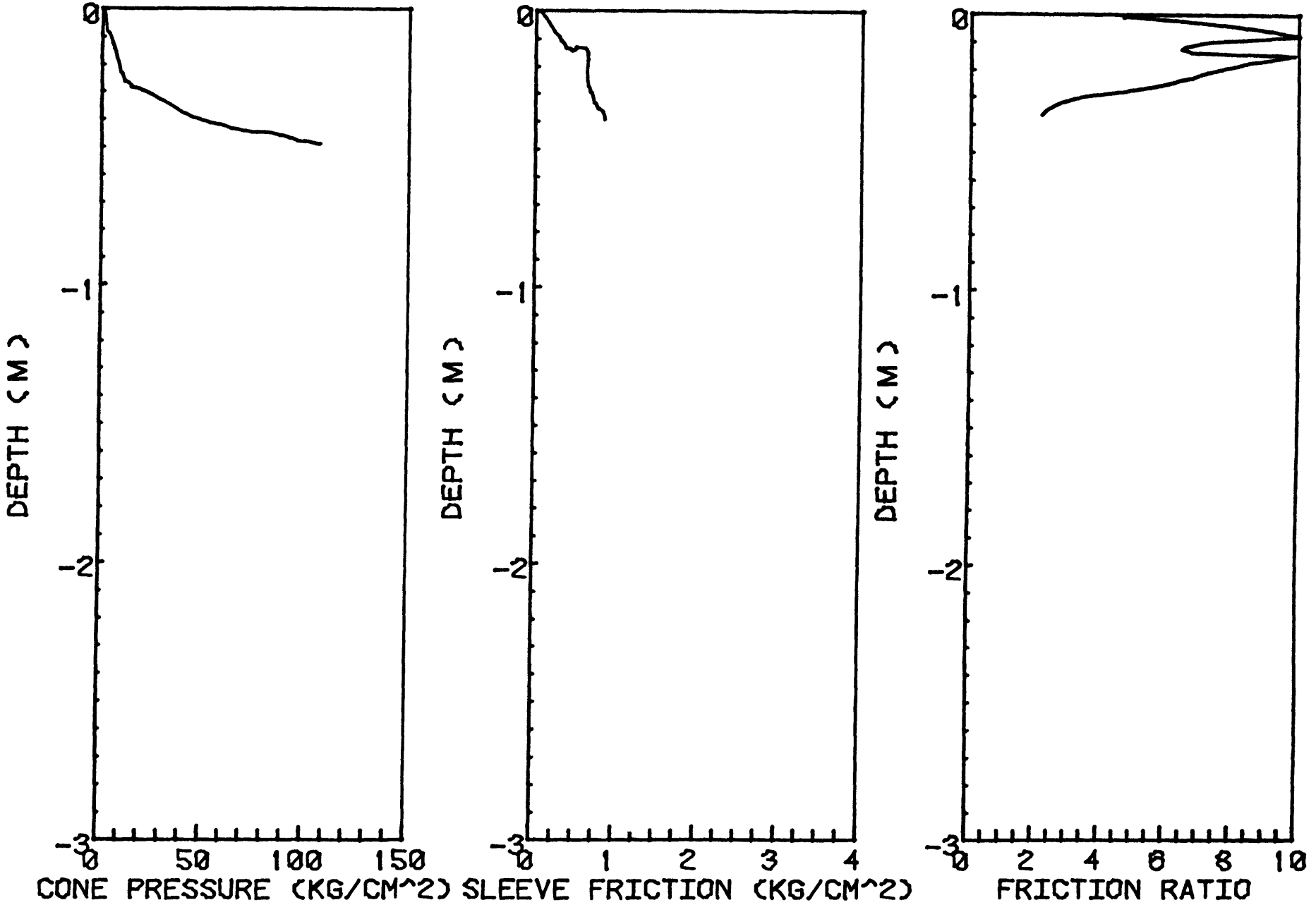

FIG. 668X1. W. YUKON DELTA - PROTECTED. ALASKA. 8/8/81

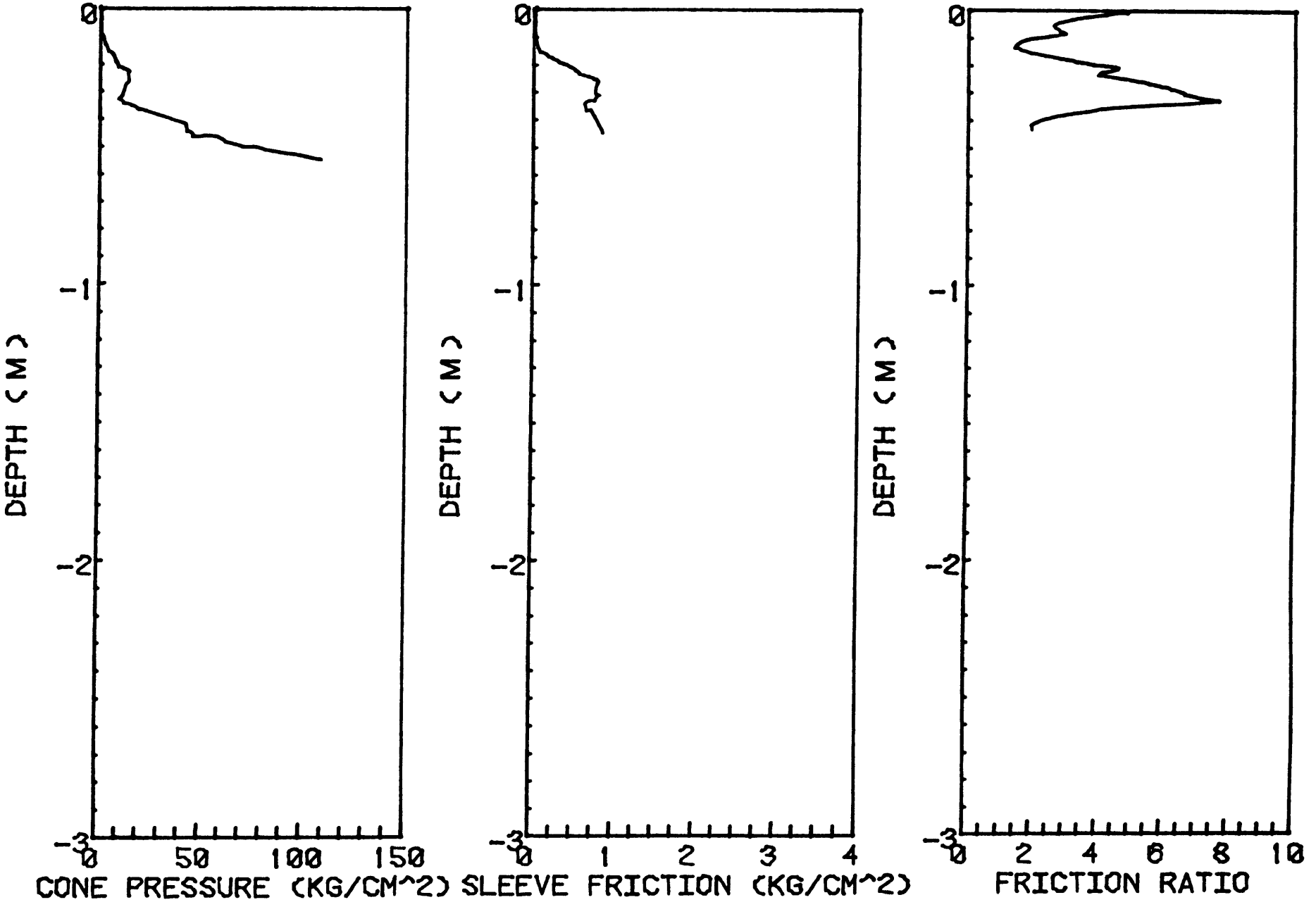

FIG. A668X2. W. YUKON DELTA - EXPOSED. ALASKA. 8/8/81

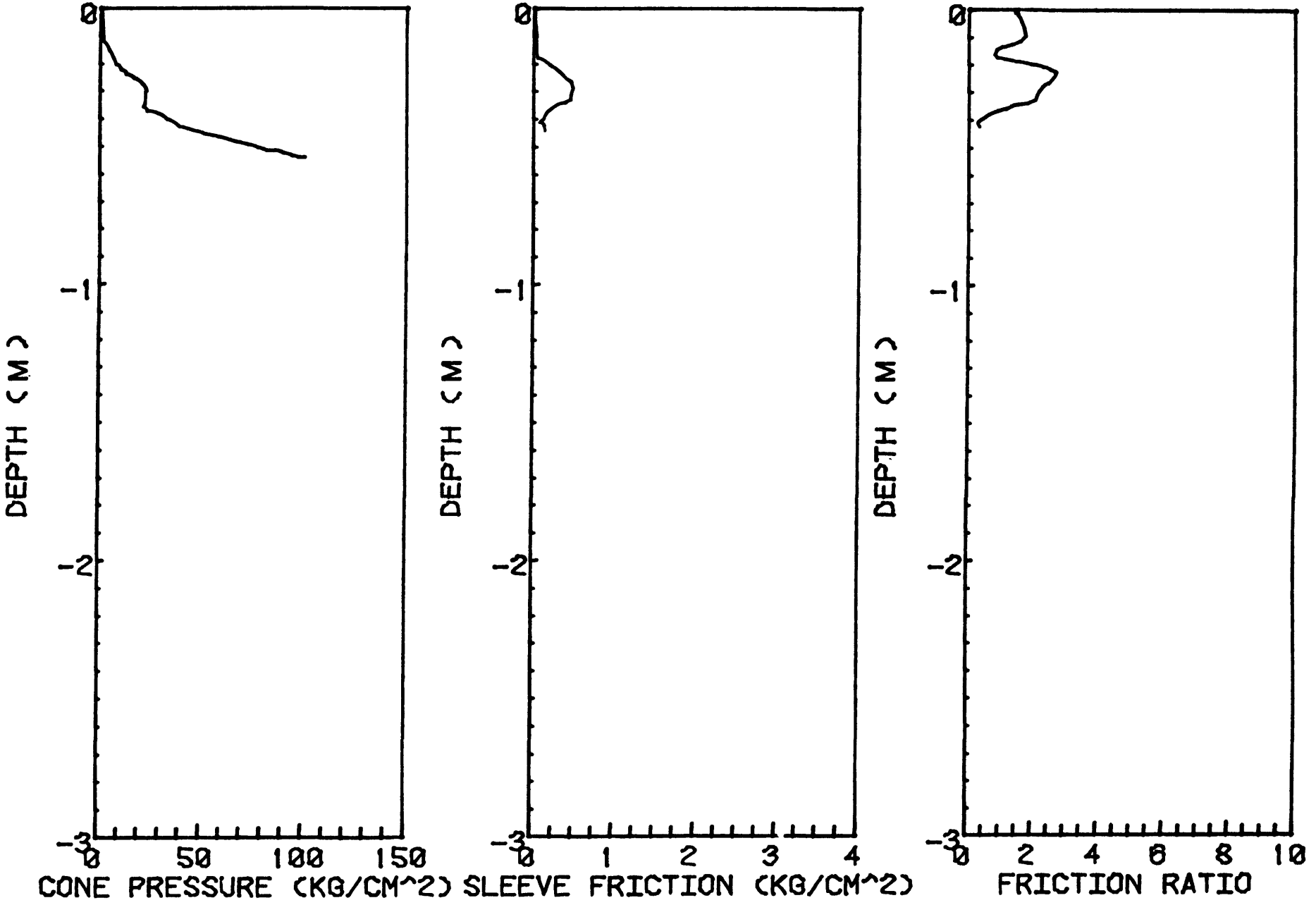

FIG. 668X3. W. OF YUKON DELTA - EXPOSED. ALASKA. 8/8/81

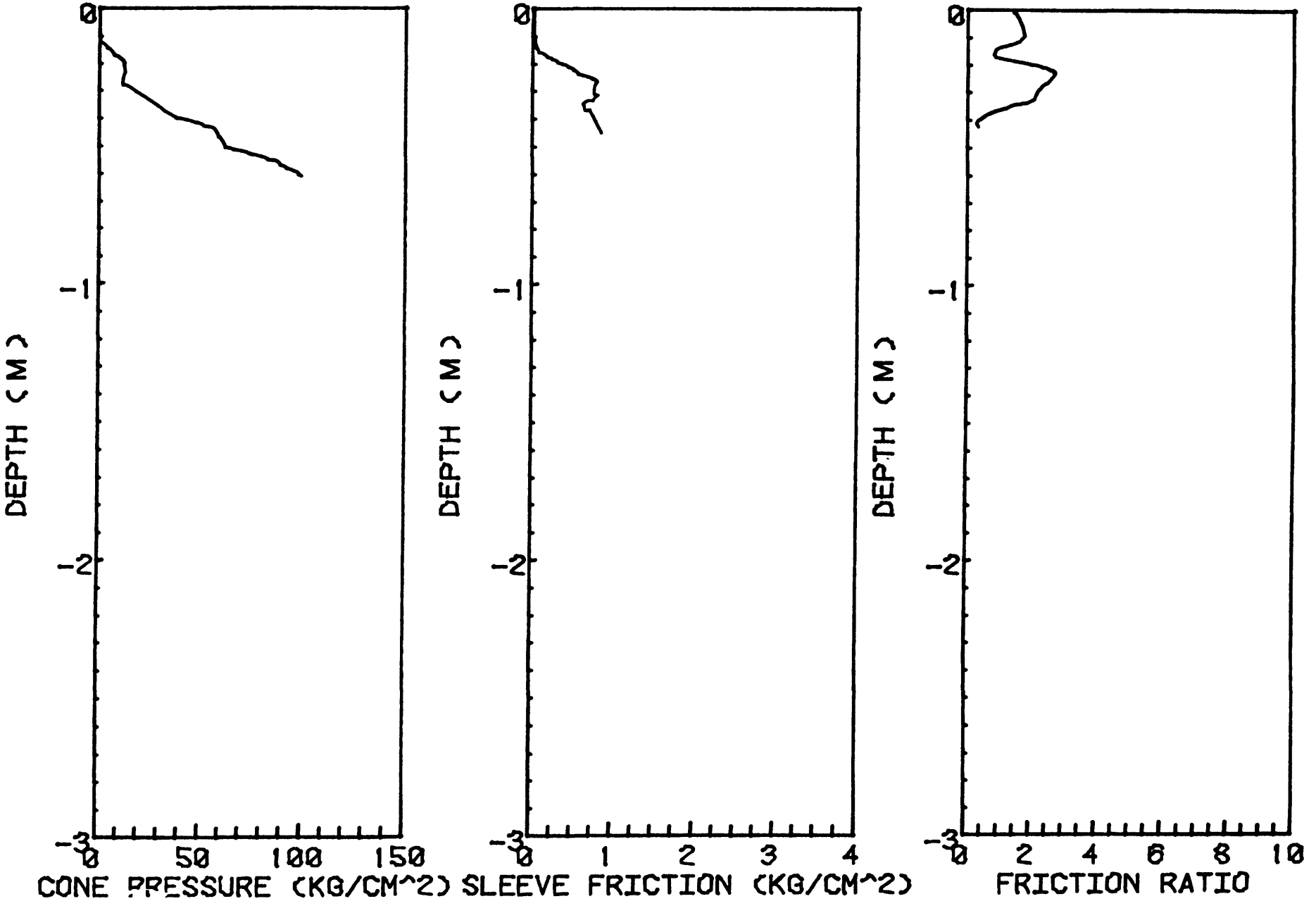

FIG. 668X4. W. OF YUKON DELTA - EXPOSED. ALASKA. 8/8/81

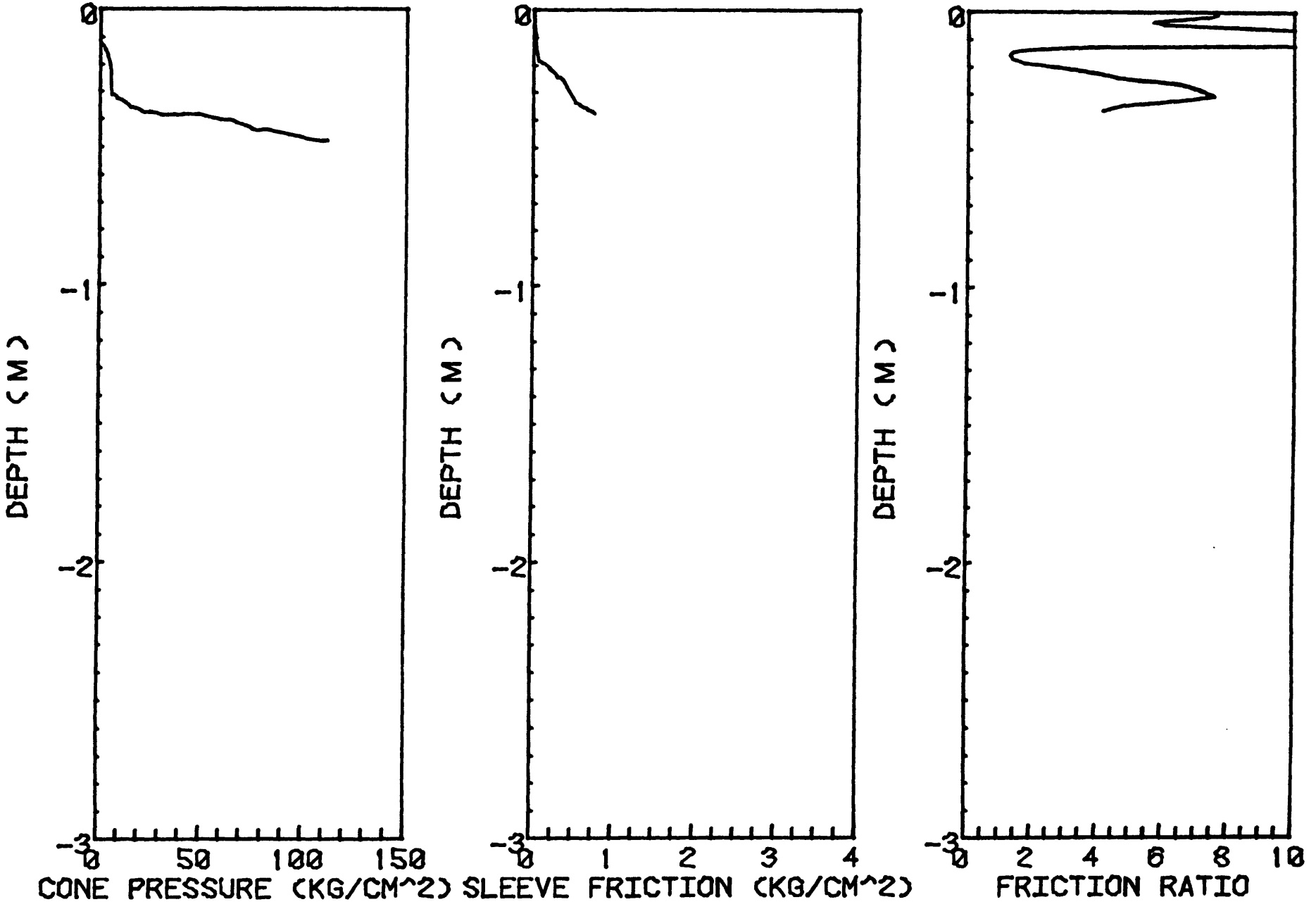

FIG. 669X1 . W. OF YUKON DELTA - EXPOSED. ALASKA. 8/8/81

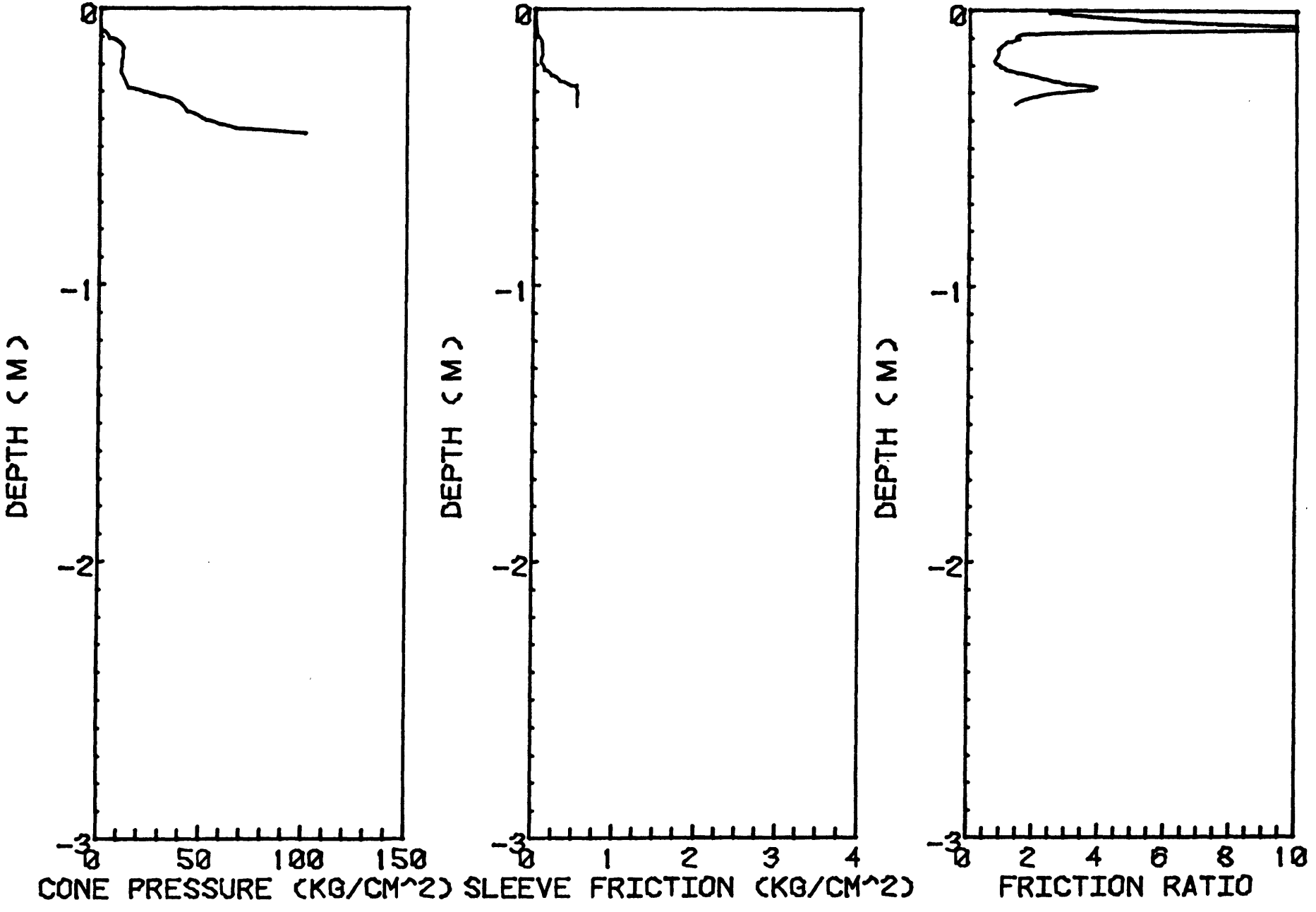

FIG. 669X2. W. YUKON DELTA - EXPOSED. ALASKA. 8/8/81

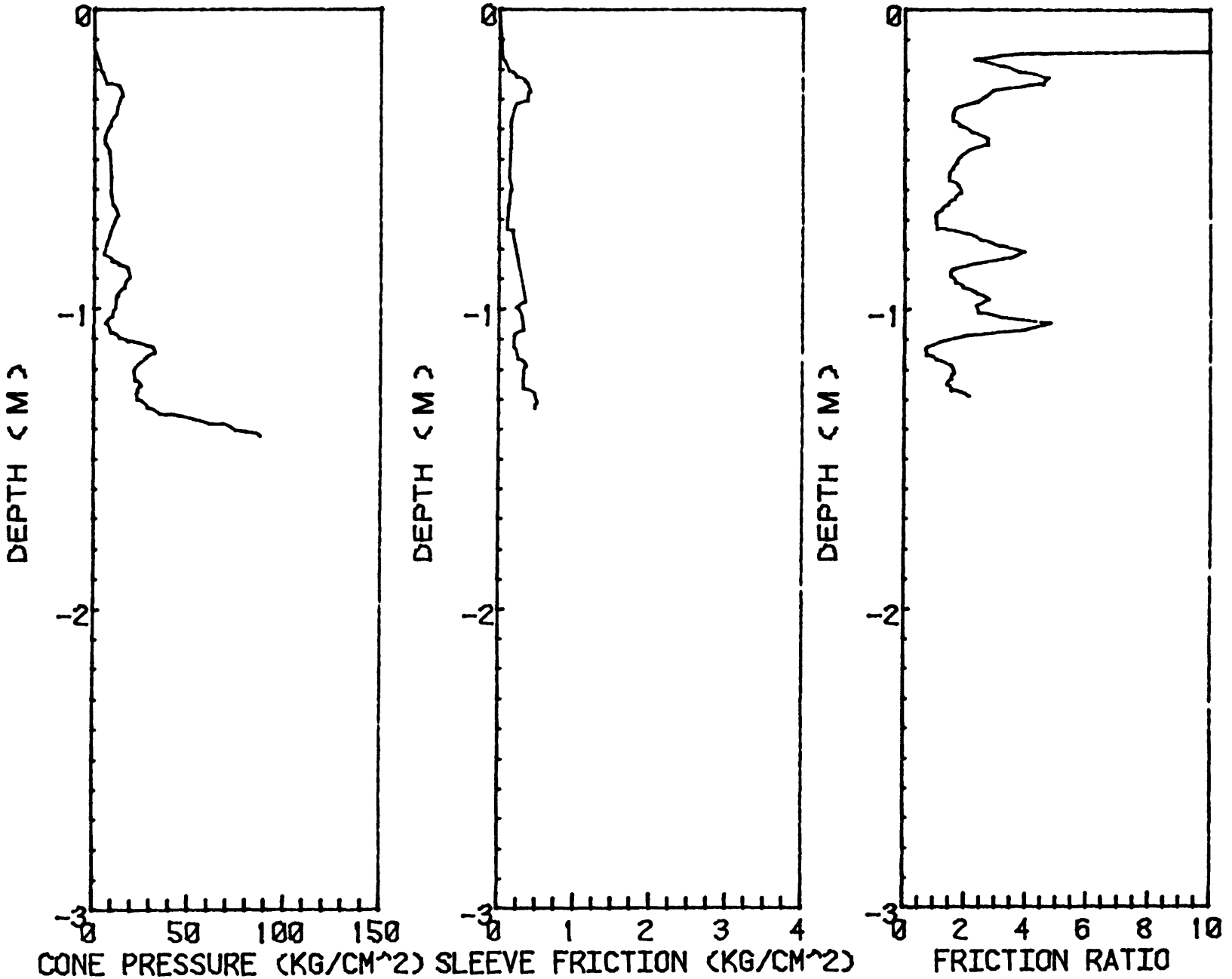

FTG 6702X1 N. N. W. YUKON DELTA - PROTECTED. ALASKA. 8/9/81

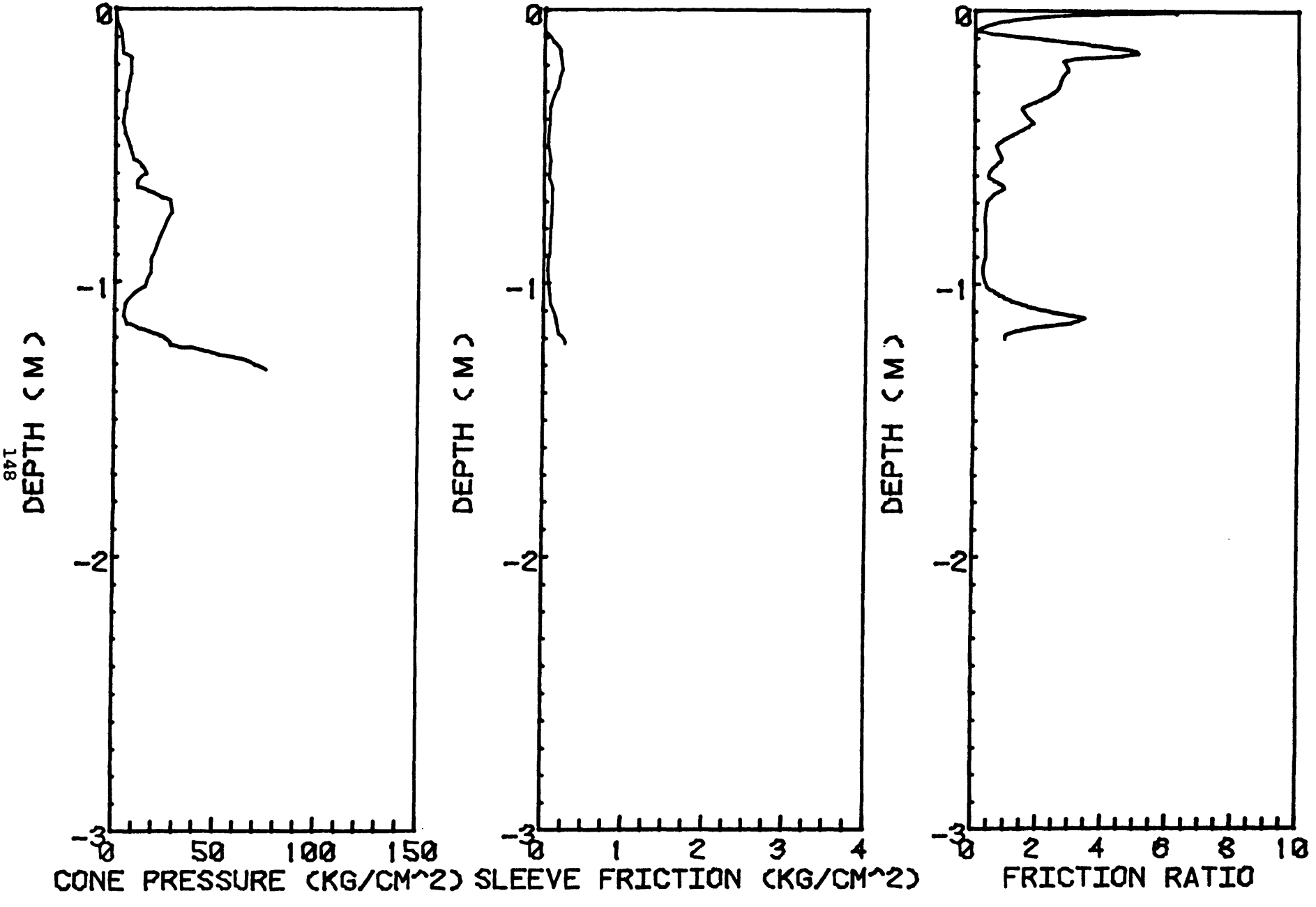

FIG. 670X3. N. N. W. YUKON DELTA - PROTECTED. ALASKA. 8/9/81

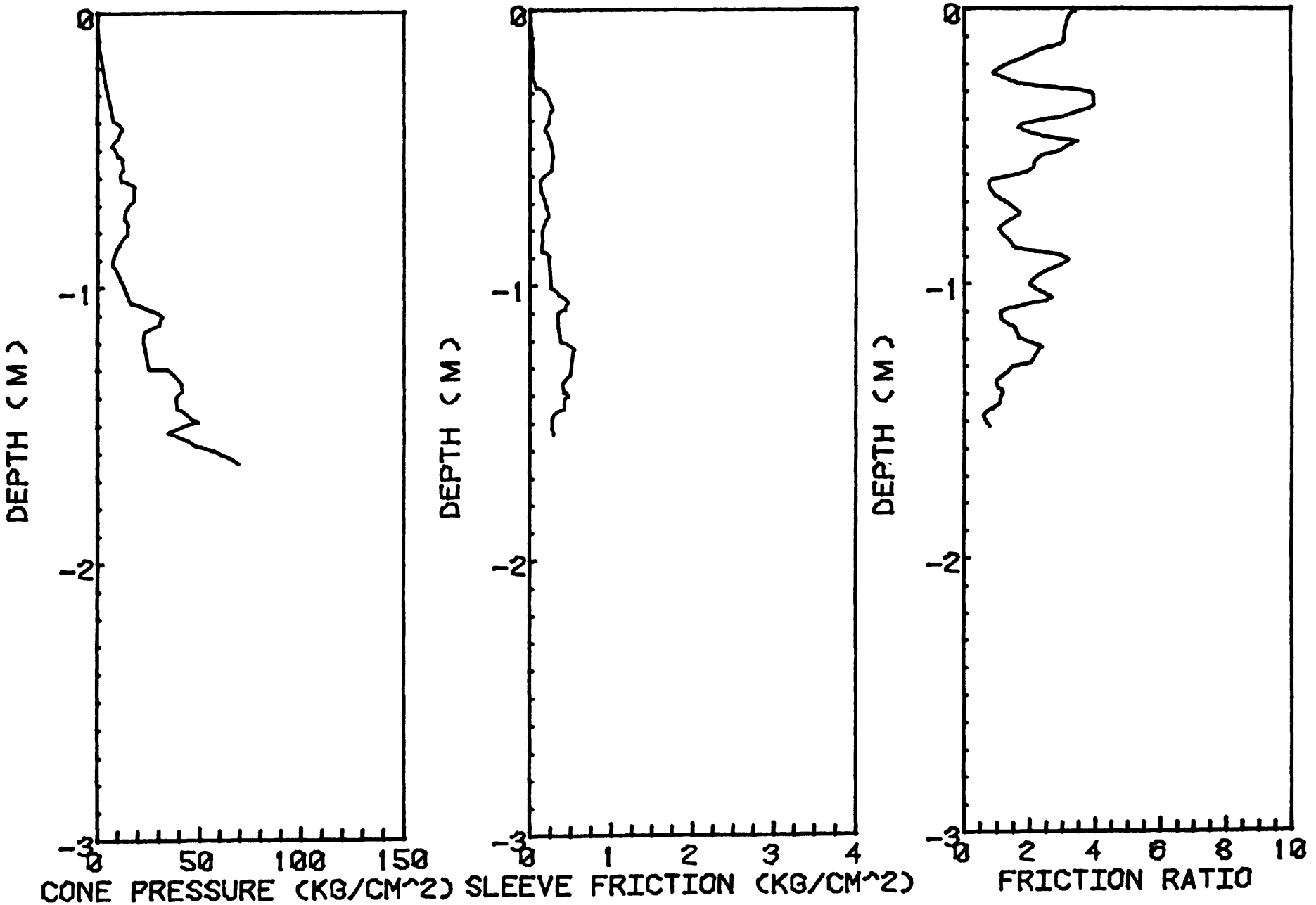

FIG. 670X4. N. N. W. YUKON DELTA - PROTECTED. ALASKA. 8/9/81

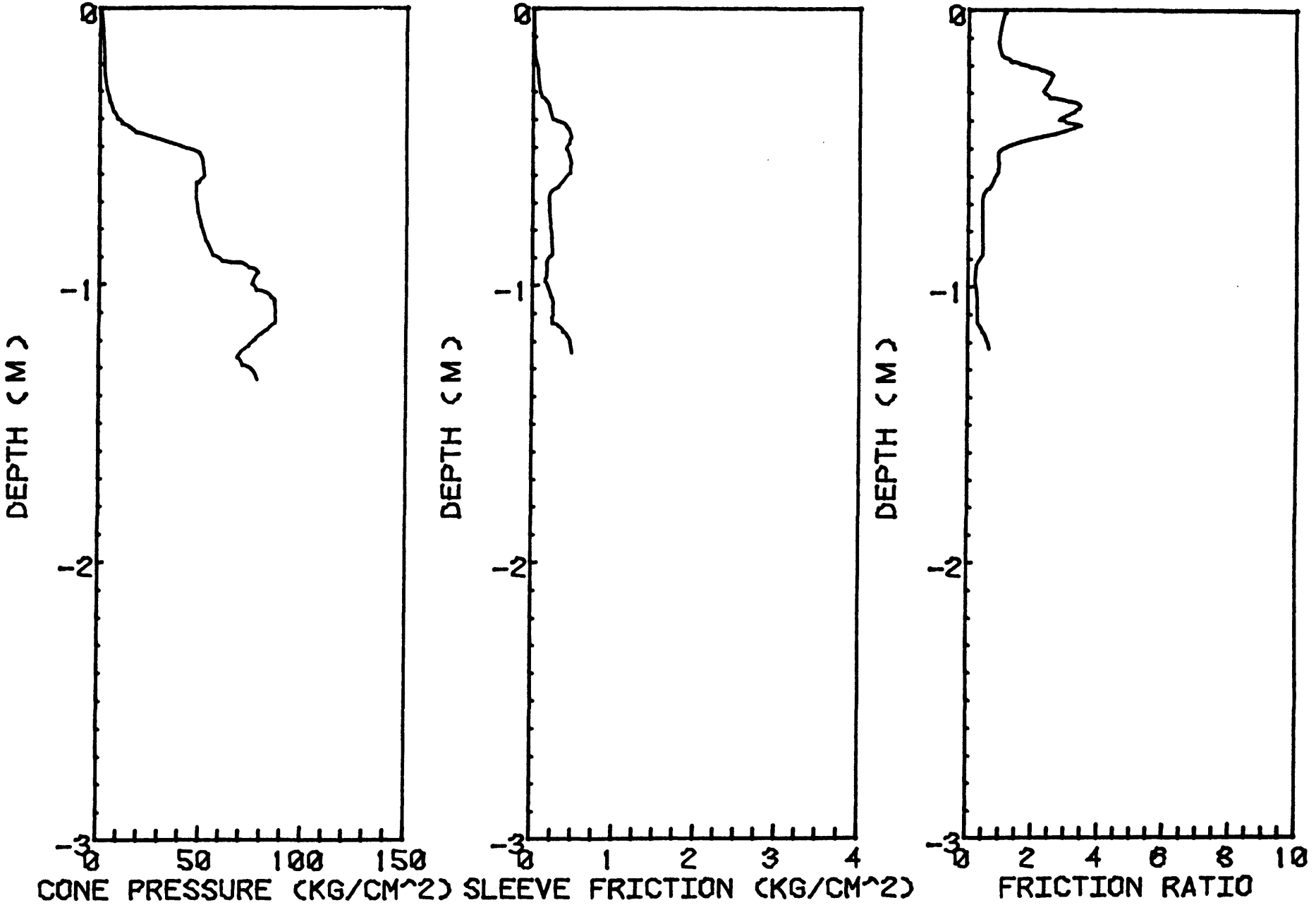

FIG. 671X1. E. OF THERMOGENIC GAS ZONE. ALASKA. 8/9/81

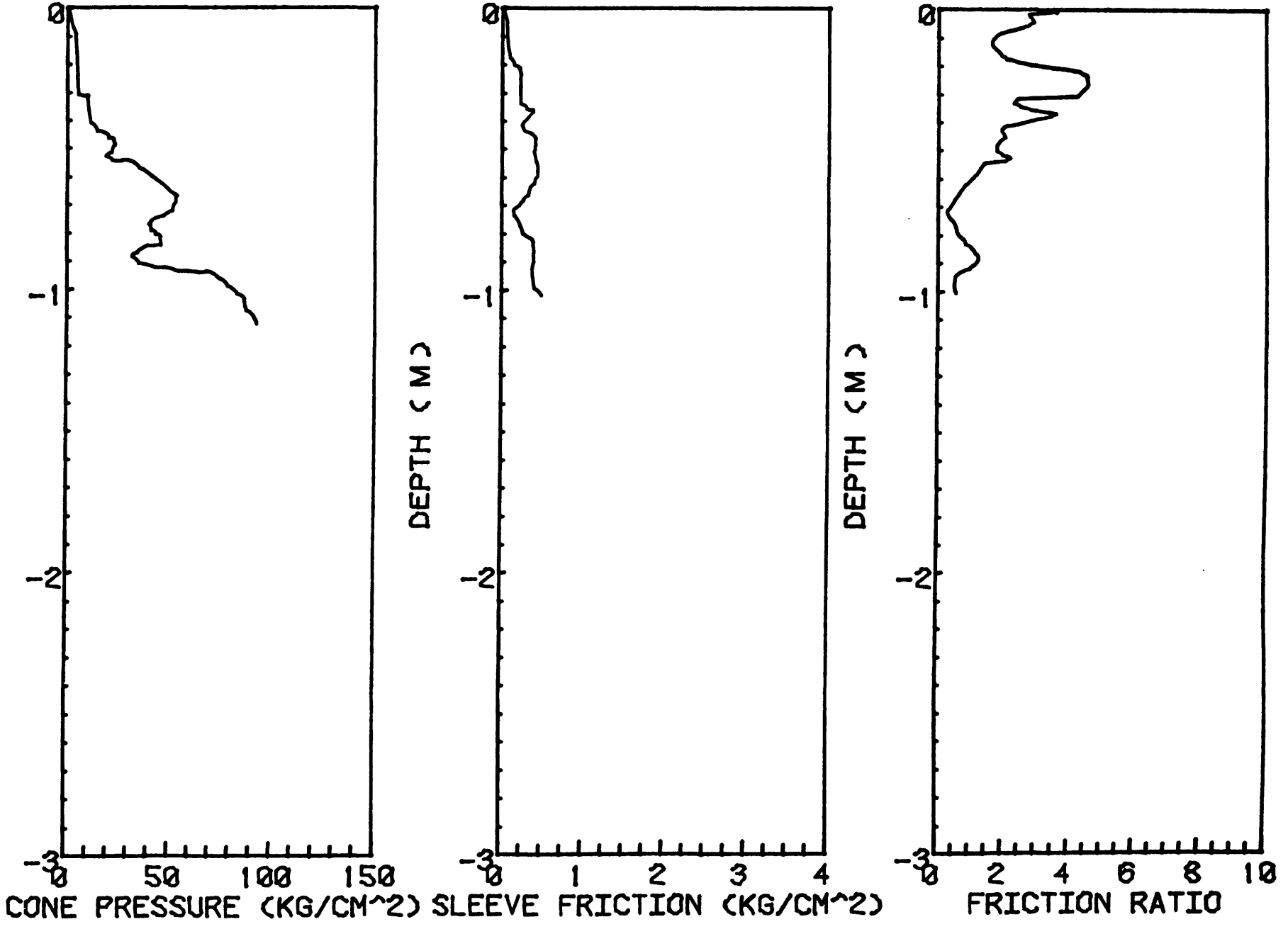

FIG. 671X2. E. OF THERMOGENIC GAS ZONE. ALASKA. 8/9/81

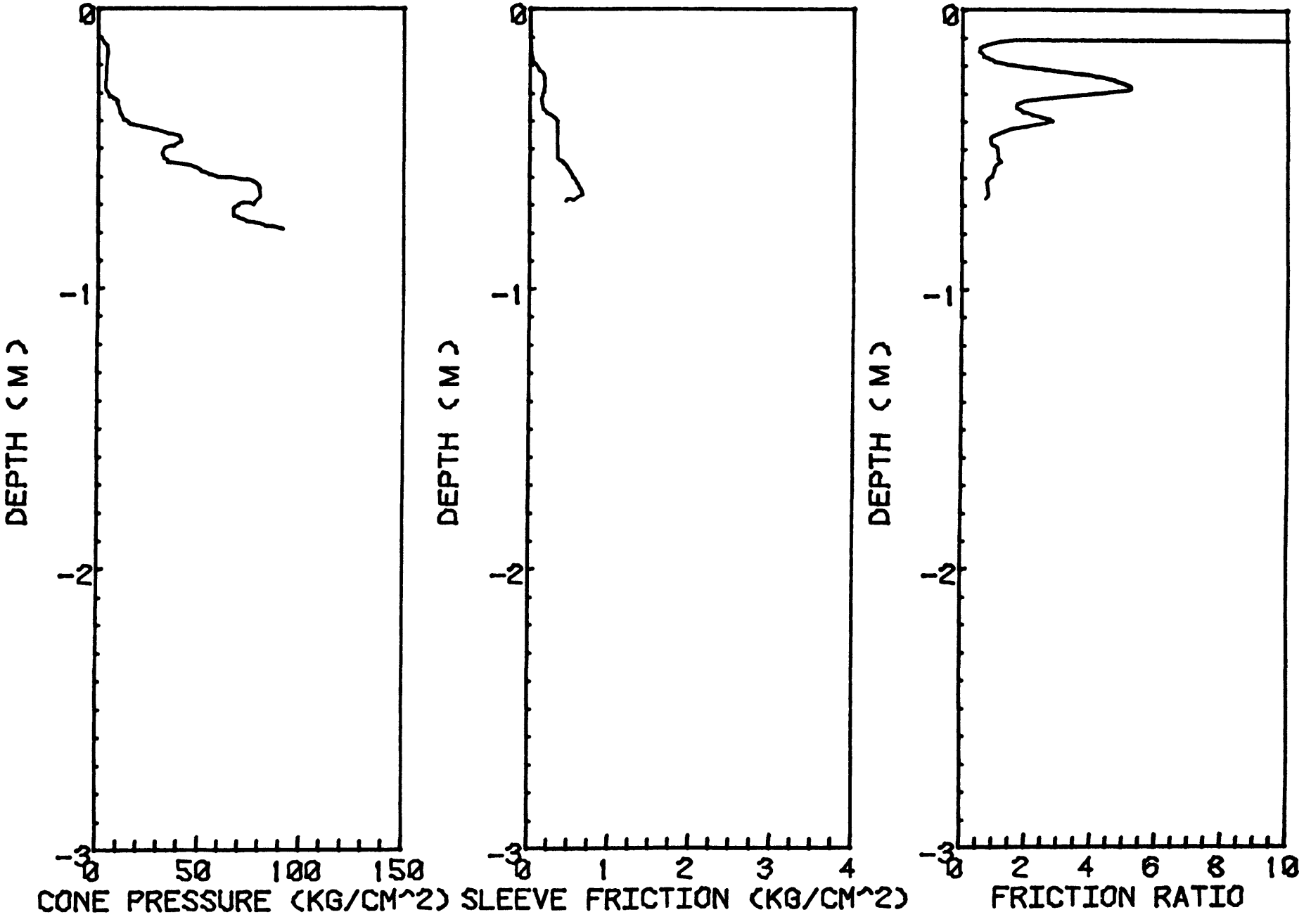

FIG. 671X3. E. OF THERMOGENIC GAS ZONE. ALASKA. 8/9/81

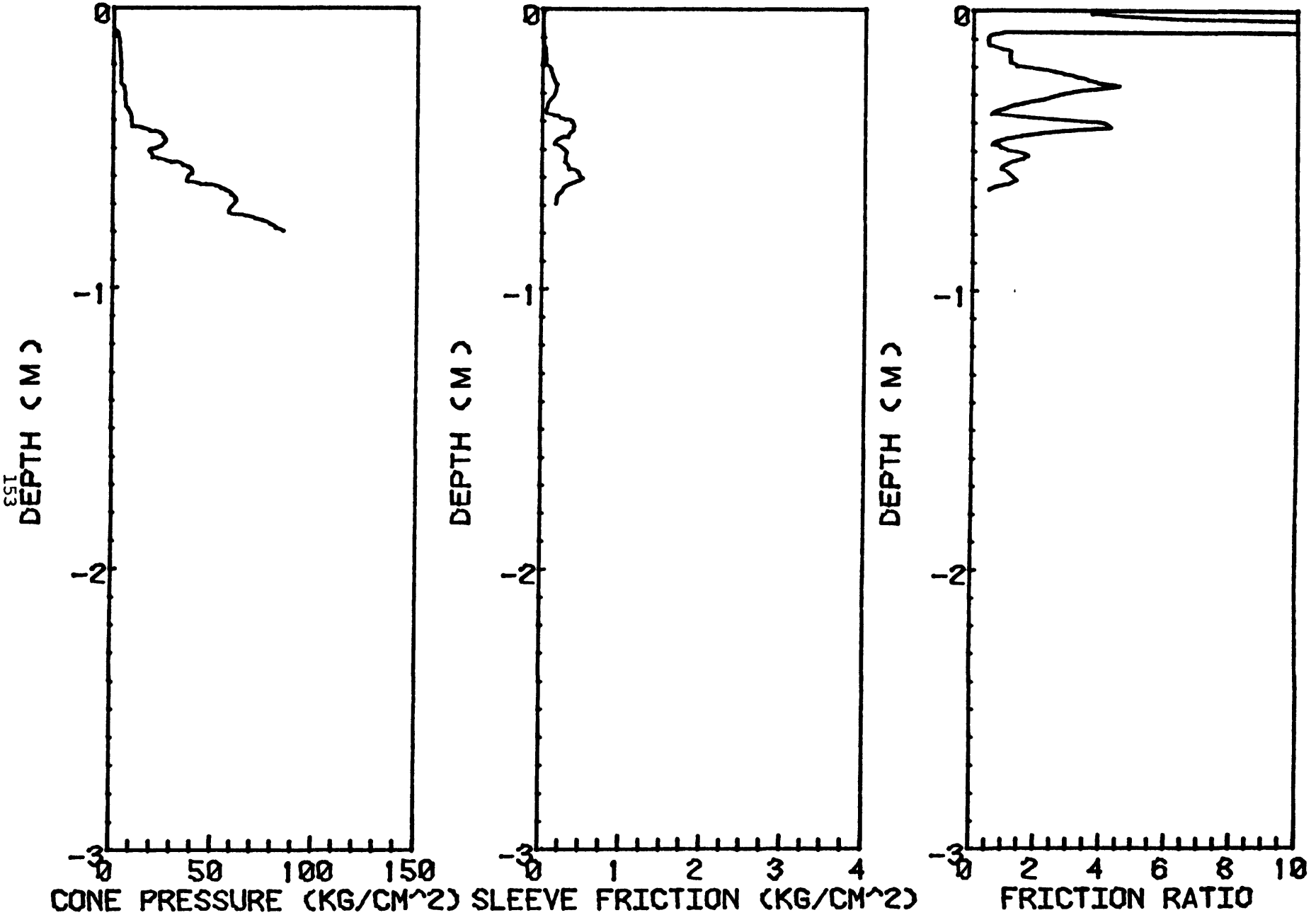

FIG. 671X4. E OF THERMOGENIC GAS ZONE. ALASKA. 8/9/81

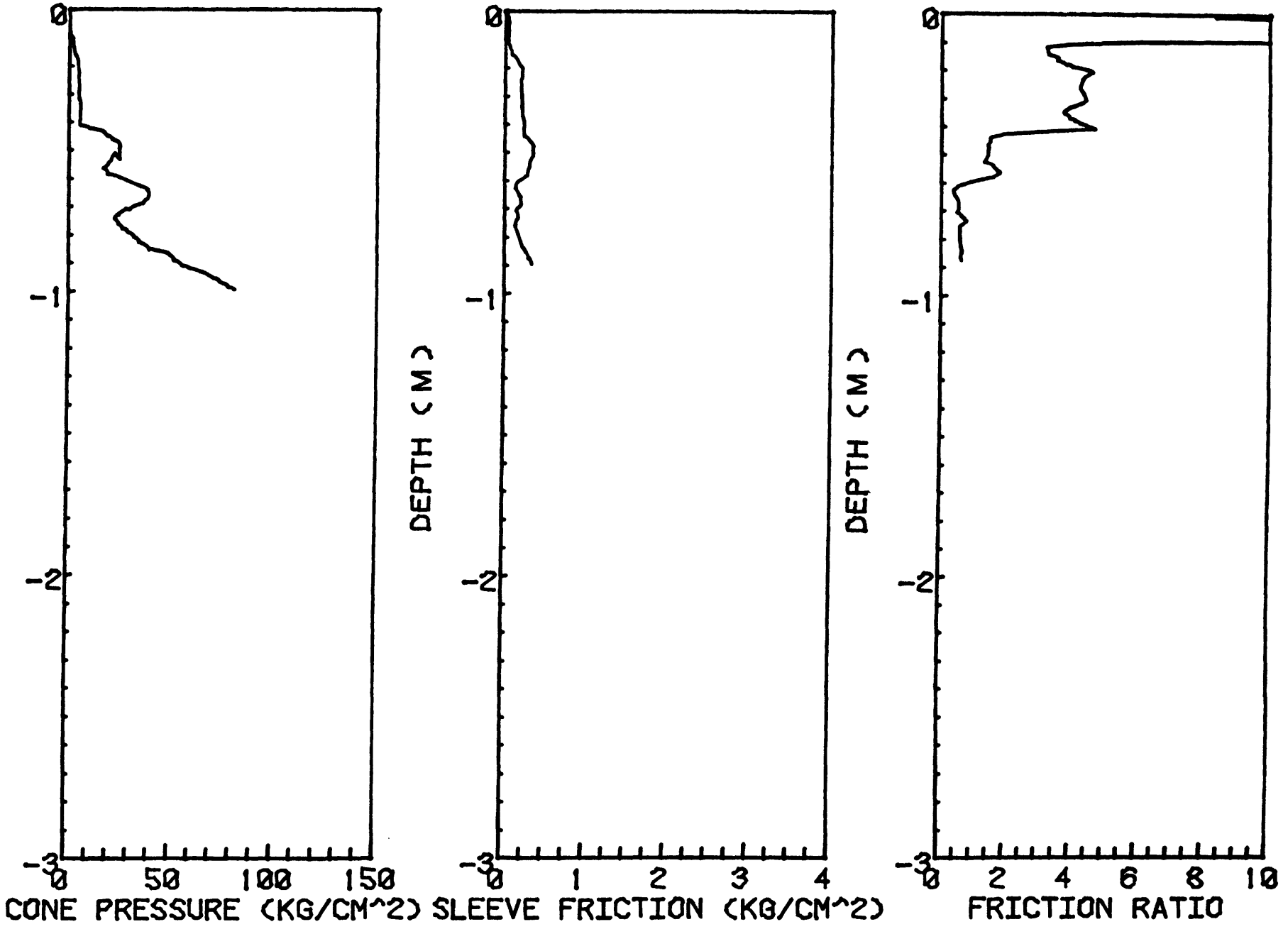

FIG. 671X5. E. OF THERMOGENIC GAS ZONE. ALASKA. 8/9/81

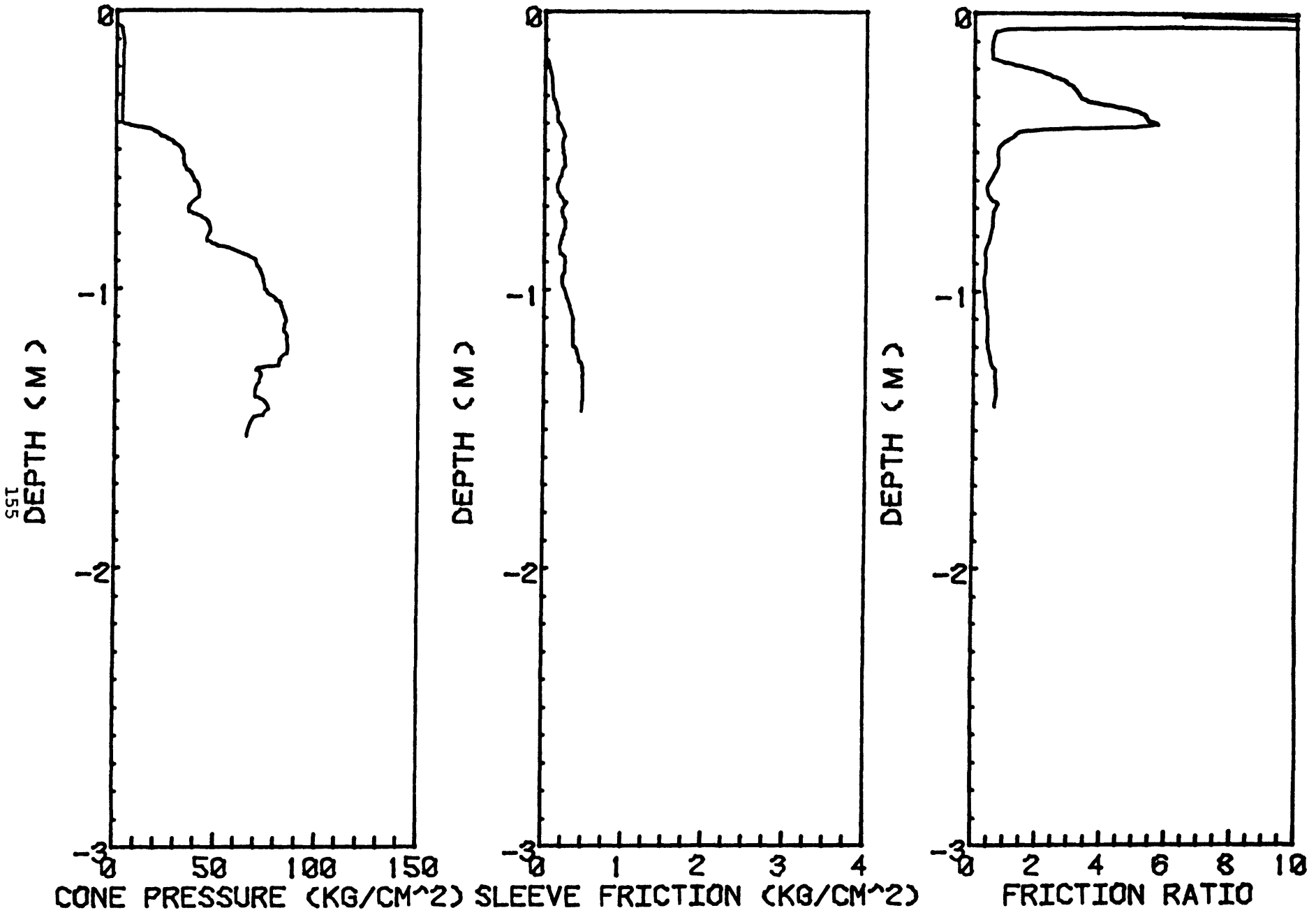

FIG. 671X6. E. OF THERMOGENIC GAS ZONE. ALASKA. 8/9/81

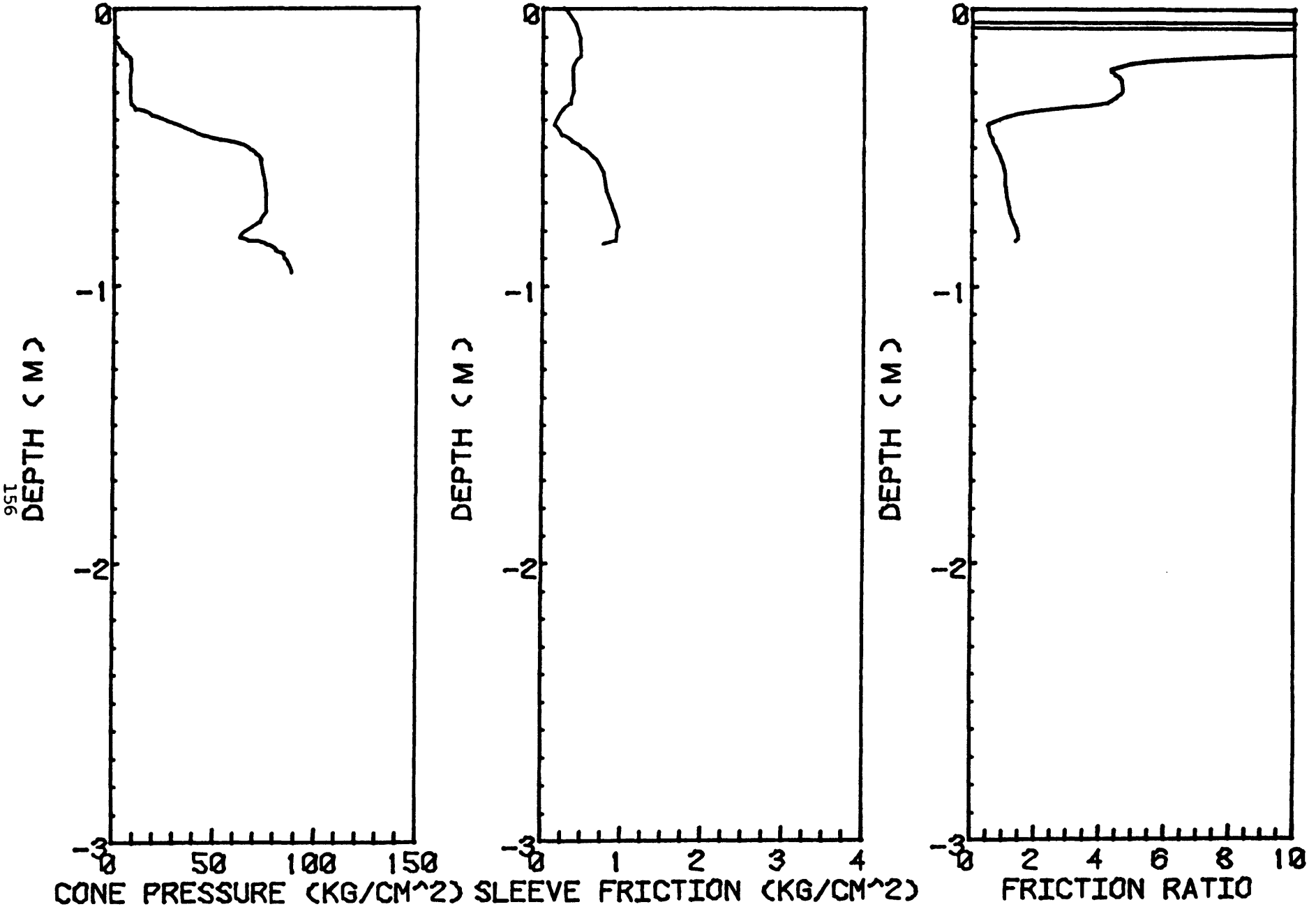

FIG. 671X7. E. OF THERMOGENIC GAS ZONE. ALASKA. 8/9/81

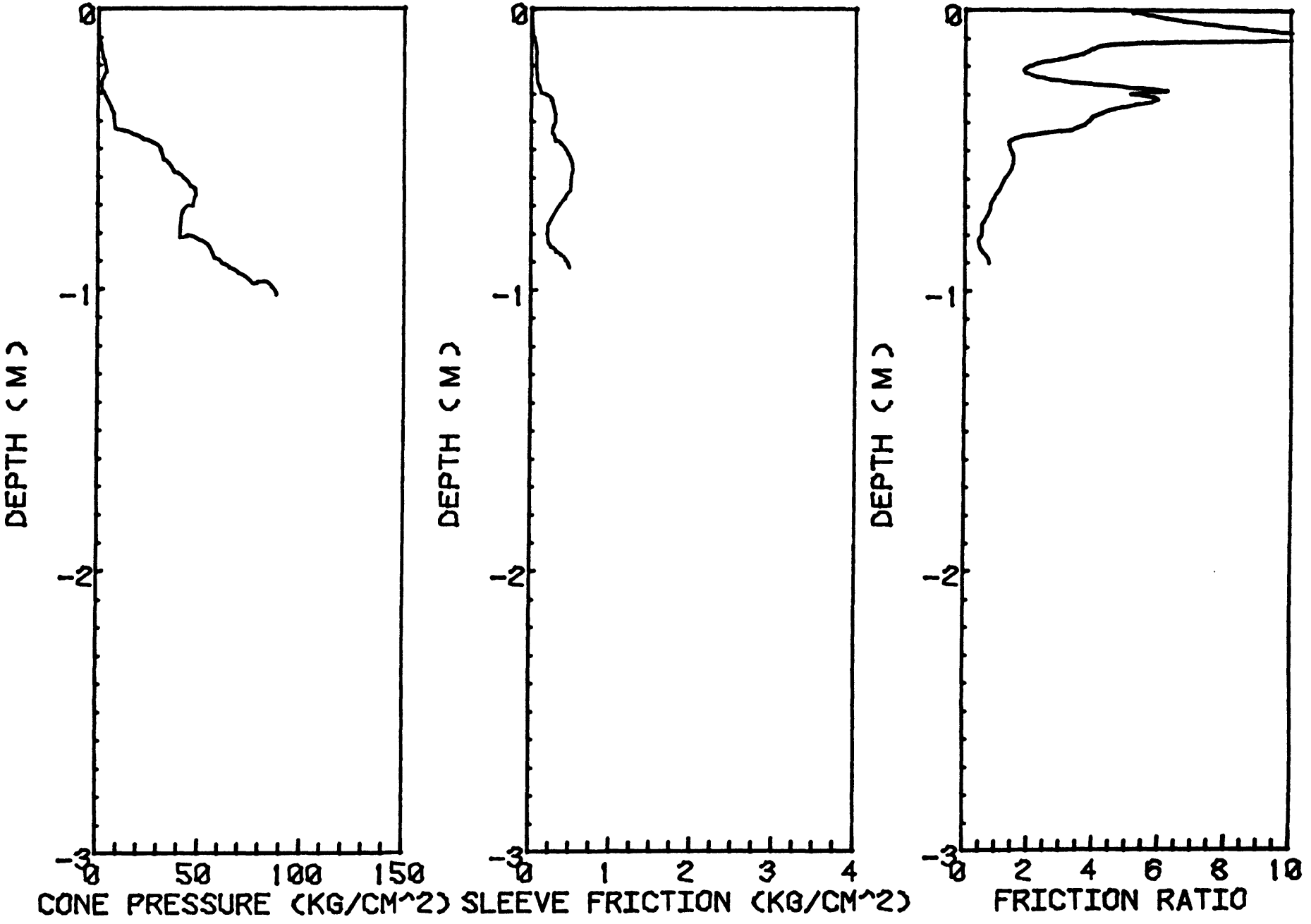

FIG. 671X8. E. OF THERMOGENIC GAS ZONE. ALASKA. 8/9/81

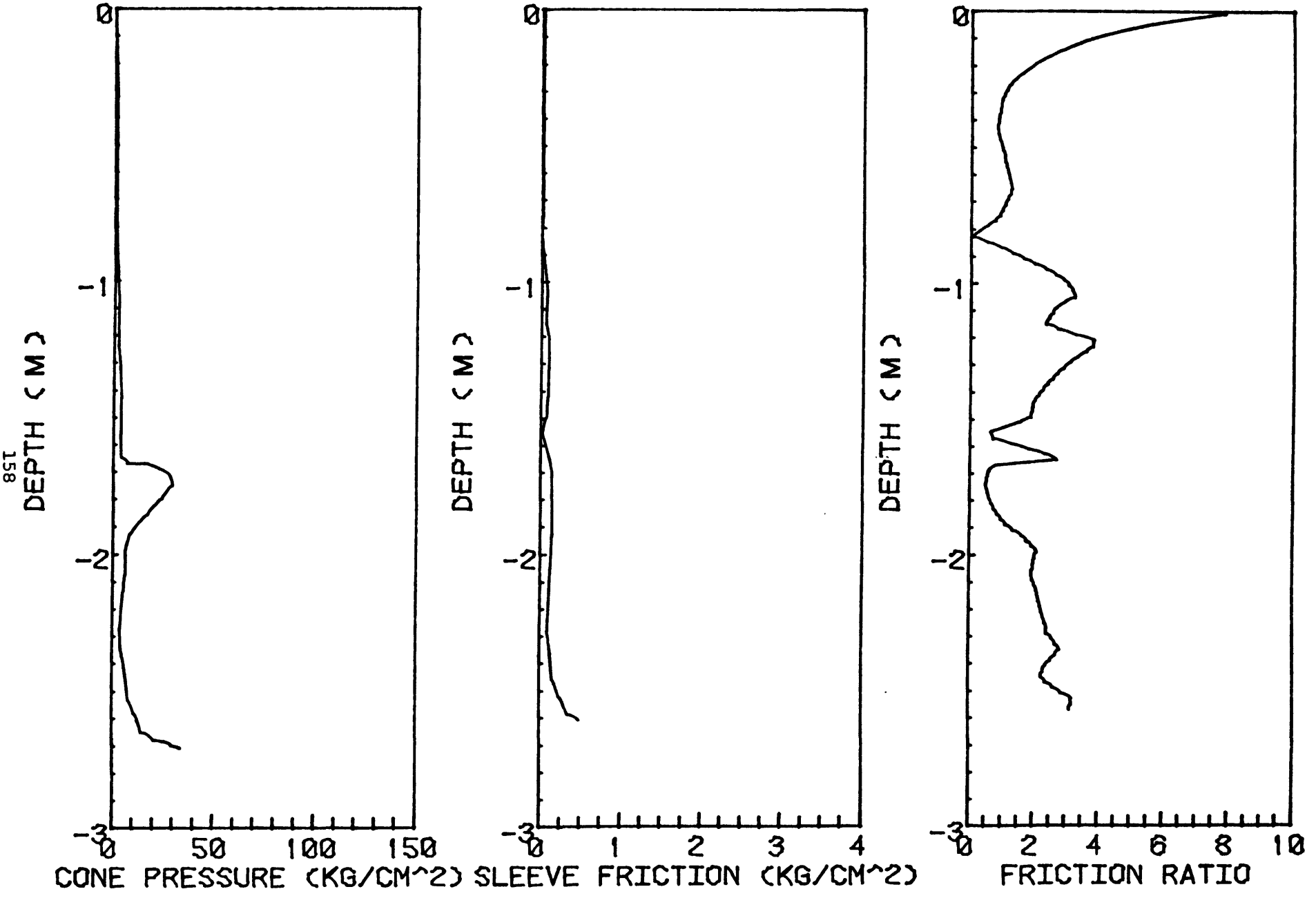

FIG. 672X2. CENTRAL FAR E. NORTON SOUND. ALASKA. 8/10/81

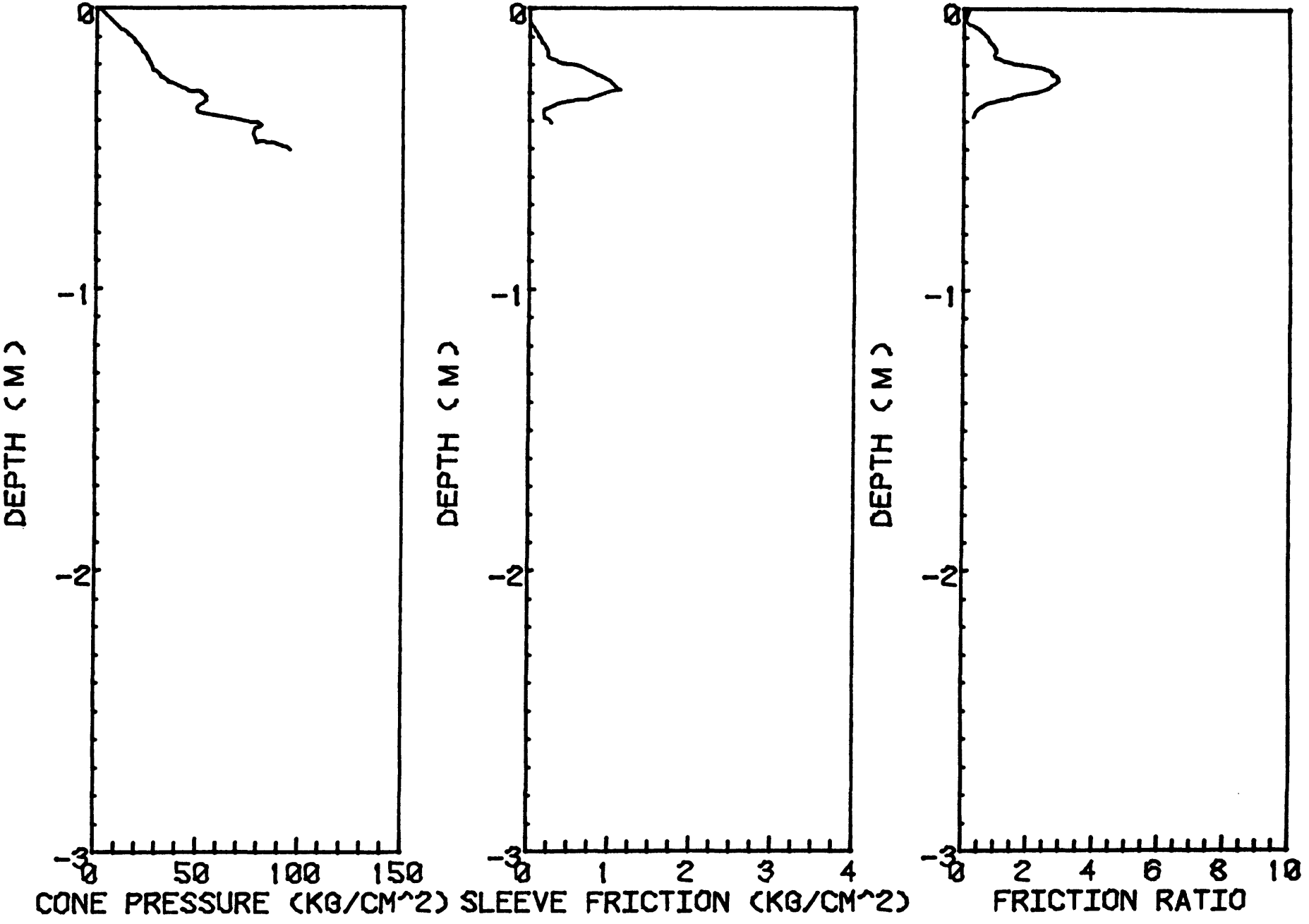

FIG. 673X1. CENTRAL E. NORTON SOUND. ALASKA. 8/10/81

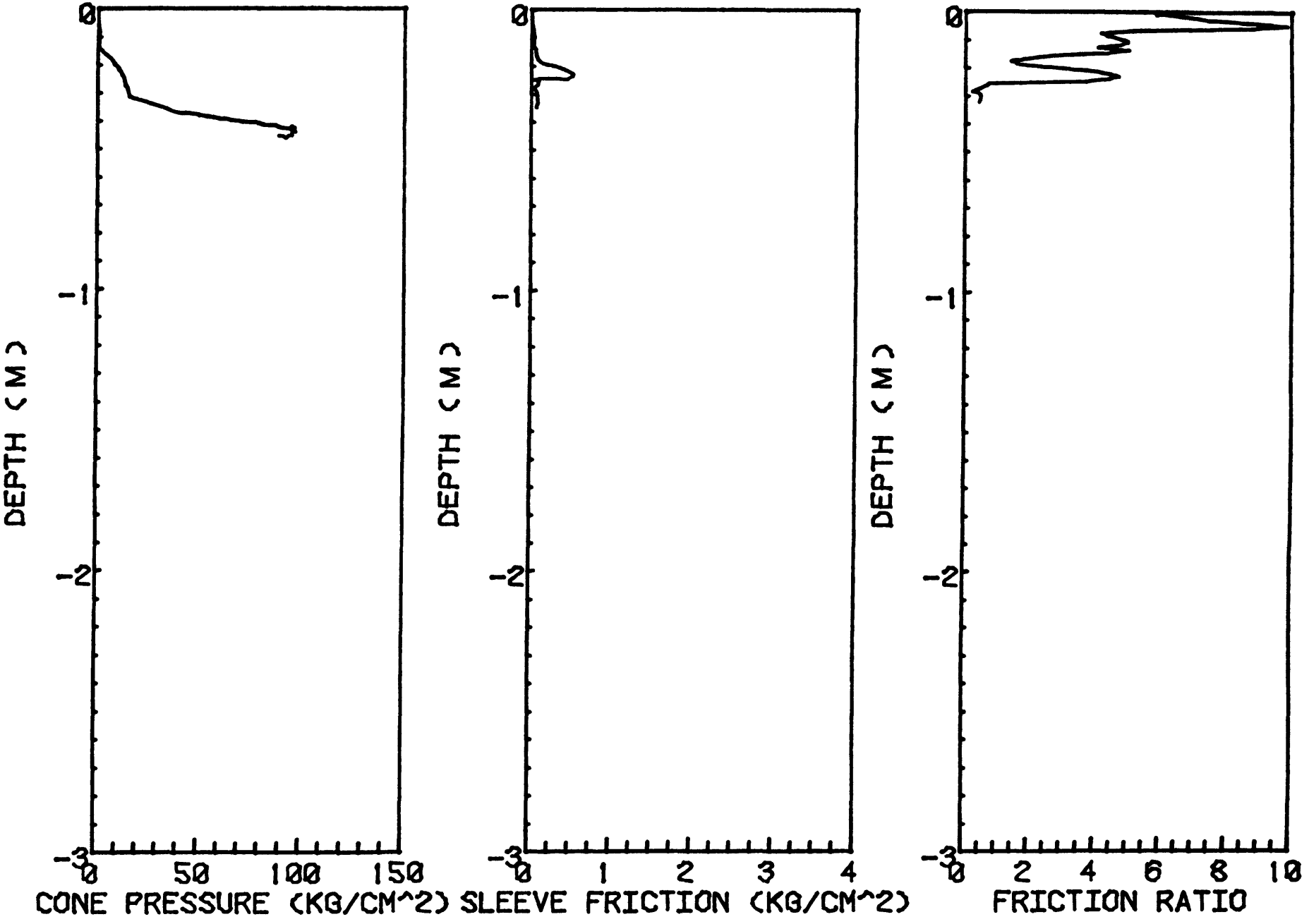

FIG. 673X2. CENTRAL E. NORTON SOUND. ALASKA. 8/10/81

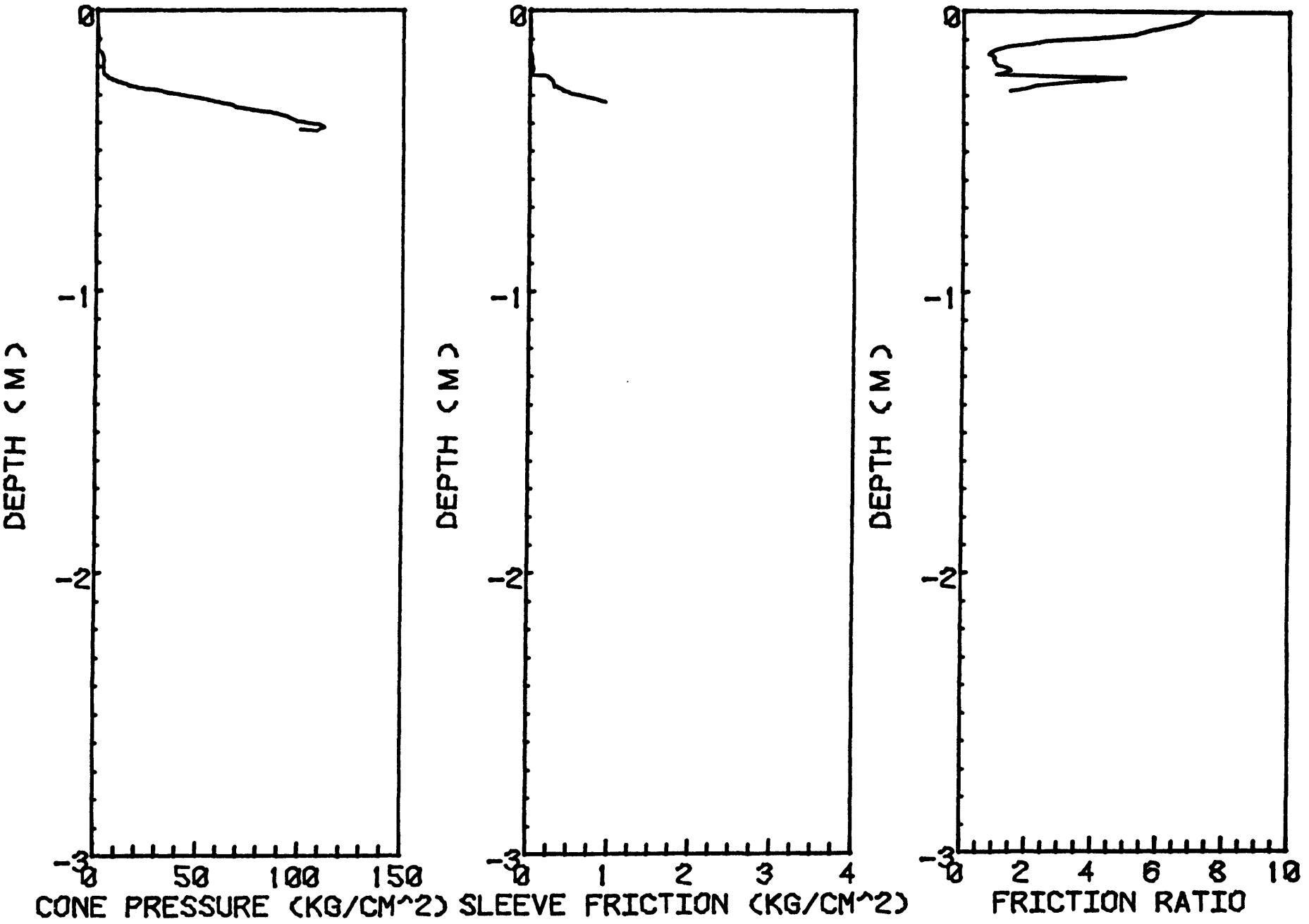

FIG. 673X3. CENTRAL E. NORTON SOUND. ALASKA. 8/10/81

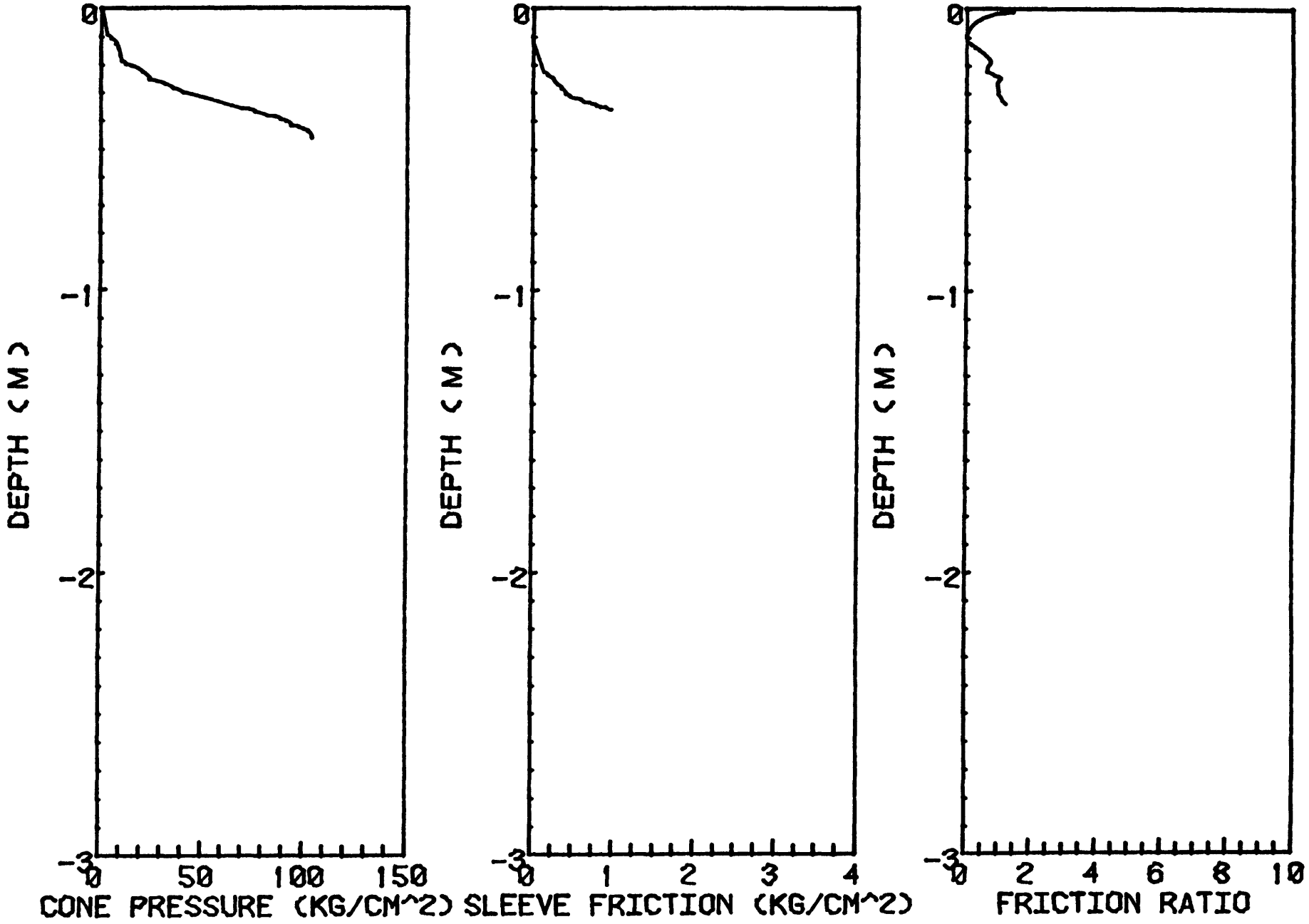

FIG. 673X4. CENTRAL E. NORTON SOUND. ALASKA. 8/10/81

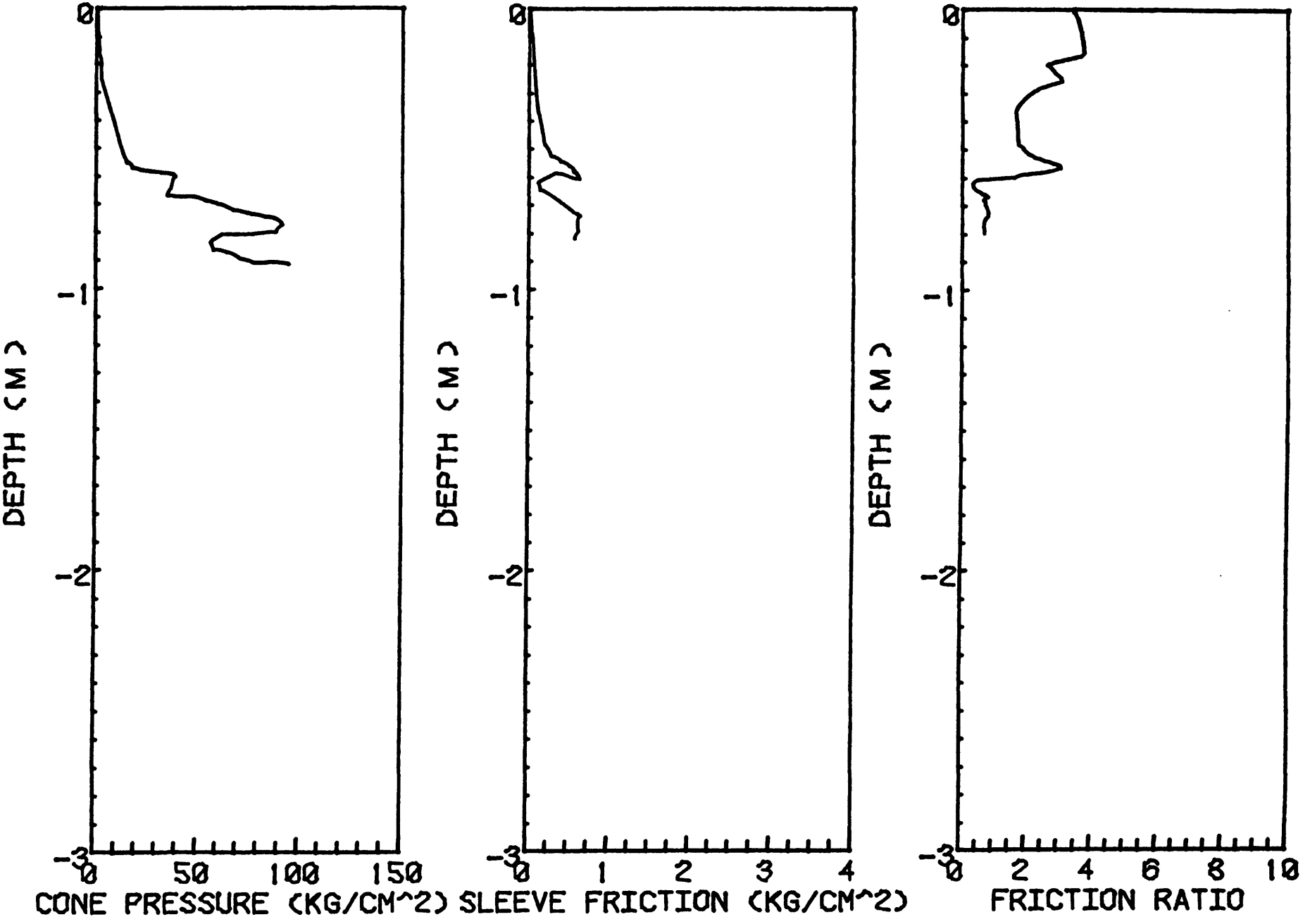

FIG. 674X1. N. YUKON DELTA ICE GOUGE AREA. ALASKA. 8/11/81

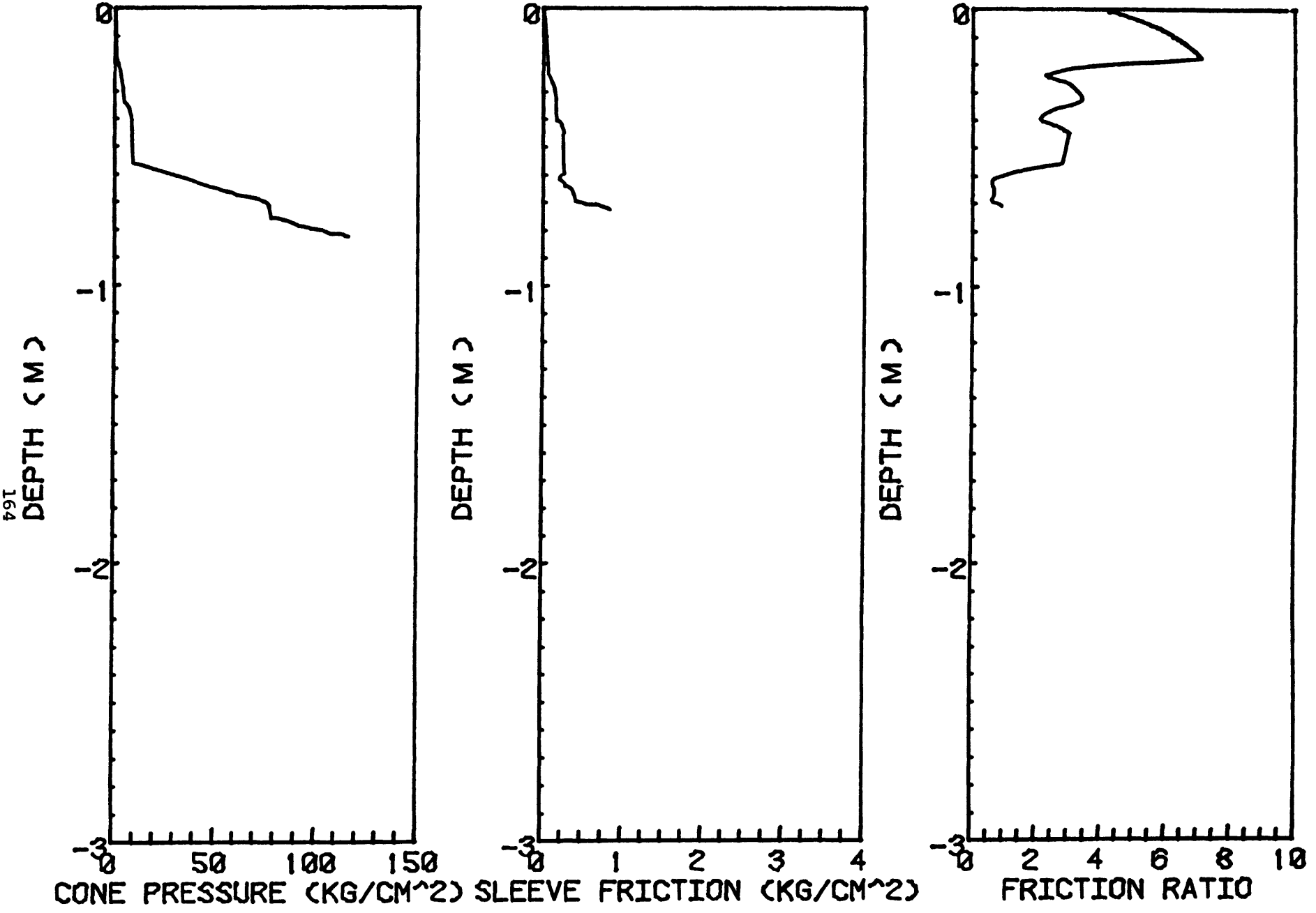

FIG. 674X2. N. YUKON DELTA ICE GOUGE AREA. ALASKA. 8/11/81

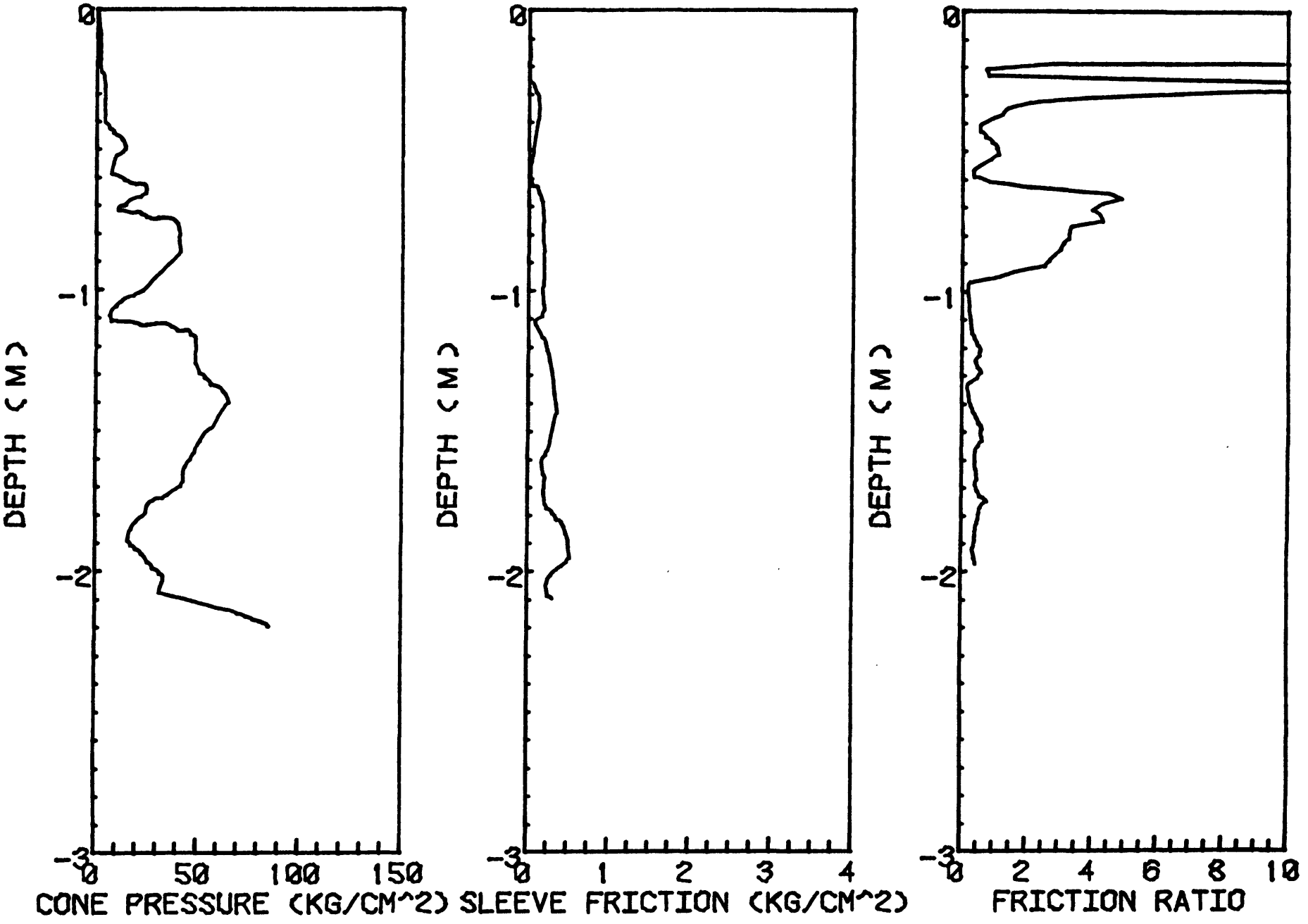

FIG. 675X1. THERMOGENIC GAS ZONE. ALASKA. 8/11/81

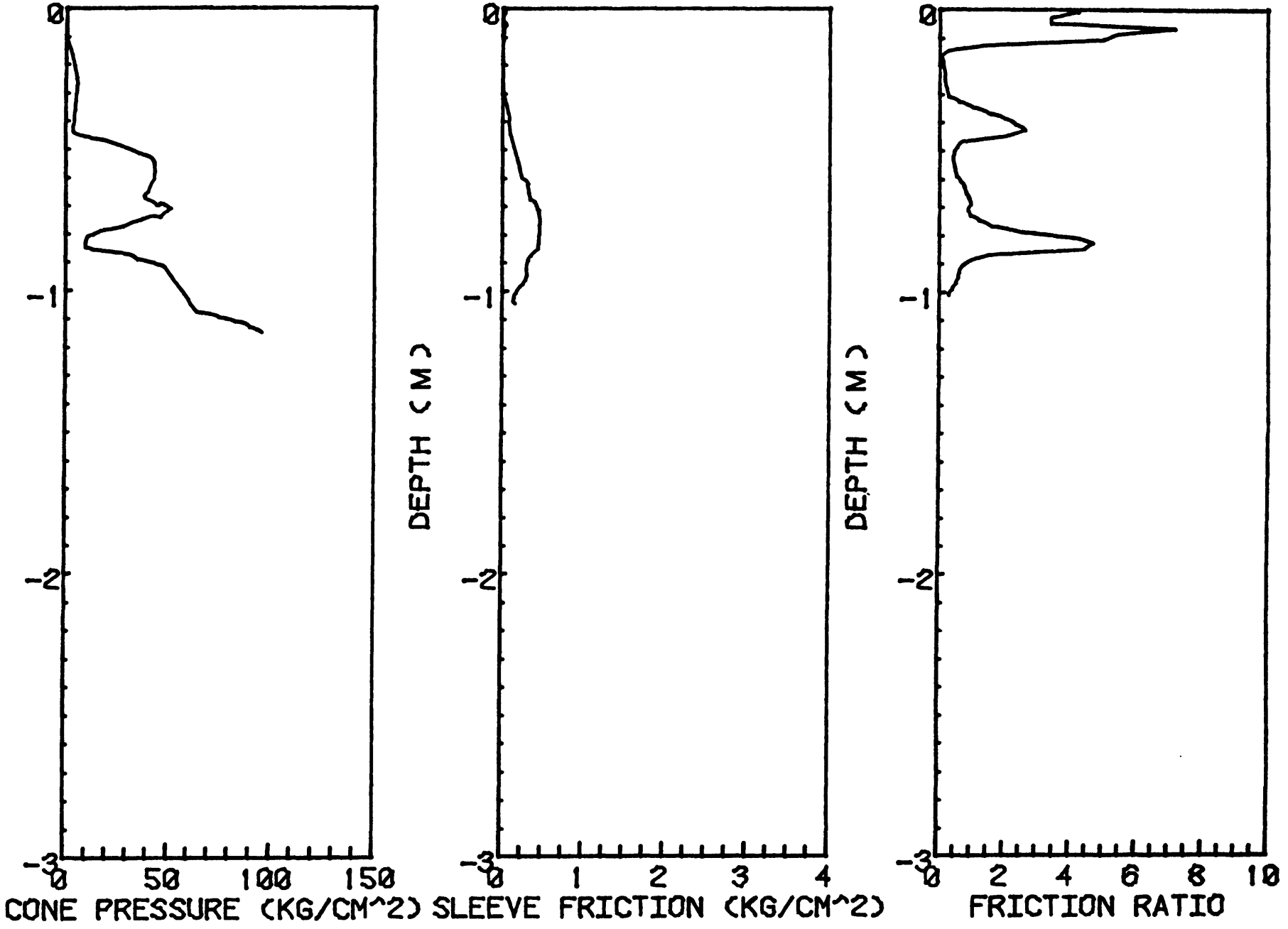

FIG. 675X2. THERMOGENIC GAS ZONE. ALASKA. 8/11/81

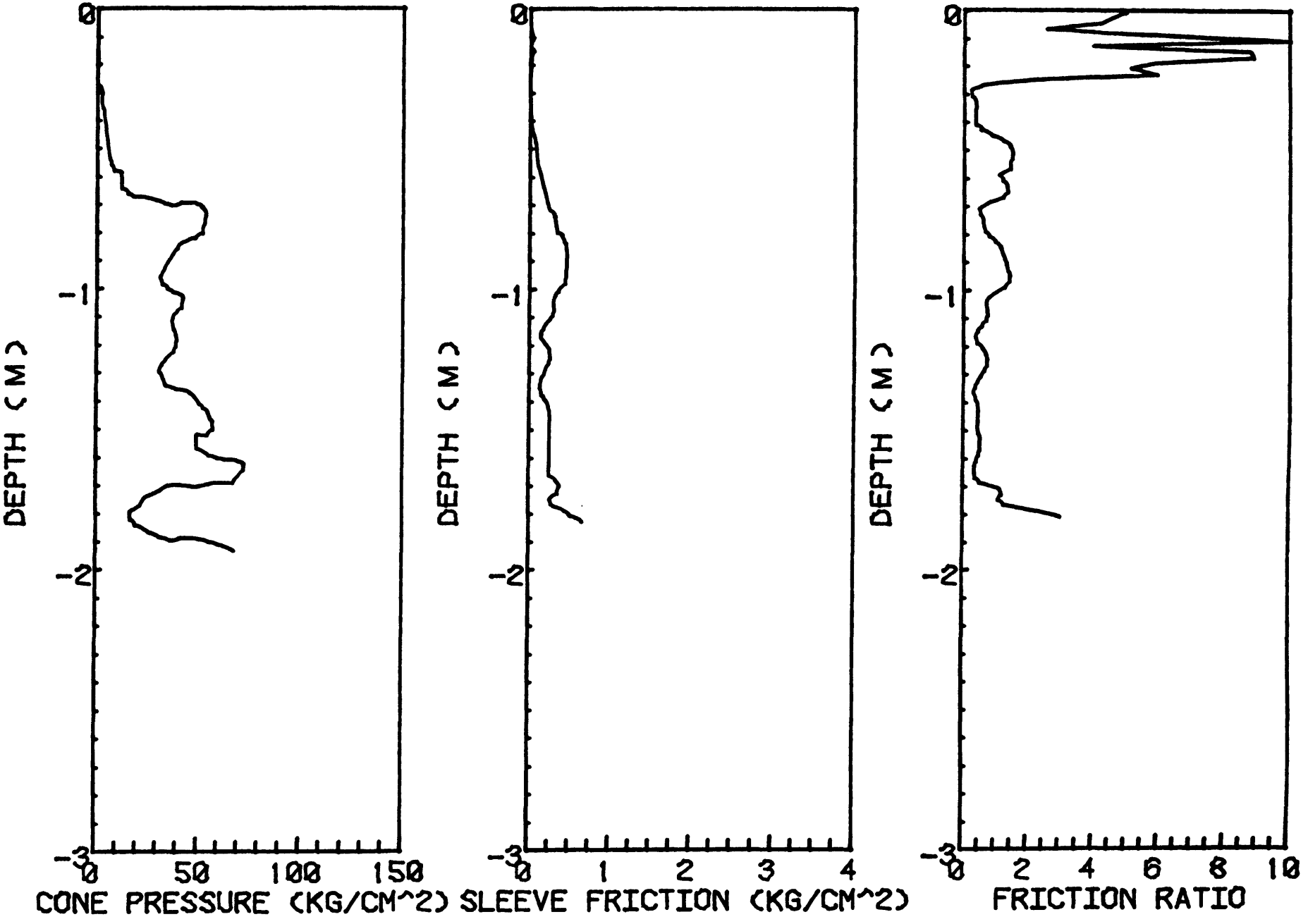

FIG. 675X3. THERMOGENIC GAS ZONE. ALASKA. 8/11/81

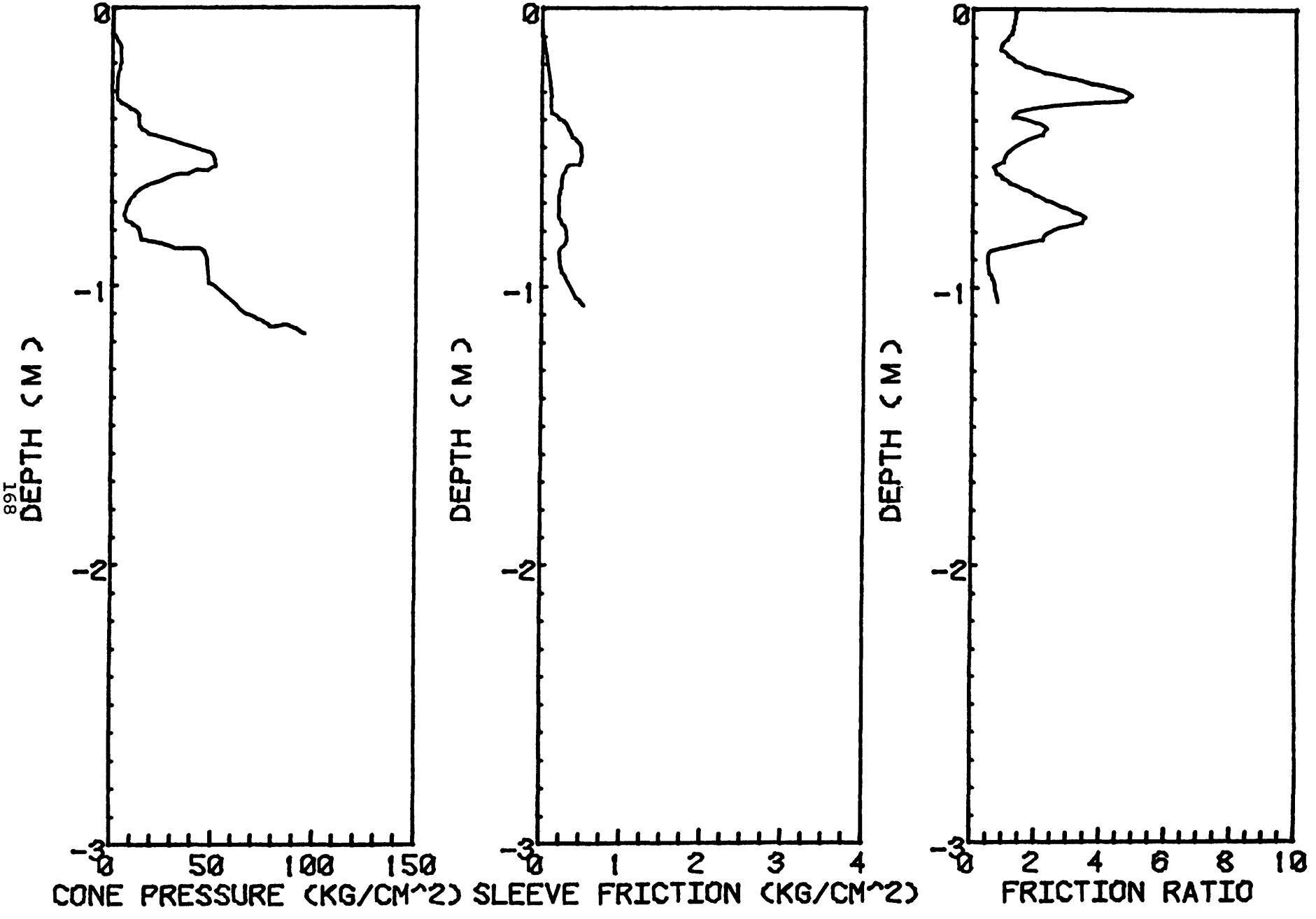

FIG. 675X4. THERMOGENIC GAS ZONE. ALASKA. 8/11/81

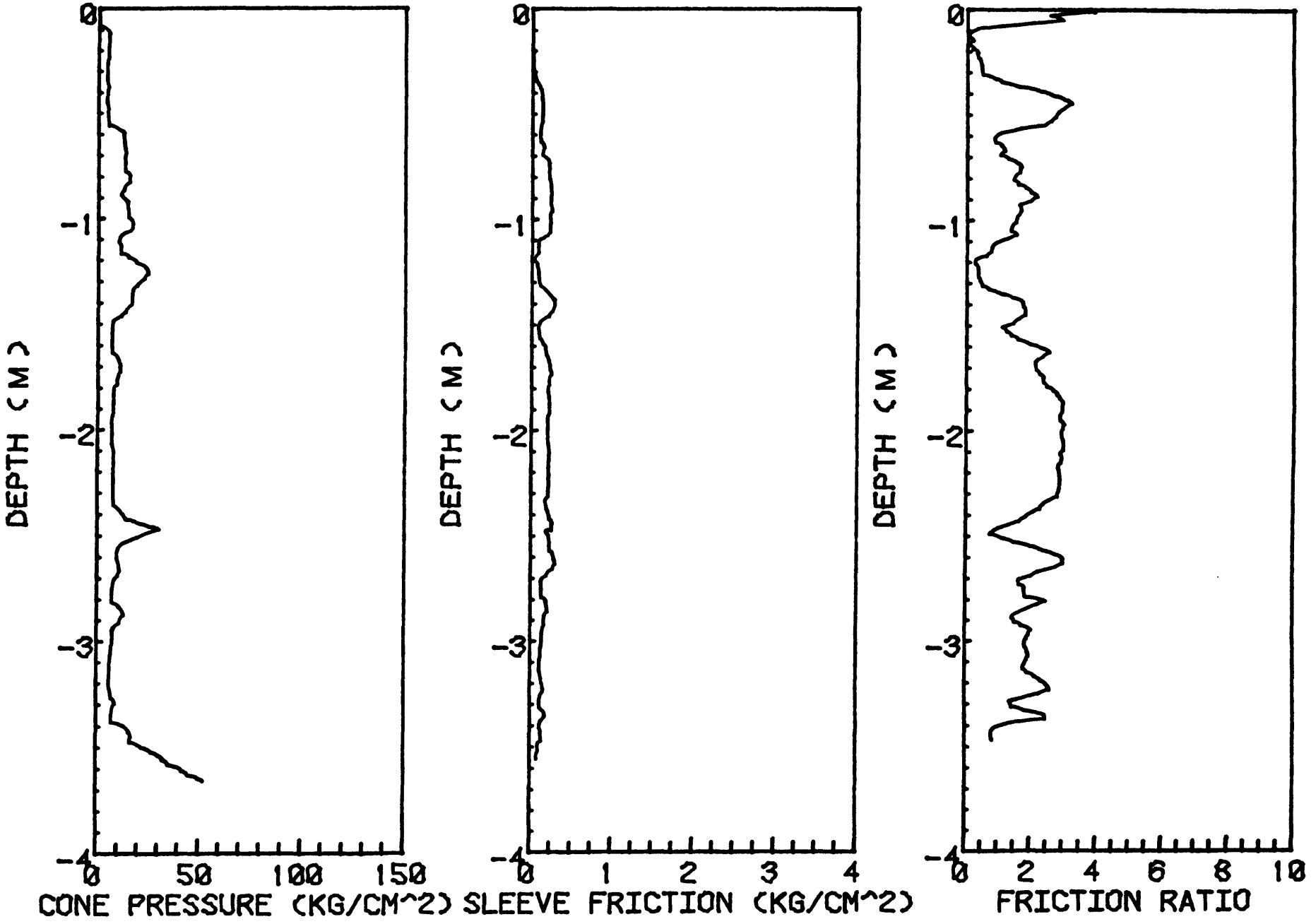

FIG. 676X1. BIOGENIC GAS ZONE. ALASKA. 8/12/81

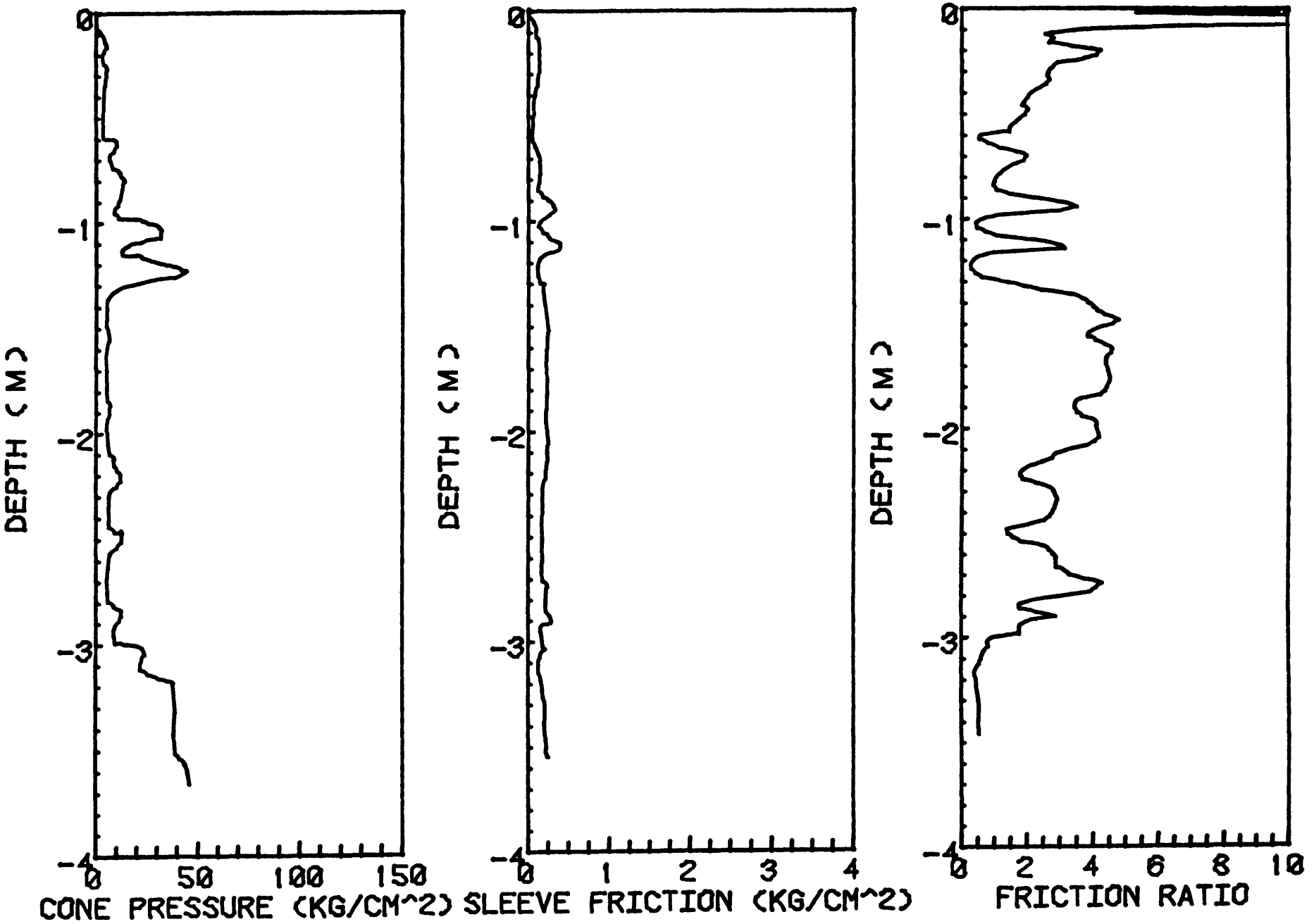

FIG. 676X2. BIOGENIC GAS ZONE. ALASKA. 8/12/81

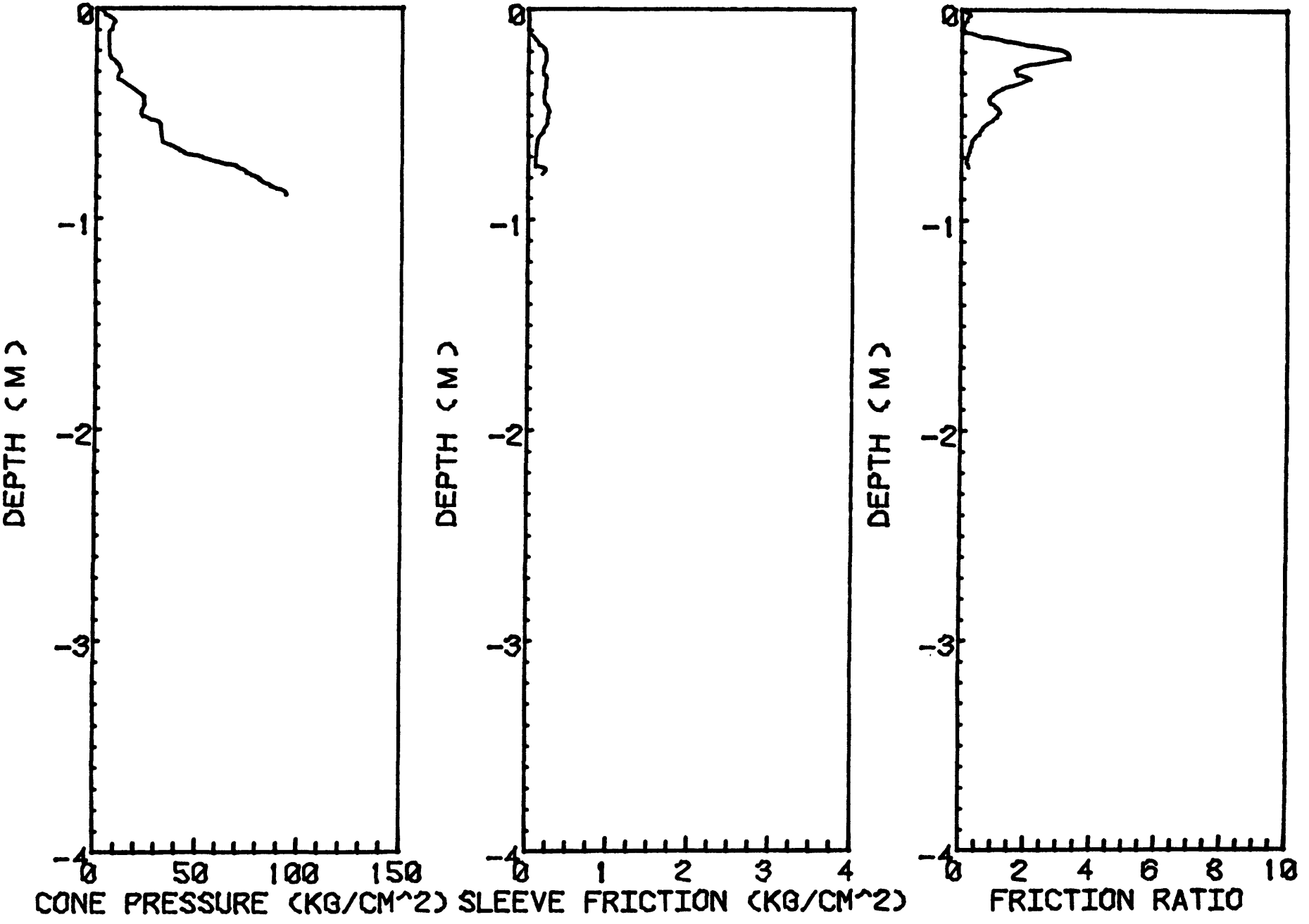

FIG. 677X1. W. OF THERMOGENIC GAS ZONE. ALASKA. 8/12/81

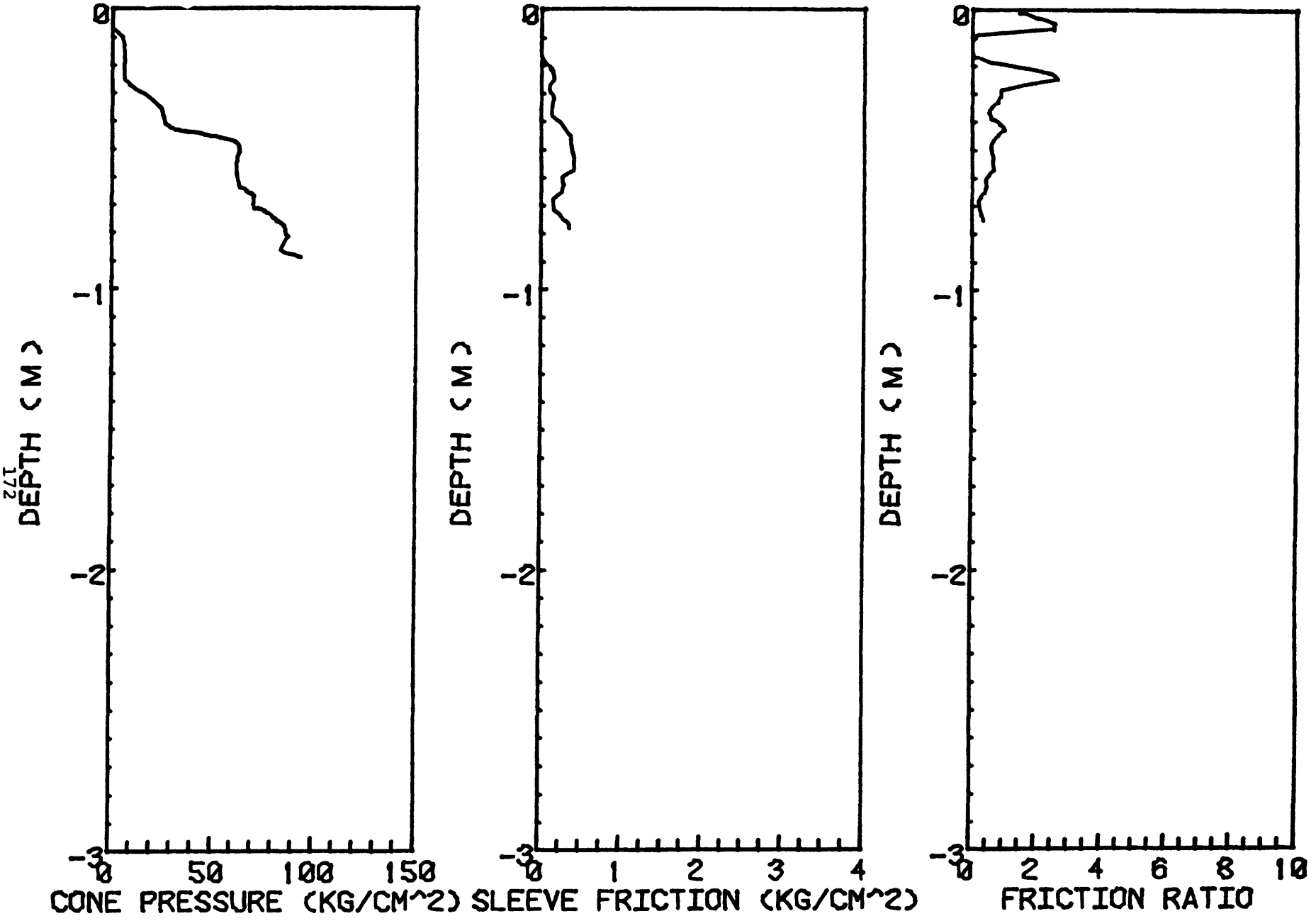

FIG. 677X2. W. OF THERMOGENIC GAS ZONE. ALASKA. 8/12/81

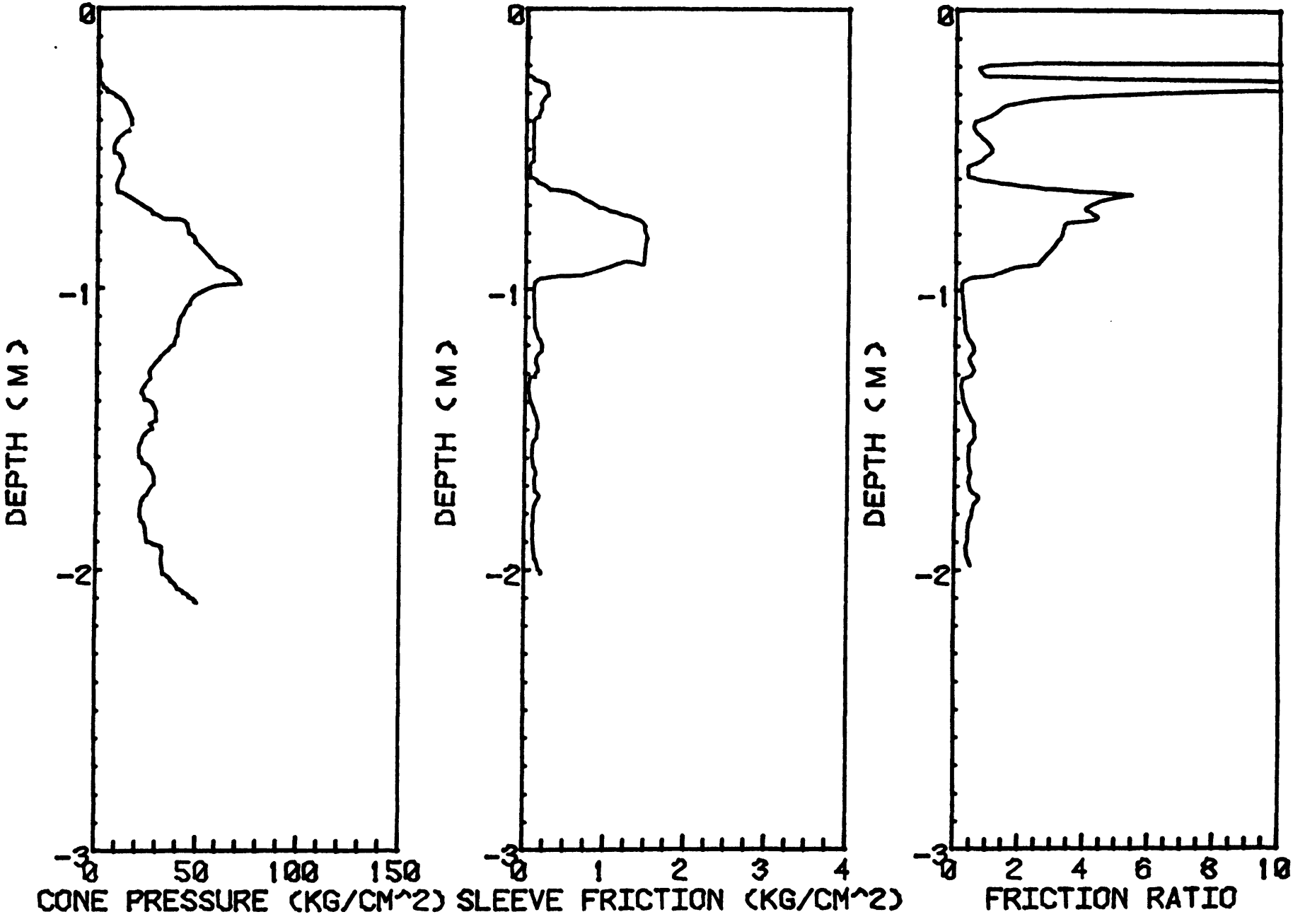

FIG. 678X1. CHIRIKOV BASIN SAND RIDGE AREA - TROUGH. ALASKA. 8/13/81

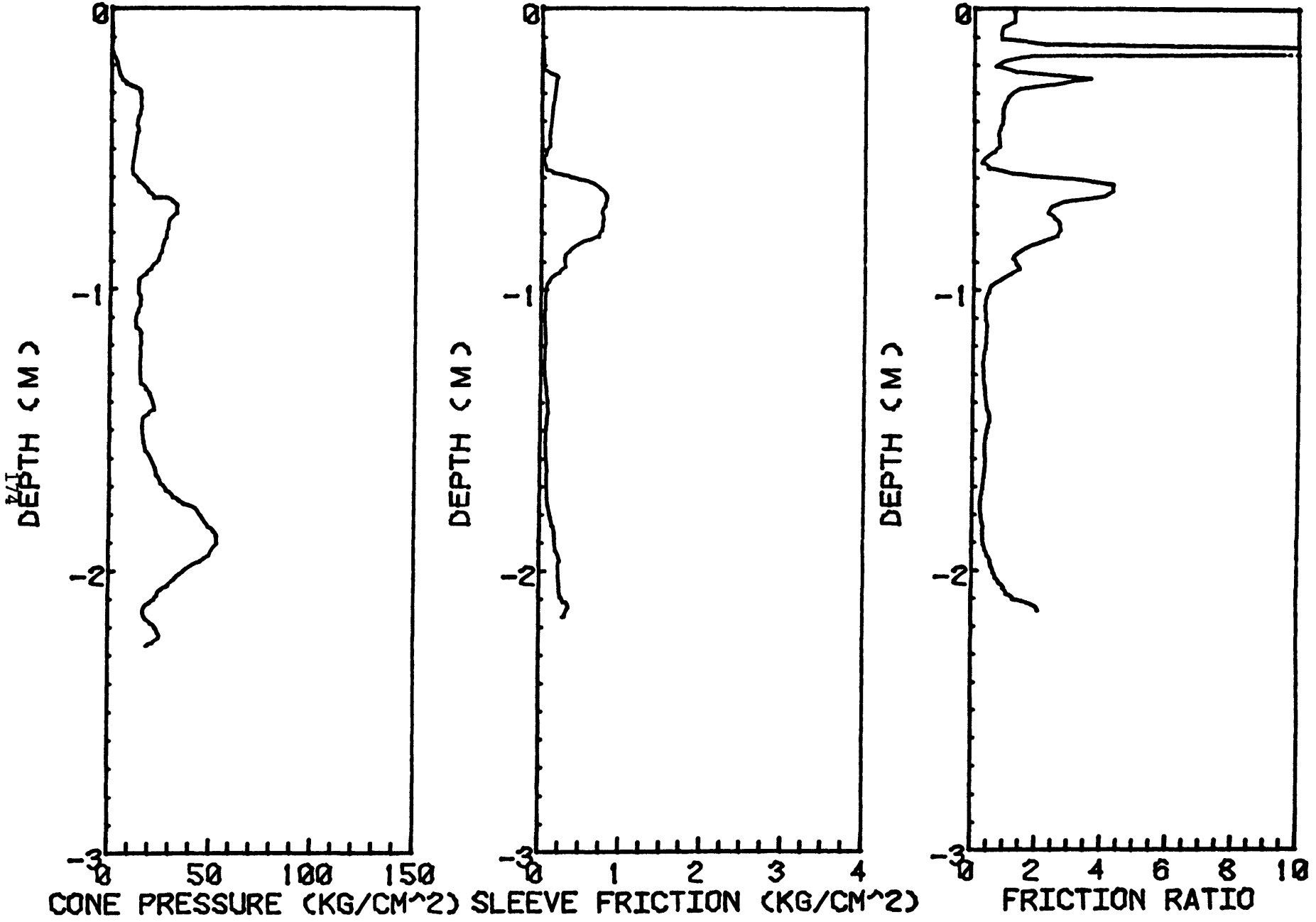

FIG. 678X2. CHIRIKOV BASIN SAND RIDGE AREA - TROUGH. ALASKA. 8/13/81

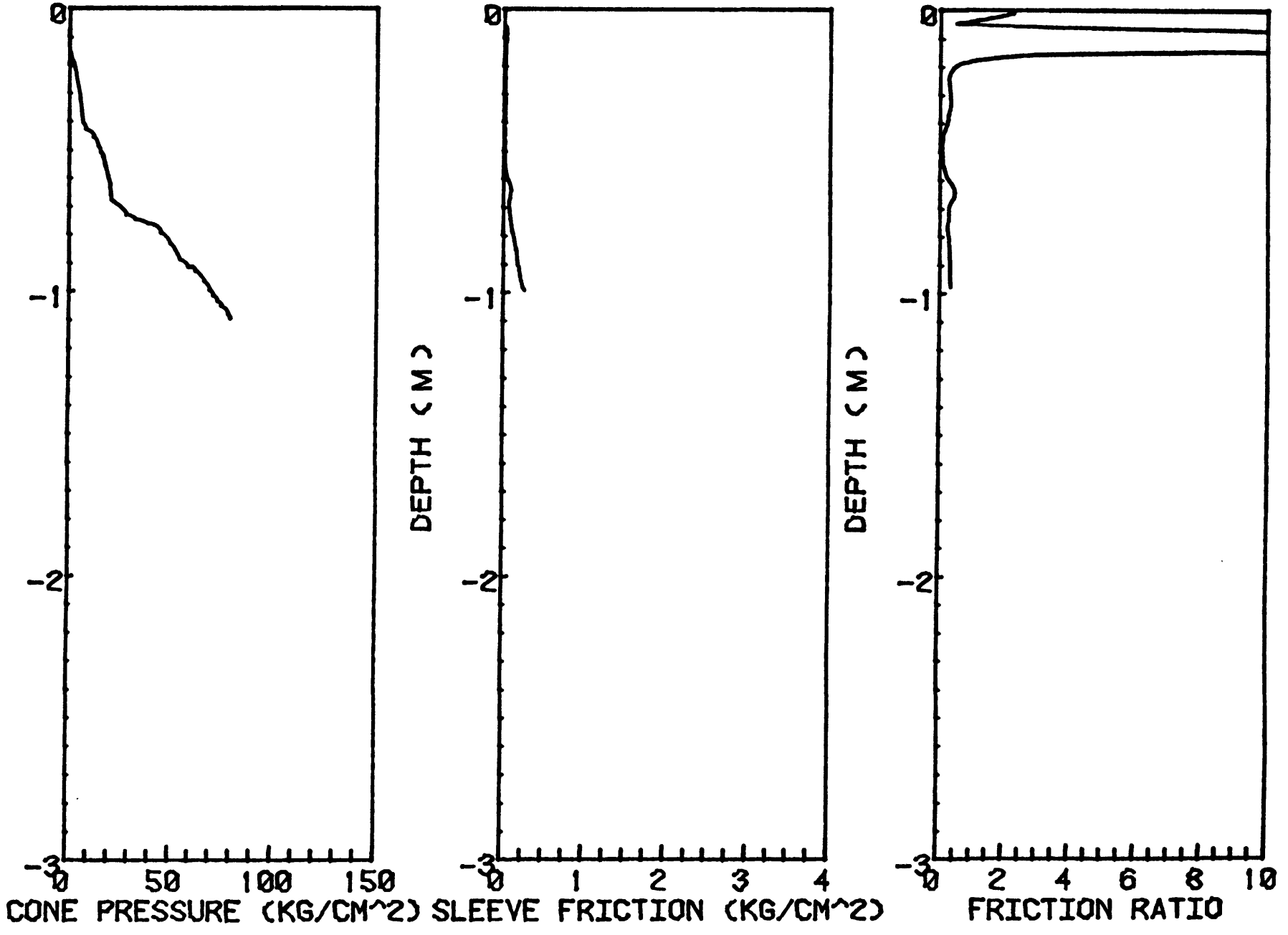

FIG. 679X1. CHIRIKOV BASIN SAND RIDGE AREA - CREST. ALASKA. 8/13/81

Appendix C. Relative density plots.

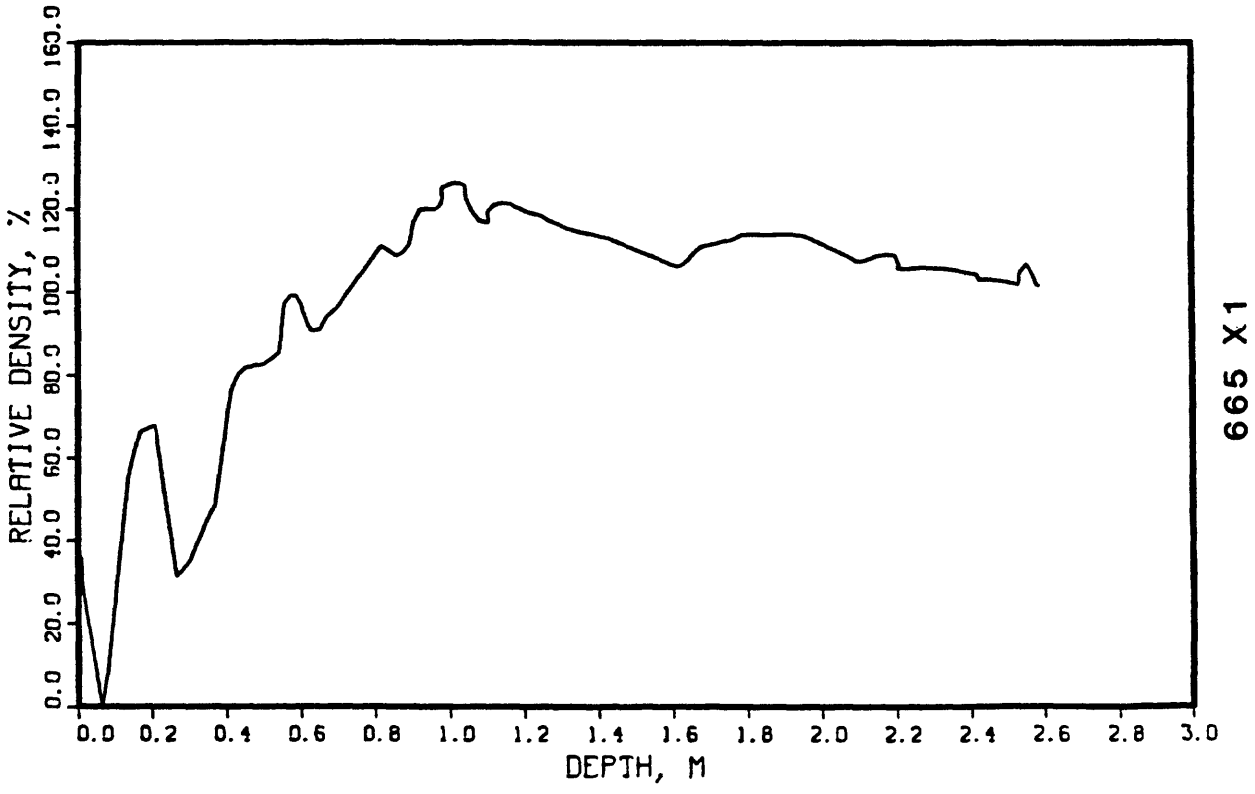
RELATIVE DENSITY, %
0.0
20.0
40.0
60.0
80.0
100.0
120.0
140.0
160.0
0.0
0.2
0.4
0.6
0.8
1.0
1.2
1.4
1.6
1.8
2.0
2.2
2.4
2.6
2.8
3.0
DEPTH, M
665 X1

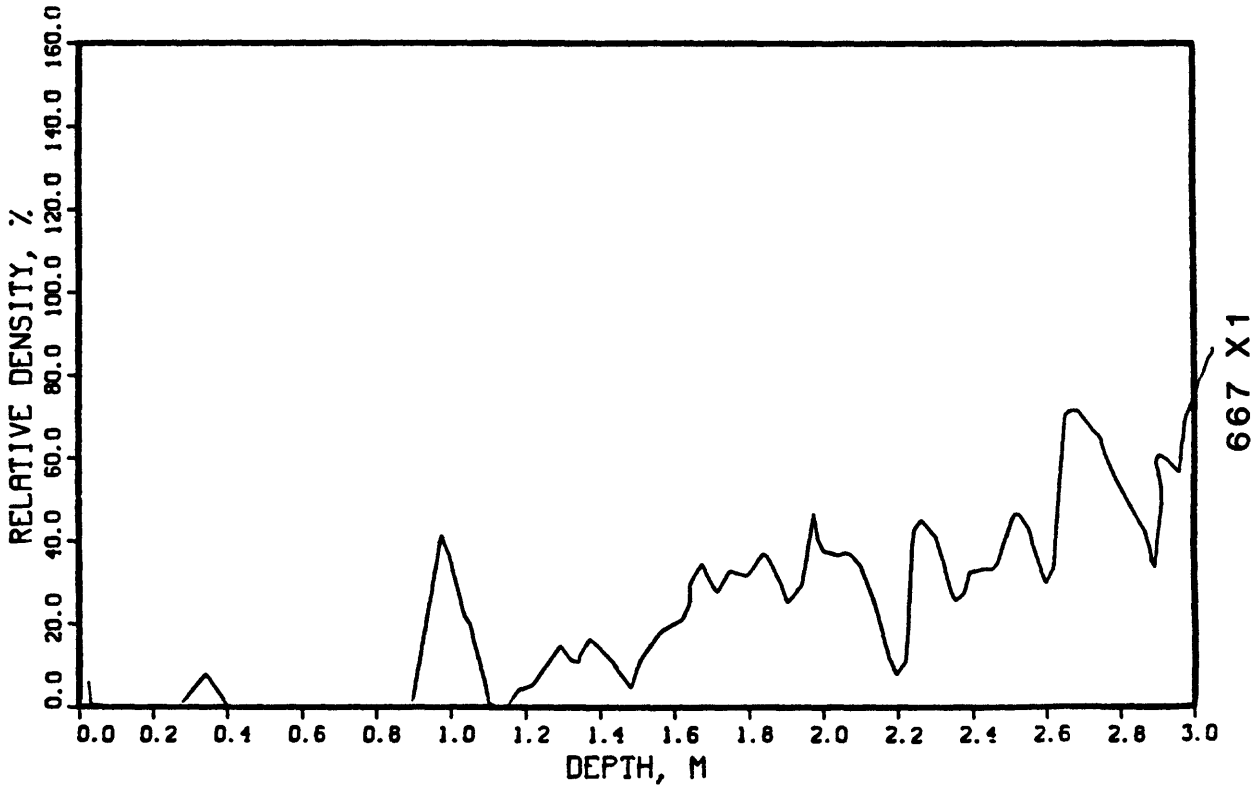
RELATIVE DENSITY, %
0.0
20.0
40.0
60.0
80.0
100.0
120.0
140.0
160.0
0.0
0.2
0.4
0.6
0.8
1.0
1.2
1.4
1.6
1.8
2.0
2.2
2.4
2.6
2.8
3.0
DEPTH, M
667 X1

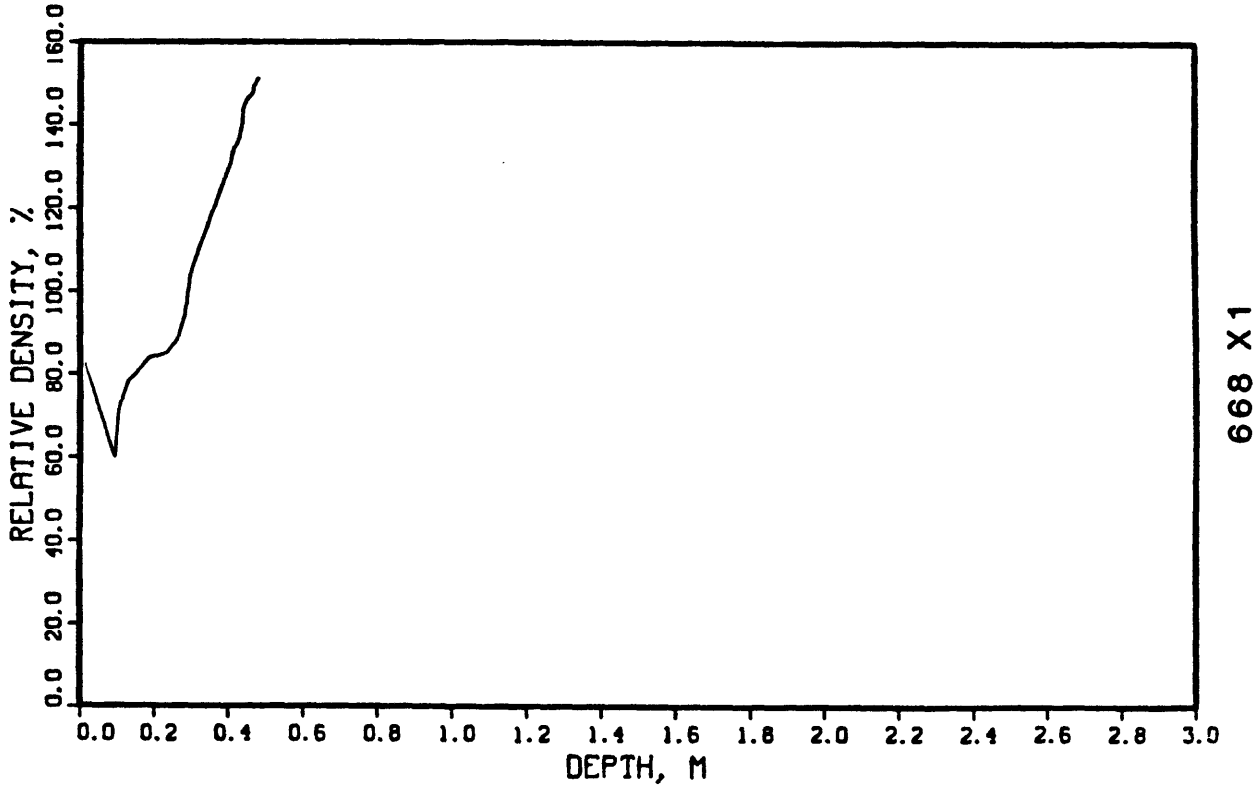
RELATIVE DENSITY, %
0.0
20.0
40.0
60.0
80.0
100.0
120.0
140.0
160.0
0.0
0.2
0.4
0.6
0.8
1.0
1.2
1.4
1.6
1.8
2.0
2.2
2.4
2.6
2.8
3.0
DEPTH, M
668 X1

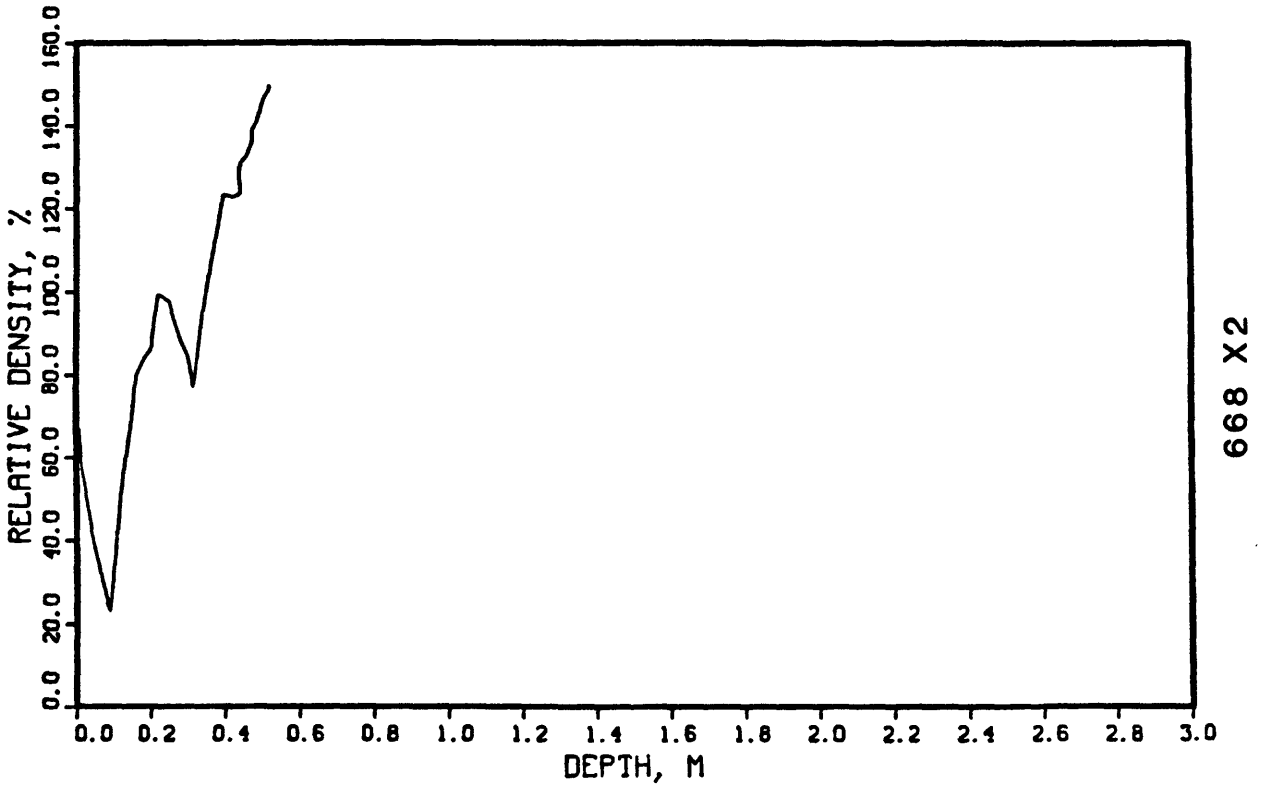
RELATIVE DENSITY, %
0.0
20.0
40.0
60.0
80.0
100.0
120.0
140.0
160.0
0.0
0.2
0.4
0.6
0.8
1.0
1.2
1.4
1.6
1.8
2.0
2.2
2.4
2.6
2.8
3.0
DEPTH, M
668 X2

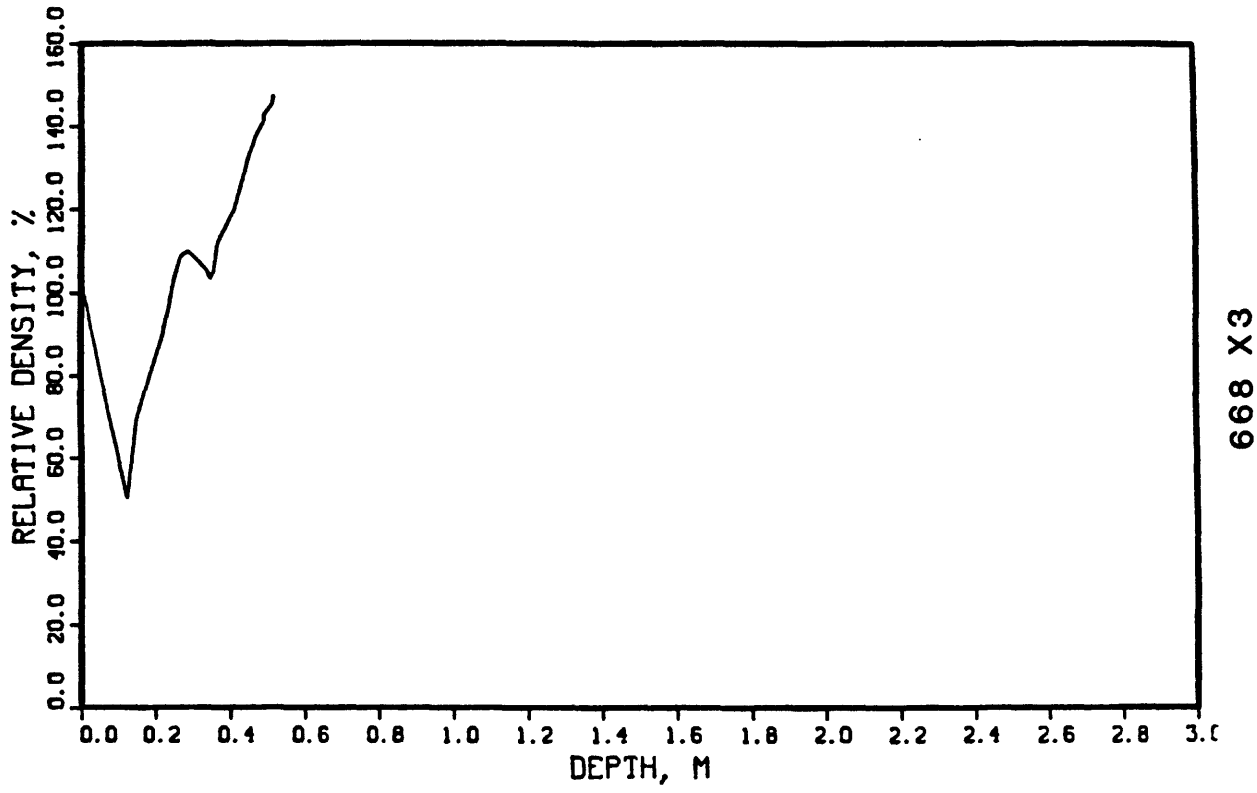
RELATIVE DENSITY, %
0.0
20.0
40.0
60.0
80.0
100.0
120.0
140.0
160.0
0.0 0.2 0.4 0.6 0.8 1.0 1.2 1.4 1.6 1.8 2.0 2.2 2.4 2.6 2.8 3.0
DEPTH, M
668 X3

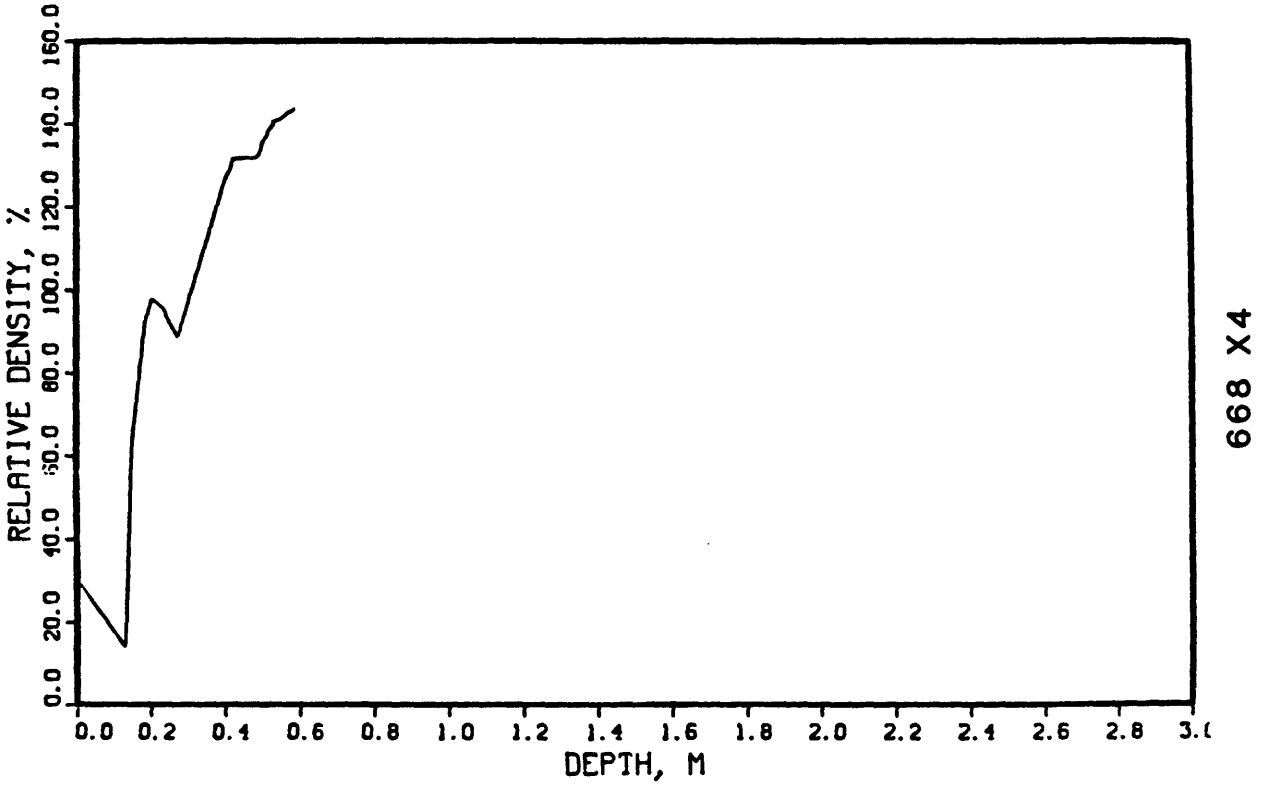
RELATIVE DENSITY, %
0.0
20.0
40.0
60.0
80.0
100.0
120.0
140.0
160.0
0.0
0.2
0.4
0.6
0.8
1.0
1.2
1.4
1.6
1.8
2.0
2.2
2.4
2.6
2.8
DEPTH, M
668 X4

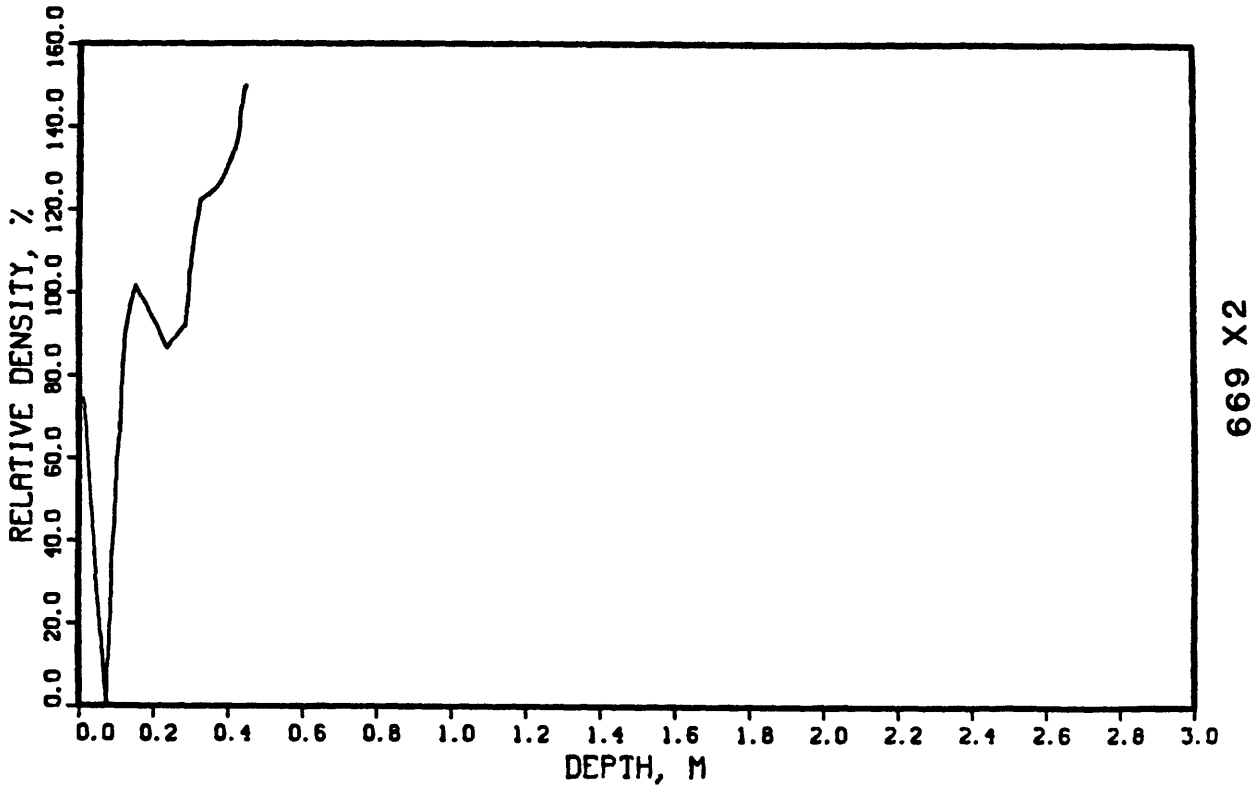
RELATIVE DENSITY, %
0.0
20.0
40.0
60.0
80.0
100.0
120.0
140.0
160.0
0.0
0.2
0.4
0.6
0.8
1.0
1.2
1.4
1.6
1.8
2.0
2.2
2.4
2.6
2.8
3.0
DEPTH, M
669 X2

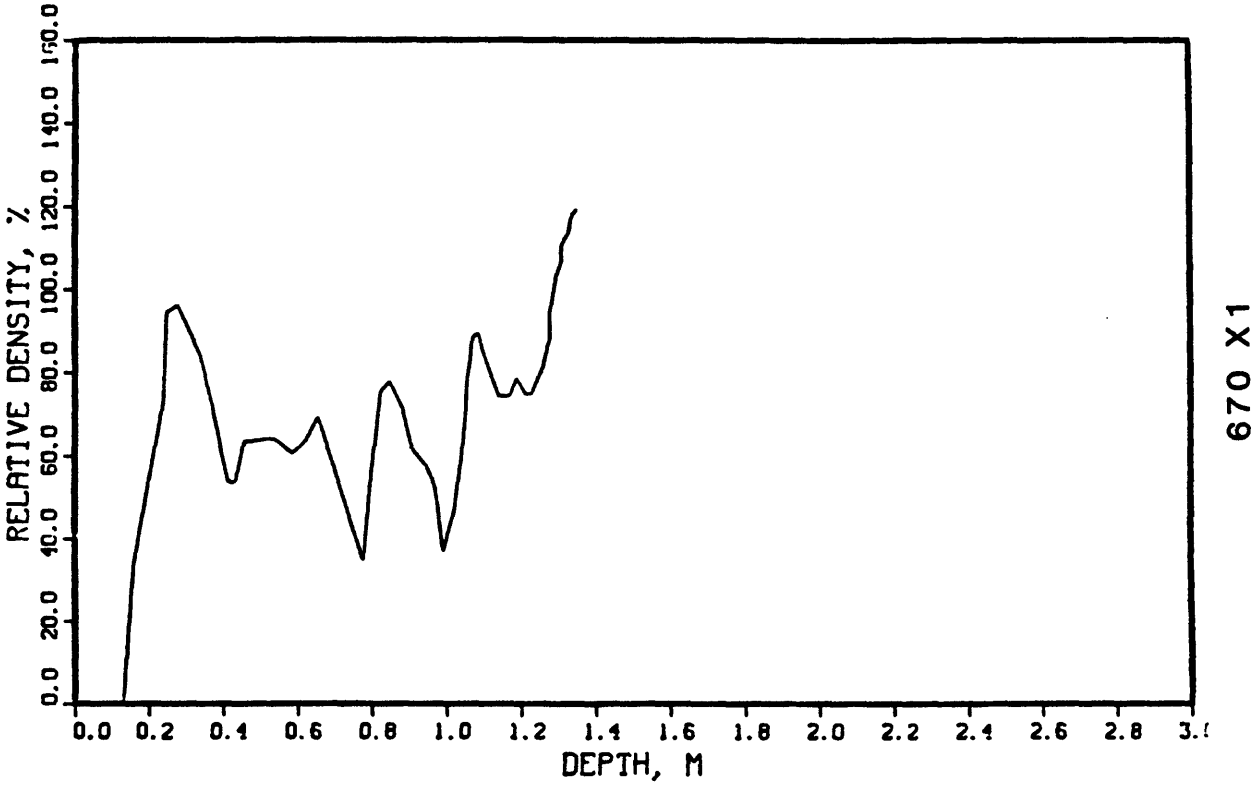
RELATIVE DENSITY, %
0.0
20.0
40.0
60.0
80.0
100.0
120.0
140.0
160.0
0.0
0.2
0.4
0.6
0.8
1.0
1.2
1.4
1.6
1.8
2.0
2.2
2.4
2.6
2.8
DEPTH, M
670 X1

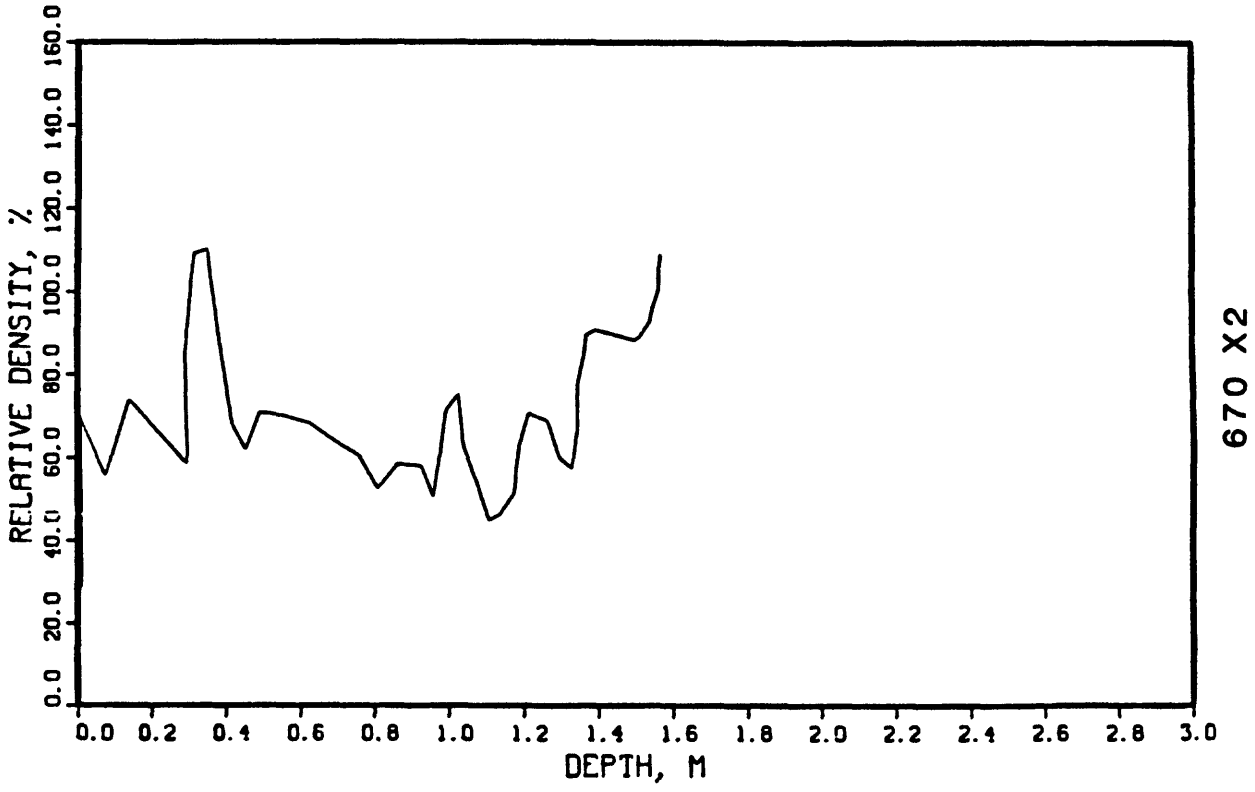
RELATIVE DENSITY, %
0.0
20.0
40.0
60.0
80.0
100.0
120.0
140.0
160.0
0.0 0.2 0.4 0.6 0.8 1.0 1.2 1.4 1.6 1.8 2.0 2.2 2.4 2.6 2.8 3.0
DEPTH, M
670 X2

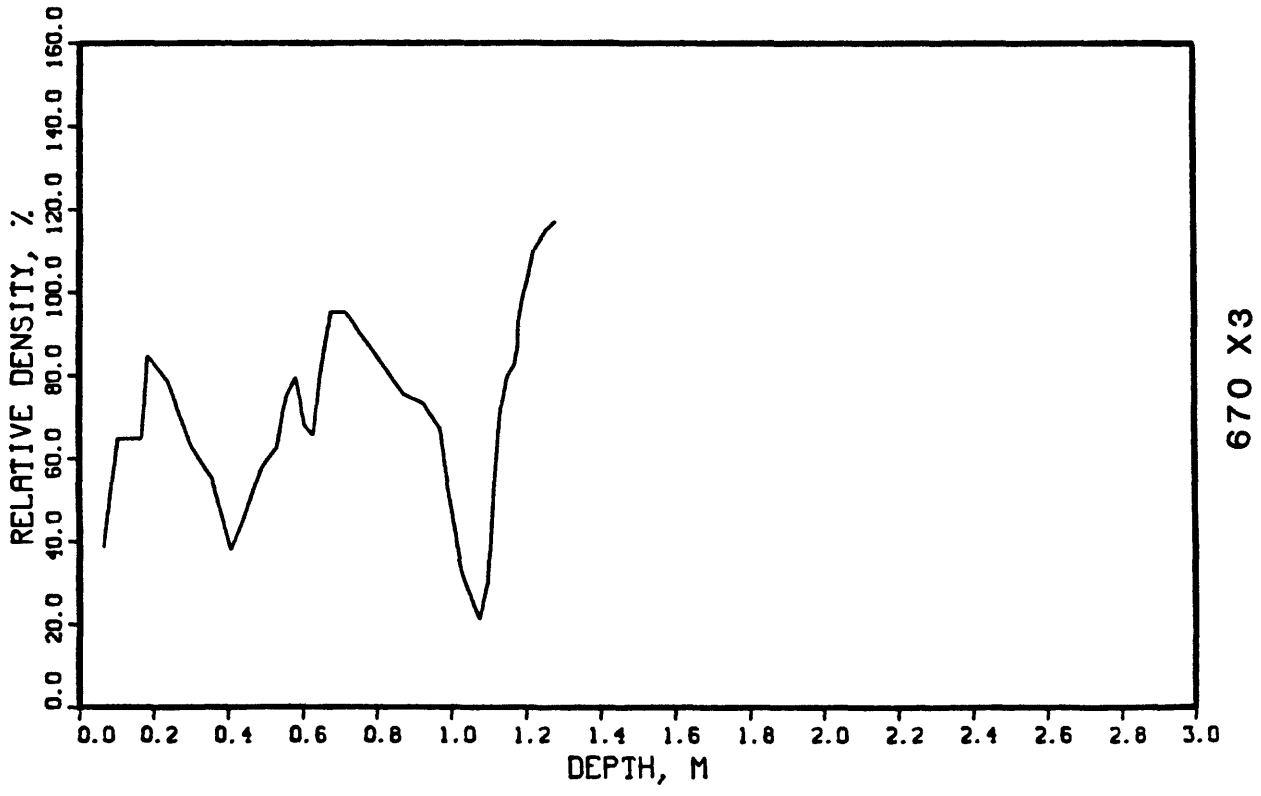
RELATIVE DENSITY, %
0.0
20.0
40.0
60.0
80.0
100.0
120.0
140.0
160.0
0.0
0.2
0.4
0.6
0.8
1.0
1.2
1.4
1.6
1.8
2.0
2.2
2.4
2.6
2.8
3.0
DEPTH, M
670 X3

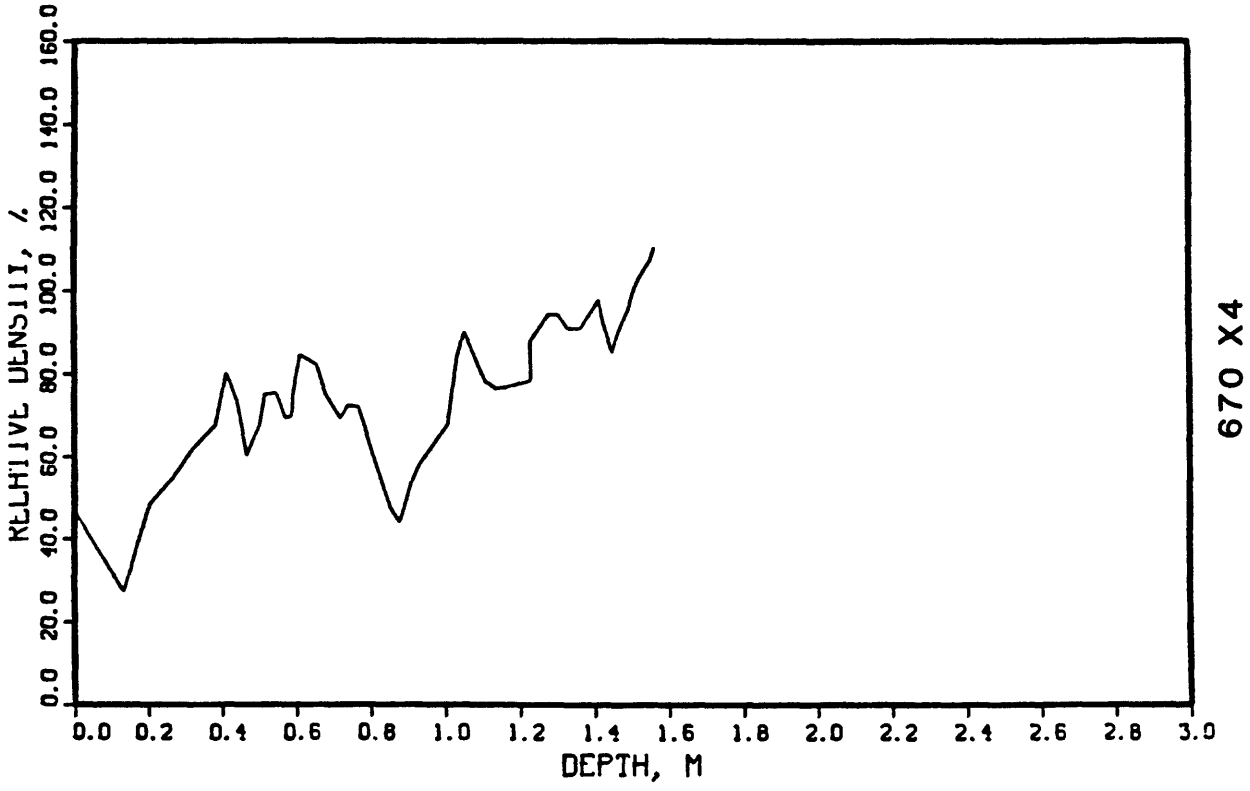
RELATIVE DENSITY, %
0.0
20.0
40.0
60.0
80.0
100.0
120.0
140.0
160.0
0.0
0.2
0.4
0.6
0.8
1.0
1.2
1.4
1.6
1.8
2.0
2.2
2.4
2.6
2.8
3.0
DEPTH, M
670 X4

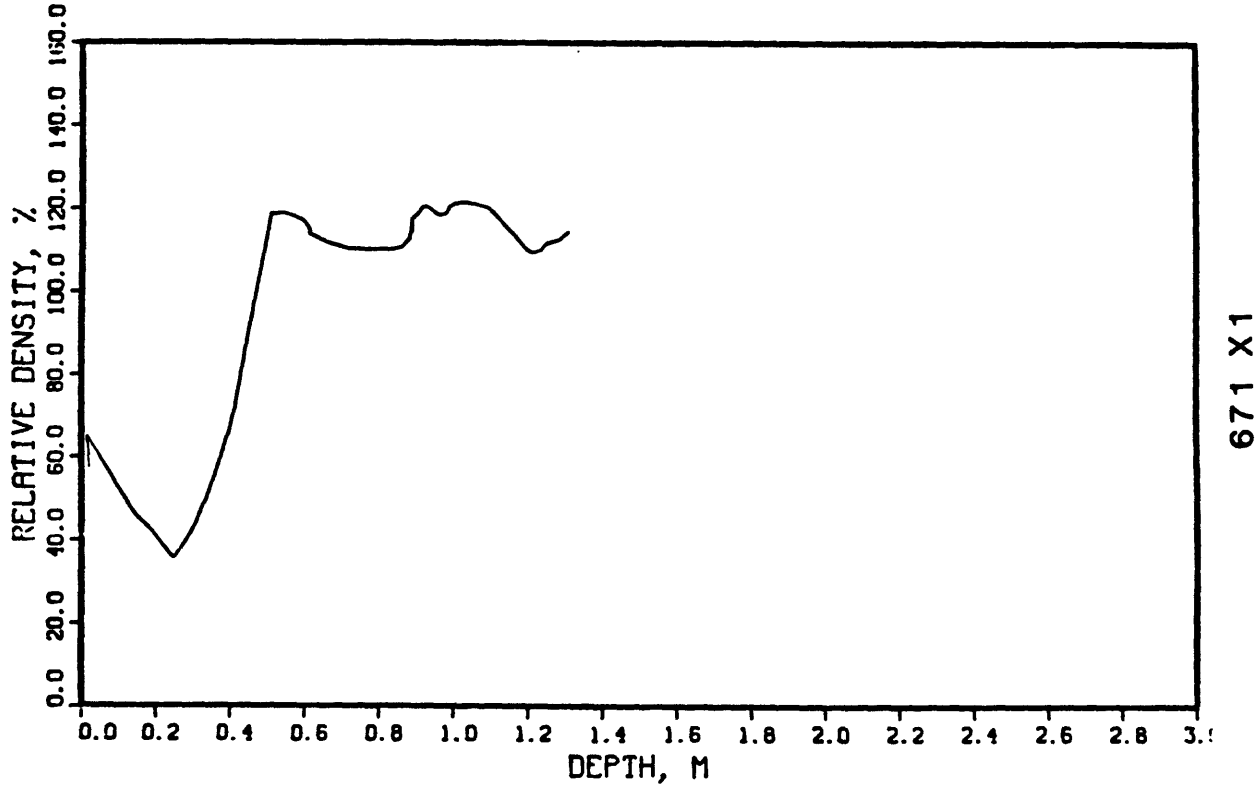
RELATIVE DENSITY, %
0.0
20.0
40.0
60.0
80.0
100.0
120.0
140.0
160.0
0.0 0.2 0.4 0.6 0.8 1.0 1.2 1.4 1.6 1.8 2.0 2.2 2.4 2.6 2.8
DEPTH, M
671 X1

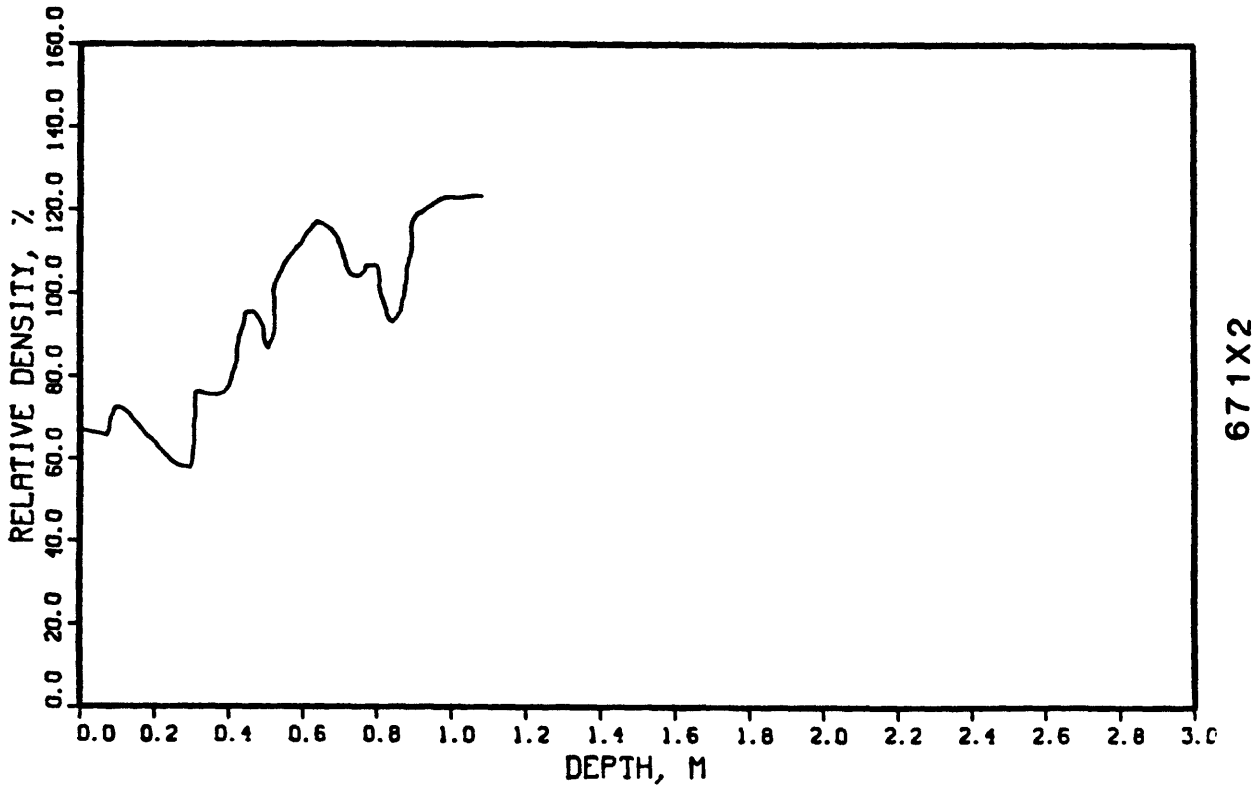
RELATIVE DENSITY, %
0.0
20.0
40.0
60.0
80.0
100.0
120.0
140.0
160.0
0.0
0.2
0.4
0.6
0.8
1.0
1.2
1.4
1.6
1.8
2.0
2.2
2.4
2.6
2.8
3.0
DEPTH, M
671X2

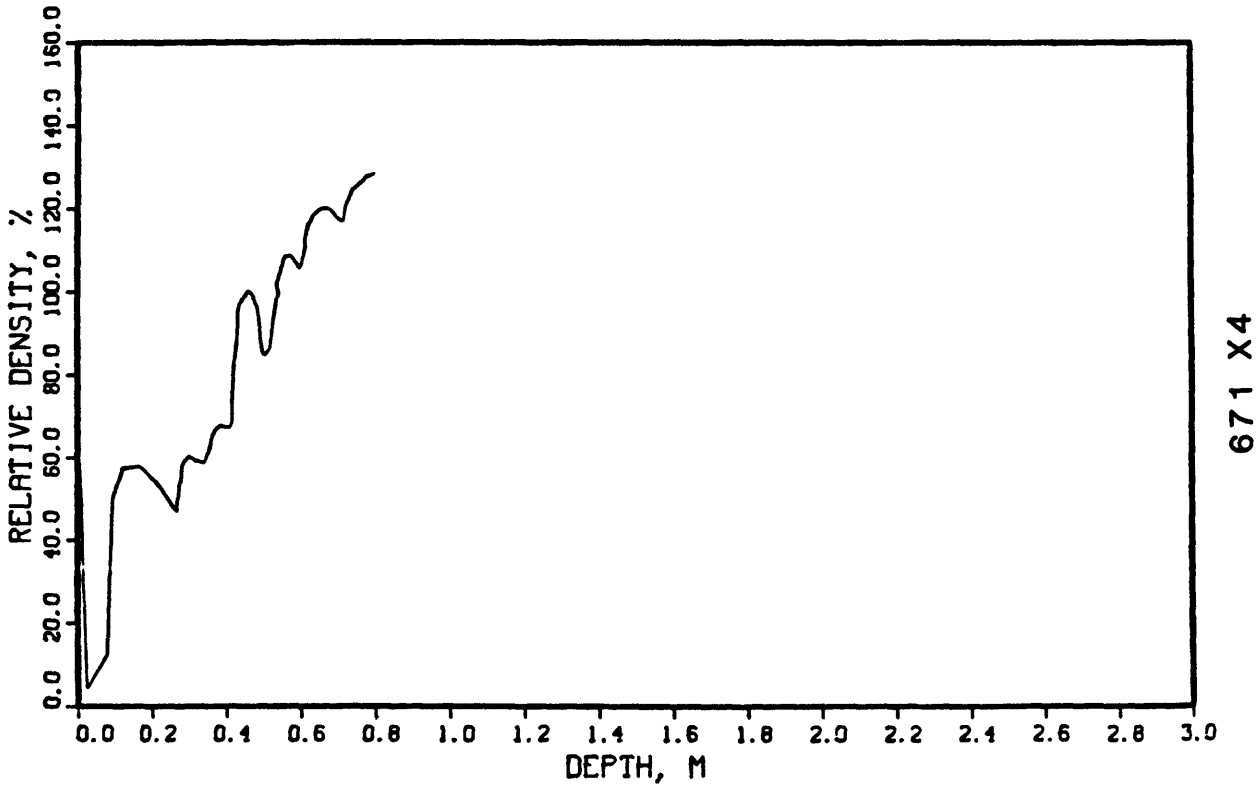
RELATIVE DENSITY, %
0.0
20.0
40.0
60.0
80.0
100.0
120.0
140.0
160.0
0.0
0.2
0.4
0.6
0.8
1.0
1.2
1.4
1.6
1.8
2.0
2.2
2.4
2.6
2.8
3.0
DEPTH, M
671 X4

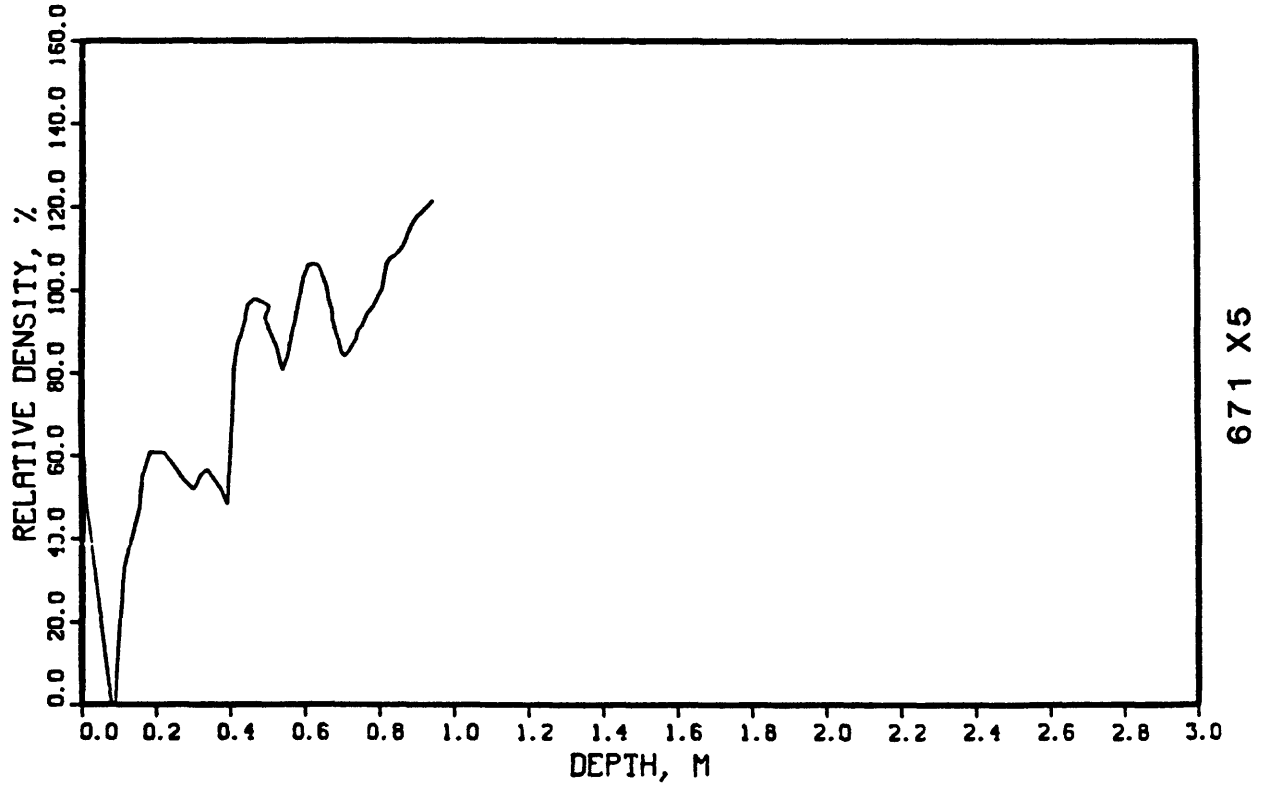
RELATIVE DENSITY, %
0.0
20.0
40.0
60.0
80.0
100.0
120.0
140.0
160.0
0.0
0.2
0.4
0.6
0.8
1.0
1.2
1.4
1.6
1.8
2.0
2.2
2.4
2.6
2.8
3.0
DEPTH, M
671 X5

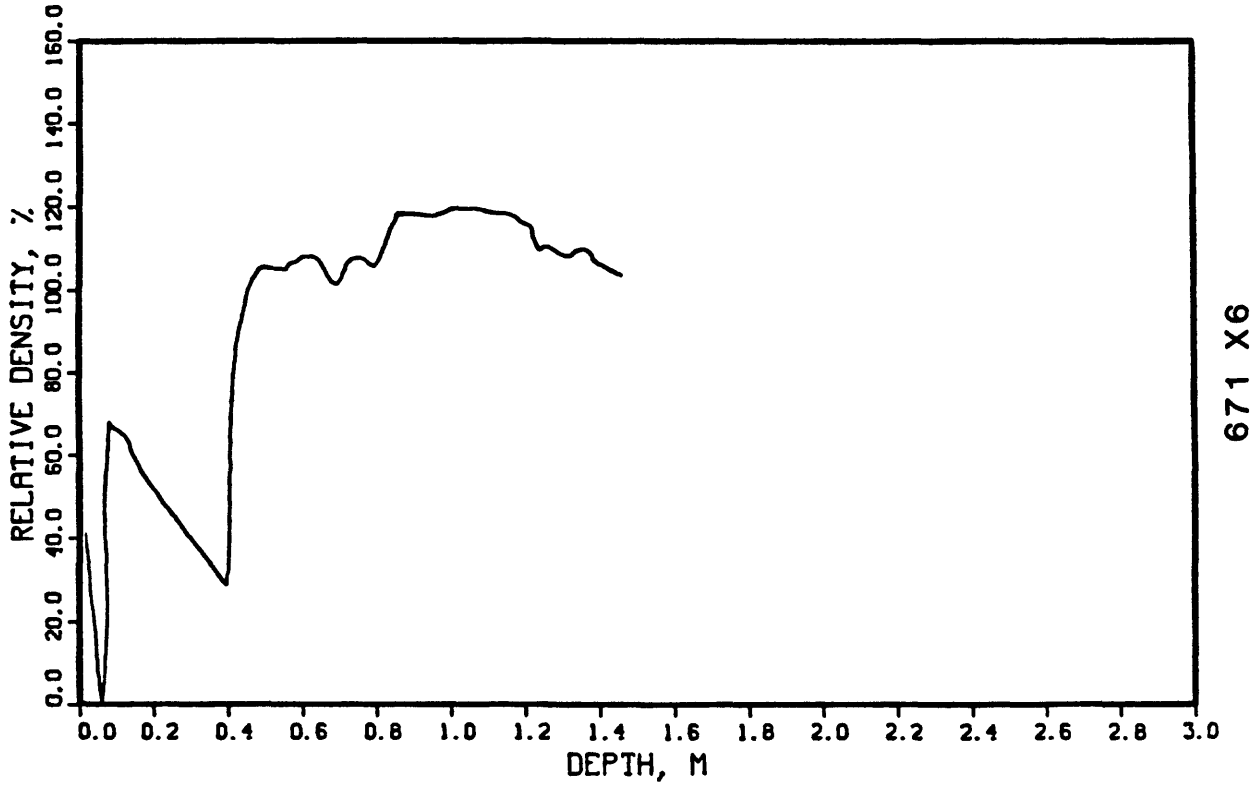
RELATIVE DENSITY, %
0.0
20.0
40.0
60.0
80.0
100.0
120.0
140.0
160.0
0.0
0.2
0.4
0.6
0.8
1.0
1.2
1.4
1.6
1.8
2.0
2.2
2.4
2.6
2.8
3.0
DEPTH, M
671 X6

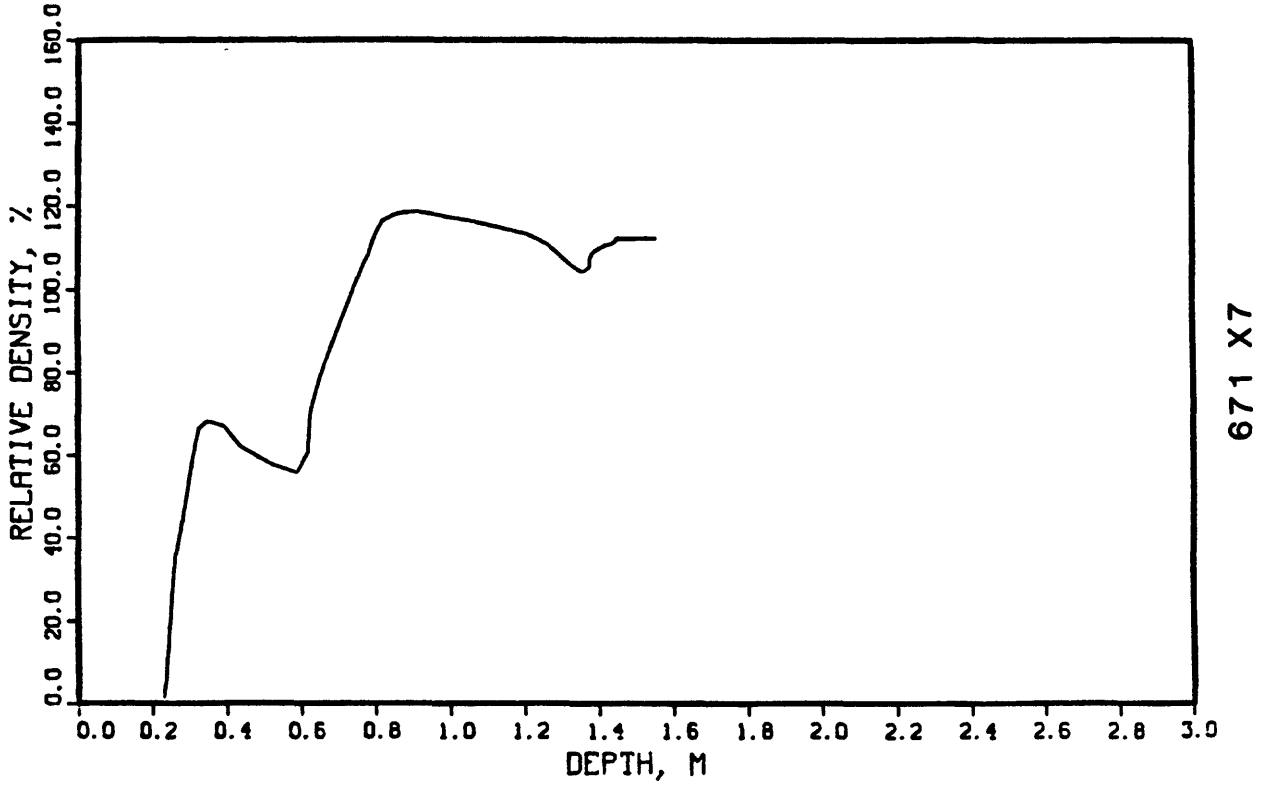
RELATIVE DENSITY, %
0.0
20.0
40.0
60.0
80.0
100.0
120.0
140.0
160.0
0.0
0.2
0.4
0.6
0.8
1.0
1.2
1.4
1.6
1.8
2.0
2.2
2.4
2.6
2.8
3.0
DEPTH, M
671 X7

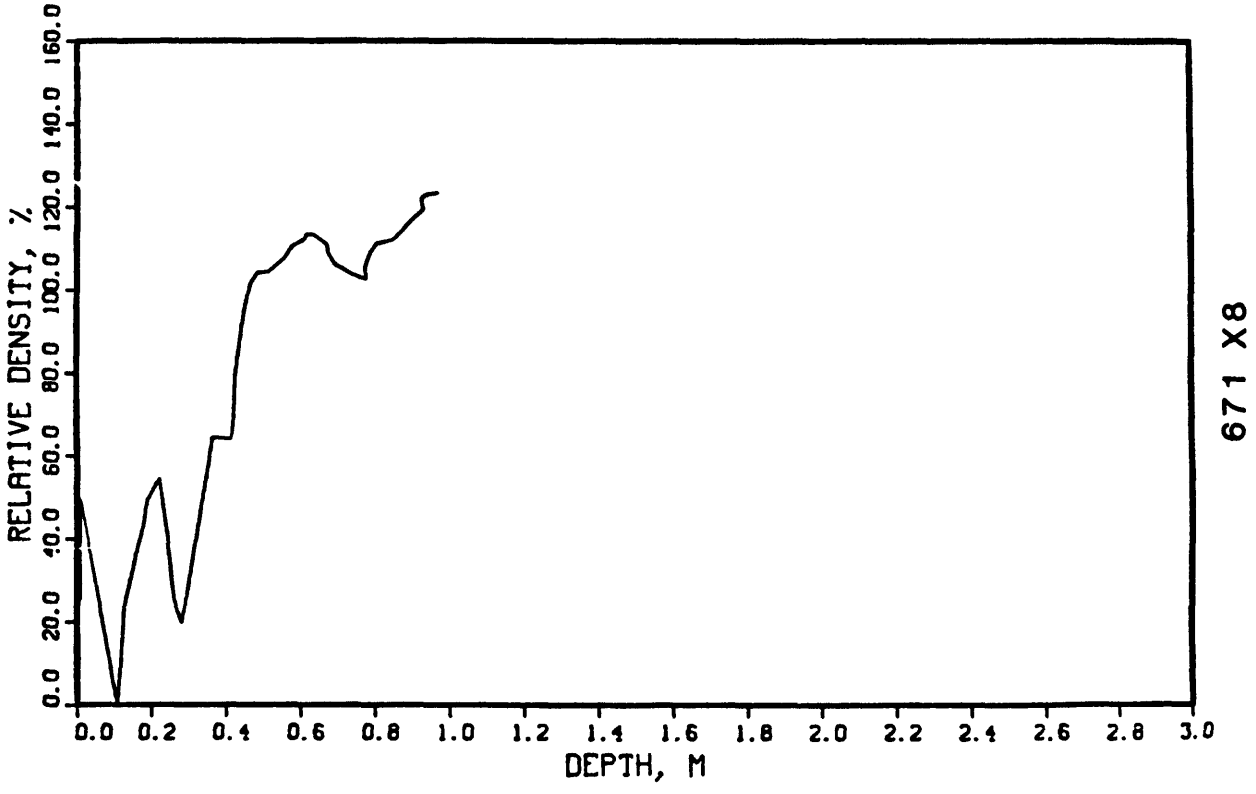
RELATIVE DENSITY, %
0.0
20.0
40.0
60.0
80.0
100.0
120.0
140.0
160.0
0.0
0.2
0.4
0.6
0.8
1.0
1.2
1.4
1.6
1.8
2.0
2.2
2.4
2.6
2.8
3.0
DEPTH, M
671 X8

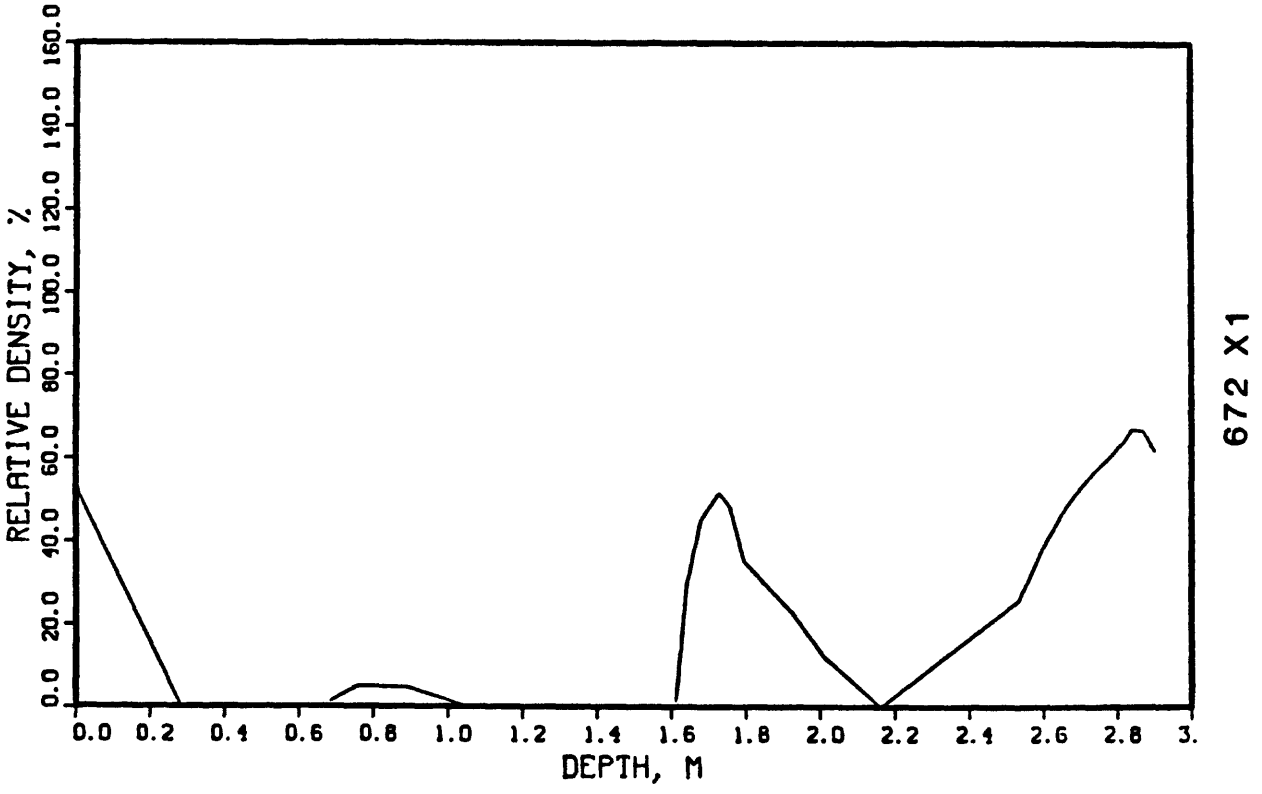
RELATIVE DENSITY, %
0.0
20.0
40.0
60.0
80.0
100.0
120.0
140.0
160.0
0.0
0.2
0.4
0.6
0.8
1.0
1.2
1.4
1.6
1.8
2.0
2.2
2.4
2.6
2.8
3.
DEPTH, M
672 X1

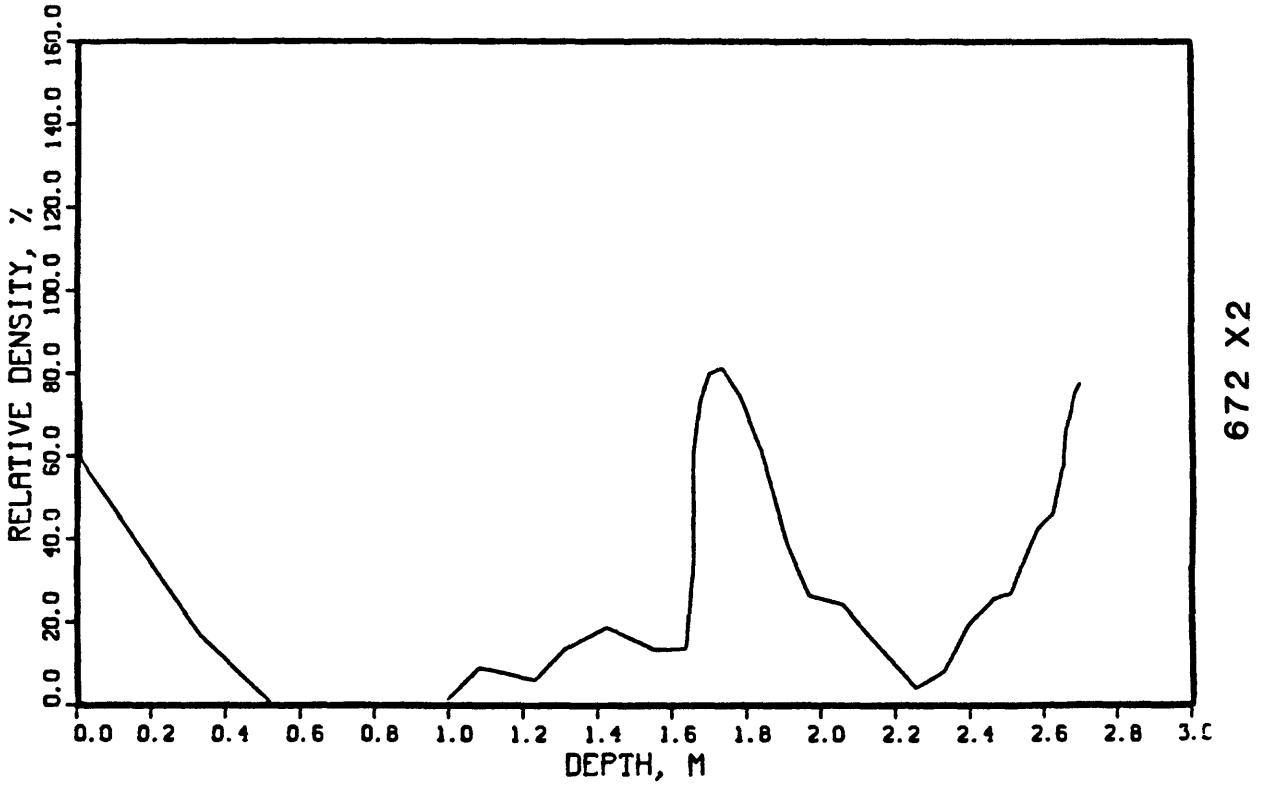
RELATIVE DENSITY, %
0.0
20.0
40.0
60.0
80.0
100.0
120.0
140.0
160.0
0.0
0.2
0.4
0.6
0.8
1.0
1.2
1.4
1.6
1.8
2.0
2.2
2.4
2.6
2.8
DEPTH, M
672 X2

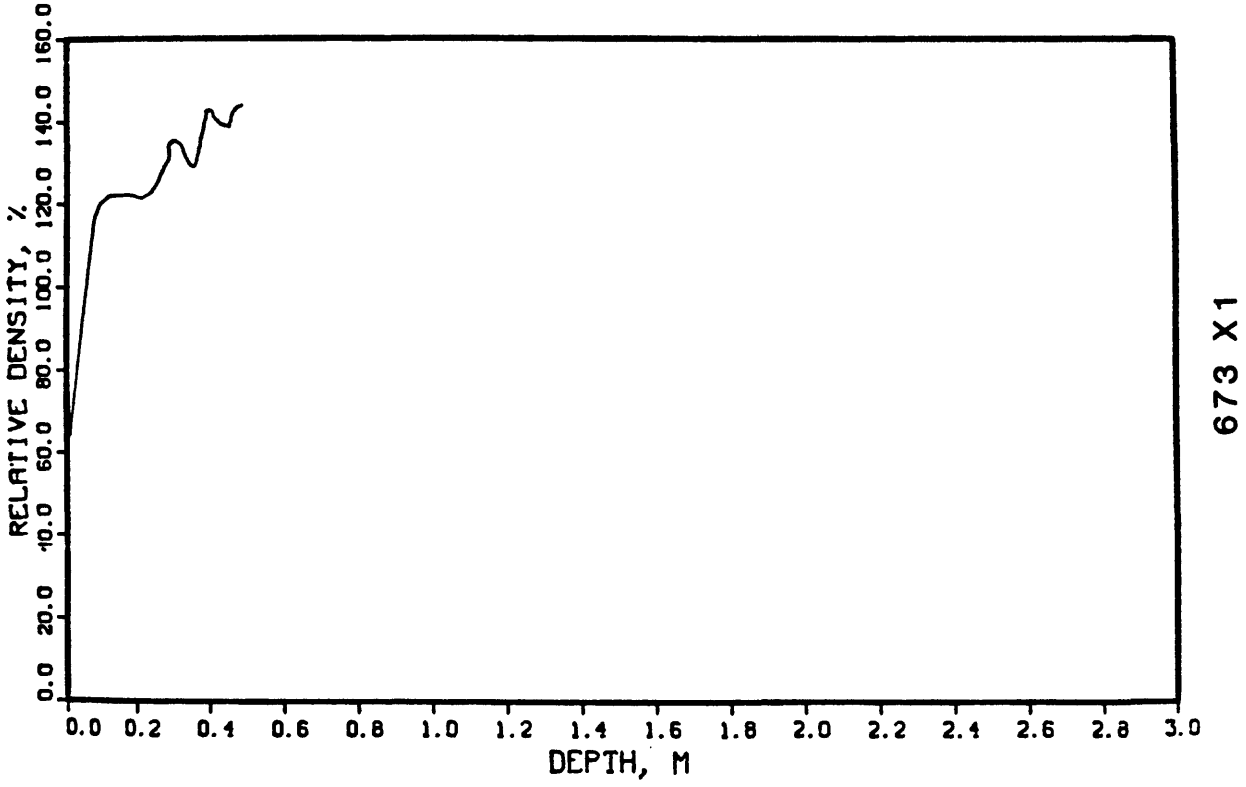
RELATIVE DENSITY, %
0.0
20.0
40.0
60.0
80.0
100.0
120.0
140.0
160.0
0.0 0.2 0.4 0.6 0.8 1.0 1.2 1.4 1.6 1.8 2.0 2.2 2.4 2.6 2.8 3.0
DEPTH, M
673 X1

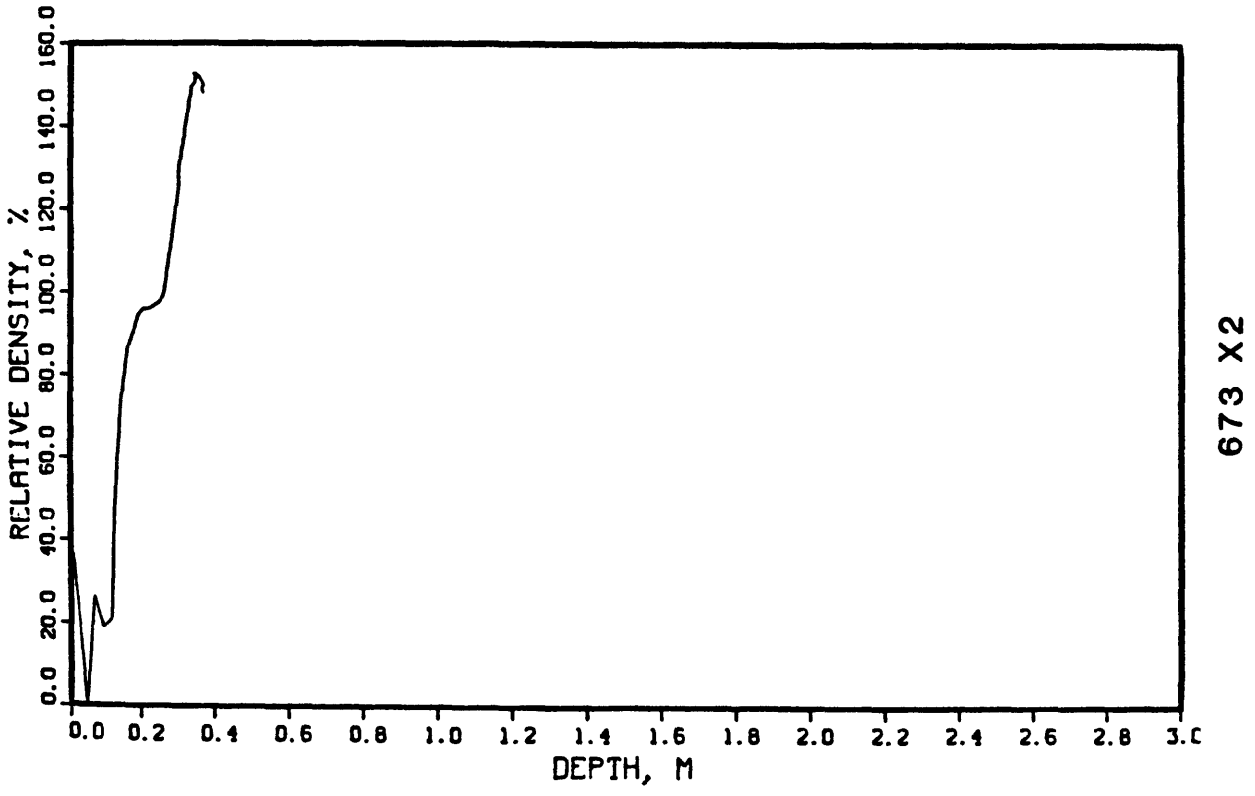
RELATIVE DENSITY, %
0.0
20.0
40.0
60.0
80.0
100.0
120.0
140.0
160.0
0.0
0.2
0.4
0.6
0.8
1.0
1.2
1.4
1.6
1.8
2.0
2.2
2.4
2.6
2.8
DEPTH, M
673 X2

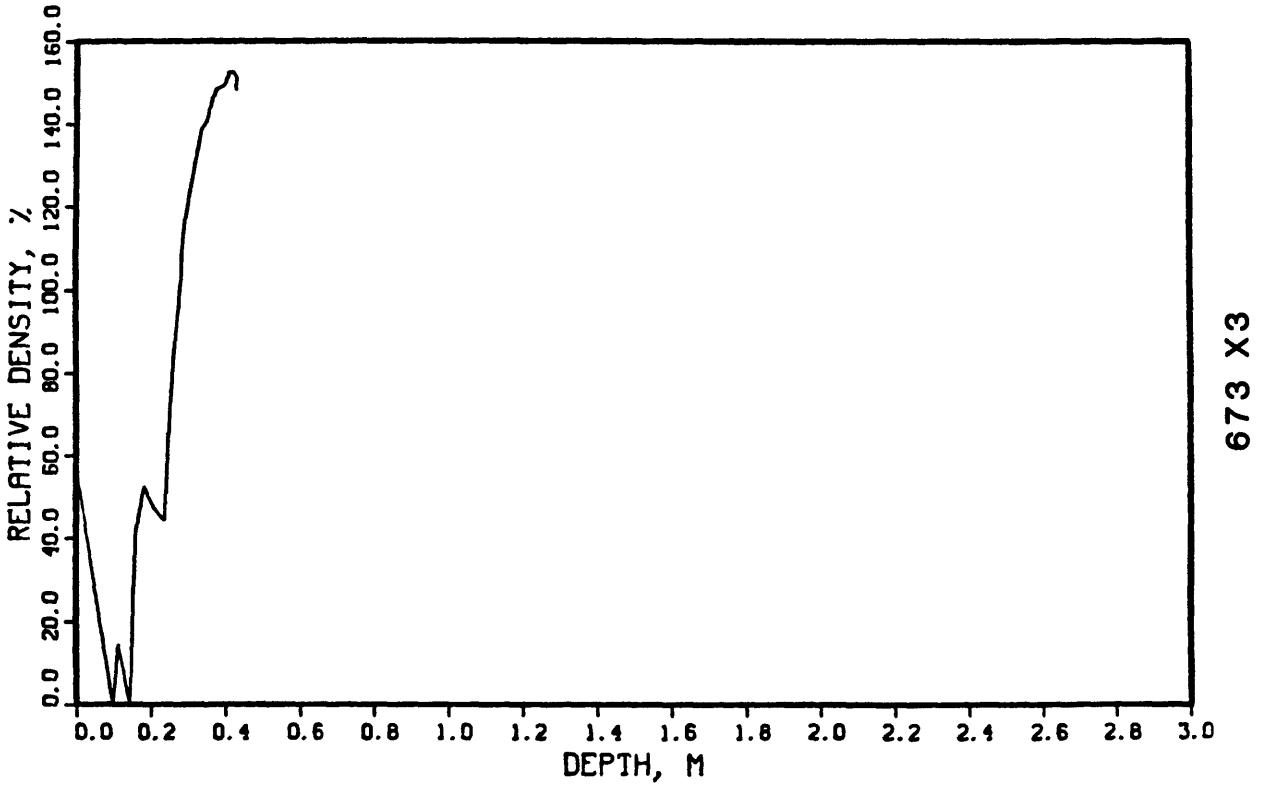
RELATIVE DENSITY, %
0.0
20.0
40.0
60.0
80.0
100.0
120.0
140.0
160.0
0.0
0.2
0.4
0.6
0.8
1.0
1.2
1.4
1.6
1.8
2.0
2.2
2.4
2.6
2.8
3.0
DEPTH, M
673 X3

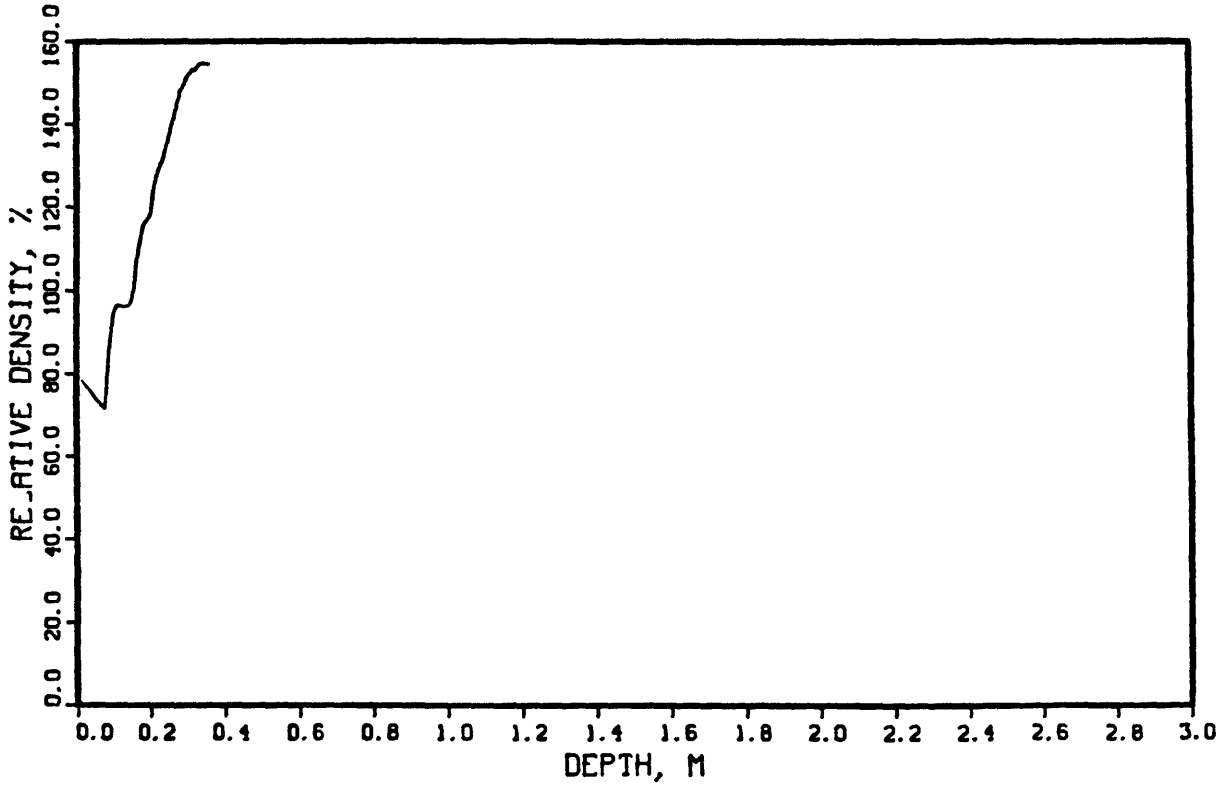
RELATIVE DENSITY, %
0.0
20.0
40.0
60.0
80.0
100.0
120.0
140.0
160.0
0.0
0.2
0.4
0.6
0.8
1.0
1.2
1.4
1.6
1.8
2.0
2.2
2.4
2.6
2.8
3.0
DEPTH, M
673 X4

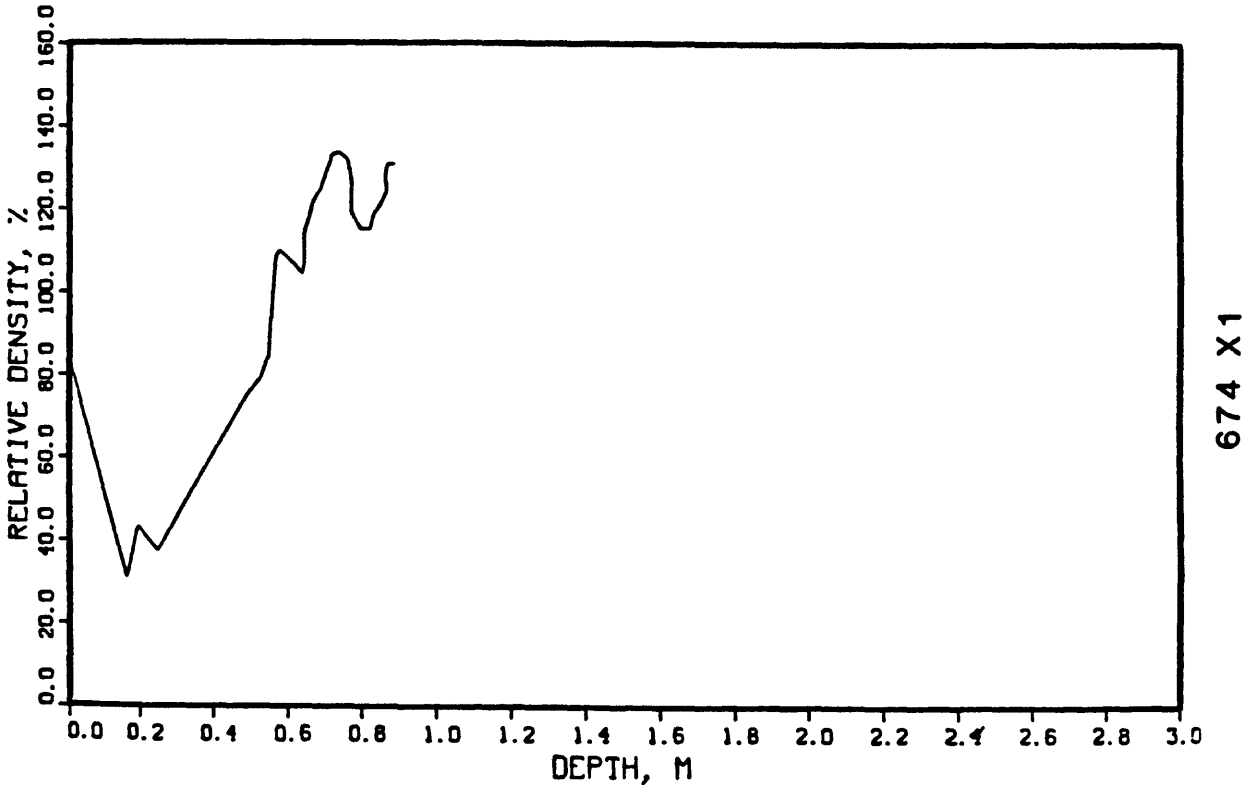
RELATIVE DENSITY, %
0.0
20.0
40.0
60.0
80.0
100.0
120.0
140.0
160.0
0.0
0.2
0.4
0.6
0.8
1.0
1.2
1.4
1.6
1.8
2.0
2.2
2.4
2.6
2.8
3.0
DEPTH, M
674 X1

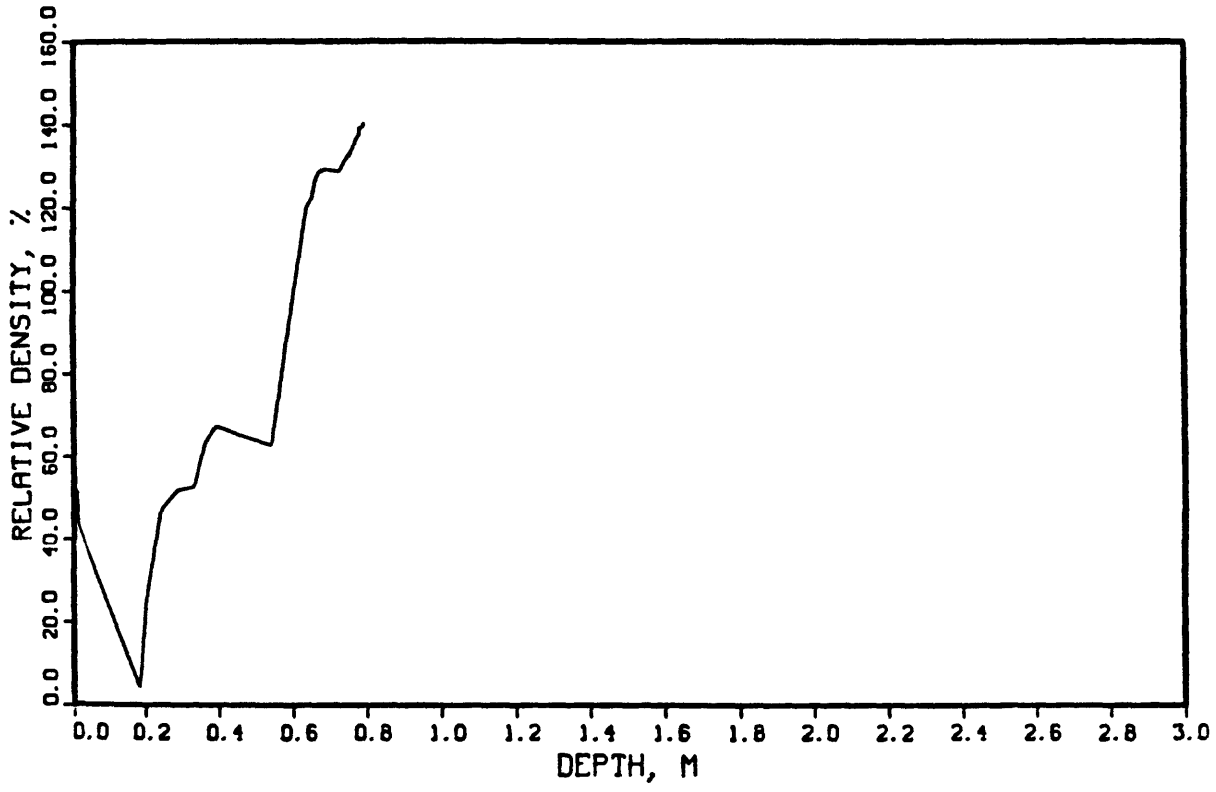
RELATIVE DENSITY, %
0.0
20.0
40.0
60.0
80.0
100.0
120.0
140.0
160.0
0.0 0.2 0.4 0.6 0.8 1.0 1.2 1.4 1.6 1.8 2.0 2.2 2.4 2.6 2.8 3.0
DEPTH, M
674 X2

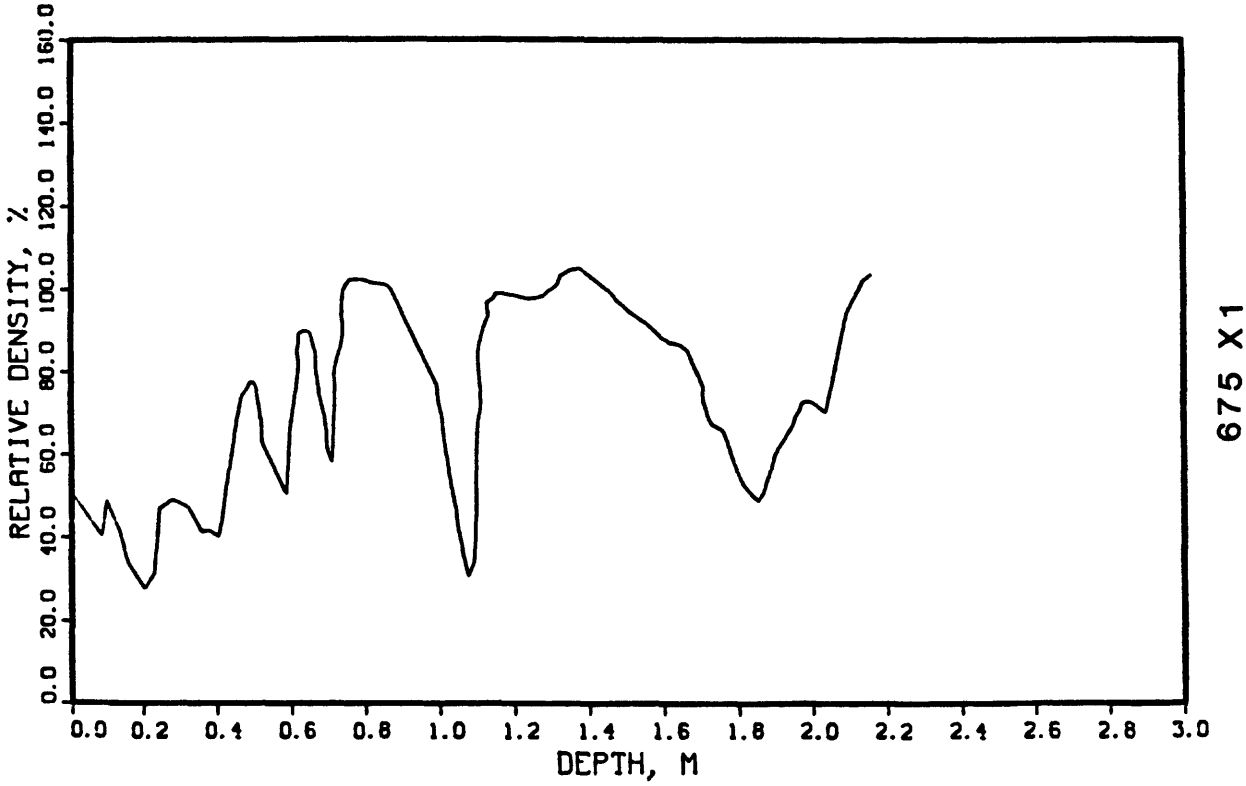
RELATIVE DENSITY, %
0.0
20.0
40.0
60.0
80.0
100.0
120.0
140.0
160.0
0.0
0.2
0.4
0.6
0.8
1.0
1.2
1.4
1.6
1.8
2.0
2.2
2.4
2.6
2.8
3.0
DEPTH, M
675 X 1

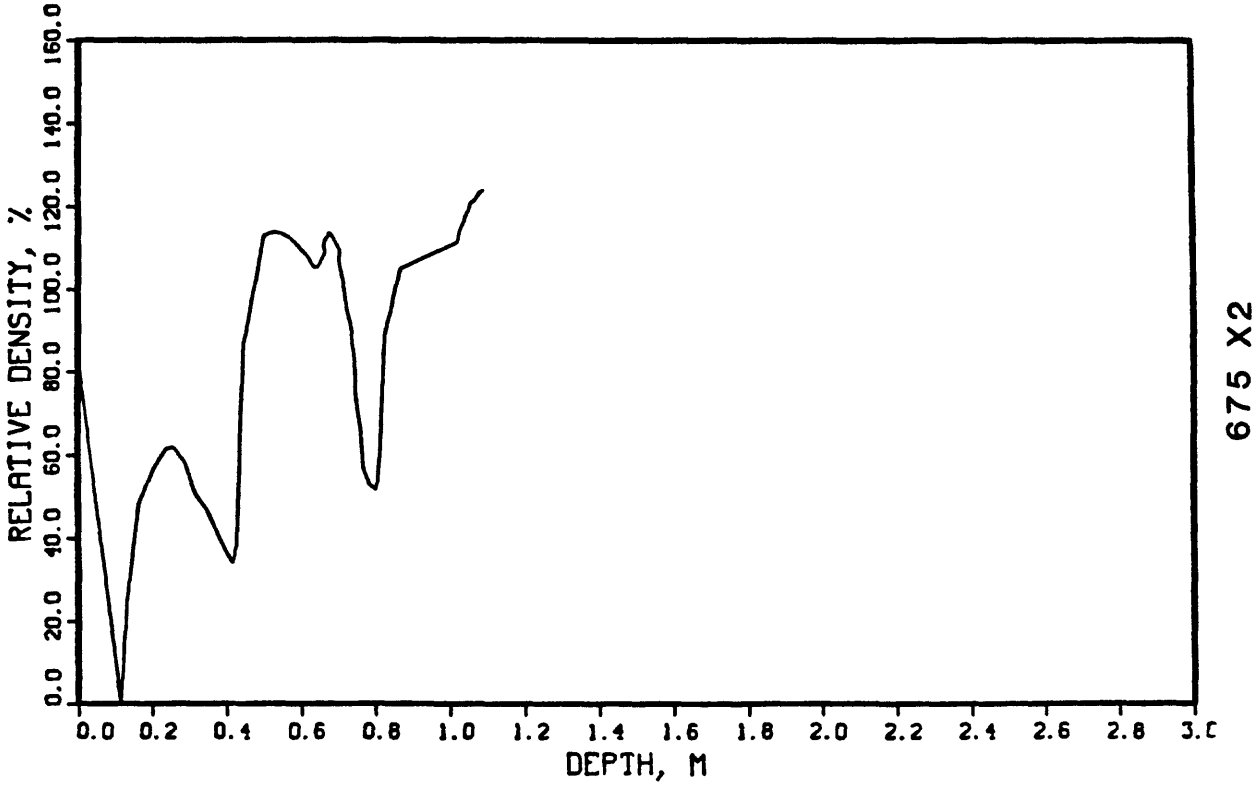
RELATIVE DENSITY, %
0.0
20.0
40.0
60.0
80.0
100.0
120.0
140.0
160.0
0.0
0.2
0.4
0.6
0.8
1.0
1.2
1.4
1.6
1.8
2.0
2.2
2.4
2.6
2.8
3.0
DEPTH, M
675 X2

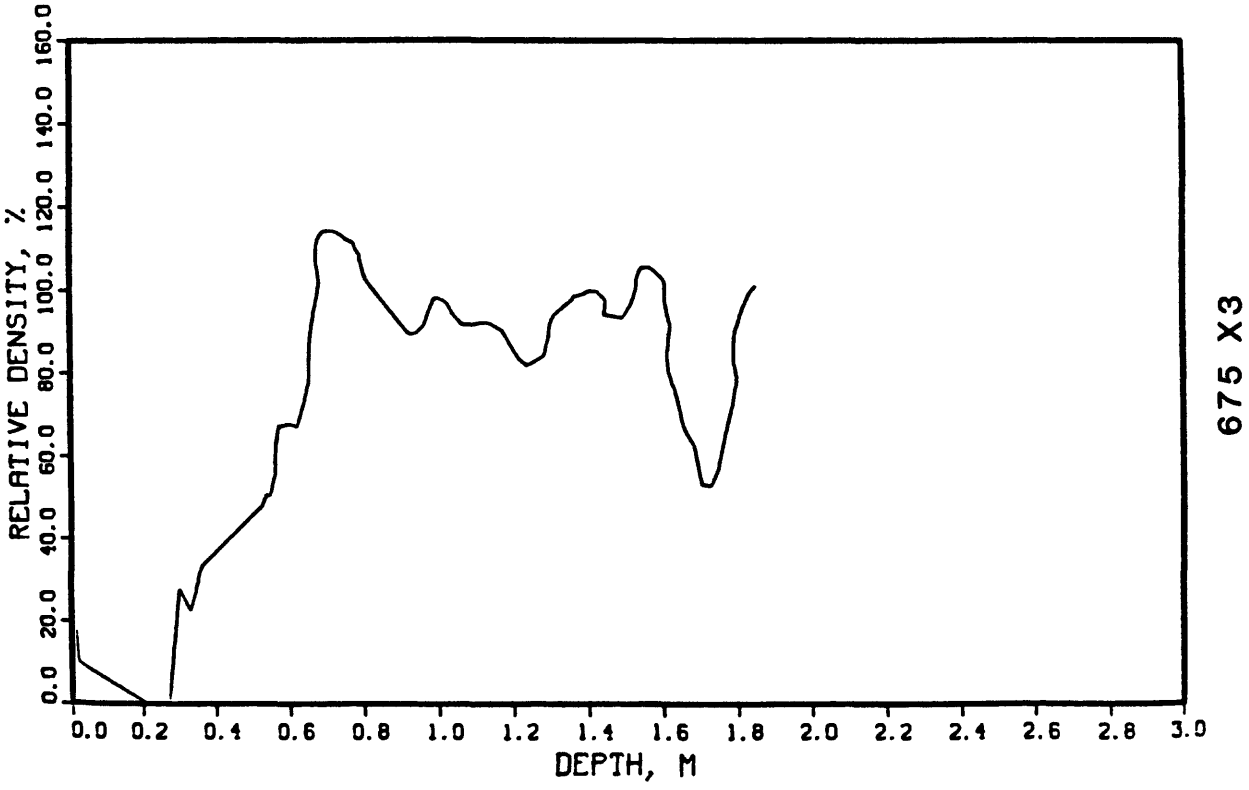
RELATIVE DENSITY, %
0.0
20.0
40.0
60.0
80.0
100.0
120.0
140.0
160.0
0.0
0.2
0.4
0.6
0.8
1.0
1.2
1.4
1.6
1.8
2.0
2.2
2.4
2.6
2.8
3.0
DEPTH, M
675 X3

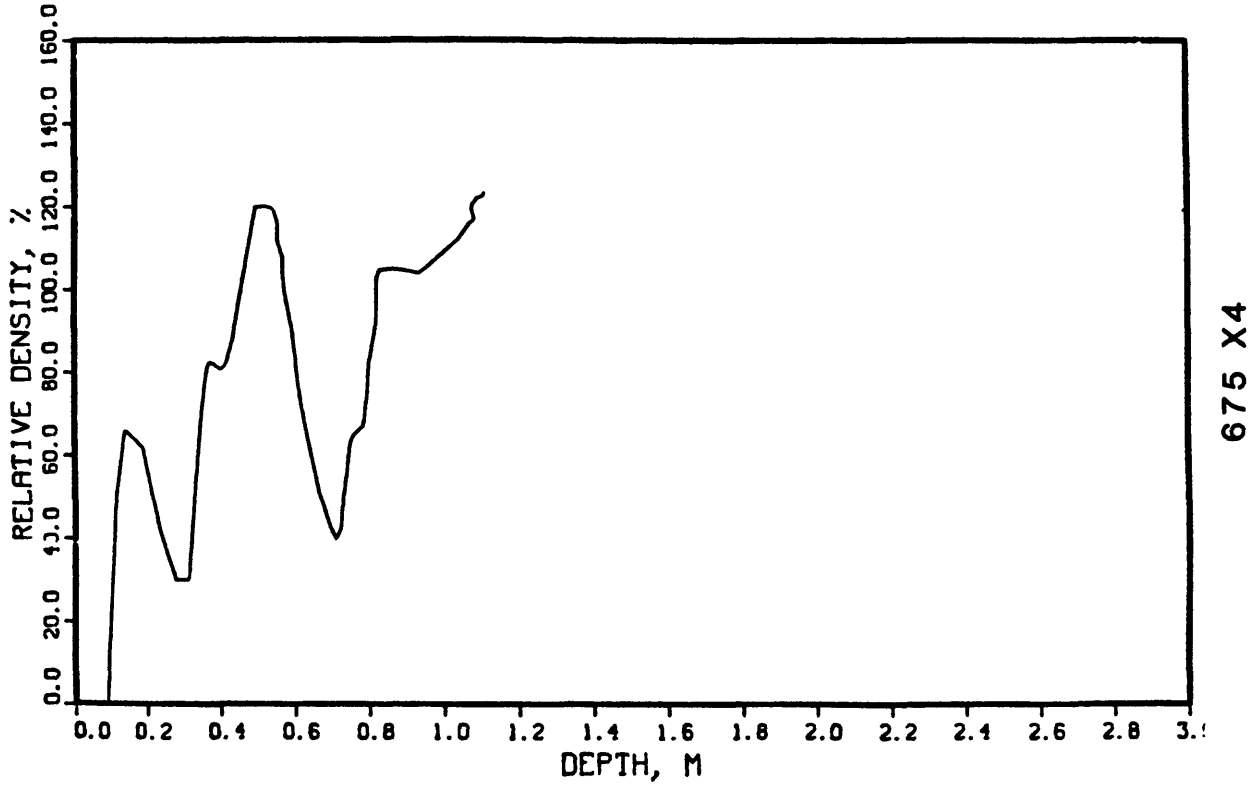
RELATIVE DENSITY, %
0.0
20.0
40.0
60.0
80.0
100.0
120.0
140.0
160.0
0.0
0.2
0.4
0.6
0.8
1.0
1.2
1.4
1.6
1.8
2.0
2.2
2.4
2.6
2.8
DEPTH, M
675 X4

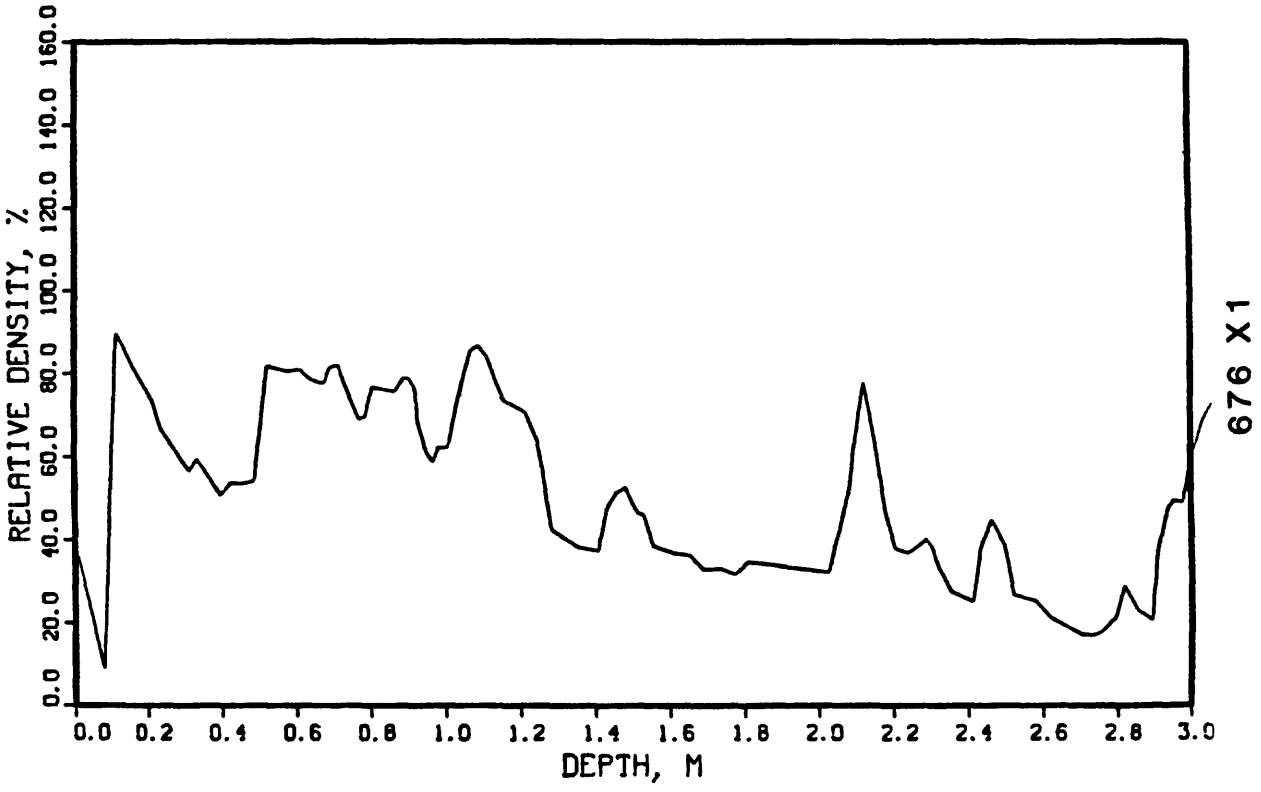
RELATIVE DENSITY, %
0.0
20.0
40.0
60.0
80.0
100.0
120.0
140.0
160.0
0.0
0.2
0.4
0.6
0.8
1.0
1.2
1.4
1.6
1.8
2.0
2.2
2.4
2.6
2.8
3.0
DEPTH, M
676 X1

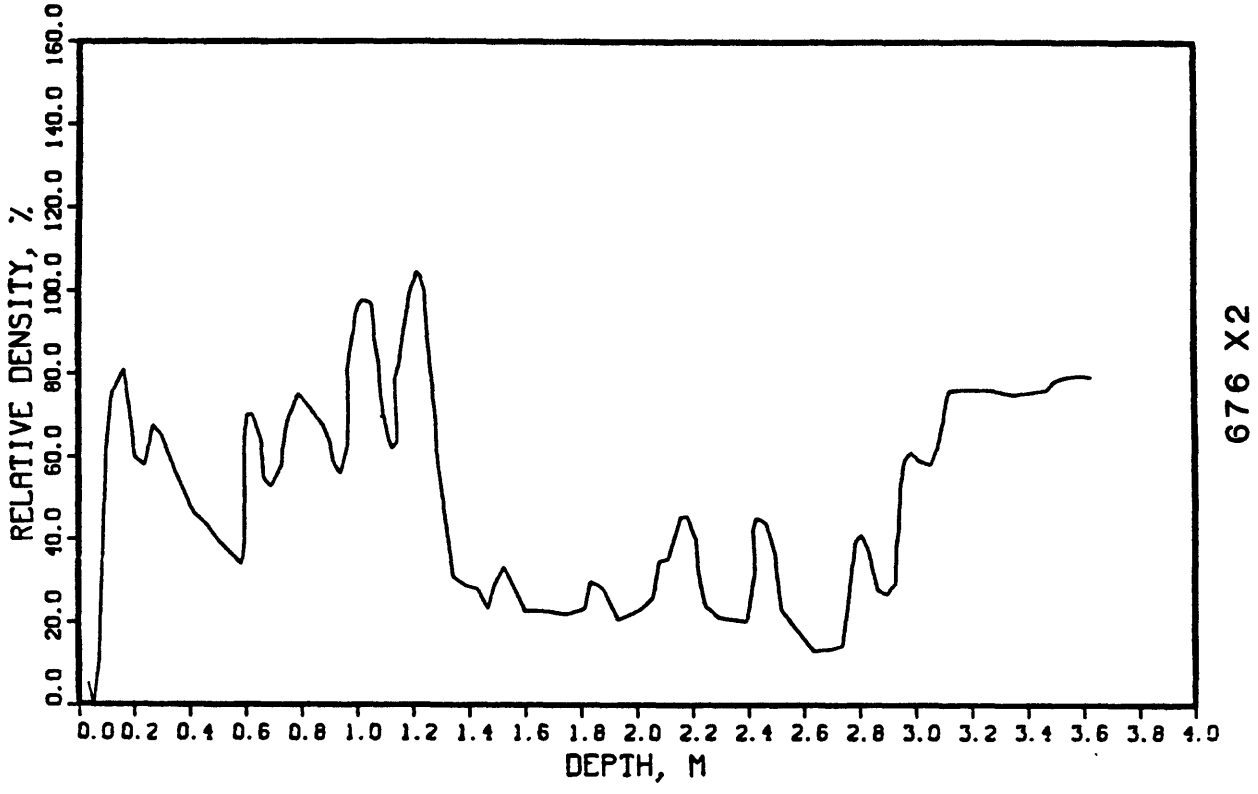
RELATIVE DENSITY, %
0.0
20.0
40.0
60.0
80.0
100.0
120.0
140.0
160.0
0.0 0.2 0.4 0.6 0.8 1.0 1.2 1.4 1.6 1.8 2.0 2.2 2.4 2.6 2.8 3.0 3.2 3.4 3.6 3.8 4.0
DEPTH, M
676 X2

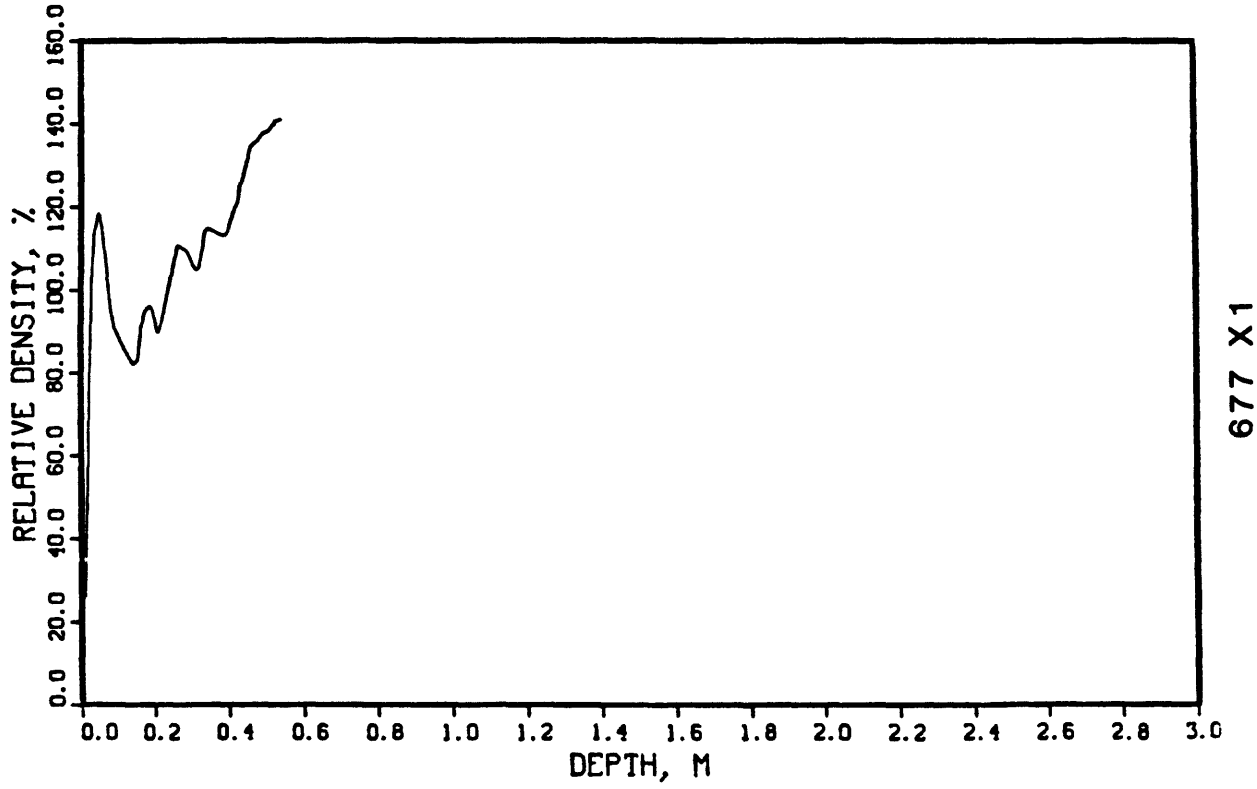
RELATIVE DENSITY, %
0.0
20.0
40.0
60.0
80.0
100.0
120.0
140.0
160.0
0.0
0.2
0.4
0.6
0.8
1.0
1.2
1.4
1.6
1.8
2.0
2.2
2.4
2.6
2.8
3.0
DEPTH, M
677 X1

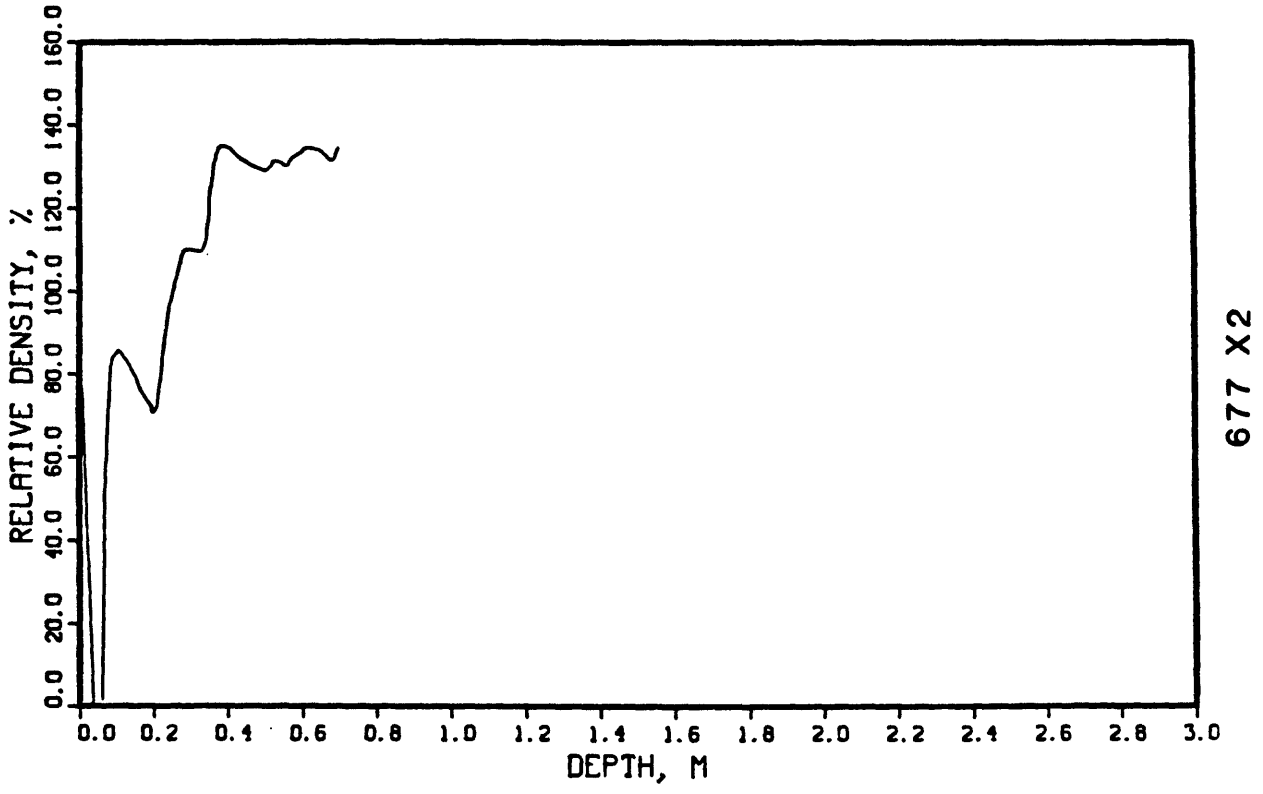
RELATIVE DENSITY, %
0.0
20.0
40.0
60.0
80.0
100.0
120.0
140.0
160.0
0.0
0.2
0.4
0.6
0.8
1.0
1.2
1.4
1.6
1.8
2.0
2.2
2.4
2.6
2.8
3.0
DEPTH, M
677 X2

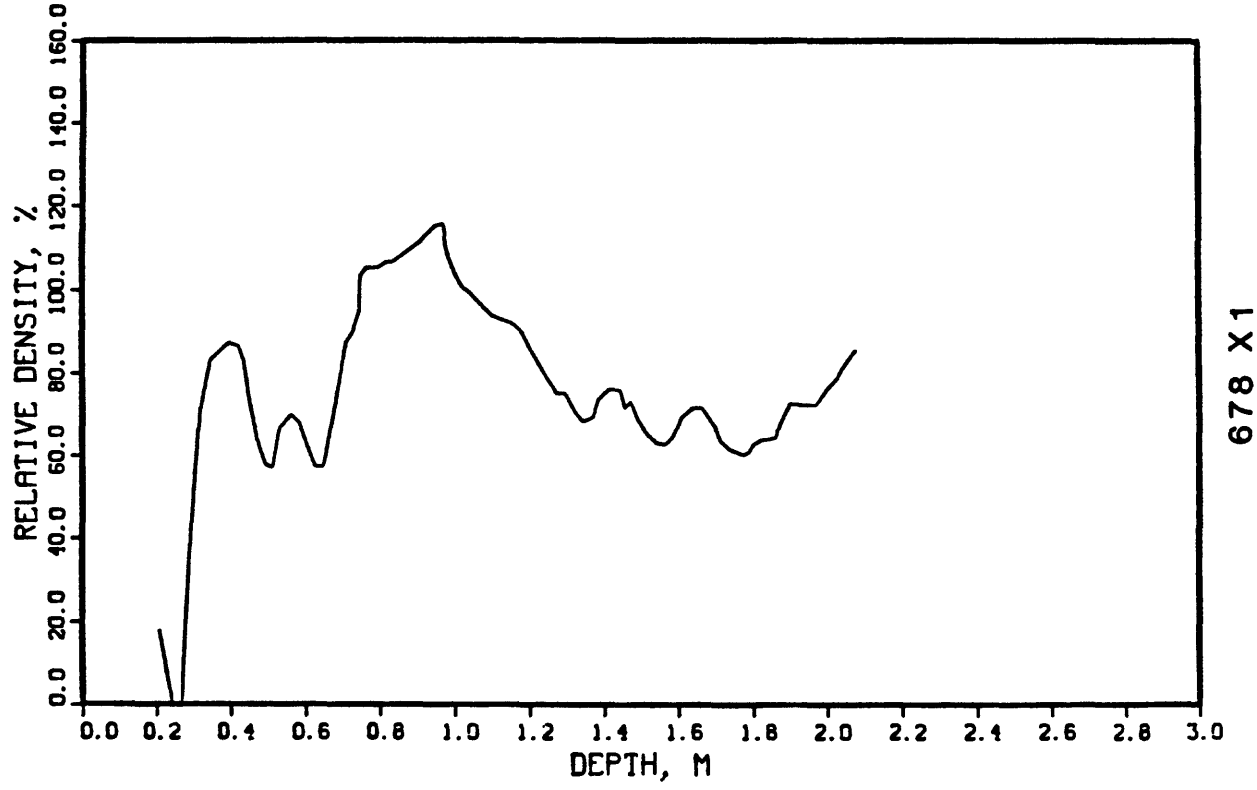
RELATIVE DENSITY, %
0.0
20.0
40.0
60.0
80.0
100.0
120.0
140.0
160.0
0.0
0.2
0.4
0.6
0.8
1.0
1.2
1.4
1.6
1.8
2.0
2.2
2.4
2.6
2.8
3.0
DEPTH, M
678 X 1

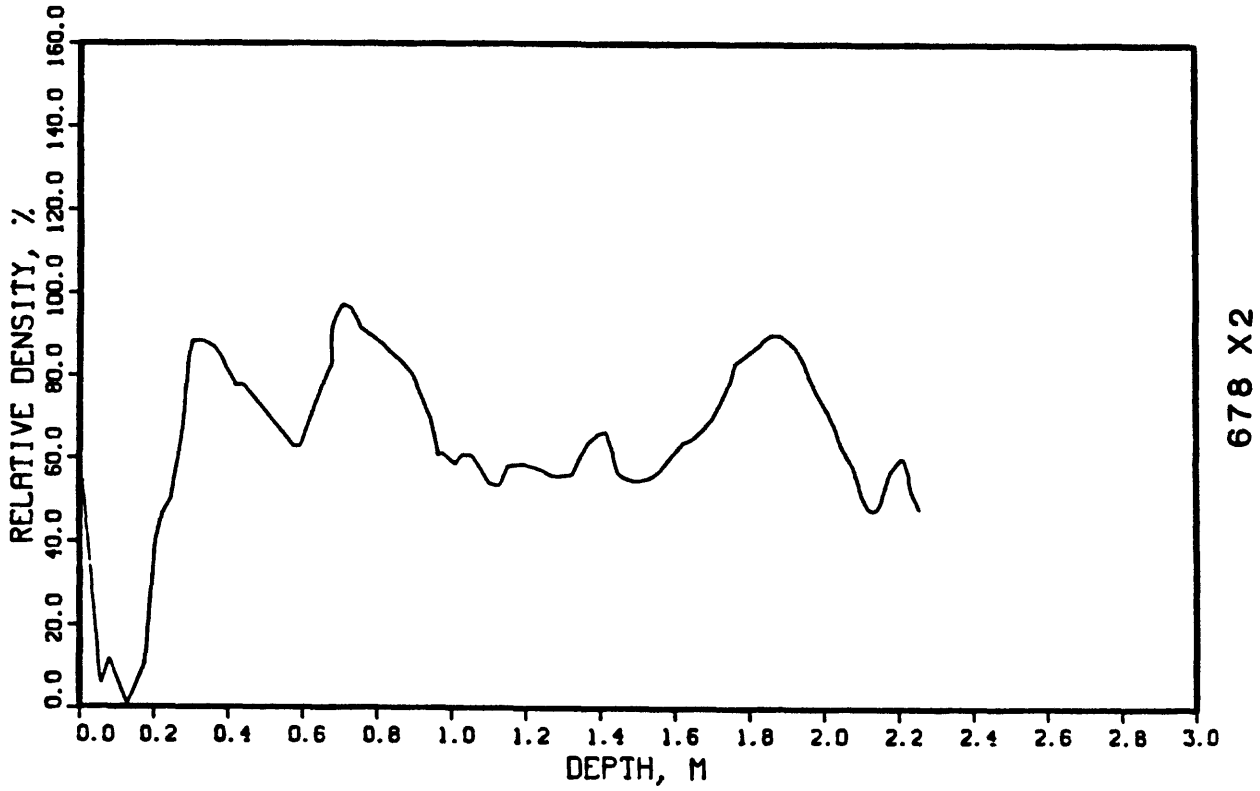
RELATIVE DENSITY, %
0.0
20.0
40.0
60.0
80.0
100.0
120.0
140.0
160.0
0.0
0.2
0.4
0.6
0.8
1.0
1.2
1.4
1.6
1.8
2.0
2.2
2.4
2.6
2.8
3.0
DEPTH, M
678 X2

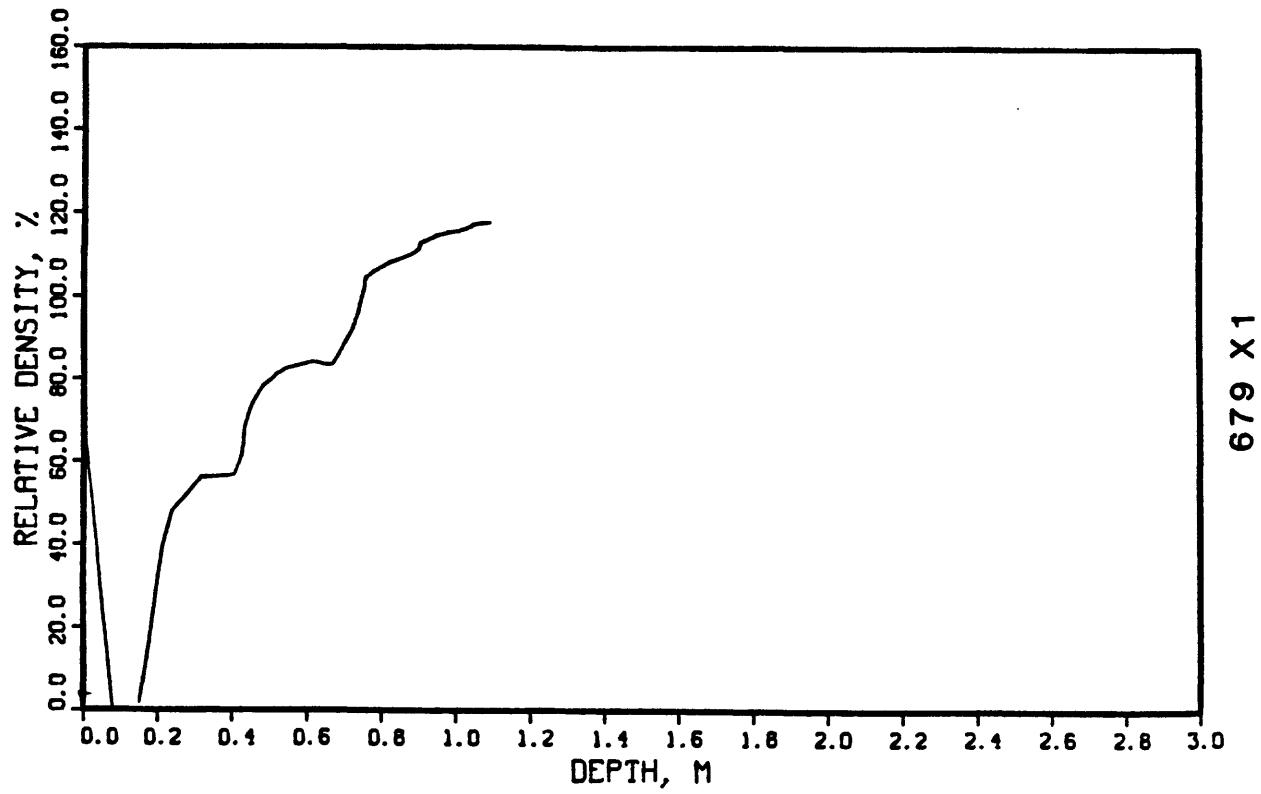
RELATIVE DENSITY, %
0.0
20.0
40.0
60.0
80.0
100.0
120.0
140.0
160.0
0.0
0.2
0.4
0.6
0.8
1.0
1.2
1.4
1.6
1.8
2.0
2.2
2.4
2.6
2.8
3.0
DEPTH, M
679 X1

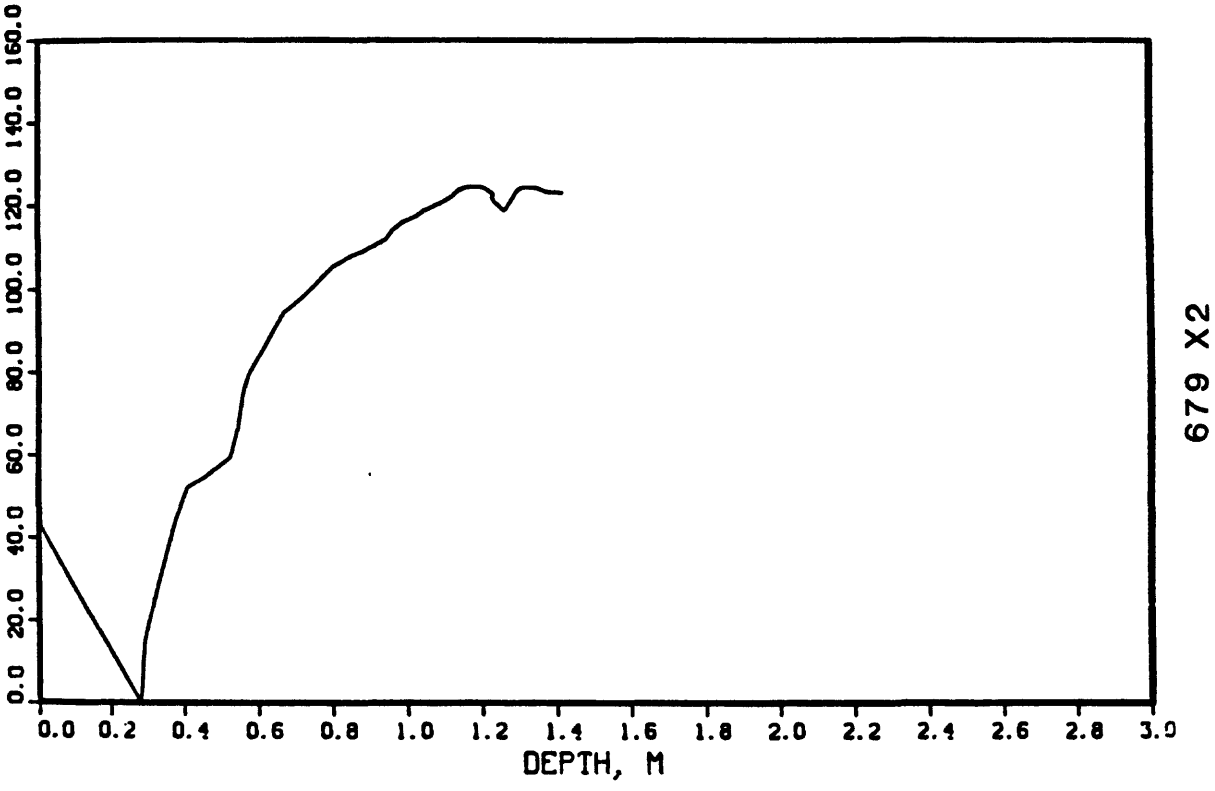
0.0
20.0
40.0
60.0
80.0
100.0
120.0
140.0
160.0
0.0 0.2 0.4 0.6 0.8 1.0 1.2 1.4 1.6 1.8 2.0 2.2 2.4 2.6 2.8 3.0
DEPTH, M
679 X2

Appendix D. Consolidation test plots.

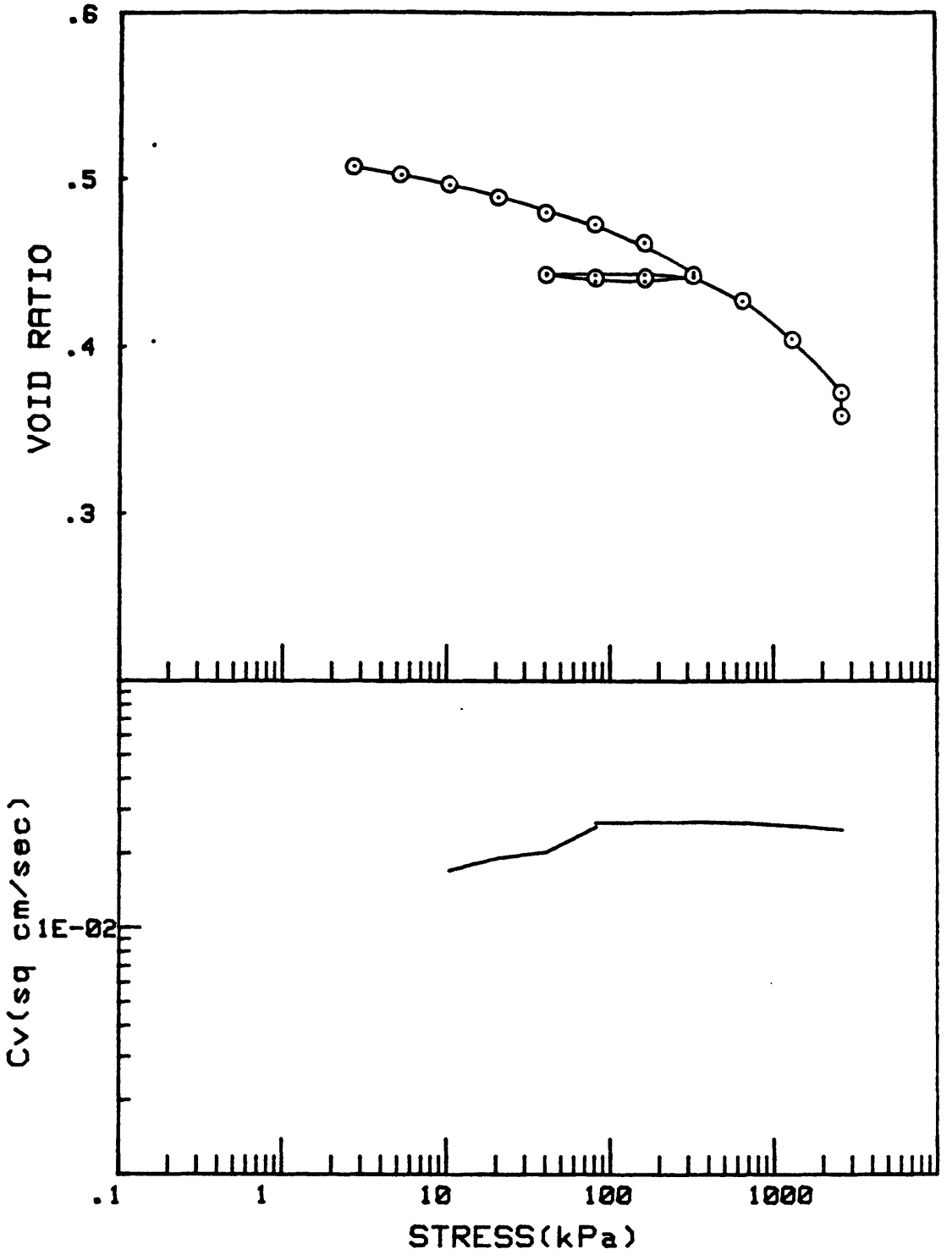

CRUISE DC4-81-NS		INCREMENT (cm)	212-214
CORE NO.	681A2	TEST NO.	OE36

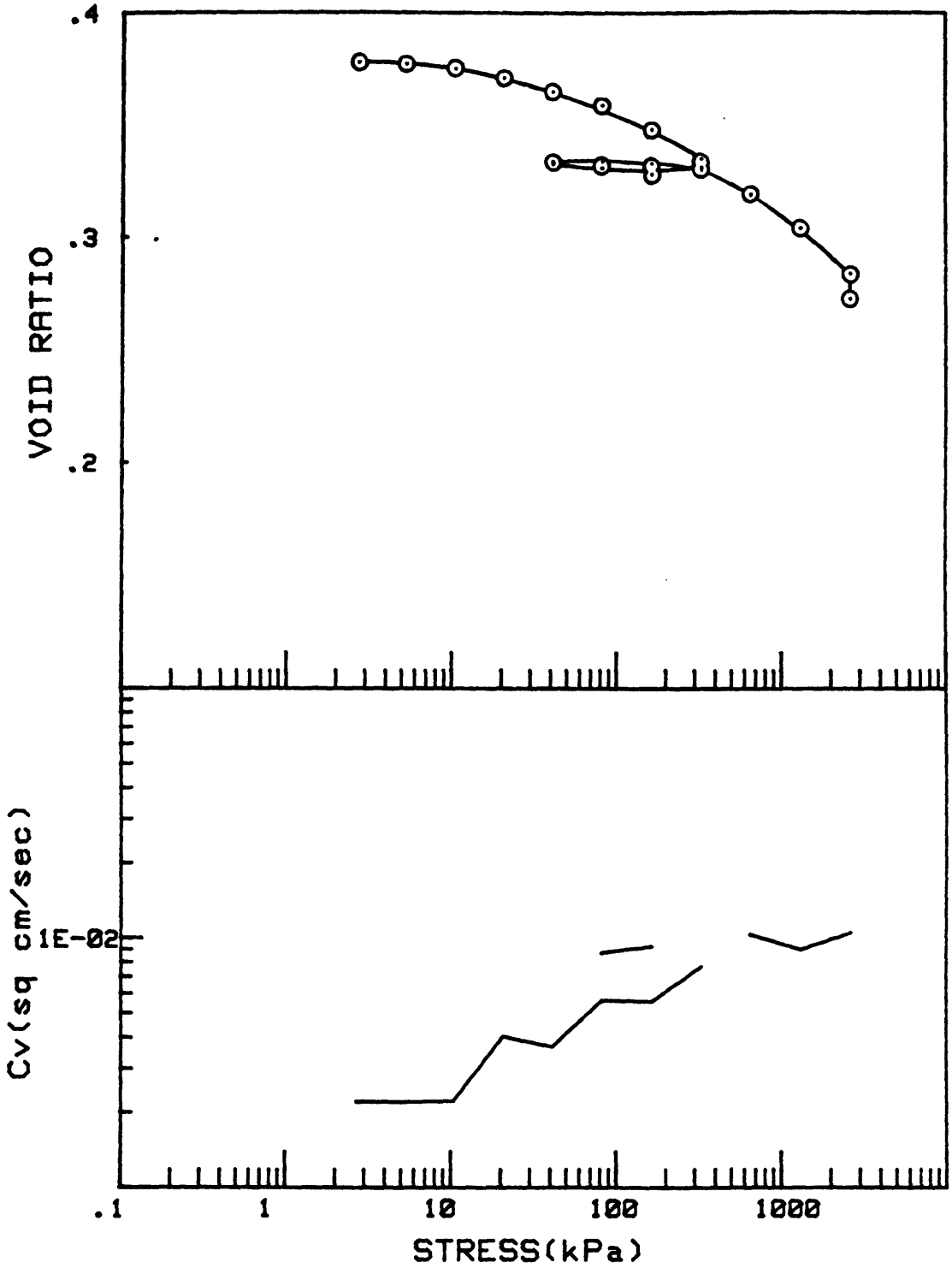

CRUISE DC4-81-NS		INCREMENT (cm)	552-554
CORE NO.	681A2	TEST NO.	OE38

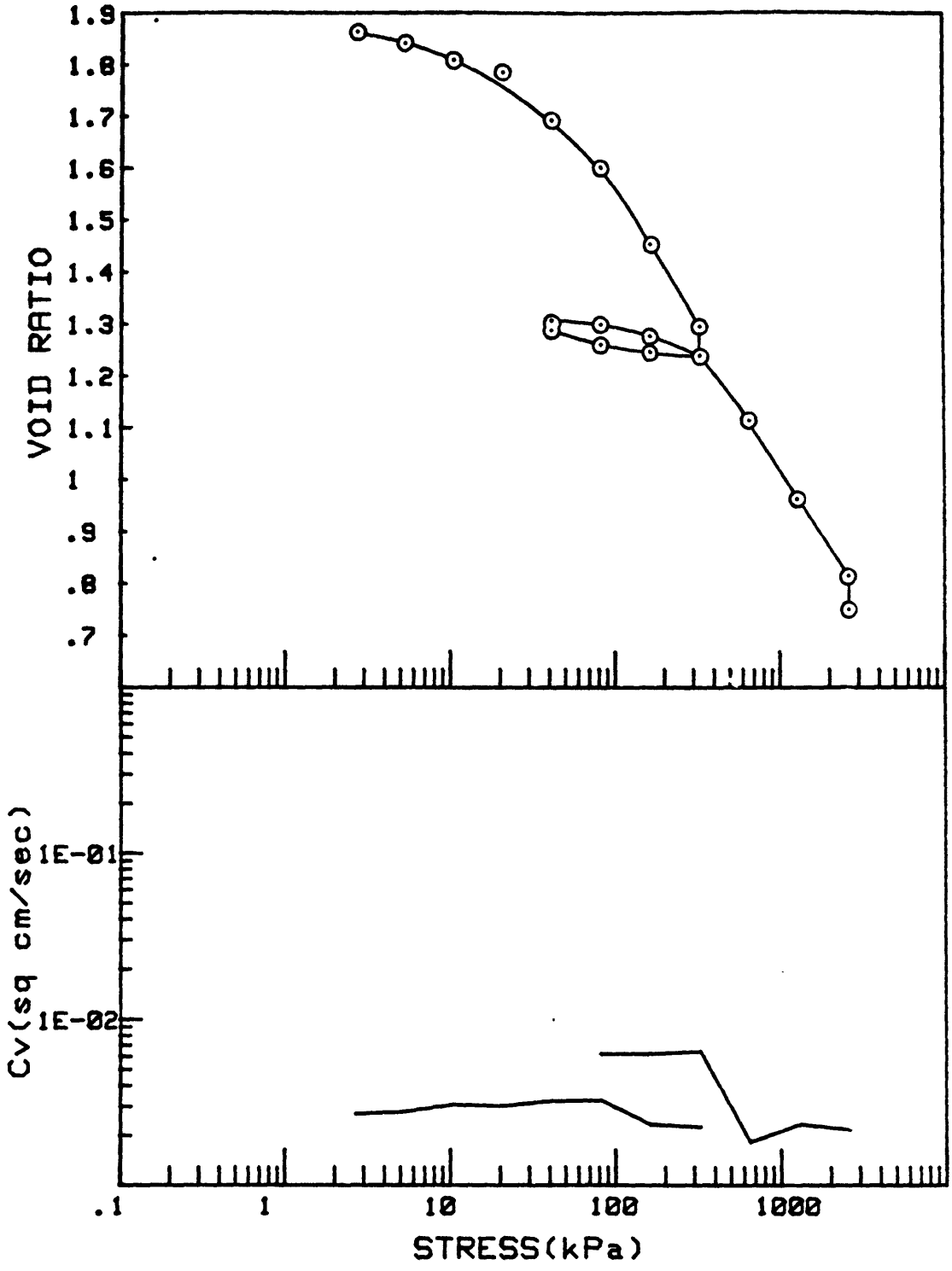

CRUISE DC4-81-NS	INCREMENT (cm) 146-148
CORE NO. 682A1	TEST NO. 0E34

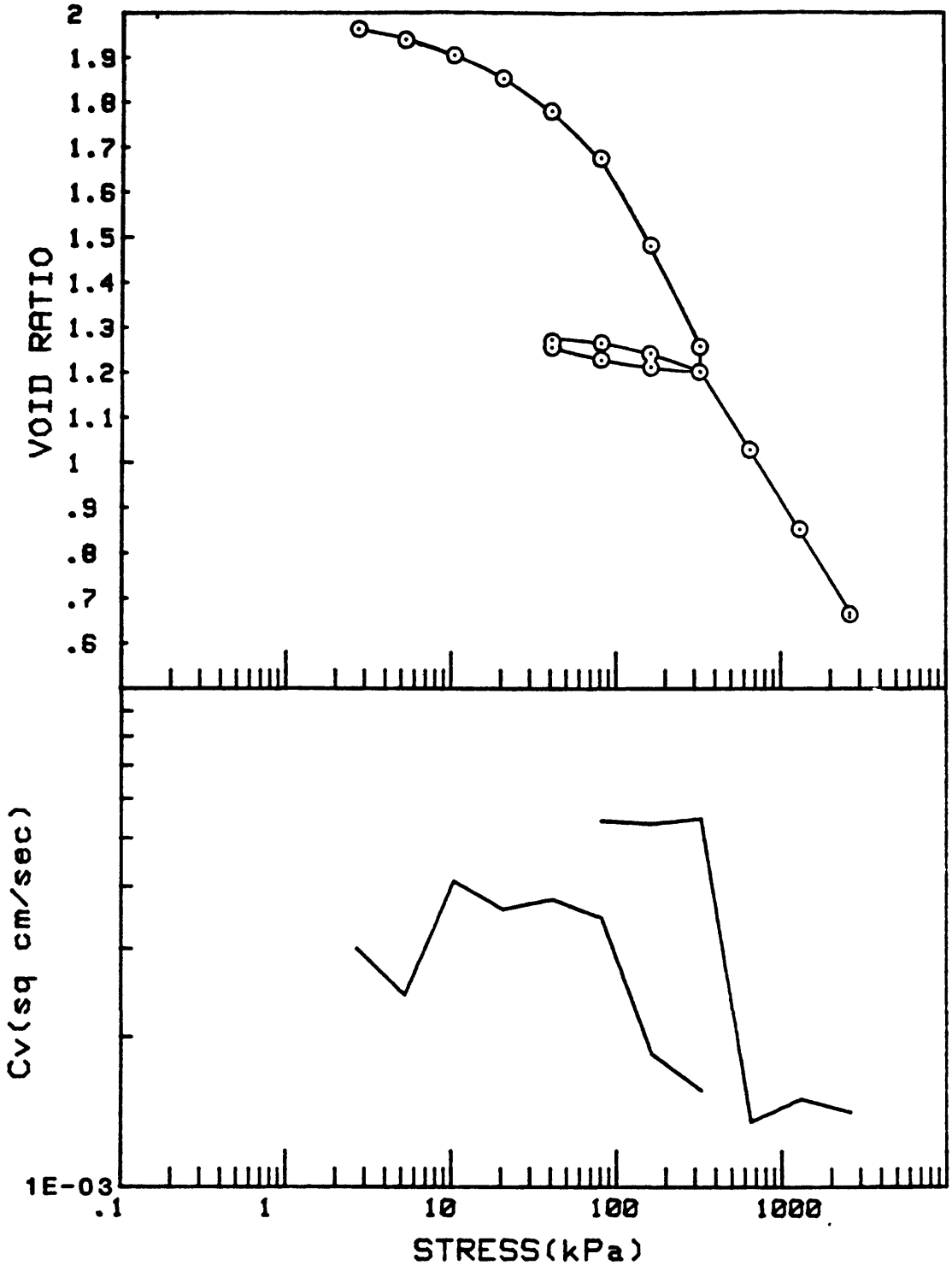

CRUISE DC4-81-NS		INCREMENT (cm)	290-292
CORE NO.	682A1	TEST NO.	OE35

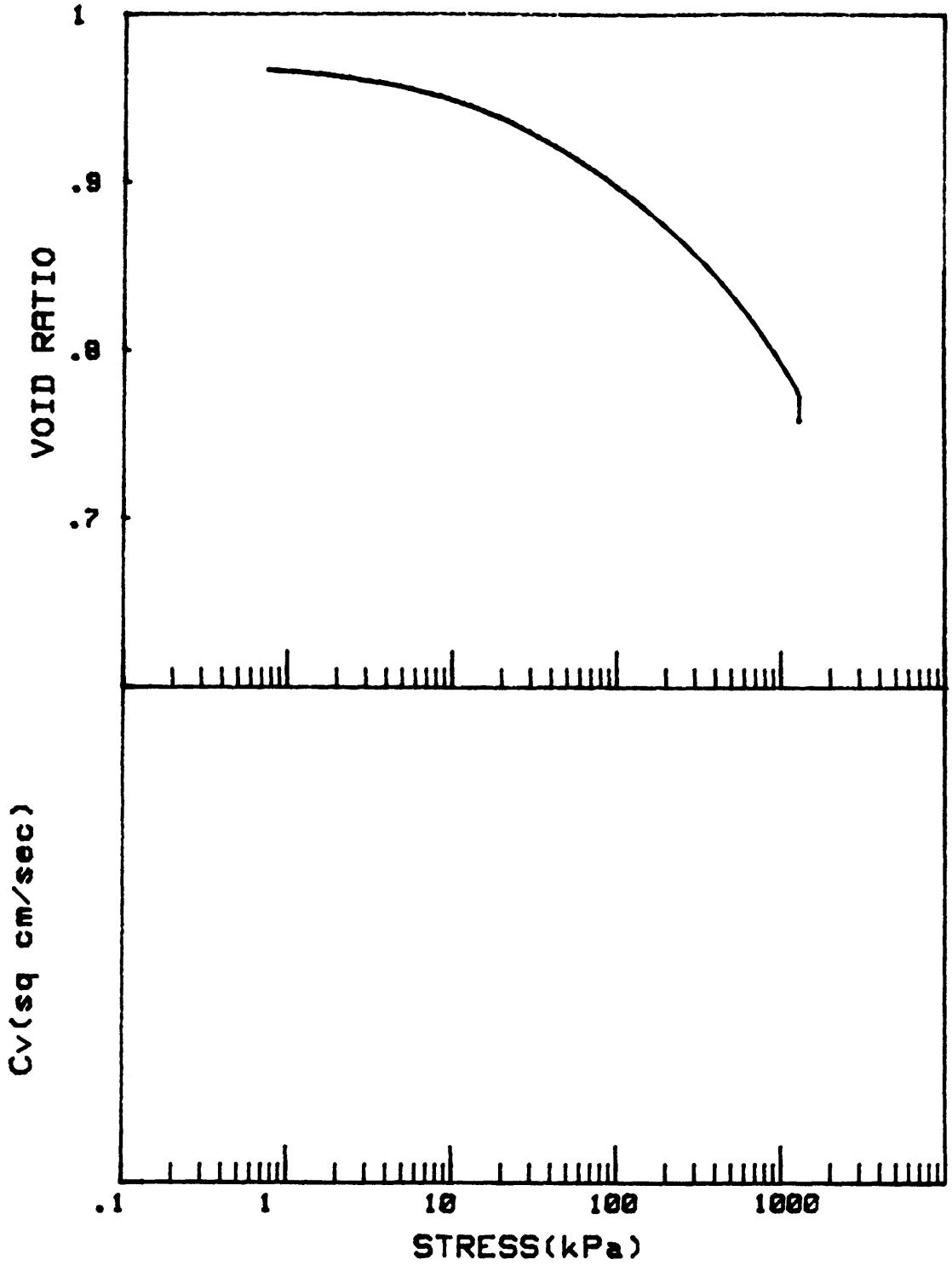

CRUISE DC4-81-NS		INCREMENT (cm)	458-464
CORE NO.	682A1	TEST NO.	CE19

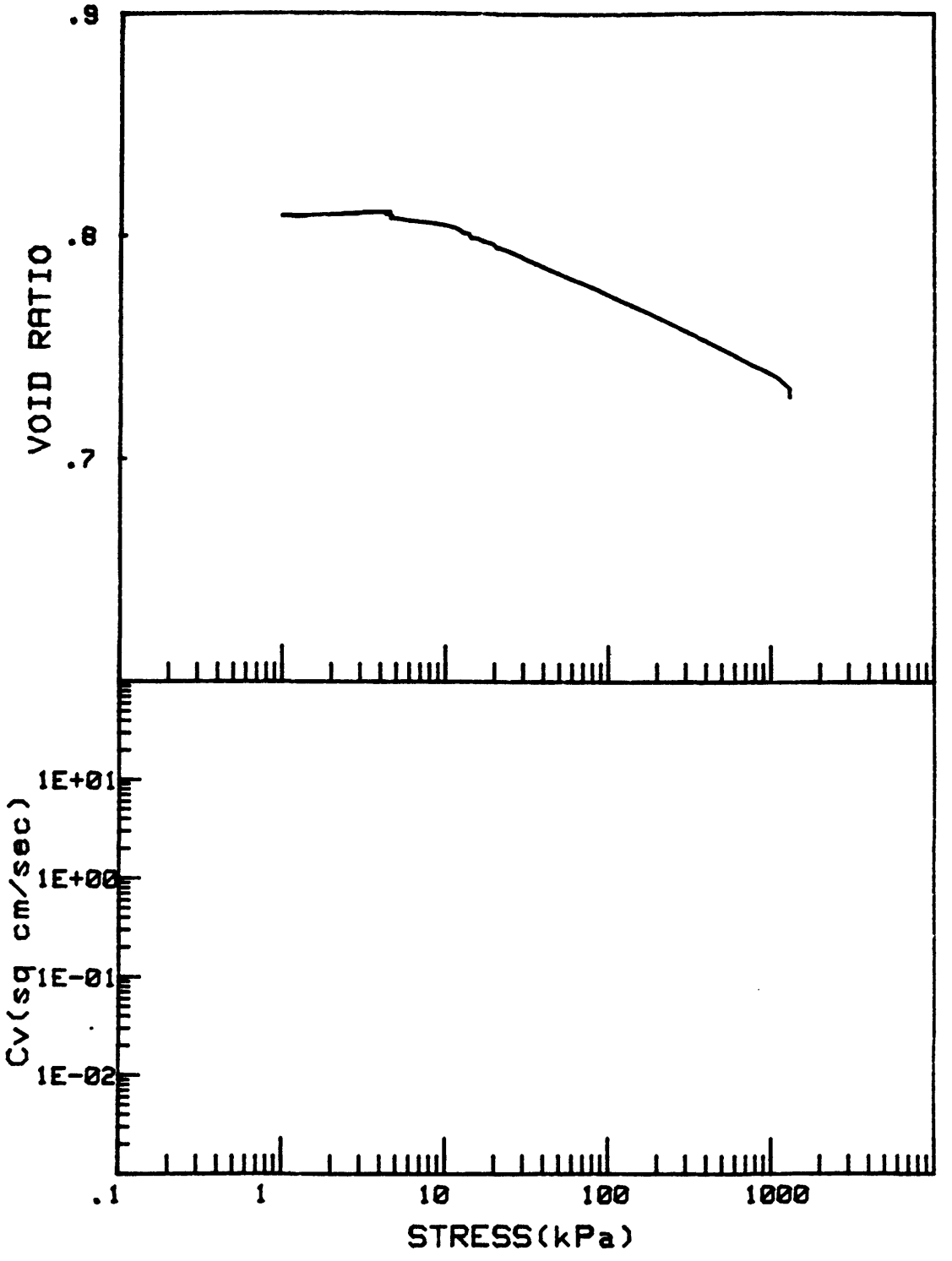

CRUISE DC4-81-NS		INCREMENT (cm)	147-152
CORE NO.	683A1	TEST NO.	CE34

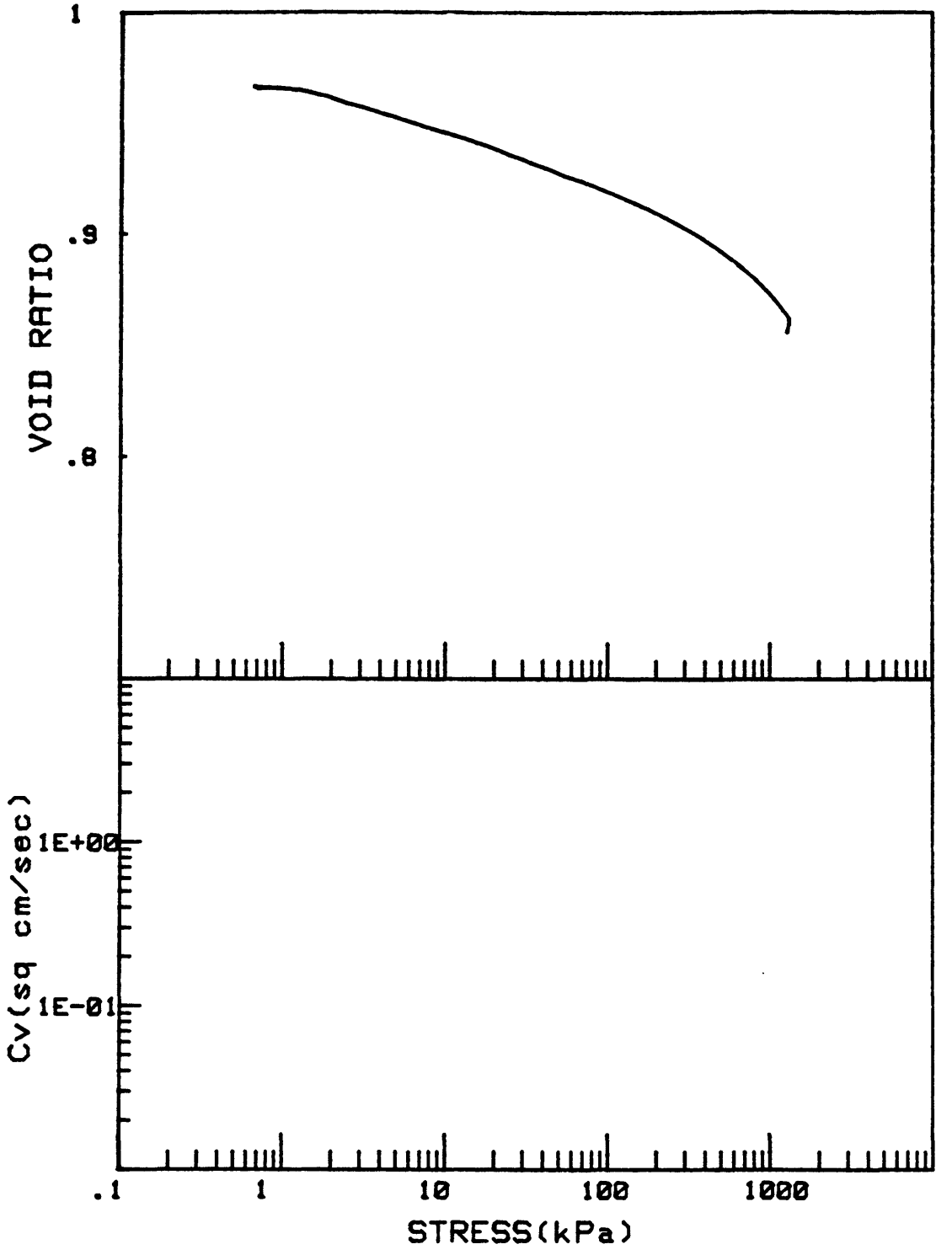

CRUISE DC4-81-NS		INCREMENT (cm)	252-257
CORE NO.	683A1	TEST NO.	CE35

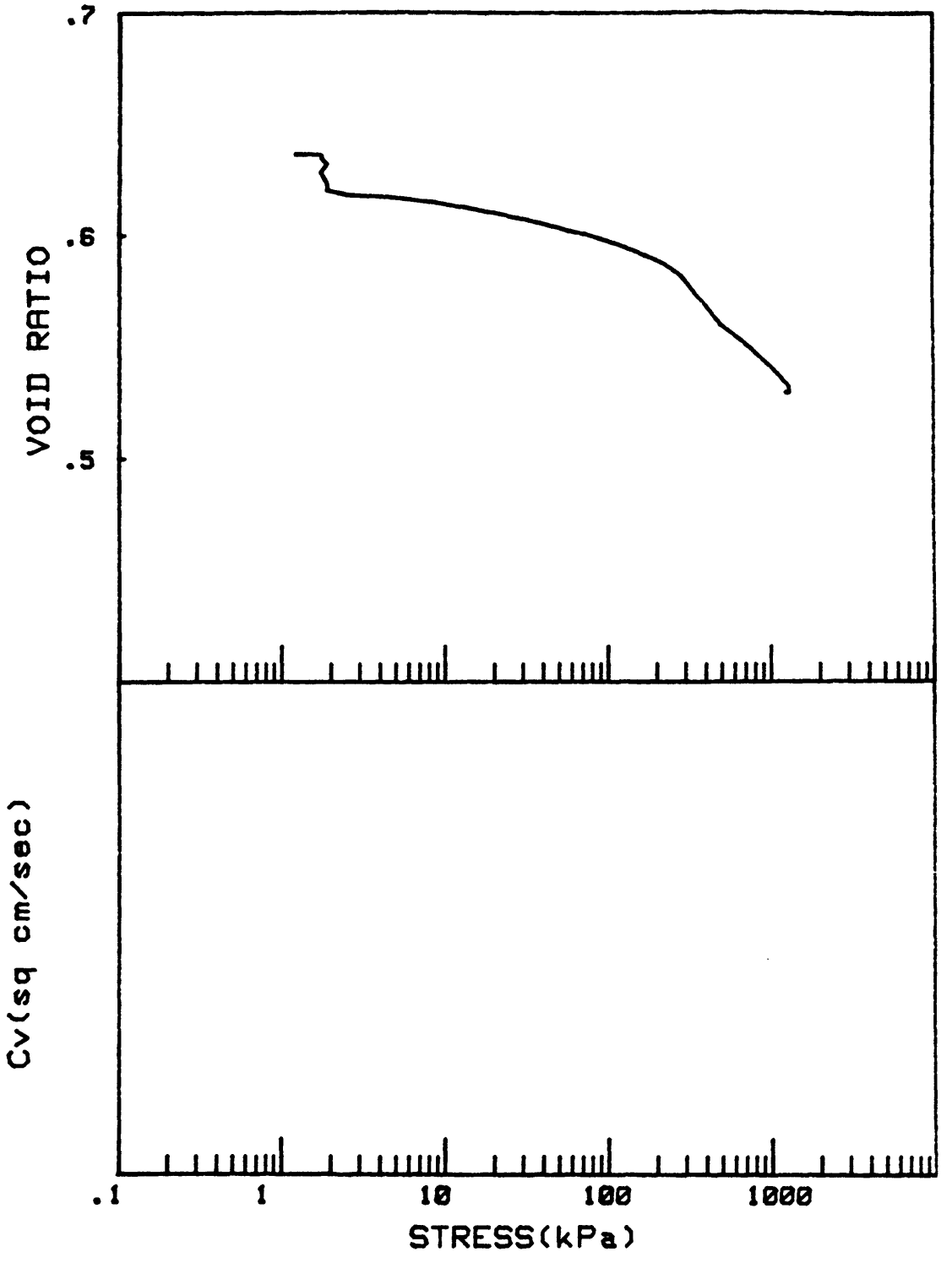

CRUISE DC4-81-NS		INCREMENT (cm)	446-448
CORE NO.	683A1	TEST NO.	CE43

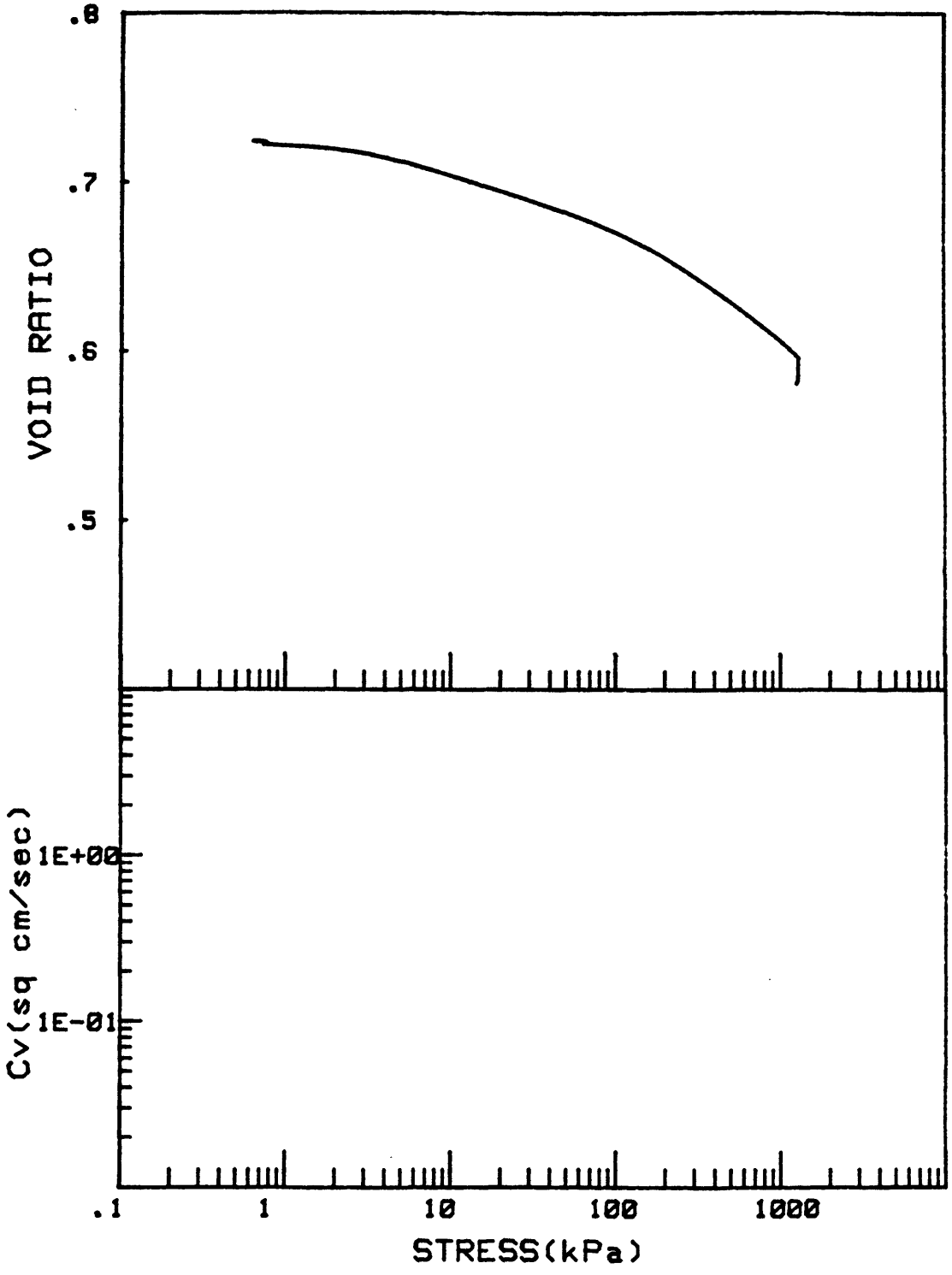

CRUISE DC4-81-NS		INCREMENT (cm)	35-40
CORE NO.	684A1	TEST NO.	CE37

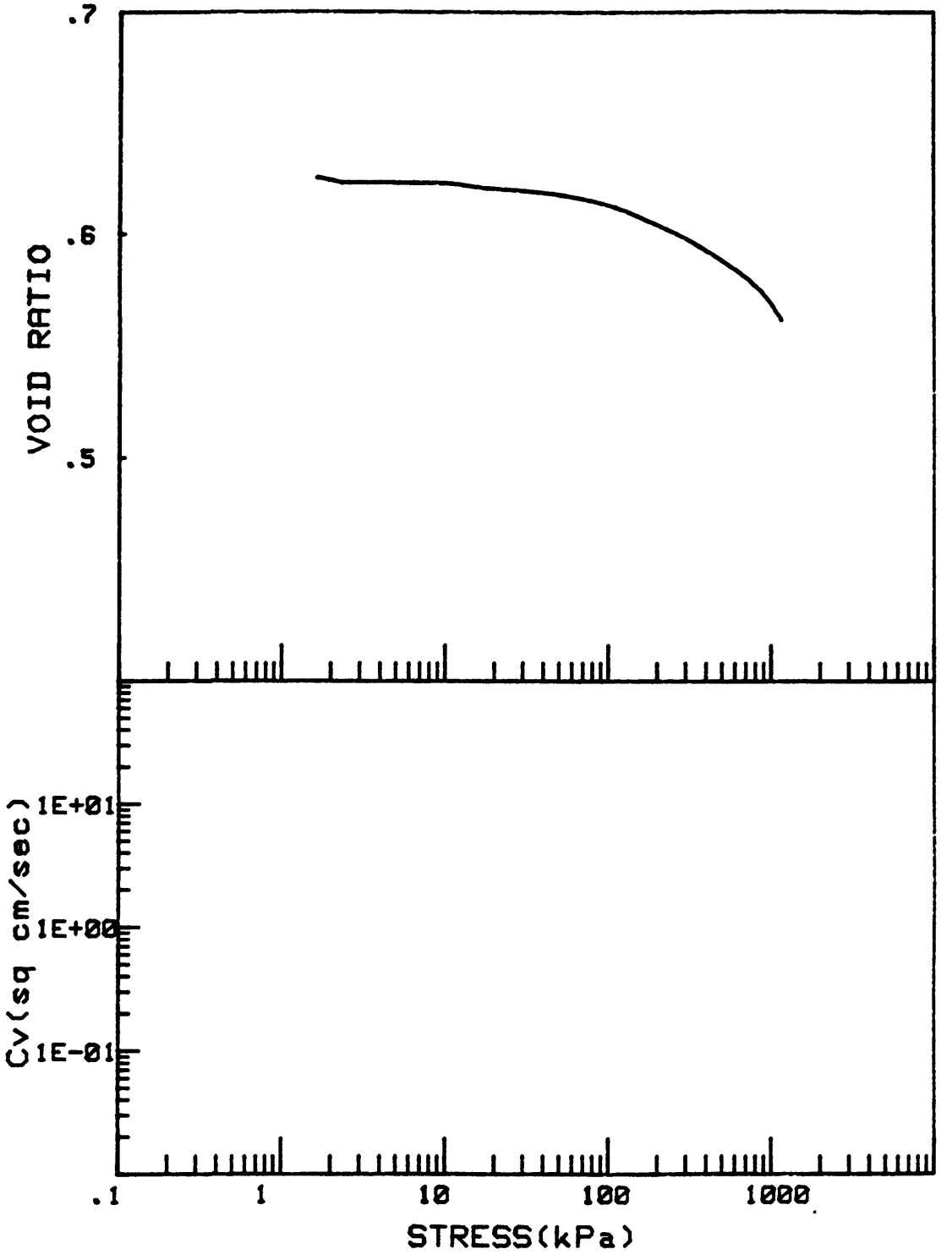

CRUISE DC4-81-NS		INCREMENT (cm)	106-108
CORE NO.	684A1	TEST NO.	CE47

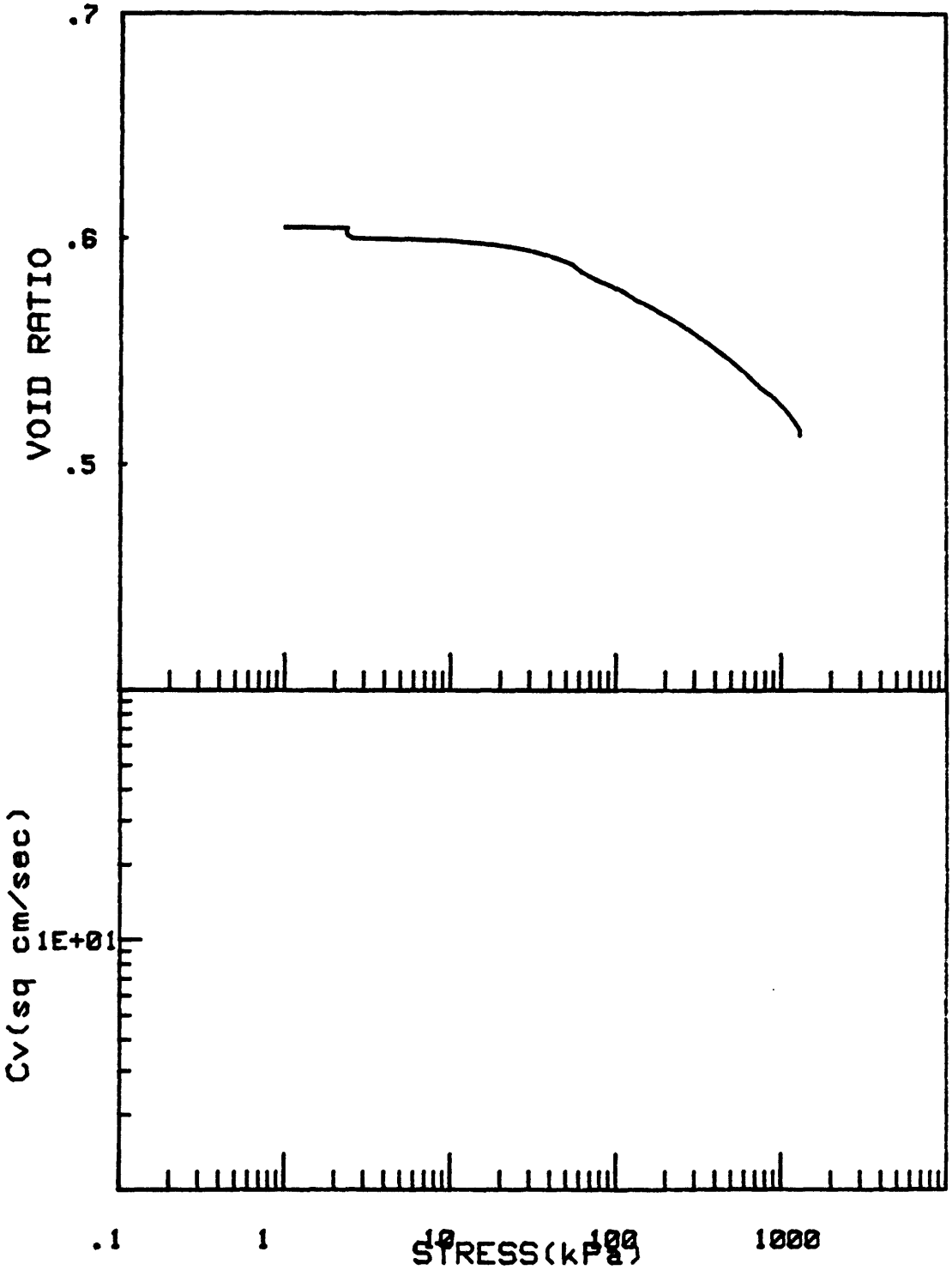

CRUISE DC4-81-NS		INCREMENT (cm)	236-238
CORE NO.	684A1	TEST NO.	CE49

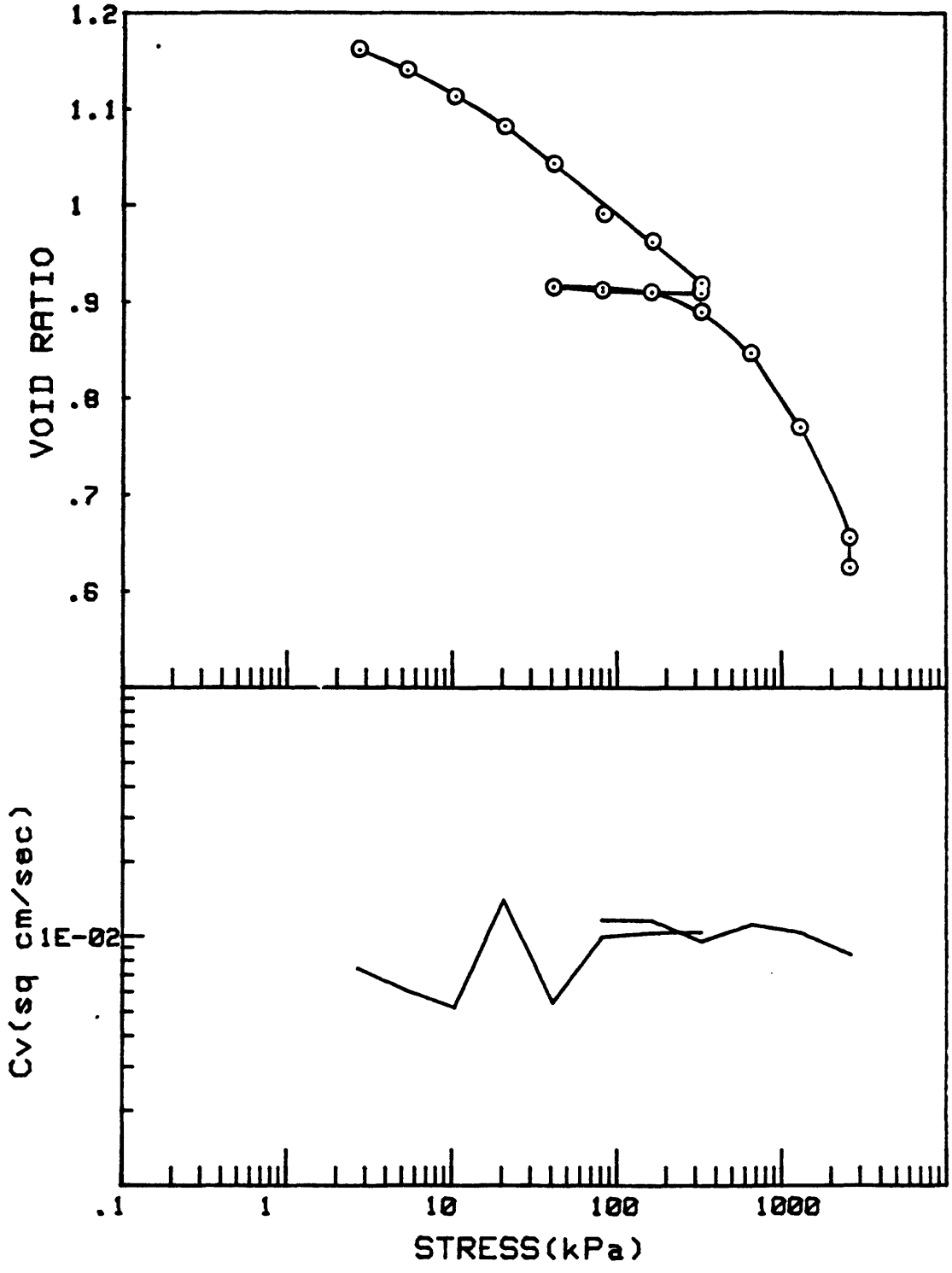

CRUISE DC4-81-NS		INCREMENT (cm)	76-78
CORE NO.	685A2	TEST NO.	0E39

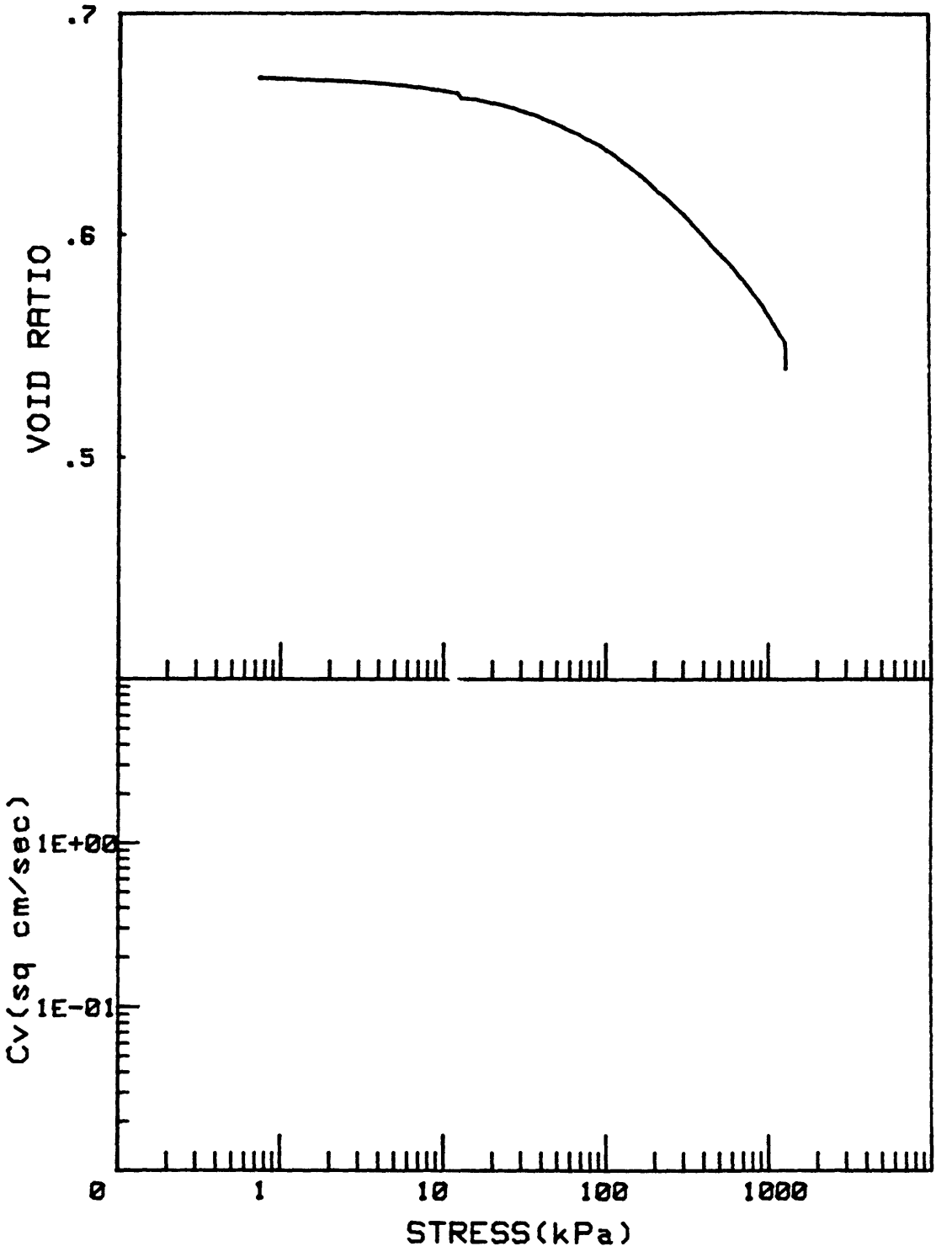

CRUISE DC4-81-NS	INCREMENT (cm) 150-156
CORE NO. 685A2	TEST NO. CE20

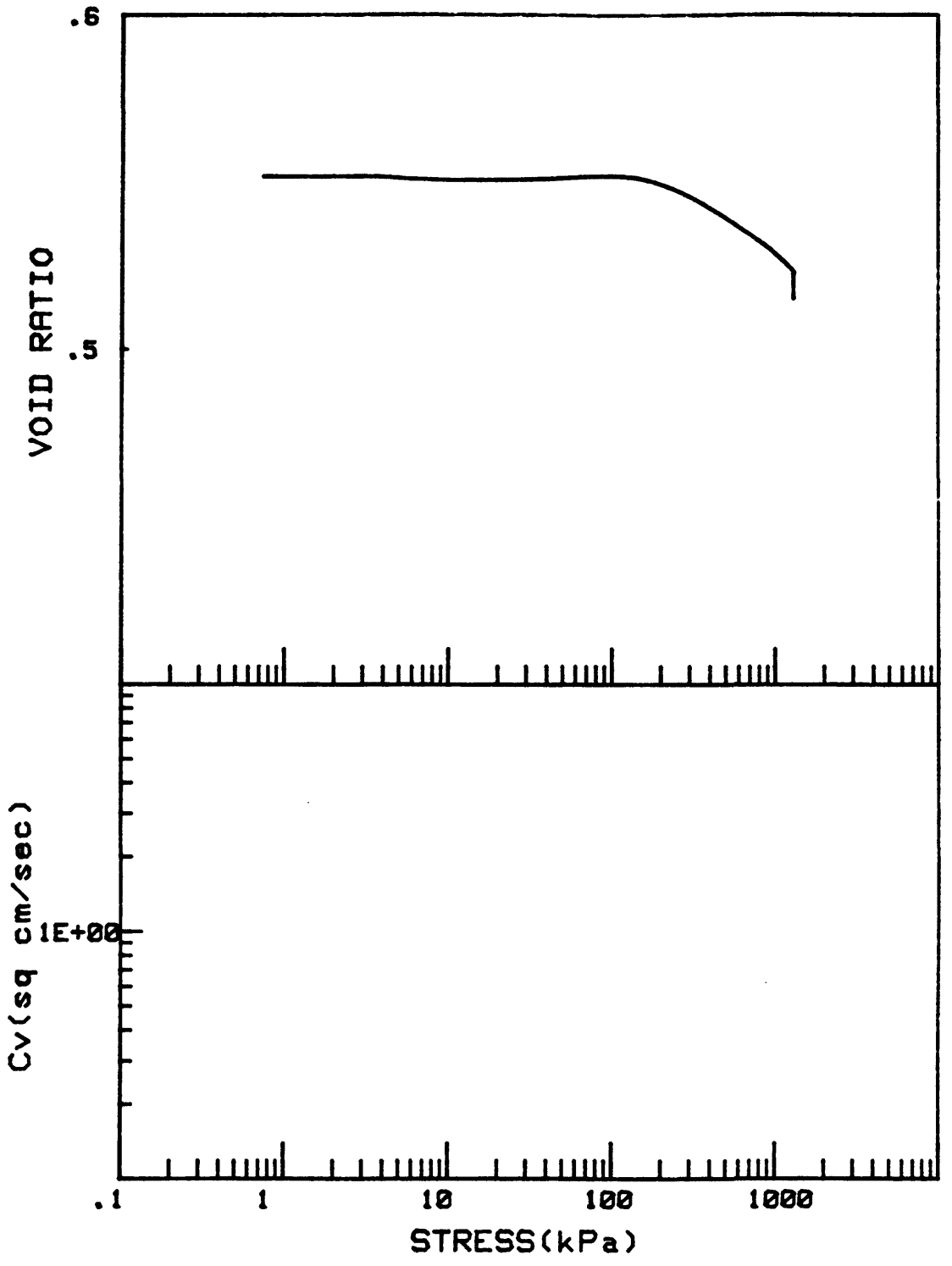

CRUISE DC4-81-NS		INCREMENT (cm)	180-182
CORE NO.	685A2	TEST NO.	CE21

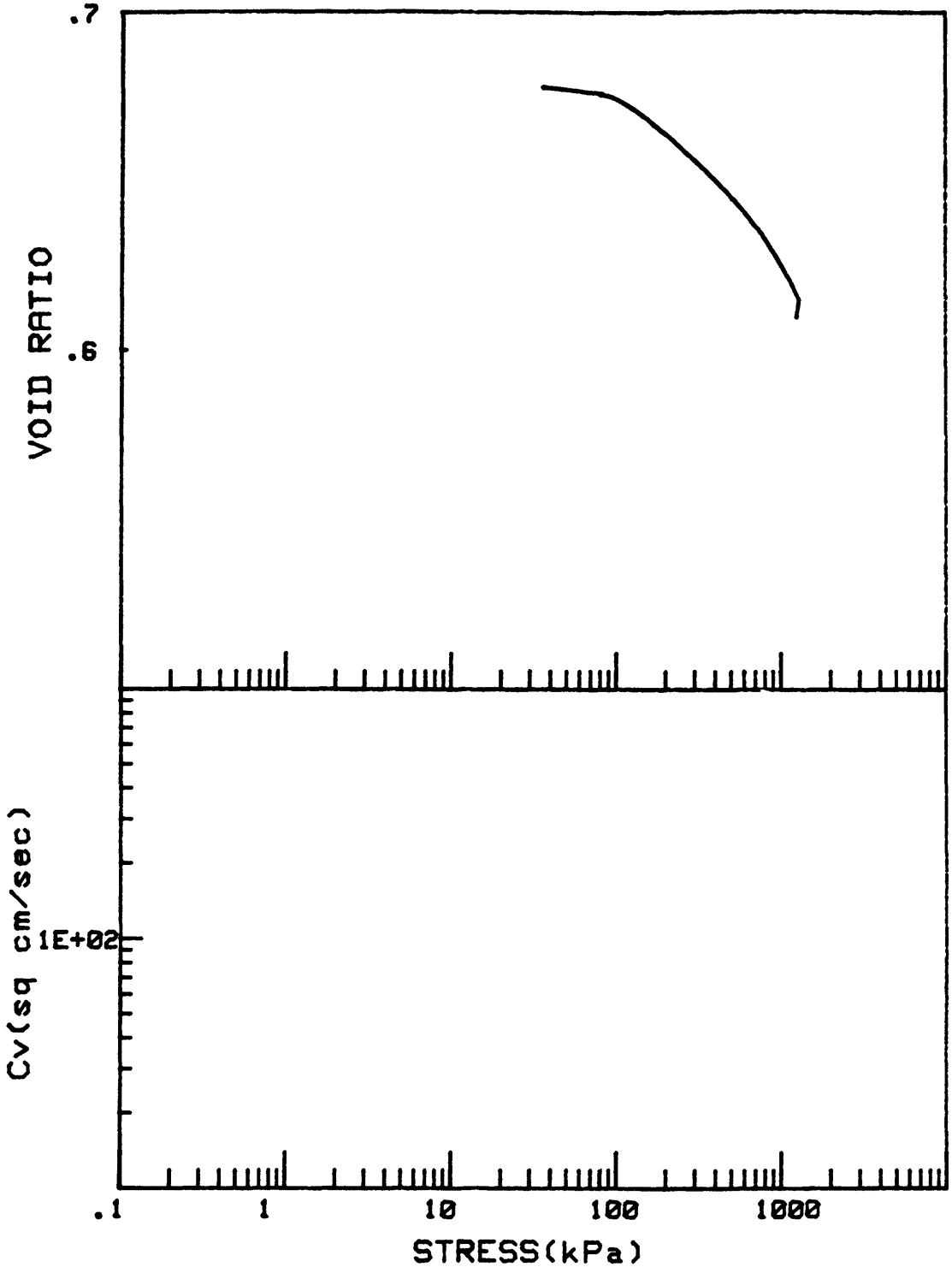

CRUISE DC4-81-NS		INCREMENT (cm)	25-30
CORE NO.	686A1	TEST NO.	CE39

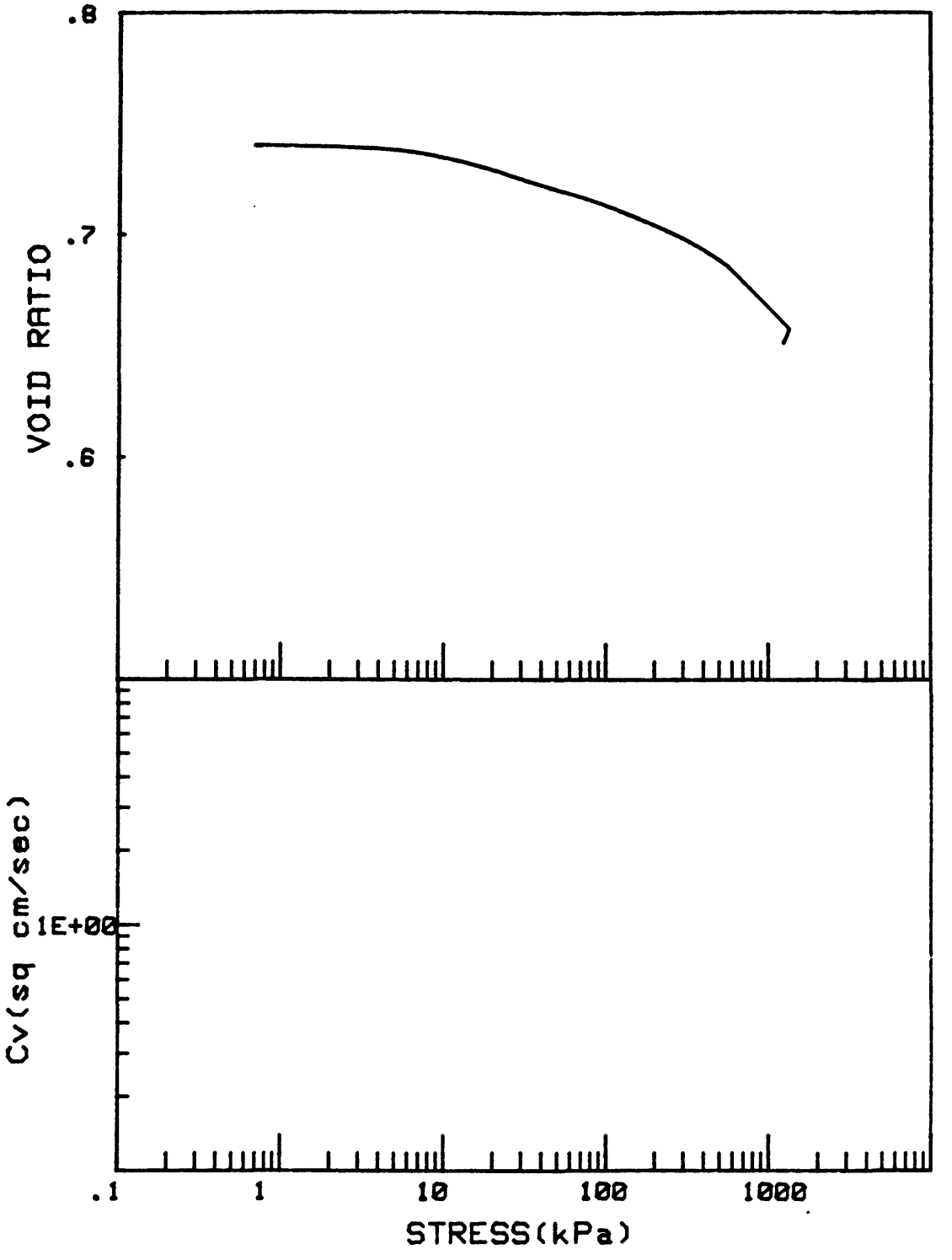

CRUISE DC4-81-NS		INCREMENT (cm)	75-80
CORE NO.	686A1	TEST NO.	CE41

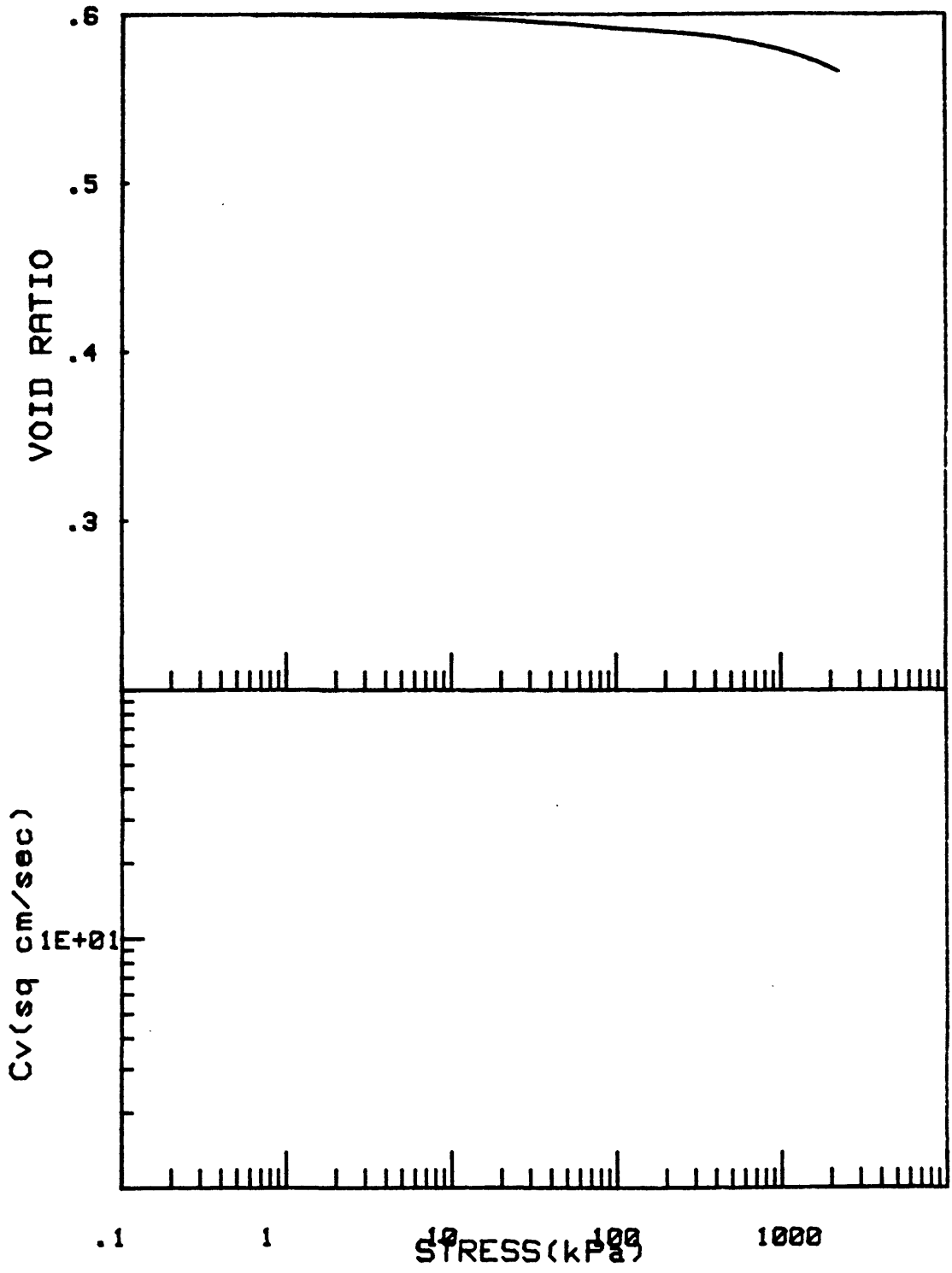

CRUISE DC4-81-NS	INCREMENT (cm) 180-185
CORE NO. 686A1	TEST NO. CE40

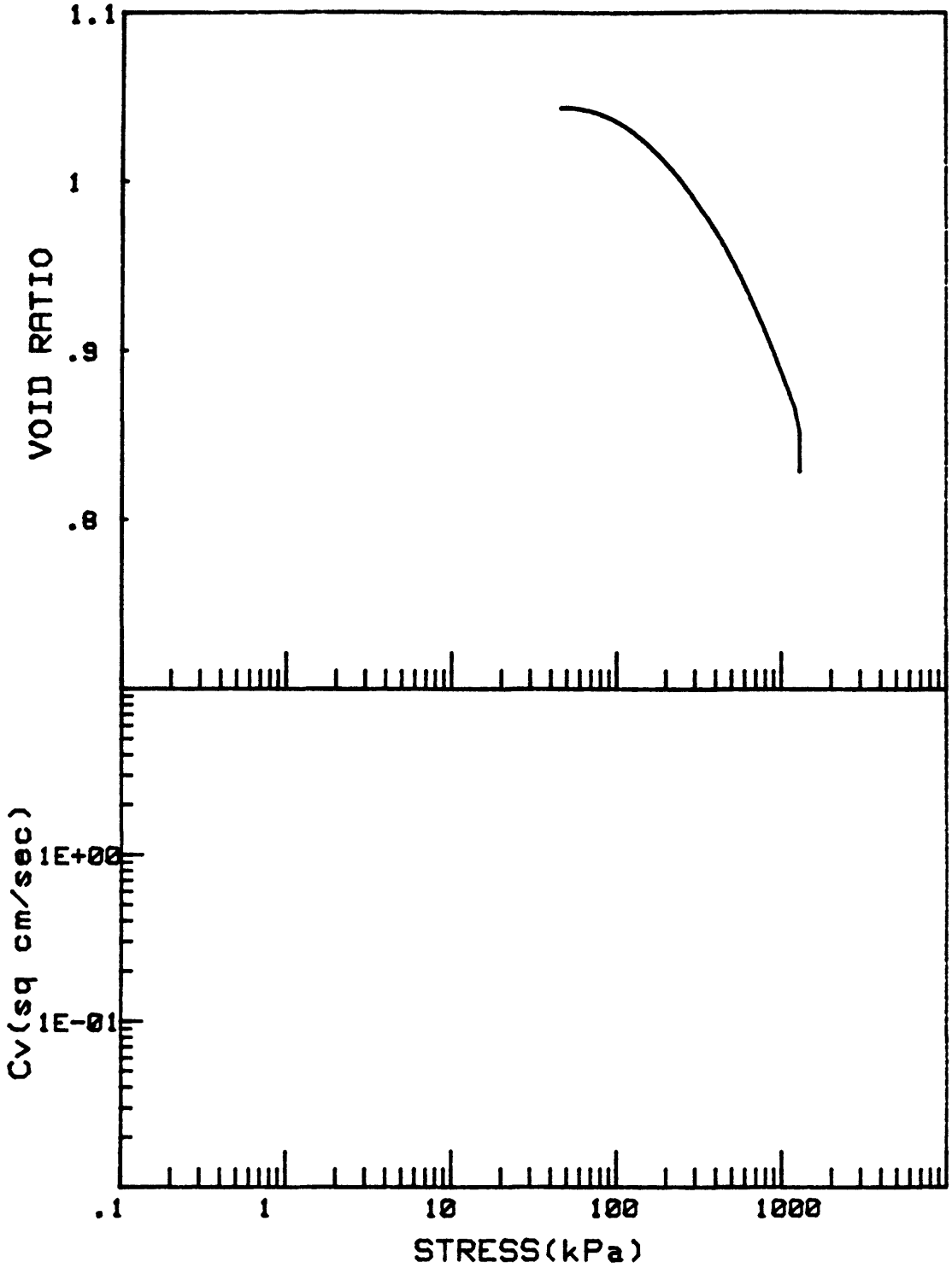

CRUISE DC4-81-NS		INCREMENT (cm)	284-289
CORE NO.	686A1	TEST NO.	CE42

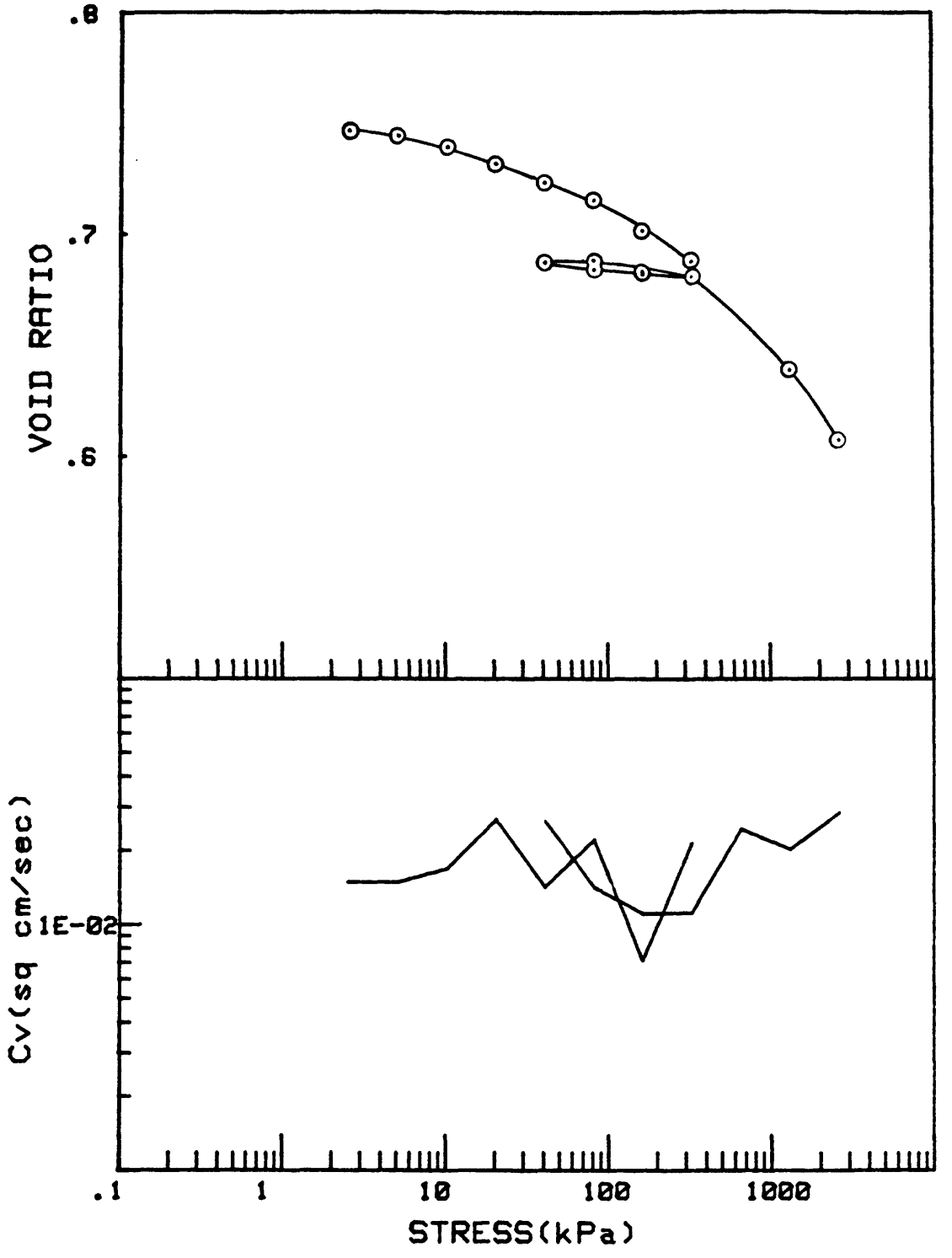

CRUISE DC4-81-NS		INCREMENT (cm)	65-70
CORE NO.	687A1	TEST NO.	OE42

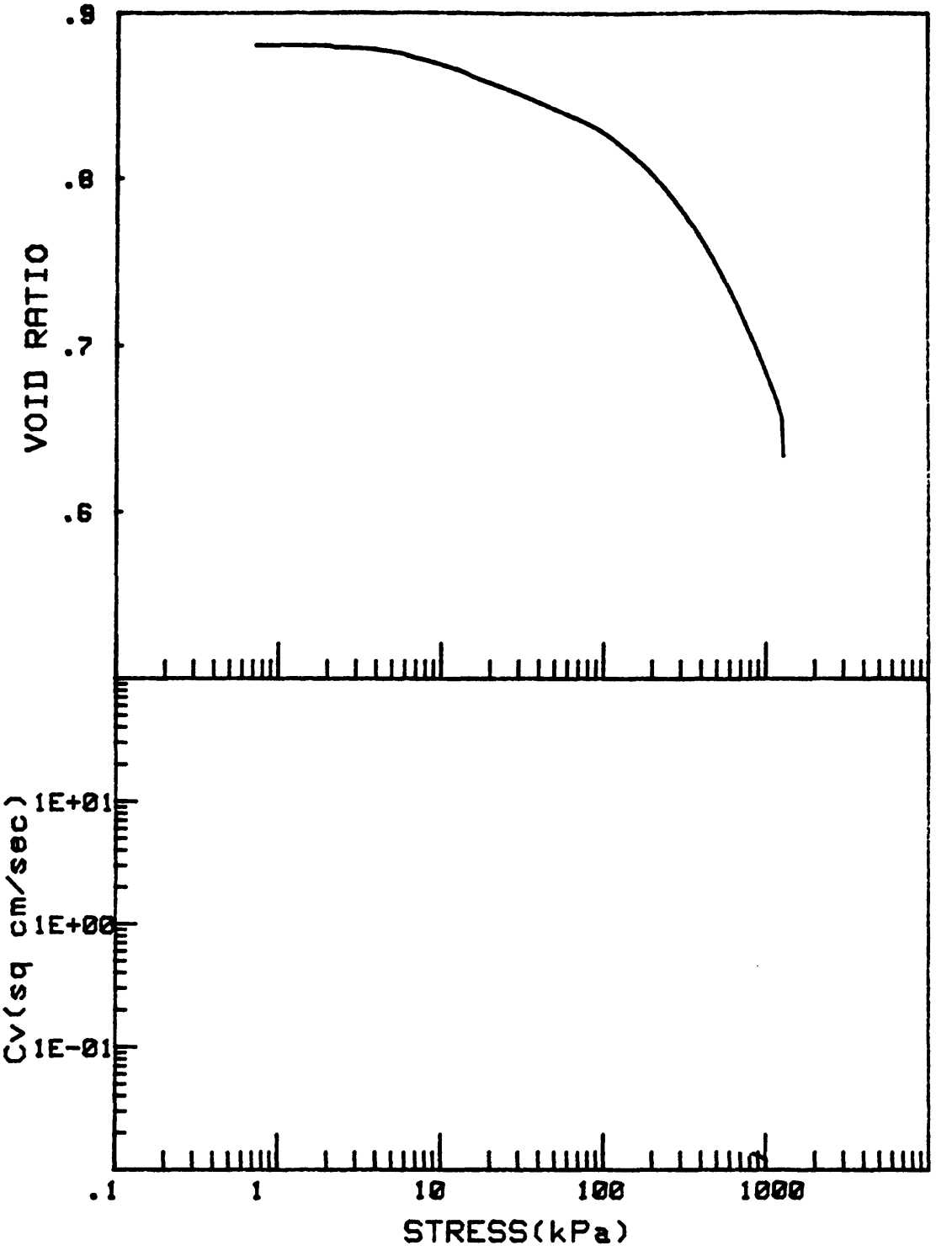

CRUISE DC4-81-NS		INCREMENT (cm)	106-108
CORE NO.	687A1	TEST NO.	CE48

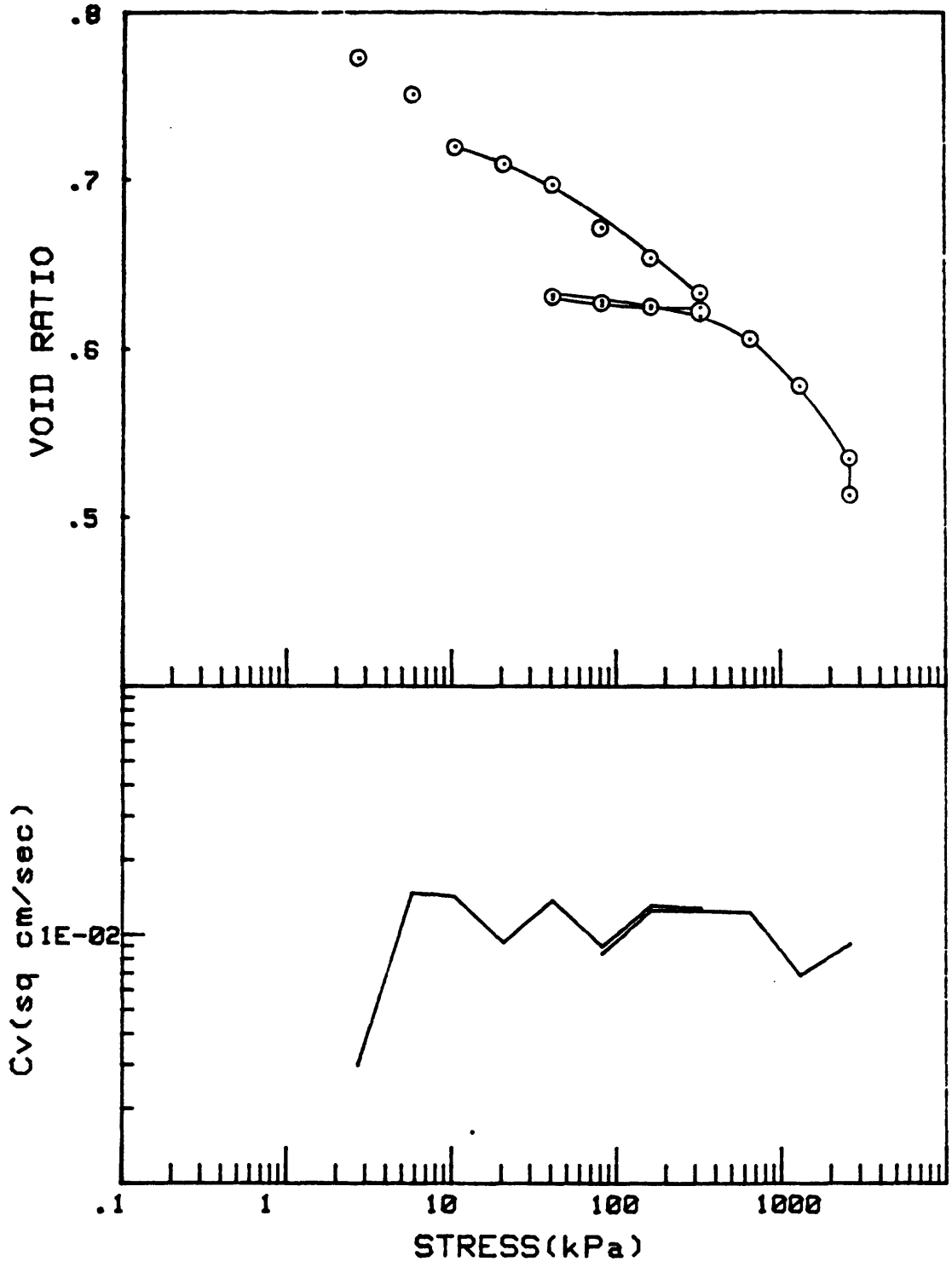

CRUISE DC4-81-NS		INCREMENT (cm)	216-222
CORE NO.	687A1	TEST NO.	OE43

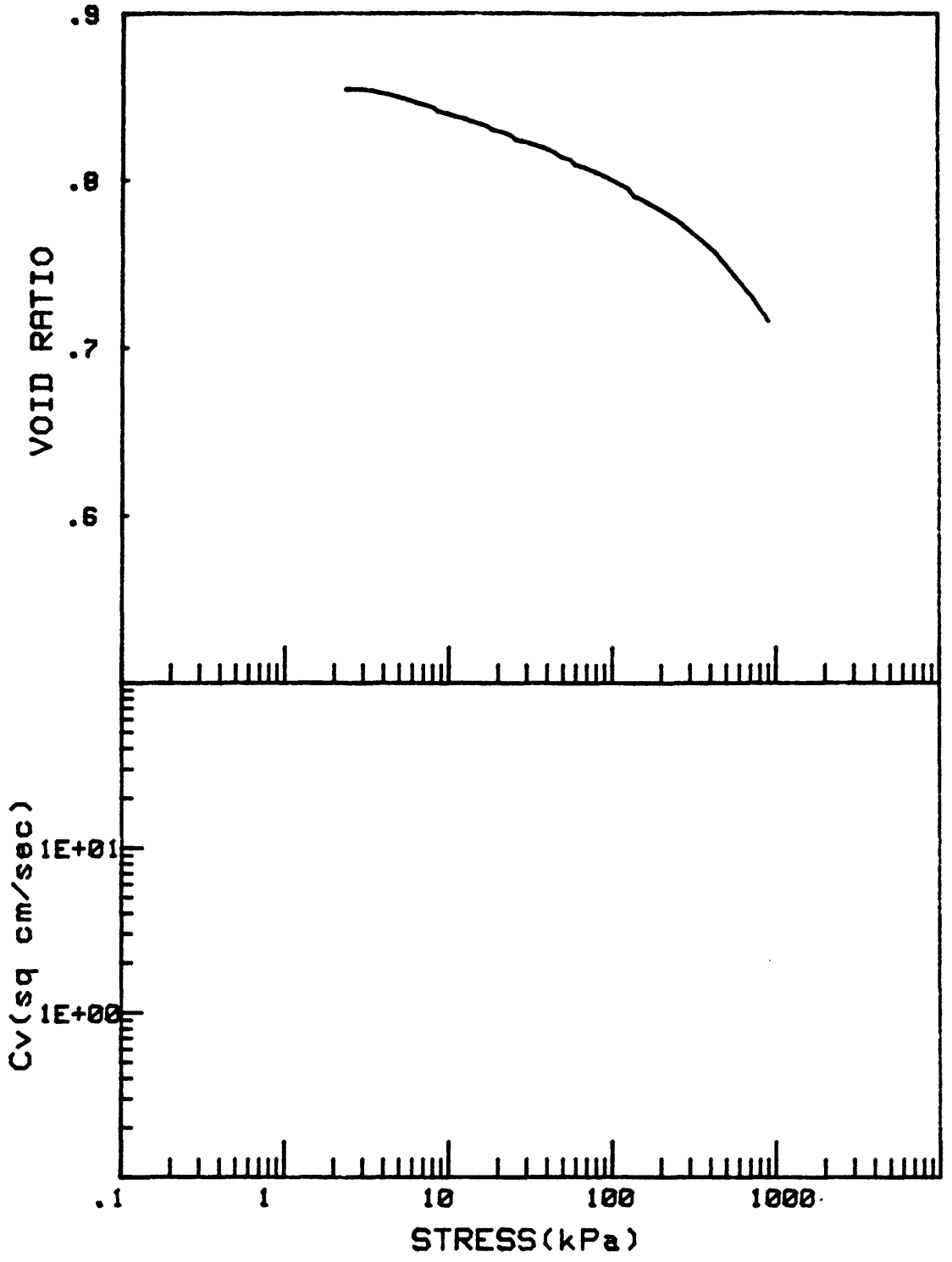

CRUISE DC4-81-NS		INCREMENT (cm)	362-364
CORE NO.	687A1	TEST NO.	CE44

Appendix E. Static triaxial test plots.

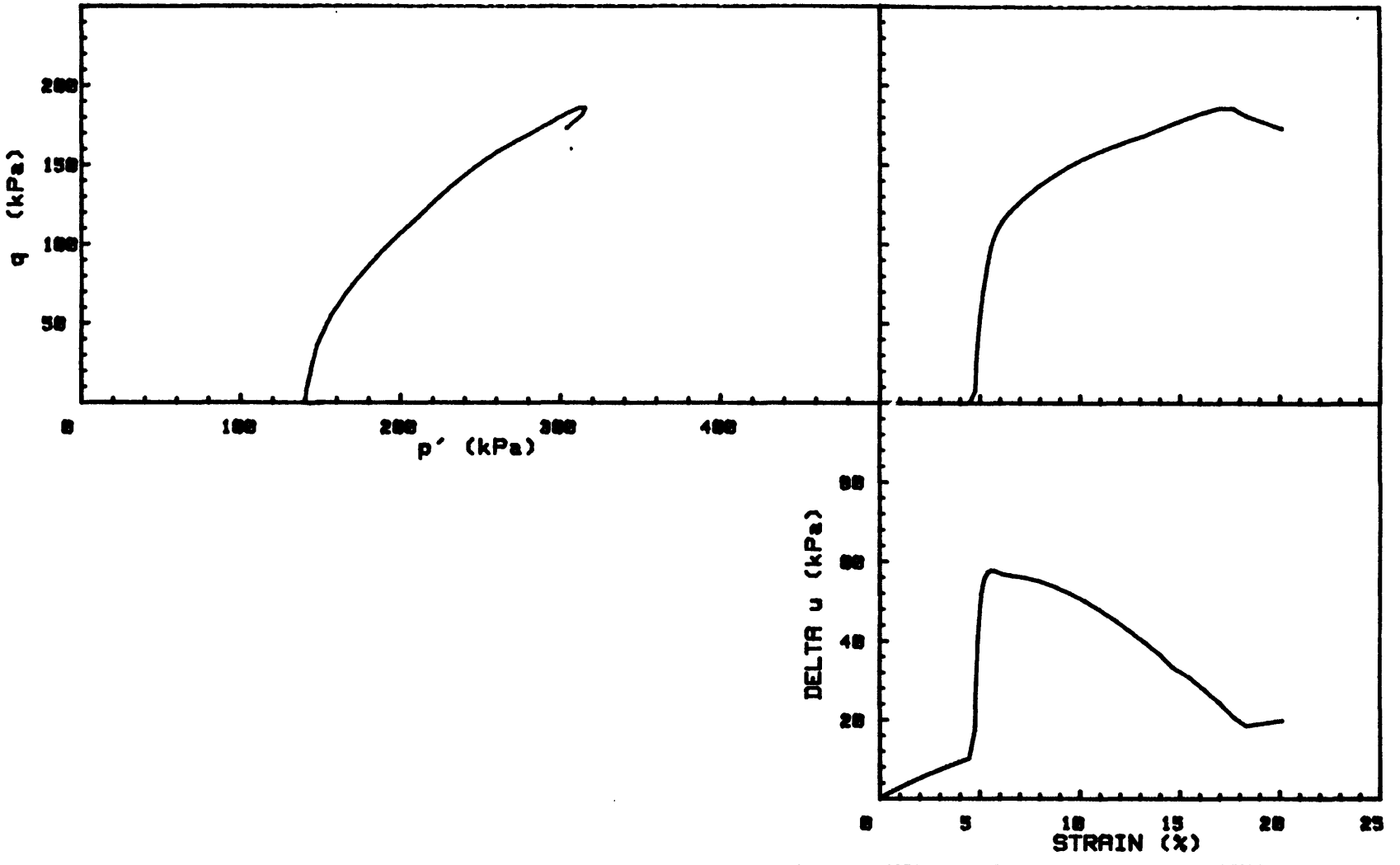

CRUISE DC4-81-NS		INCREMENT (cm)	131-140
CORE NO.	681A2	TEST NO.	TE107
SIG1c'(kPa)	151.0		
SIG3c'(kPa)	151.0		
INDUCED OCR	1.0		

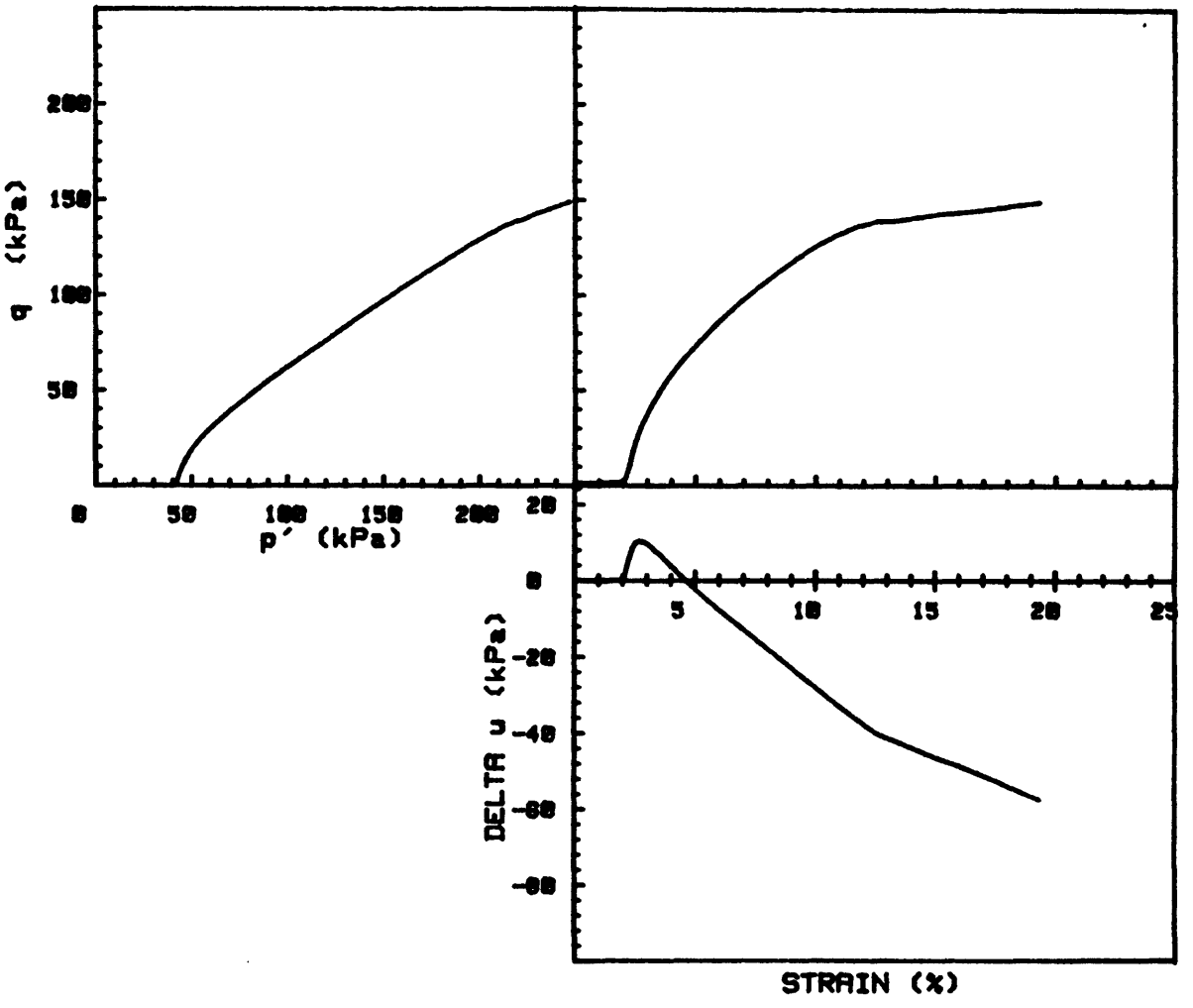

CRUISE DC4-81-NS		INCREMENT (cm)	131-140
CORE NO.	681A2	TEST NO.	TE108

SIG1c'(kPa)	40.7
SIG3c'(kPa)	40.7
INDUCED OCR	6.0

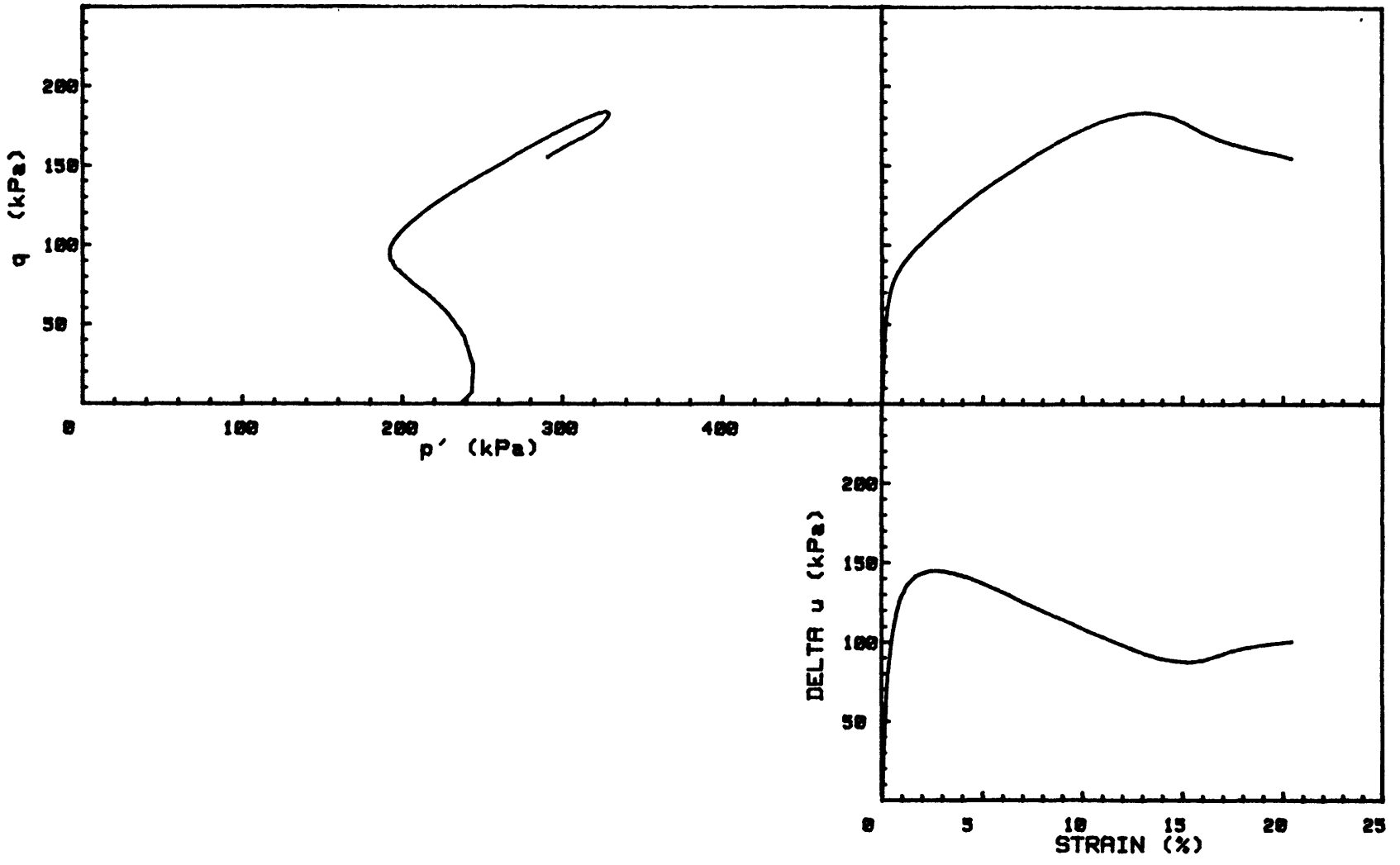

CRUISE DC4-81-NS		INCREMENT (cm)	107-116
CORE NO.	682A1	TEST NO.	TE76

SIG1c'(kPa)	236.7
SIG3c'(kPa)	236.7
INDUCED OCR	1.0

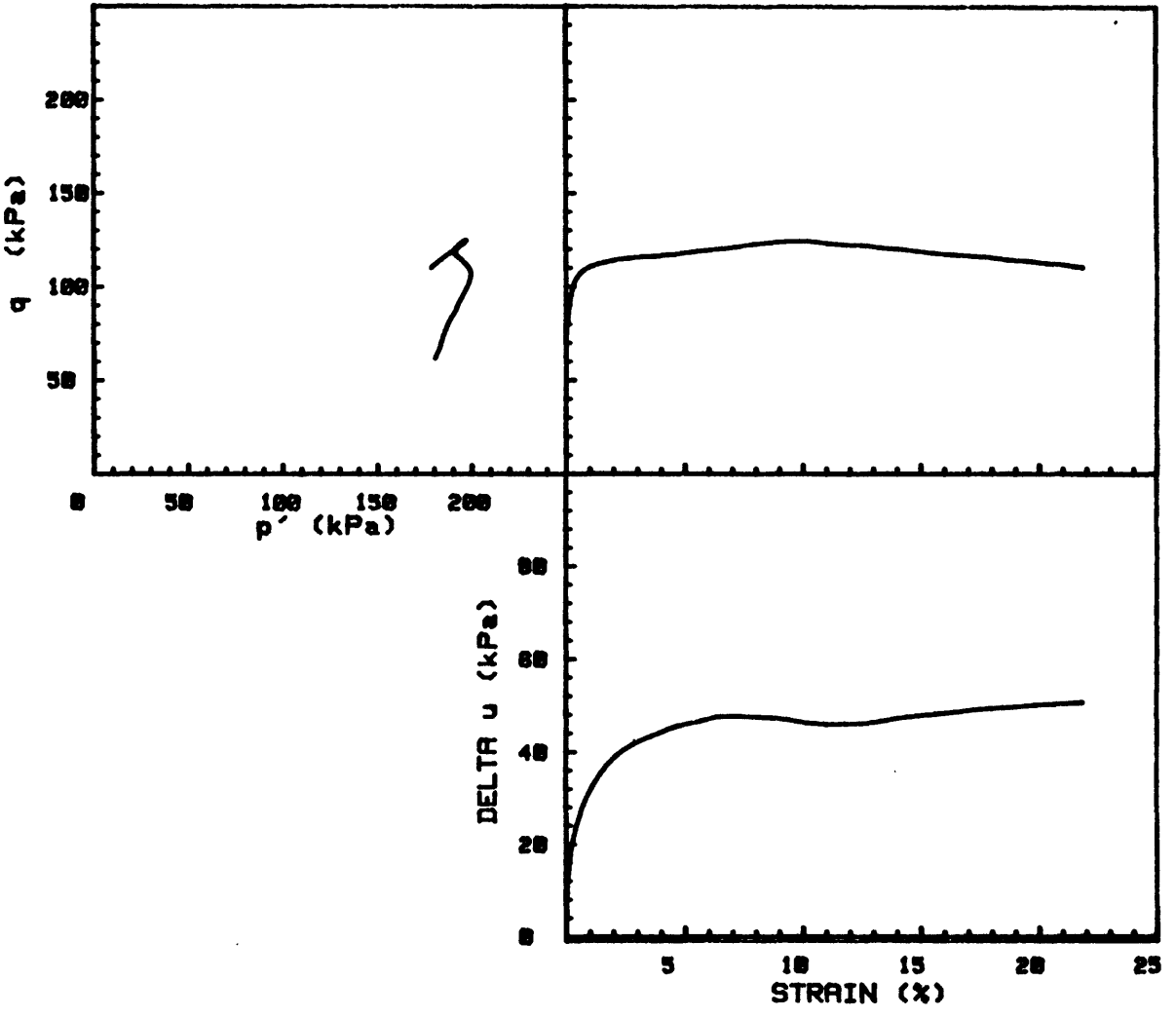

CRUISE DC4-81-NS		INCREMENT (cm)	106-117
CORE NO.	682A1	TEST NO.	TE77

SIG1c'(kPa)	242.3
SIG3c'(kPa)	119.2
INDUCED OCR	1.0

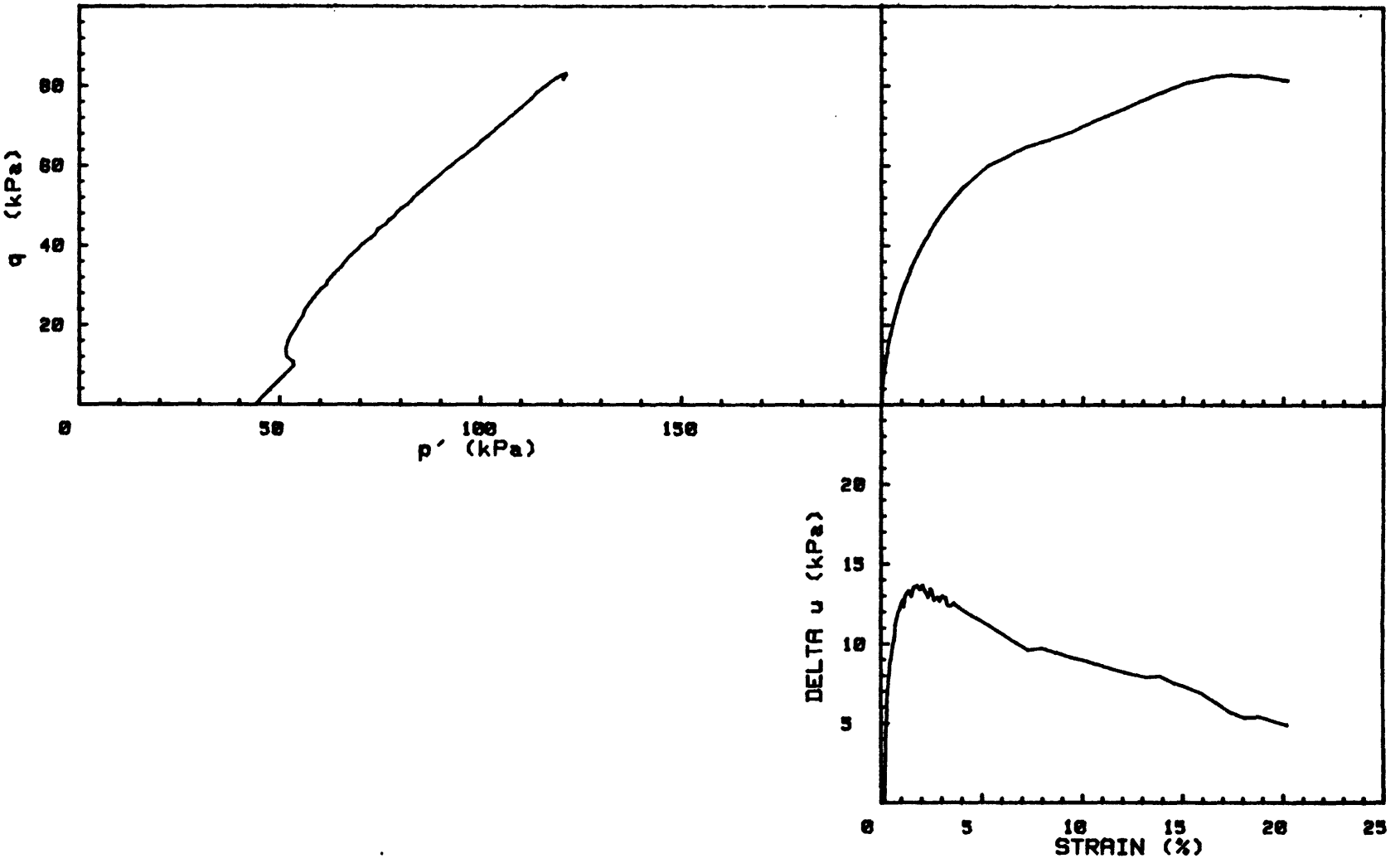

CRUISE DC4-81-NS		INCREMENT (cm)	121-132
CORE NO.	682A1	TEST NO.	TE85

SIG1c'(kPa)	44.1
SIG3c'(kPa)	44.1
INDUCED OCR	6.0

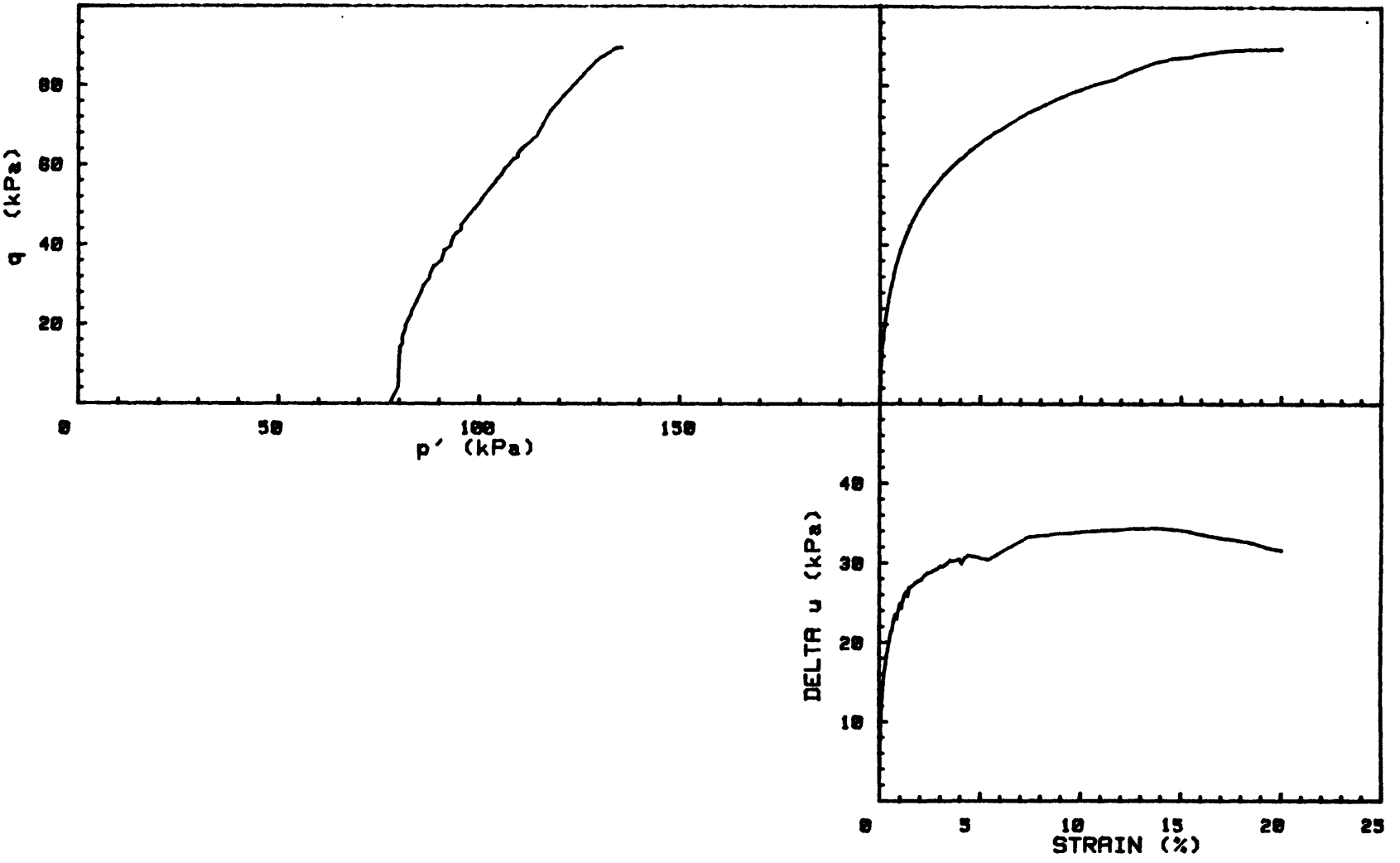

CRUISE DC4-81-NS		INCREMENT (cm)	121-132
CORE NO.	682A1	TEST NO.	TE86

SIG1c'(kPa)	77.9
SIG3c'(kPa)	77.9
INDUCED OCR	3.0

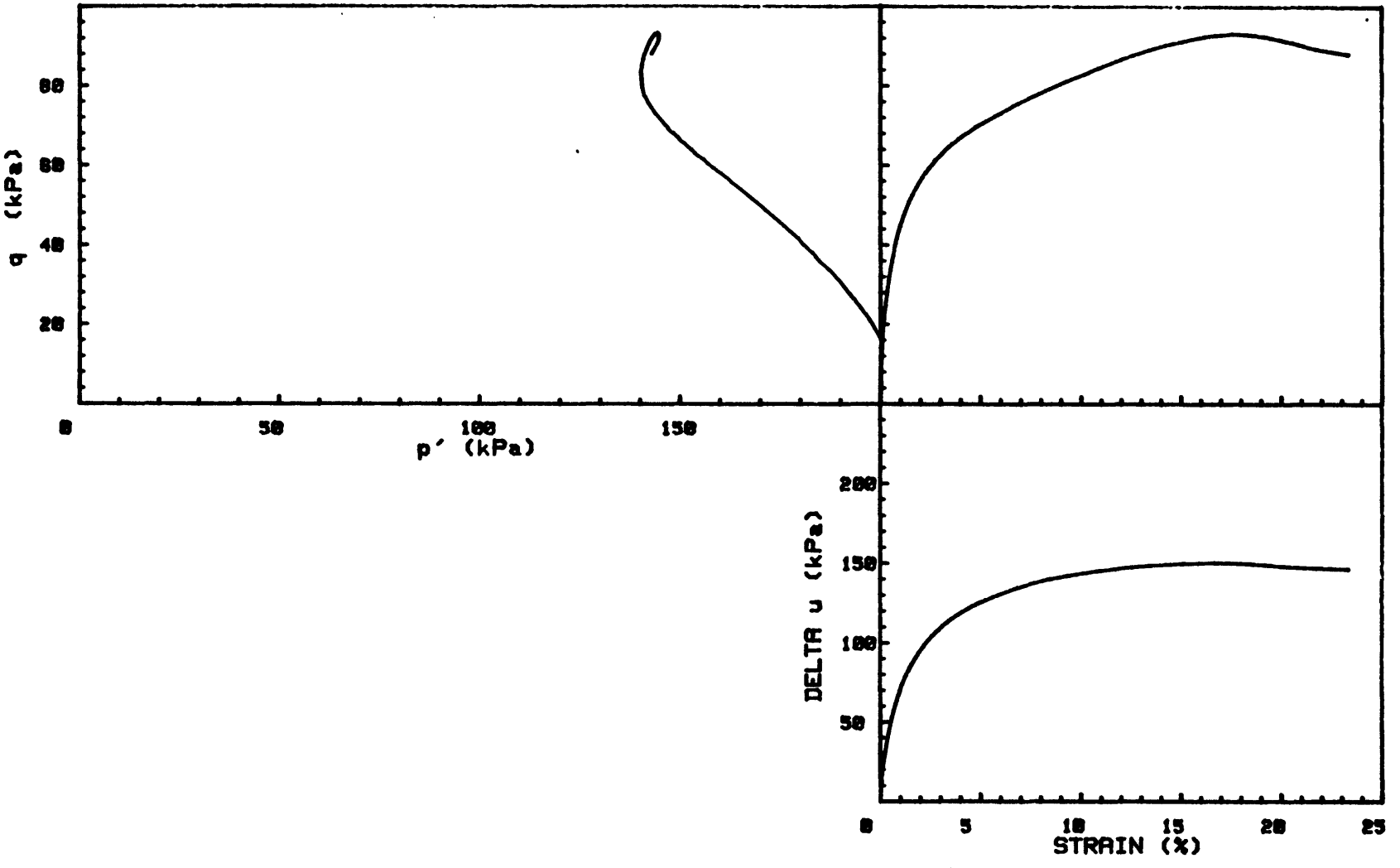

CRUISE DC4-81-NS		INCREMENT (cm)	174-183
CORE NO.	682A1	TEST NO.	TE98

SIG1c'(kPa)	201.3
SIG3c'(kPa)	201.3
INDUCED OCR	1.0

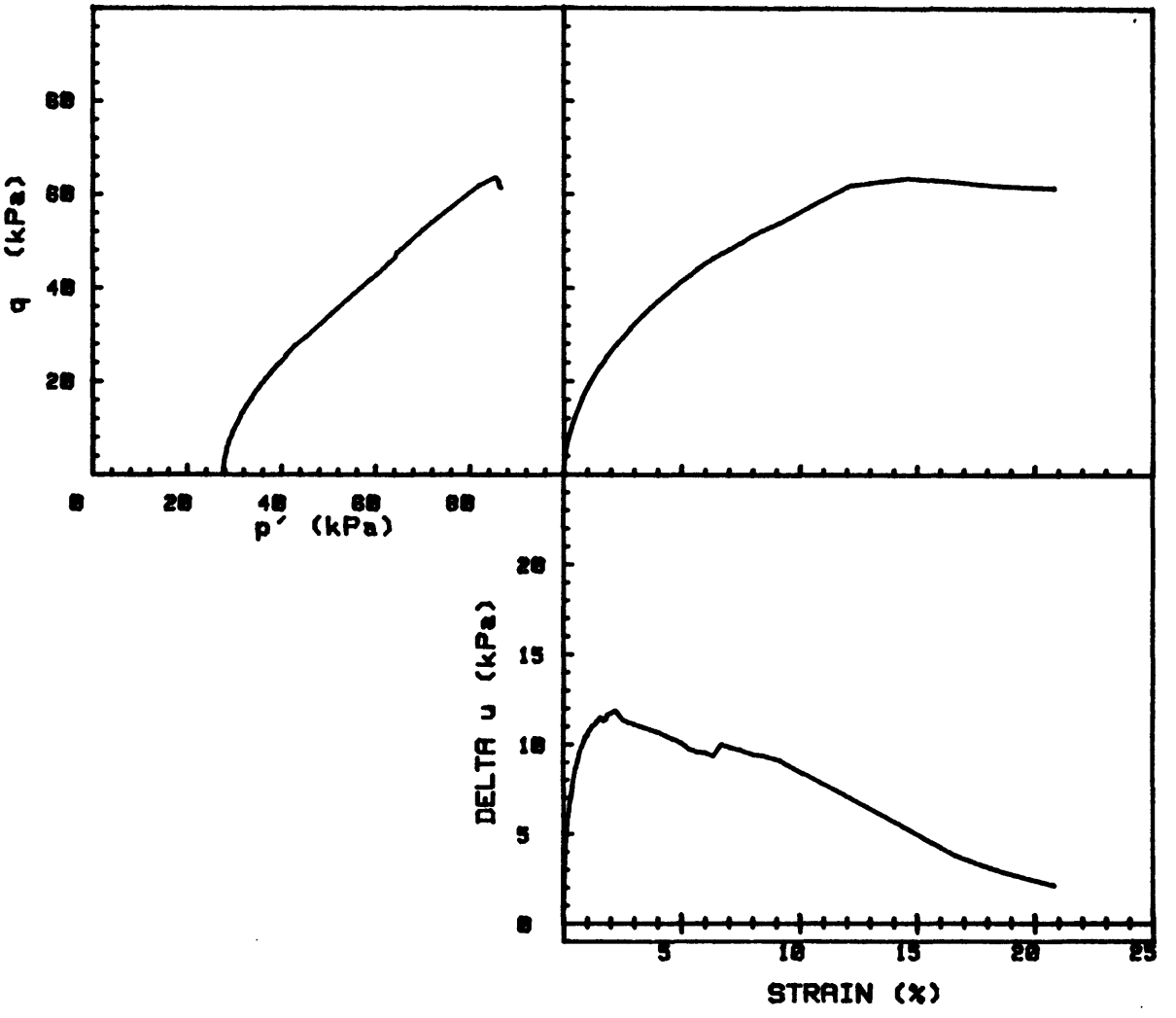

CRUISE DC4-81-NS		INCREMENT (cm)	175-183
CORE NO.	682A1	TEST NO.	TE99

SIG1c'(kPa)	27.3
SIG3c'(kPa)	27.3
INDUCED OCR	6.0

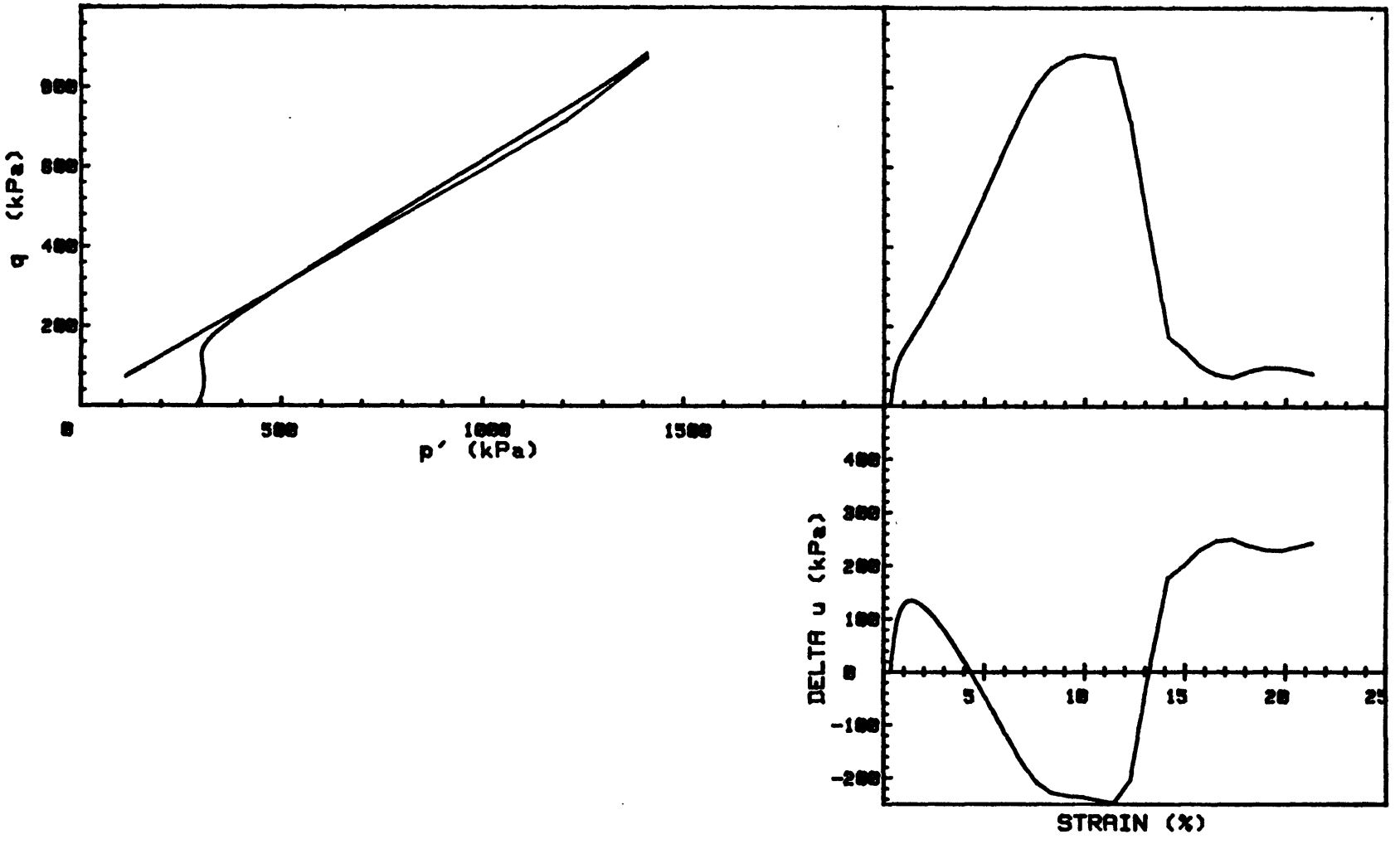

CRUISE DC4-81-NS		INCREMENT (cm)	421-430
CORE NO.	683A1	TEST NO.	TE109

SIG1c'(kPa)	289.7
SIG3c'(kPa)	289.7
INDUCED OCR	1.0

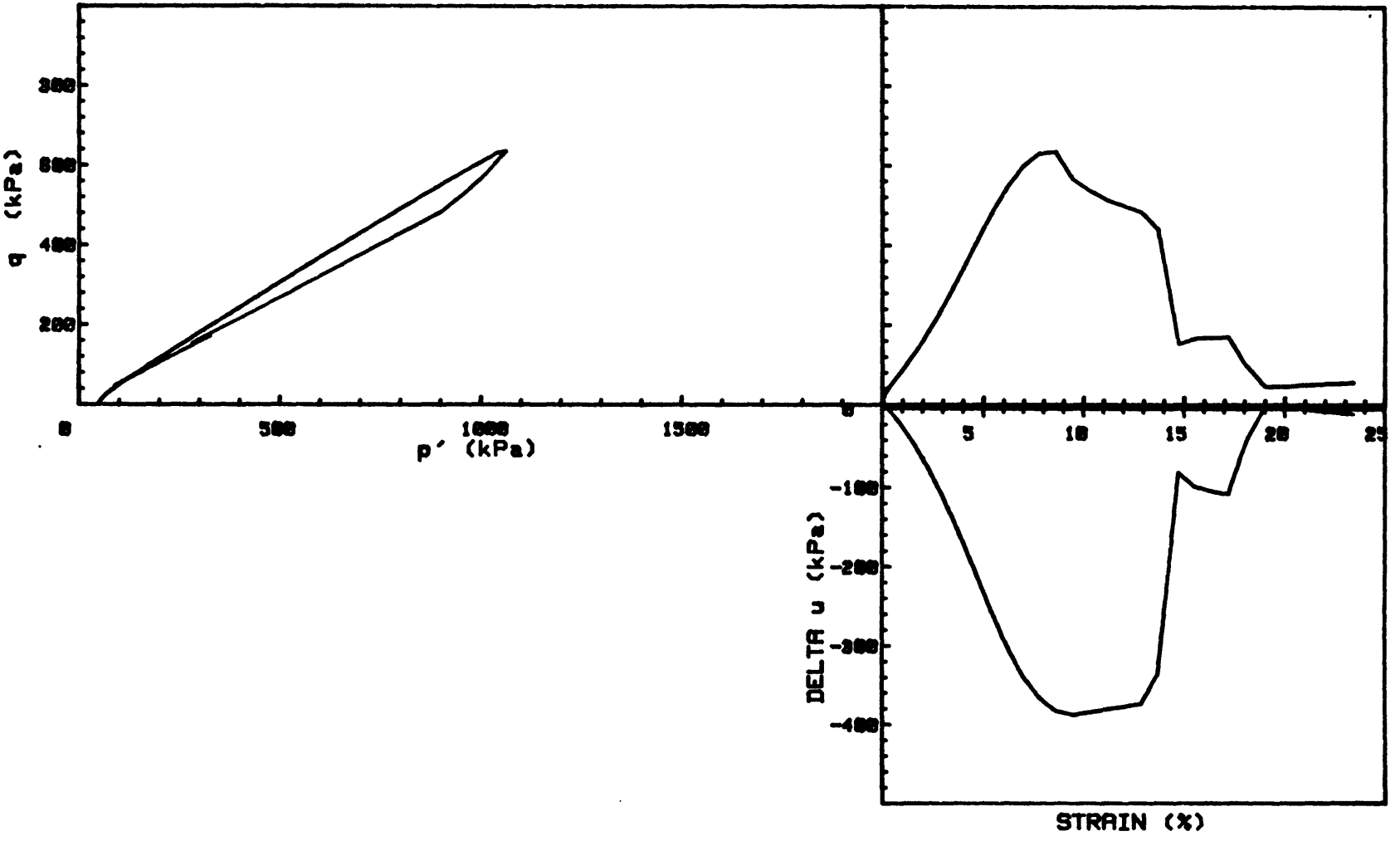

CRUISE DC4-81-NS		INCREMENT (cm)	421-430
CORE NO.	683A1	TEST NO.	TE110
SIG1c'(kPa)	47.4		
SIG3c'(kPa)	47.4		
INDUCED OCR	6.0		

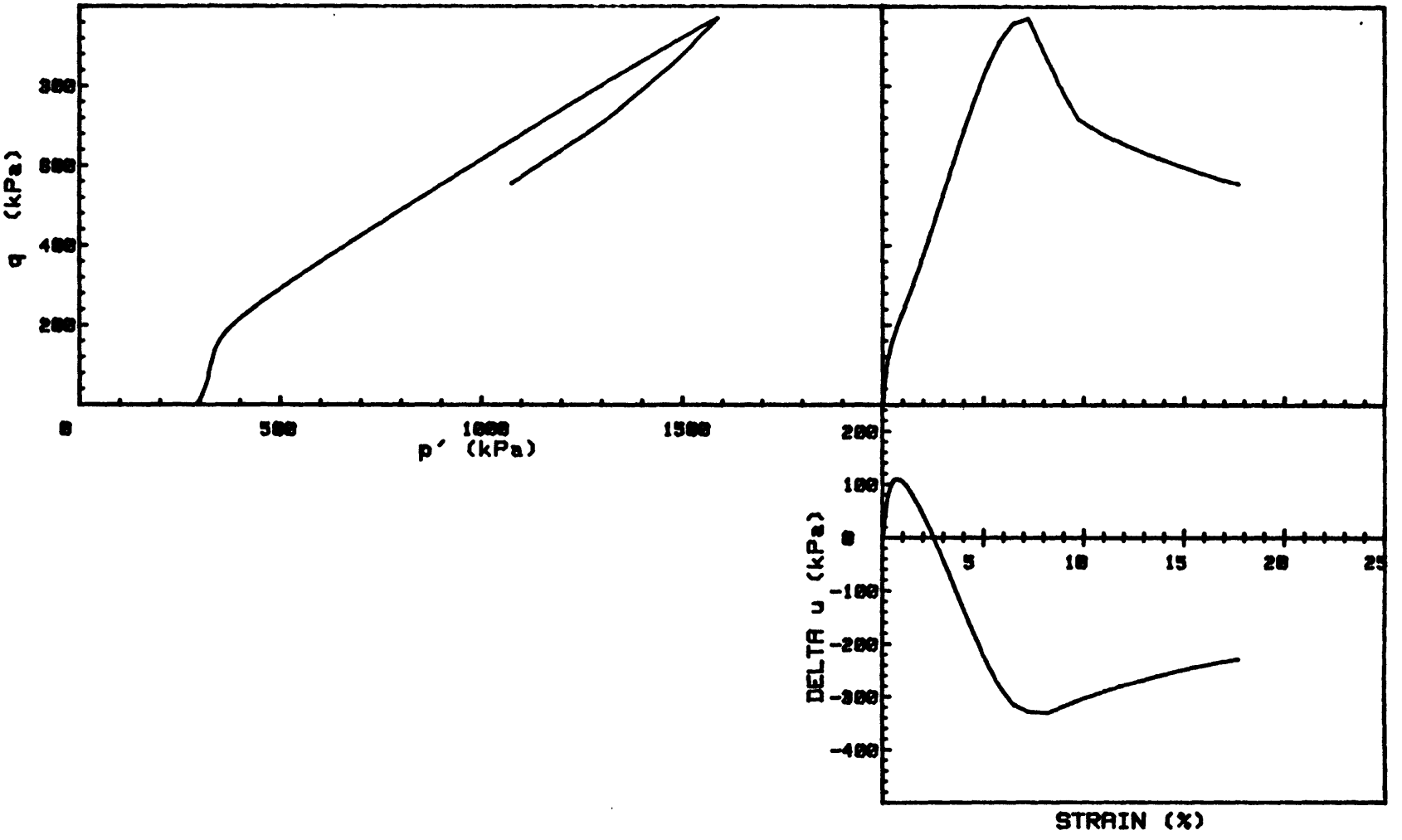

CRUISE DC4-81-NS		INCREMENT (cm)	90-99
CORE NO.	684A1	TEST NO.	TE105

SIG1c'(kPa)	293.0
SIG3c'(kPa)	293.0
INDUCED OCR	1.0

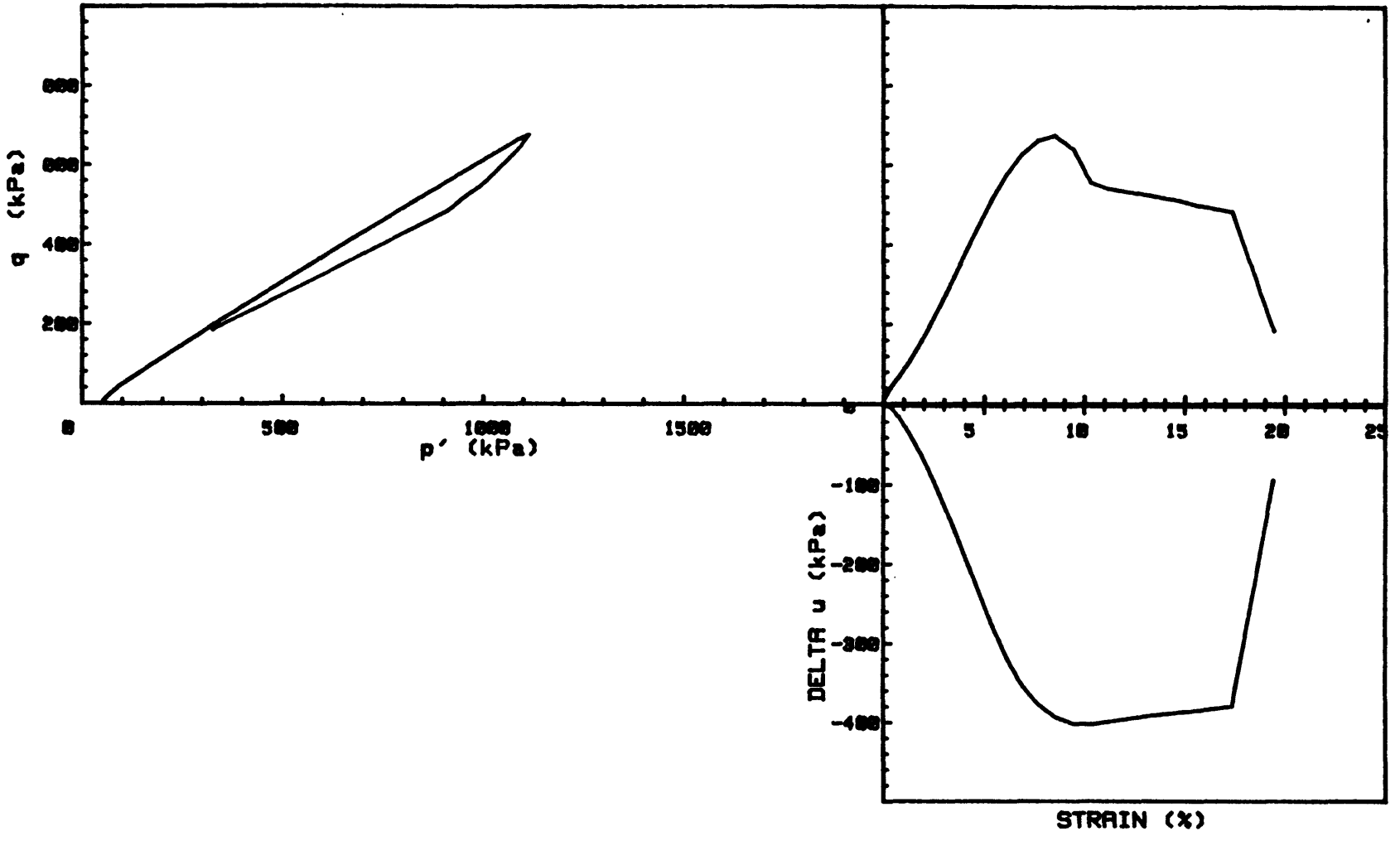

CRUISE DC4-81-NS		INCREMENT (cm)	90-99
CORE NO.	684A1	TEST NO.	TE106
SIG1c'(kPa)	48.1		
SIG3c'(kPa)	48.1		
INDUCED OCR	6.0		

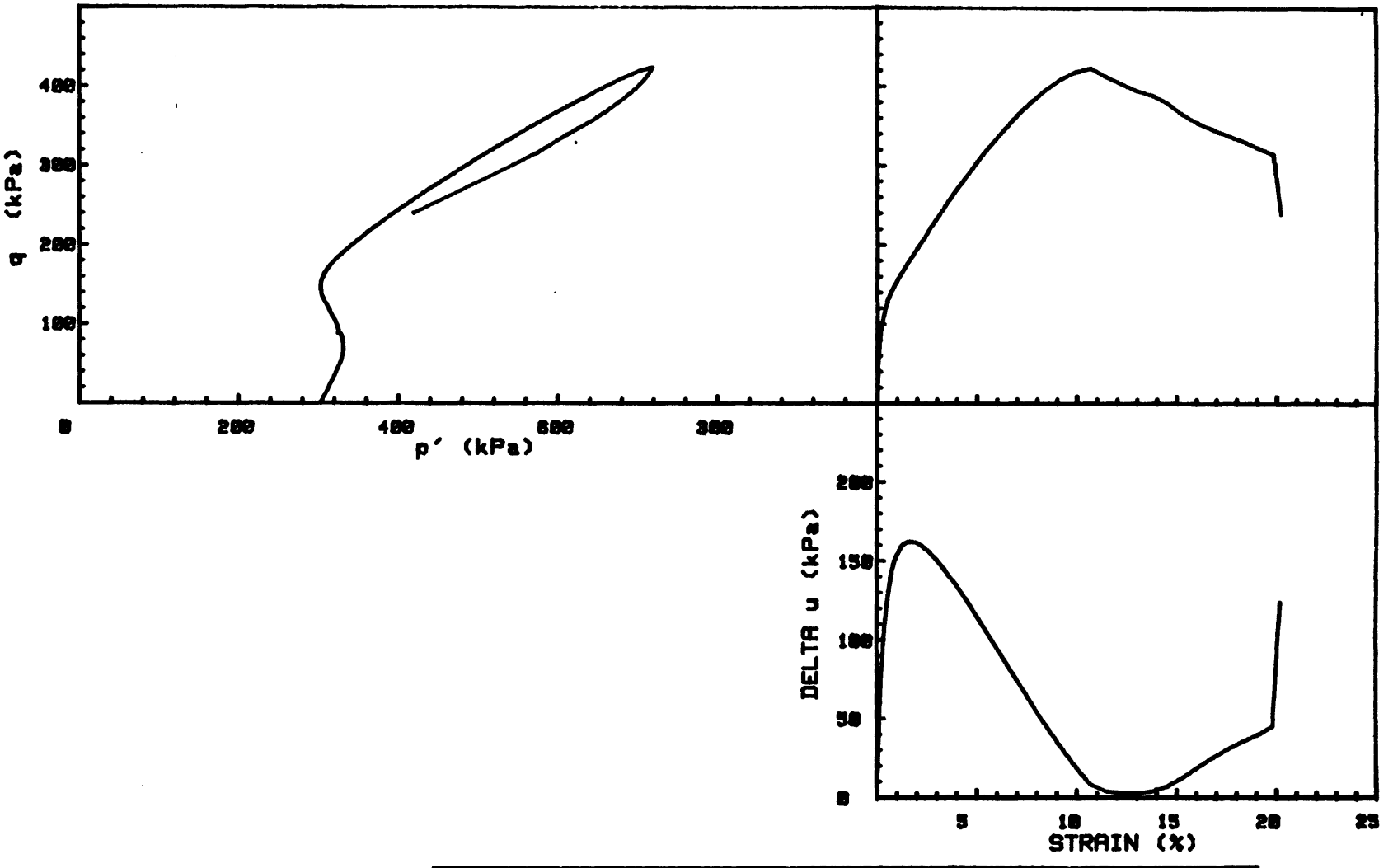

CRUISE DC4-81-NS		INCREMENT (cm)	50-59
CORE NO.	685A1	TEST NO.	TE103

SIG1c'(kPa)	303.8
SIG3c'(kPa)	303.8
INDUCED OCR	1.0

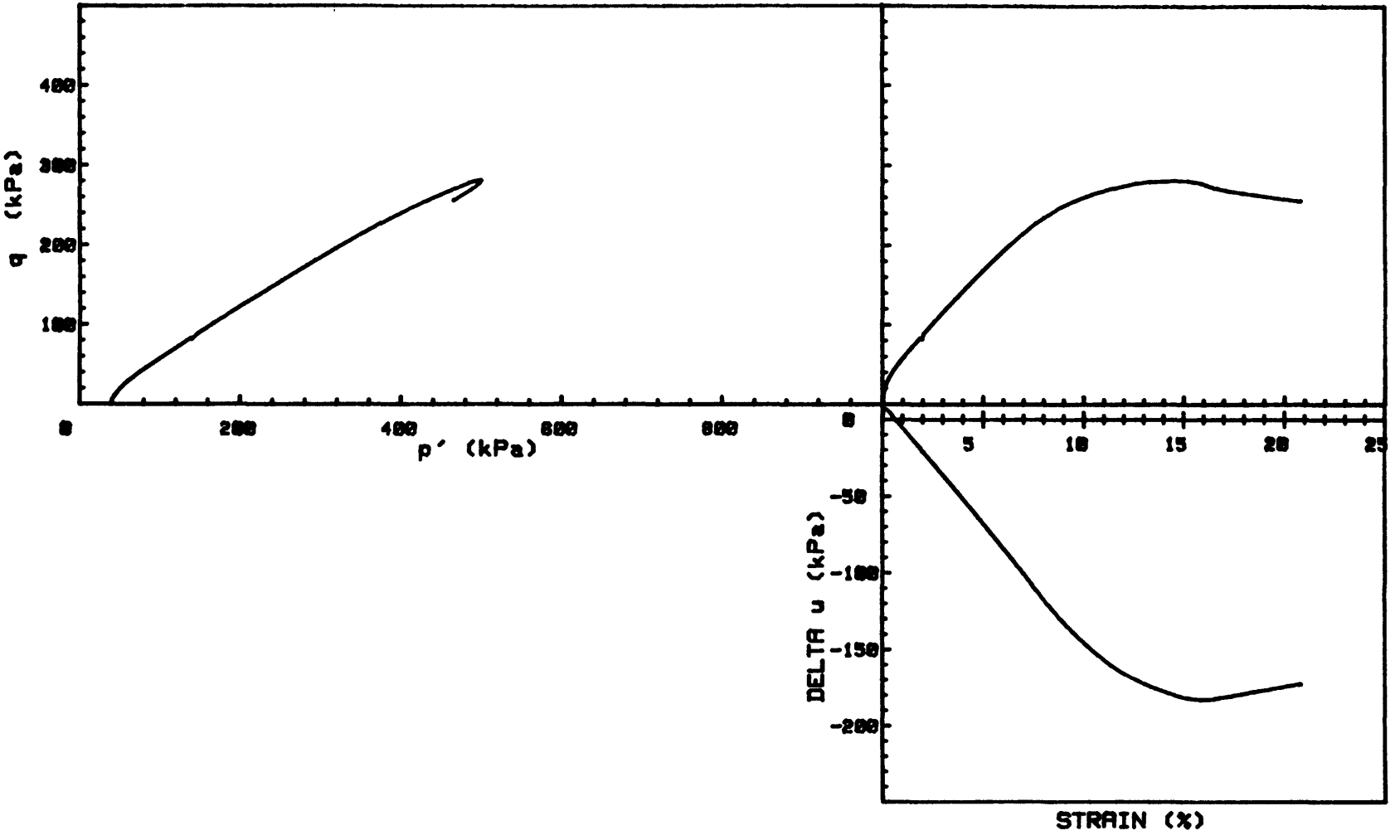

CRUISE DC4-81-NS		INCREMENT (cm)	50-59
CORE NO.	685A2	TEST NO.	TE104
SIG1c'(kPa)	38.3		
SIG3c'(kPa)	38.3		
INDUCED OCR	6.0		

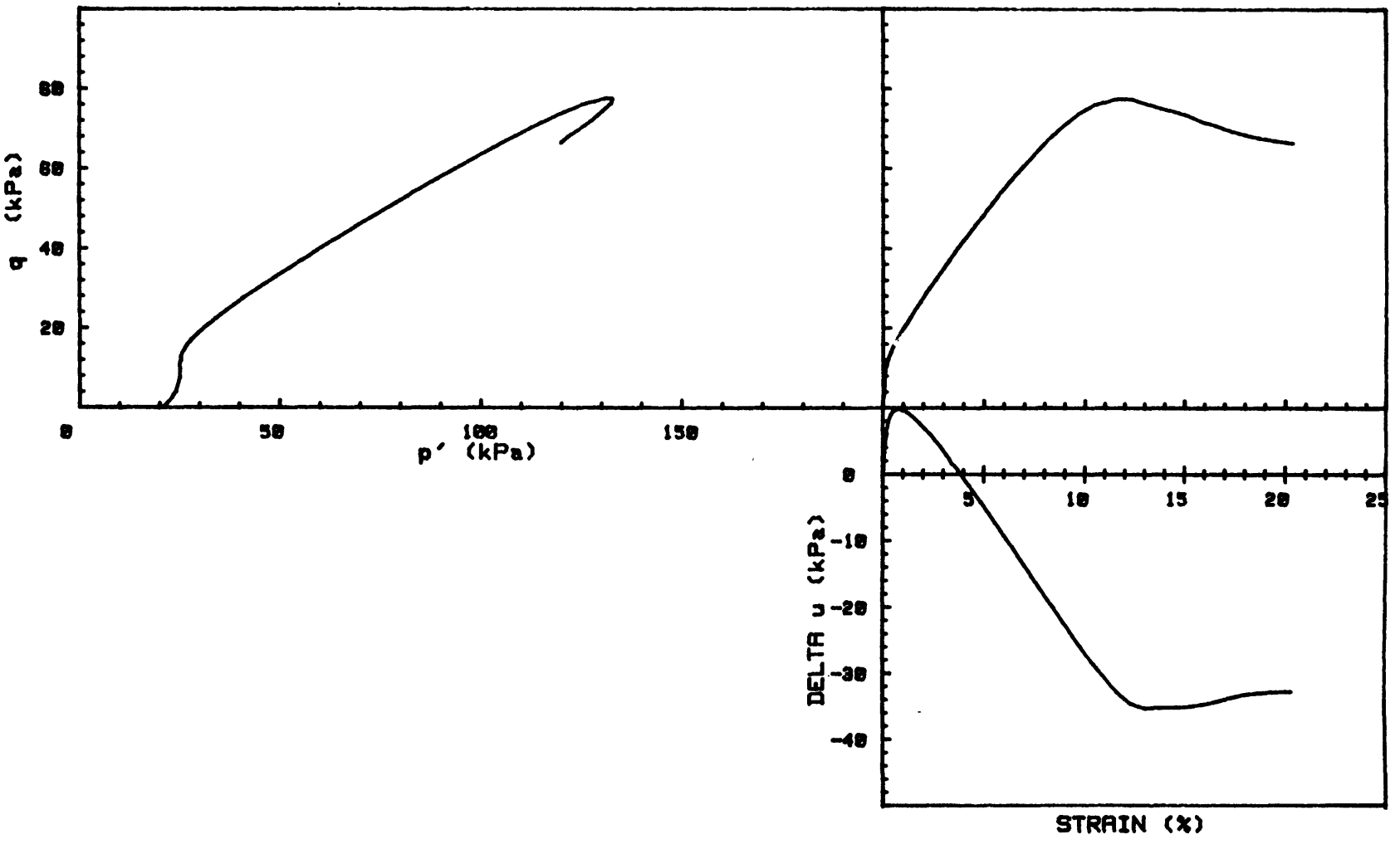

CRUISE DC4-81-NS		INCREMENT (cm)	131-140
CORE NO.	685A2	TEST NO.	TE119
SIG1c'(kPa)	20.9		
SIG3c'(kPa)	20.9		
INDUCED OCR	1.0		

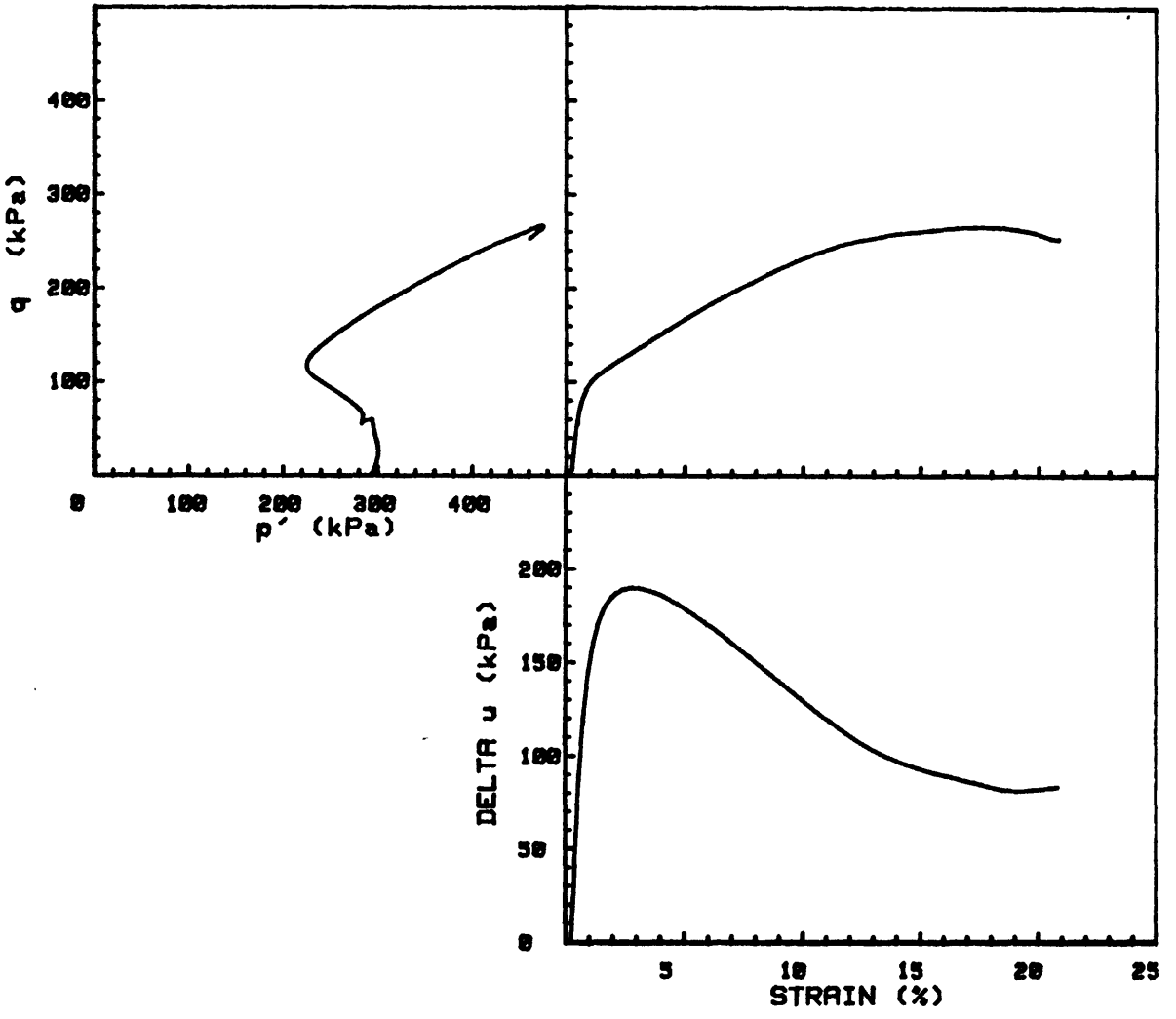

CRUISE DC4-81-NS		INCREMENT (cm)	131-140
CORE NO.	685A2	TEST NO.	TE120

SIG1c'(kPa)	292.0
SIG3c'(kPa)	292.0
INDUCED OCR	1.0

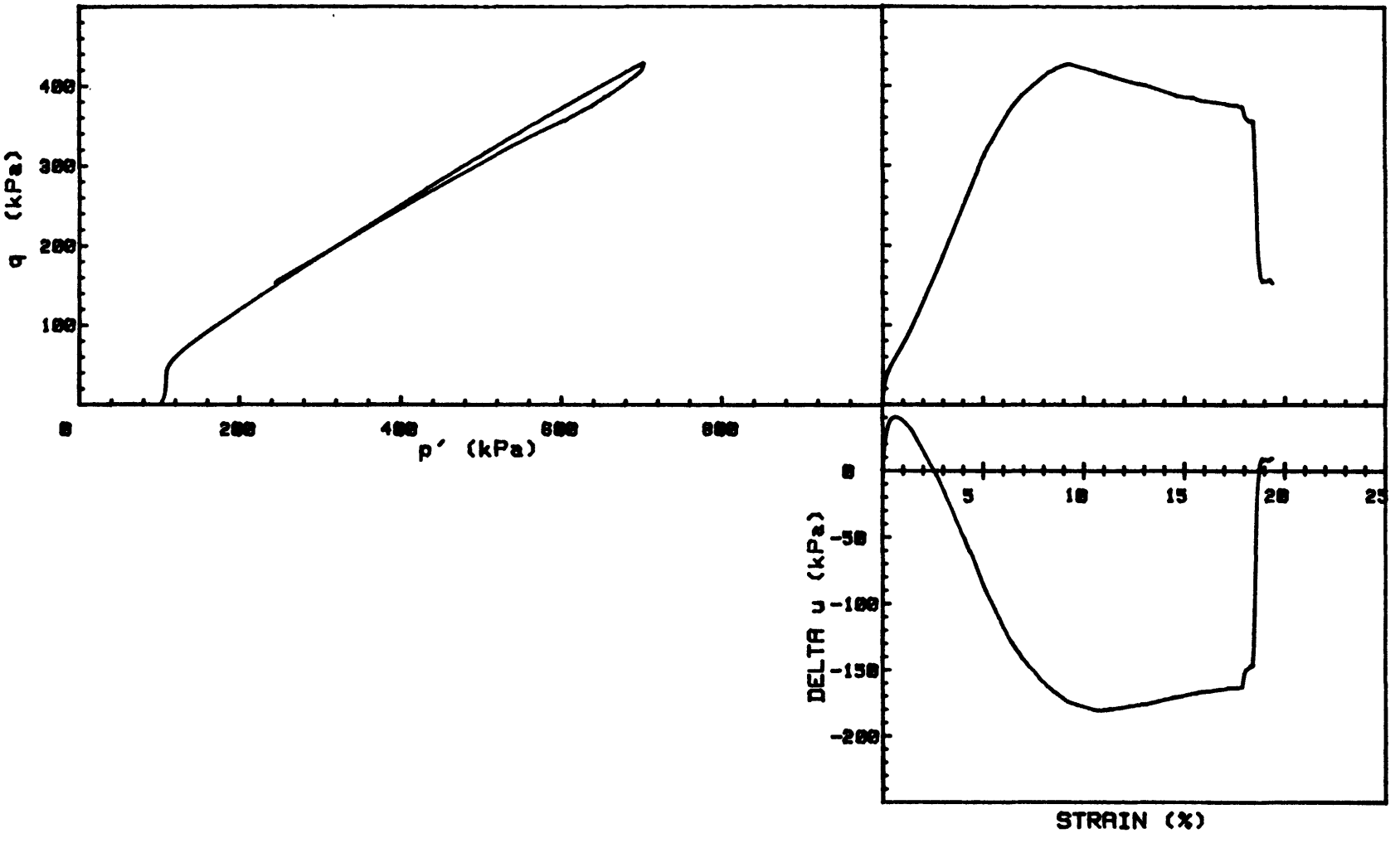

CRUISE DC4-81-NS		INCREMENT (cm)	231-240
CORE NO.	685A2	TEST NO.	TE94
SIG1c'(kPa)	101.5		
SIG3c'(kPa)	101.5		
INDUCED OCR	1.0		

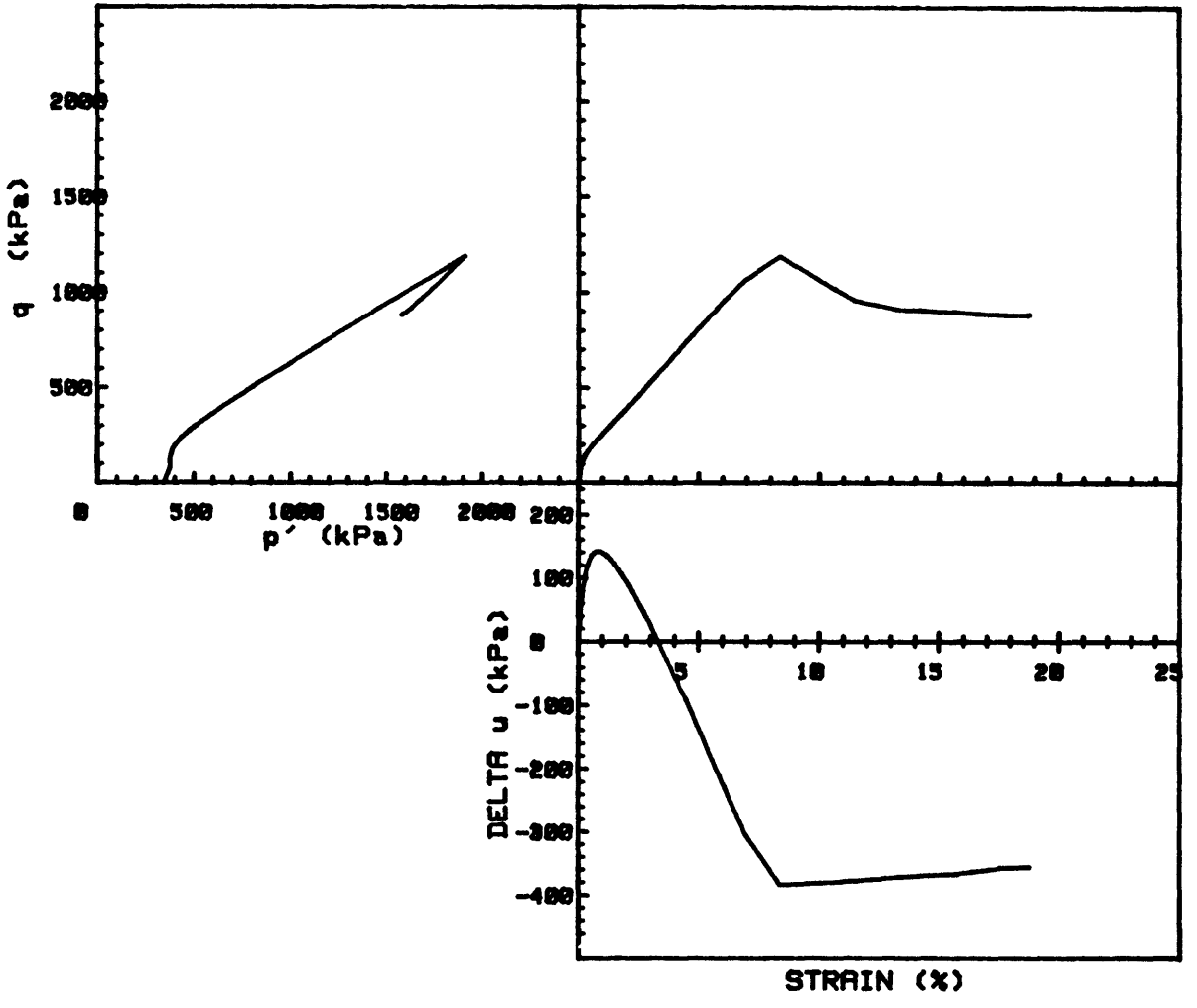

CRUISE DC4-81-NS		INCREMENT (cm)	242-251
CORE NO.	685A2	TEST NO.	TE95

SIG1c'(kPa)	343.2
SIG3c'(kPa)	343.2
INDUCED OCR	1.0

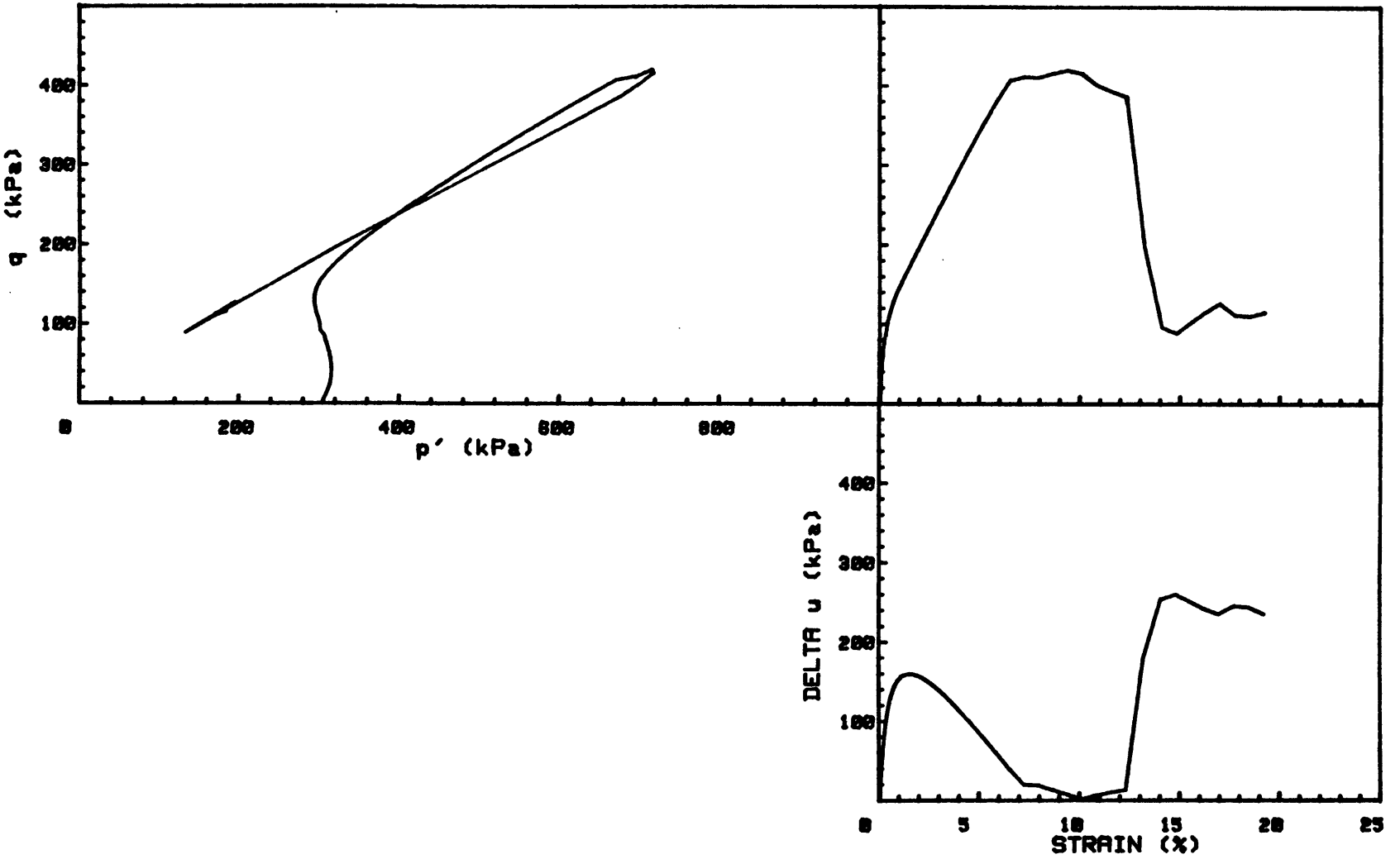

CRUISE DC4-81-NS		INCREMENT (cm)	170-179
CORE NO.	686A1	TEST NO.	TE100

SIG1c'(kPa)	304.2
SIG3c'(kPa)	304.2
INDUCED OCR	1.0

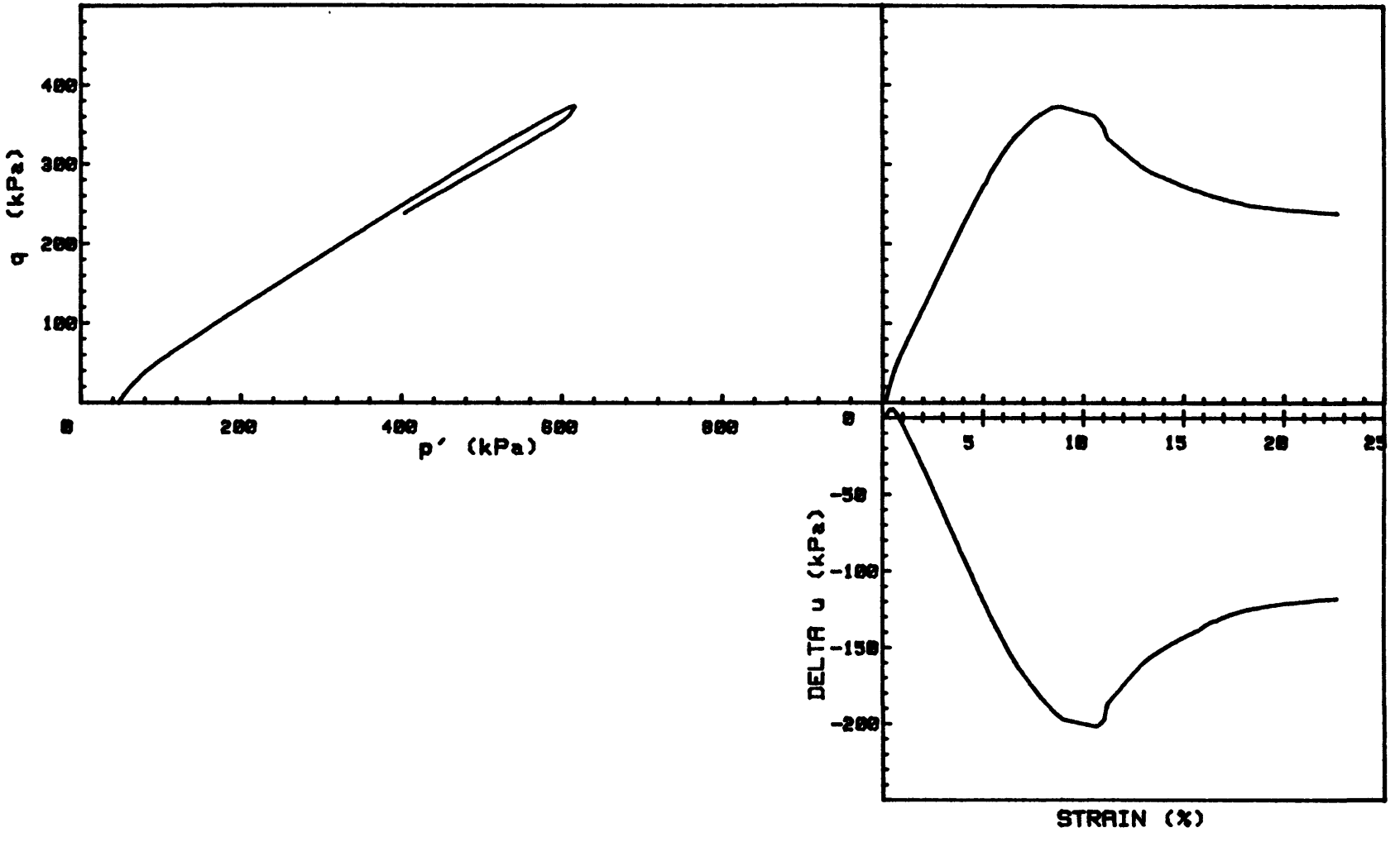

CRUISE DC4-81-NS		INCREMENT (cm)	170-179
CORE NO.	686A1	TEST NO.	TE101

SIG1c'(kPa)	47.7
SIG3c'(kPa)	47.7
INDUCED OCR	6.0

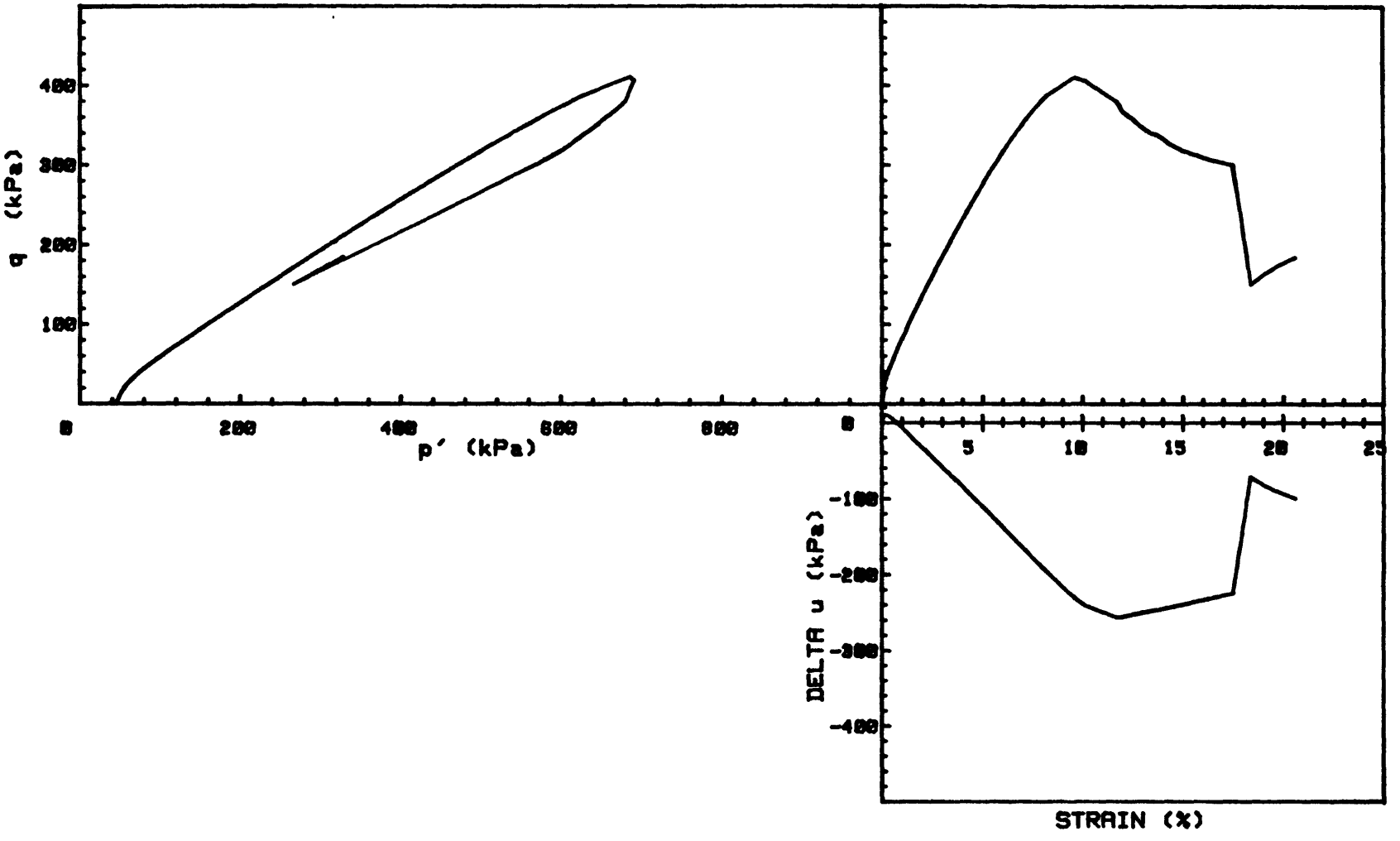

CRUISE DC4-81-NS		INCREMENT (cm)	55-64
CORE NO.	687A1	TEST NO.	TE102
SIG1c'(kPa)	45.1		
SIG3c'(kPa)	45.1		
INDUCED OCR	6.0		

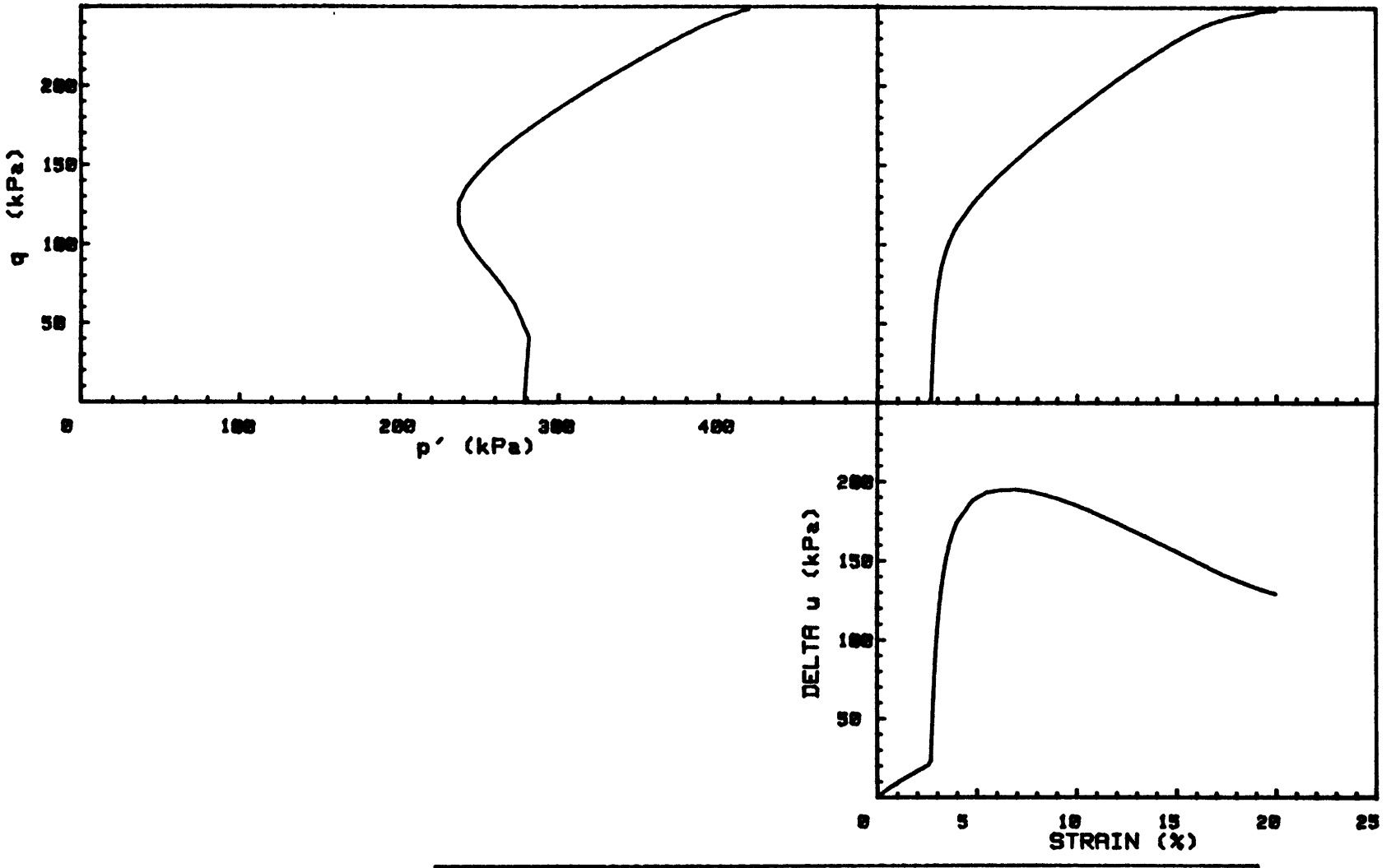

CRUISE DC4-81-NS		INCREMENT (cm)	111-120
CORE NO.	687A1	TEST NO.	TE96

SIG1c'(kPa)	299.6
SIG3c'(kPa)	299.6
INDUCED OCR	1.0

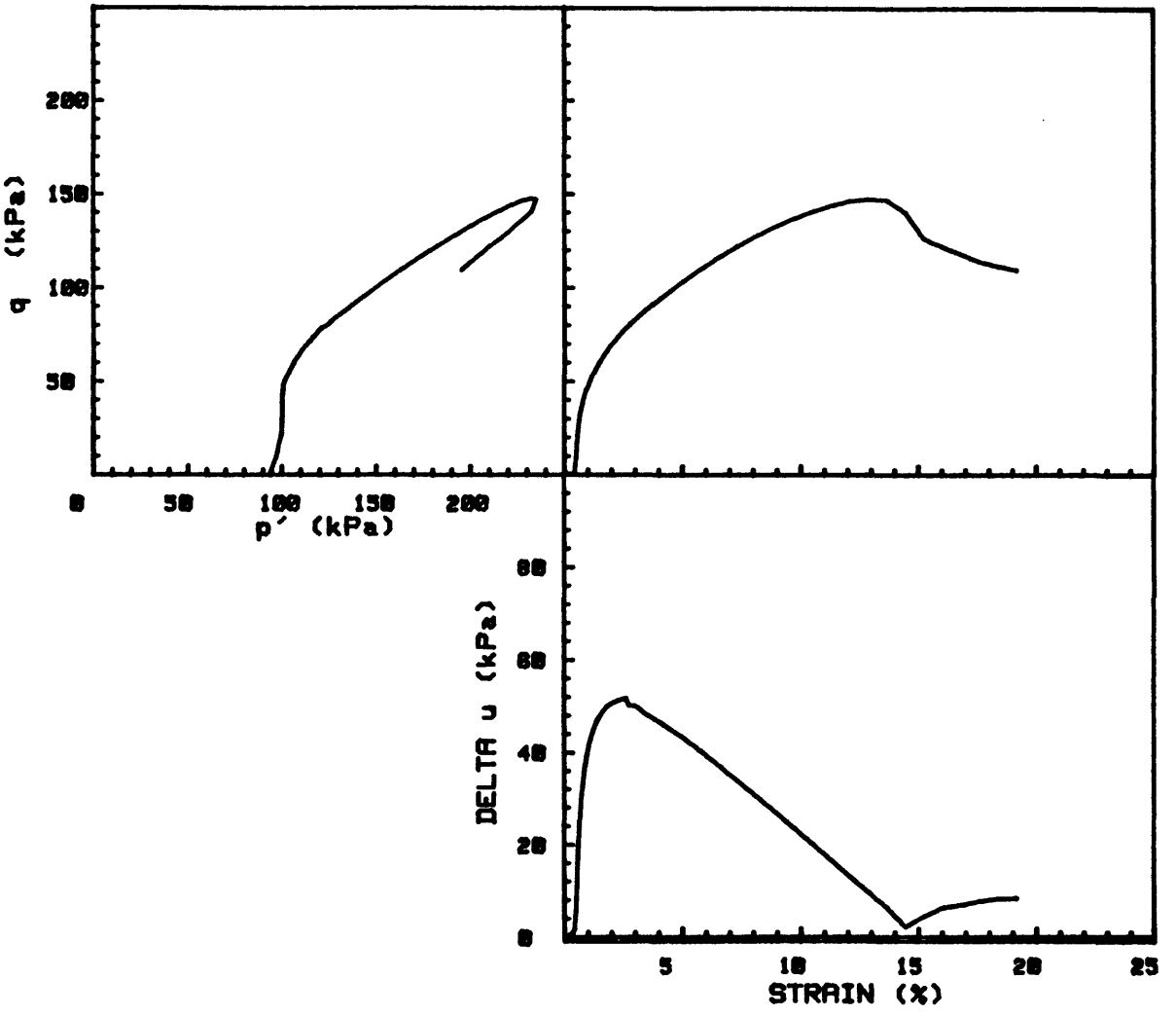

CRUISE DC4-81-NS		INCREMENT (cm)	111-120
CORE NO.	687A1	TEST NO.	TE97

SIG1c'(kPa)	94.4
SIG3c'(kPa)	94.4
INDUCED OCR	1.0

Appendix F. Cyclic triaxial test plots.

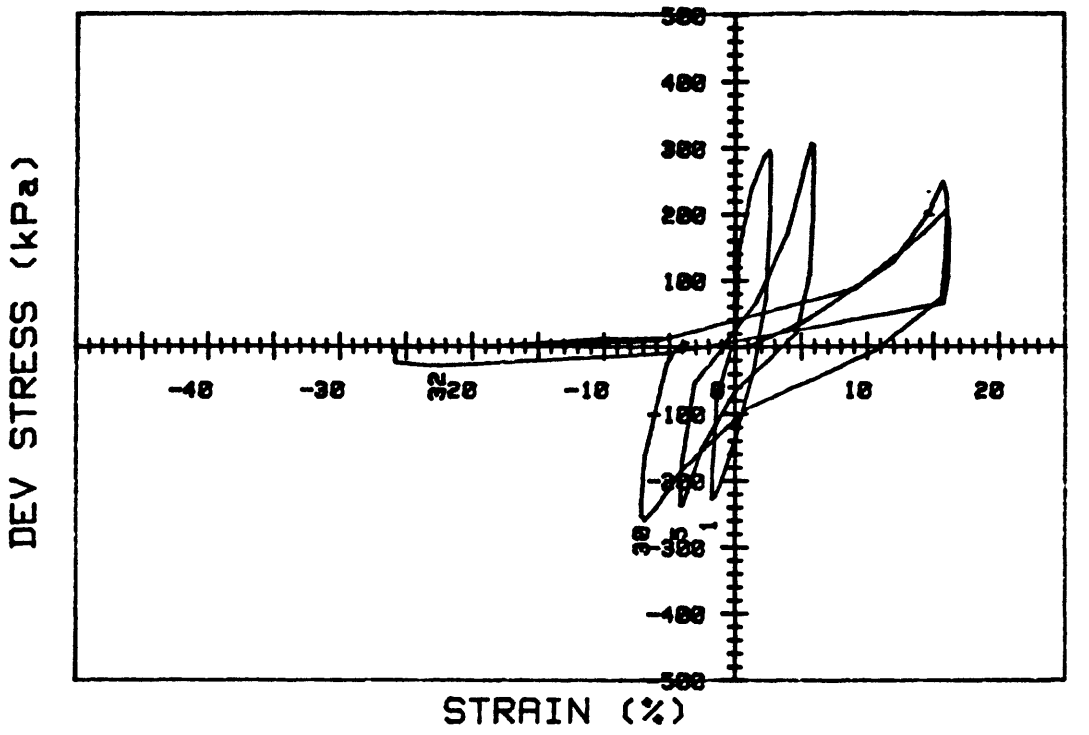

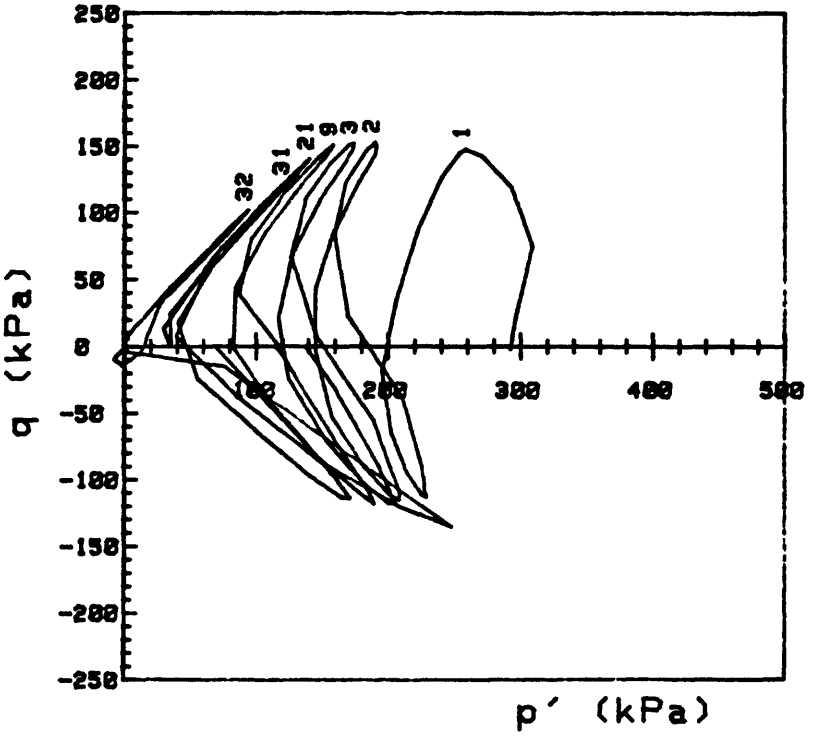

CRUISE DC4-81-NS		INCREMENT (cm)	142-150
CORE NO. 681A2		TEST NO.	D100
SIG1c'(kPa)	294.5	STATIC qf (kPa)	300.0
SIG3c'(kPa)	294.5	AVG MAX q (kPa)	141.0 (47.0%)
INDUCED OCR	1.0	AVG MIN q (kPa)	-115.5 (38.5%)

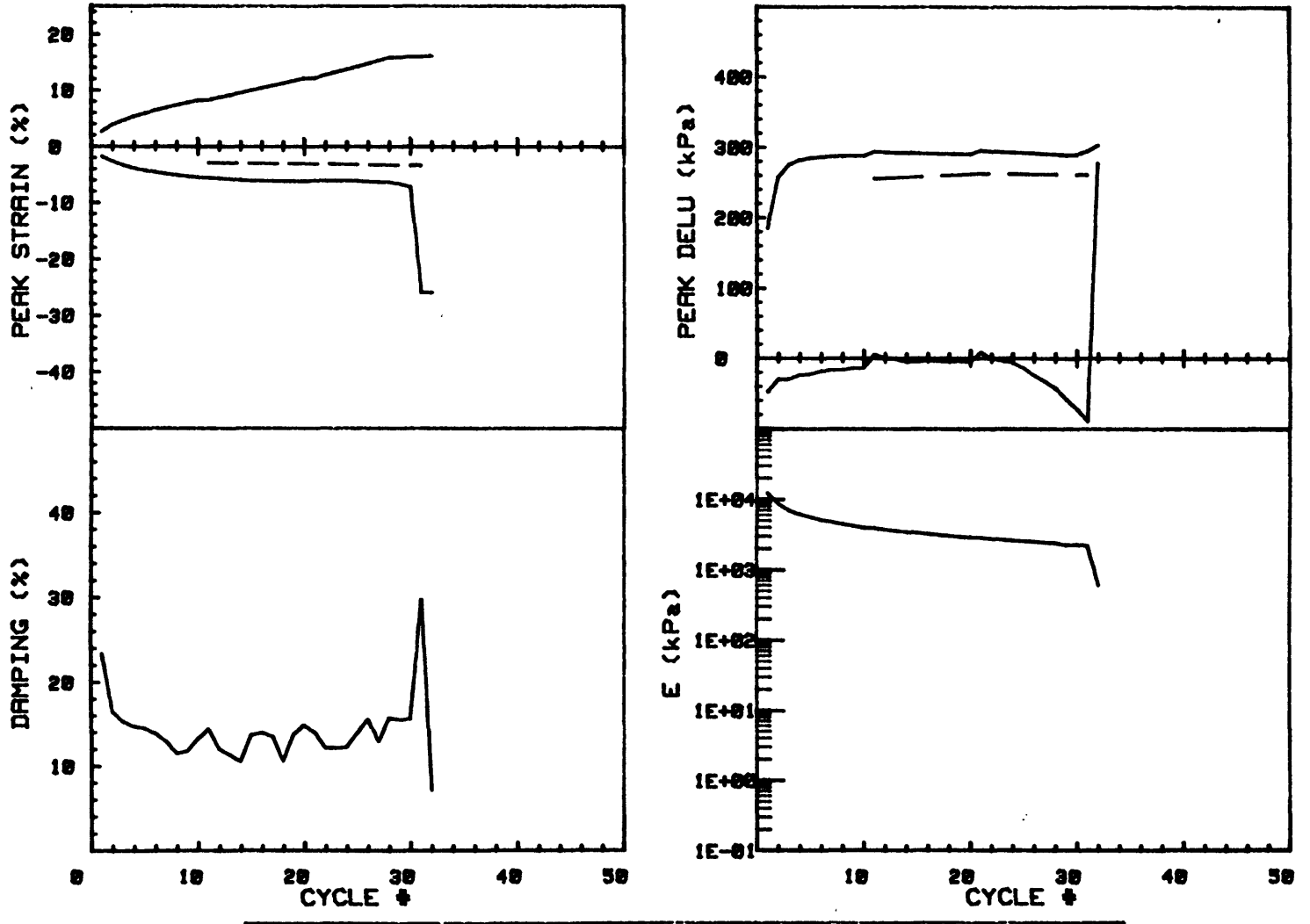

CRUISE DC4-81-NS		INCREMENT (cm)	142-150
CORE NO. 681A2		TEST NO.	D100
SIG1c'(kPa)	294.5	STATIC qf (kPa)	300.0
SIG3c'(kPa)	294.5	AVG MAX q (kPa)	141.0 (47.0%)
INDUCED OCR	1.0	AVG MIN q (kPa)	-115.5 (38.5%)

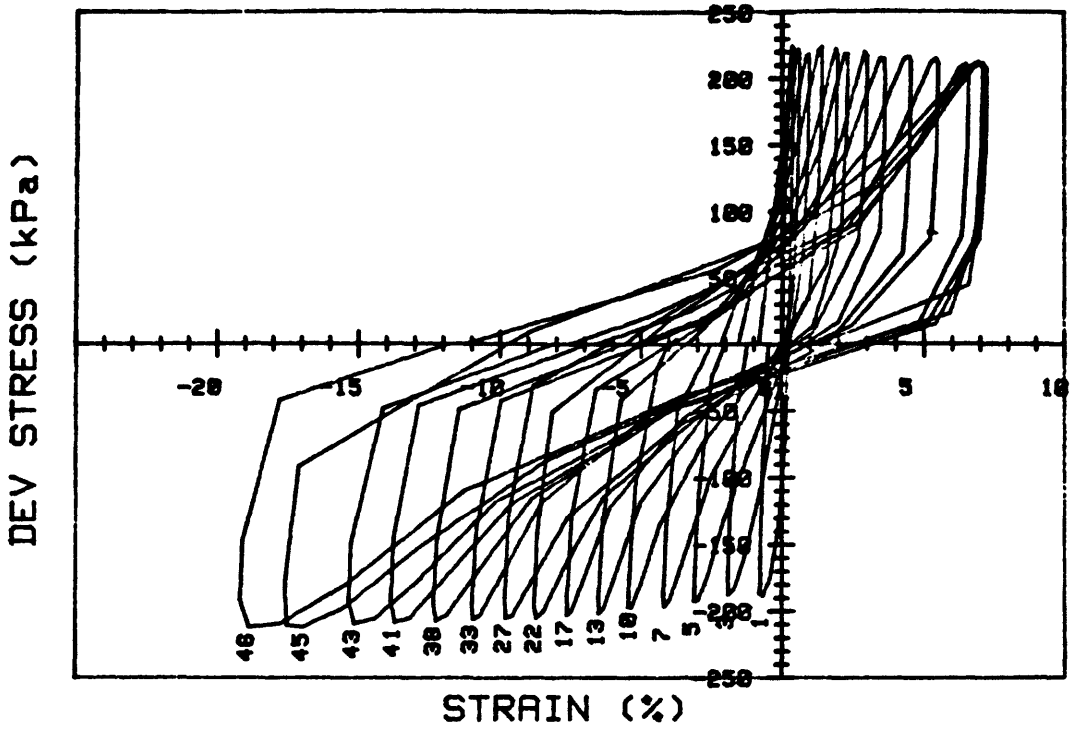

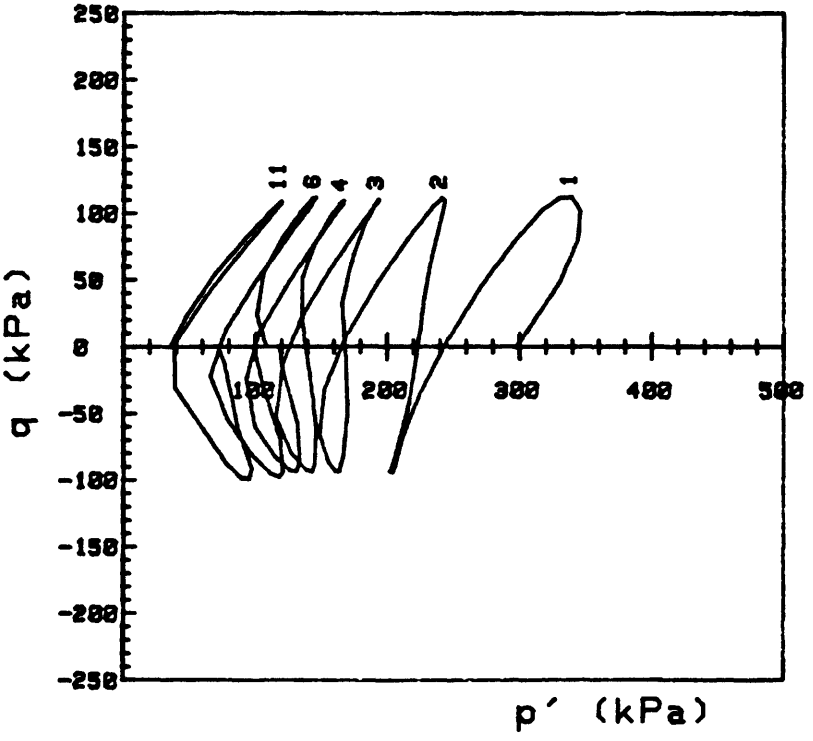

CRUISE DC4-81-NS		INCREMENT (cm)	142-149
CORE NO.	681A2	TEST NO.	D101
SIG1c′(kPa)	298.4	STATIC qf (kPa)	300.0
SIG3c′(kPa)	298.4	AVG MAX q (kPa)	108.2 (36.1%)
INDUCED OCR	1.0	AVG MIN q (kPa)	-101.5 (33.8%)

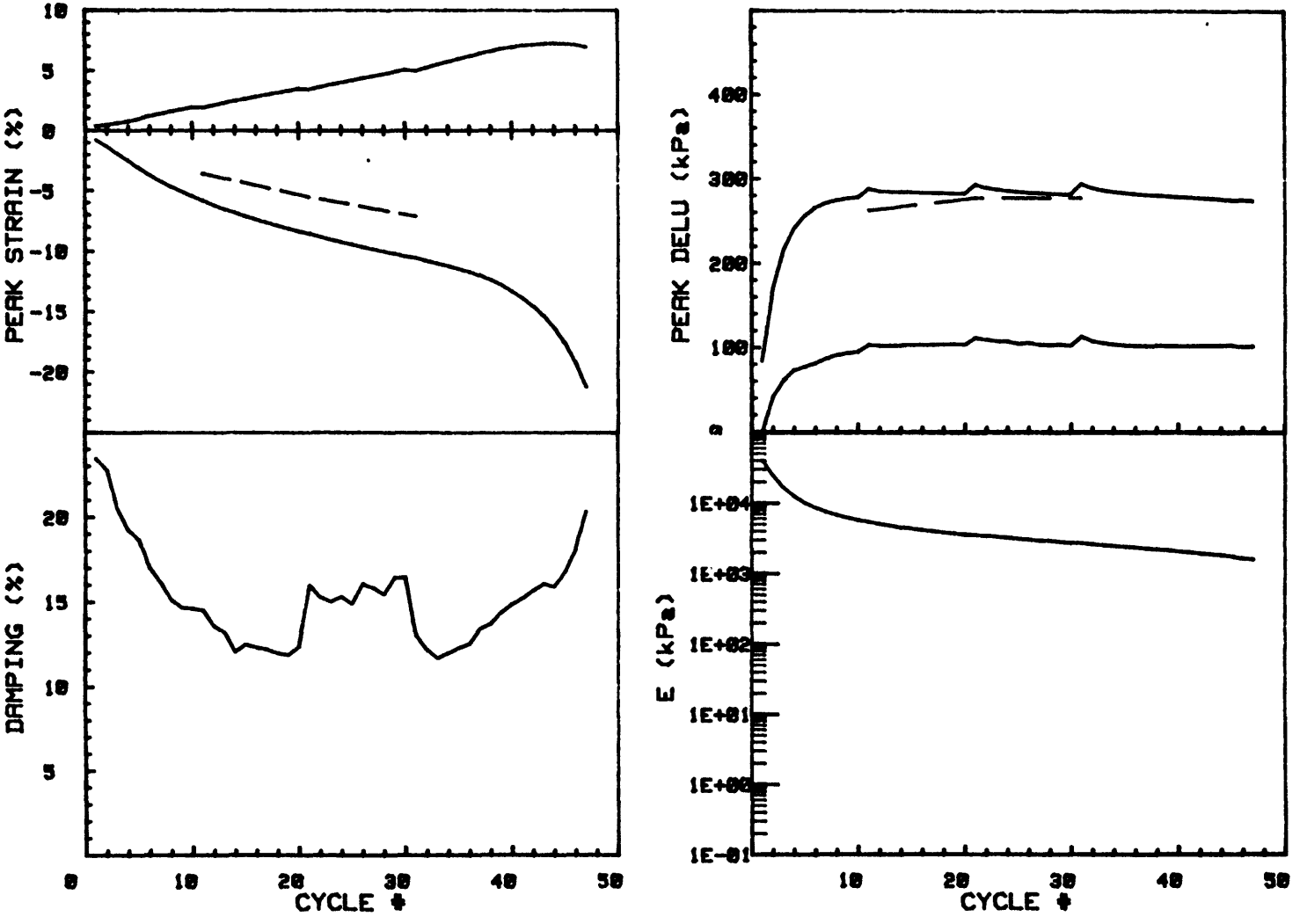

CRUISE DC4-81-NS		INCREMENT (cm)	142-149
CORE NO. 681A2		TEST NO.	D101
SIG1c'(kPa)	298.4	STATIC qf (kPa)	300.0
SIG3c'(kPa)	298.4	AVG MAX q (kPa)	108.2 (36.1%)
INDUCED OCR	1.0	AVG MIN q (kPa)	-101.5 (33.8%)

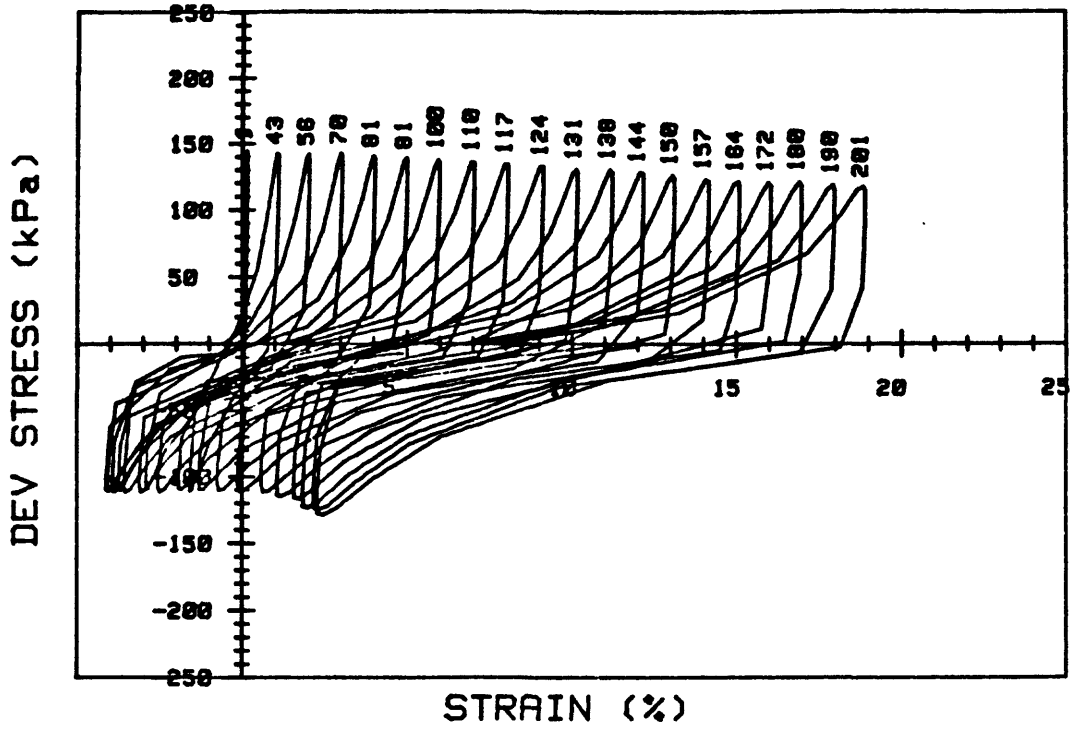

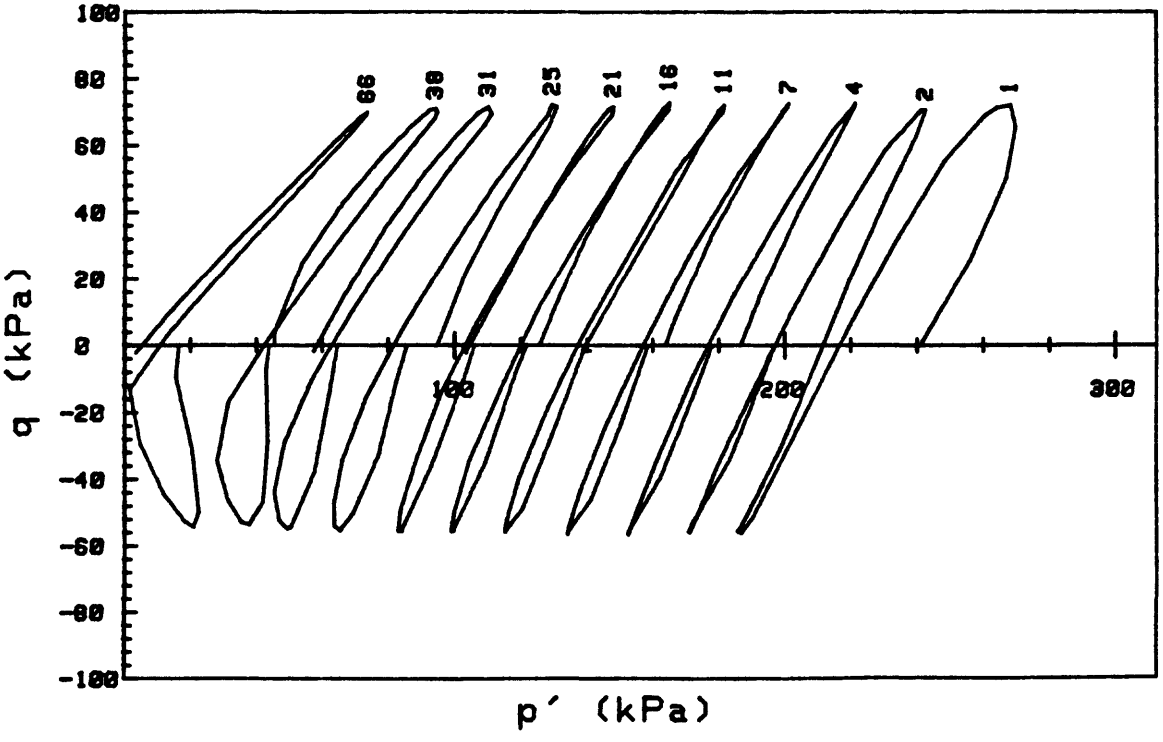

CRUISE DC4-81-NS		INCREMENT (cm)	76-83
CORE NO.	682A1	TEST NO.	TC44
SIG1c'(kPa)	241.8	STATIC qf (kPa)	184.0
SIG3c'(kPa)	241.8	AVG MAX q (kPa)	65.8 (35.8%)
INDUCED OCR	1.0	AVG MIN q (kPa)	-56.9 (30.9%)

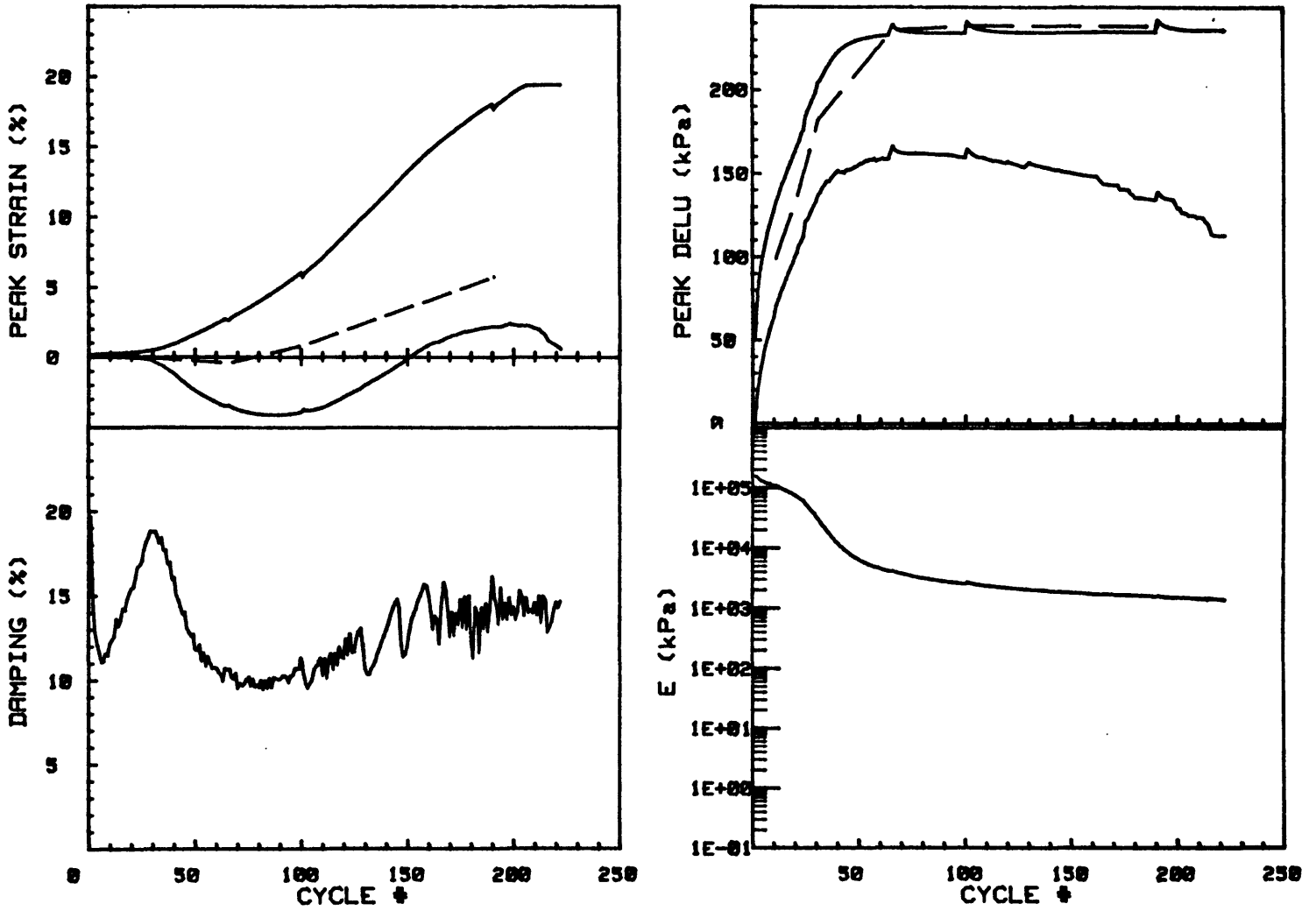

CRUISE DC4-81-NS		INCREMENT (cm)	76-83
CORE NO.	682A1	TEST NO.	TC44
SIG1c'(kPa)	241.8	STATIC qf (kPa)	184.0
SIG3c'(kPa)	241.8	AVG MAX q (kPa)	65.8 (35.8%)
INDUCED OCR	1.0	AVG MIN q (kPa)	-56.9 (30.9%)

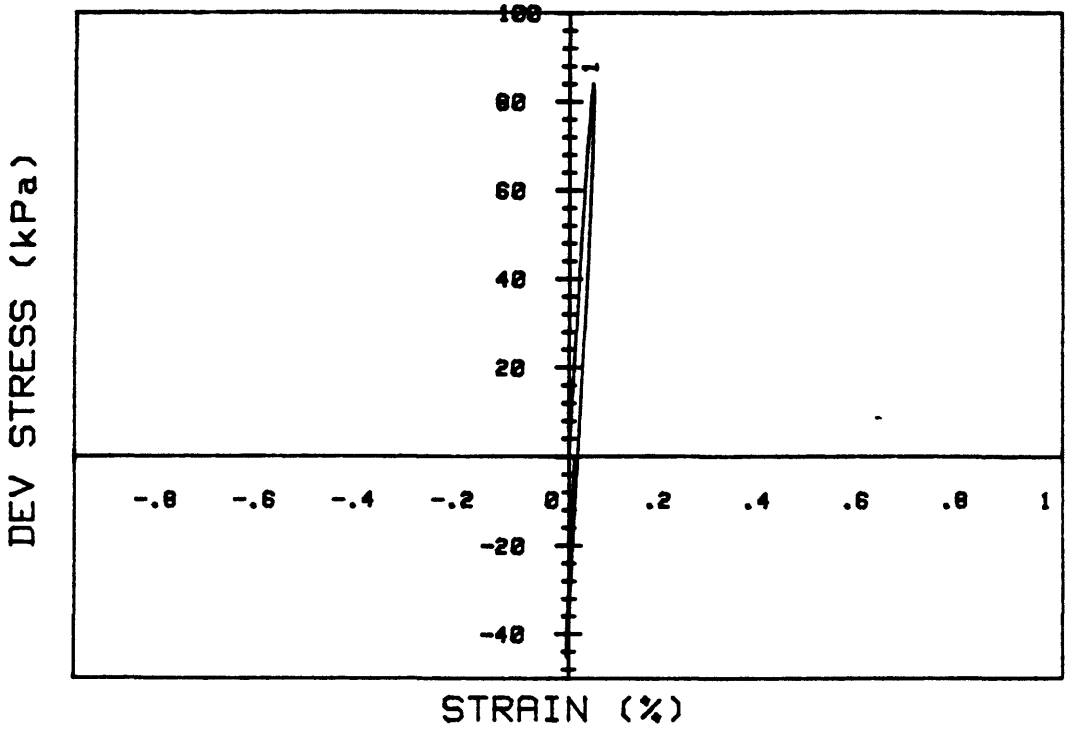

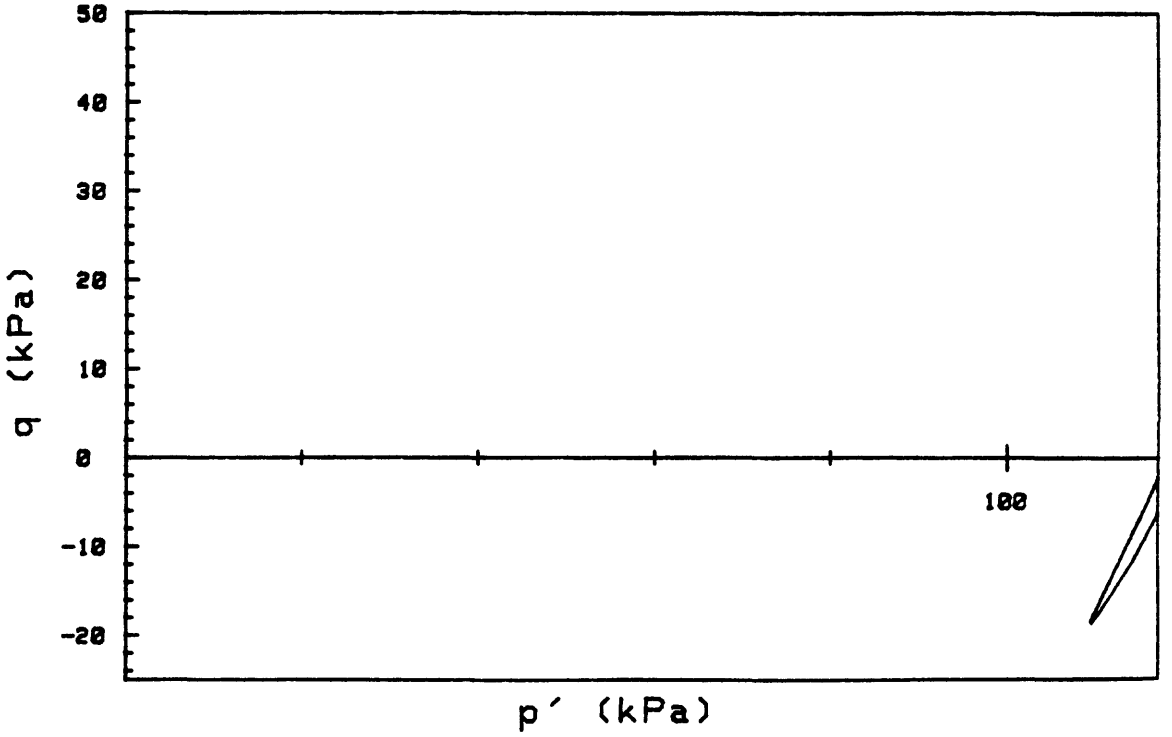

CRUISE DC4-81-NS		INCREMENT (cm)	76-84
CORE NO.	682A1	TEST NO.	TC45
SIG1c'(kPa)	239.4	STATIC qf (kPa)	183.9
SIG3c'(kPa)	239.4	AVG MAX q (kPa)	41.6 (22.6%)
INDUCED OCR	1.0	AVG MIN q (kPa)	-19.4 (10.5%)

Cycles 1-470

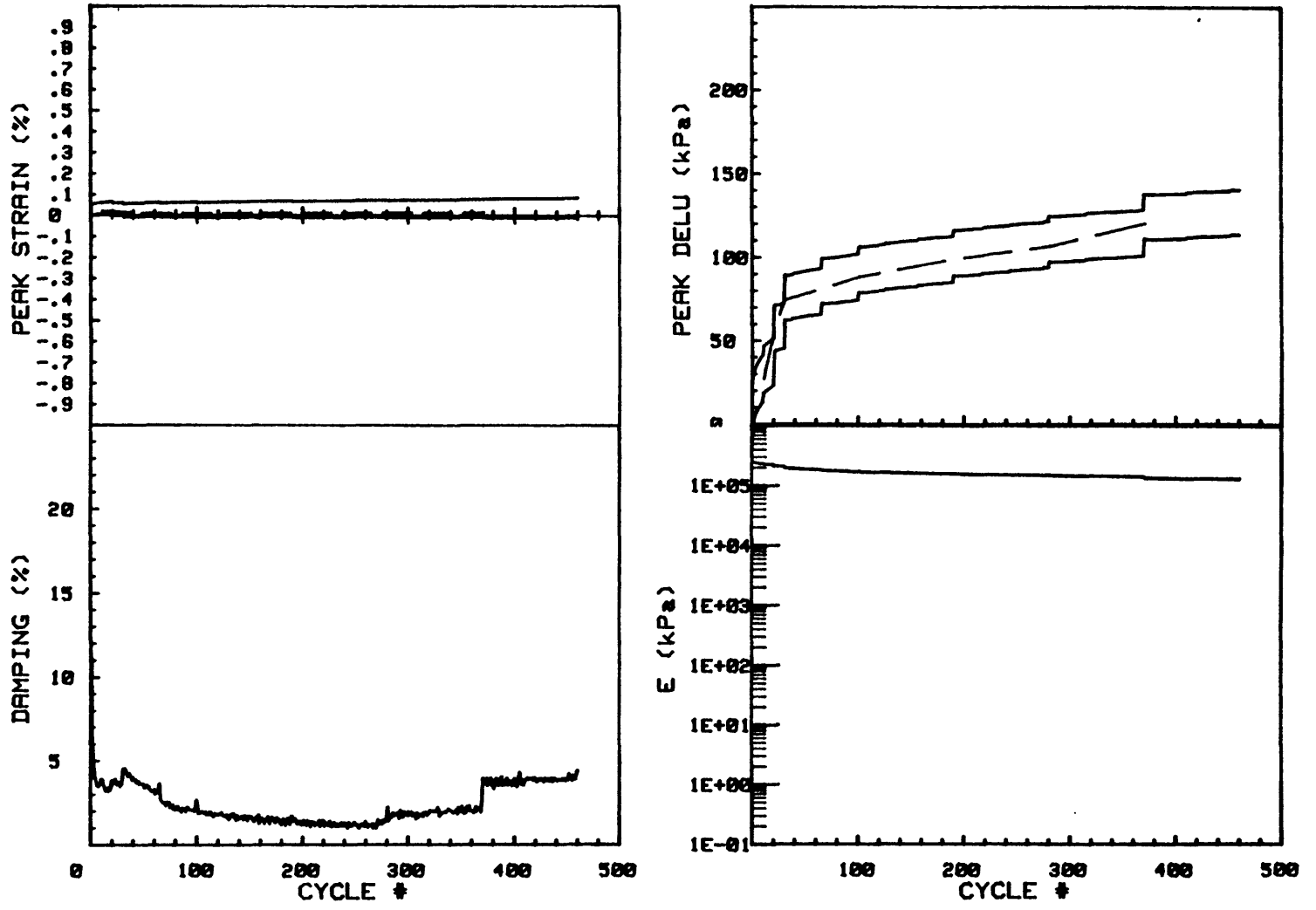

CRUISE DC4-81-NS		INCREMENT (cm)	76-84
CORE NO.	682A1	TEST NO.	TC45
SIG1c'(kPa)	239.4	STATIC qf (kPa)	183.9
SIG3c'(kPa)	239.4	AVG MAX q (kPa)	41.6 (22.6%)
INDUCED OCR	1.0	AVG MIN q (kPa)	-19.4 (10.5%)

Cycles 1-470

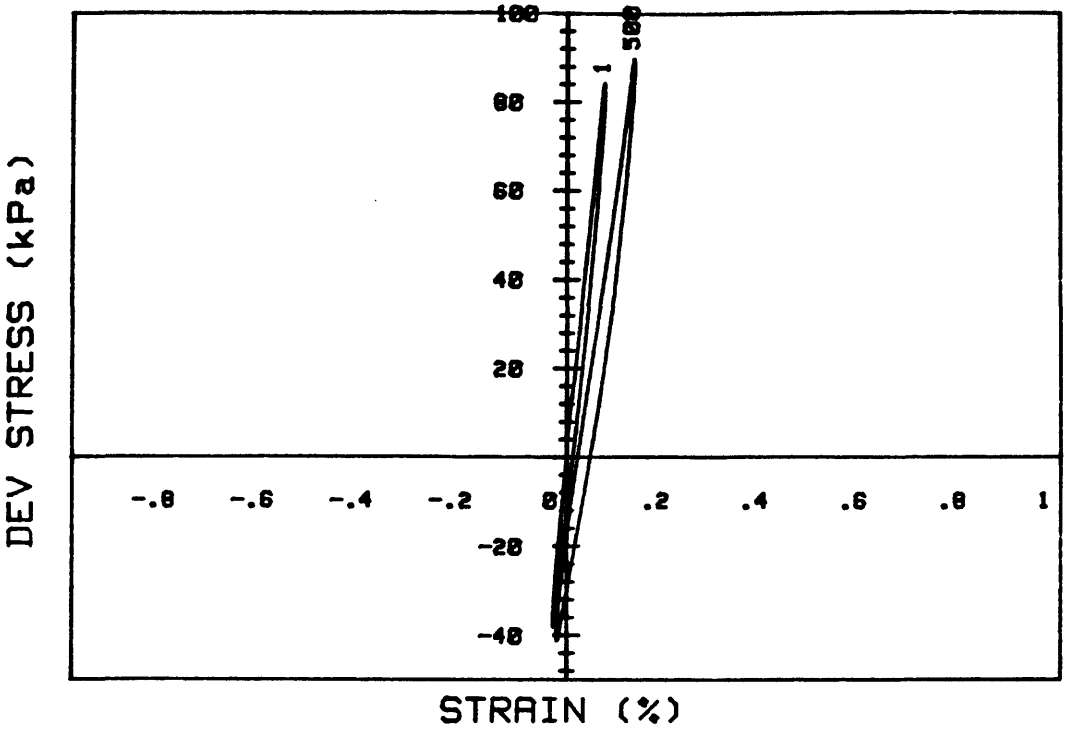

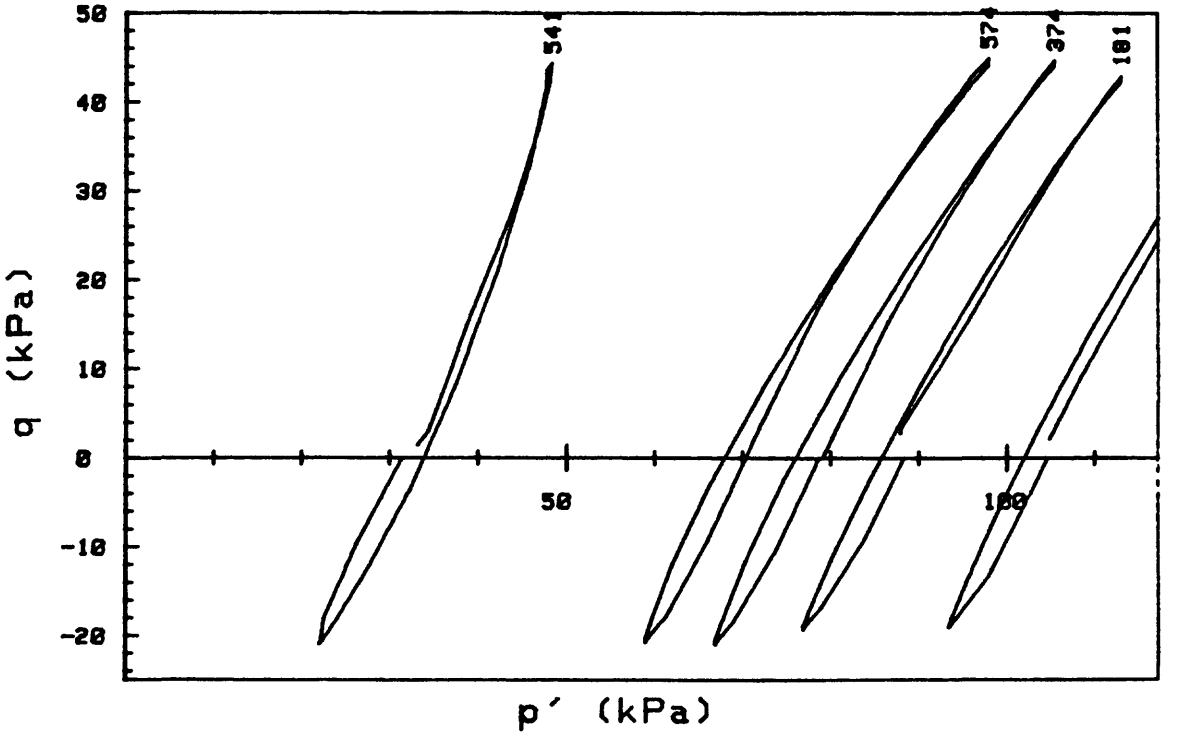

CRUISE DC4-81-NS		INCREMENT (cm)	76-84
CORE NO. 682A1		TEST NO.	TC45
SIG1c'(kPa)	102.7	STATIC qf (kPa)	183.9
SIG3c'(kPa)	102.7	AVG MAX q (kPa)	43.9 (23.9%)
INDUCED OCR	1.0	AVG MIN q (kPa)	-20.3 (11.0%)

Cycles 741 - 1370

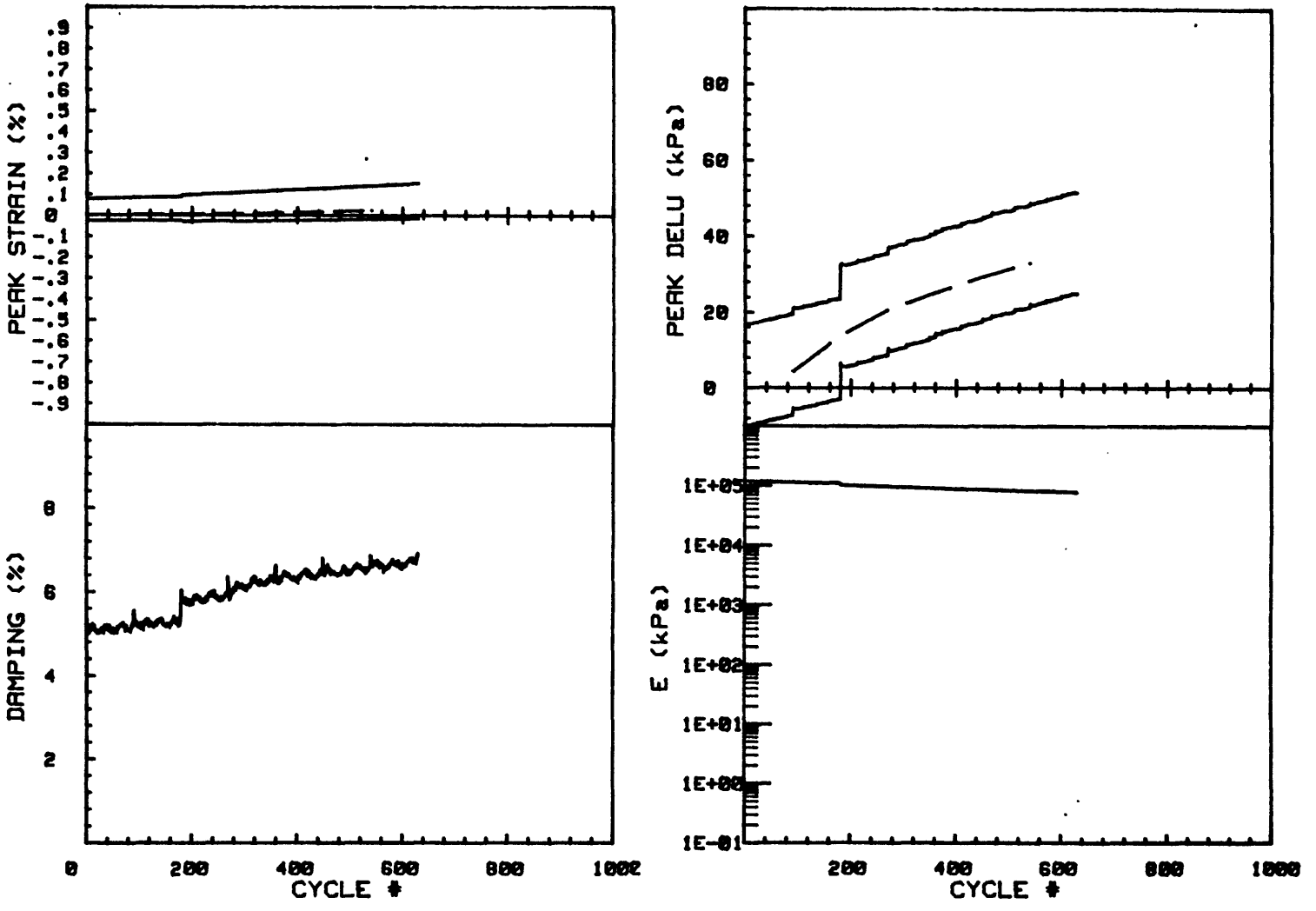

CRUISE DC4-81-NS		INCREMENT (cm)	76-84
CORE NO. 682A1		TEST NO.	TC45
SIG1c'(kPa)	102.7	STATIC qf (kPa)	183.9
SIG3c'(kPa)	102.7	AVG MAX q (kPa)	43.9 (23.9%)
INDUCED OCR	1.0	AVG MIN q (kPa)	-20.3 (11.0%)

Cycles 741 - 1370

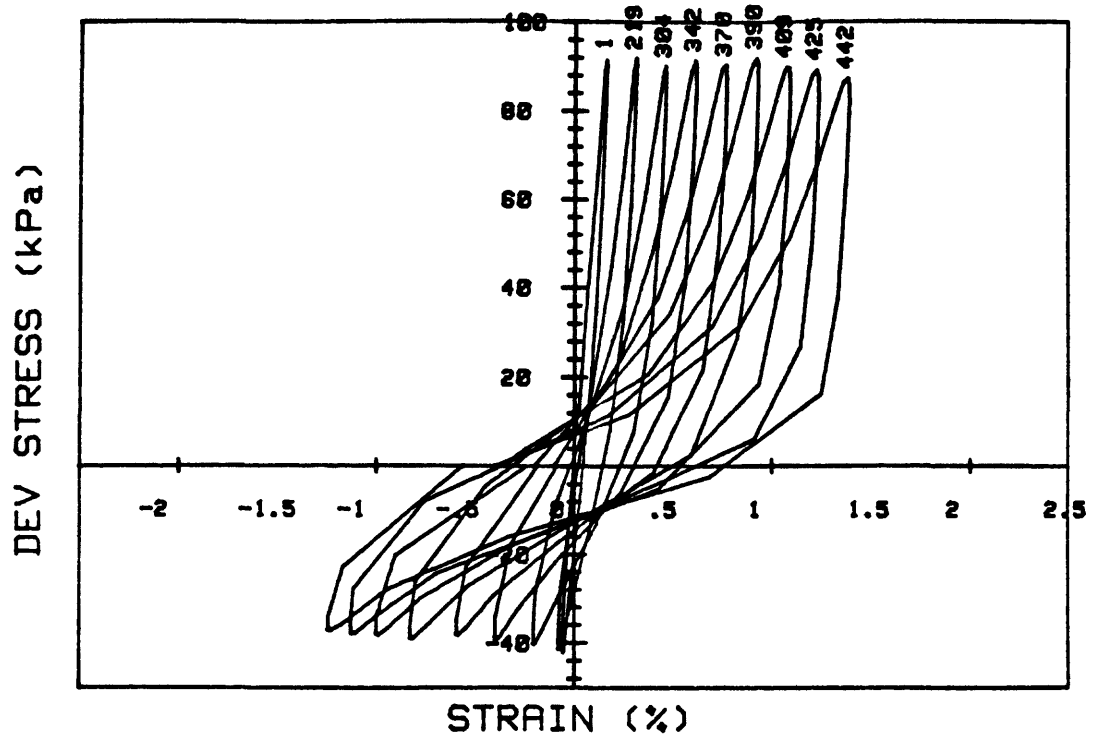

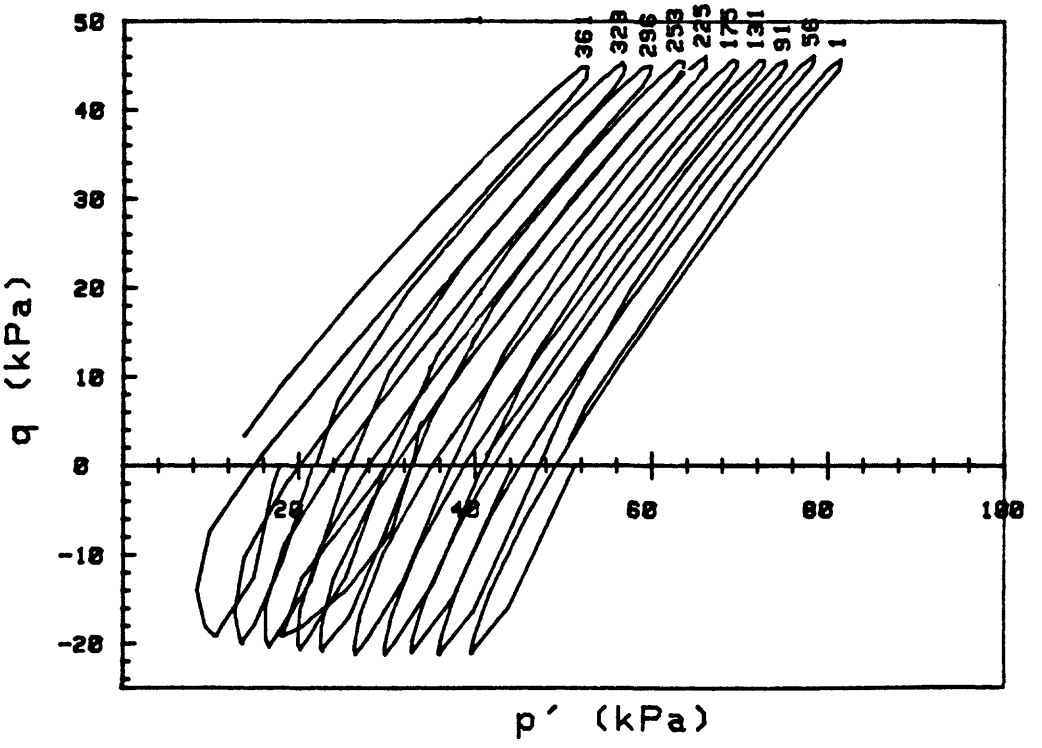

CRUISE DC4-81-NS		INCREMENT (cm)	76-84
CORE NO.	682A1	TEST NO.	TC45
SIG1c'(kPa)	47.8	STATIC qf (kPa)	183.9
SIG3c'(kPa)	47.8	AVG MAX q (kPa)	45.5 (24.7%)
INDUCED OCR	1.0	AVG MIN q (kPa)	-20.4 (11.1%)

Cycles 1461 - 1910

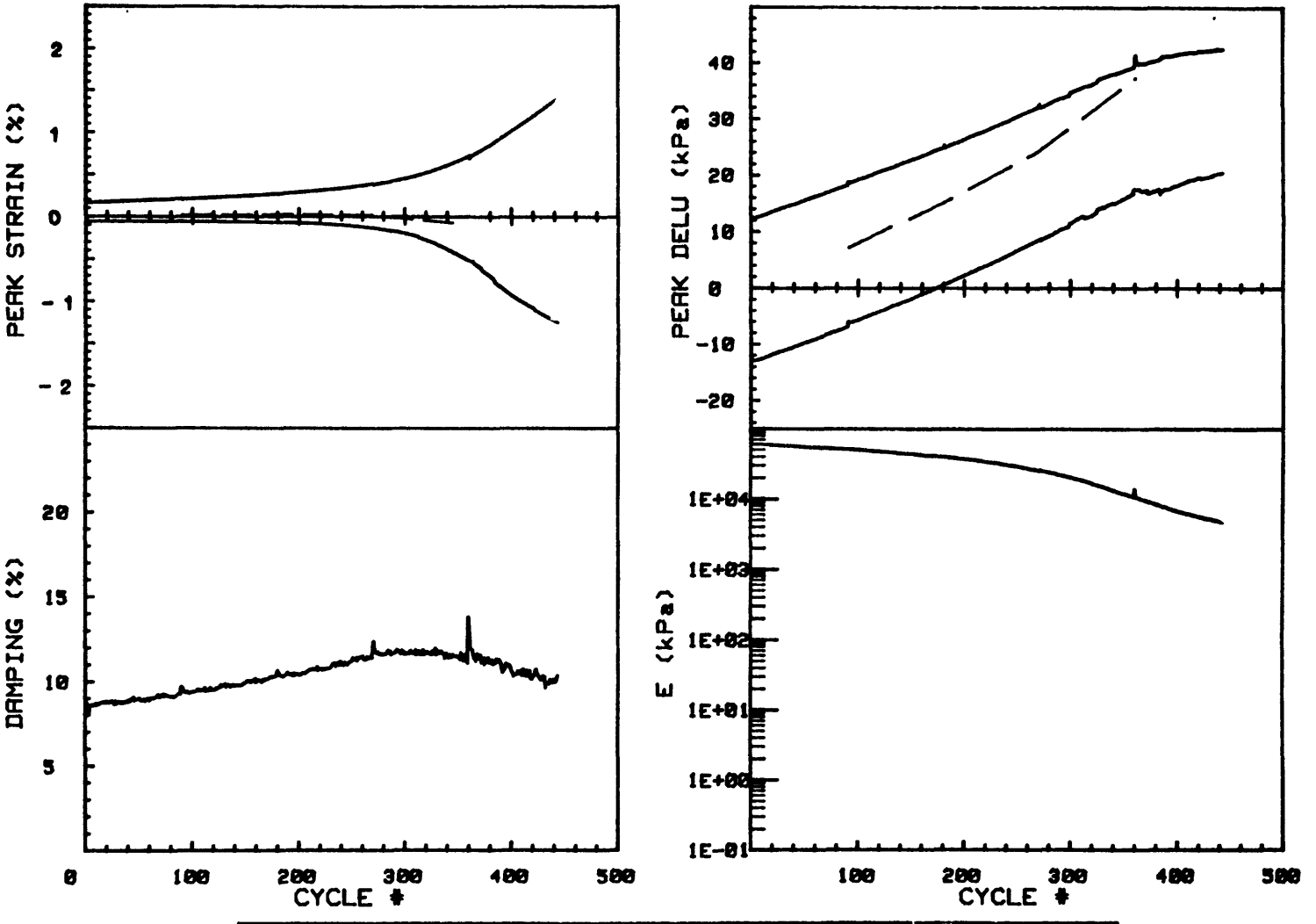

CRUISE DC4-81-NS		INCREMENT (cm)	76-84
CORE NO.	682A1	TEST NO.	TC45
SIG1c'(kPa)	47.8	STATIC qf (kPa)	183.9
SIG3c'(kPa)	47.8	AVG MAX q (kPa)	45.5 (24.7%)
INDUCED OCR	1.0	AVG MIN q (kPa)	-20.4 (11.1%)

Cycles 1461 - 1910

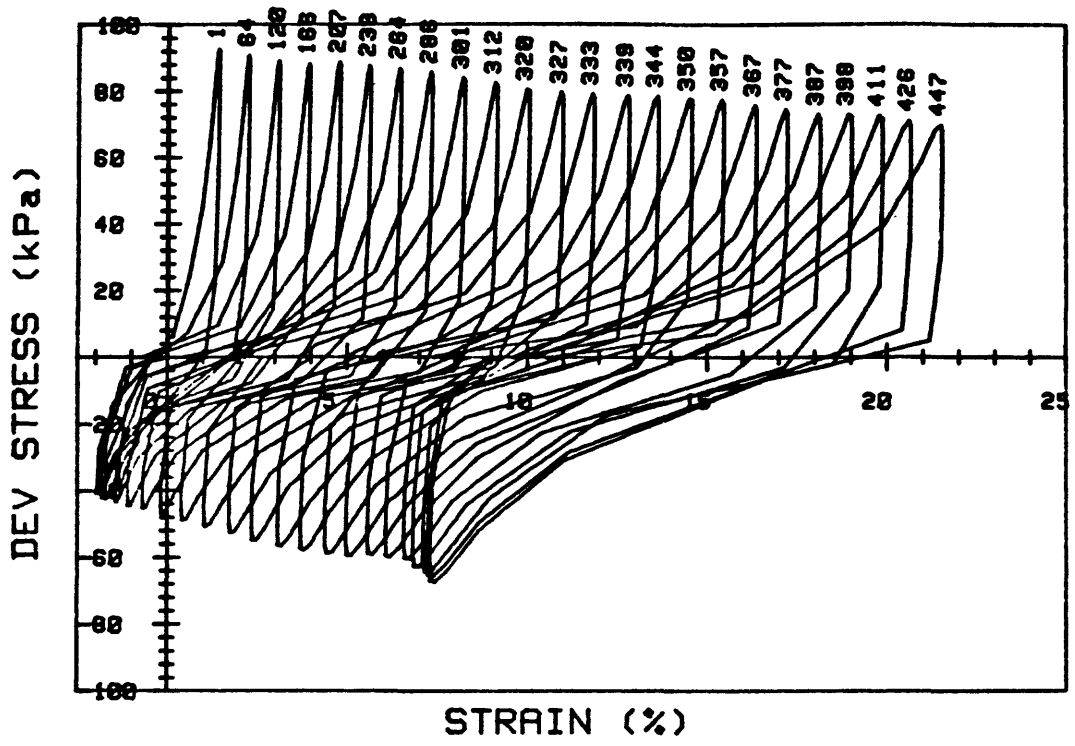

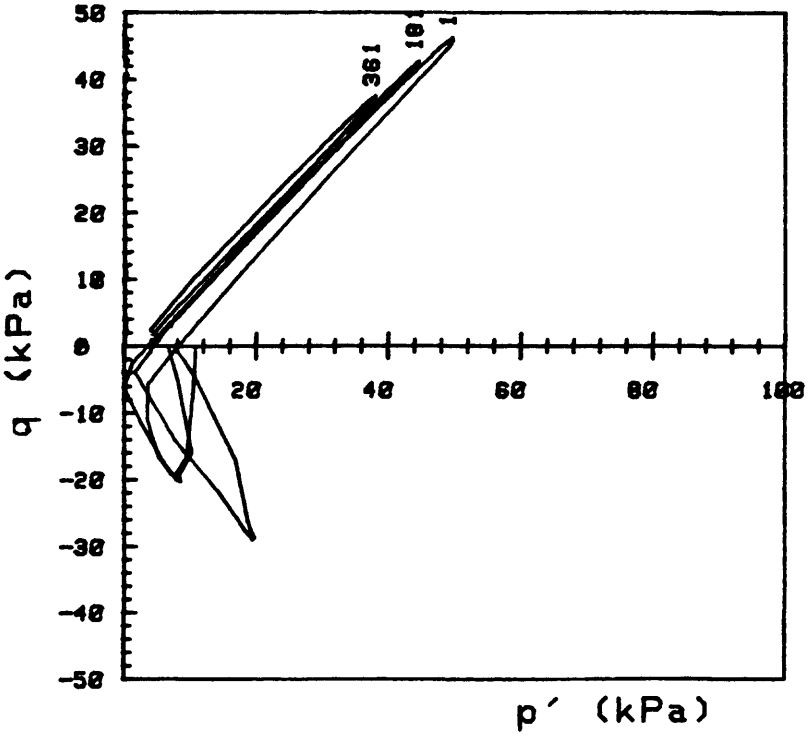

CRUISE DC4-81-NS		INCREMENT (cm)	76-84
CORE NO.	682A1	TEST NO.	TC45
SIG1c'(kPa)	4.2	STATIC qf (kPa)	183.9
SIG3c'(kPa)	4.2	AVG MAX q (kPa)	42.0 (22.8%)
INDUCED OCR	1.0	AVG MIN q (kPa)	-23.8 (12.9%)

Cycles 1911 - 2360

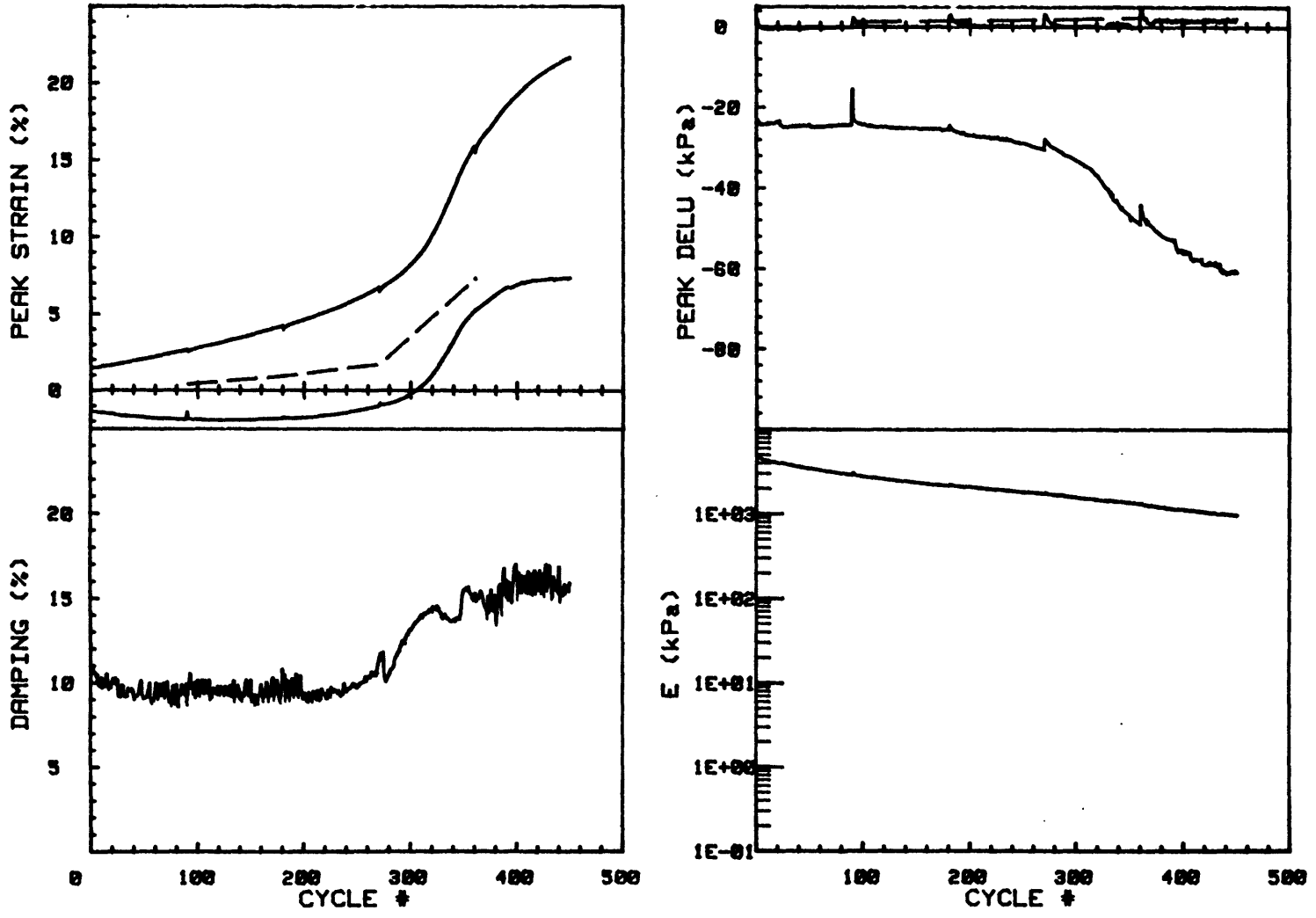

CRUISE DC4-81-NS		INCREMENT (cm)	76-84
CORE NO.	682A1	TEST NO.	TC45
SIG1c'(kPa)	4.2	STATIC qf (kPa)	183.9
SIG3c'(kPa)	4.2	AVG MAX q (kPa)	42.0 (22.8%)
INDUCED OCR	1.0	AVG MIN q (kPa)	-23.8 (12.9%)

Cycles 1911 - 2360

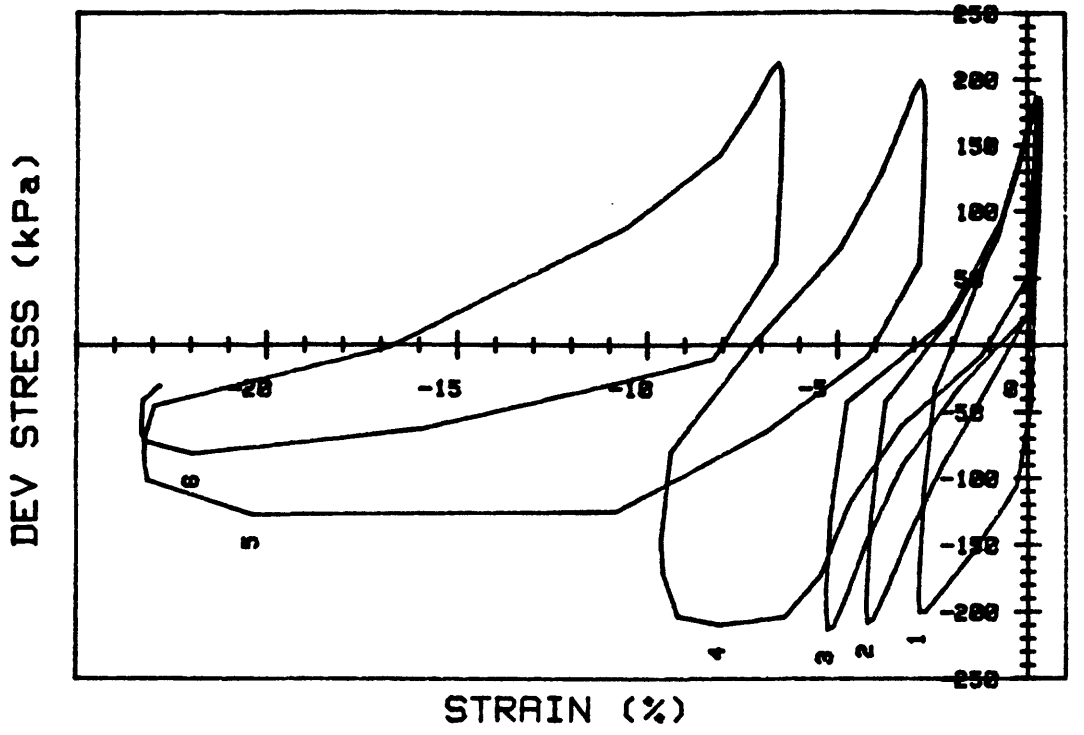

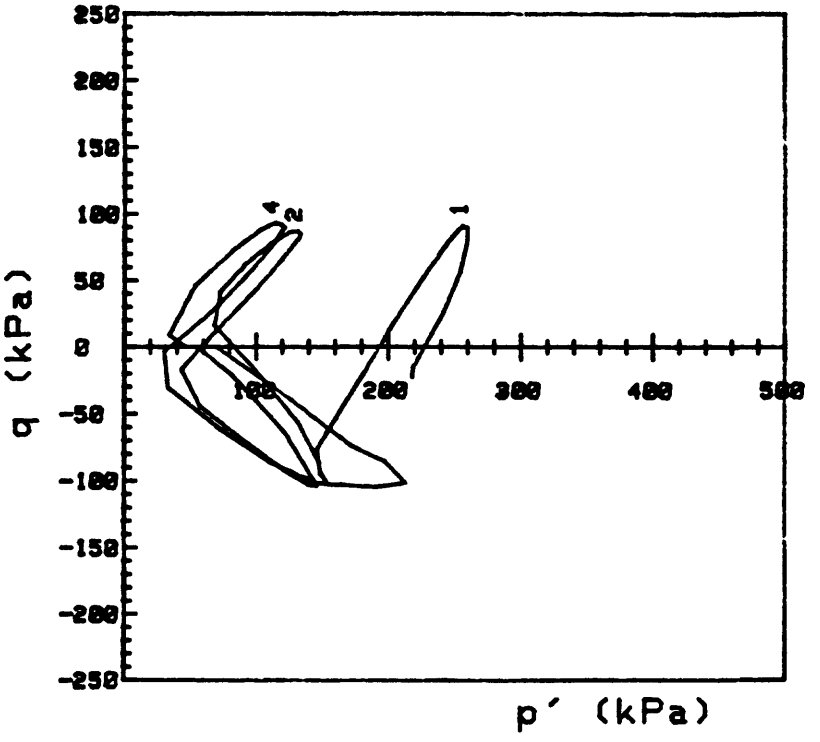

CRUISE DC4-81-NS		INCREMENT (cm)	86-93
CORE NO.	682A1	TEST NO.	TC40
SIG1c'(kPa)	240.4	STATIC qf (kPa)	183.9
SIG3c'(kPa)	240.4	AVG MAX q (kPa)	94.9 (51.6%)
INDUCED OCR	1.0	AVG MIN q (kPa)	-86.7 (47.1%)

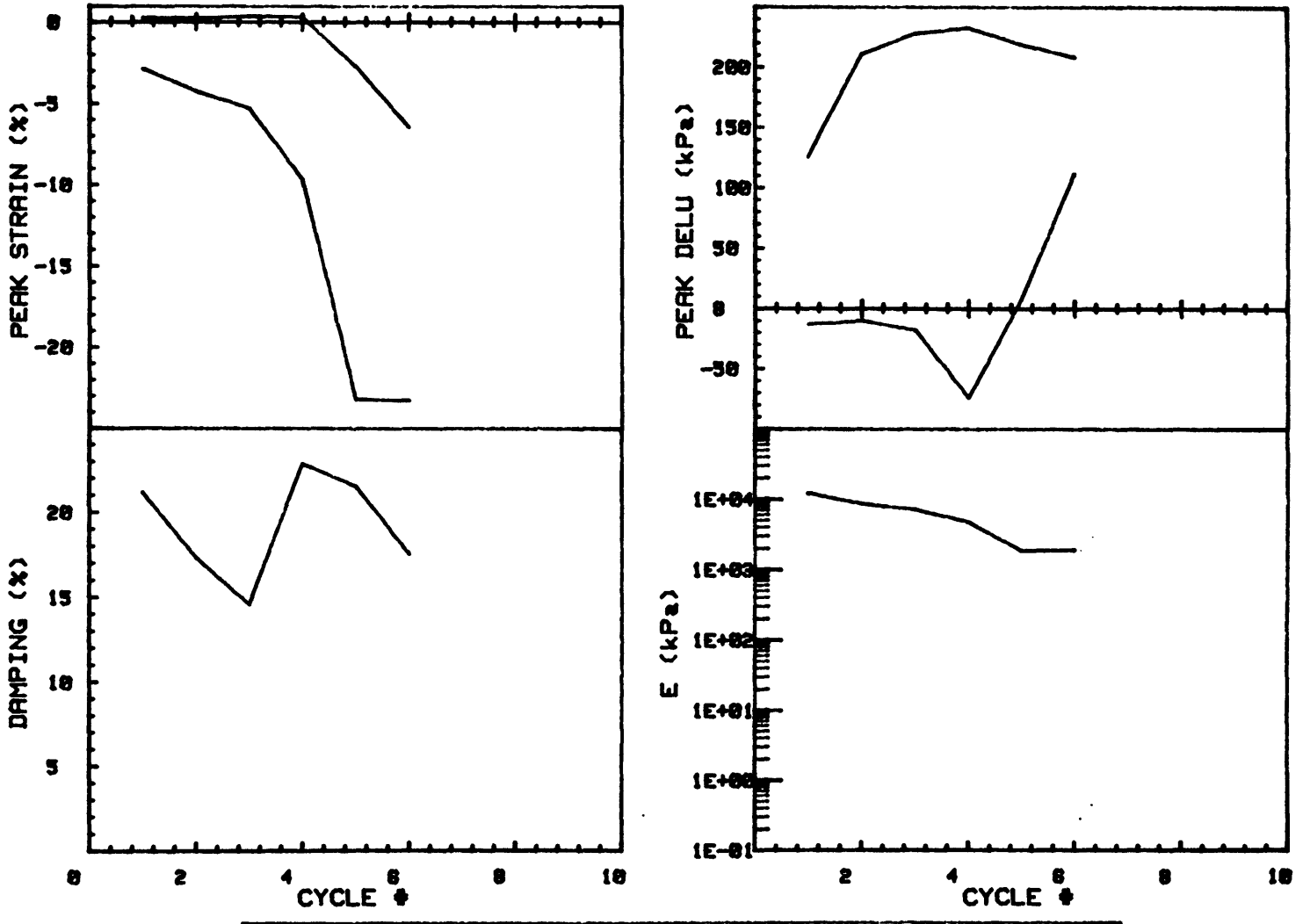

CRUISE DC4-81-NS		INCREMENT (cm)	86-93
CORE NO.	682A1	TEST NO.	TC40
SIG1c'(kPa)	240.4	STATIC qf (kPa)	183.9
SIG3c'(kPa)	240.4	AVG MAX q (kPa)	94.9 (51.6%)
INDUCED OCR	1.0	AVG MIN q (kPa)	-86.7 (47.1%)

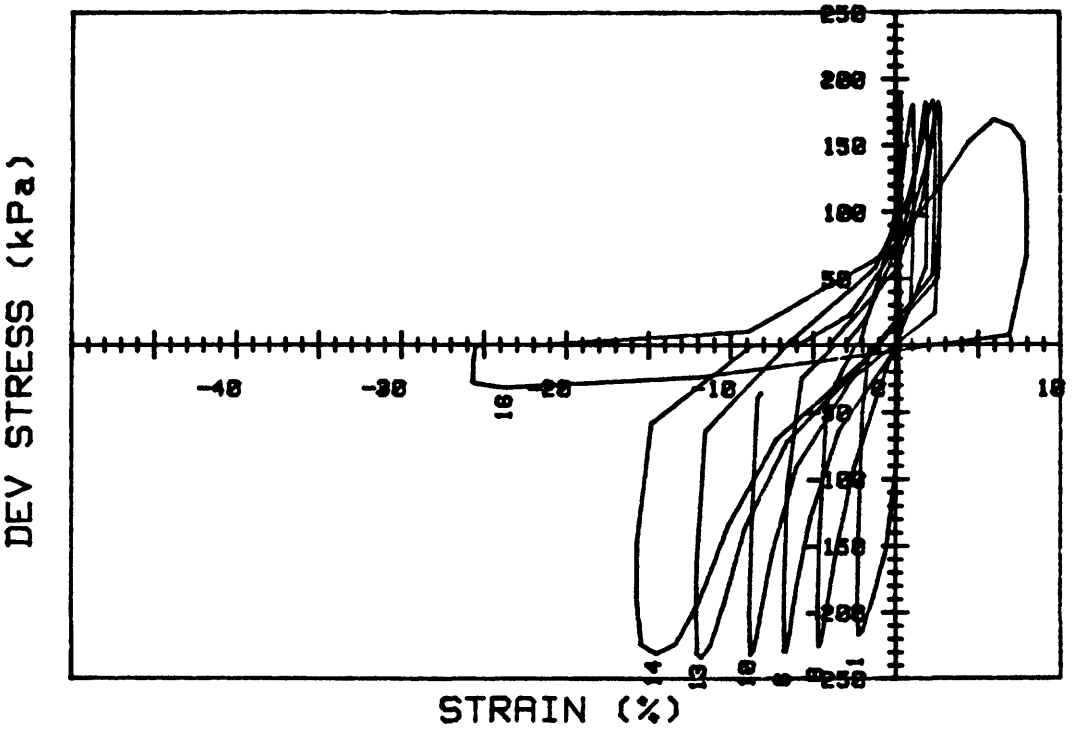

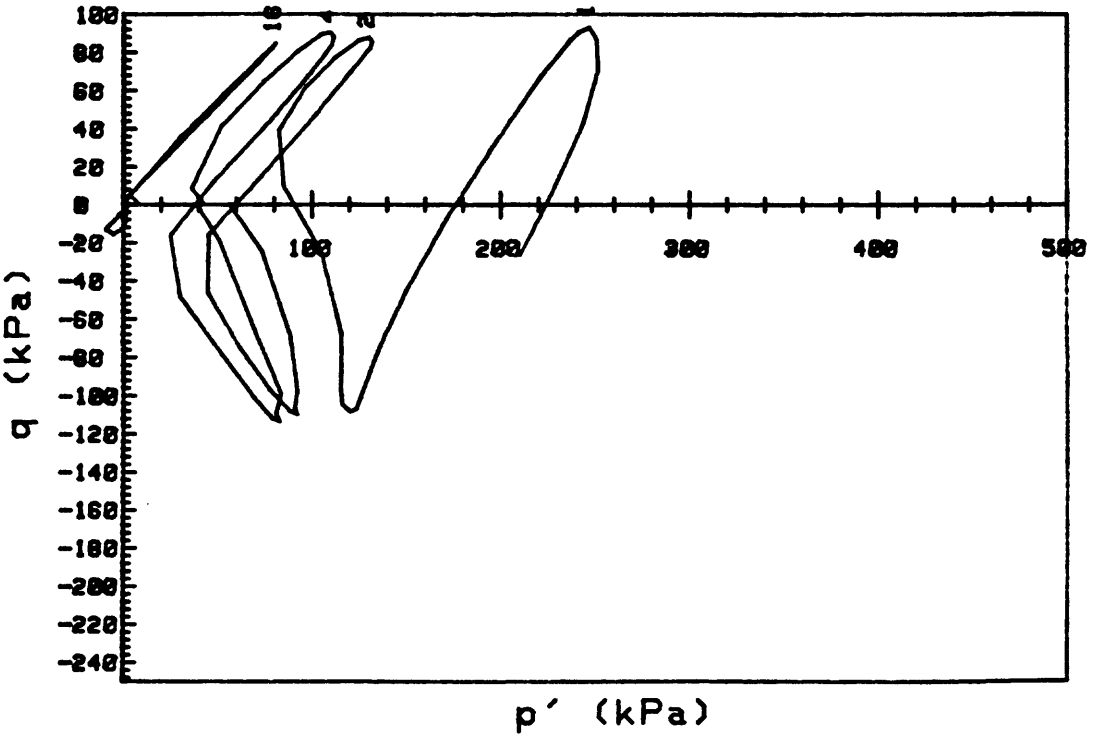

CRUISE DC4-81-NS		INCREMENT (cm)	86-93
CORE NO.	682A1	TEST NO.	TC41
SIG1c'(kPa)	236.8	STATIC qf (kPa)	183.9
SIG3c'(kPa)	236.8	AVG MAX q (kPa)	90.4 (49.2%)
INDUCED OCR	1.0	AVG MIN q (kPa)	-105.7 (57.5%)

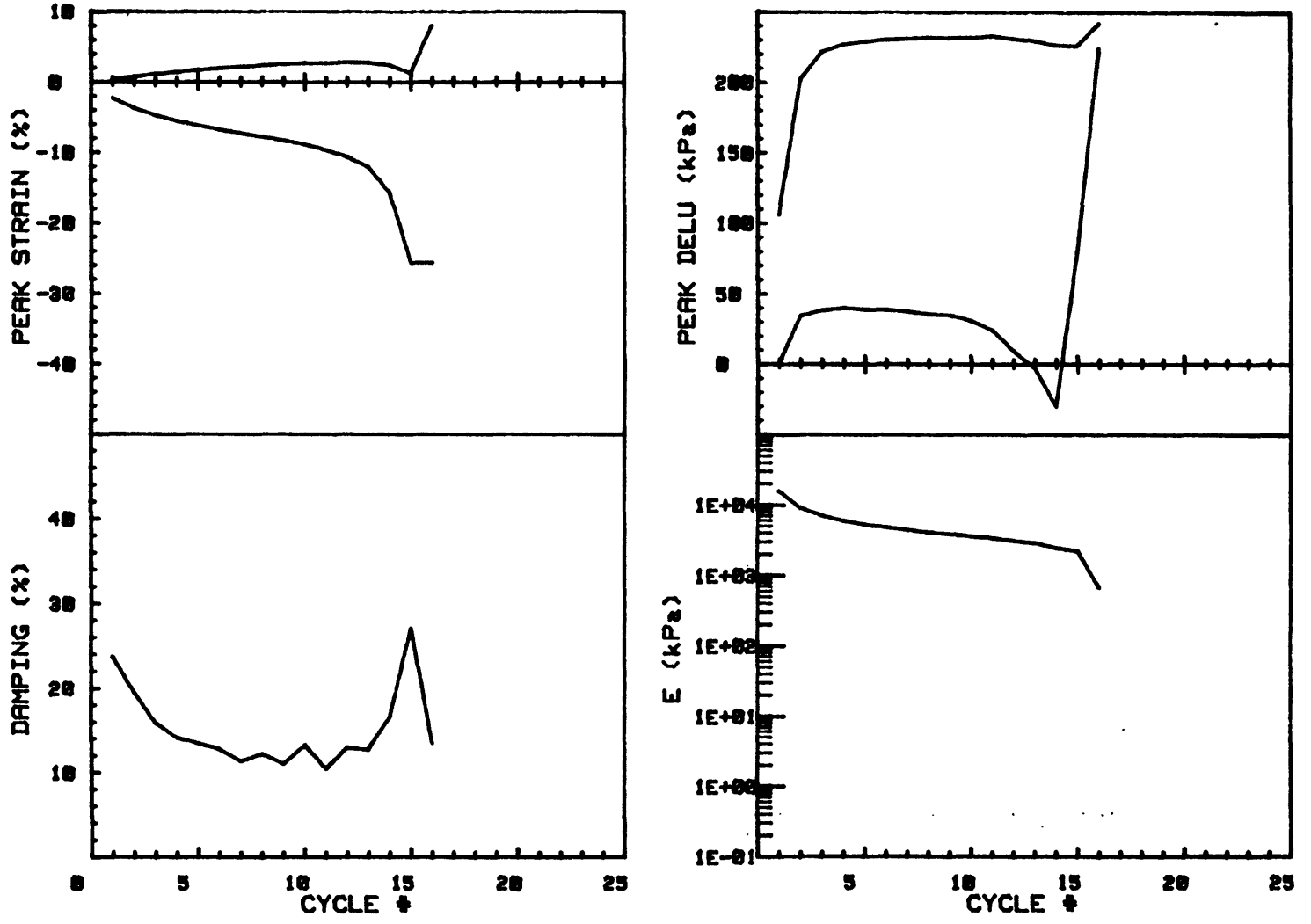

CRUISE DC4-81-NS		INCREMENT (cm)	86-93
CORE NO.	682A1	TEST NO.	TC41
SIG1c'(kPa)	236.8	STATIC qf (kPa)	183.9
SIG3c'(kPa)	236.8	AVG MAX q (kPa)	90.4 (49.2%)
INDUCED OCR	1.0	AVG MIN q (kPa)	-105.7 (57.5%)

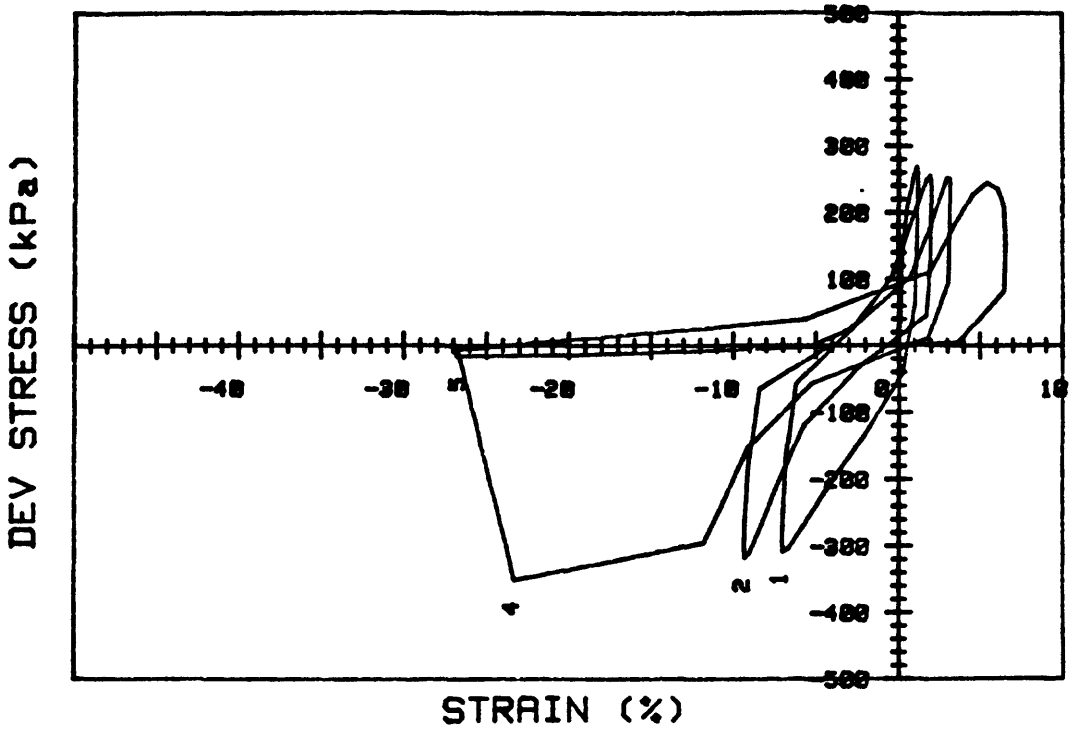

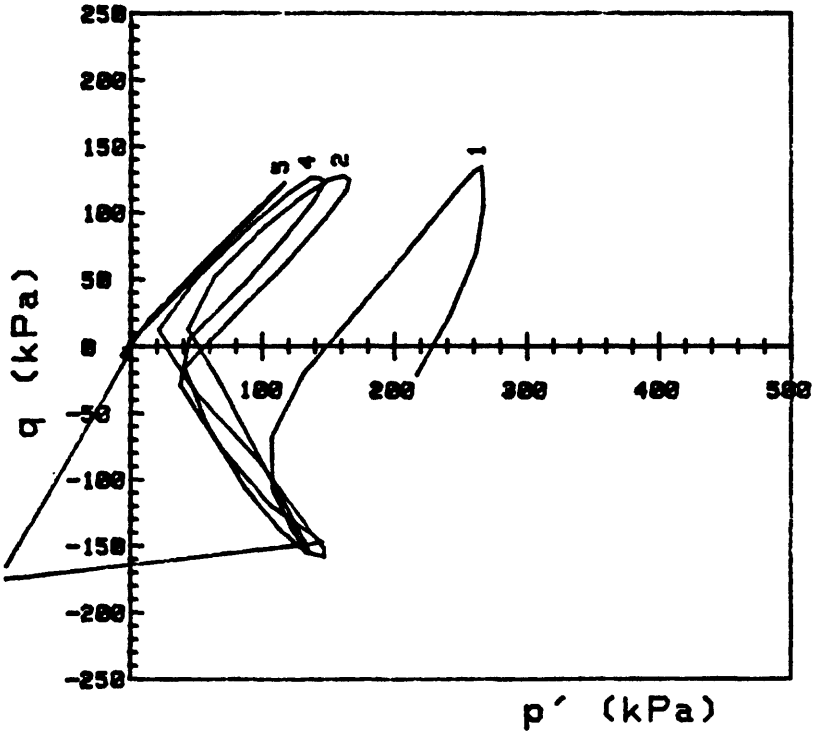

CRUISE DC4-81-NS		INCREMENT (cm)	95-106
CORE NO.	682A1	TEST NO.	TC38
SIG1c'(kPa)	238.4	STATIC qf (kPa)	183.9
SIG3c'(kPa)	238.4	AVG MAX q (kPa)	127.3 (69.2%)
INDUCED OCR	1.0	AVG MIN q (kPa)	-131.1 (71.3%)

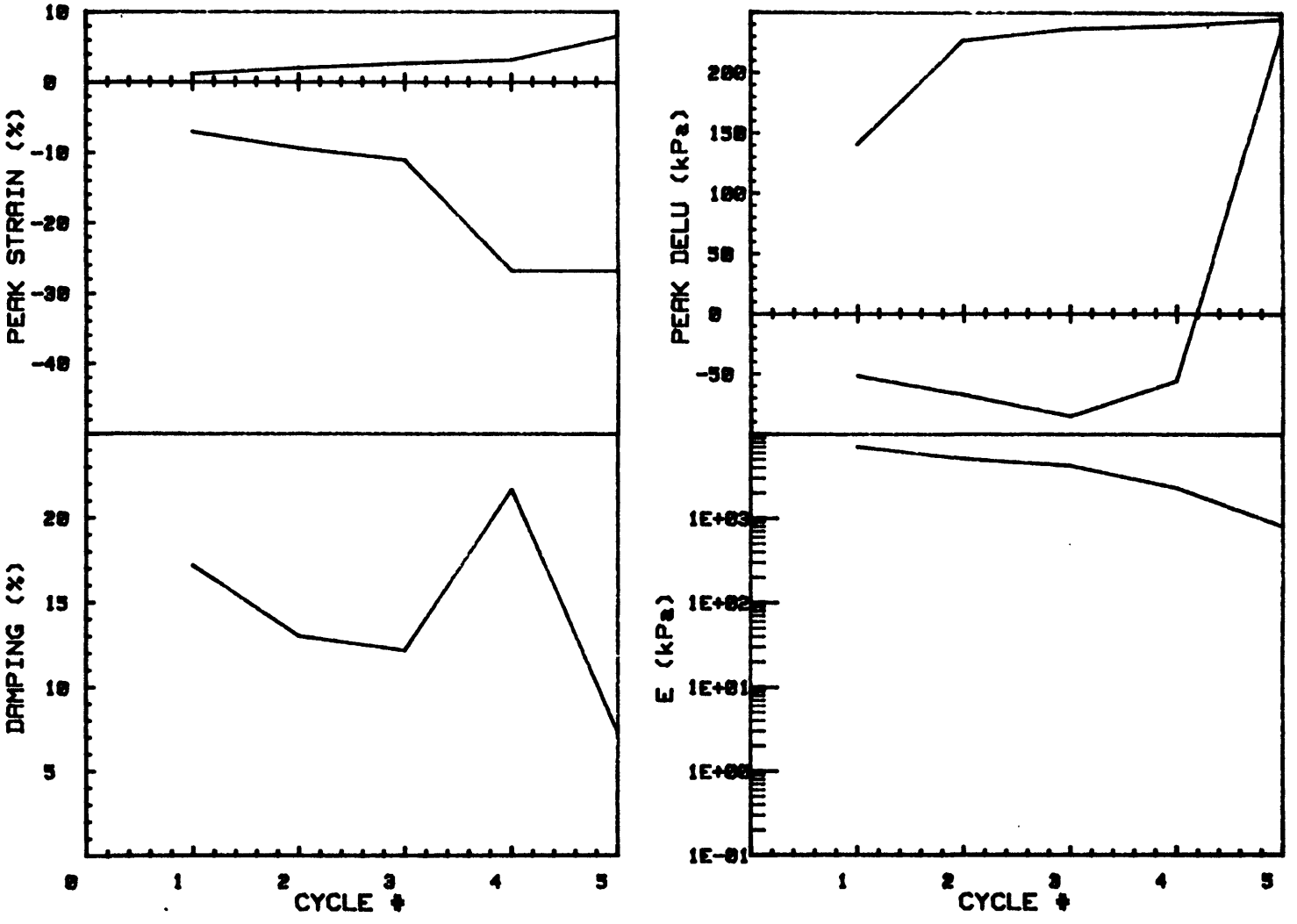

CRUISE DC4-81-NS		INCREMENT (cm)	95-106
CORE NO.	682A1	TEST NO.	TC38
SIG1c'(kPa)	238.4	STATIC qf (kPa)	183.9
SIG3c'(kPa)	238.4	AVG MAX q (kPa)	127.3 (69.2%)
INDUCED OCR	1.0	AVG MIN q (kPa)	-131.1 (71.3%)

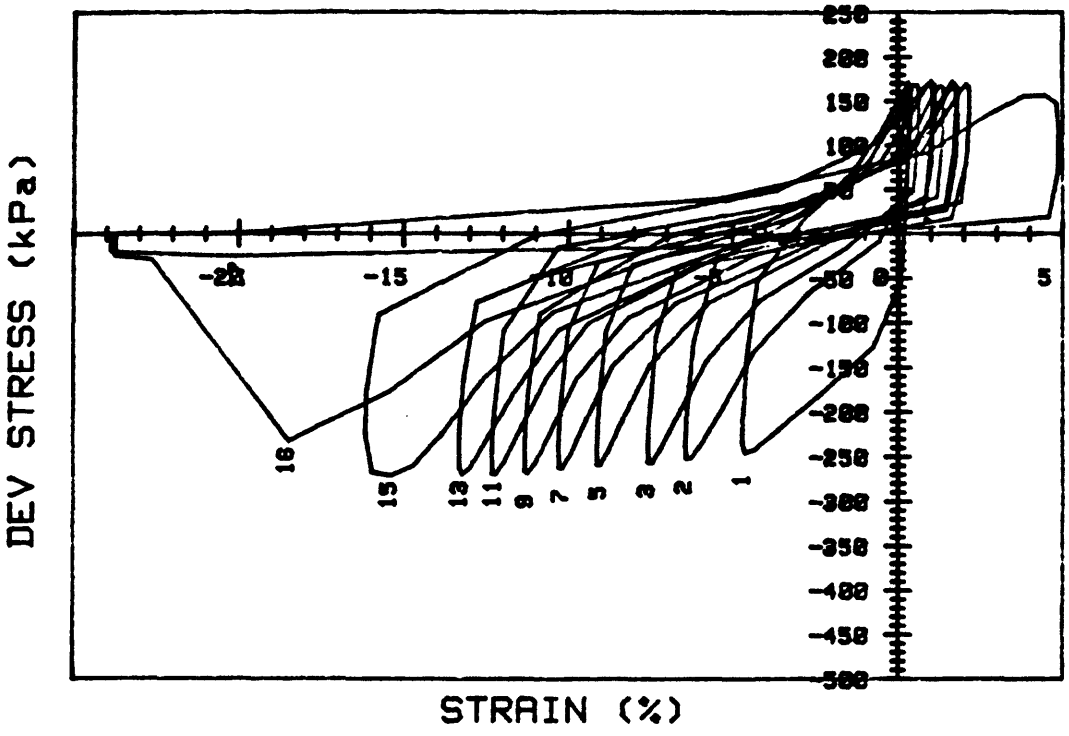

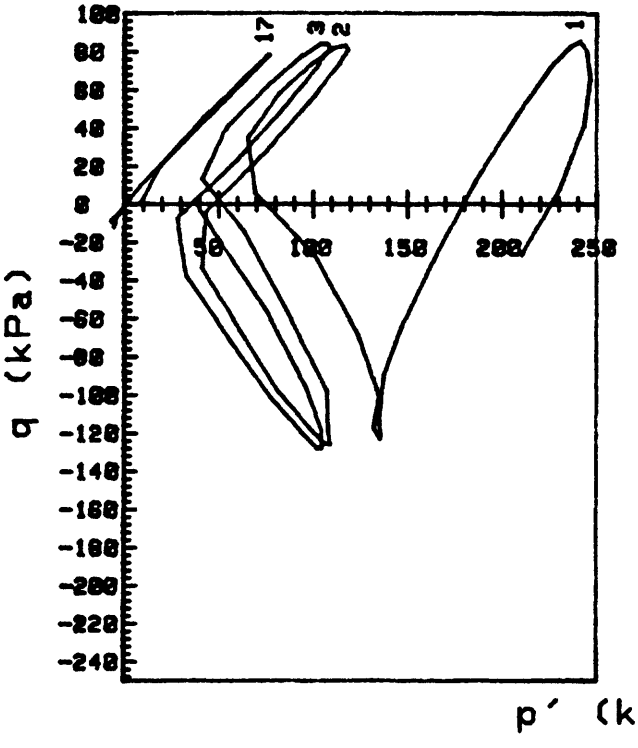

CRUISE DC4-81-NS		INCREMENT (cm)	95-106
CORE NO. 682A1		TEST NO.	TC39
SIG1c'(kPa)	237.3	STATIC qf (kPa)	183.9
SIG3c'(kPa)	237.3	AVG MAX q (kPa)	84.2 (45.8%)
INDUCED OCR	1.0	AVG MIN q (kPa)	-123.6 (67.2%)

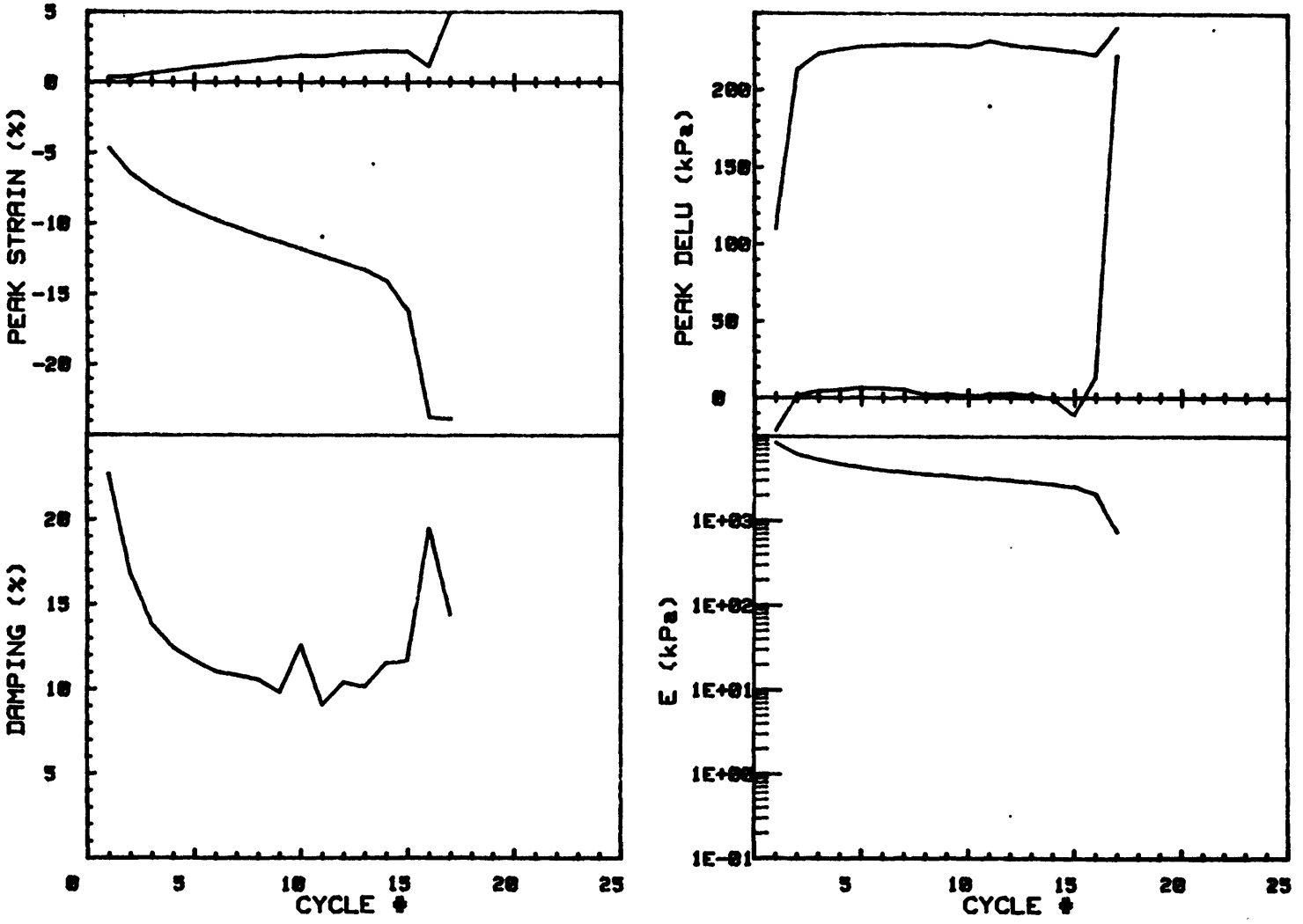

CRUISE DC4-81-NS		INCREMENT (cm)	95-106
CORE NO.	682A1	TEST NO.	TC39
SIG1c'(kPa)	237.3	STATIC qf (kPa)	183.9
SIG3c'(kPa)	237.3	AVG MAX q (kPa)	84.2 (45.8%)
INDUCED OCR	1.0	AVG MIN q (kPa)	-123.6 (67.2%)

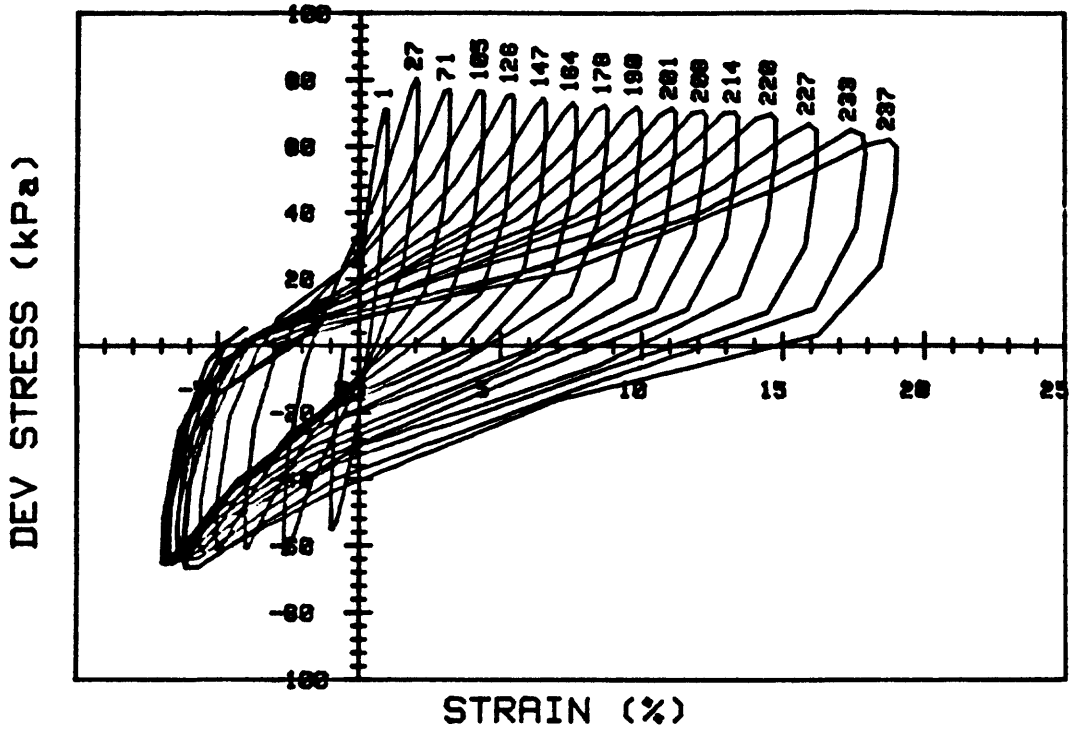

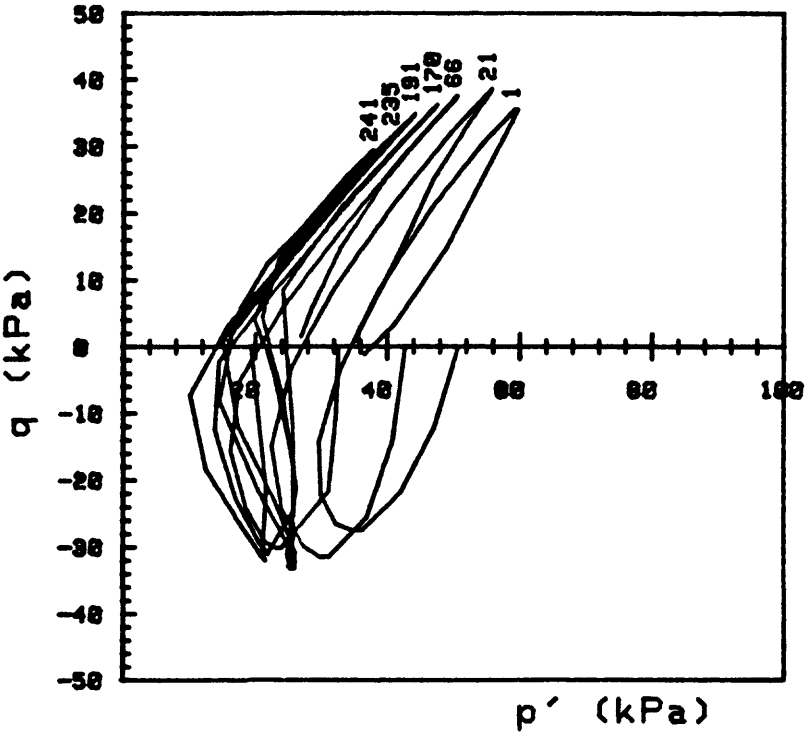

CRUISE DC4-81-NS		INCREMENT (cm)	134-142
CORE NO. 682A1		TEST NO.	TC78
SIG1c'(kPa)	37.8	STATIC qf (kPa)	82.9
SIG3c'(kPa)	37.8	AVG MAX q (kPa)	37.1 (44.8%)
INDUCED OCR	6.3	AVG MIN q (kPa)	-31.1 (37.5%)

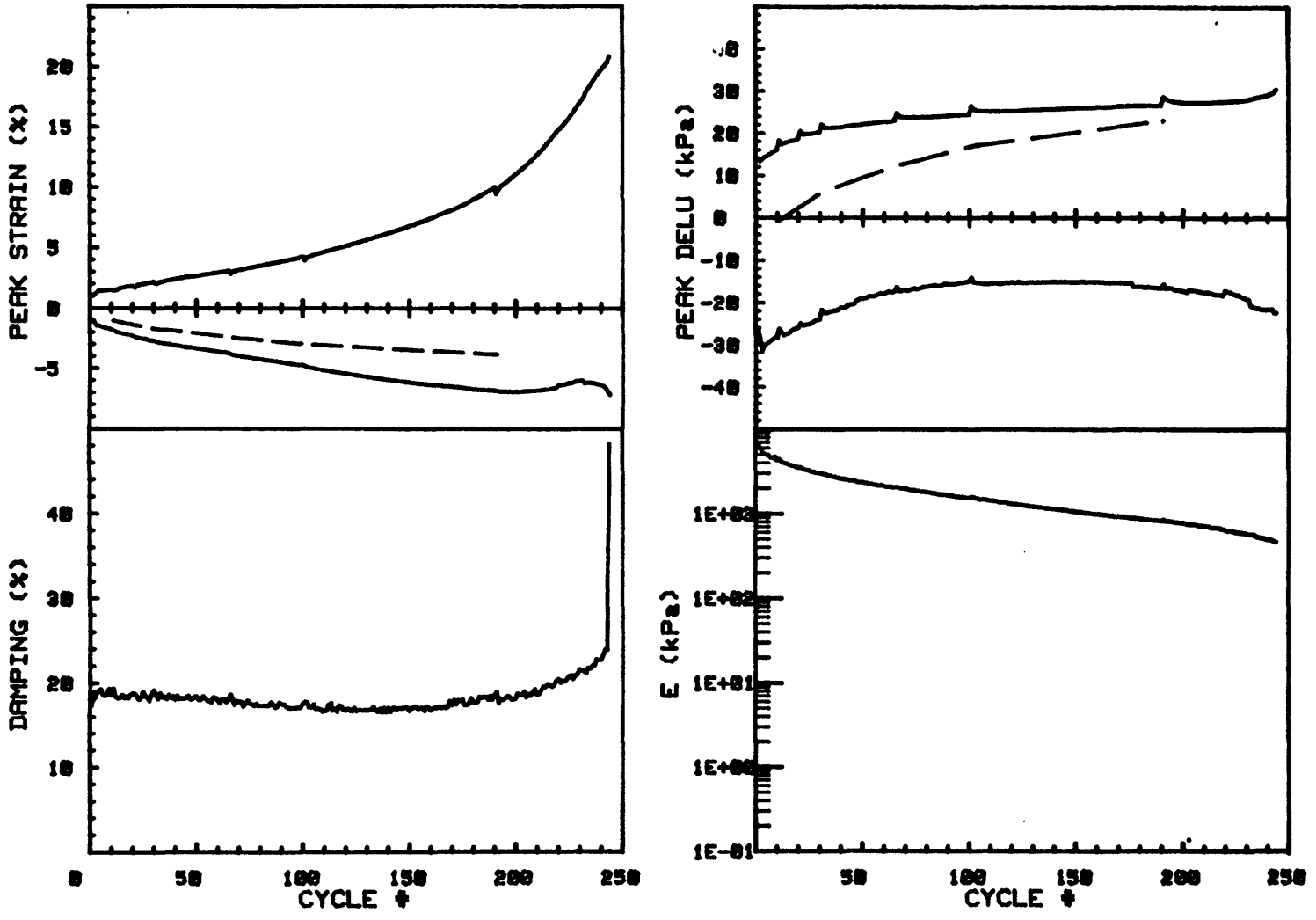

CRUISE DC4-81-NS		INCREMENT (cm)	134-142
CORE NO.	682A1	TEST NO.	TC78
SIG1c'(kPa)	37.8	STATIC qf (kPa)	82.9
SIG3c'(kPa)	37.8	AVG MAX q (kPa)	37.1 (44.8%)
INDUCED OCR	6.3	AVG MIN q (kPa)	-31.1 (37.5%)

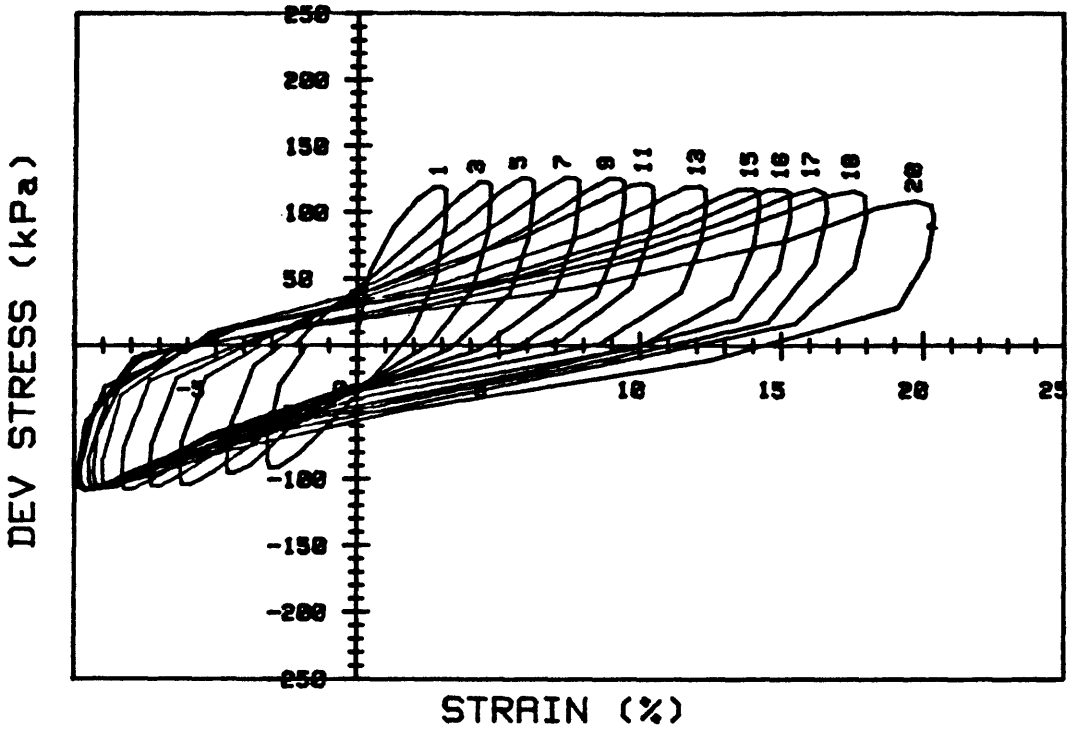

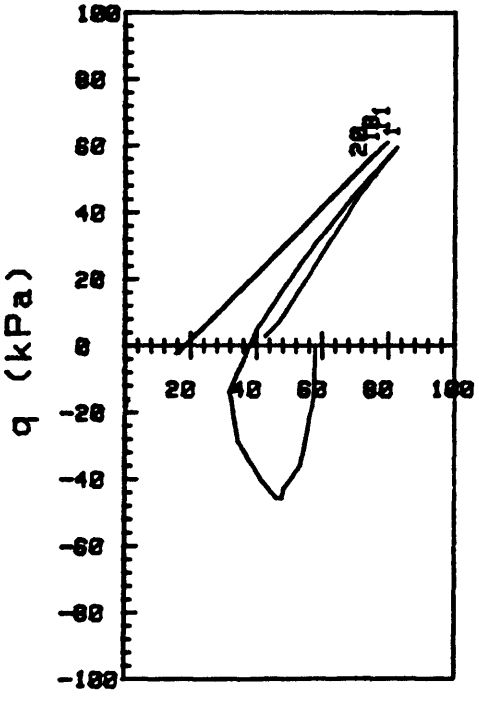

CRUISE DC4-81-NS		INCREMENT (cm)	134-142
CORE NO.	682A1	TEST NO.	TC79
SIG1c'(kPa)	39.8	STATIC qf (kPa)	82.9
SIG3c'(kPa)	39.8	AVG MAX q (kPa)	60.3 (72.7%)
INDUCED OCR	6.0	AVG MIN q (kPa)	-52.2 (63.0%)

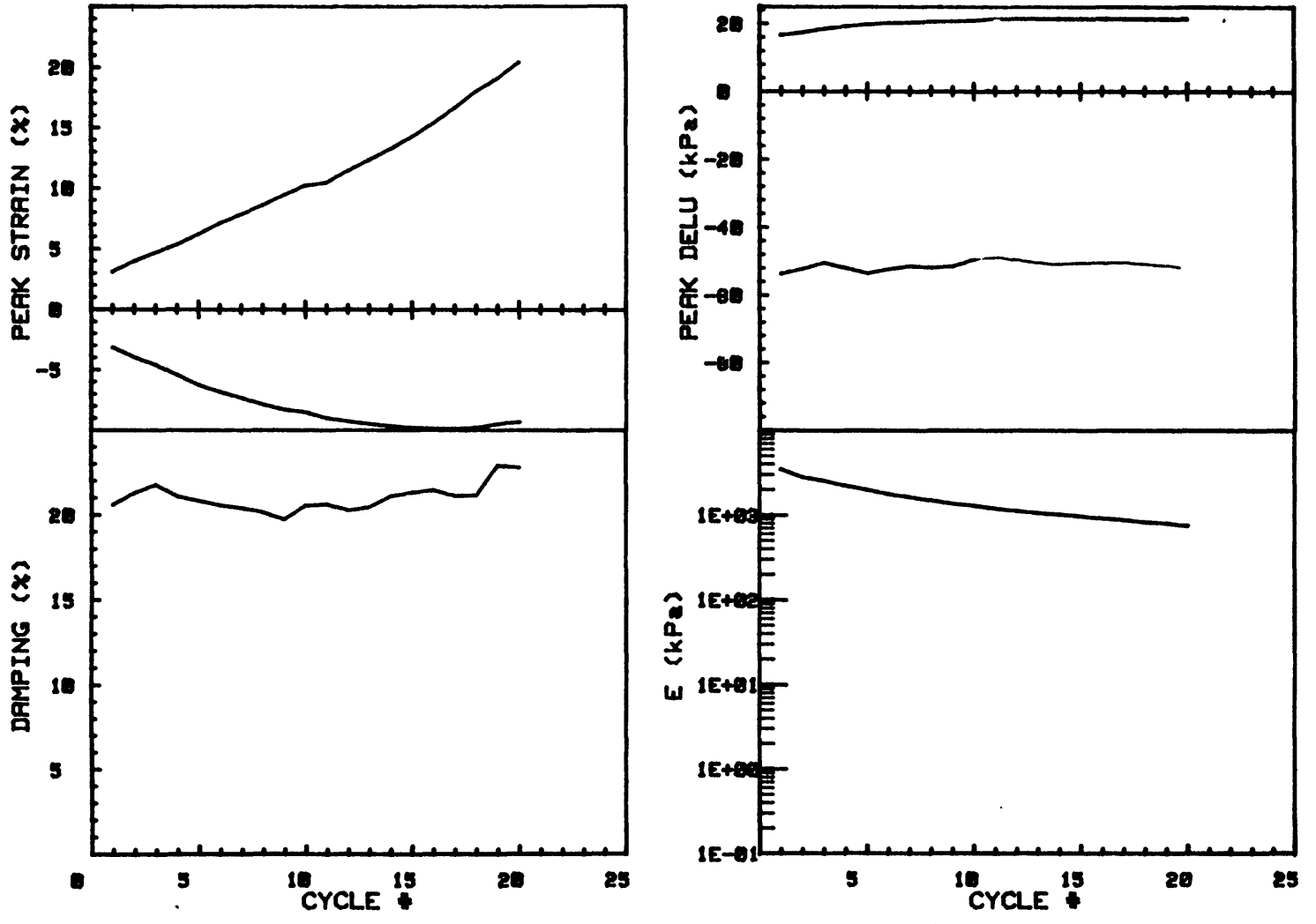

CRUISE DC4-81-NS		INCREMENT (cm)	134-142
CORE NO.	682A1	TEST NO.	TC79
SIG1c'(kPa)	39.8	STATIC qf (kPa)	82.9
SIG3c'(kPa)	39.8	AVG MAX q (kPa)	60.3 (72.7%)
INDUCED OCR	6.0	AVG MIN q (kPa)	-52.2 (63.0%)

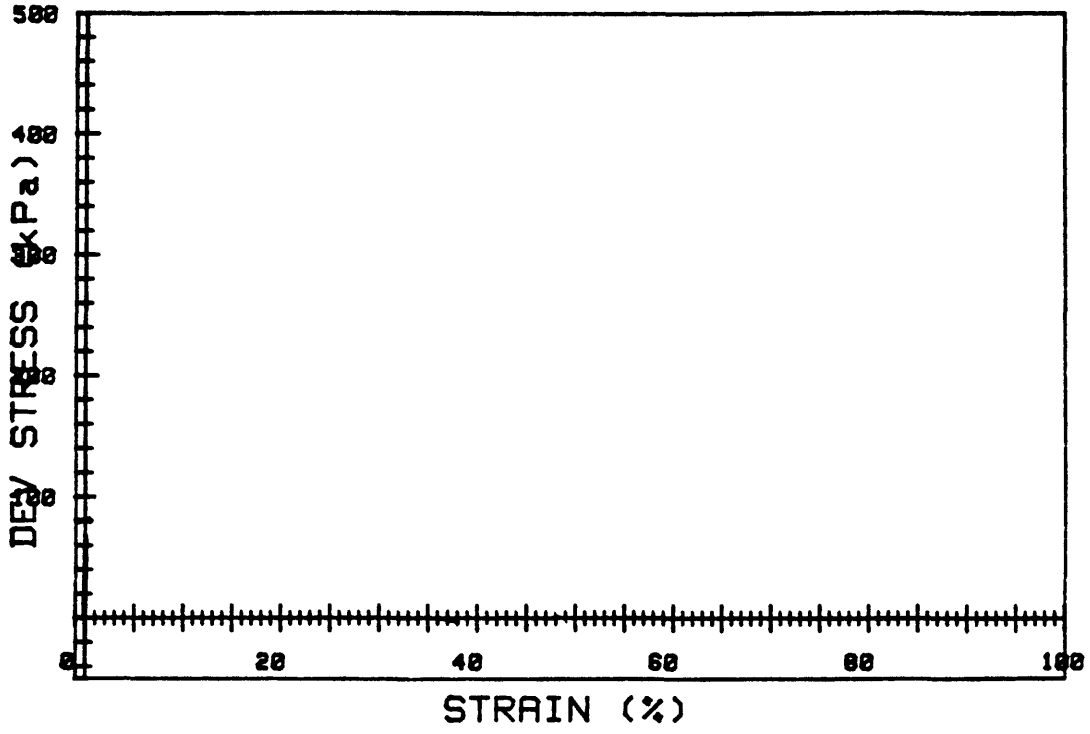

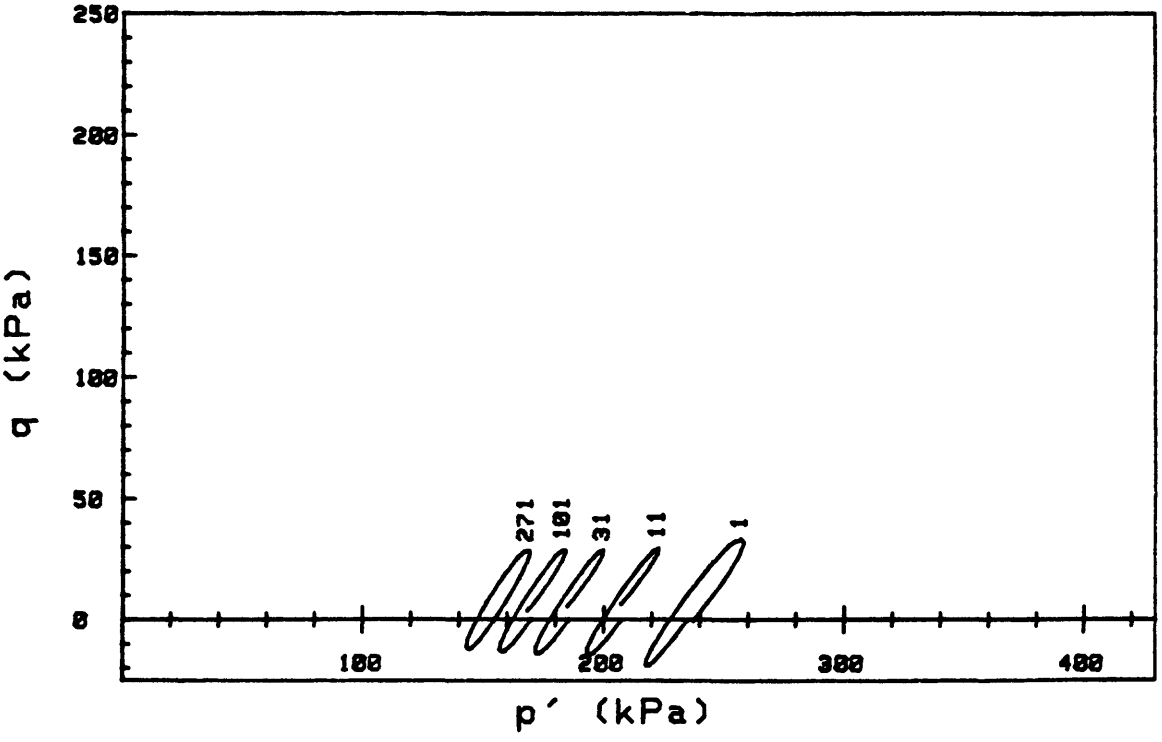

CRUISE DC4-81-NS		INCREMENT (cm)	186-193
CORE NO.	682A1	TEST NO.	TC76
SIG1c'(kPa)	238.0	STATIC qf (kPa)	93.2
SIG3c'(kPa)	233.0	AVG MAX q (kPa)	29.3 (31.4%)
INDUCED OCR	1.0	AVG MIN q (kPa)	-12.4 (13.3%)

Cycles 1 - 500

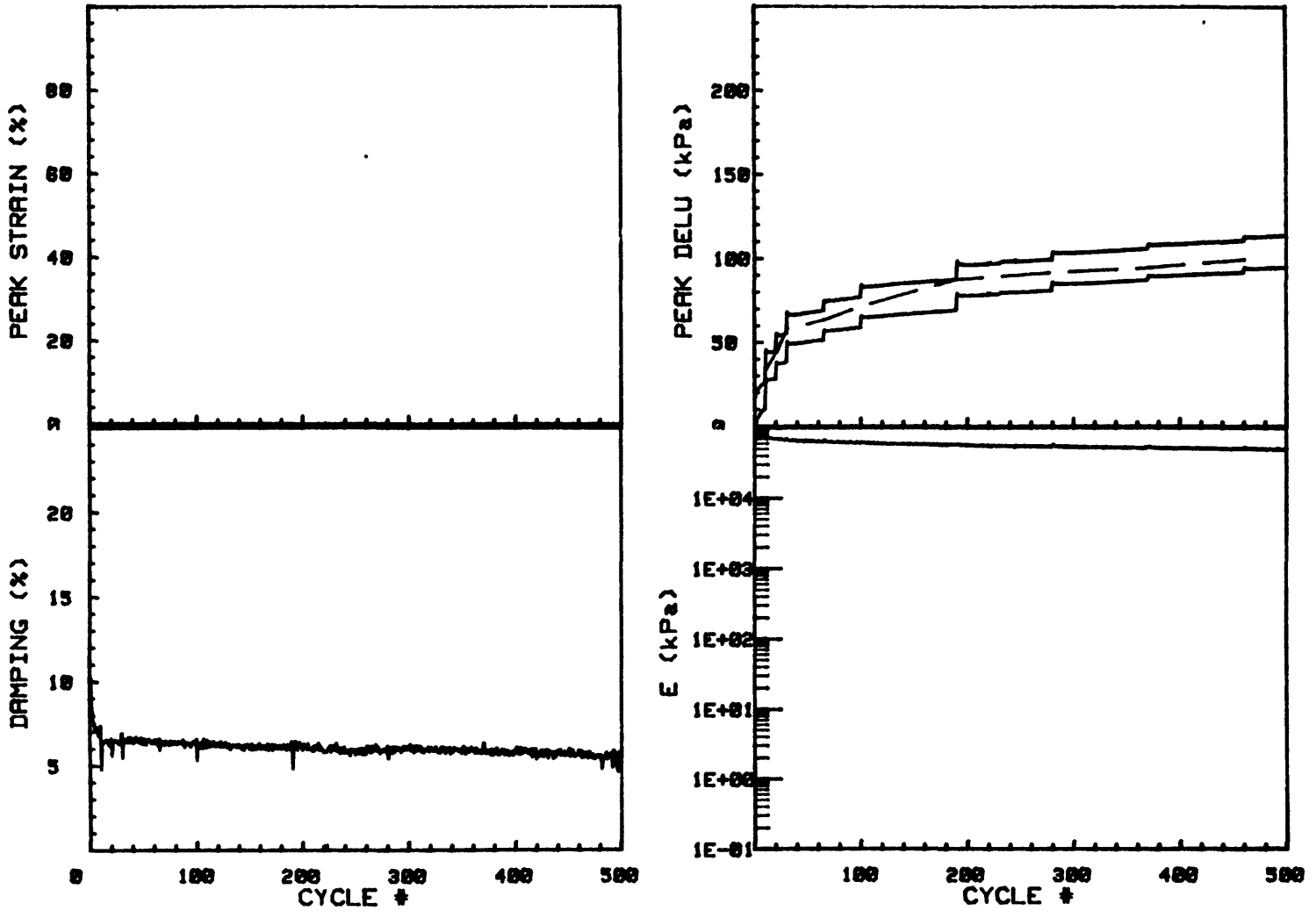

CRUISE DC4-81-NS		INCREMENT (cm)	186-193
CORE NO.	682A1	TEST NO.	TC76
SIG1c'(kPa)	238.0	STATIC qf (kPa)	93.2
SIG3c'(kPa)	238.0	AVG MAX q (kPa)	29.3 (31.4%)
INDUCED OCR	1.0	AVG MIN q (kPa)	-12.4 (13.3%)

Cycles 1 - 500

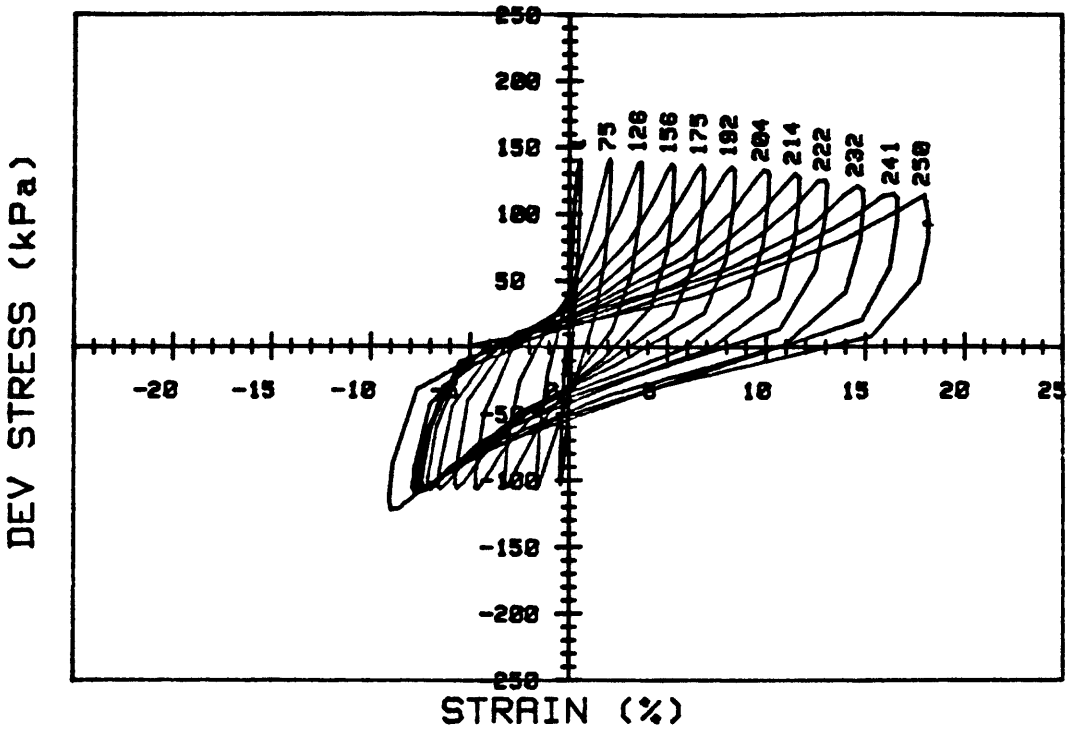

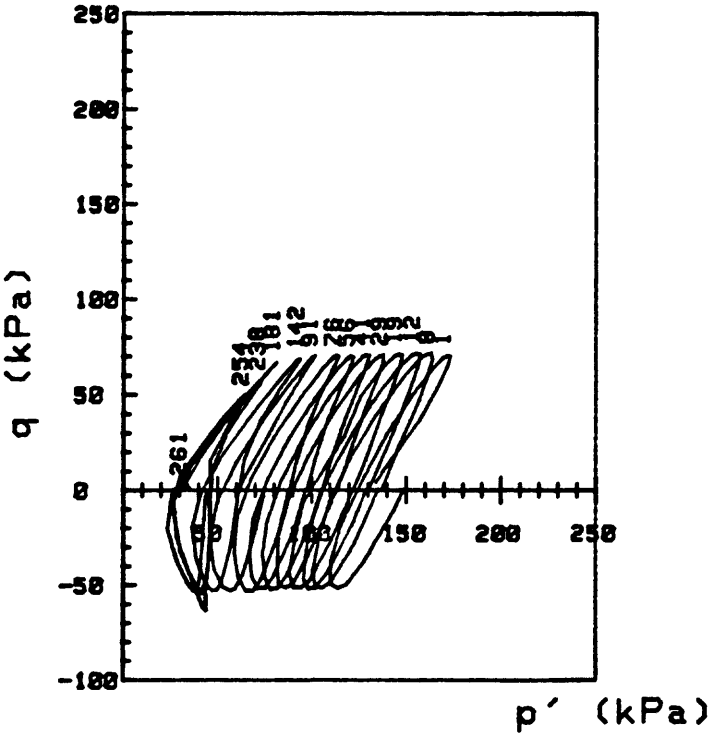

CRUISE DC4-81-NS		INCREMENT (cm)	186-193
CORE NO.	682A1	TEST NO.	TC76
SIG1c′(kPa)	130.4	STATIC qf (kPa)	93.2
SIG3c′(kPa)	130.4	AVG MAX q (kPa)	67.3 (72.2%)
INDUCED OCR	1.0	AVG MIN q (kPa)	-53.2 (57.1%)

Cycles 501 - 761

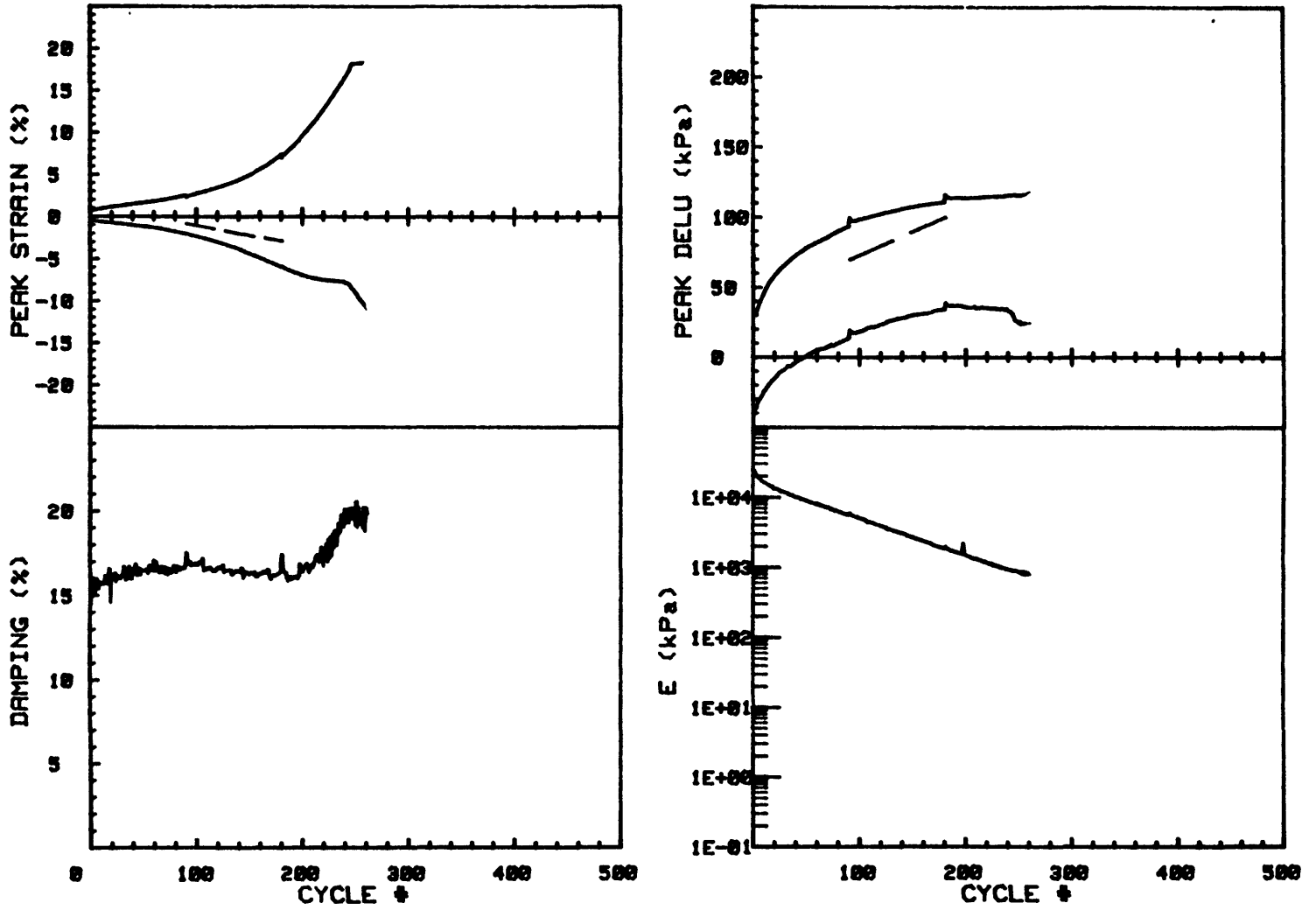

CRUISE DC4-81-NS		INCREMENT (cm)	186-193
CORE NO. 682A1		TEST NO.	TC76
SIG1c'(kPa)	130.4	STATIC qf (kPa)	93.2
SIG3c'(kPa)	130.4	AVG MAX q (kPa)	67.3 (72.2%)
INDUCED OCR	1.0	AVG MIN q (kPa)	-53.2 (57.1%)

Cycles 501 - 761

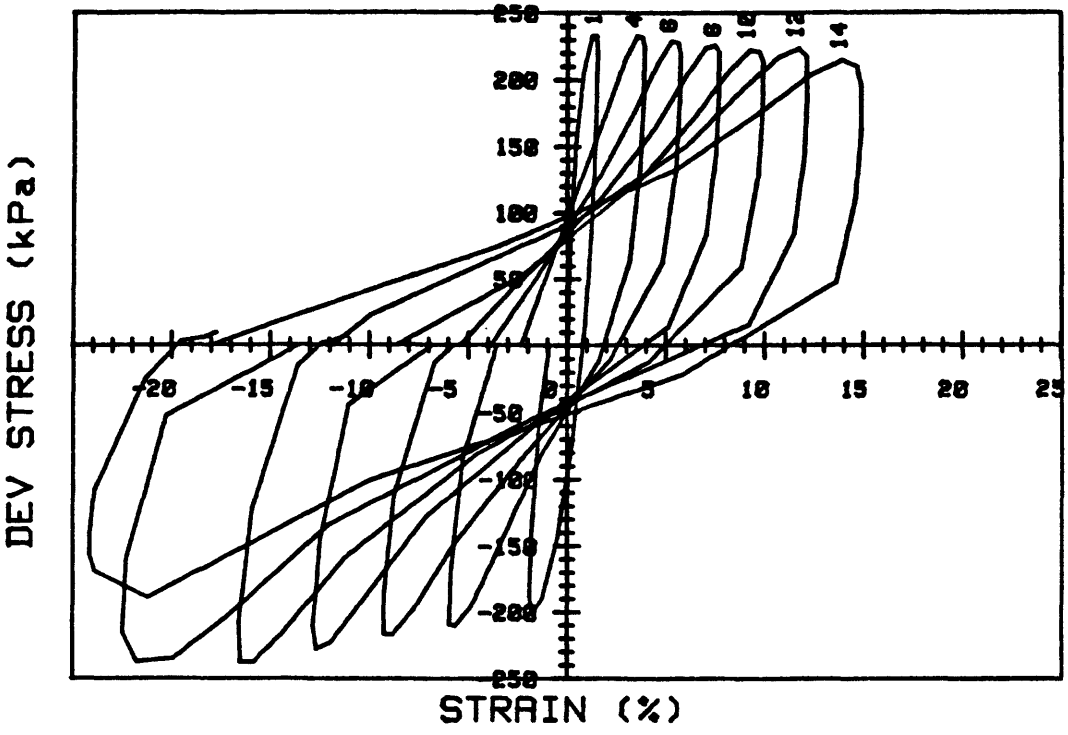

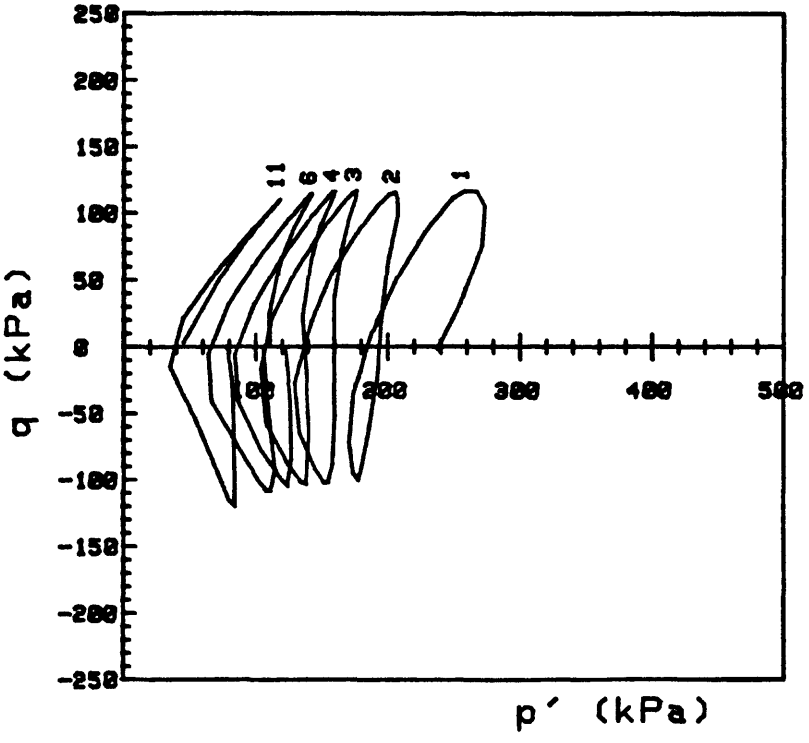

CRUISE DC4-81-NS		INCREMENT (cm)	186-194
CORE NO.	682A1	TEST NO.	TC77
SIG1c'(kPa)	239.1	STATIC qf (kPa)	93.2
SIG3c'(kPa)	239.1	AVG MAX q (kPa)	113.0 (121.2%)
INDUCED OCR	1.0	AVG MIN q (kPa)	-108.9 (116.8%

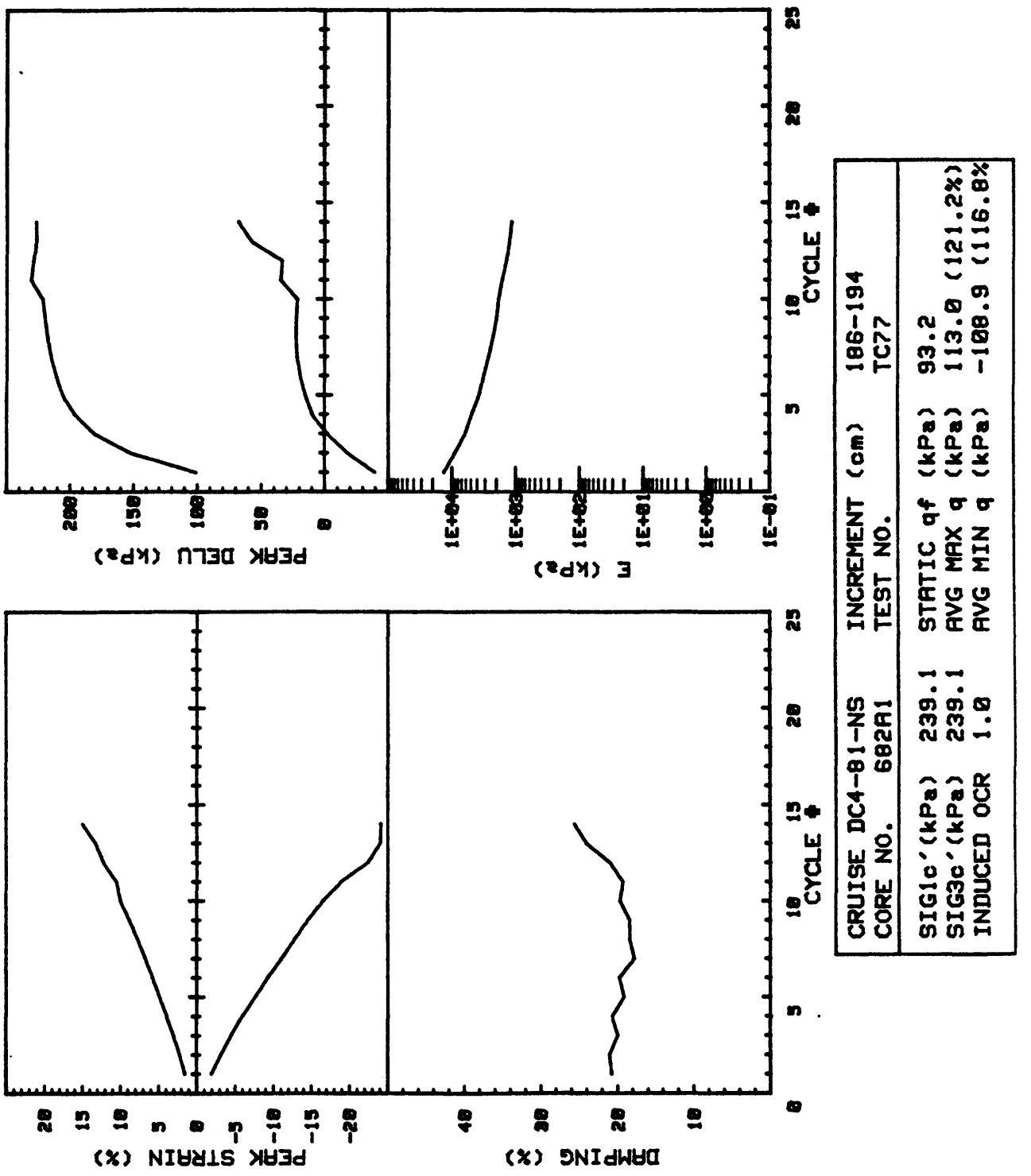
PEAK DELU (kPa)
E (kPa)
CYCLE #
PEAK STRAIN (%)
DAMPING (%)
CRUISE DC4-81-NS
CORE NO. 682A1
INCREMENT (cm) 186-194
TEST NO. TC77
SIG1c'(kPa) 239.1
SIG3c'(kPa) 239.1
INDUCED OCR 1.0
STATIC qf (kPa) 93.2
AVG MAX q (kPa) 113.0 (121.2%)
AVG MIN q (kPa) -108.9 (116.8%

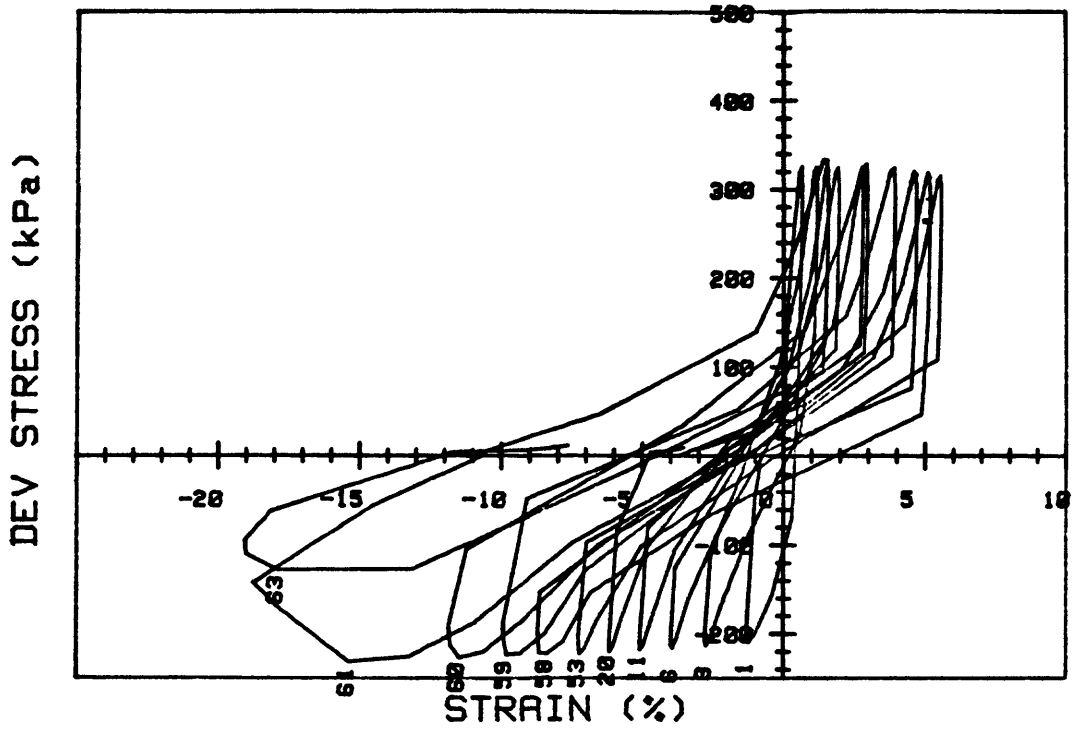

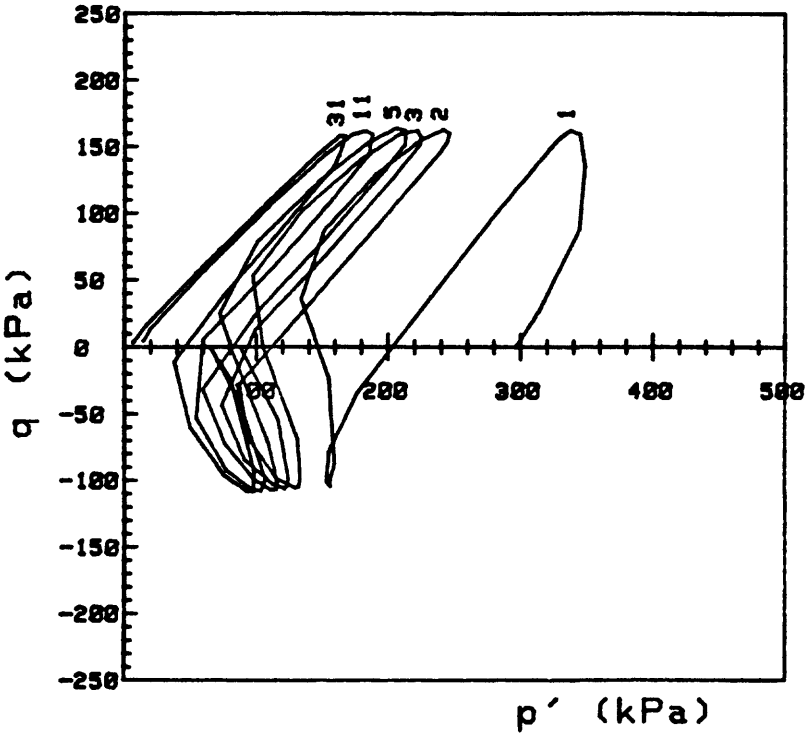

CRUISE DC4-81-NS		INCREMENT (cm)	62-70
CORE NO. 684A1		TEST NO.	TC90
SIG1c'(kPa)	296.6	STATIC qf (kPa)	300.0
SIG3c'(kPa)	296.6	AVG MAX q (kPa)	160.4 (53.5%)
INDUCED OCR	1.0	AVG MIN q (kPa)	-108.2 (36.1%)

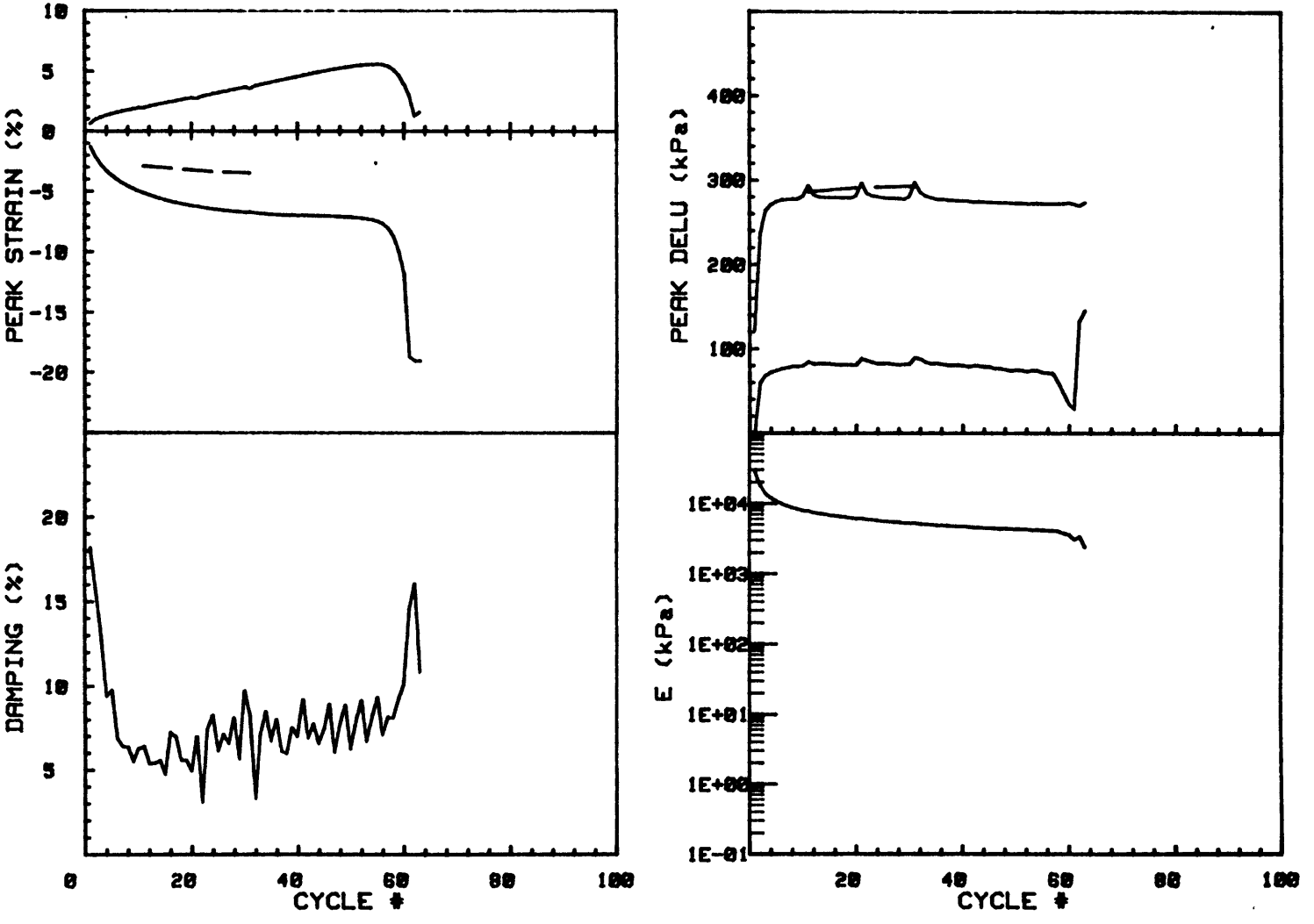

CRUISE DC4-81-NS		INCREMENT (cm)	62-70
CORE NO.	684A1	TEST NO.	TC90
SIG1c'(kPa)	296.6	STATIC qf (kPa)	300.0
SIG3c'(kPa)	296.6	AVG MAX q (kPa)	160.4 (53.5%)
INDUCED OCR	1.0	AVG MIN q (kPa)	-108.2 (36.1%)

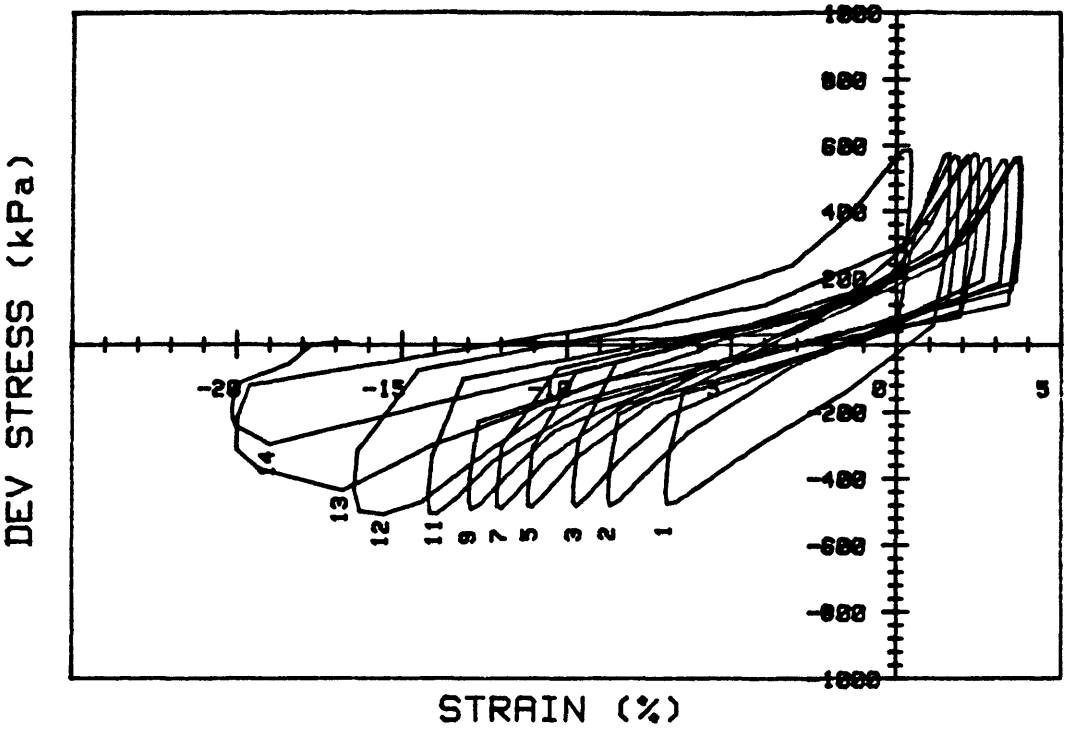

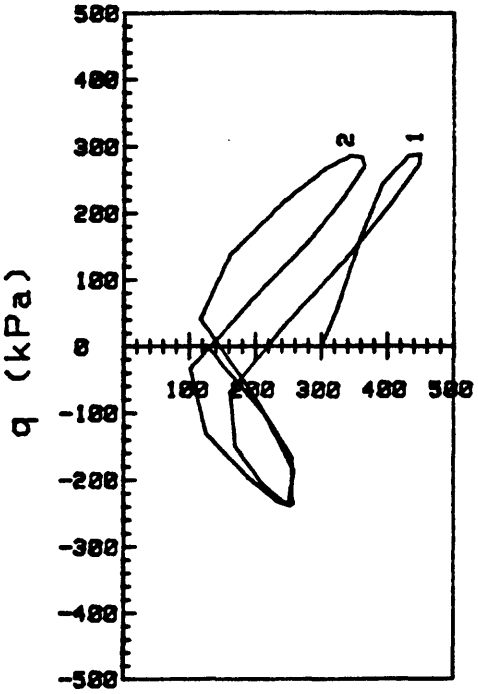

CRUISE DC4-81-NS		INCREMENT (cm)	62-70
CORE NO. 684A1		TEST NO.	TC91
SIG1c'(kPa)	297.2	STATIC qf (kPa)	300.0
SIG3c'(kPa)	297.2	AVG MAX q (kPa)	281.8 (93.9%)
INDUCED OCR	1.0	AVG MIN q (kPa)	-236.5 (78.8%)

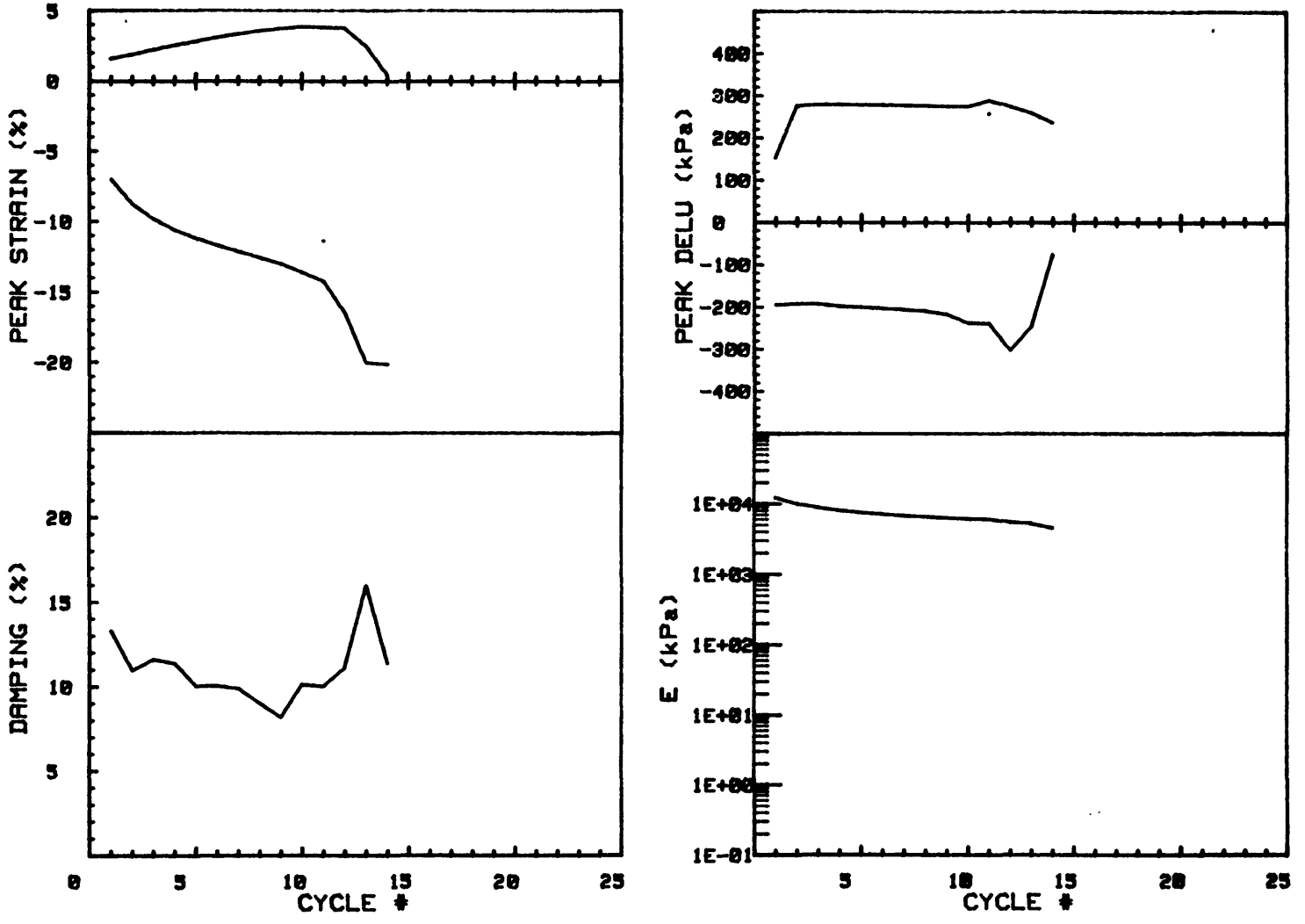

CRUISE DC4-81-NS		INCREMENT (cm)	62-70
CORE NO.	684A1	TEST NO.	TC91
SIG1c'(kPa)	297.2	STATIC qf (kPa)	300.0
SIG3c'(kPa)	297.2	AVG MAX q (kPa)	281.8 (93.9%)
INDUCED OCR	1.0	AVG MIN q (kPa)	-236.5 (78.8%)

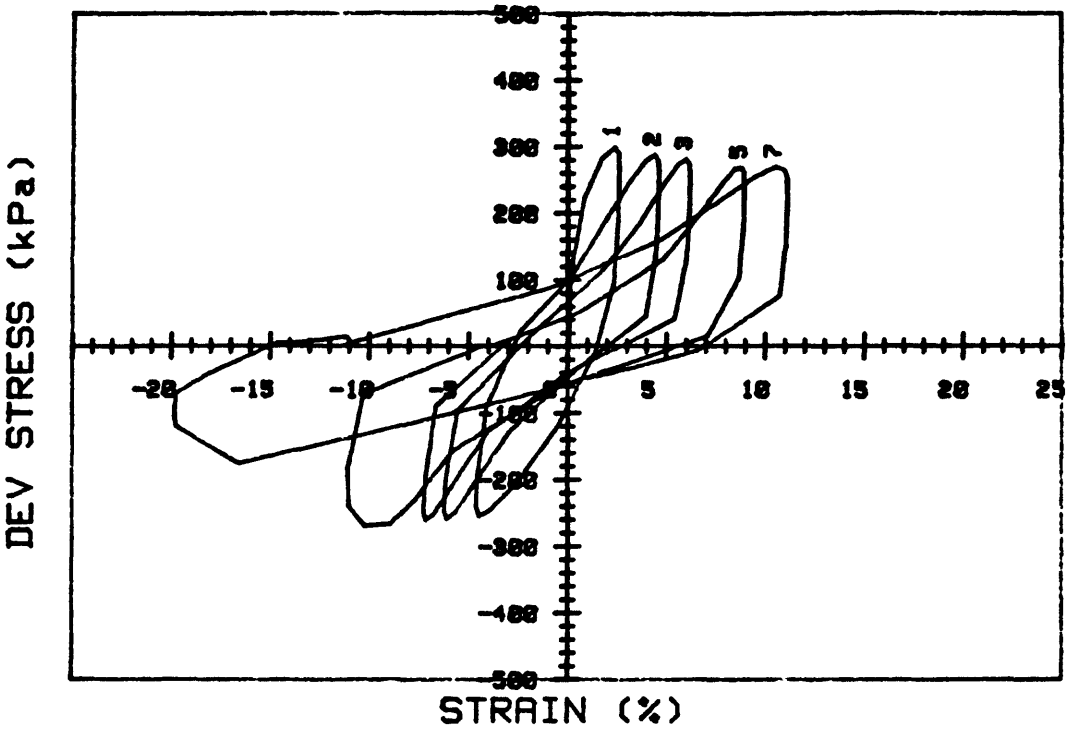

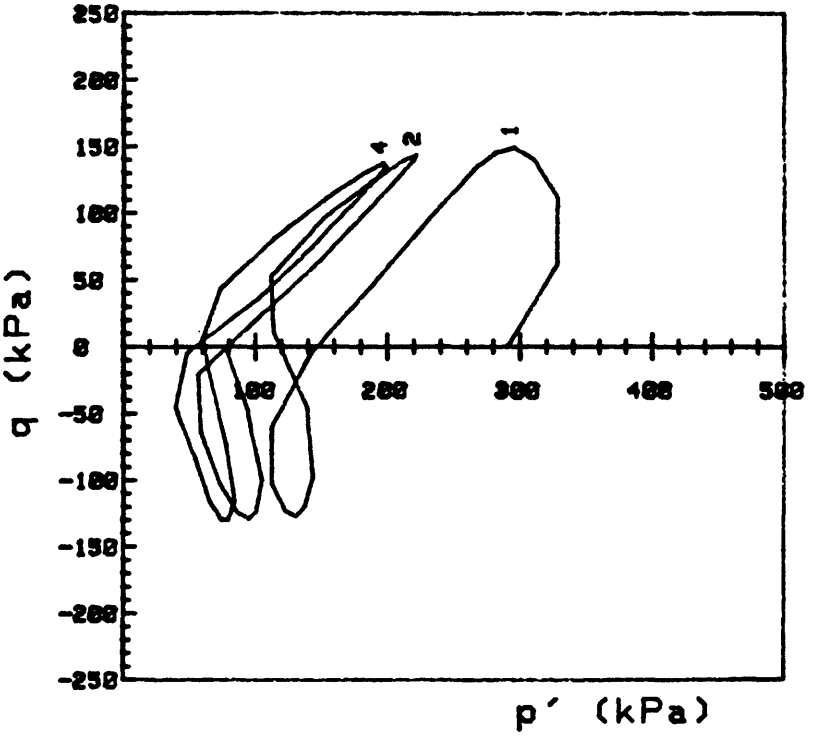

CRUISE DC4-81-NS		INCREMENT (cm)	30-37
CORE NO. 685A2		TEST NO.	D111
SIG1c'(kPa)	292.6	STATIC qf (kPa)	300.0
SIG3c'(kPa)	292.6	AVG MAX q (kPa)	139.3 (46.4%)
INDUCED OCR	1.0	AVG MIN q (kPa)	-122.4 (40.8%)

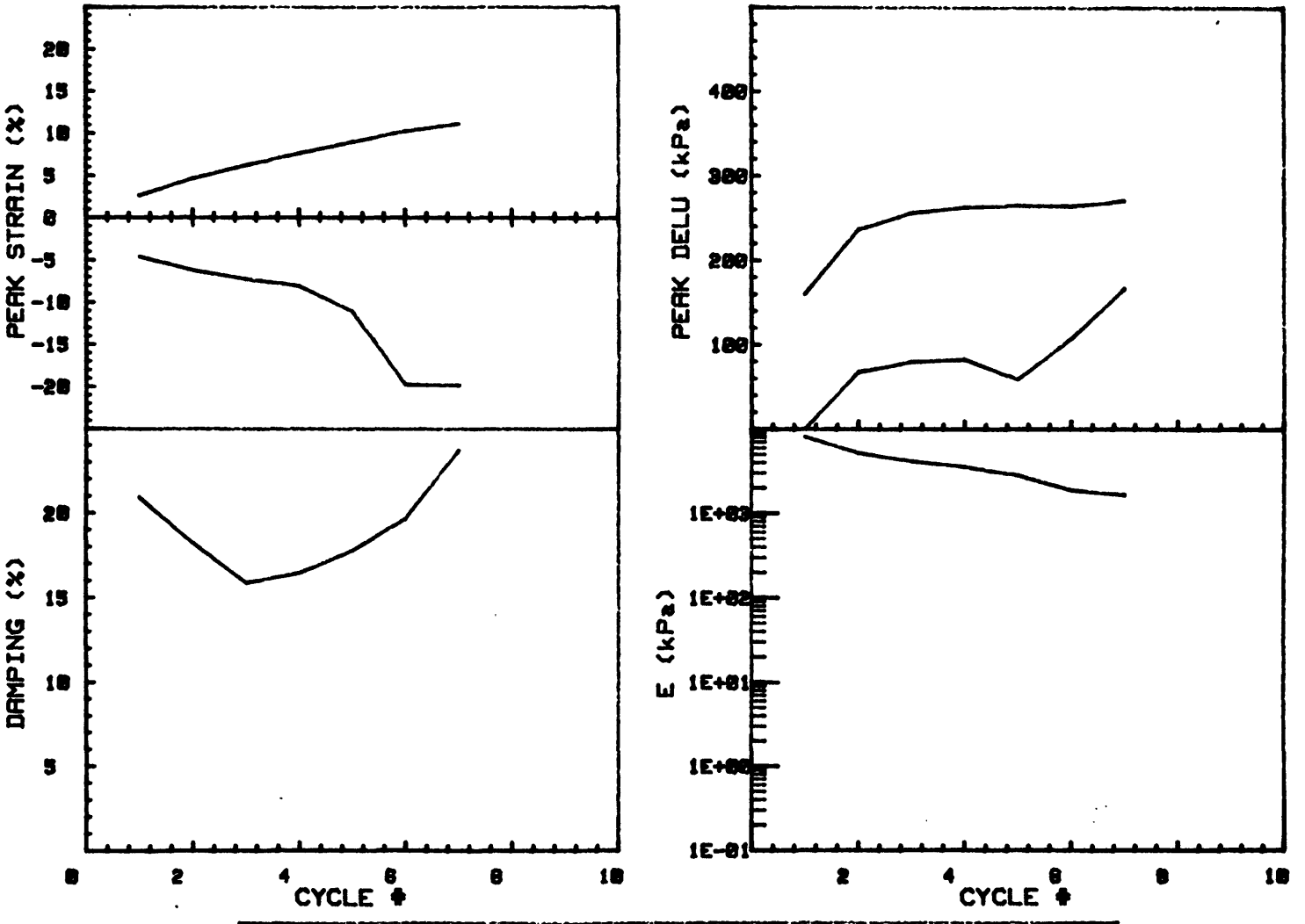

CRUISE DC4-81-NS		INCREMENT (cm)	30-37
CORE NO.	685A2	TEST NO.	D111
SIG1c'(kPa)	292.6	STATIC qf (kPa)	300.0
SIG3c'(kPa)	292.6	AVG MAX q (kPa)	139.3 (46.4%)
INDUCED OCR	1.0	AVG MIN q (kPa)	-122.4 (40.8%)

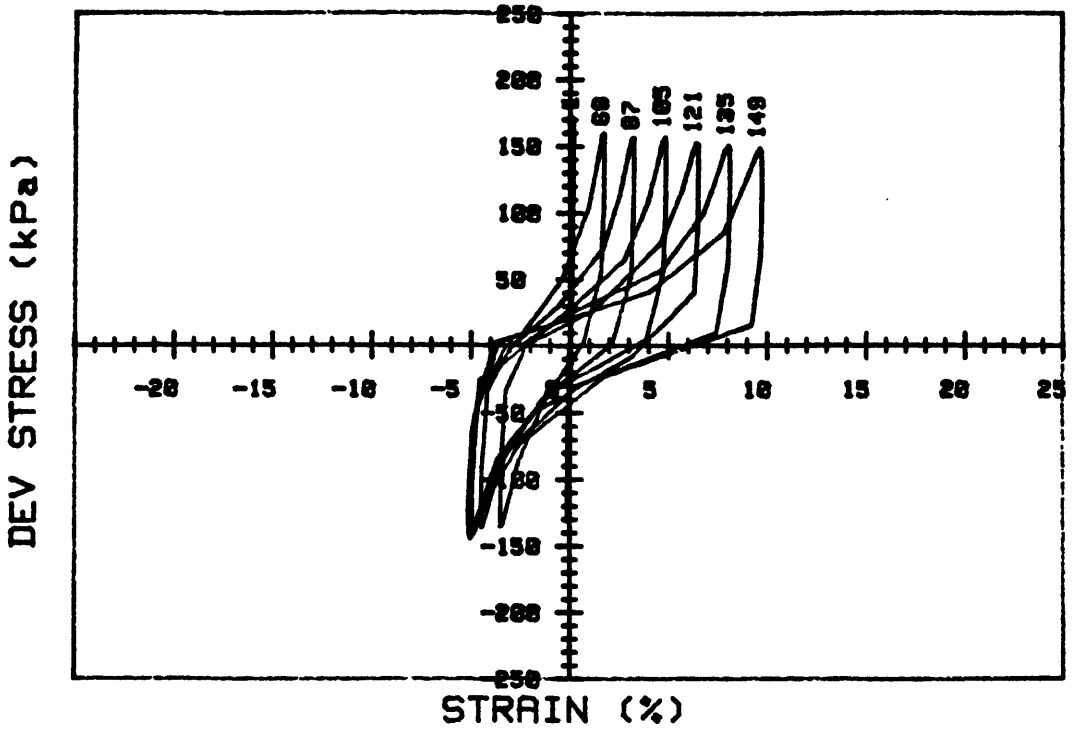

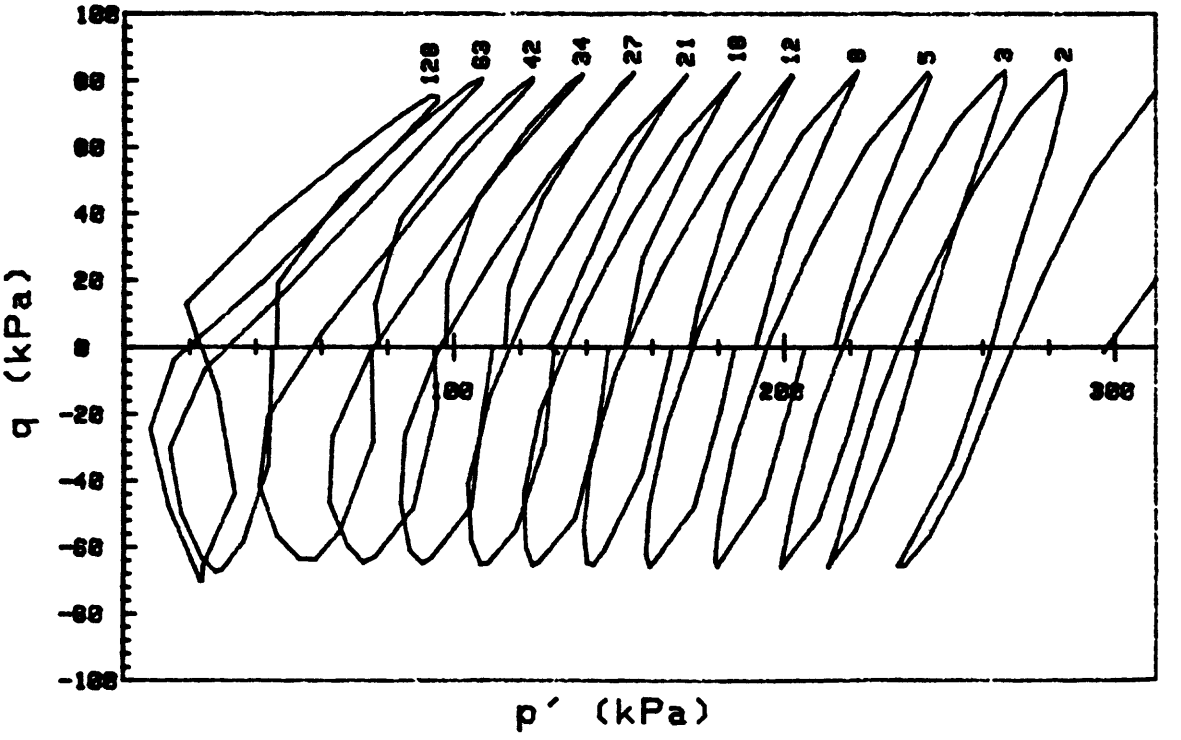

CRUISE DC4-81-NS		INCREMENT (cm)	30-37
CORE NO. 685A2		TEST NO.	D112
SIG1c'(kPa)	298.0	STATIC qf (kPa)	300.0
SIG3c'(kPa)	298.0	AVG MAX q (kPa)	78.6 (26.2%)
INDUCED OCR	1.0	AVG MIN q (kPa)	-68.0 (22.7%)

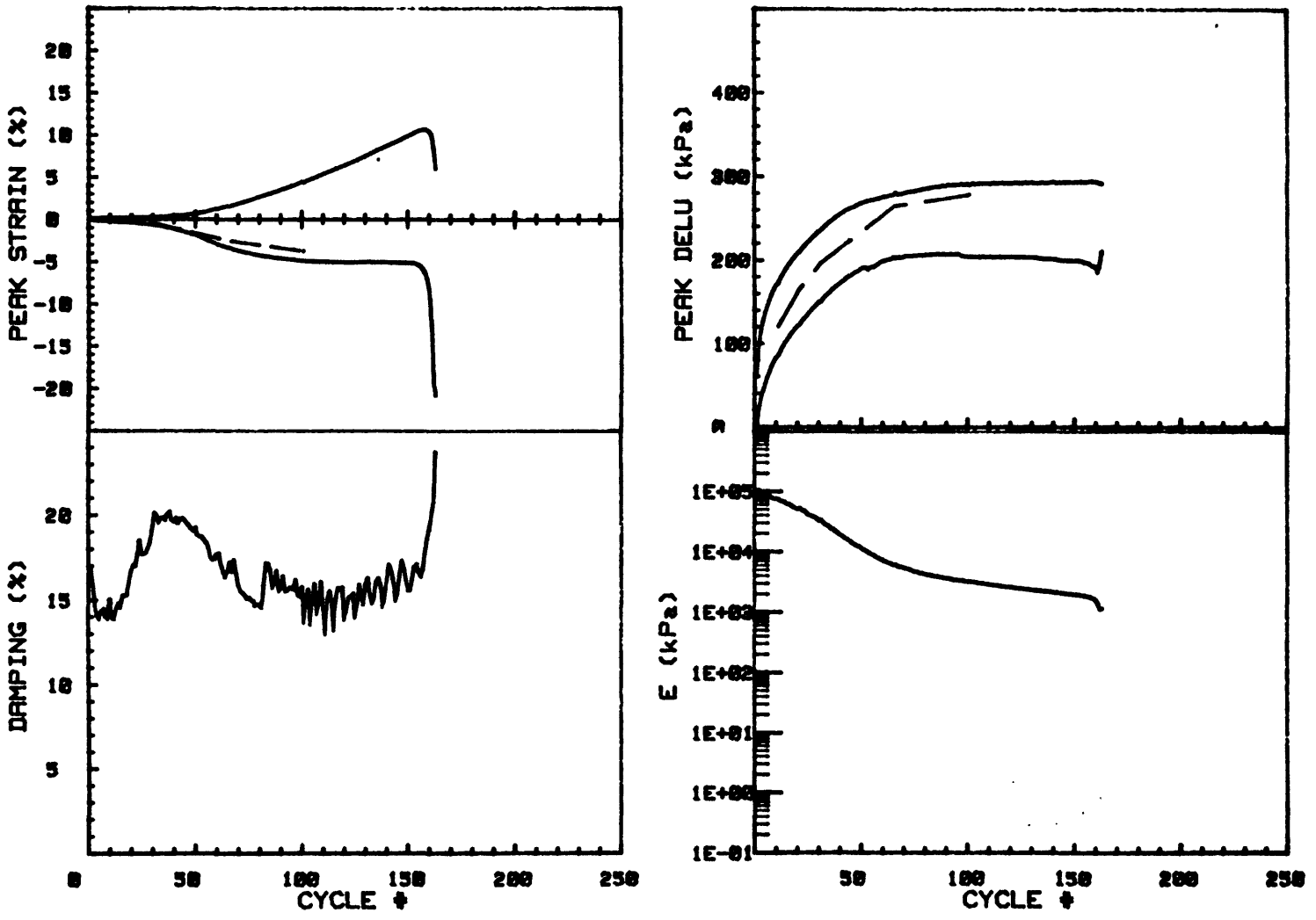

CRUISE DC4-81-NS		INCREMENT (cm)	30-37
CORE NO.	685A2	TEST NO.	D112
SIG1c'(kPa)	298.0	STATIC qf (kPa)	300.0
SIG3c'(kPa)	298.0	AVG MAX q (kPa)	78.6 (26.2%)
INDUCED OCR	1.0	AVG MIN q (kPa)	-68.0 (22.7%)

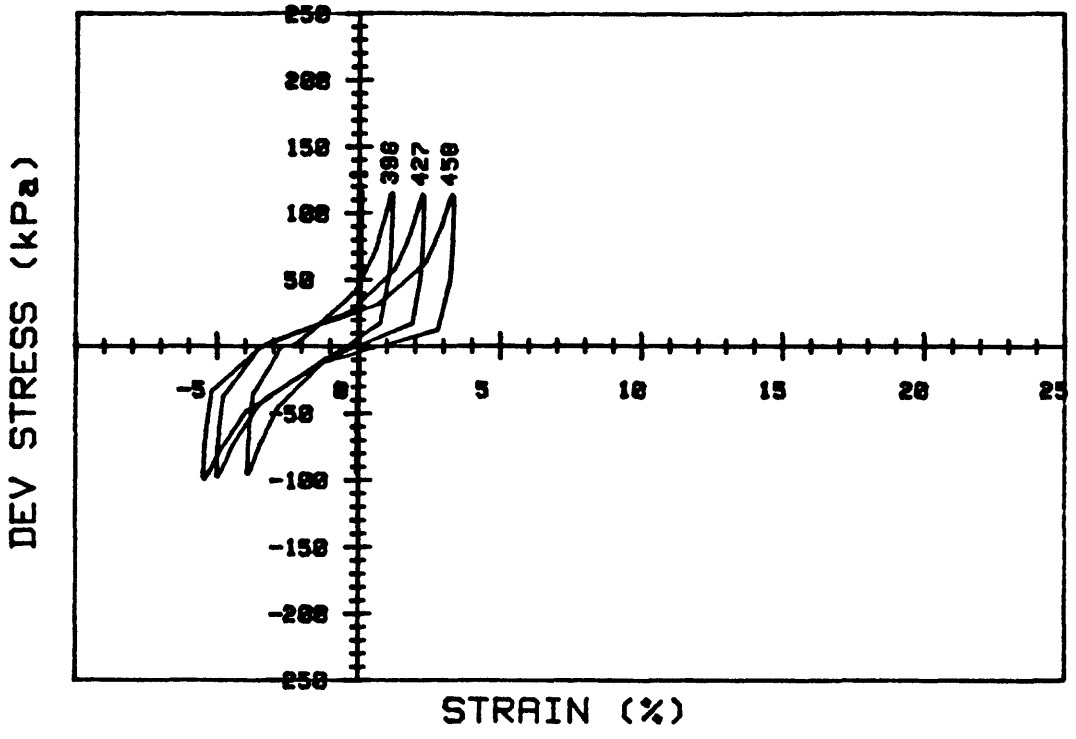

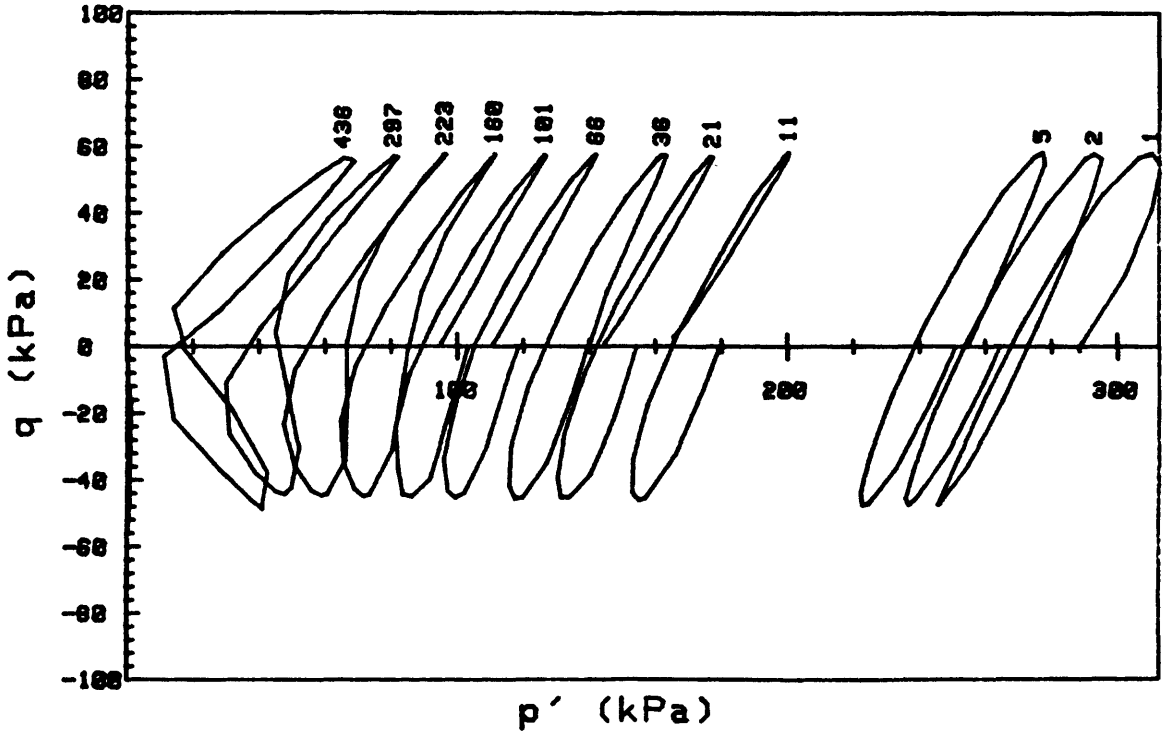

CRUISE DC4-81-NS		INCREMENT (cm)	40-48
CORE NO.	685A2	TEST NO.	TC80
SIG1c′(kPa)	289.8	STATIC qf (kPa)	300.0
SIG3c′(kPa)	289.8	AVG MAX q (kPa)	56.5 (18.8%)
INDUCED OCR	1.0	AVG MIN q (kPa)	-46.8 (15.6%)

Cycles 1 - 640

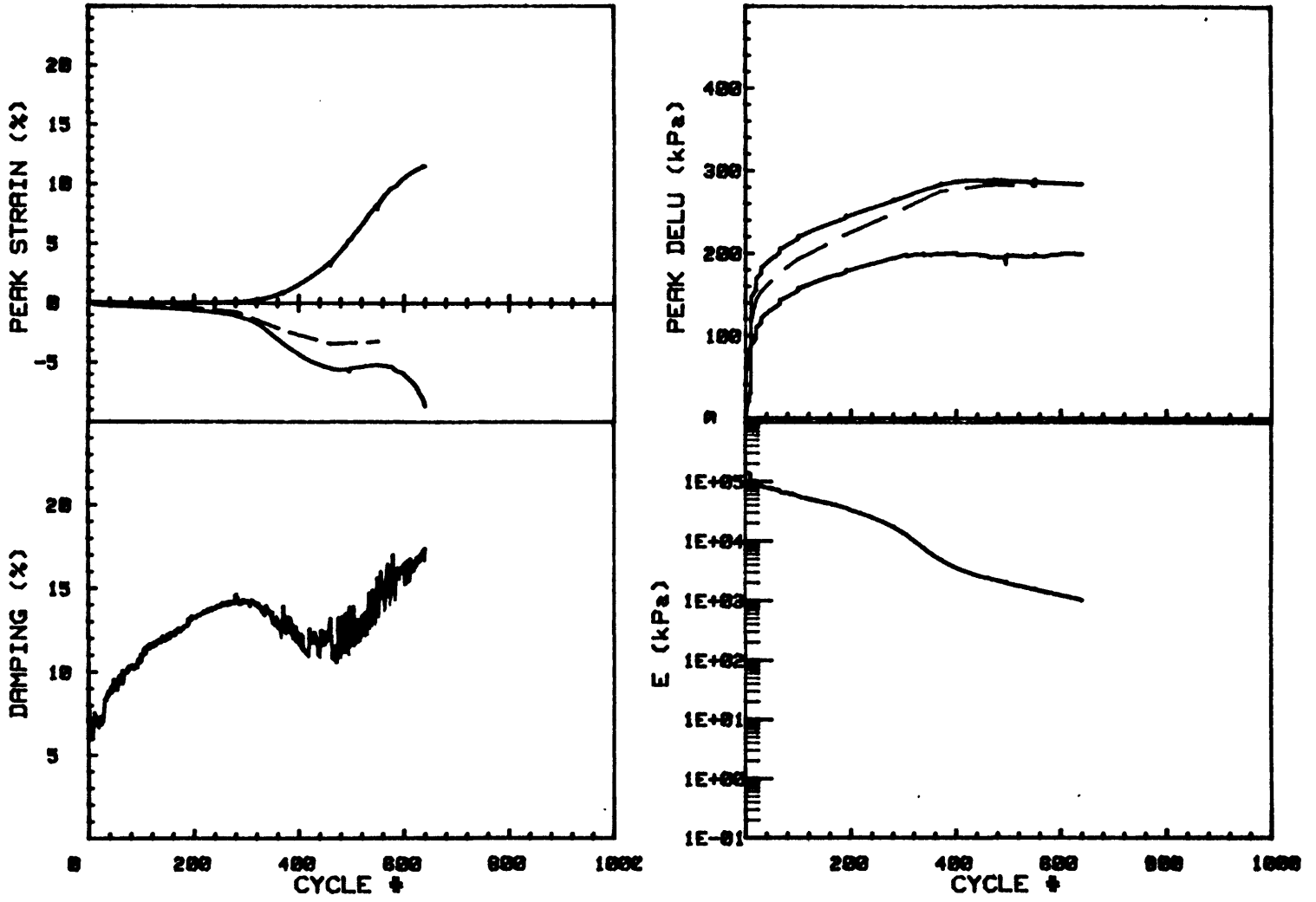

CRUISE DC4-81-NS		INCREMENT (cm)	40-48
CORE NO.	685A2	TEST NO.	TC80
SIG1c'(kPa)	289.8	STATIC qf (kPa)	300.0
SIG3c'(kPa)	289.8	AVG MAX q (kPa)	56.5 (18.8%)
INDUCED OCR	1.0	AVG MIN q (kPa)	-46.8 (15.6%)

Cycles 1 - 640

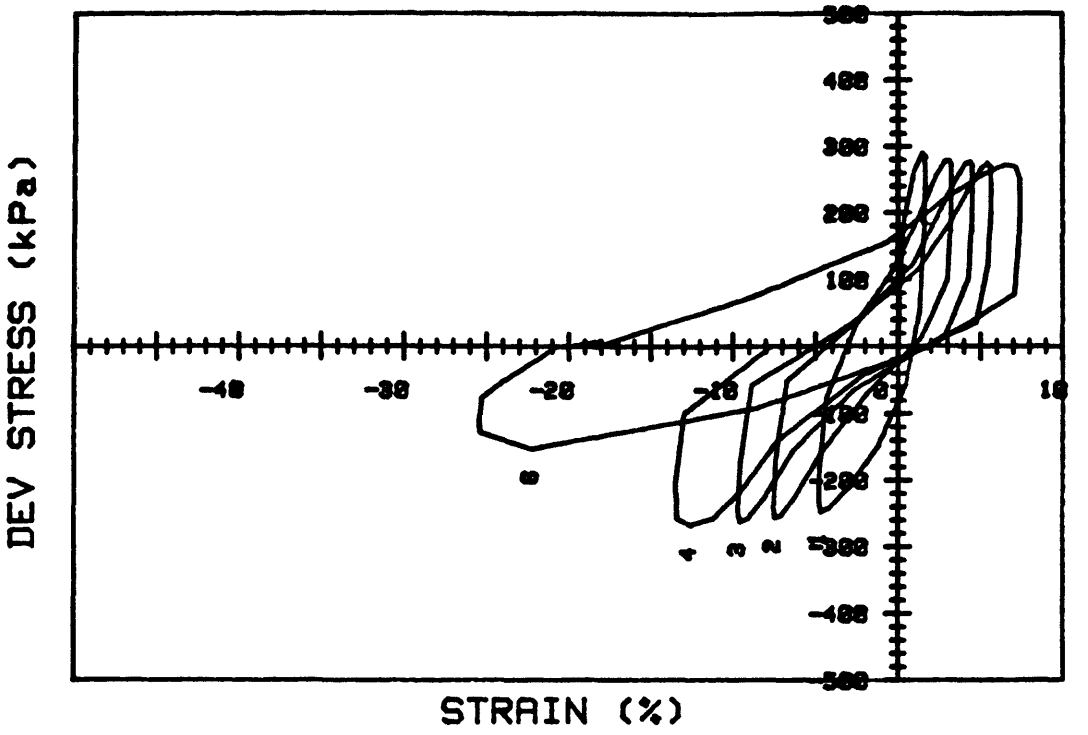

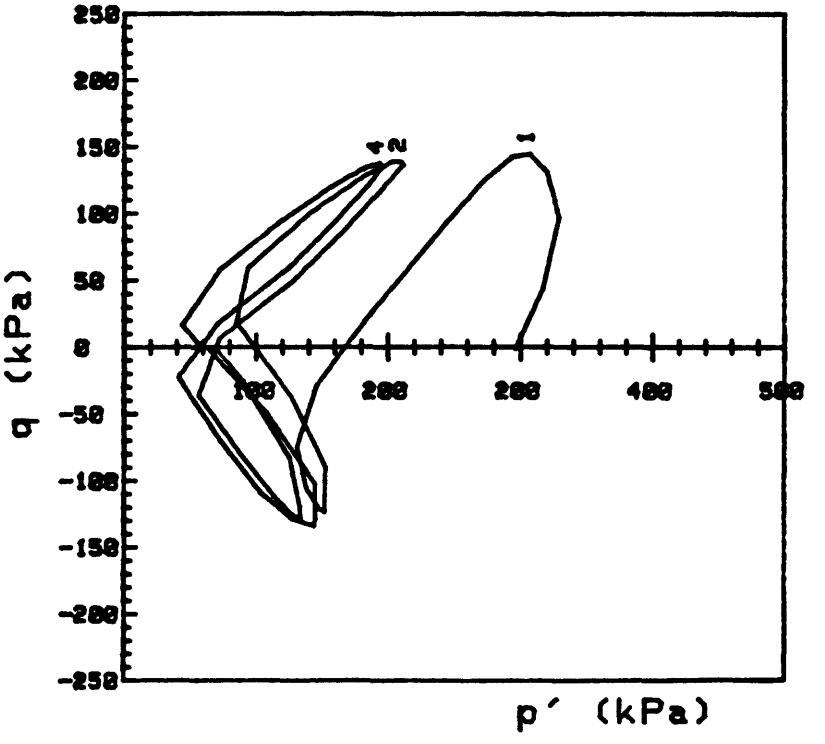

CRUISE DC4-81-NS		INCREMENT (cm)	40-40
CORE NO.	685A2	TEST NO.	TC81
SIG1c'(kPa)	297.4	STATIC qf (kPa)	300.0
SIG3c'(kPa)	297.4	AVG MAX q (kPa)	139.0 (46.3%)
INDUCED OCR	1.0	AVG MIN q (kPa)	-117.4 (39.1%)

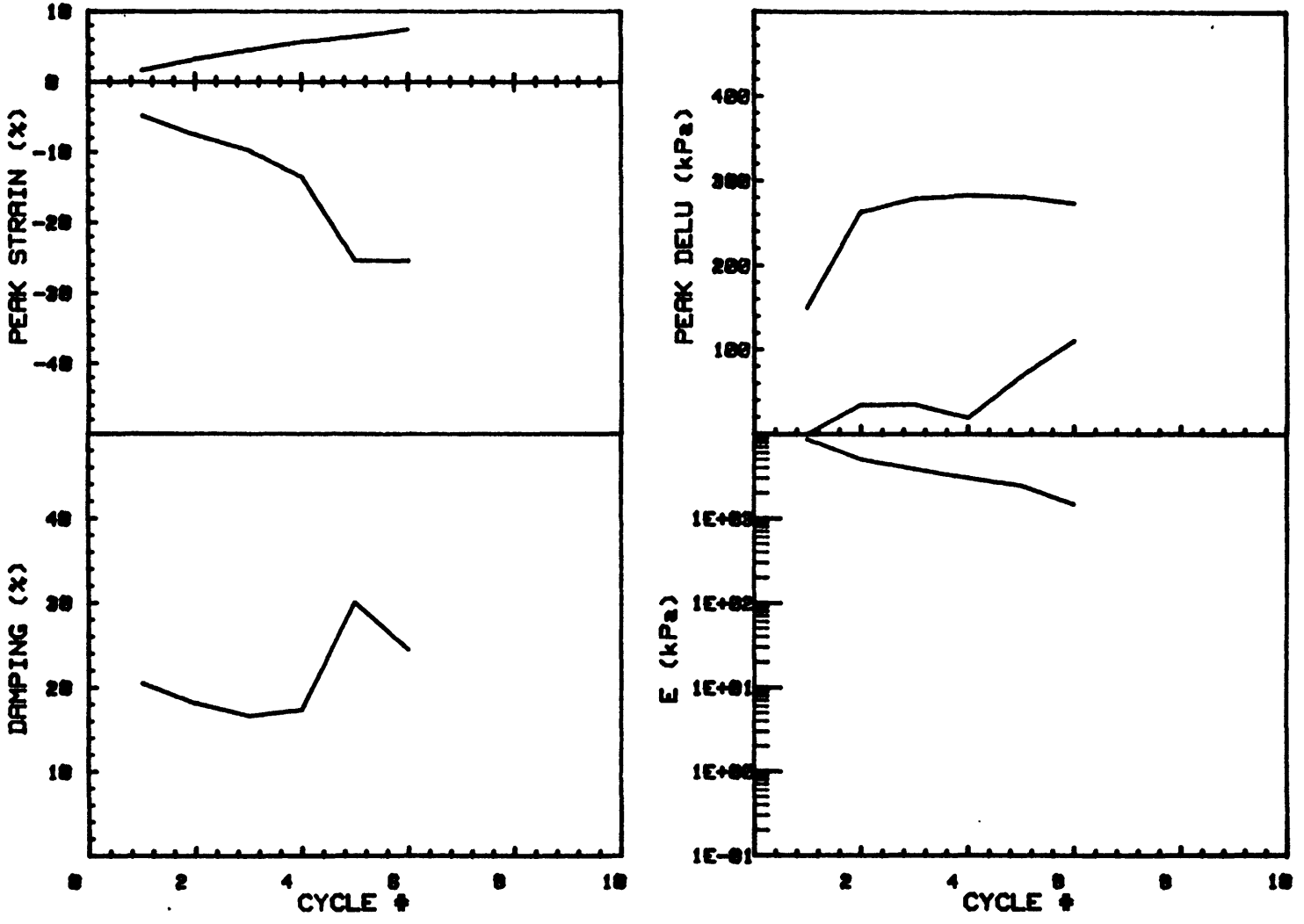

CRUISE DC4-81-NS		INCREMENT (cm)	40-48
CORE NO.	685A2	TEST NO.	TC81
SIG1c'(kPa)	297.4	STATIC qf (kPa)	300.0
SIG3c'(kPa)	297.4	AVG MAX q (kPa)	139.0 (46.3%)
INDUCED OCR	1.0	AVG MIN q (kPa)	-117.4 (39.1%)

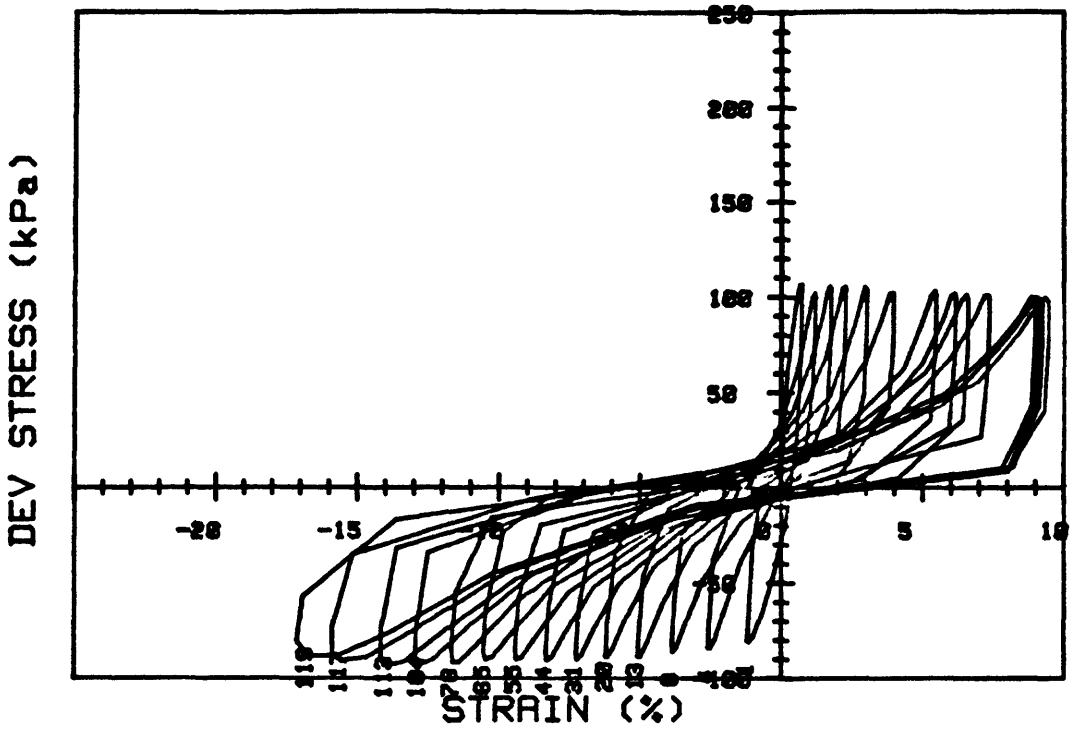

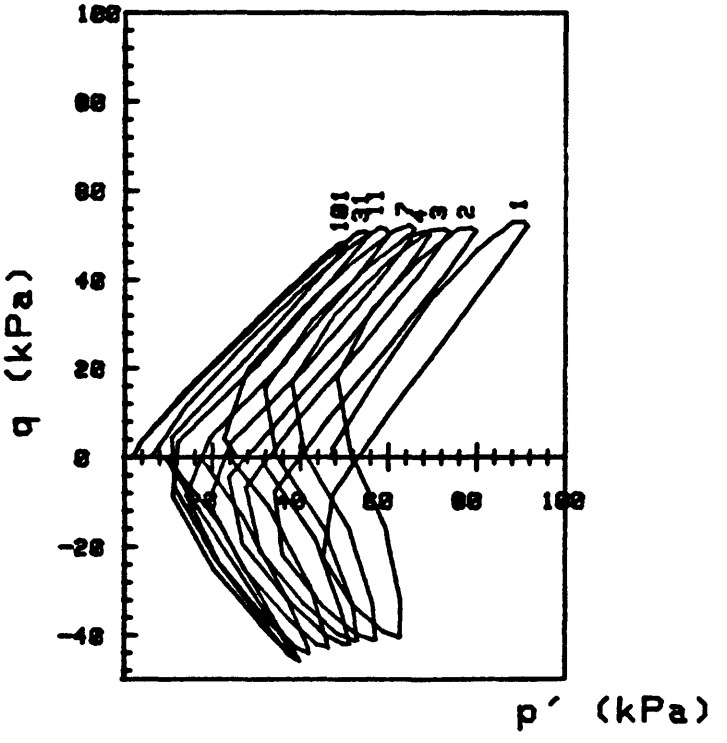

CRUISE DC4-81-NS		INCREMENT (cm)	61-69
CORE NO.	685A2	TEST NO.	TC82
SIG1c´(kPa)	46.7	STATIC qf (kPa)	50.0
SIG3c´(kPa)	46.7	AVG MAX q (kPa)	50.8 (101.6%)
INDUCED OCR	6.0	AVG MIN q (kPa)	-45.0 (90.0%)

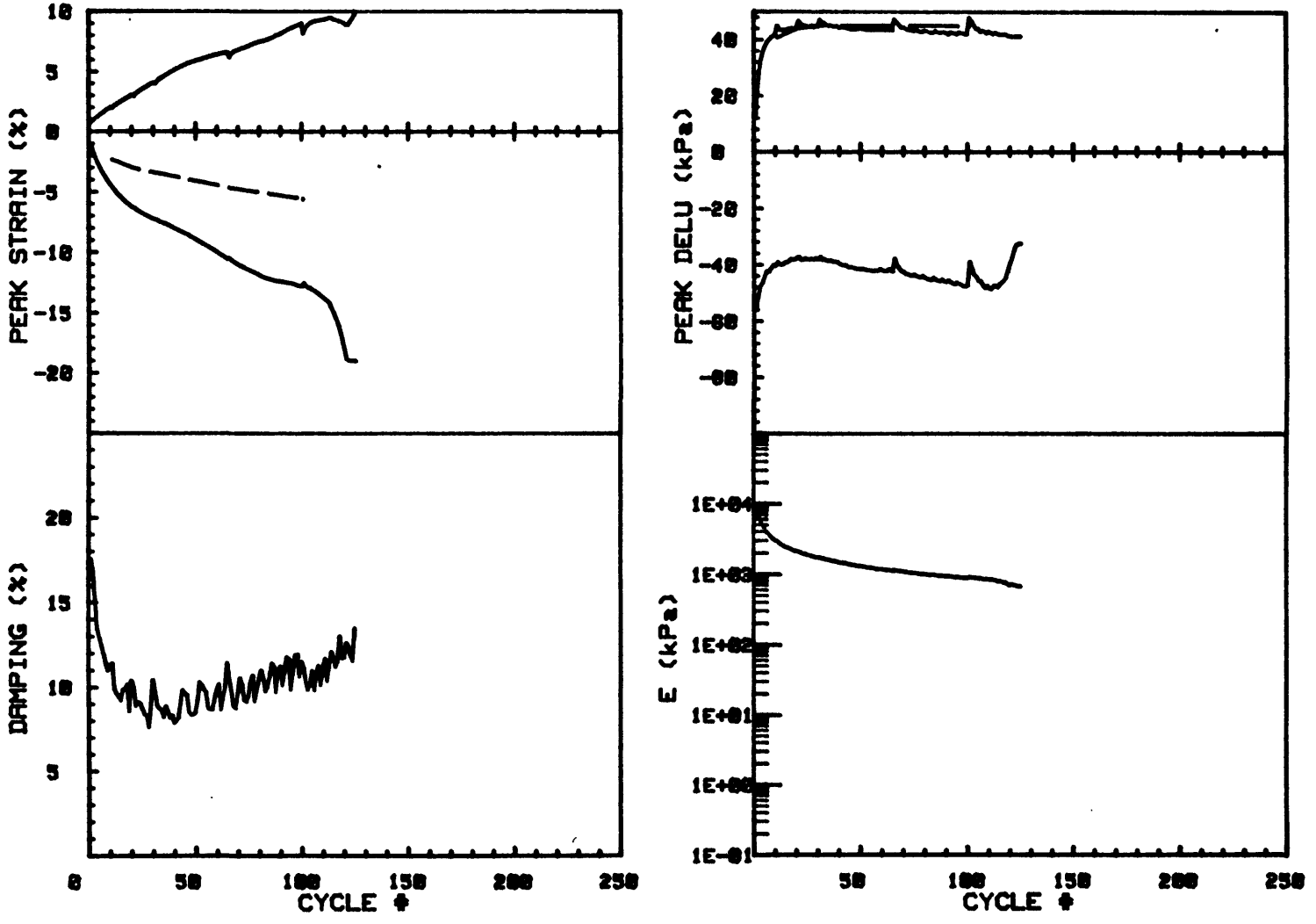

CRUISE DC4-81-NS		INCREMENT (cm)	61-69
CORE NO.	685A2	TEST NO.	TC82
SIG1c'(kPa)	46.7	STATIC qf (kPa)	50.0
SIG3c'(kPa)	46.7	AVG MAX q (kPa)	50.8 (101.6%)
INDUCED OCR	6.0	AVG MIN q (kPa)	-45.0 (90.0%)

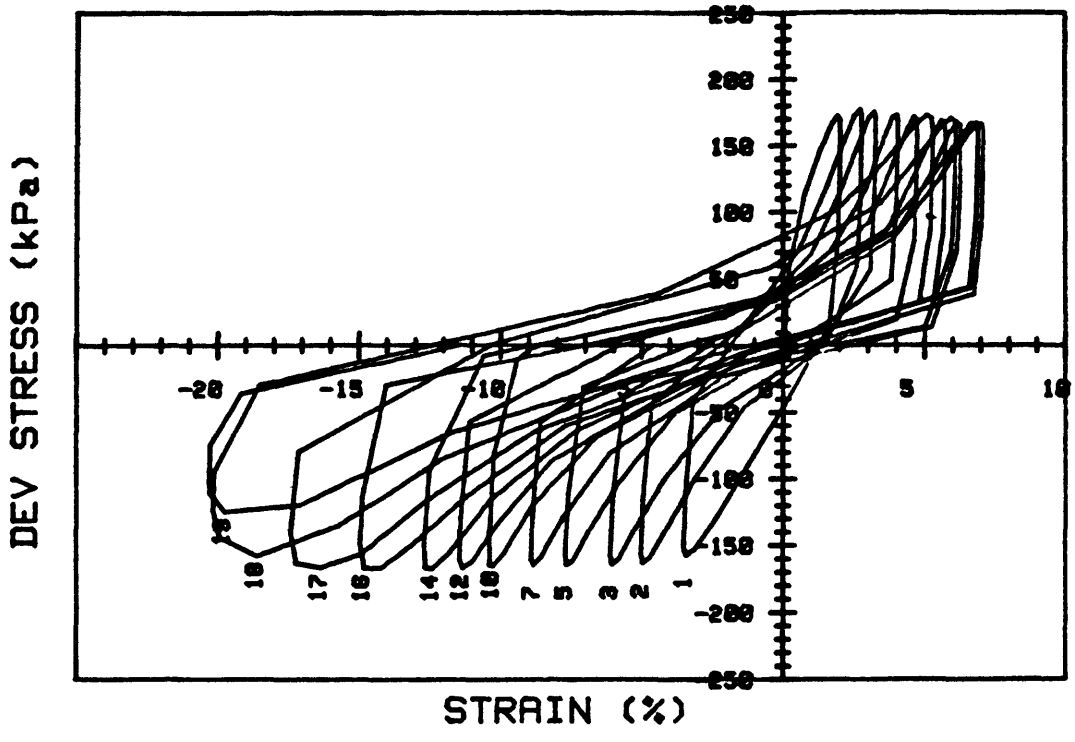

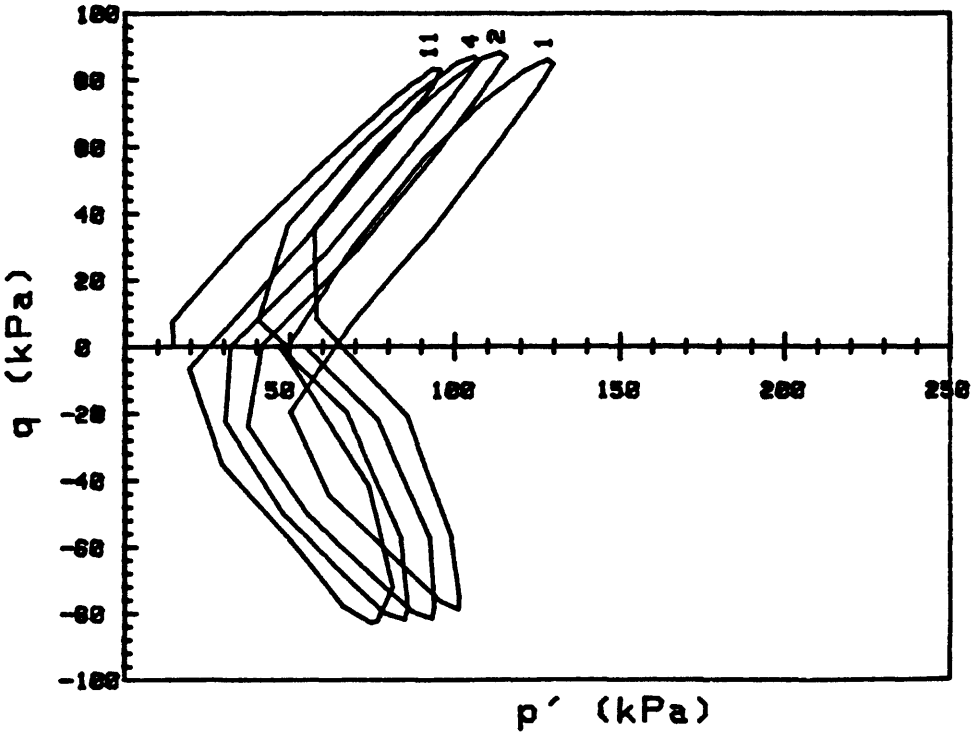

CRUISE DC4-81-NS		INCREMENT (cm)	61-69
CORE NO.	685A2	TEST NO.	TC83
SIG1c'(kPa)	49.7	STATIC qf (kPa)	50.0
SIG3c'(kPa)	49.7	AVG MAX q (kPa)	85.0 (170.0%)
INDUCED OCR	6.0	AVG MIN q (kPa)	-80.1 (160.2%)

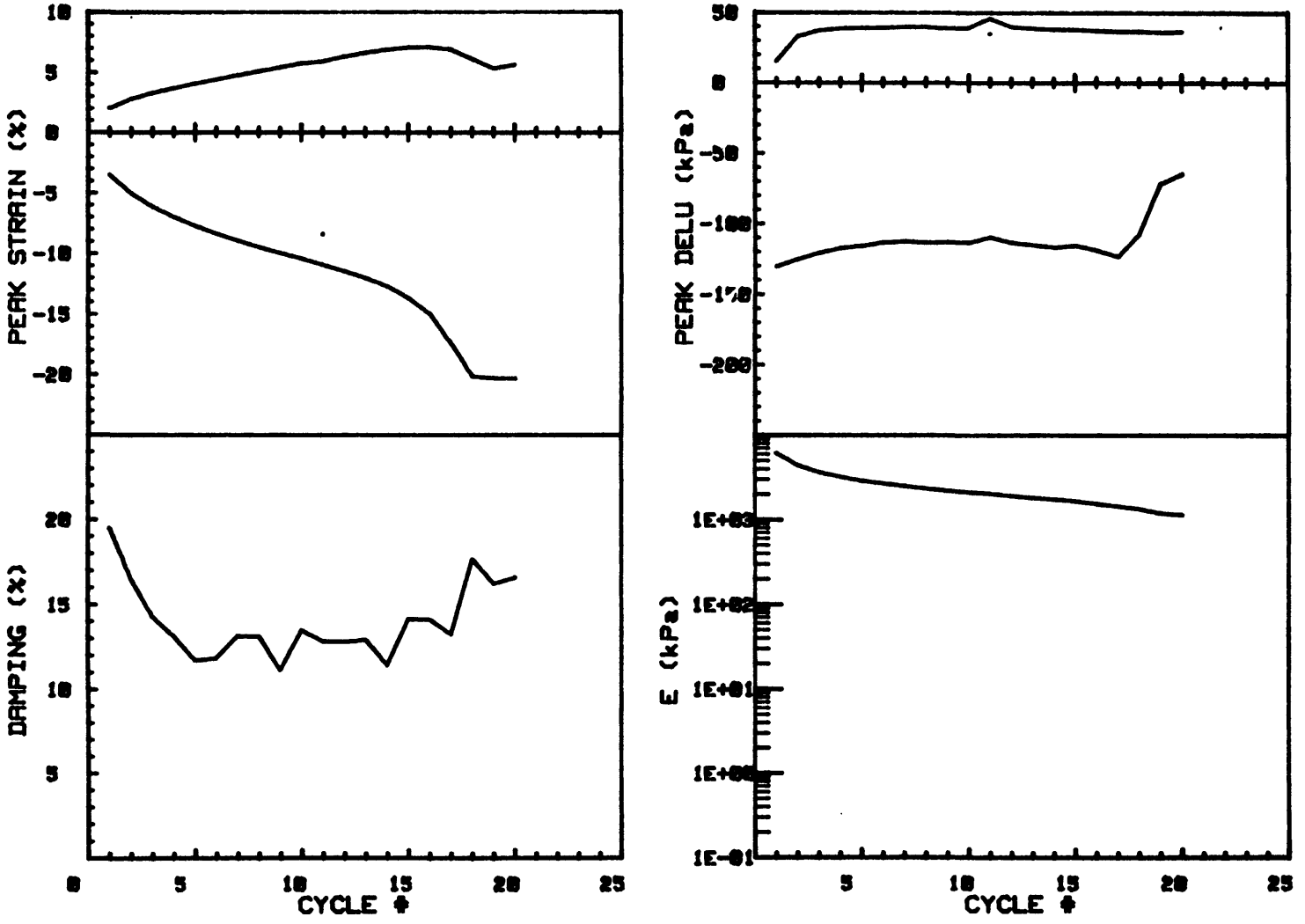

CRUISE DC4-81-NS		INCREMENT (cm)	61-69
CORE NO.	685A2	TEST NO.	TC83
SIG1c'(kPa)	49.7	STATIC qf (kPa)	50.0
SIG3c'(kPa)	49.7	AVG MAX q (kPa)	85.0 (170.0%)
INDUCED OCR	6.0	AVG MIN q (kPa)	-80.1 (160.2%)

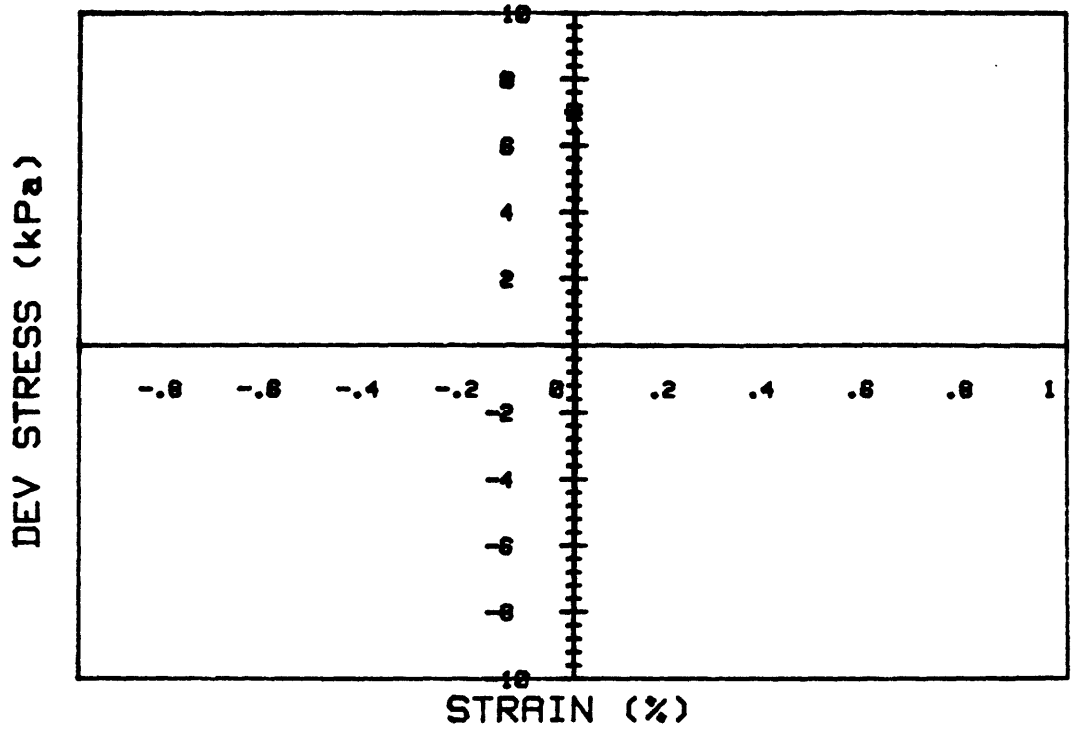

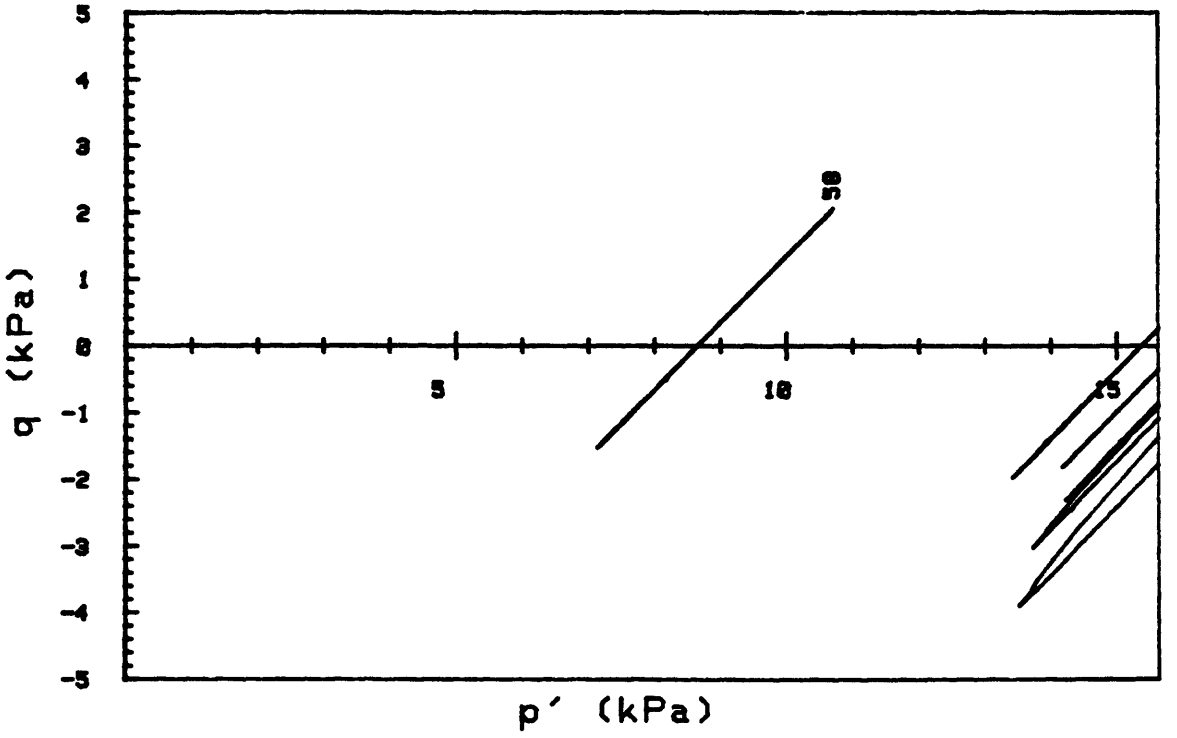

CRUISE DC4-81-NS		INCREMENT (cm)	101-109
CORE NO. 685A2		TEST NO.	TC62
SIG1c'(kPa)	17.4	STATIC qf (kPa)	18.0
SIG3c'(kPa)	17.4	AVG MAX q (kPa)	1.5 (8.3%)
INDUCED OCR	1.0	AVG MIN q (kPa)	-2.1 (11.7%)

Cycles 1 - 500

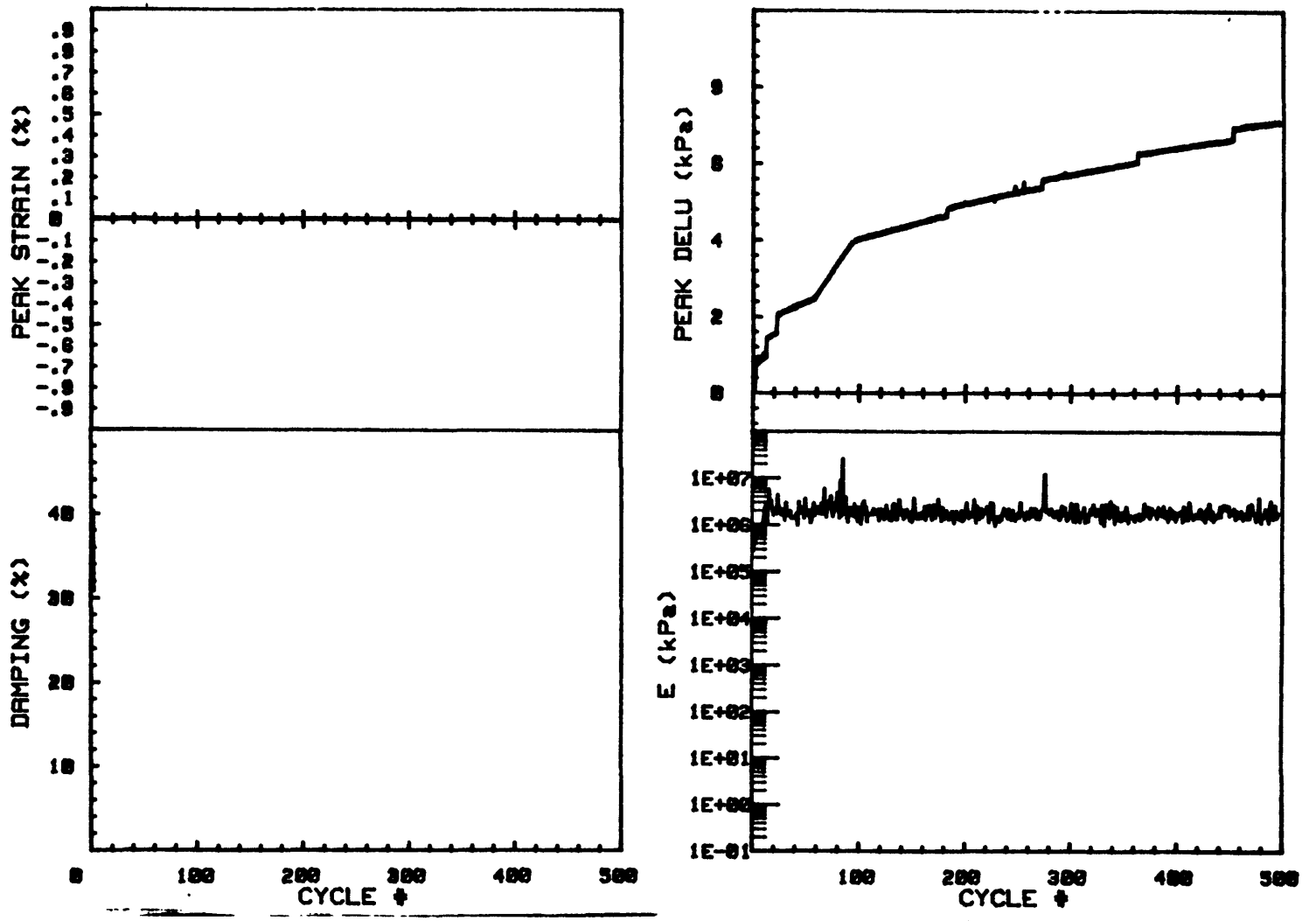

CRUISE DC4-81-NS		INCREMENT (cm)	101-109
CORE NO.	685A2	TEST NO.	TC62
SIG1c'(kPa)	17.4	STATIC qf (kPa)	18.0
SIG3c'(kPa)	17.4	AVG MAX q (kPa)	1.5 (8.3%)
INDUCED OCR	1.0	AVG MIN q (kPa)	-2.1 (11.7%)

Cycles 1 - 500

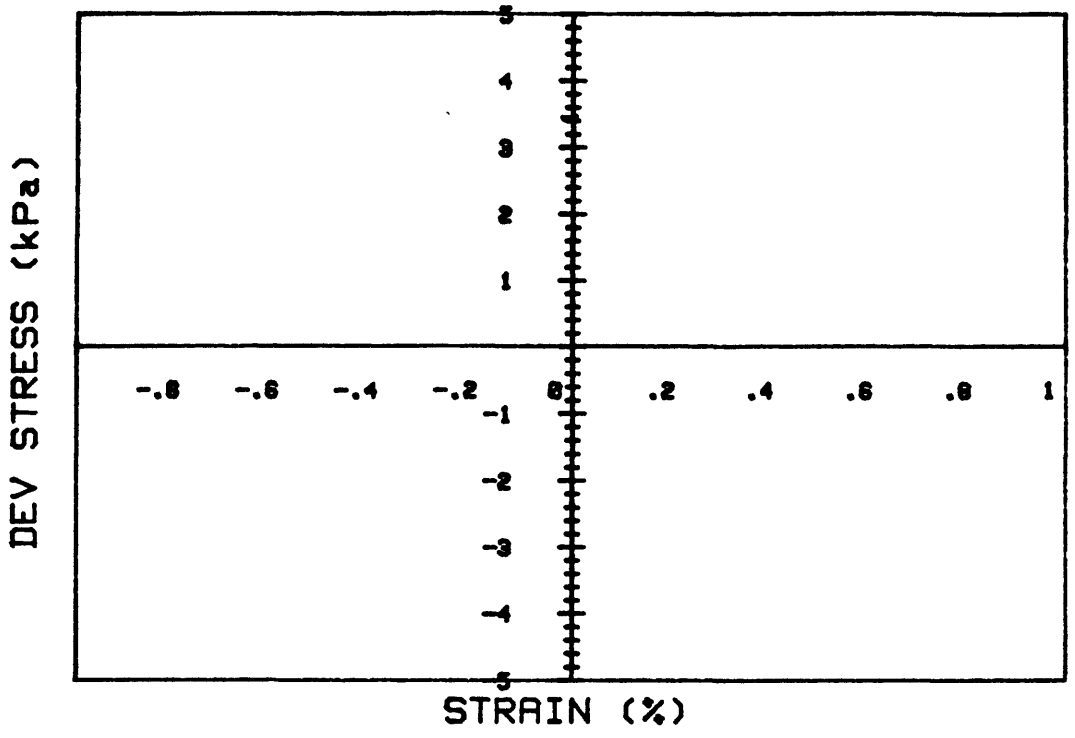

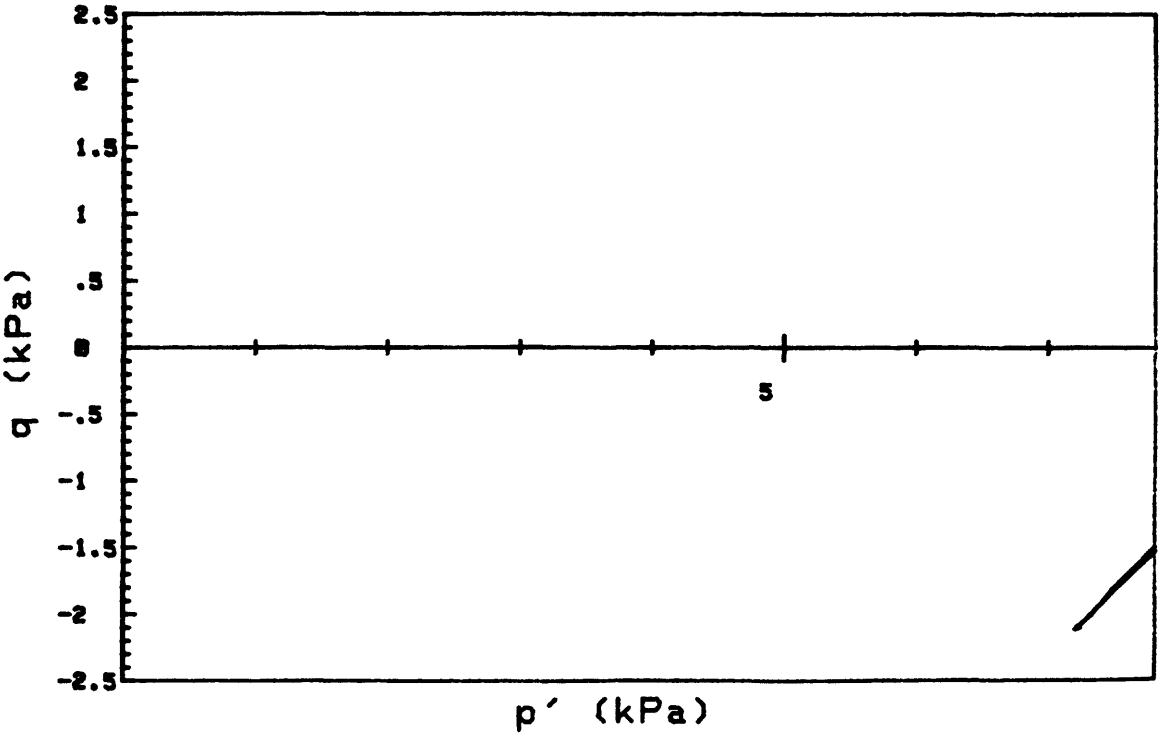

CRUISE DC4-81-NS		INCREMENT (cm)	101-109
CORE NO.	685A2	TEST NO.	TC62
SIG1c'(kPa)	10.2	STATIC qf (kPa)	18.0
SIG3c'(kPa)	10.2	AVG MAX q (kPa)	1.6 (8.9%)
INDUCED OCR	1.0	AVG MIN q (kPa)	-2.0 (11.1%)

Cycles 501 - 860

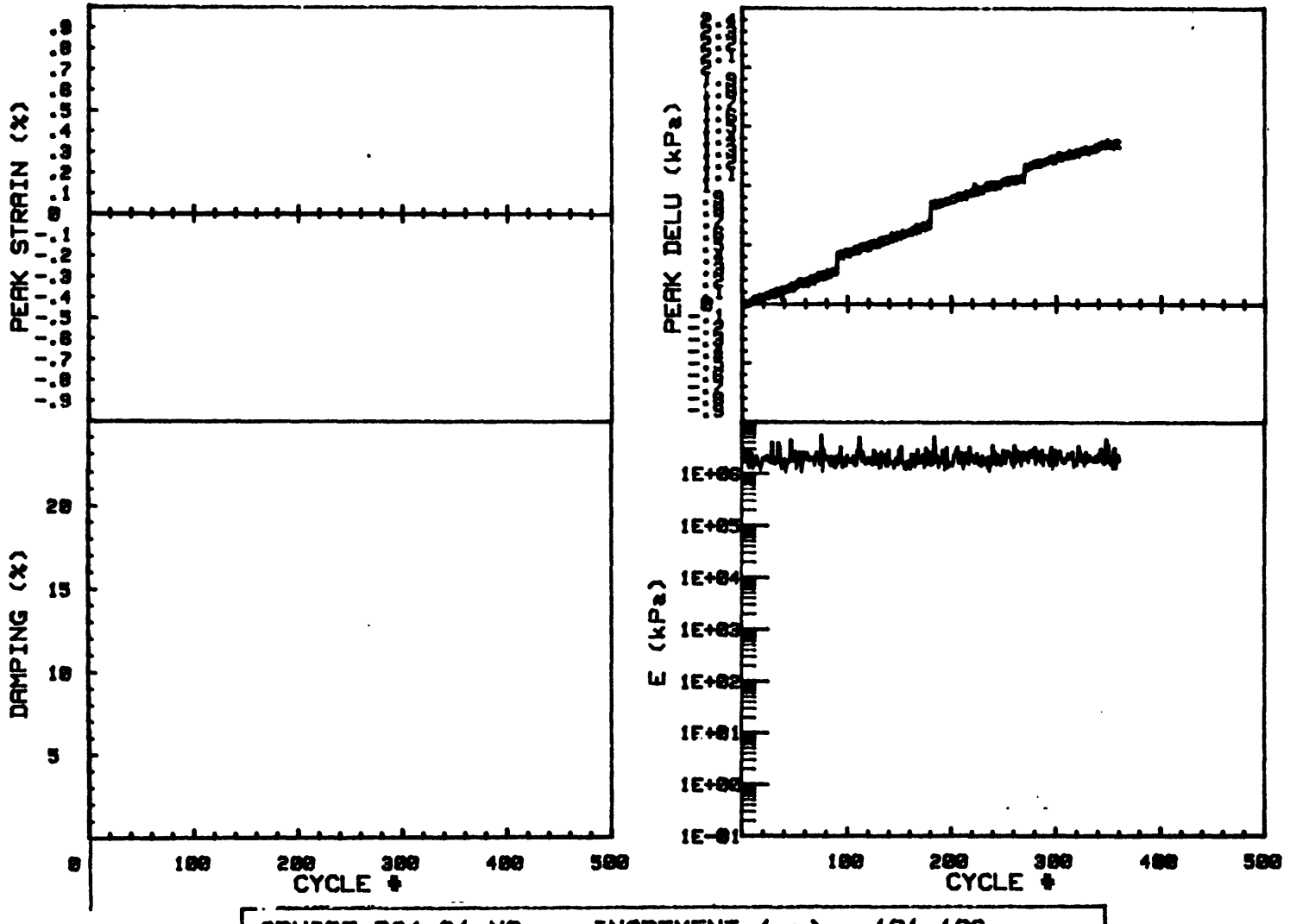

CRUISE DC4-81-NS		INCREMENT (cm)	101-109
CORE NO.	685A2	TEST NO.	TC62
SIG1c'(kPa)	10.2	STATIC qf (kPa)	18.0
SIG3c'(kPa)	10.2	AVG MAX q (kPa)	1.6 (8.9%)
INDUCED OCR	1.0	AVG MIN q (kPa)	-2.0 (11.1%)

Cycles 501 - 860

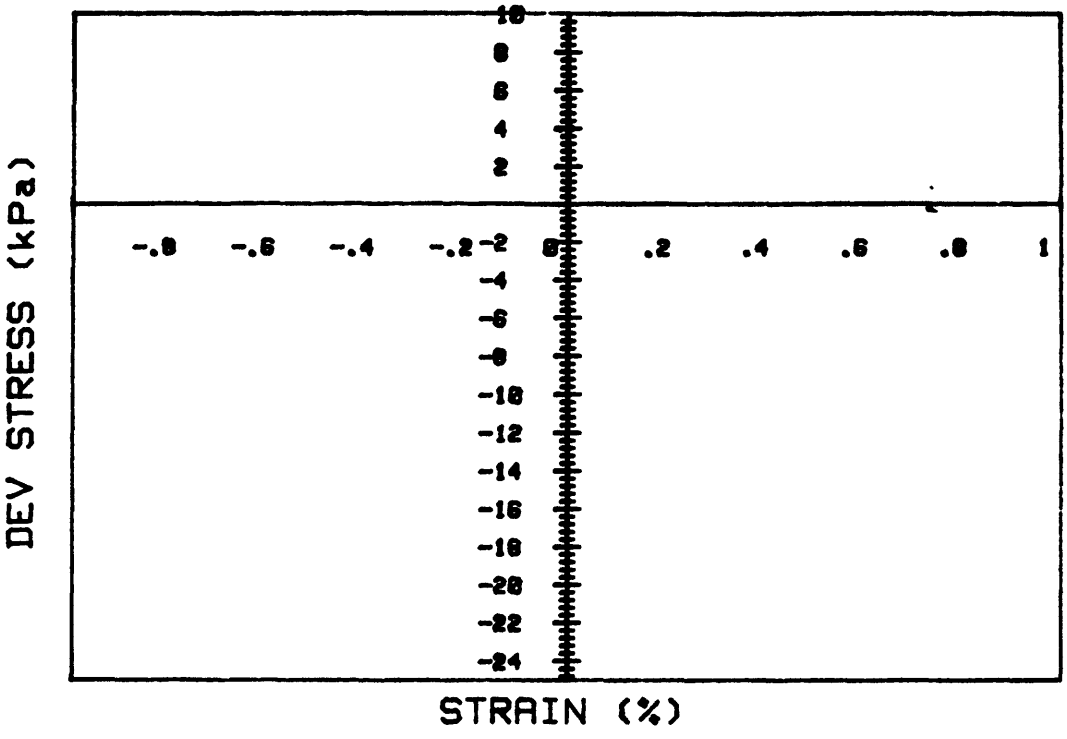

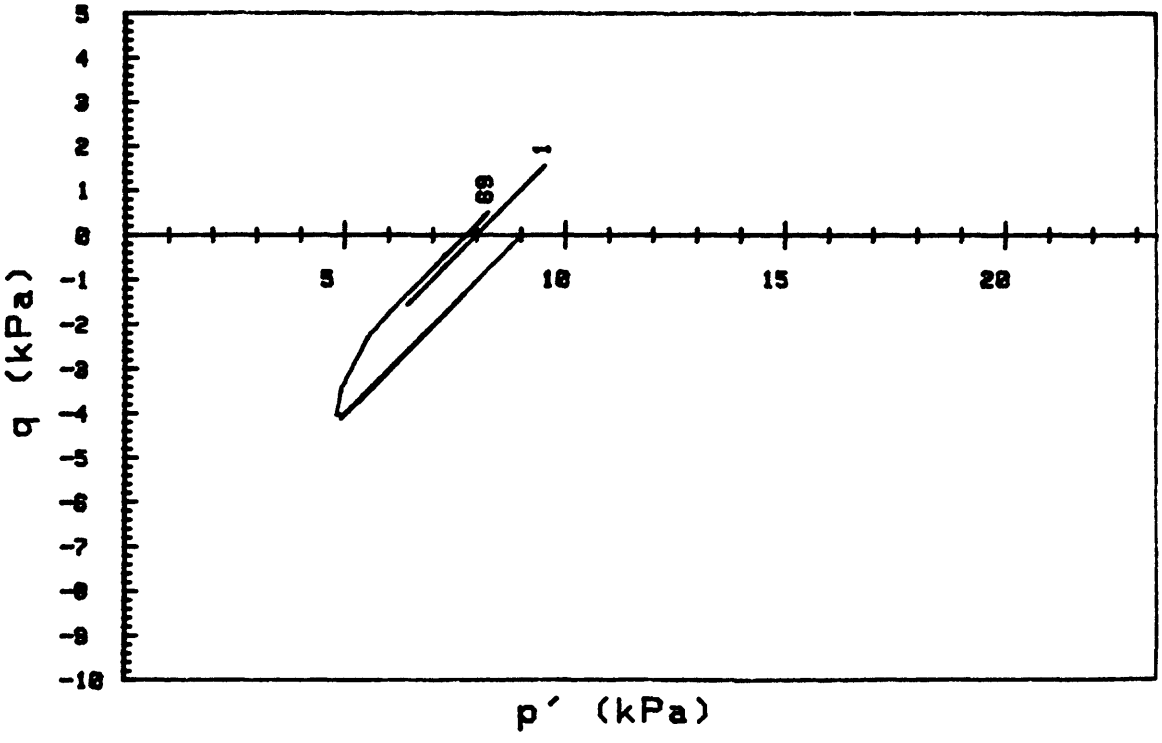

CRUISE DC4-81-NS		INCREMENT (cm)	101-109
CORE NO.	685A2	TEST NO.	TC62
SIG1c'(kPa)	8.0	STATIC qf (kPa)	10.0
SIG3c'(kPa)	8.0	AVG MAX q (kPa)	1.7 (9.4%)
INDUCED OCR	1.0	AVG MIN q (kPa)	-1.7 (9.4%)

Cycles 1147 - 1600

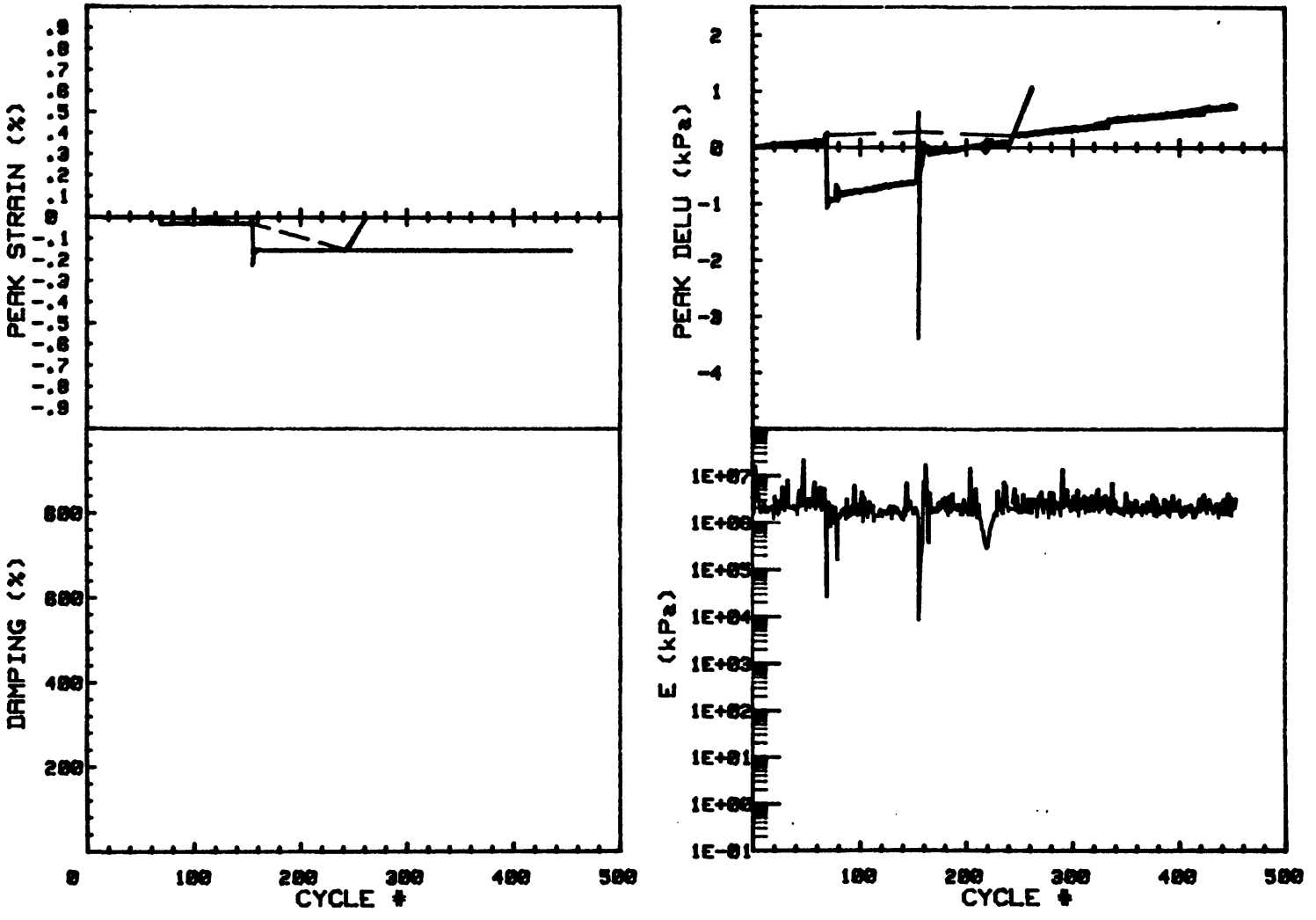

CRUISE DC4-81-NS		INCREMENT (cm)	101-109
CORE NO.	685A2	TEST NO.	TC62
SIG1c'(kPa)	8.0	STATIC qf (kPa)	18.0
SIG3c'(kPa)	8.0	AVG MAX q (kPa)	1.7 (9.4%)
INDUCED OCR	1.0	AVG MIN q (kPa)	-1.7 (9.4%)

Cycles 1147 - 1600

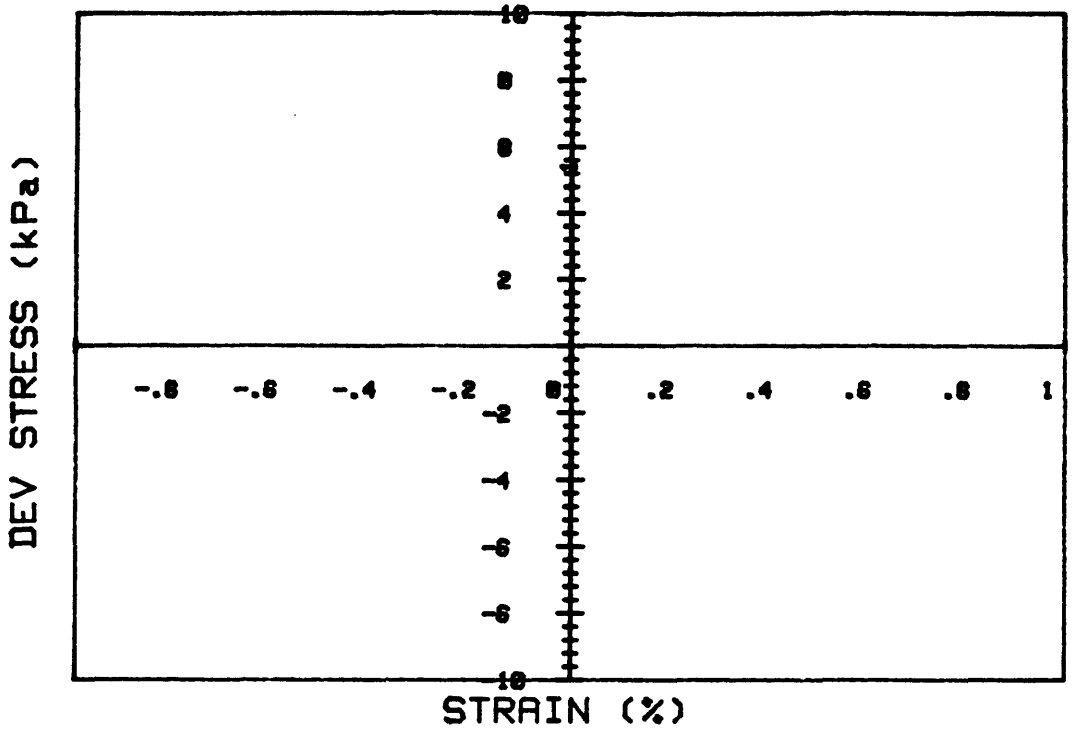

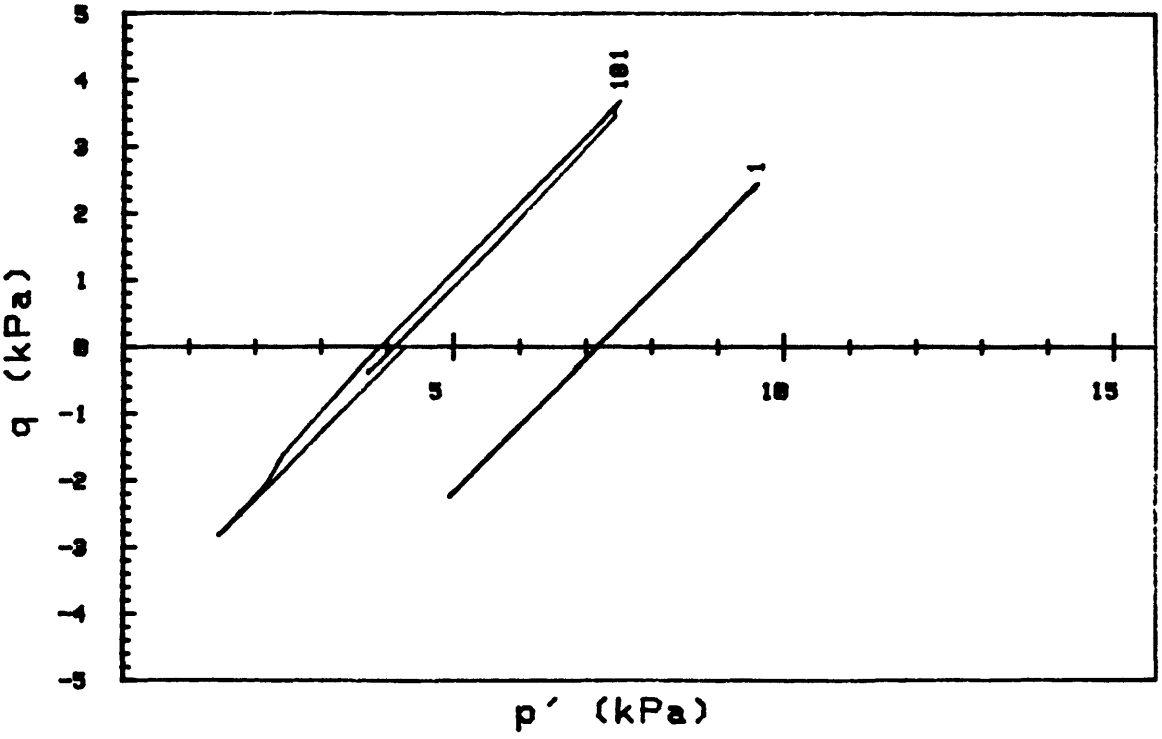

CRUISE DC4-81-NS		INCREMENT (cm)	101-109
CORE NO.	685A2	TEST NO.	TC62
SIG1c'(kPa)	7.2	STATIC qf (kPa)	18.0
SIG3c'(kPa)	7.2	AVG MAX q (kPa)	3.9 (21.7%)
INDUCED OCR	1.0	AVG MIN q (kPa)	-3.5 (19.4%)

Cycles 1601 - 2000

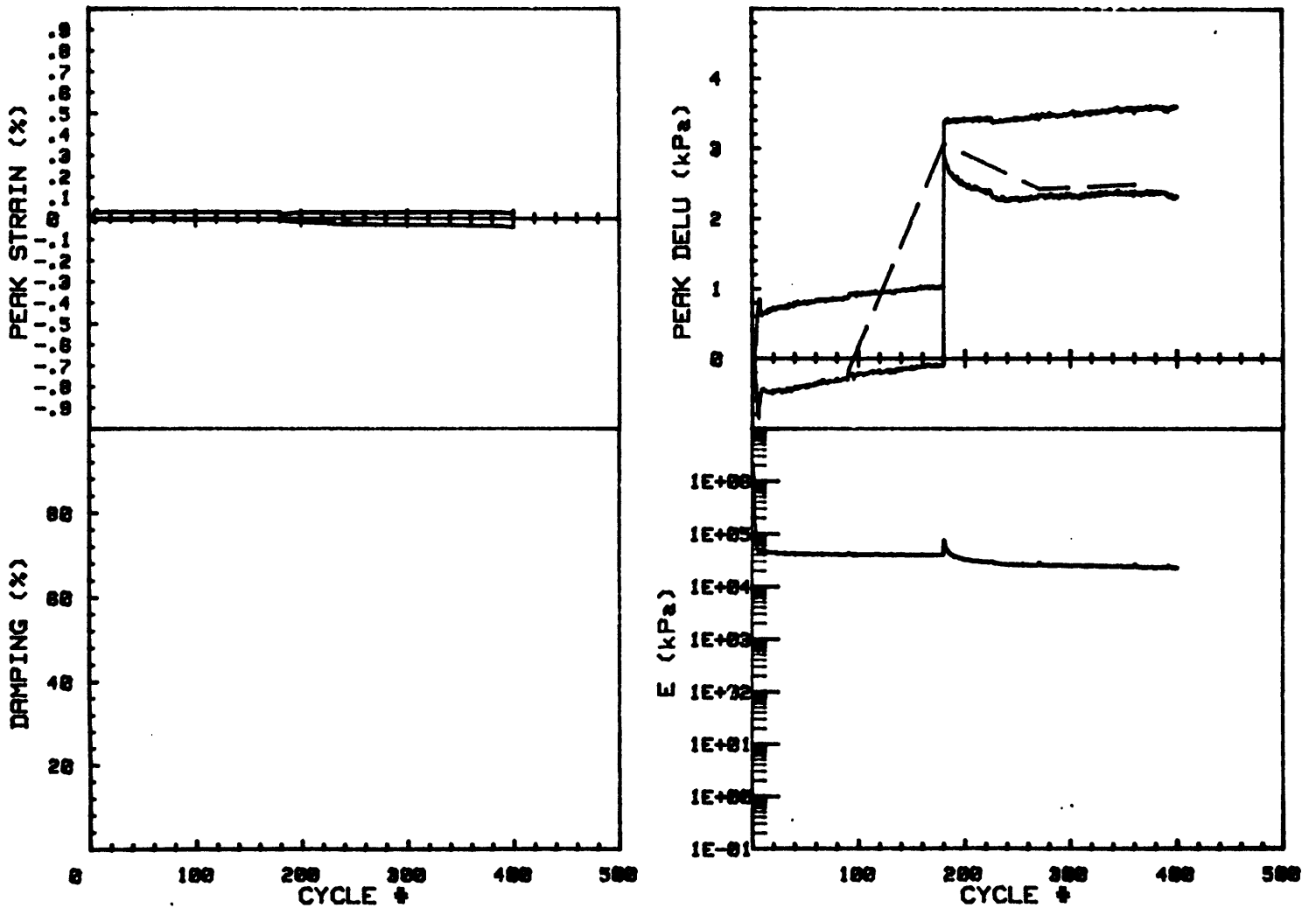

CRUISE DC4-81-NS		INCREMENT (cm)	101-109
CORE NO.	685A2	TEST NO.	TC62
SIG1c'(kPa)	7.2	STATIC qf (kPa)	18.0
SIG3c'(kPa)	7.2	AVG MAX q (kPa)	3.9 (21.7%)
INDUCED OCR	1.0	AVG MIN q (kPa)	-3.5 (19.4%)

Cycles 1601 - 2000

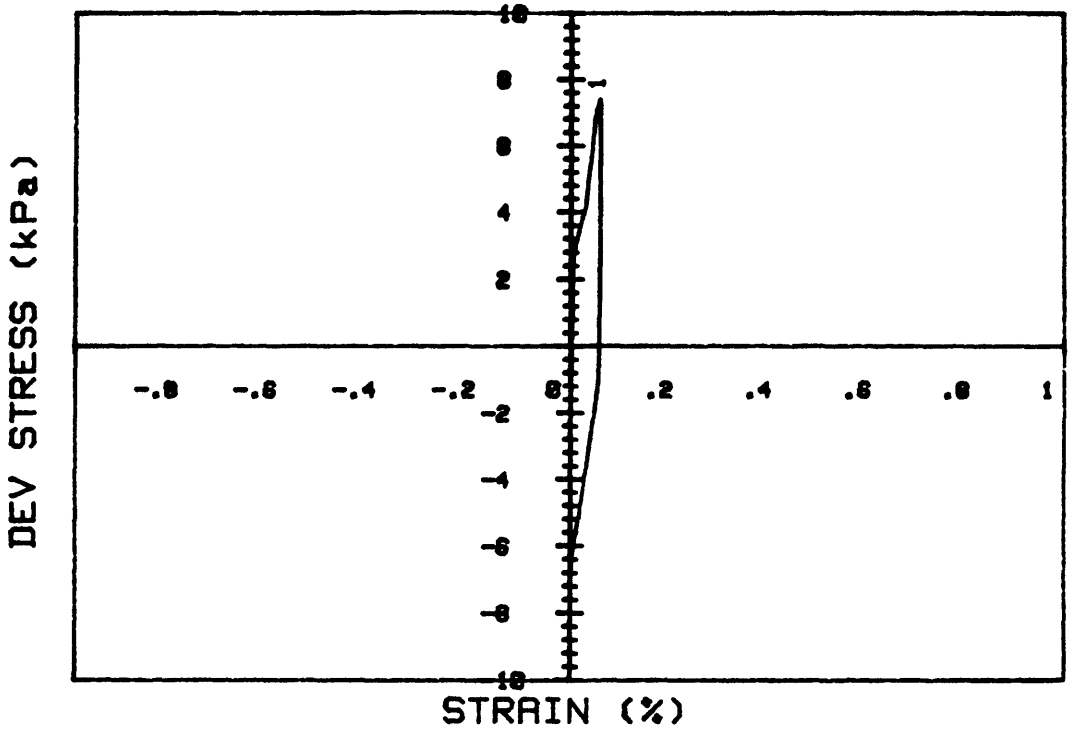

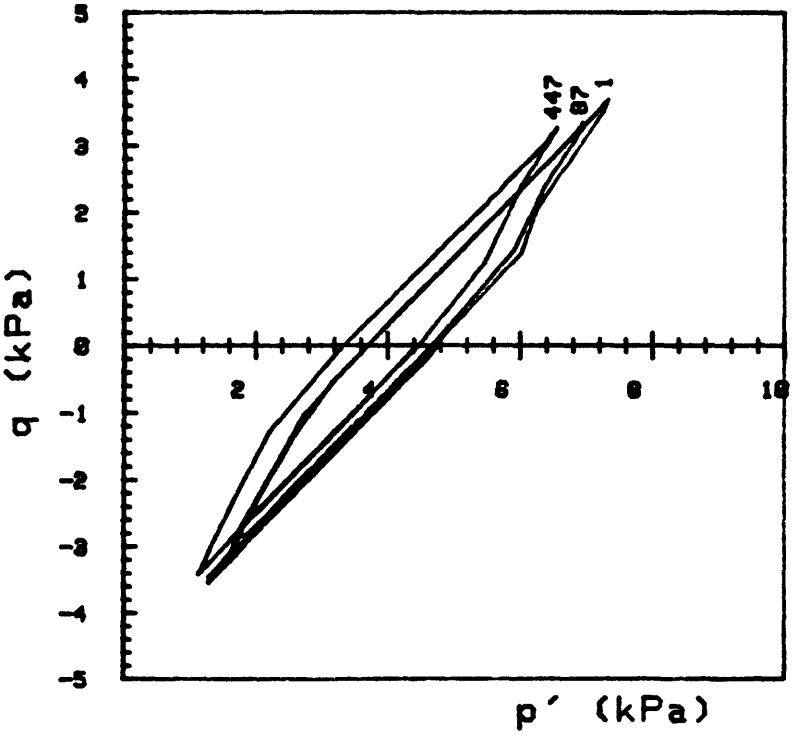

CRUISE DC4-81-NS		INCREMENT (cm)	101-109
CORE NO. 685A2		TEST NO.	TC62
SIG1c'(kPa)	4.7	STATIC qf (kPa)	18.0
SIG3c'(kPa)	4.7	AVG MAX q (kPa)	3.6 (20.0%)
INDUCED OCR	1.0	AVG MIN q (kPa)	-3.5 (19.4%)

Cycles 2001 - 2500

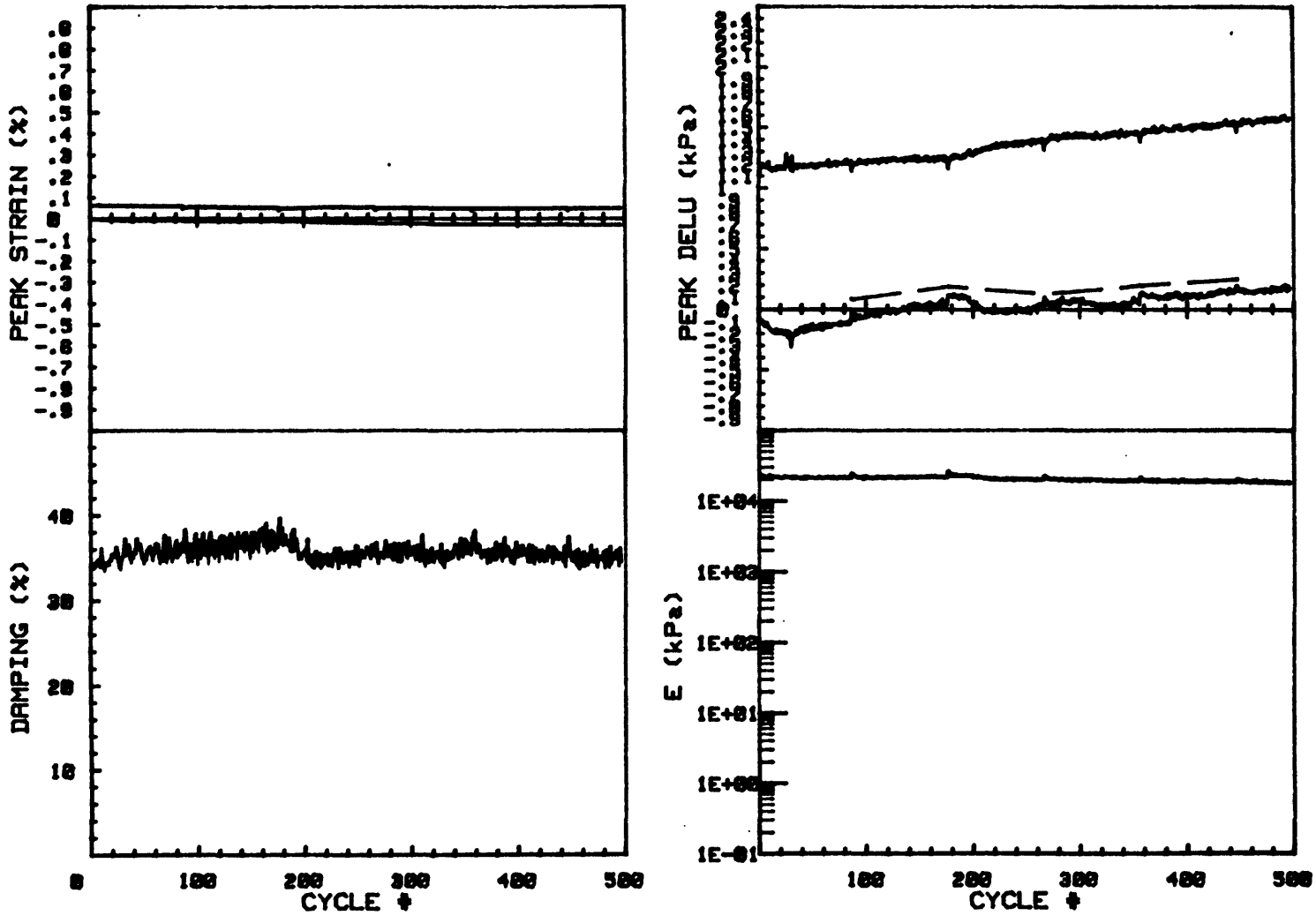

CRUISE DC4-81-NS		INCREMENT (cm)	101-109
CORE NO.	685A2	TEST NO.	TC62
SIG1c'(kPa)	4.7	STATIC qf (kPa)	18.0
SIG3c'(kPa)	4.7	AVG MAX q (kPa)	3.6 (20.0%)
INDUCED OCR	1.0	AVG MIN q (kPa)	-3.5 (19.4%)

Cycles 2001 - 2500

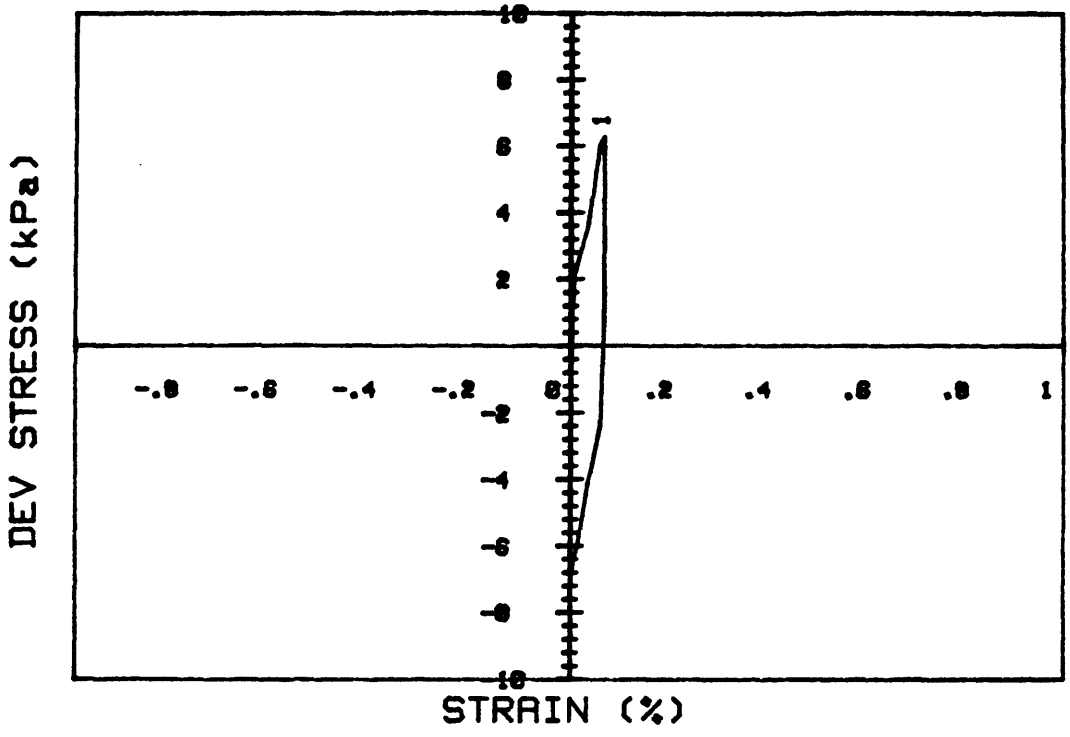

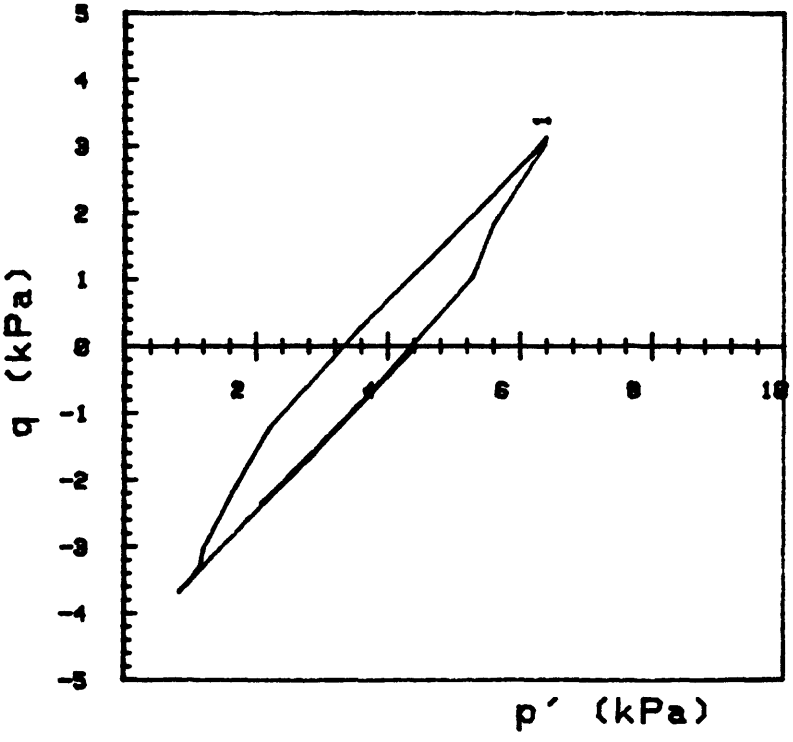

CRUISE DC4-81-NS		INCREMENT (cm)	101-109
CORE NO.	685A2	TEST NO.	TC62
SIG1c′(kPa)	4.4	STATIC qf (kPa)	18.0
SIG3c′(kPa)	4.4	AVG MAX q (kPa)	3.7 (20.6%)
INDUCED OCR	1.0	AVG MIN q (kPa)	-3.6 (20.0%)

Cycles 2501 - 3000

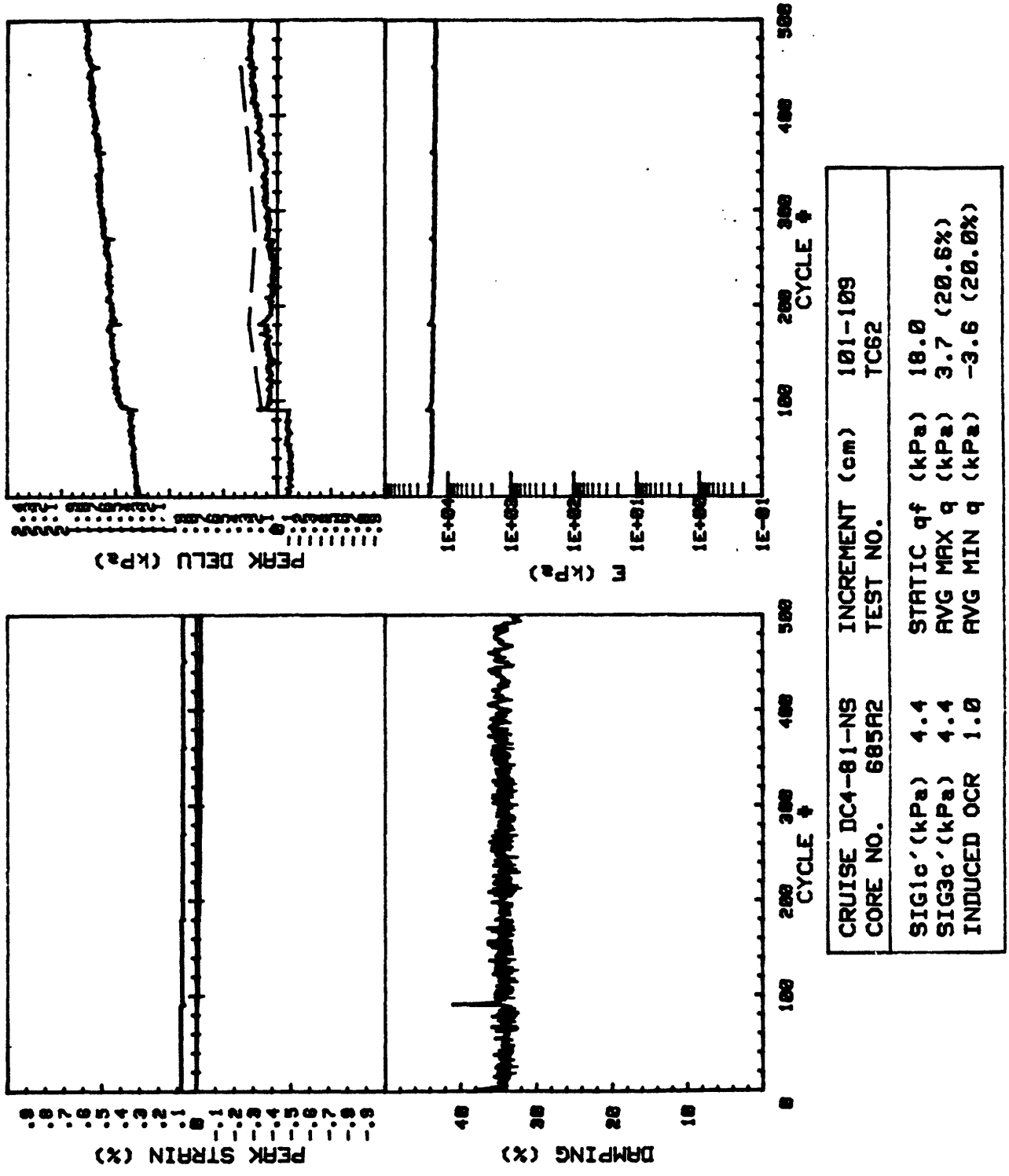

Cycles 2501 - 3000

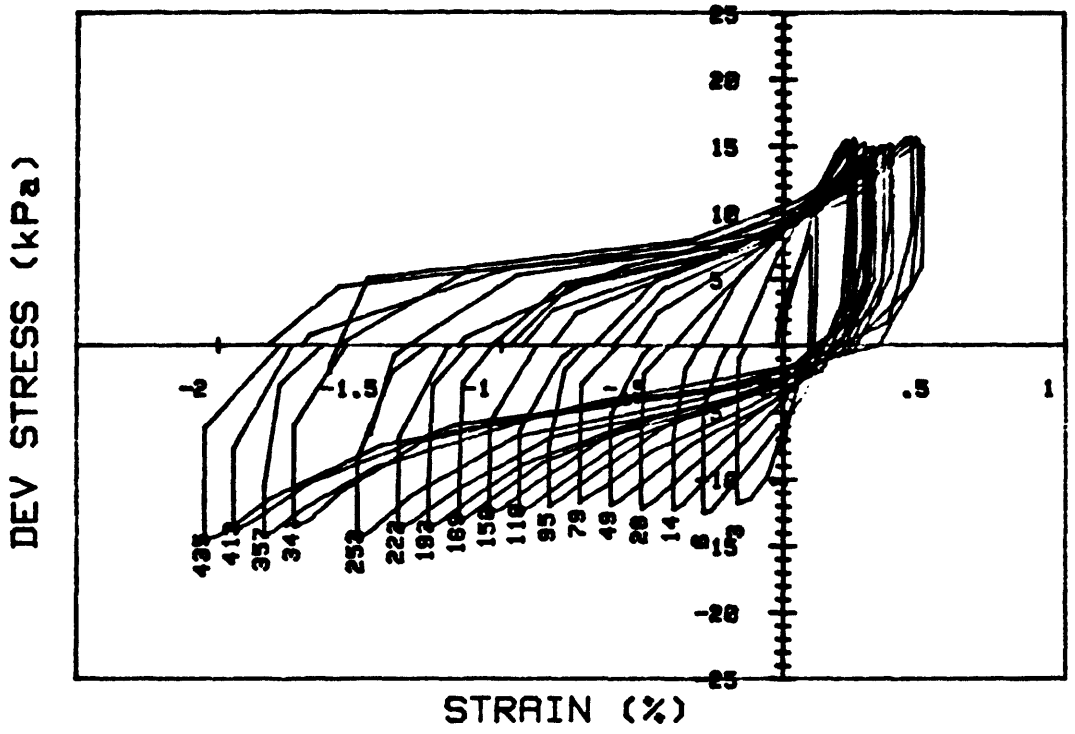

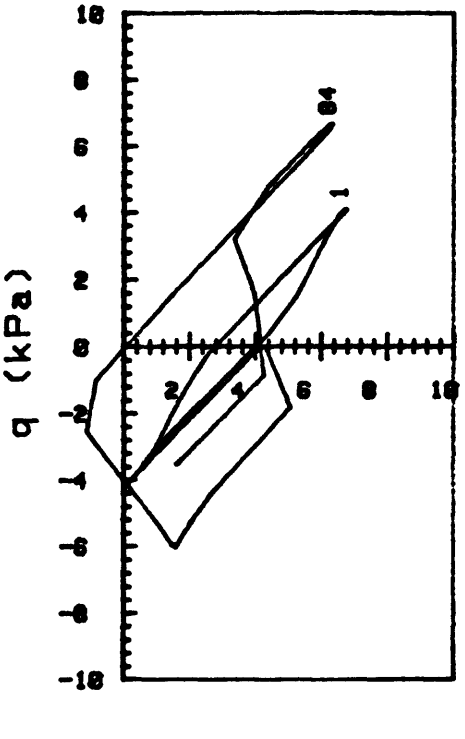

CRUISE DC4-81-NS		INCREMENT (cm)	101-109
CORE NO.	685A2	TEST NO.	TC62
SIG1c'(kPa)	4.0	STATIC qf (kPa)	18.0
SIG3c'(kPa)	4.0	AVG MAX q (kPa)	7.5 (41.7%)
INDUCED OCR	1.0	AVG MIN q (kPa)	-6.6 (36.7%)

Cycles 3001 - 3500

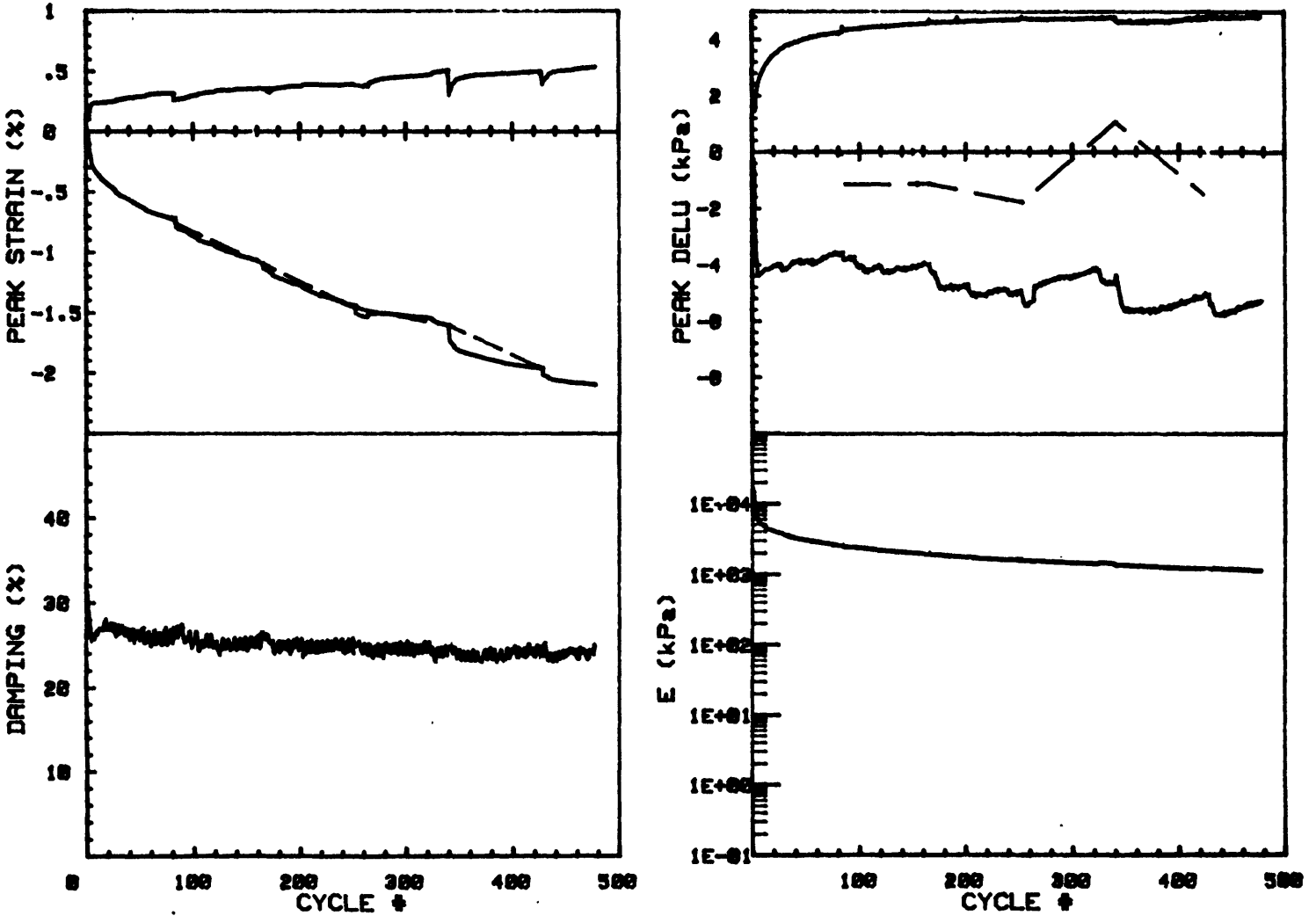

CRUISE DC4-81-NS		INCREMENT (cm)	101-109
CORE NO.	685A2	TEST NO.	TC62
SIG1c'(kPa)	4.0	STATIC qf (kPa)	18.0
SIG3c'(kPa)	4.0	AVG MAX q (kPa)	7.5 (41.7%)
INDUCED OCR	1.0	AVG MIN q (kPa)	-6.6 (36.7%)

Cycles 3001 - 3500

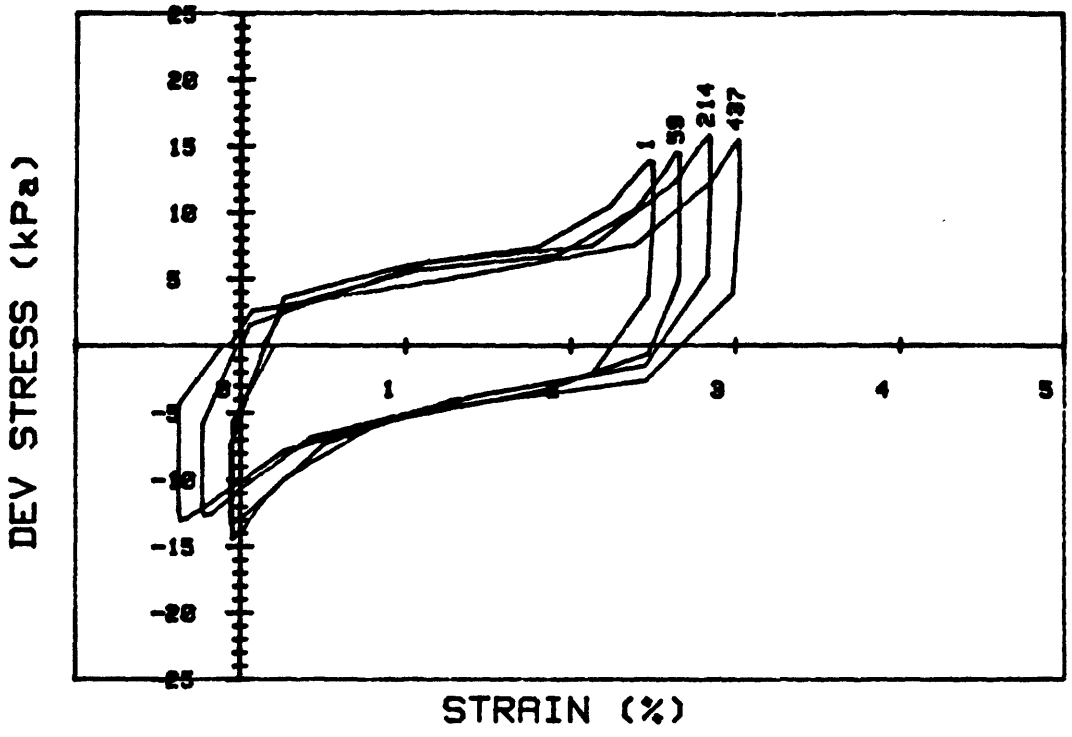

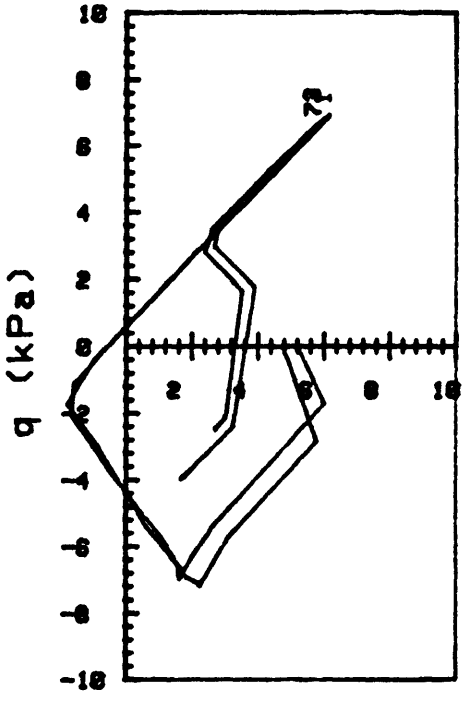

CRUISE DC4-81-NS		INCREMENT (cm)	101-109
CORE NO.	685A2	TEST NO.	TC62
SIG1c'(kPa)	5.7	STATIC qf (kPa)	18.0
SIG3c'(kPa)	5.7	AVG MAX q (kPa)	7.6 (42.2%)
INDUCED OCR	1.0	AVG MIN q (kPa)	-6.6 (36.7%)

Cycles 3501 - 4000

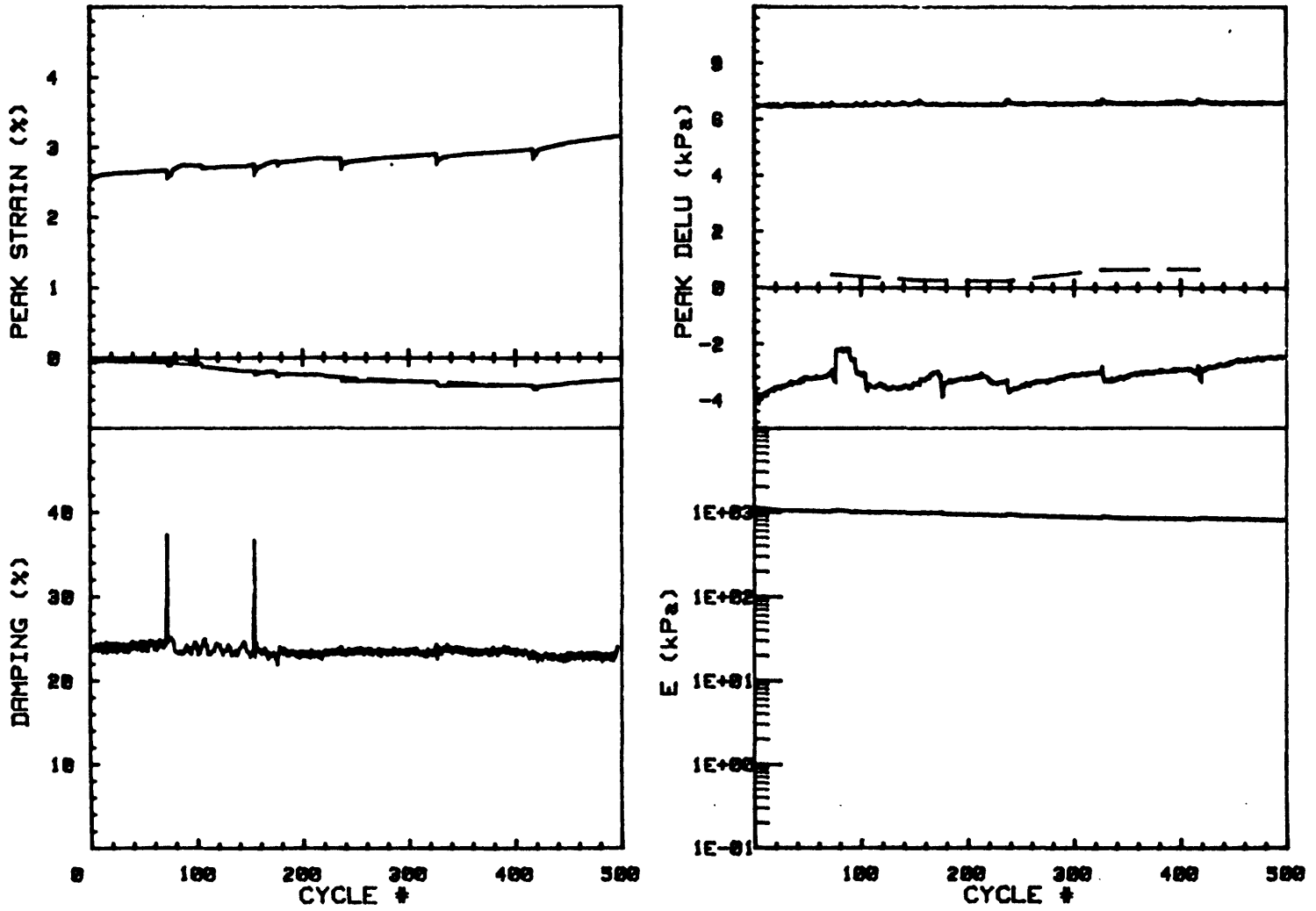

CRUISE DC4-81-NS		INCREMENT (cm)	101-109
CORE NO.	685A2	TEST NO.	TC62
SIG1c'(kPa)	5.7	STATIC qf (kPa)	18.0
SIG3c'(kPa)	5.7	AVG MAX q (kPa)	7.6 (42.2%)
INDUCED OCR	1.0	AVG MIN q (kPa)	-6.6 (36.7%)

Cycles 3501 - 4000

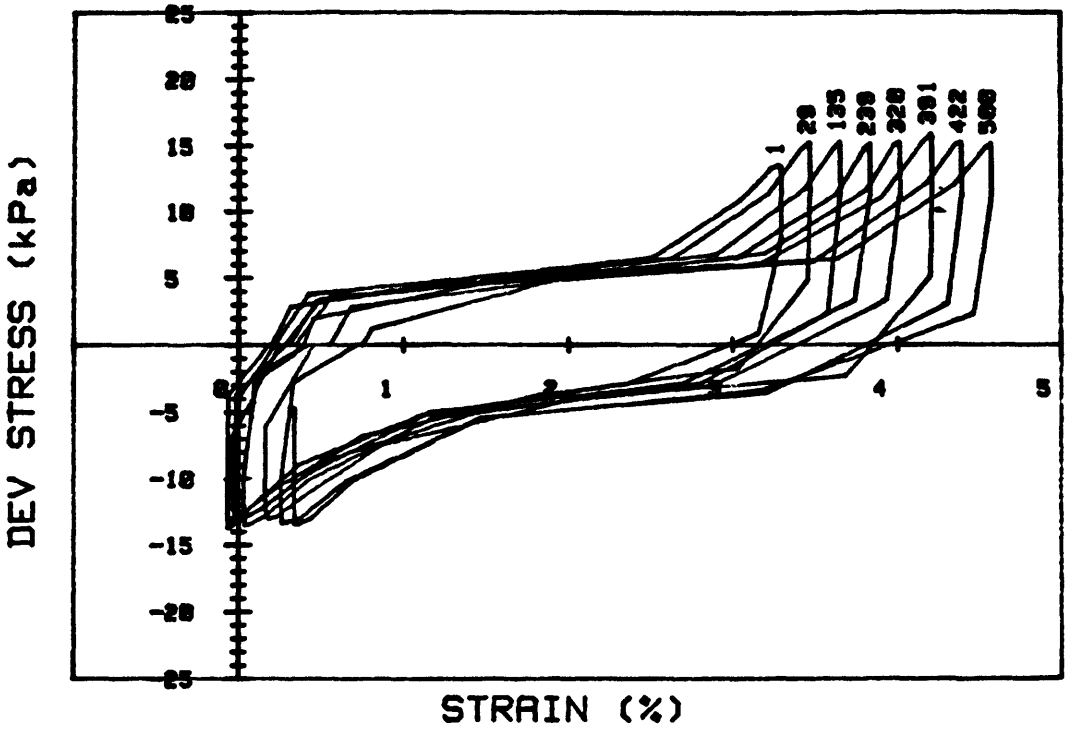

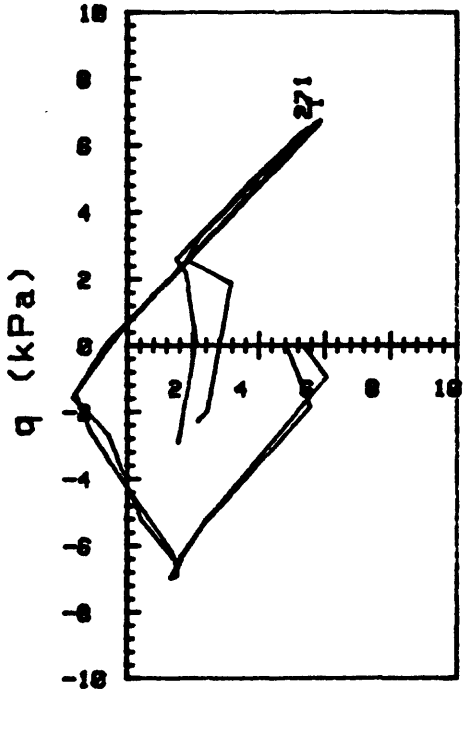

CRUISE DC4-81-NS		INCREMENT (cm)	101-109
CORE NO.	685A2	TEST NO.	TC62
SIG1c'(kPa)	4.4	STATIC qf (kPa)	18.0
SIG3c'(kPa)	4.4	AVG MAX q (kPa)	7.6 (42.2%)
INDUCED OCR	1.0	AVG MIN q (kPa)	-6.6 (36.7%)

Cycles 4001 - 4500

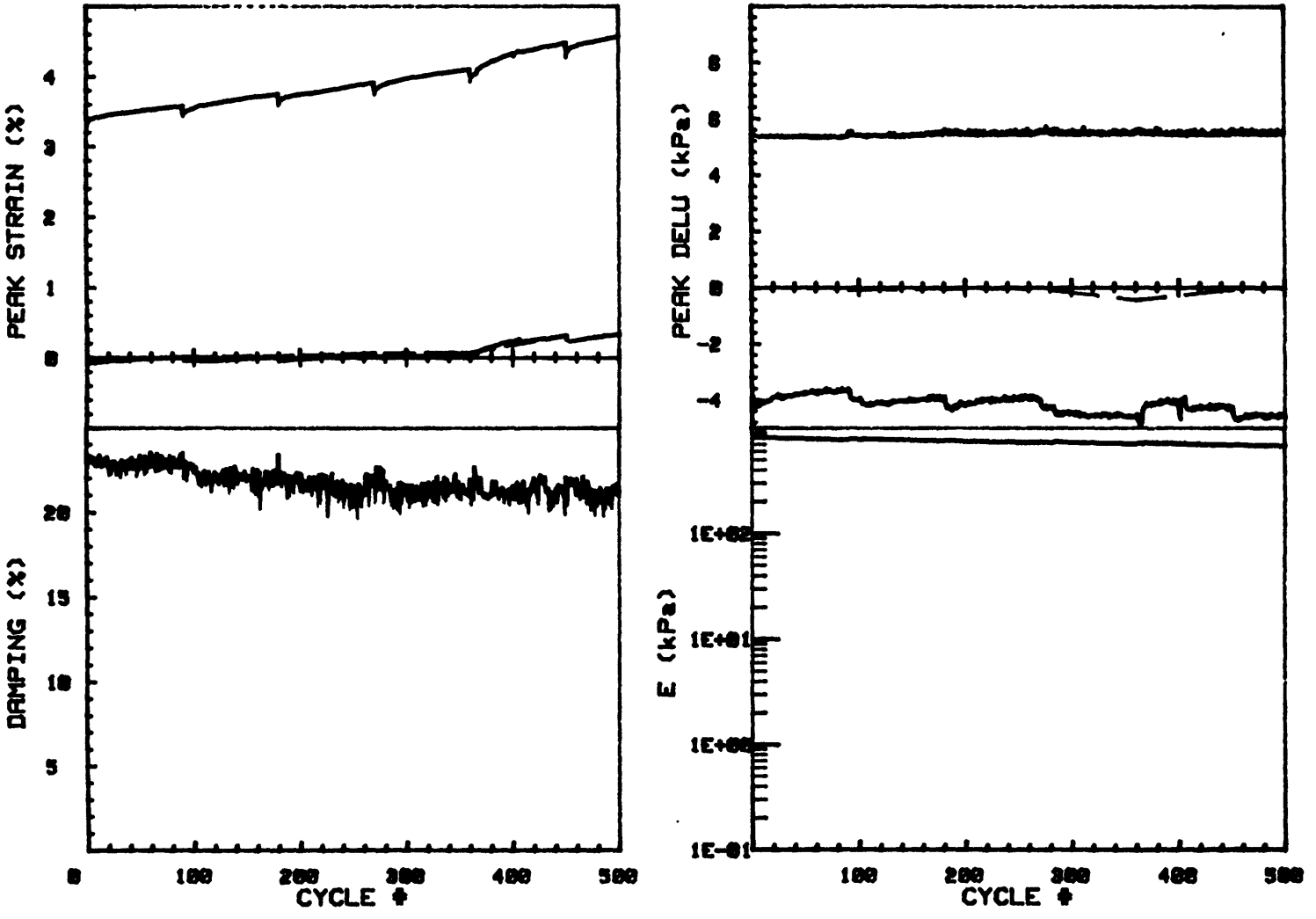

CRUISE DC4-81-NS		INCREMENT (cm)	101-109
CORE NO.	685A2	TEST NO.	TC62
SIG1c'(kPa)	4.4	STATIC qf (kPa)	18.0
SIG3c'(kPa)	4.4	AVG MAX q (kPa)	7.6 (42.2%)
INDUCED OCR	1.0	AVG MIN q (kPa)	-6.6 (36.7%)

Cycles 4001 - 4500

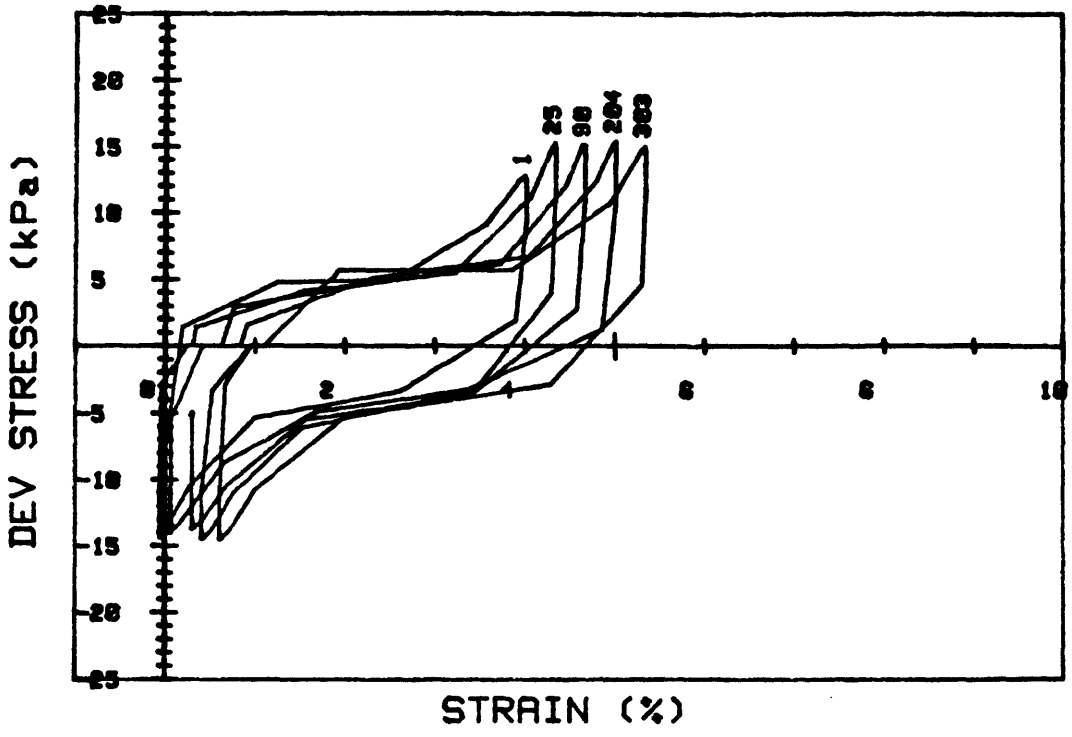

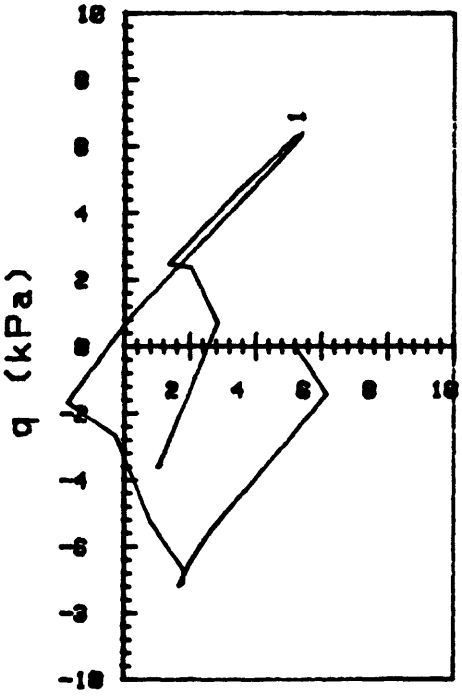

CRUISE DC4-81-NS		INCREMENT (cm)	101-109
CORE NO.	685A2	TEST NO.	TC62
SIG1c'(kPa)	4.7	STATIC qf (kPa)	18.0
SIG3c'(kPa)	4.7	AVG MAX q (kPa)	7.6 (42.2%)
INDUCED OCR	1.0	AVG MIN q (kPa)	-7.1 (39.4%)

Cycles 4501 - 4860

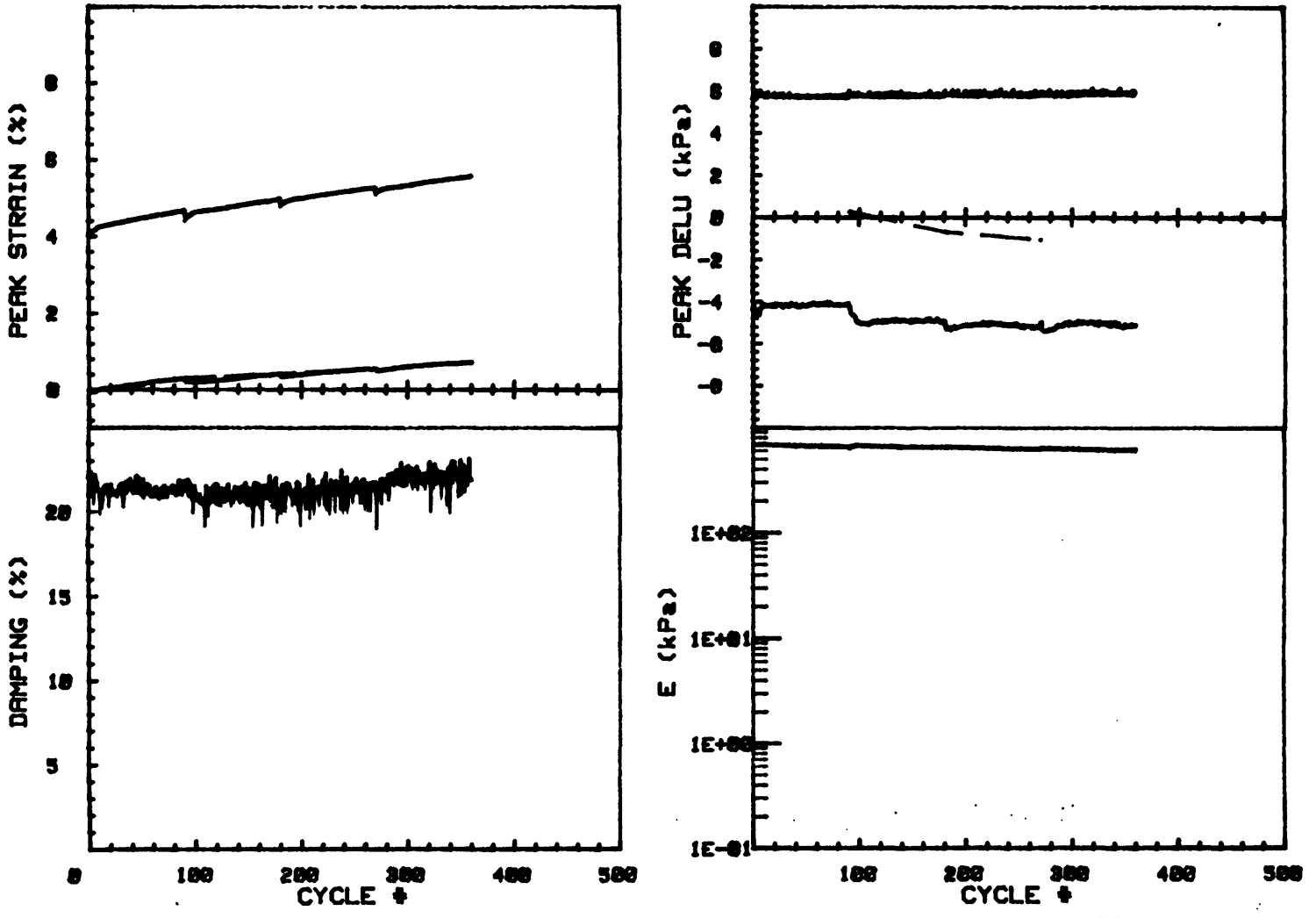

CRUISE DC4-81-NS		INCREMENT (cm)	101-109
CORE NO.	685A2	TEST NO.	TC62
SIG1c'(kPa)	4.7	STATIC qf (kPa)	18.0
SIG3c'(kPa)	4.7	AVG MAX q (kPa)	7.6 (42.2%)
INDUCED OCR	1.0	AVG MIN q (kPa)	-7.1 (39.4%)

Cycles 4501 - 4860

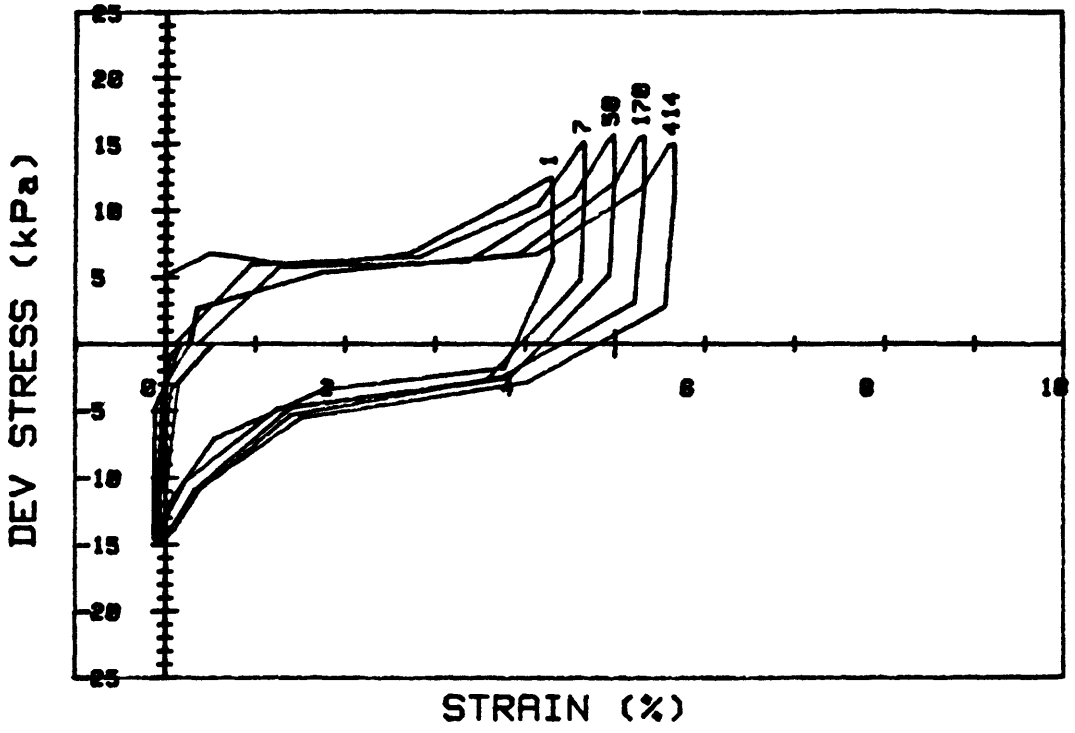

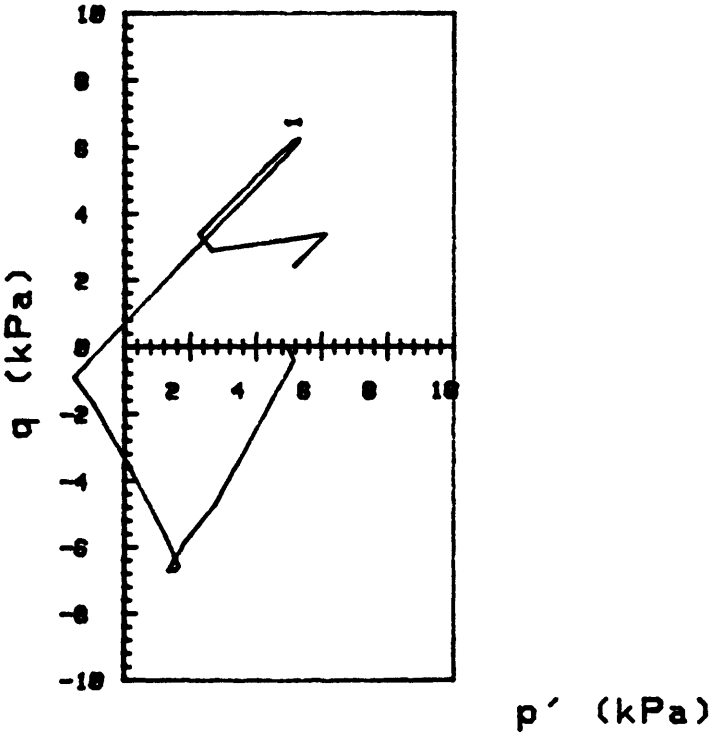

CRUISE DC4-81-NS		INCREMENT (cm)	101-109
CORE NO.	685A2	TEST NO.	TC62
SIG1c'(kPa)	2.7	STATIC qf (kPa)	18.0
SIG3c'(kPa)	2.7	AVG MAX q (kPa)	7.7 (42.8%)
INDUCED OCR	1.0	AVG MIN q (kPa)	-7.1 (39.4%)

Cycles 4861 - 5300

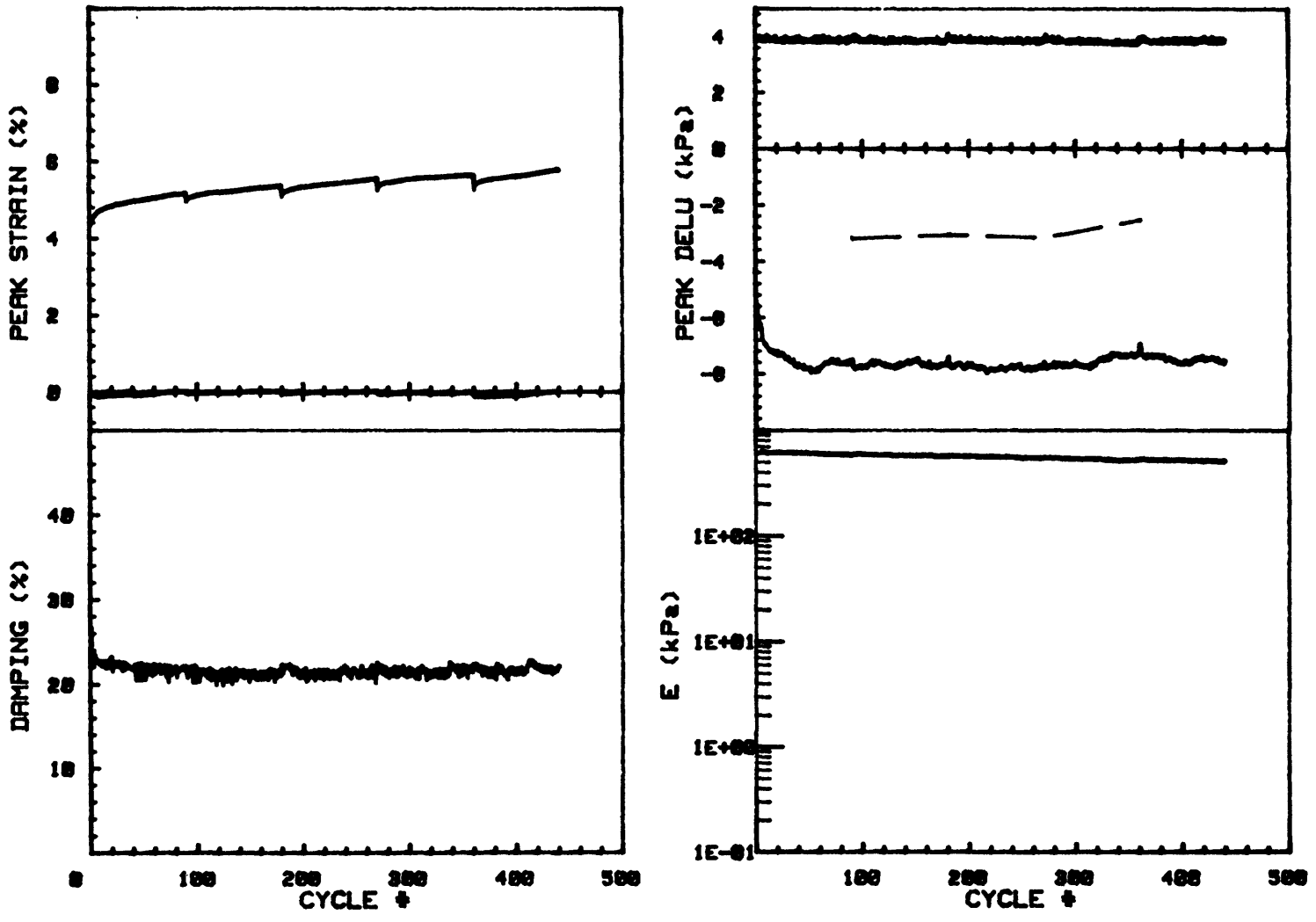

CRUISE DC4-81-NS		INCREMENT (cm)	101-109
CORE NO.	685A2	TEST NO.	TC62
SIG1c'(kPa)	2.7	STATIC qf (kPa)	18.0
SIG3c'(kPa)	2.7	AVG MAX q (kPa)	7.7 (42.8%)
INDUCED OCR	1.0	AVG MIN q (kPa)	-7.1 (39.4%)

Cycles 4861 - 5300

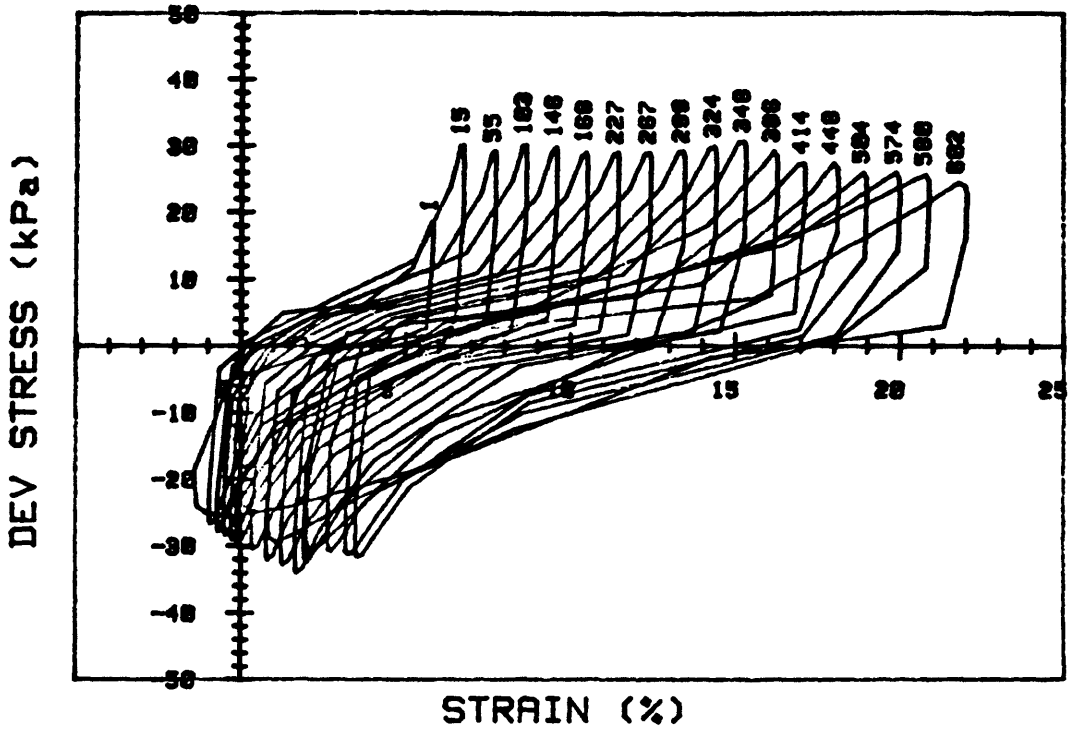

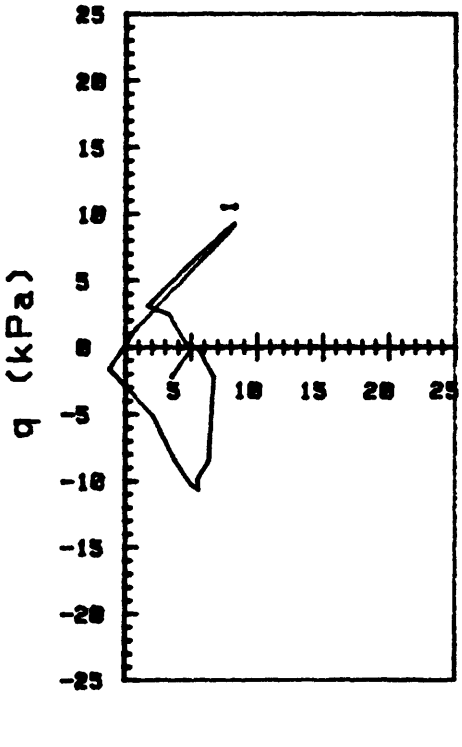

CRUISE DC4-81-NS		INCREMENT (cm)	101-109
CORE NO.	685A2	TEST NO.	TC62
SIG1c'(kPa)	5.7	STATIC qf (kPa)	18.0
SIG3c'(kPa)	5.7	AVG MAX q (kPa)	14.2 (78.9%)
INDUCED OCR	1.0	AVG MIN q (kPa)	-15.0 (83.3%)

Cycles 5301 - 5910

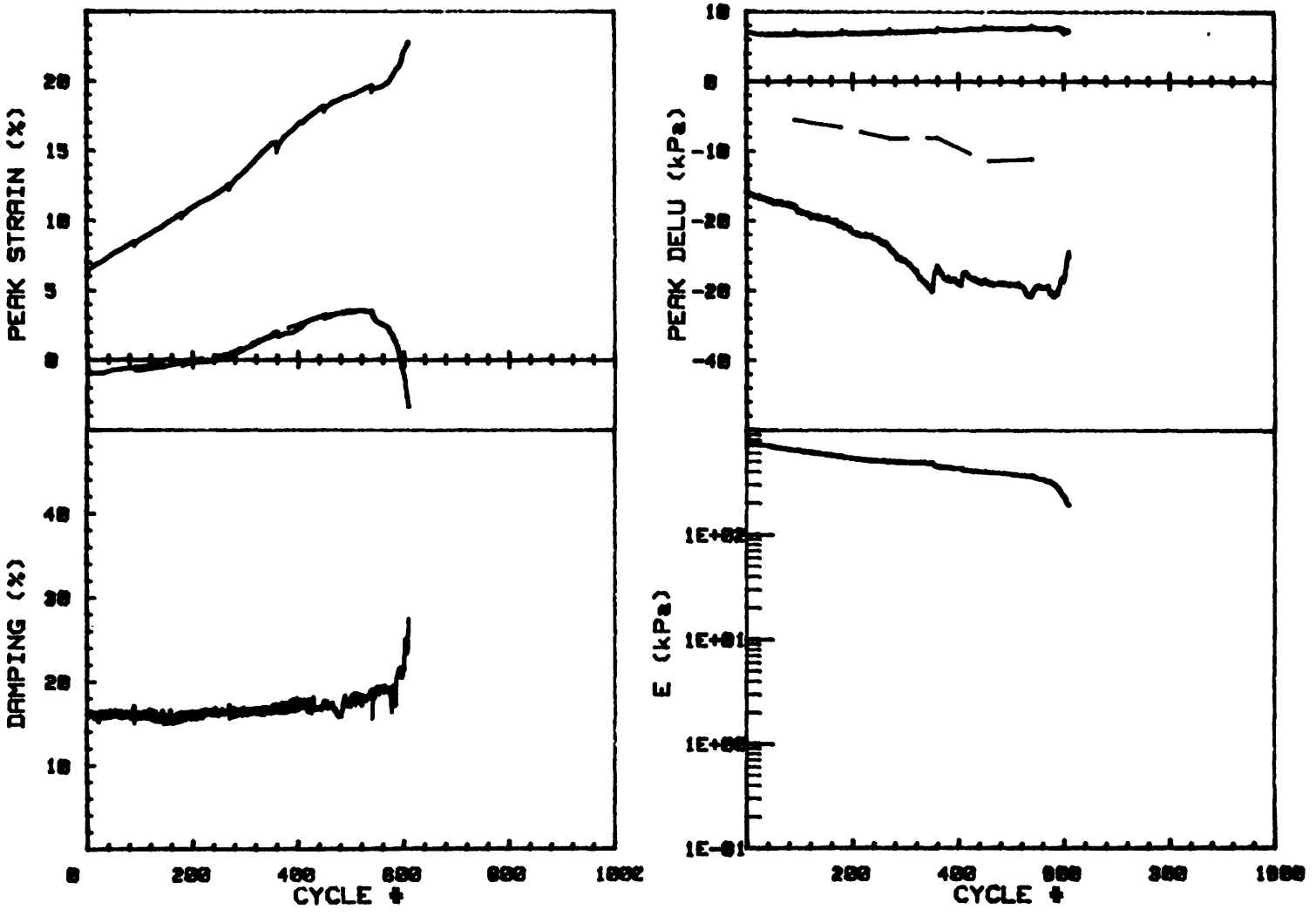

CRUISE DC4-81-NS		INCREMENT (cm)	101-109
CORE NO.	685A2	TEST NO.	TC62
SIG1c'(kPa)	5.7	STATIC qf (kPa)	18.0
SIG3c'(kPa)	5.7	AVG MAX q (kPa)	14.2 (78.9%)
INDUCED OCR	1.0	AVG MIN q (kPa)	-15.0 (83.3%)

Cycles 5301 - 5910

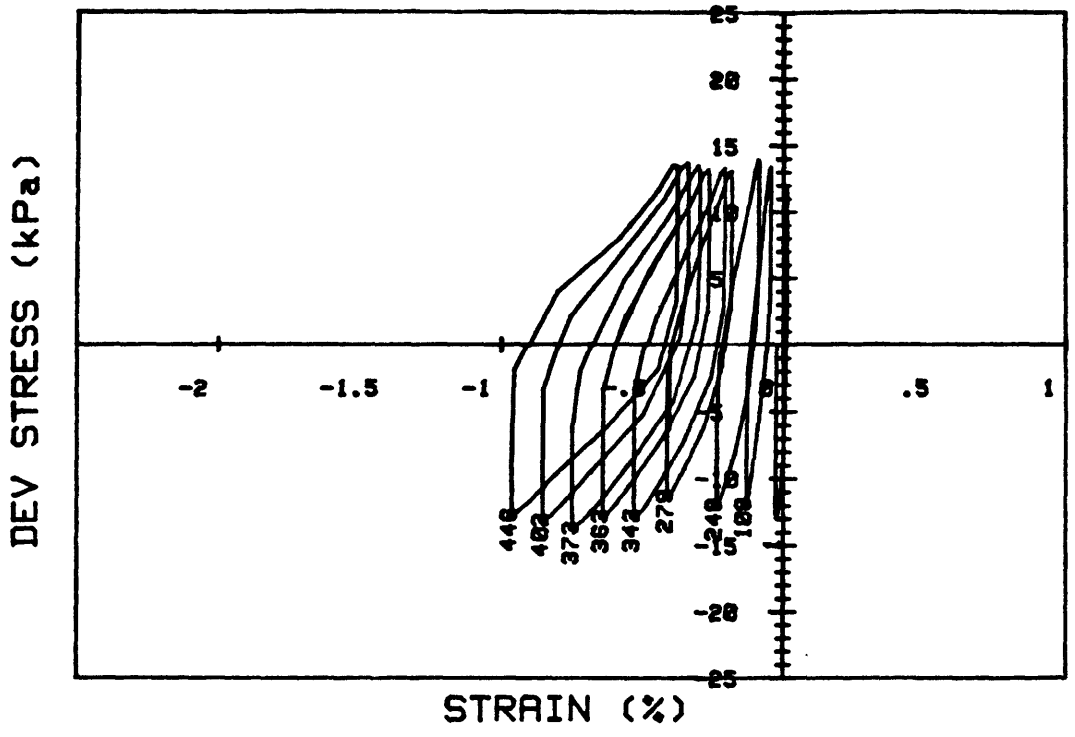

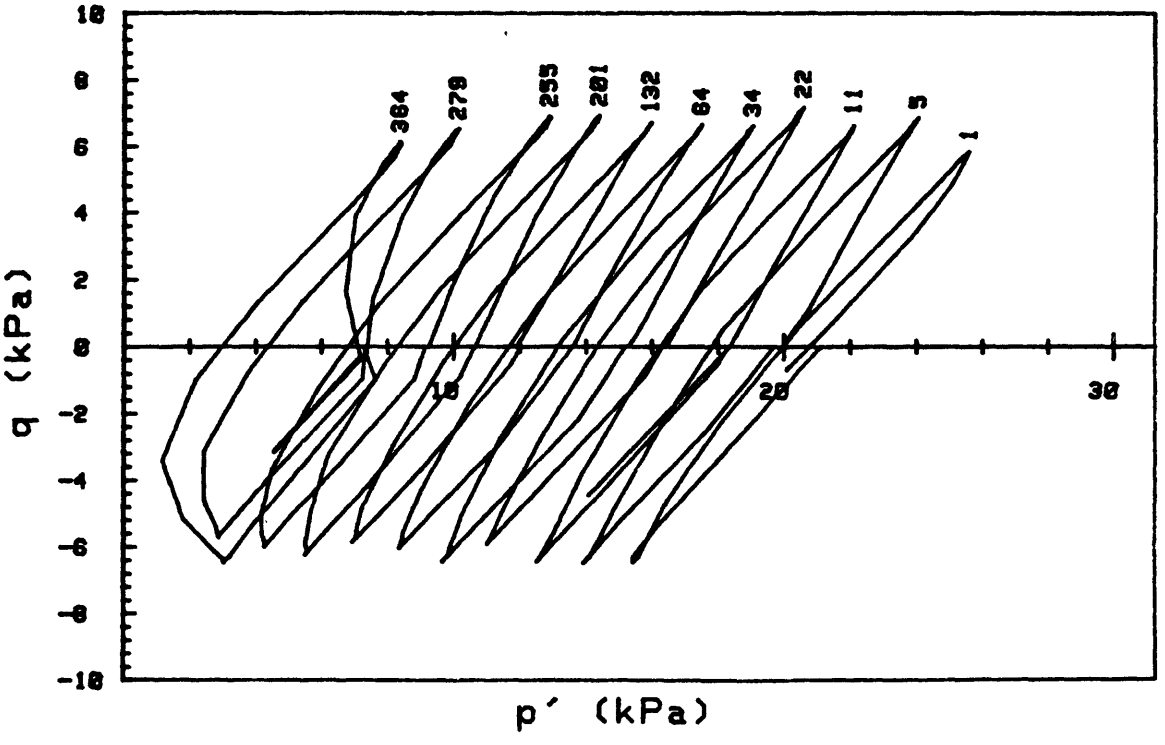

CRUISE DC4-81-NS		INCREMENT (cm)	101-109
CORE NO.	685A2	TEST NO.	TC74
SIG1c'(kPa)	20.8	STATIC qf (kPa)	20.8
SIG3c'(kPa)	20.8	AVG MAX q (kPa)	6.8 (32.7%)
INDUCED OCR	1.0	AVG MIN q (kPa)	-6.2 (29.8%)

Cycles 1 - 820

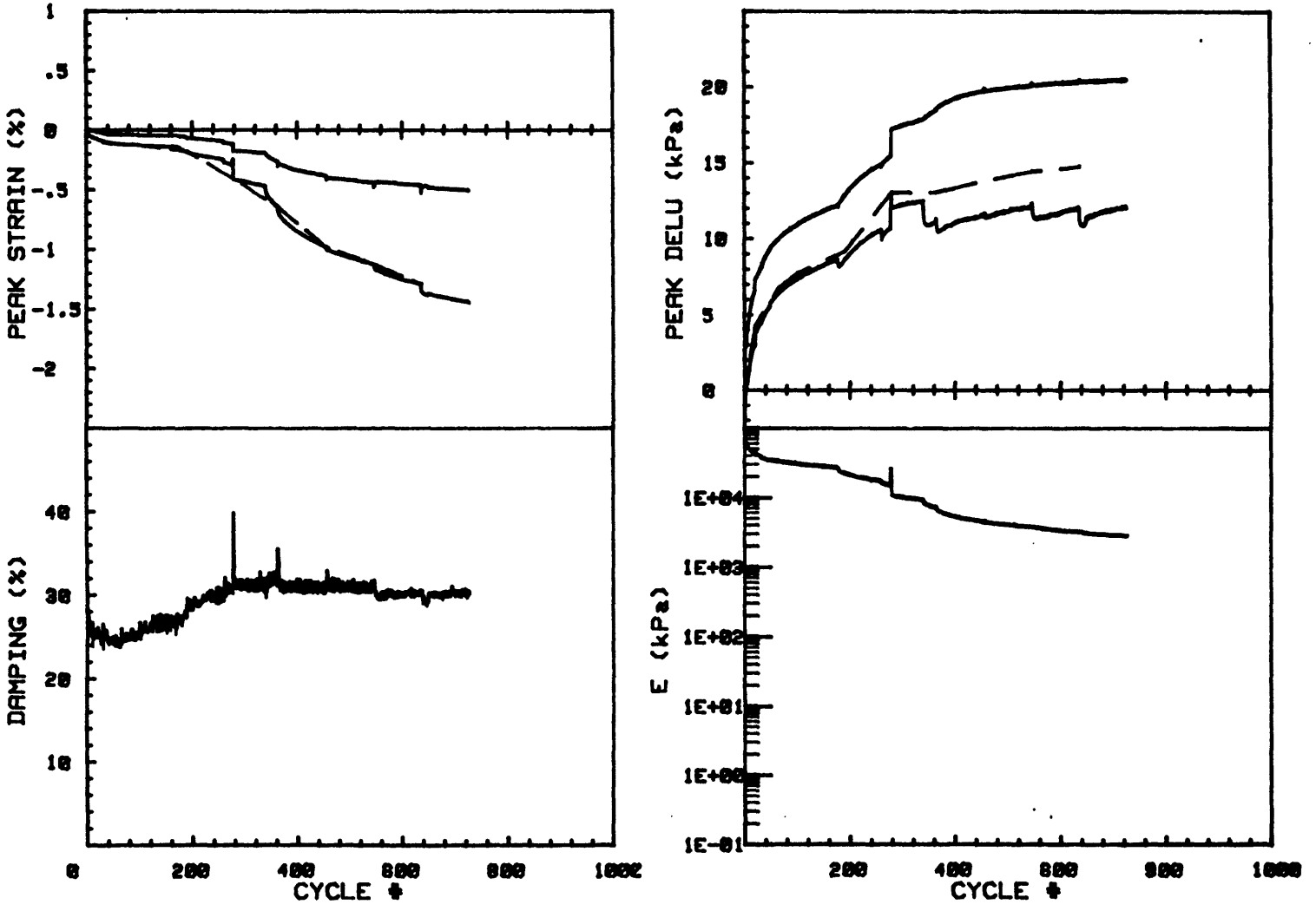

CRUISE DC4-81-NS		INCREMENT (cm)	101-109
CORE NO.	685A2	TEST NO.	TC74
SIG1c'(kPa)	20.8	STATIC qf (kPa)	20.8
SIG3c'(kPa)	20.8	AVG MAX q (kPa)	6.8 (32.7%)
INDUCED OCR	1.0	AVG MIN q (kPa)	-6.2 (29.8%)

Cycles 1 - 820

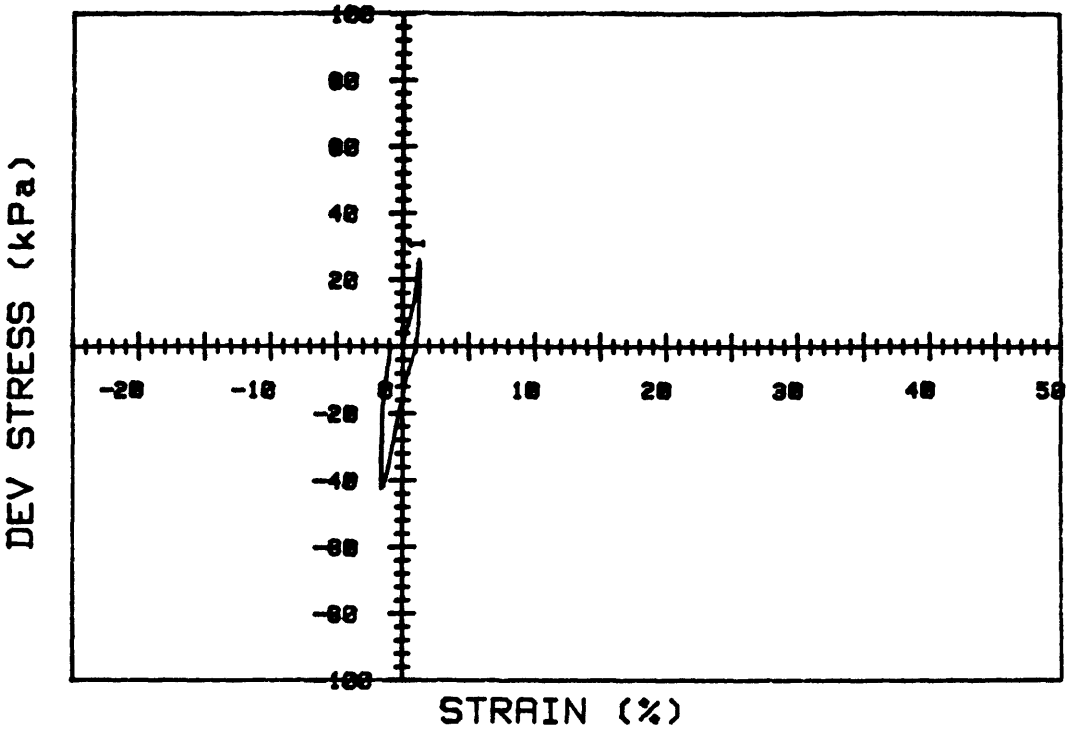

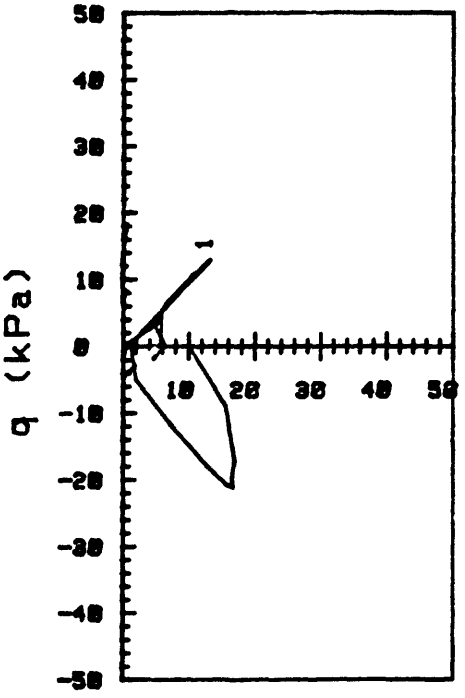

CRUISE DC4-81-NS		INCREMENT (cm)	101-109
CORE NO.	685A2	TEST NO.	TC74
SIG1c'(kPa)	6.4	STATIC qf (kPa)	20.8
SIG3c'(kPa)	6.4	AVG MAX q (kPa)	29.9 (143.8%)
INDUCED OCR	1.0	AVG MIN q (kPa)	-26.6 (127.9%)

Cycles 821 - 850

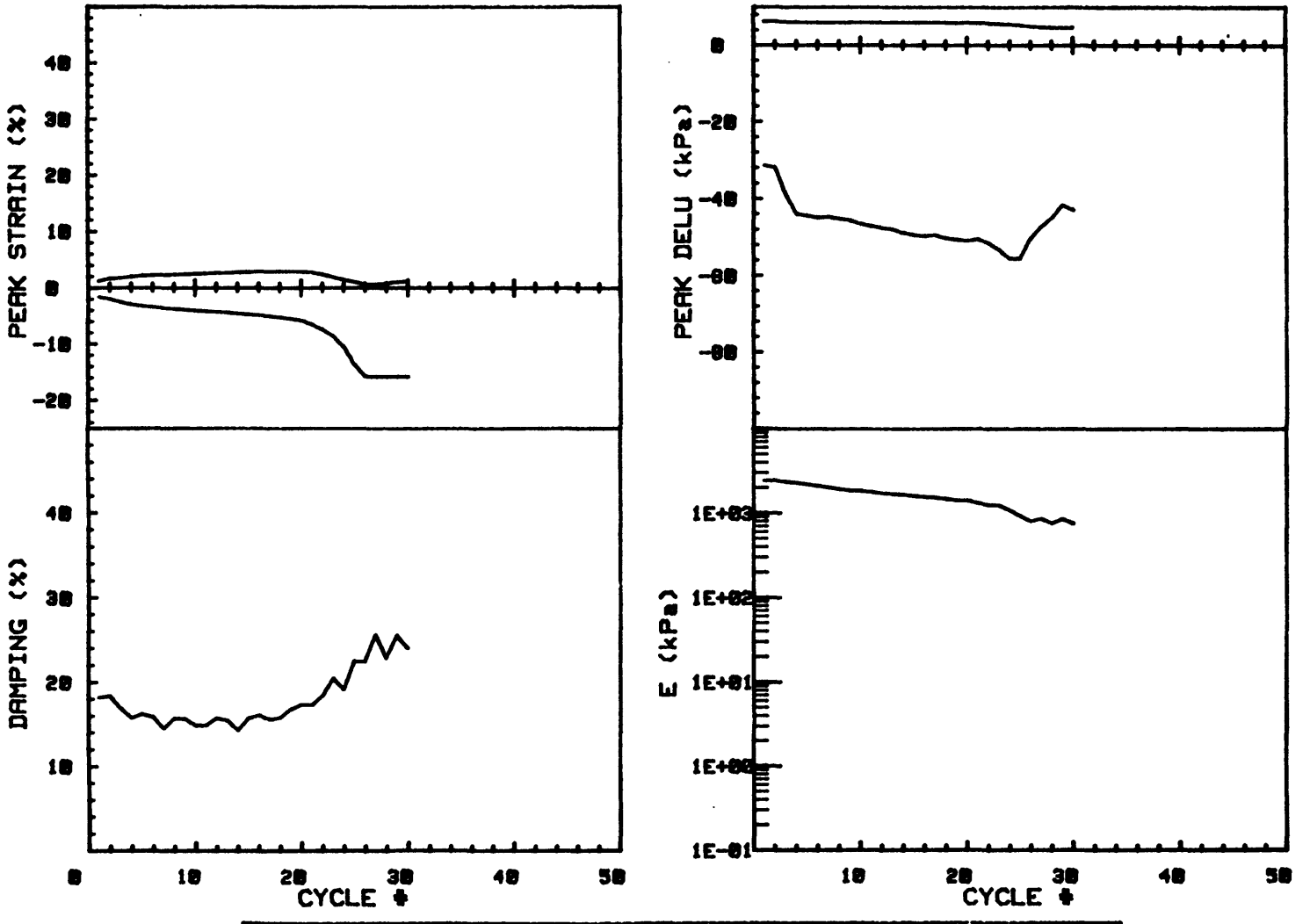

CRUISE DC4-81-NS		INCREMENT (cm)	101-109
CORE NO.	685A2	TEST NO.	TC74
SIG1c'(kPa)	6.4	STATIC qf (kPa)	20.8
SIG3c'(kPa)	6.4	AVG MAX q (kPa)	29.9 (143.8%)
INDUCED OCR	1.0	AVG MIN q (kPa)	-26.6 (127.9%)

Cycles 821 - 850

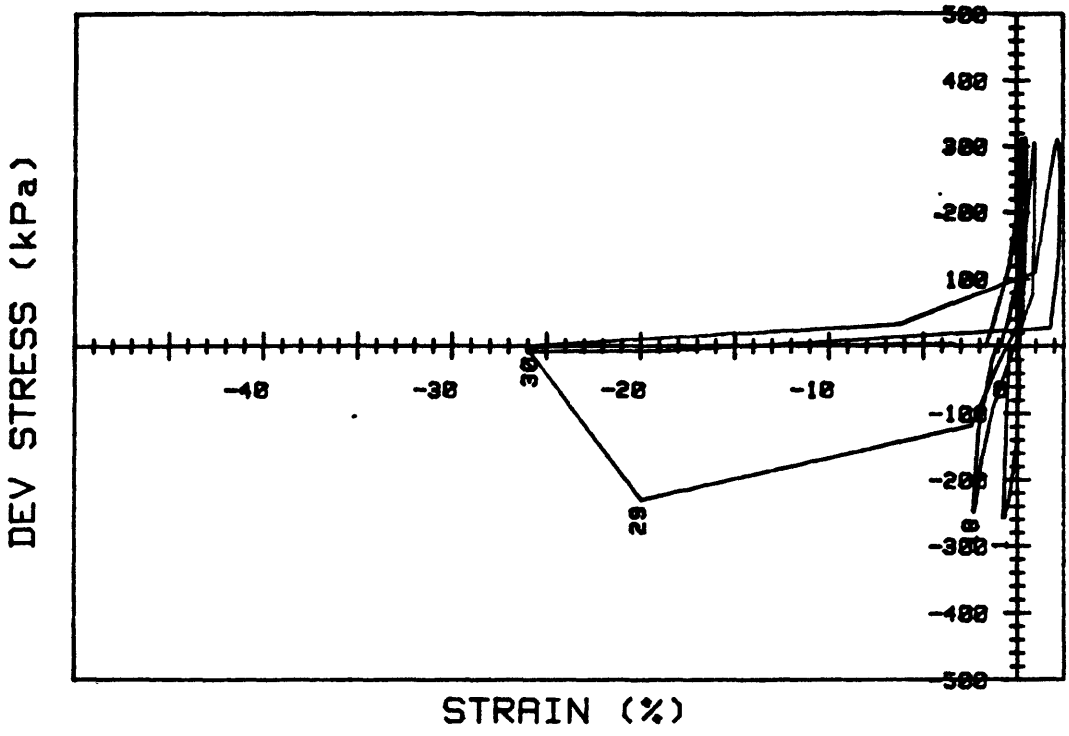

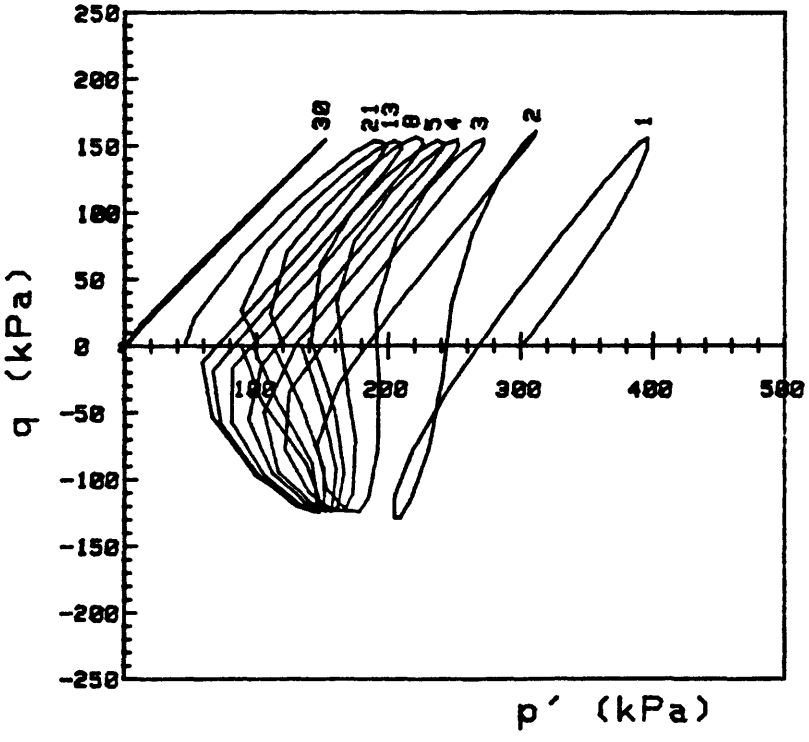

CRUISE DC4-81-NS		INCREMENT (cm)	200-210
CORE NO. 685A2		TEST NO.	TC50
SIG1c'(kPa)	301.0	STATIC qf (kPa)	300.0
SIG3c'(kPa)	301.0	AVG MAX q (kPa)	154.6 (51.5%)
INDUCED OCR	1.0	AVG MIN q (kPa)	-120.4 (40.1%)

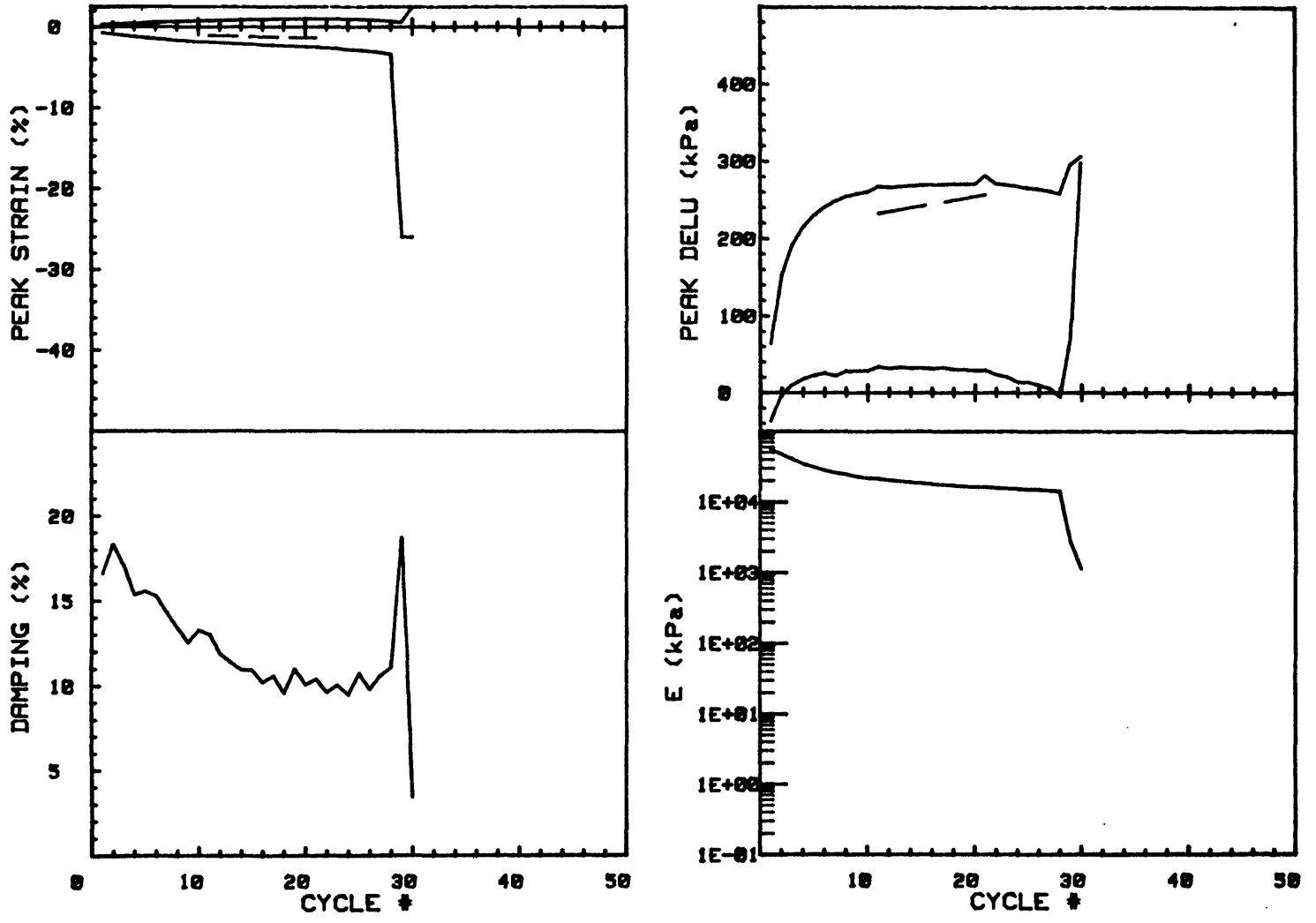

CRUISE DC4-81-NS		INCREMENT (cm)	200-210
CORE NO.	685A2	TEST NO.	TC50
SIG1c'(kPa)	301.0	STATIC qf (kPa)	300.0
SIG3c'(kPa)	301.0	AVG MAX q (kPa)	154.6 (51.5%)
INDUCED OCR	1.0	AVG MIN q (kPa)	-120.4 (40.1%)

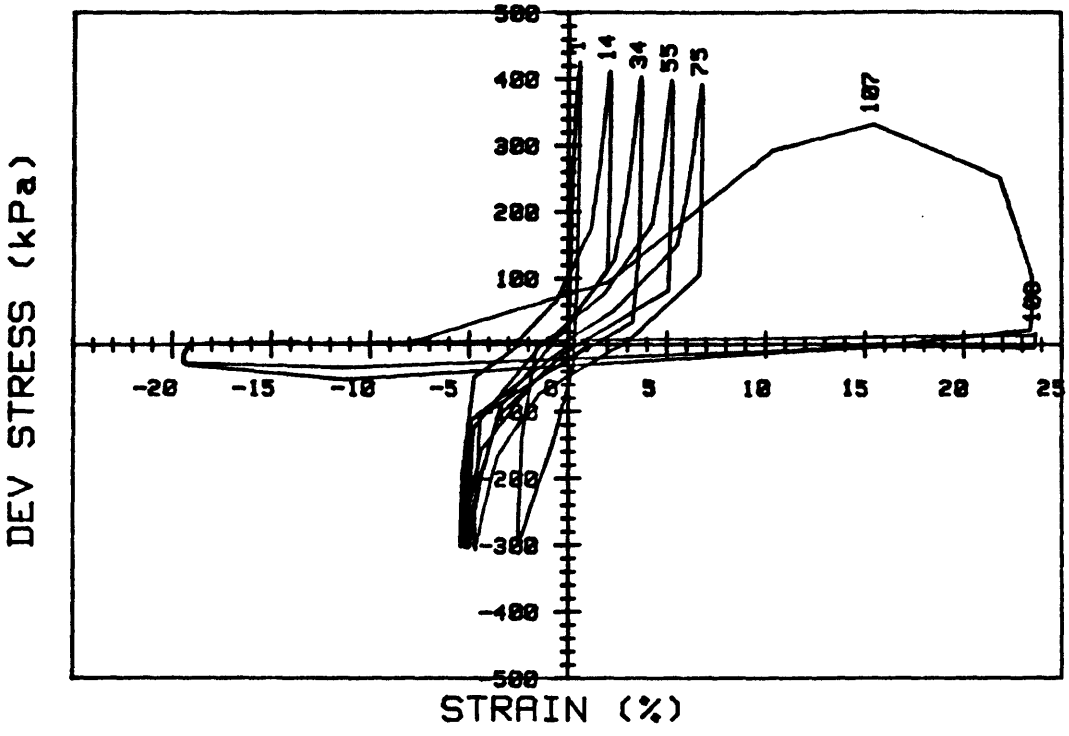

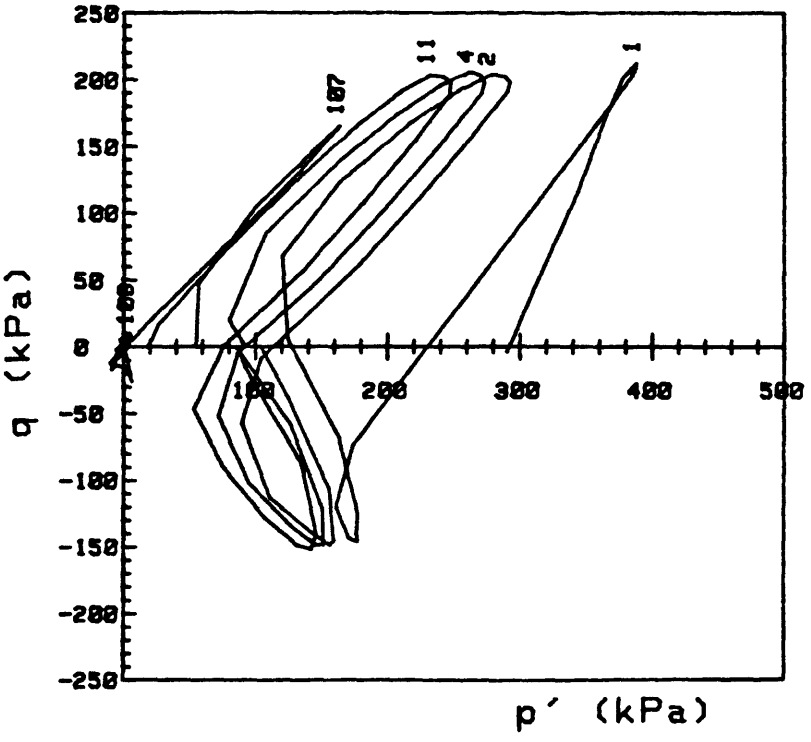

CRUISE DC4-81-NS		INCREMENT (cm)	200-210
CORE NO. 685A2		TEST NO.	TC51
SIG1c´(kPa)	294.1	STATIC qf (kPa)	300.0
SIG3c´(kPa)	294.1	AVG MAX q (kPa)	194.7 (64.9%)
INDUCED OCR	1.0	AVG MIN q (kPa)	-147.4 (49.1%)

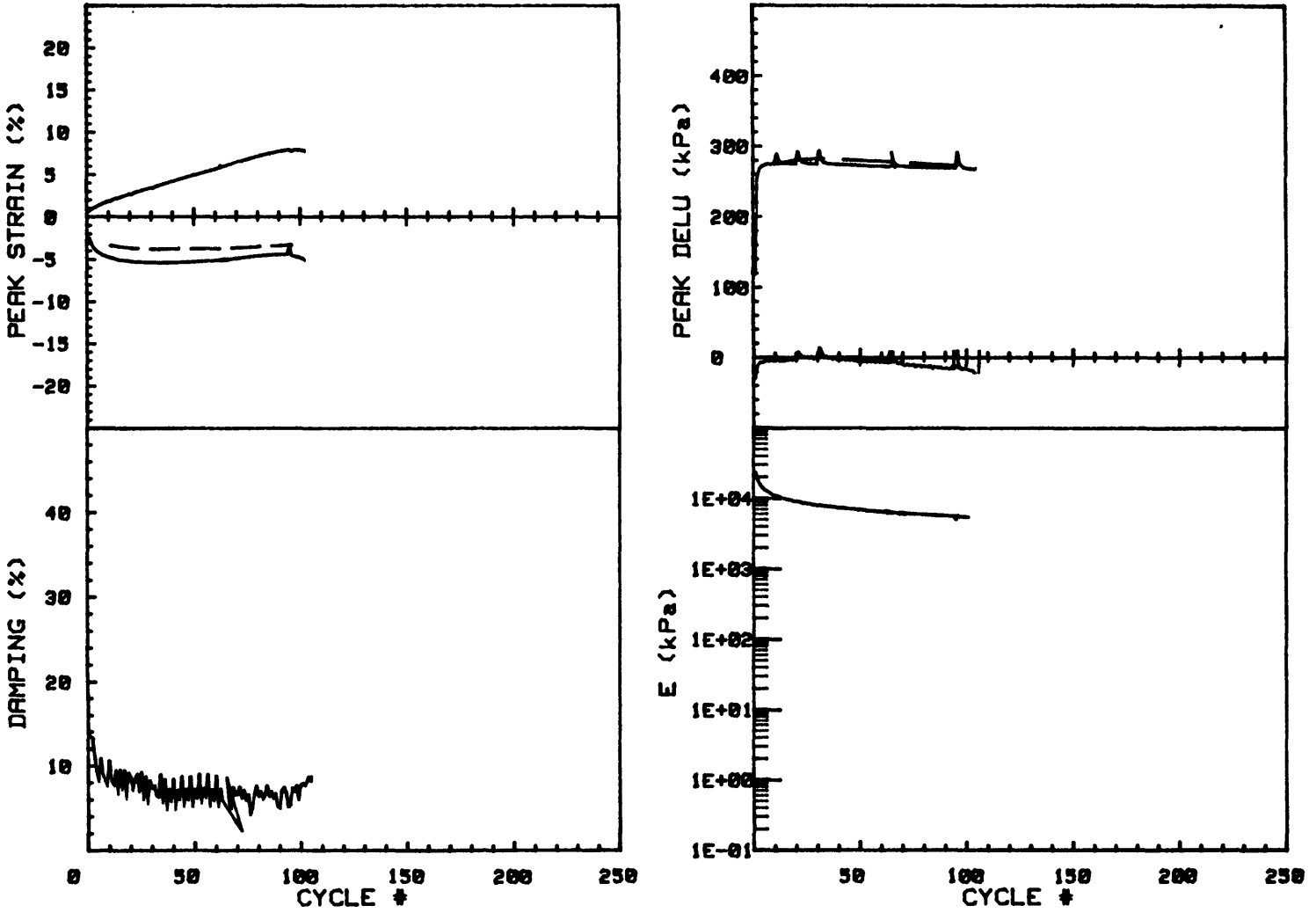

CRUISE DC4-81-NS		INCREMENT (cm)	200-210
CORE NO.	685A2	TEST NO.	TC51
SIG1c'(kPa)	294.1	STATIC qf (kPa)	300.0
SIG3c'(kPa)	294.1	AVG MAX q (kPa)	194.7 (64.9%)
INDUCED OCR	1.0	AVG MIN q (kPa)	-147.4 (49.1%)

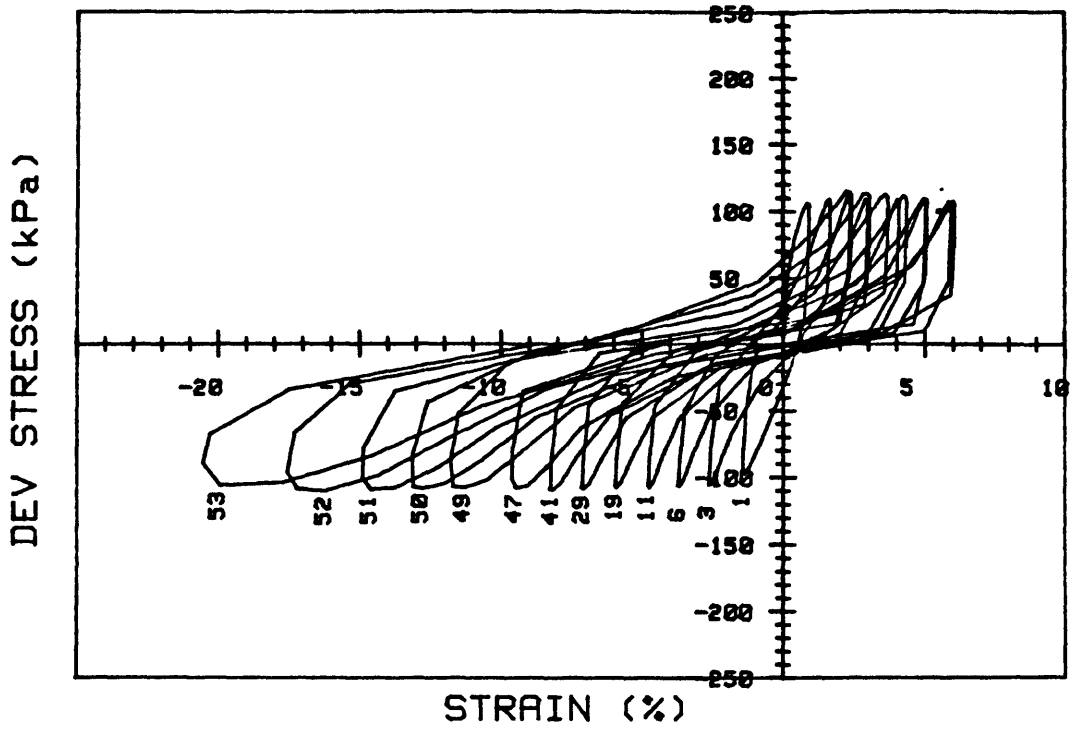

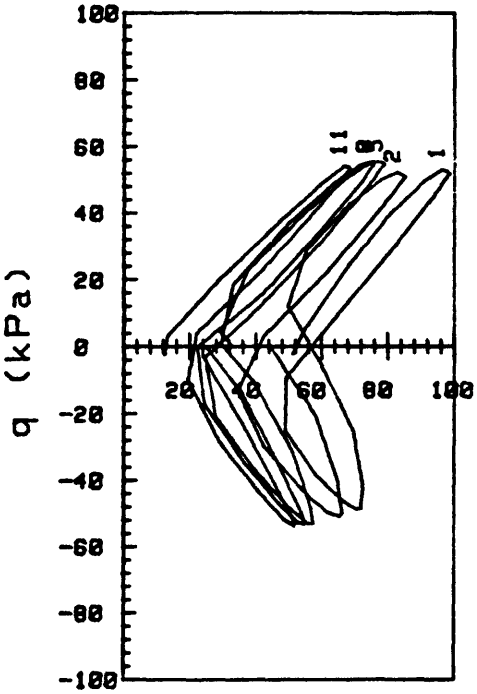

CRUISE DC4-81-NS		INCREMENT (cm)	16-24
CORE NO.	686A1	TEST NO.	TC88
SIG1c′(kPa)	53.4	STATIC qf (kPa)	50.0
SIG3c′(kPa)	53.4	AVG MAX q (kPa)	54.2 (108.4%)
INDUCED OCR	6.0	AVG MIN q (kPa)	-53.5 (107.0%)

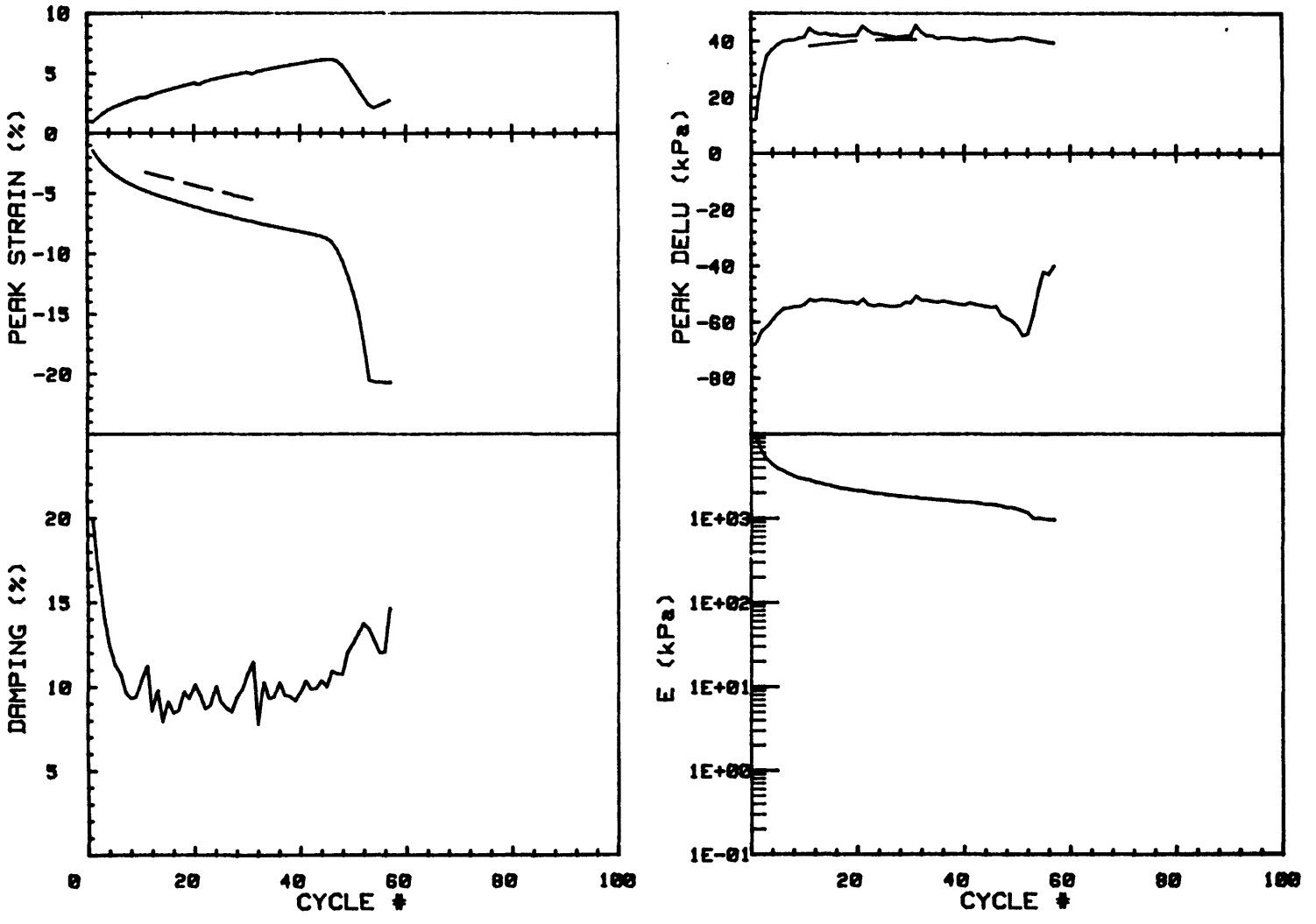

CRUISE DC4-81-NS		INCREMENT (cm)	16-24
CORE NO.	686A1	TEST NO.	TC88
SIG1c'(kPa)	53.4	STATIC qf (kPa)	50.0
SIG3c'(kPa)	53.4	AVG MAX q (kPa)	54.2 (108.4%)
INDUCED OCR	6.0	AVG MIN q (kPa)	-53.5 (107.0%)

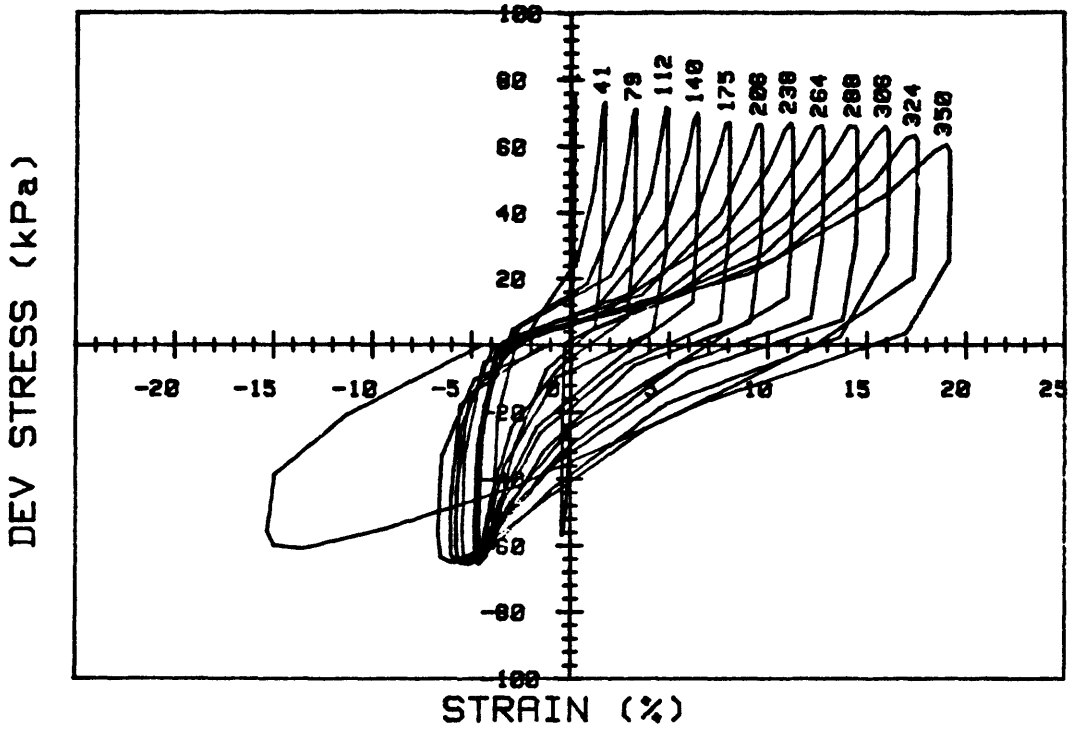

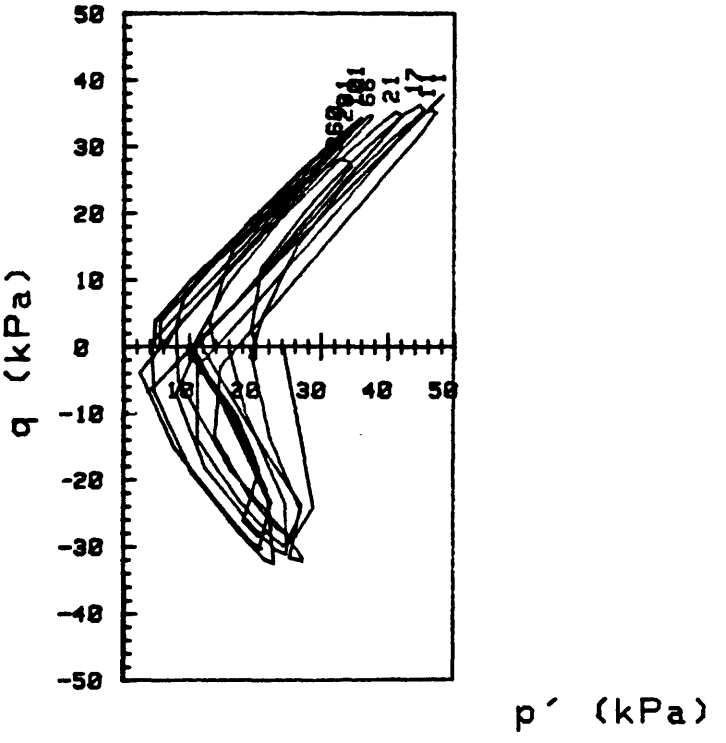

CRUISE DC4-81-NS		INCREMENT (cm)	16-24
CORE NO.	686A1	TEST NO.	TC89
SIG1c´(kPa)	50.0	STATIC qf (kPa)	50.0
SIG3c´(kPa)	50.0	AVG MAX q (kPa)	34.1 (68.2%)
INDUCED OCR	6.0	AVG MIN q (kPa)	-31.8 (63.6%)

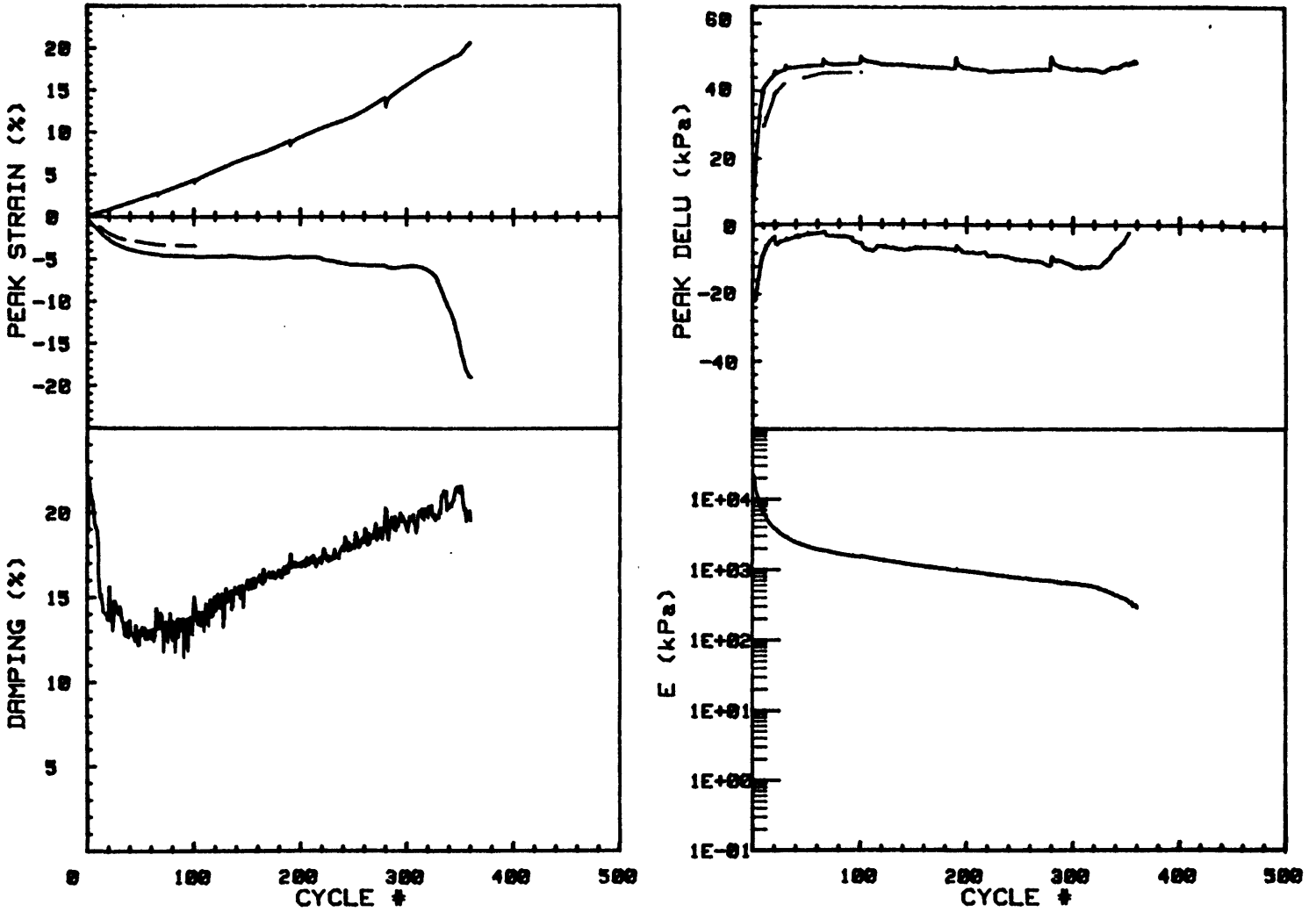

CRUISE DC4-81-NS		INCREMENT (cm)	16-24
CORE NO.	686A1	TEST NO.	TC89
SIG1c'(kPa)	50.0	STATIC qf (kPa)	50.0
SIG3c'(kPa)	50.0	AVG MAX q (kPa)	34.1 (68.2%)
INDUCED OCR	6.0	AVG MIN q (kPa)	-31.8 (63.6%)

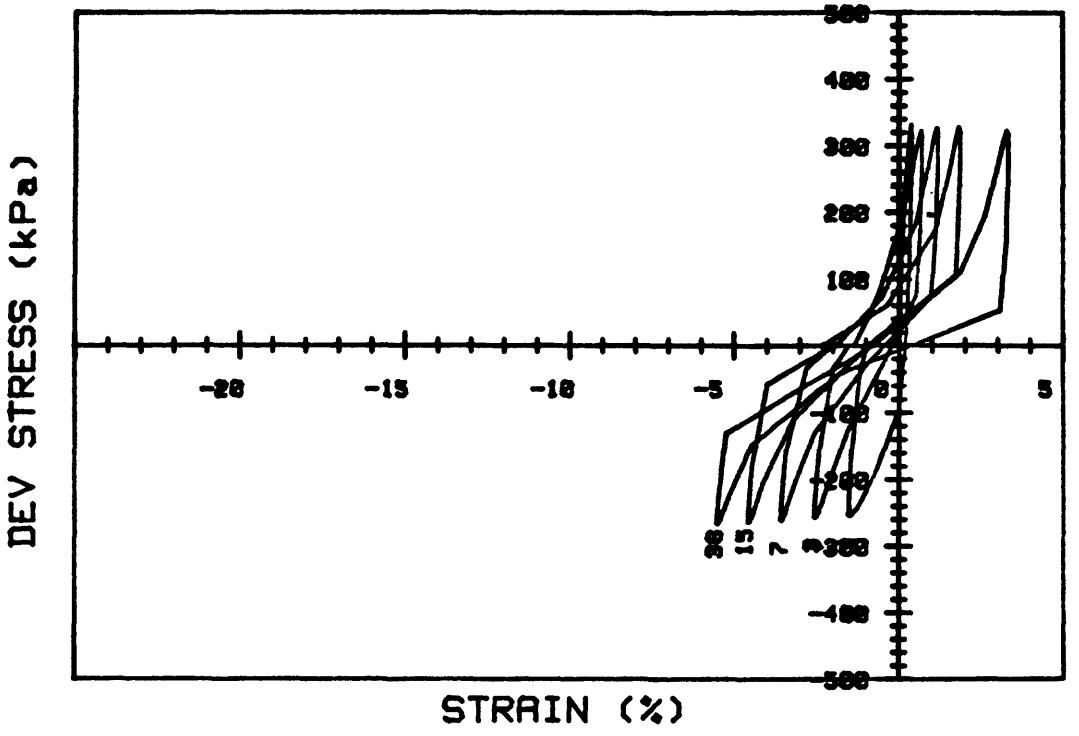

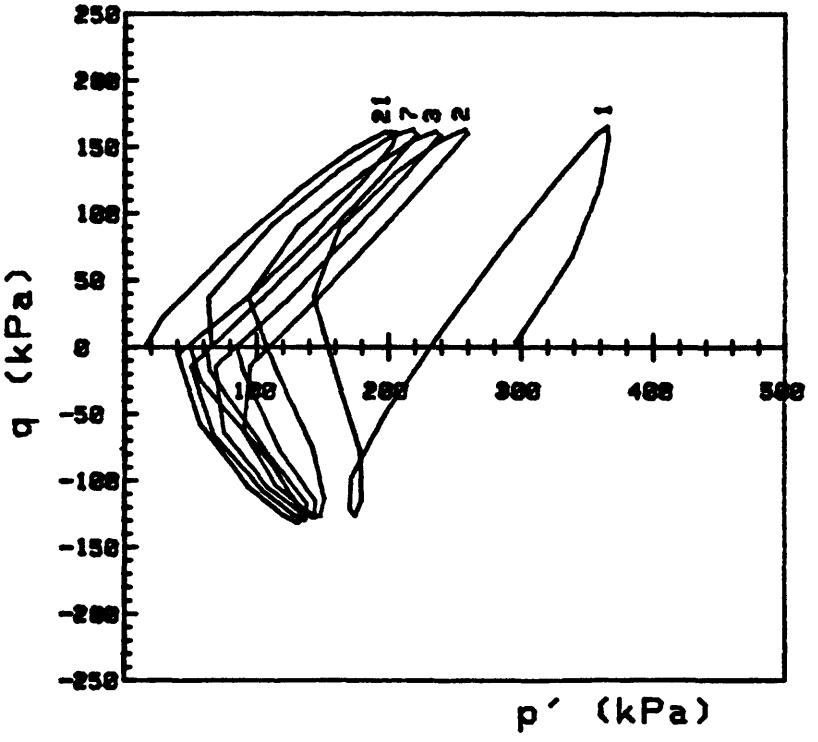

CRUISE DC4-81-NS		INCREMENT (cm)	31-39
CORE NO. 686A1		TEST NO.	TC84
SIG1c'(kPa)	296.7	STATIC qf (kPa)	300.0
SIG3c'(kPa)	296.7	AVG MAX q (kPa)	161.4 (53.8%)
INDUCED OCR	1.0	AVG MIN q (kPa)	-132.0 (44.0%)

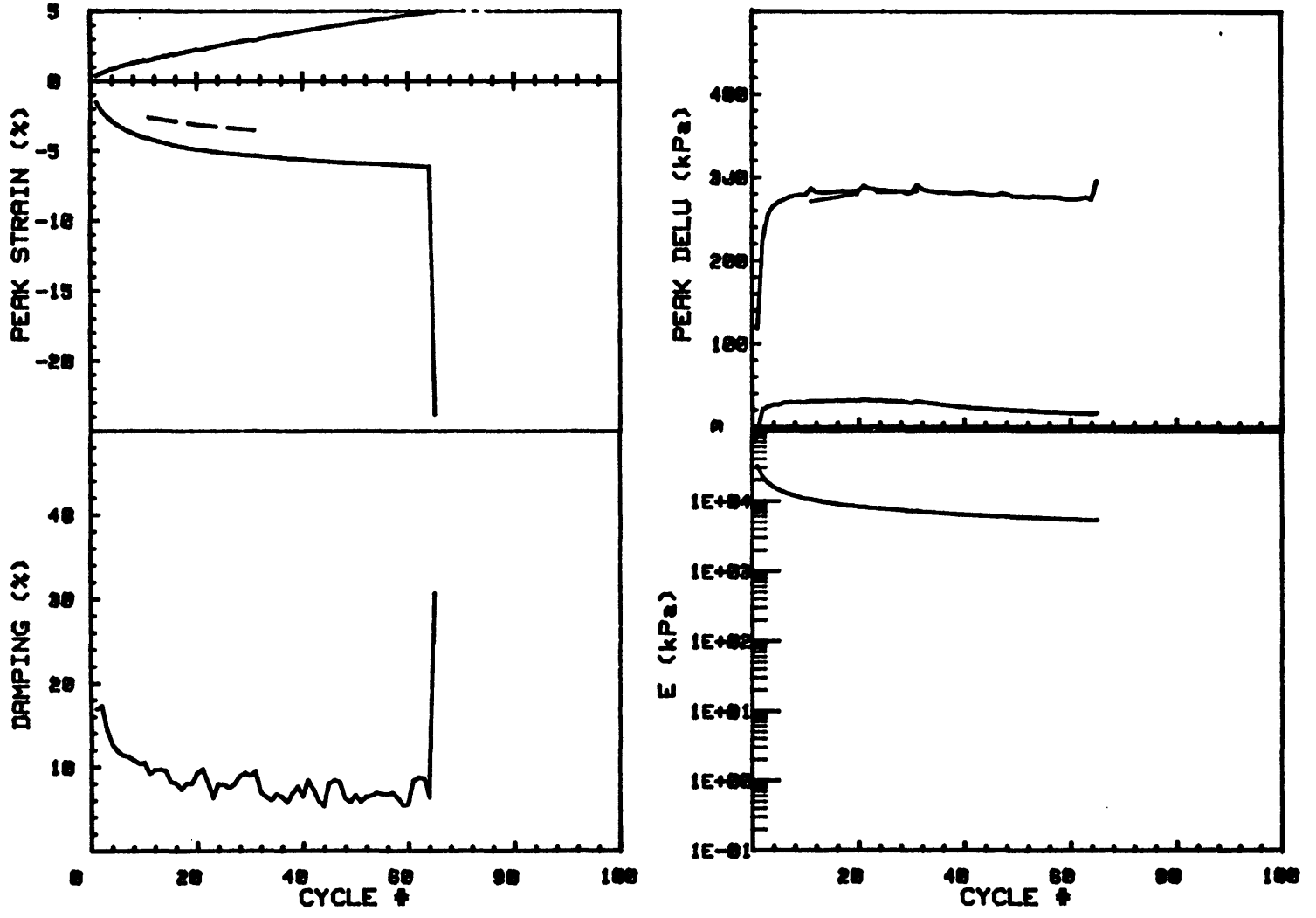

CRUISE DC4-81-NS		INCREMENT (cm)	31-39
CORE NO. 686A1		TEST NO.	TC84
SIG1c'(kPa)	296.7	STATIC qf (kPa)	300.0
SIG3c'(kPa)	296.7	AVG MAX q (kPa)	161.4 (53.8%)
INDUCED OCR	1.0	AVG MIN q (kPa)	-132.0 (44.0%)

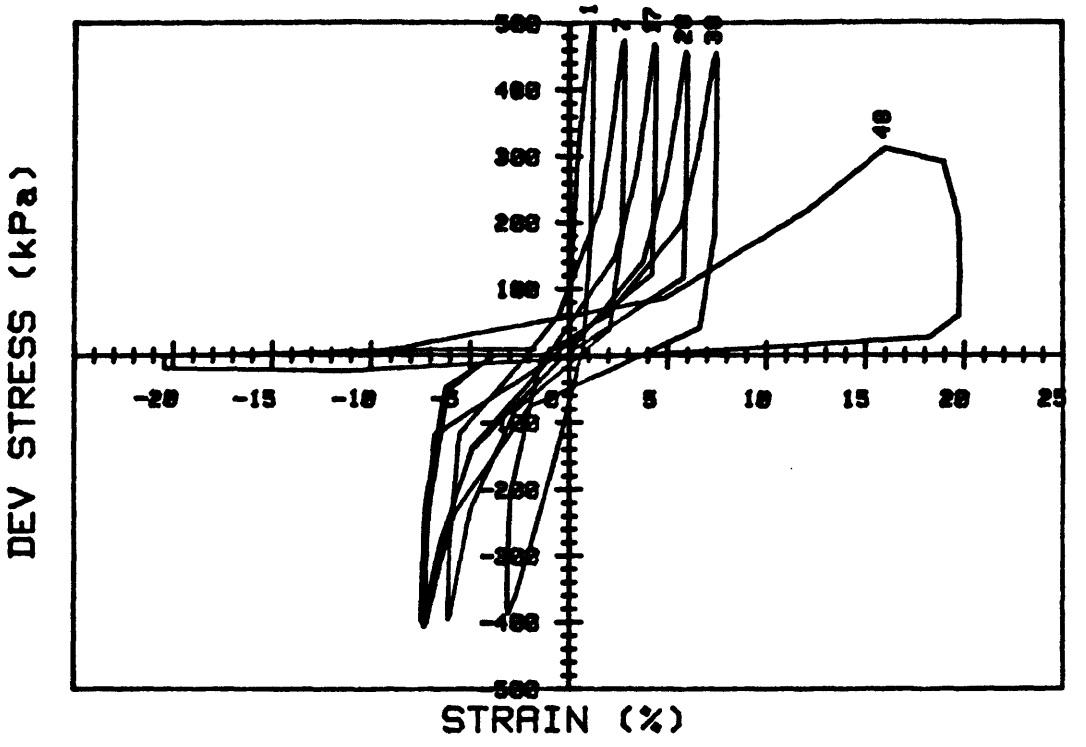

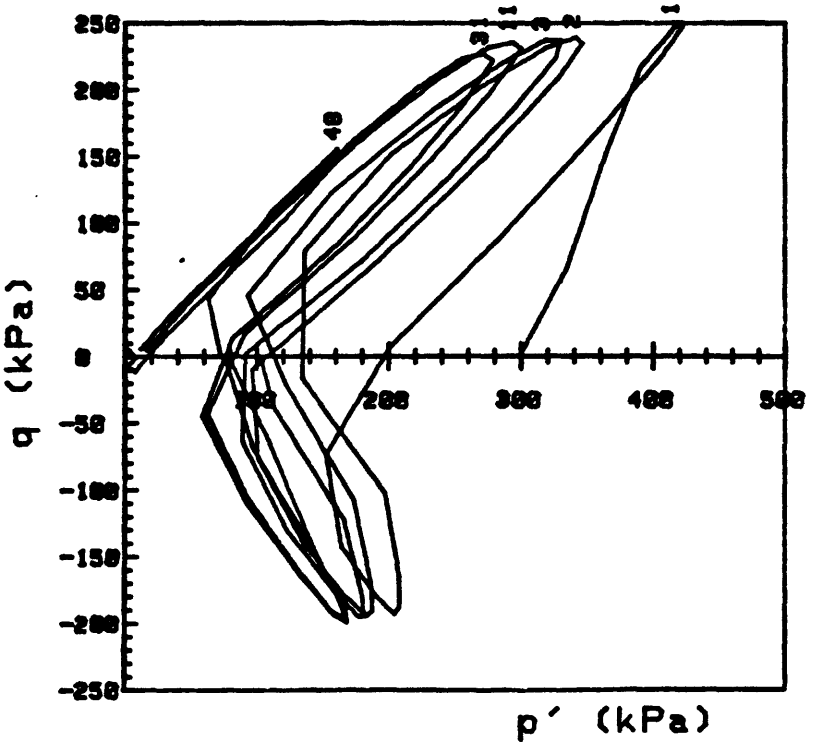

CRUISE DC4-81-NS		INCREMENT (cm)	31-39
CORE NO. 686A1		TEST NO.	TC85
SIG'c'(kPa)	298.9	STATIC qf (kPa)	300.0
SIG3c'(kPa)	298.9	AVG MAX q (kPa)	229.6 (76.5%)
INDUCED OCR	1.0	AVG MIN q (kPa)	-196.4 (65.5%)

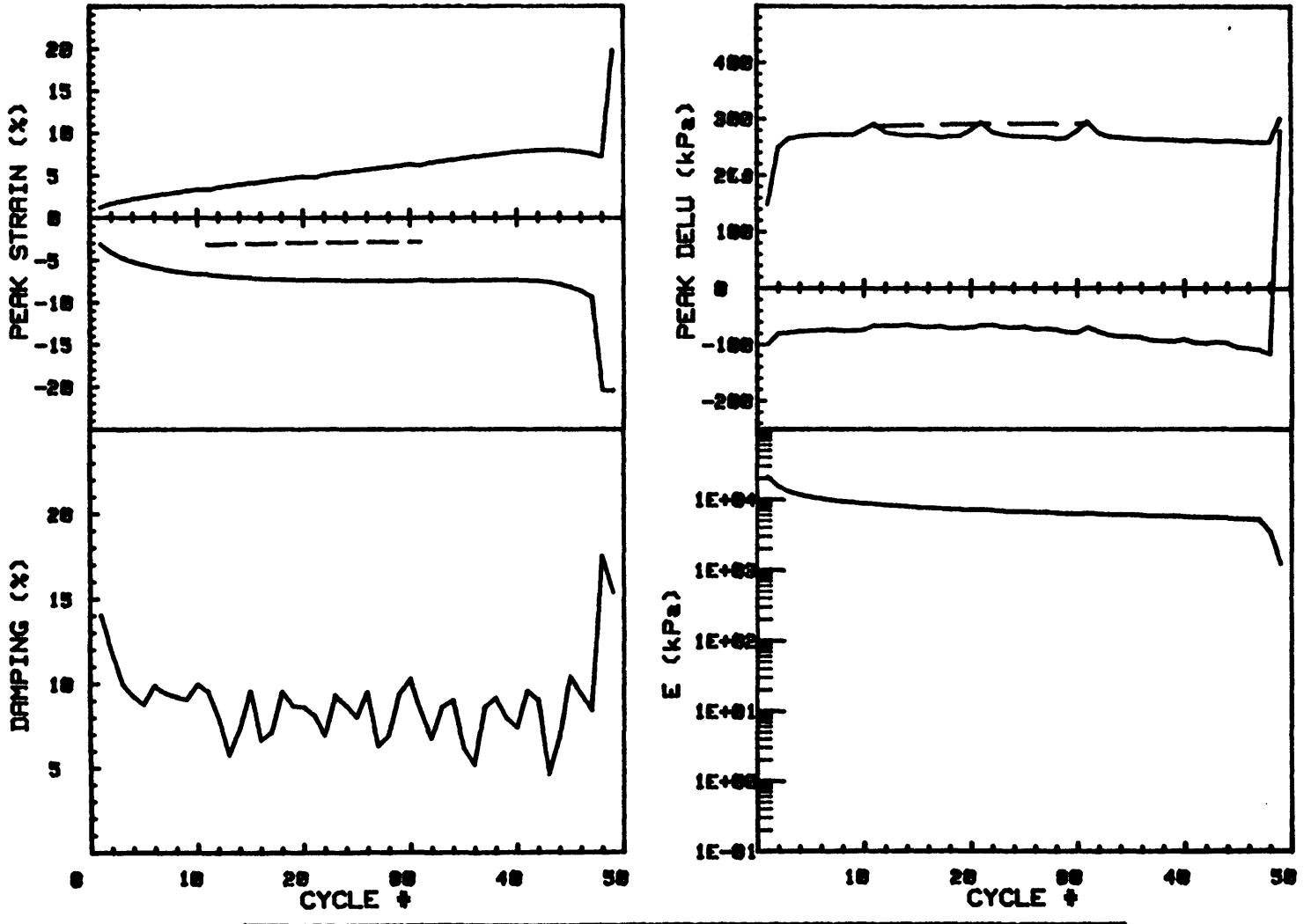

CRUISE DC4-81-NS		INCREMENT (cm)	31-39
CORE NO.	686A1	TEST NO.	TC85
SIG1c'(kPa)	298.9	STATIC qf (kPa)	300.0
SIG3c'(kPa)	298.9	AVG MAX q (kPa)	229.6 (76.5%)
INDUCED OCR	1.0	AVG MIN q (kPa)	-196.4 (65.5%)

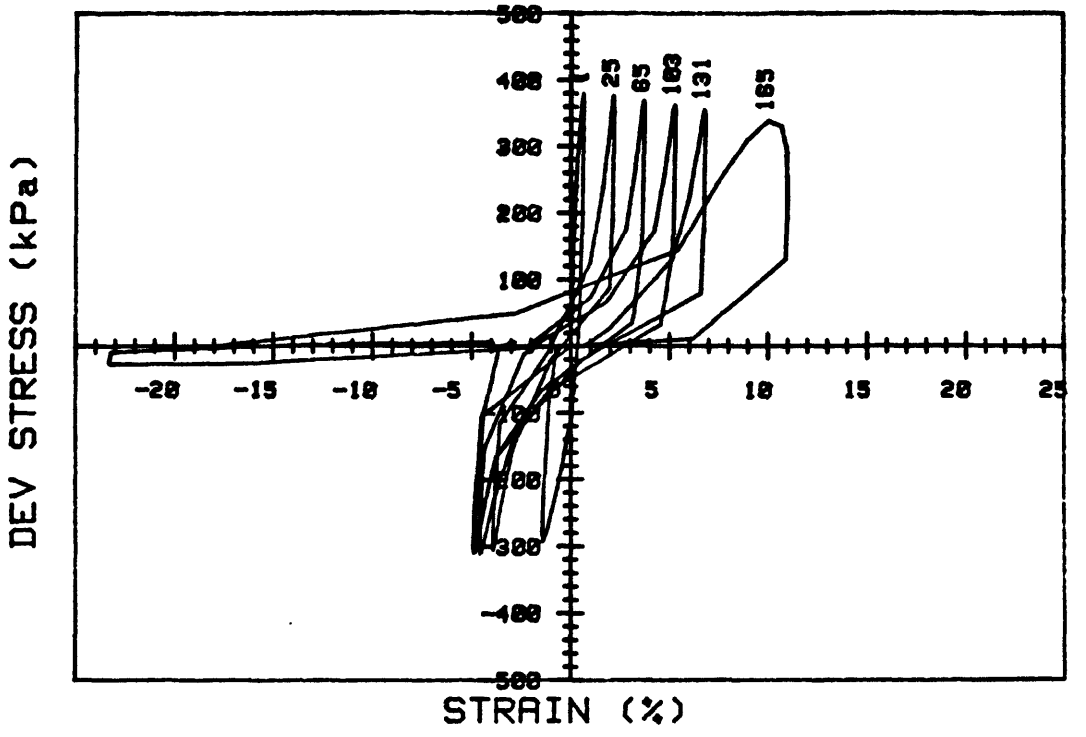

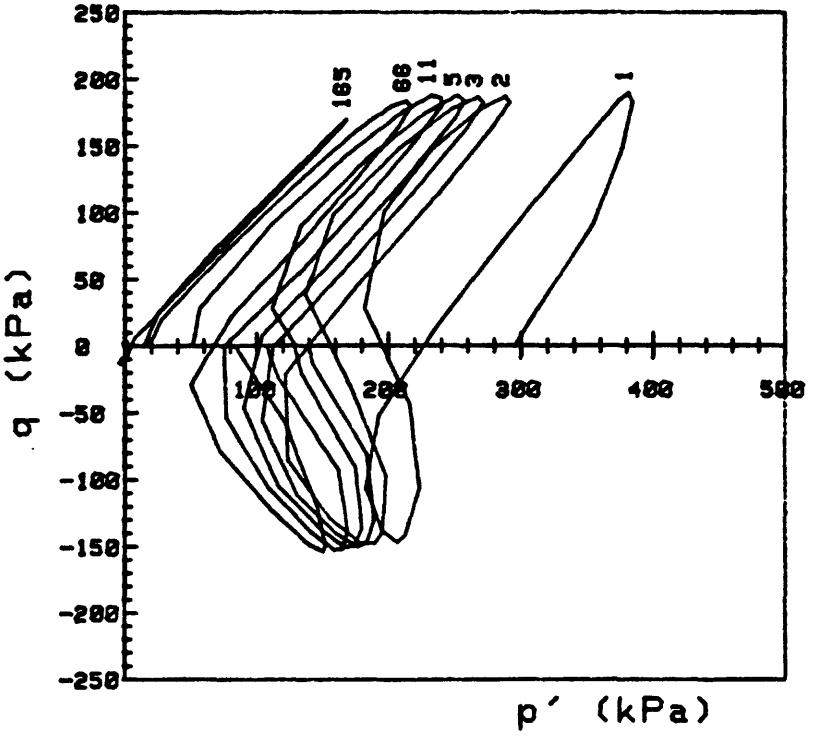

CRUISE DC4-81-NS		INCREMENT (cm)	41-49
CORE NO.	686A1	TEST NO.	TC96
SIG1c′(kPa)	295.5	STATIC qf (kPa)	300.0
SIG3c′(kPa)	295.5	AVG MAX q (kPa)	182.1 (60.7%)
INDUCED OCR	1.0	AVG MIN q (kPa)	-153.5 (51.2%)

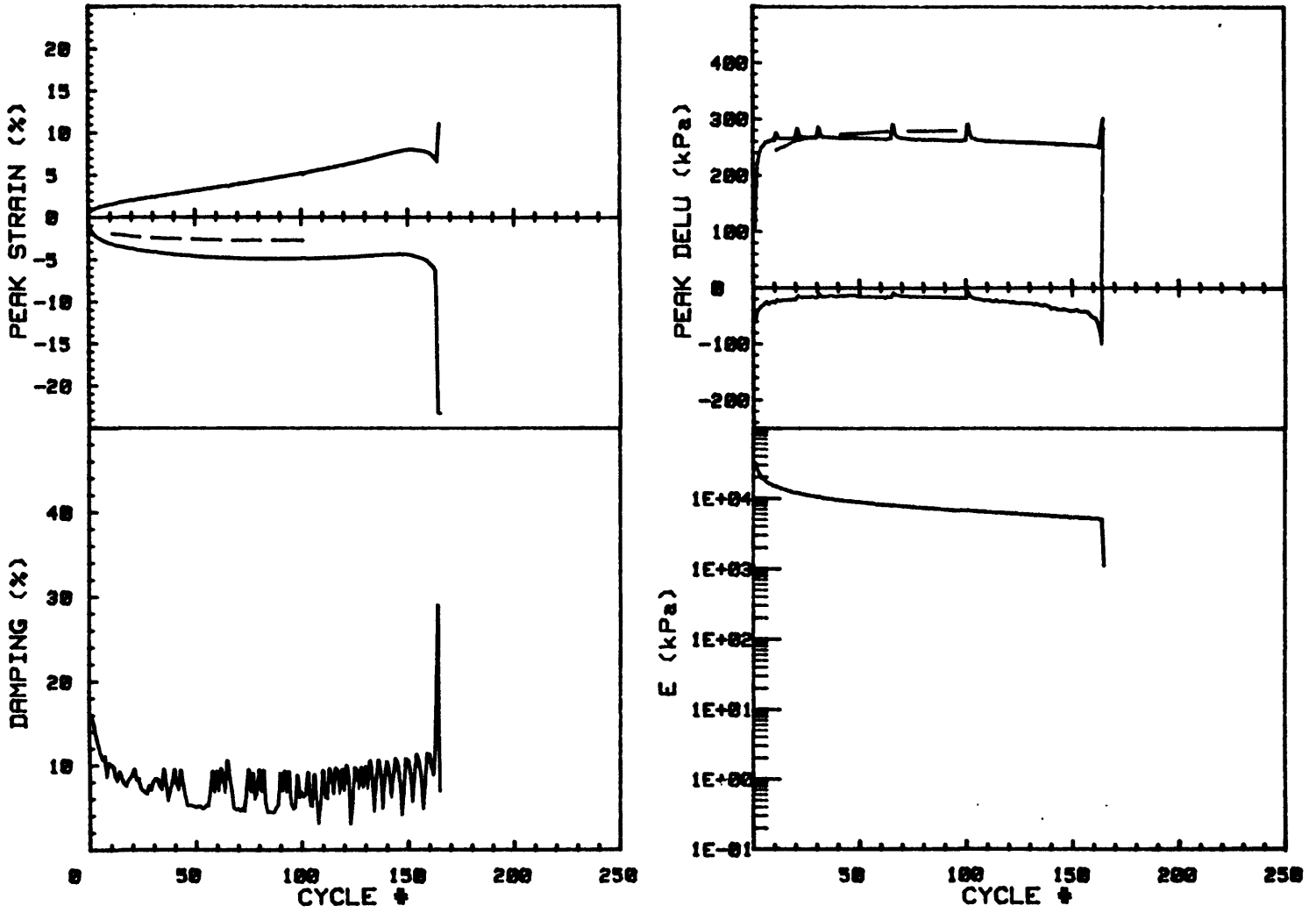

CRUISE DC4-81-NS		INCREMENT (cm)	41-49
CORE NO. 686A1		TEST NO.	TC96
SIG1c'(kPa)	295.5	STATIC qf (kPa)	300.0
SIG3c'(kPa)	295.5	AVG MAX q (kPa)	182.1 (60.7%)
INDUCED OCR	1.0	AVG MIN q (kPa)	-153.5 (51.2%)

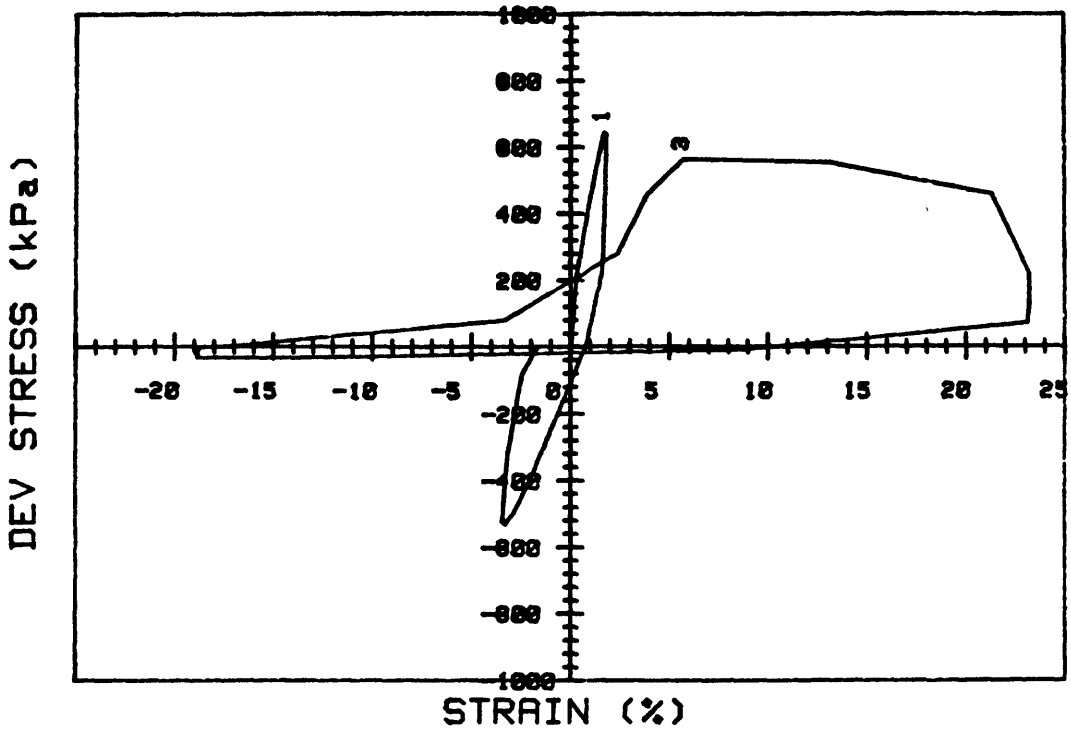

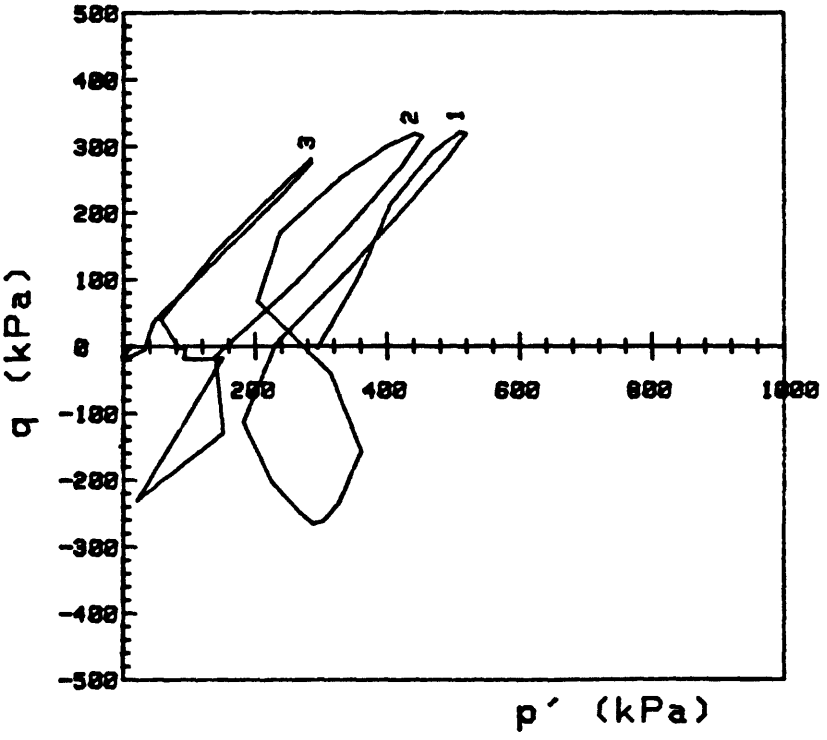

CRUISE DC4-81-NS		INCREMENT (cm)	41-49
CORE NO. 686A1		TEST NO.	TC97
SIG1c'(kPa)	298.1	STATIC qf (kPa)	300.0
SIG3c'(kPa)	298.1	AVG MAX q (kPa)	307.0 (102.3%)
INDUCED OCR	1.0	AVG MIN q (kPa)	-171.4 (57.1%)

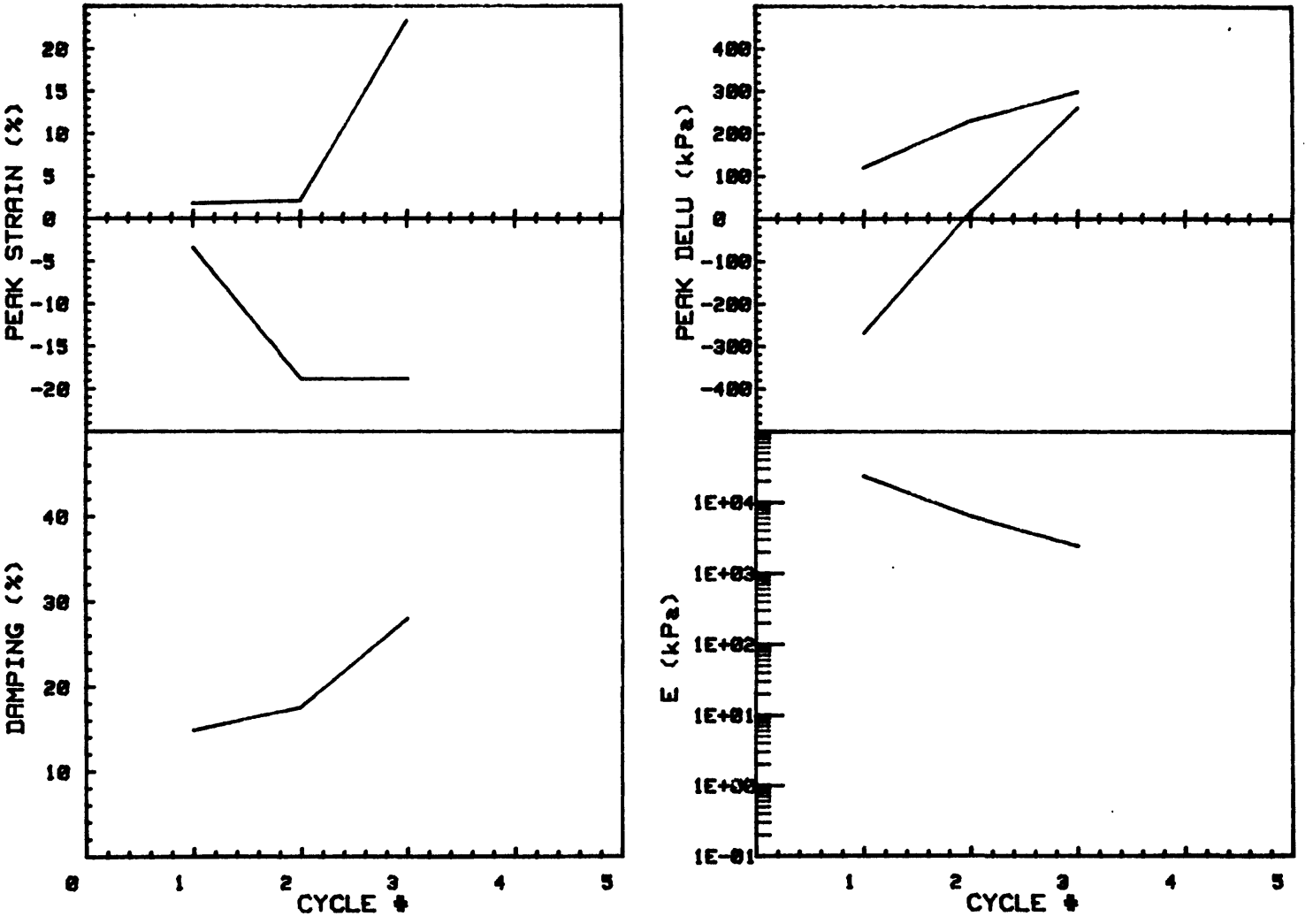

CRUISE DC4-81-NS		INCREMENT (cm)	41-49
CORE NO.	686A1	TEST NO.	TC97
SIG1c'(kPa)	298.1	STATIC qf (kPa)	300.0
SIG3c'(kPa)	298.1	AVG MAX q (kPa)	307.0 (102.3%)
INDUCED OCR	1.0	AVG MIN q (kPa)	-171.4 (57.1%)

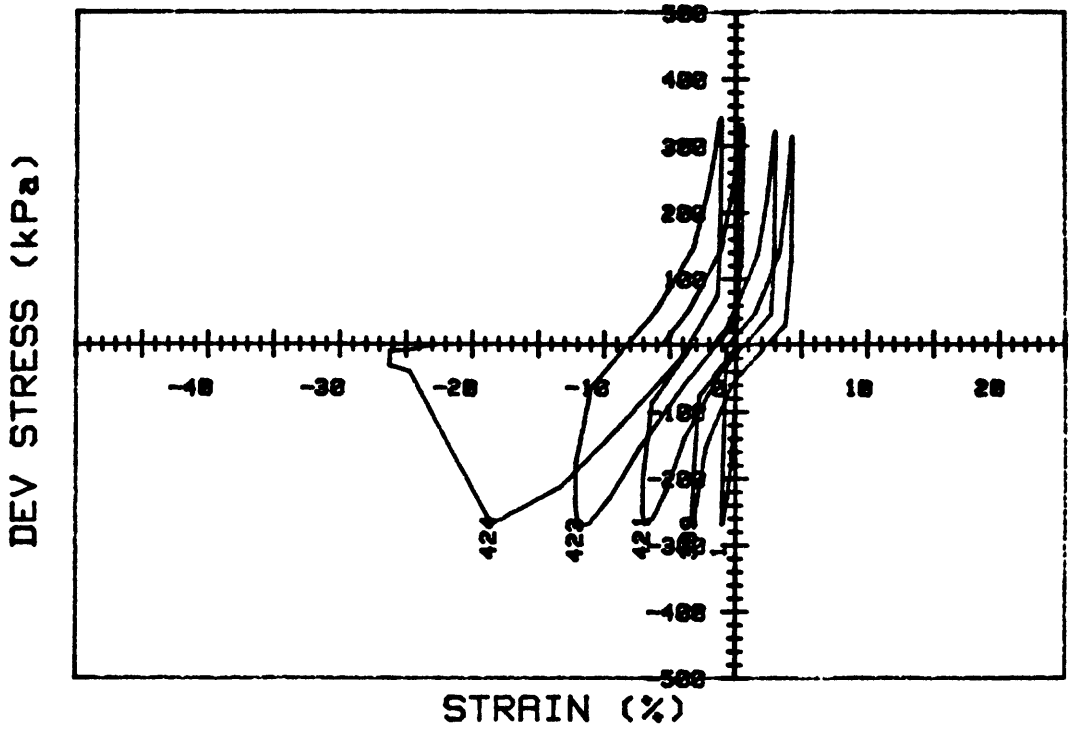

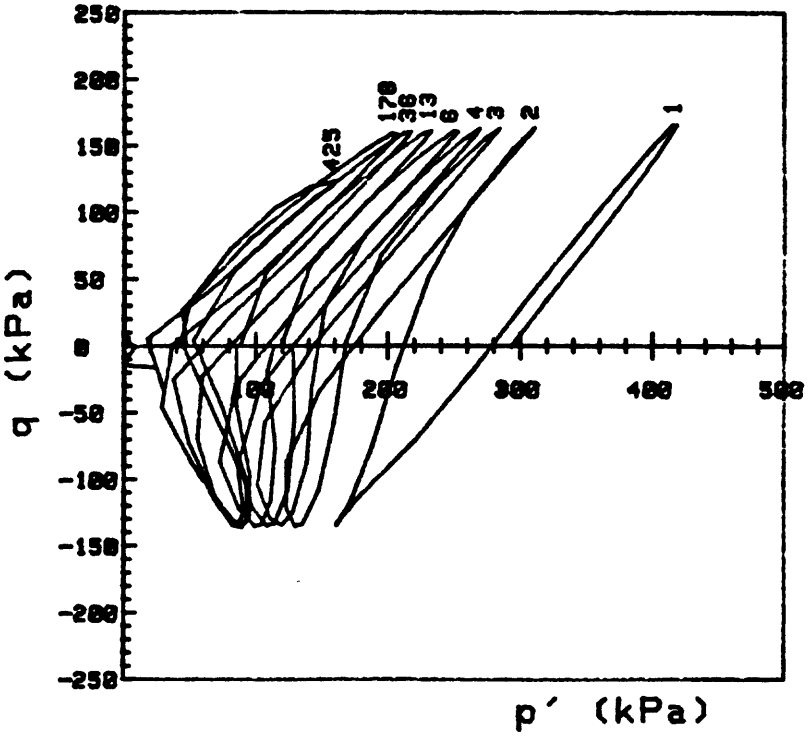

CRUISE DC4-81-NS		INCREMENT (cm)	52-59
CORE NO. 686A1		TEST NO.	D109
SIG1c'(kPa)	293.6	STATIC qf (kPa)	300.0
SIG3c'(kPa)	293.6	AVG MAX q (kPa)	159.1 (53.0%)
INDUCED OCR	1.0	AVG MIN q (kPa)	-135.6 (45.2%)

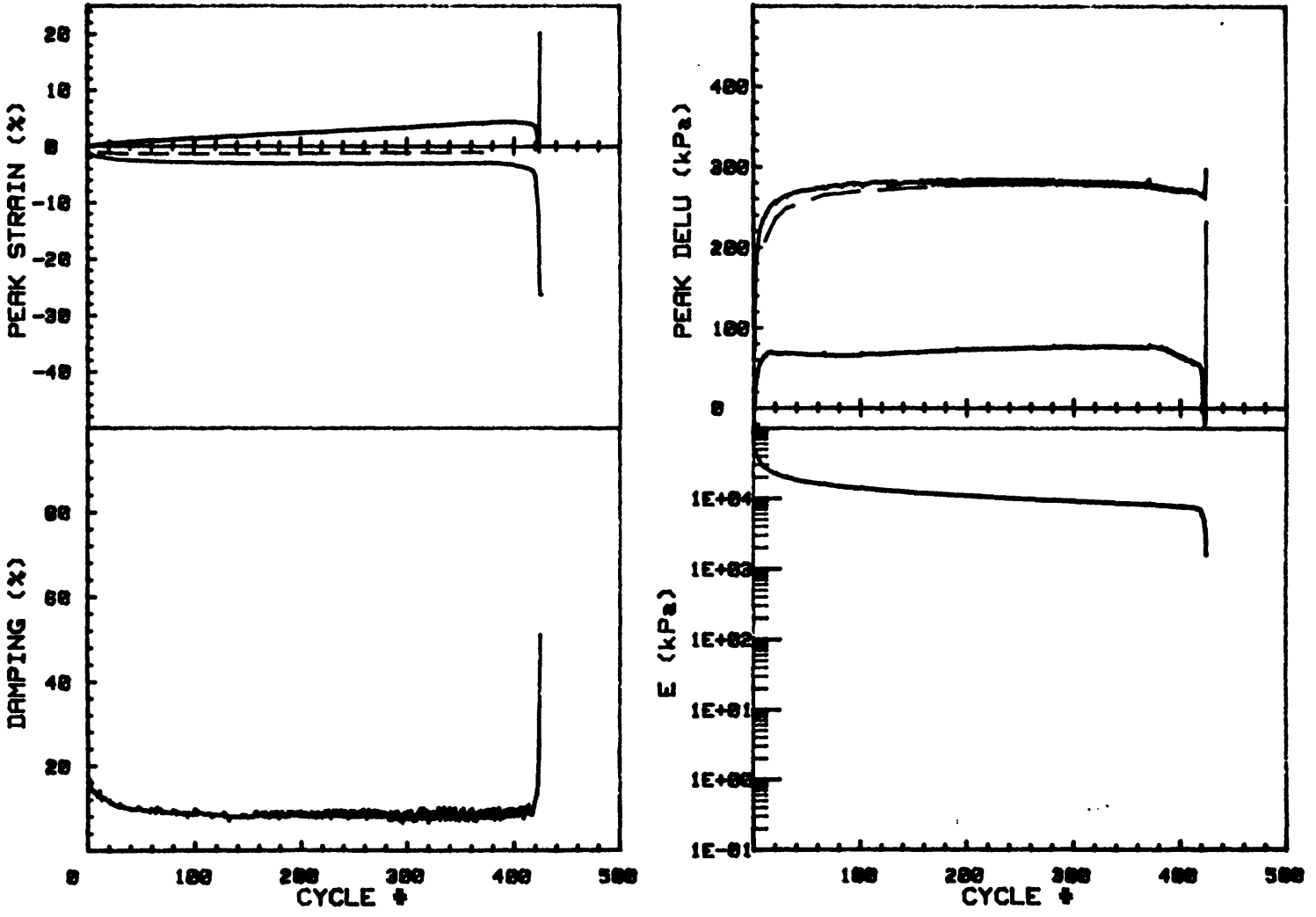

CRUISE DC4-81-NS		INCREMENT (cm)	52-59
CORE NO.	686A1	TEST NO.	D109
SIG1c'(kPa)	293.6	STATIC qf (kPa)	300.0
SIG3c'(kPa)	293.6	AVG MAX q (kPa)	159.1 (53.0%)
INDUCED OCR	1.0	AVG MIN q (kPa)	-135.6 (45.2%)

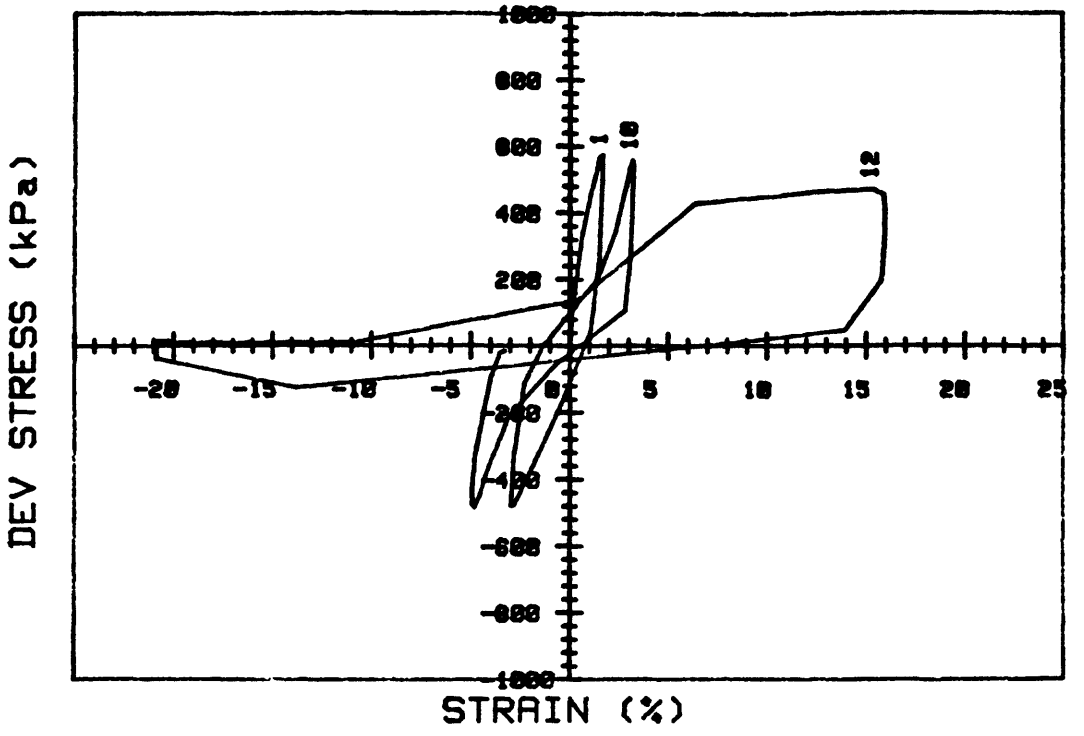

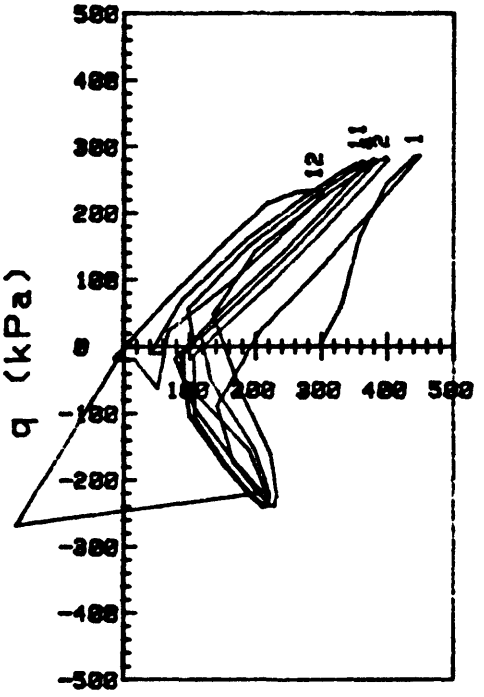

CRUISE DC4-81-NS		INCREMENT (cm)	52-59
CORE NO. 686A1		TEST NO.	D110
SIG1c'(kPa)	297.1	STATIC qf (kPa)	300.0
SIG3c'(kPa)	297.1	AVG MAX q (kPa)	276.6 (92.2%)
INDUCED OCR	1.0	AVG MIN q (kPa)	-228.5 (76.2%)

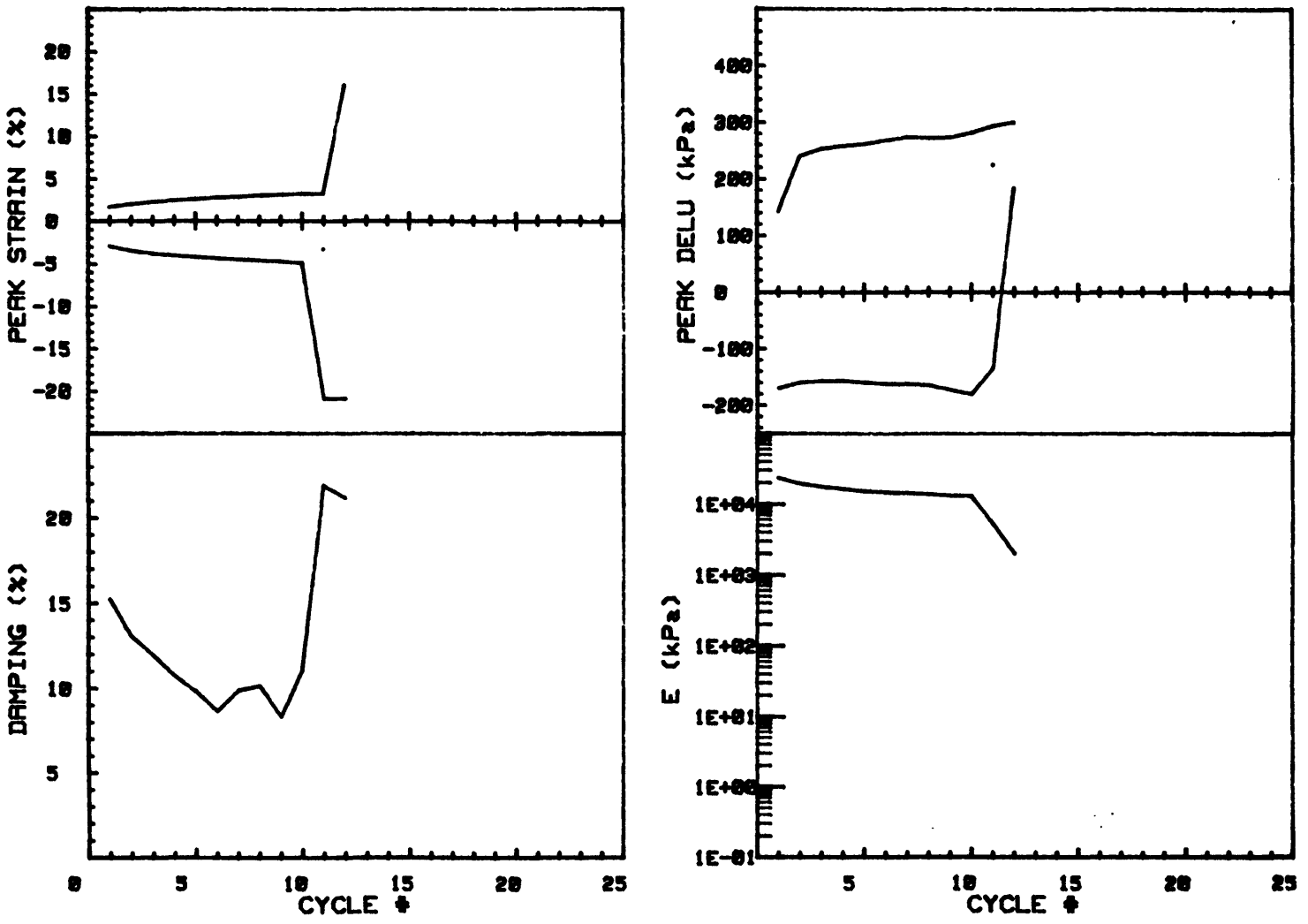

CRUISE DC4-81-NS		INCREMENT (cm)	52-59
CORE NO. 686A1		TEST NO.	D110
SIG1c'(kPa)	297.1	STATIC qf (kPa)	300.0
SIG3c'(kPa)	297.1	AVG MAX q (kPa)	276.6 (92.2%)
INDUCED OCR	1.0	AVG MIN q (kPa)	-228.5 (76.2%)

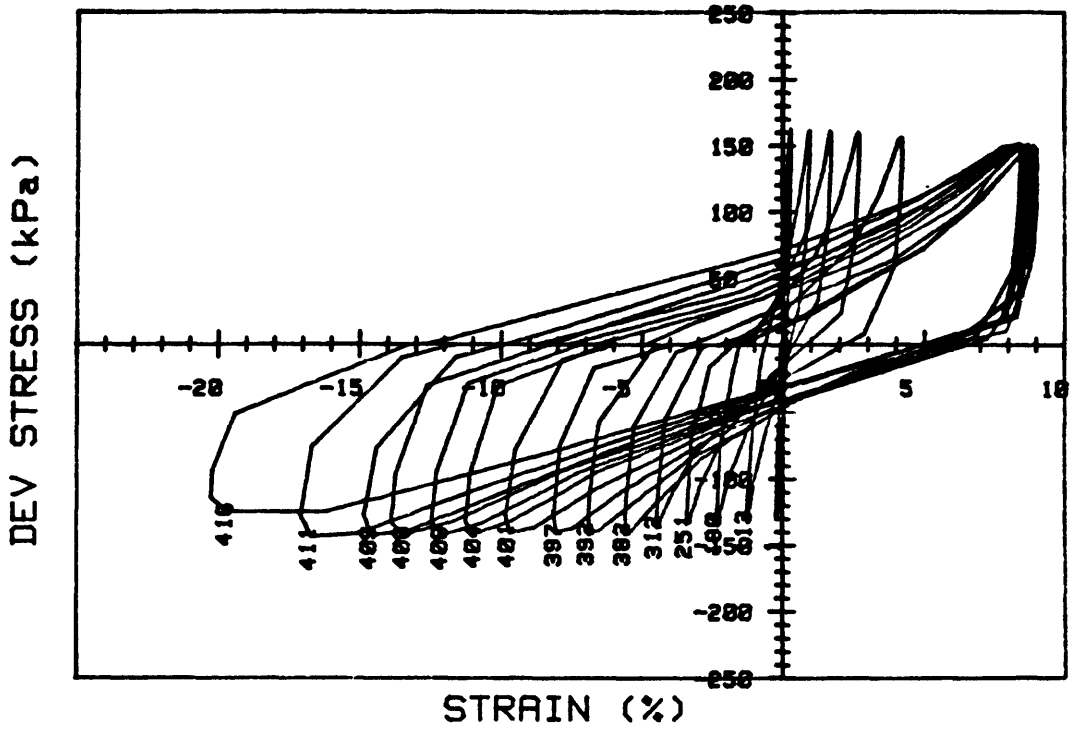

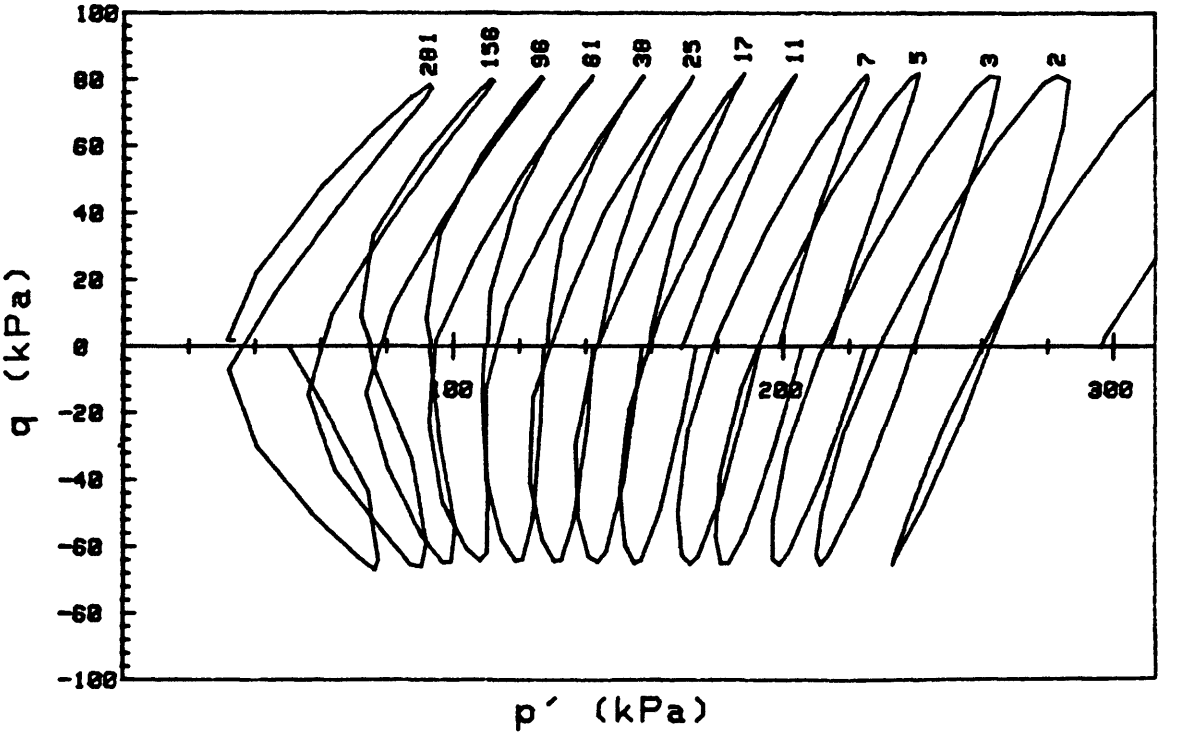

CRUISE DC4-81-NS		INCREMENT (cm)	45-53
CORE NO. 687A1		TEST NO.	TC94
SIG1c'(kPa)	296.7	STATIC qf (kPa)	300.0
SIG3c'(kPa)	296.7	AVG MAX q (kPa)	79.2 (26.4%)
INDUCED OCR	1.0	AVG MIN q (kPa)	-66.8 (22.3%)

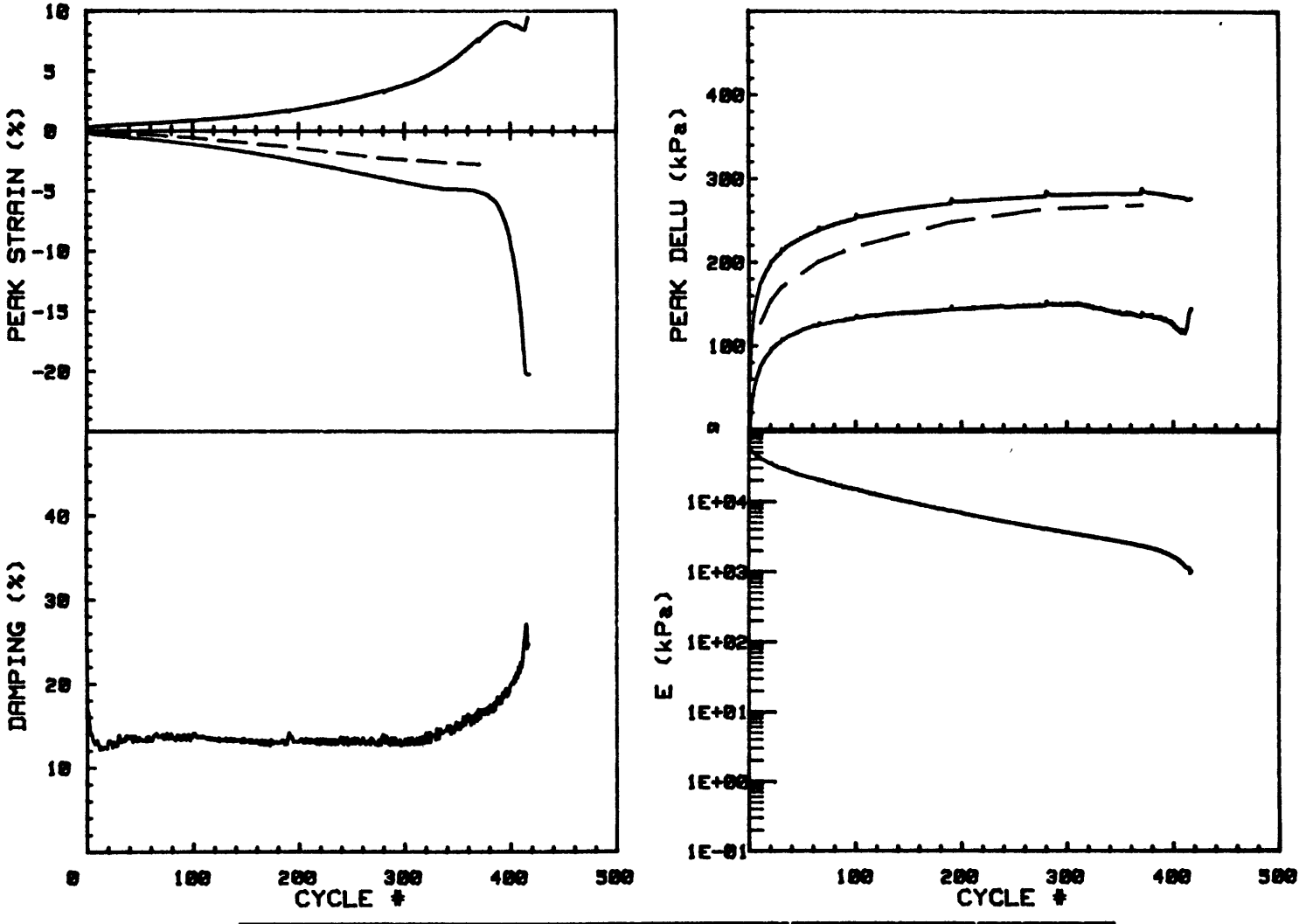

CRUISE DC4-81-NS		INCREMENT (cm)	45-53
CORE NO. 687A1		TEST NO.	TC94
SIG1c'(kPa)	296.7	STATIC qf (kPa)	300.0
SIG3c'(kPa)	296.7	AVG MAX q (kPa)	79.2 (26.4%)
INDUCED OCR	1.0	AVG MIN q (kPa)	-66.8 (22.3%)

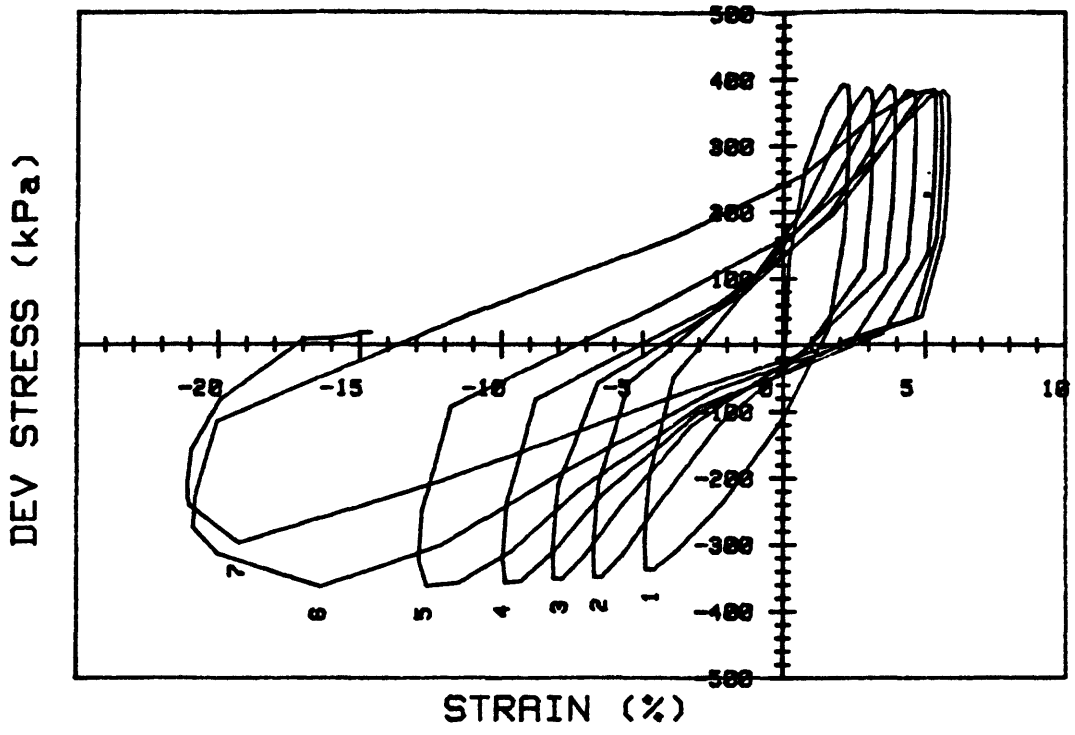

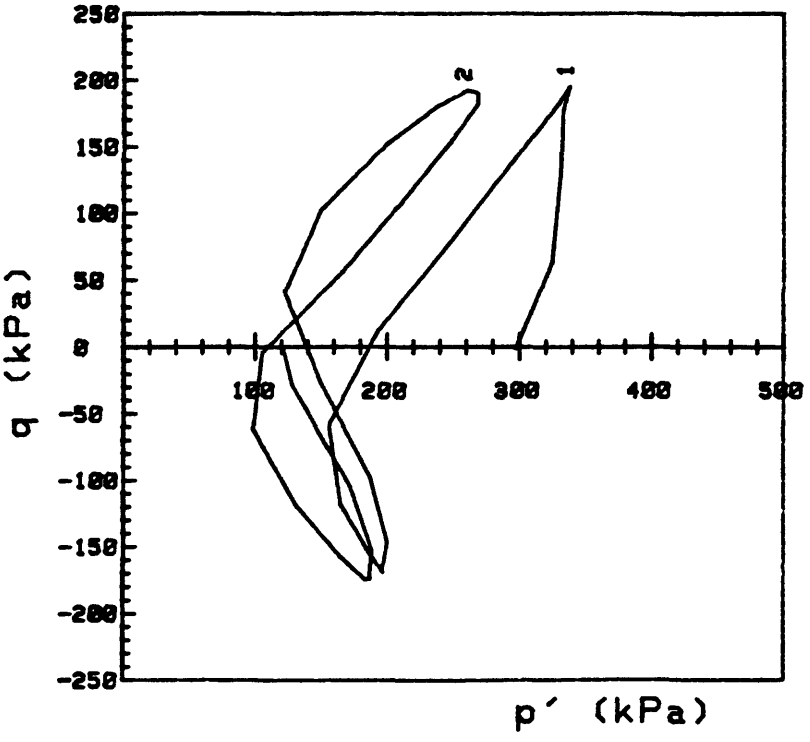

CRUISE DC4-81-NS		INCREMENT (cm)	45-53
CORE NO.	687A1	TEST NO.	TC95
SIG1c′(kPa)	298.7	STATIC qf (kPa)	300.0
SIG3c′(kPa)	298.7	AVG MAX q (kPa)	192.1 (64.0%)
INDUCED OCR	1.0	AVG MIN q (kPa)	-172.7 (57.6%)

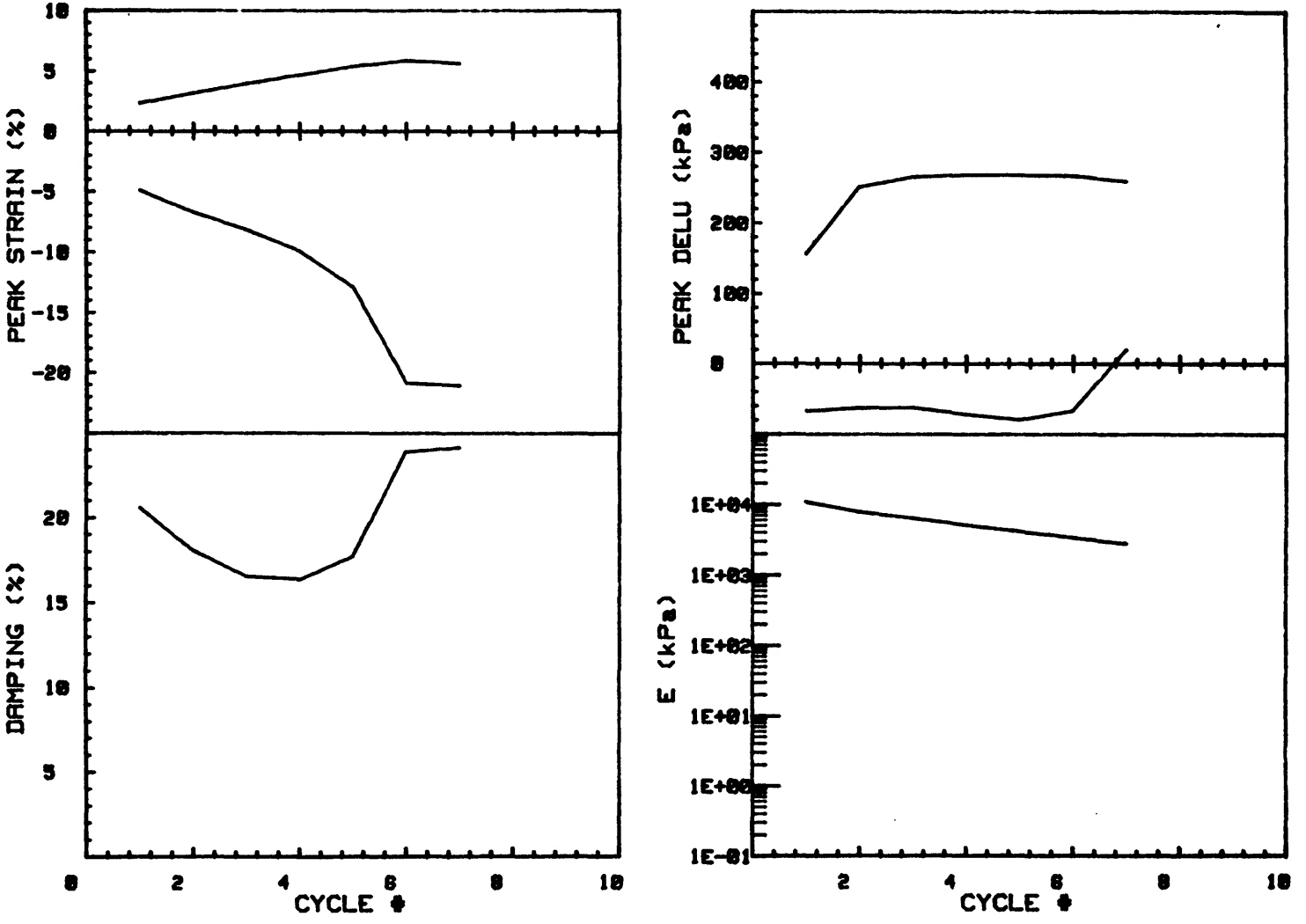

CRUISE DC4-81-NS		INCREMENT (cm)	45-53
CORE NO.	687A1	TEST NO.	TC95
SIG1c'(kPa)	298.7	STATIC qf (kPa)	300.0
SIG3c'(kPa)	298.7	AVG MAX q (kPa)	192.1 (64.0%)
INDUCED OCR	1.0	AVG MIN q (kPa)	-172.7 (57.6%)

Appendix G. Liquefaction susceptibility analyses.

Appendix G

Four liquefaction analyses, based primarily on the techniques of Seed and Idriss (1971) and Seed and Rahman (1978), were performed using cone penetration test (CPT) and cyclic triaxial test data. Because sediment types in Norton Sound are different than previously studied material, some modification of the following procedures may be necessary when more information is known about the liquefaction behavior of sandy silt. The results of the analyses are presented in Table 9. A description of the procedures follow.

Analysis 1: Earthquake accelerations that will liquefy sediment at various depths were calculated using cyclic triaxial test data.

The maximum shear stresses in a soil body are primarily caused by an upward propagation of shear waves from bedrock. The average shear stress (τ_{ave}) in a deformable body is equal to (Seed and Idriss, 1971):

$$\tau_{ave} = 0.65 \quad \gamma \quad h \quad \frac{a_{max}}{g} \quad r_d \qquad (1)$$

where: τ_{ave} = average horizontal shear stress;

γ = total unit weight of the soil estimated from consolidation tests;

h = subbottom depth of stress determination;

g = acceleration due to gravity;

a_{max} = maximum ground surface acceleration;

r_d = stress coefficient to reduce stresses from a rigid to a deformable body, determined from Fig. G1.

Cyclic triaxial tests were performed to evaluate the cyclic stress ratio ($\tau_{cyc\ ave\ max}/\sigma'_c$) necessary to cause a certain strain to occur at a particular number of loading cycles. A magnitude 5.25 earthquake may be represented by approximately 3 significant cycles at 0.65 τ_{max}, a magnitude 6.0 event contains approximately 5 cycles, and a 6.75 magnitude has approximately 10 representative cycles (Seed and Idriss, in press). Useful data can be obtained from carefully conducted cyclic triaxial tests performed to 5 percent strain for dense samples (Seed, 1979) (Fig. 9). Cyclic triaxial test results typically are adjusted to agree with field stress applications. The following equation transforms cyclic triaxial stress ratios into representative field data (Seed, 1979):

$$\left(\frac{\tau_h}{\sigma'_{vo}}\right)_{field} \approx c_m \; c_r \left(\frac{\tau_{cyc\ ave\ max}}{\sigma'_c}\right)_{triaxial} \qquad (2)$$

where: $\left(\tau_h/\sigma'_{vo}\right)_{field}$ = the horizontal shear stress caused by an earthquake normalized to its vertical in situ confining stress;

c_m = a coefficient that relates unidirectional cyclic shear tests to multidirectional shaking in the field, typically equals 0.9;

c_r = a coefficient that modifies the cyclic triaxial stress ratio to a corresponding cyclic simple shear stress ratio that is more representative of field conditions, the coefficient is dependent upon the coefficient of earth pressure at rest in the field, K_o;

$\left(\tau_{cyc\ ave\ max}/\sigma'_c\right)_{triaxial}$ =the stress ratio required to reach 5 percent strain in 3, 5 and 10 cycles as determined from cyclic triaxial tests (Fig. 9).

The triaxial to simple shear reduction coefficient, c_r, is dependent upon K_o; $c_r \approx 0.63$ for $K_o \approx 0.4$ and $c_r \approx 1.0$ for $K_o \approx 1.0$. Other values of c_r were linearly interpolated between the end values (Seed, 1979). The coefficient of earth pressure at rest was calculated from (Mayne and Kulhawy, 1982):

$$K_o = (1-\sin \phi')\ OCR^{\sin \phi'} \qquad (3)$$

where: K_o = the coefficient of earth pressure at rest;

ϕ' = the effective friction angle determined from static triaxial tests (Table 7);

OCR = overconsolidation ratio at depth of interest, estimated from Fig. G2.

Equating τ_{ave} in equation 1 with τ_h in equation 2, the maximum ground surface acceleration from an earthquake necessary to cause liquefaction at various depths was determined (Table G1):

$$a_{max} = \frac{g\ c_m\ c_r\ \sigma'_{vo}}{0.65\ \gamma\ h\ r_d} \left(\frac{\tau_{cyc\ ave\ max}}{\sigma'_c}\right)_{triaxial} \qquad (4)$$

The above analysis assumed that cyclic properties at depth were the same as measured properties of shallow subbottom sediment. Deep site specific investigations are required to determine if weaker stratas exist.

Analysis 2: Earthquake accelerations that will liquefy sediment at a shallow subbottom depth were calculated using standard correlations based on CPT data.

This analysis also is based on the simplified procedure for evaluating soil liquefaction potential of Seed and Idriss (1971) with some modification. That evaluation relies on empirical correlations between the standard penetration test (SPT) and areas of observed liquefaction caused by earthquakes. The standard penetration test is performed by dropping a weight onto drill rods and measuring the number of blows (N) required to drive a split sampling spoon 0.305 m. Representative blow counts (N) were determined from the in situ cone penetration test data obtained in Norton Sound using the relations in Fig. G3 (Schmertmann, 1976, cited in Martin and Douglas 1981). The blow counts (N) were corrected for shallow subbottom depth by multiplying by 0.75 and by C_N obtained from Fig. G4. The blow count was also increased by 7.5 to account for silt content (Seed and Idriss, in press). The equation to determine the corrected blow count, N_c, for any shallow (<3m) subbottom depth is:

$$N_c = (0.75 \quad C_N \quad N) \quad + 7.5 \qquad (5)$$

The stress ratio (τ_{cyc}/σ'_{vo}) necessary to cause liquefaction for a particular magnitude earthquake as a function of N_c is shown in Fig. G5. If the stress ratio is known, the maximum acceleration at the seafloor (a_{max}) can be calculated from equation 1 with both sides normalized by σ'_{vo}. The minimum a_{max} for each penetration is listed in Table G2.

Analysis 3: Wave heights that will liquefy shallow subbottom sediment were calculated using cyclic triaxial test data.

Storm waves traveling over sediment in shallow water depths generate shear stresses similar to those induced by earthquakes. Liquefaction may occur if the resultant pore pressures increase sufficiently. The analysis consisted of two main parts: the stresses imparted to the seafloor were determined for design storms, and the cyclic characteristics of the sediment were measured in cyclic triaxial tests.

The shear stress ratio $\frac{\tau_c}{\sigma'_{vo}}$ at any subbottom depth induced by ocean waves was determined from (Seed and Rahman, 1978):

$$\frac{\tau_c}{\sigma'_{vo}} = \frac{\pi}{\gamma'} \frac{\gamma_w}{} \frac{H}{L} \left(\exp \frac{-2\pi z}{L} \right) \left(\frac{1}{\cosh \frac{2\pi d}{L}} \right) \qquad (6)$$

where: τ_c = horizontal cyclic shear stress at a particular subbottom depth;

σ'_{vo} = vertical effective stress at a particular subbottom depth;

γ_w = unit weight of salt water;

γ' = average buoyant unit weight of sediment above a particular subbottom depth;

H = sustained storm wave height;

L = wave length, determined from Fig. G6, assuming a wave period of 10 seconds (Clukey and others, 1980);

z = subbottom depth;

d = still water depth.

The average wave height was determined by multiplying the significant wave height for different return periods by 0.63 (McCormick and Thiruvathukal, 1976, p. 119) (Table G3). The shear stress ratios for different sustained wave heights at sites in the nothern Bering Sea are presented in Table G4.

The laboratory stress ratios necessary to cause 5 percent strain after 360 cycles (a storm duration of one hour with a wave period of 10 seconds, Clukey and others, 1980) (Fig. 9) were corrected using equation 2 to simulate field conditions (Table G5). A comparison of the stresses induced by storm waves (Table G4) with the corrected cyclic sediment resistance (Table G5) revealed the sustained wave height necessary to cause liquefaction to a particular subbottom depth (Table G6). The above analysis does not account for drainage during storm events; this is a very conservative assumption.

Analysis 4: Cone penetration data was modified using an earthquake associated procedure to yield values that are related to wave heights necessary to cause liquefaction.

The final analysis consists of portions of analyses 2 and 3. The smallest shear stress ratio (τ/σ'_{vo}) (Table G2) for each CPT determined from Fig. G5 (assuming M=5.25) was compared to the cyclic shear stress ratio (τ_c/σ'_{vo}) induced by storm waves (Table G4). The minimum wave heights necessary to equalize the stress ratios are presented in Table 9. Although the values show relative susceptibility to liquefaction between stations, they do not represent actual wave heights.

Table G1. Ground surface earthquake accelerations (a_{max}) necessary to induce liquefaction at different subbottom depths (h) based on laboratory cyclic triaxial test data (determined from equation 4).

CORE	h (m)	γ (kN/m^3)	r_d	σ'_{vo} (kN/m^2)	c_m	ϕ degrees	OCR	K_o (1)	c_r	$\frac{\tau_{cyc\ ave\ max}}{\sigma'_c}$ (triaxial) M = 5.25; 3 cycles	a_{max} (g)	$\frac{\tau_{cyc\ ave\ max}}{\sigma'_c}$ (triaxial) M= 6.0; 5 cycles	a_{max} (g)	$\frac{\tau_{cyc\ ave\ max}}{\sigma'_c}$ (triaxial) M=6.75; 10 cycles	a_{max} (g)
681A2	1	20.4	0.99	10.4	0.9	37	32	1.00(3.21)	1.00	0.52	0.37	0.44	0.31	0.35	0.25
	2	20.5	0.98	20.9			22	1.00(2.56)	1.00		0.37		0.32		0.25
	6	20.8	0.95	64.5			5	1.00(1.05)	1.00		0.39		0.33		0.26
682A1	1	16.0	0.99	6.0	0.9	35	11	1.00(1.69)	1.00	0.47	0.25	0.42	0.22	0.37	0.19
	2	16.1	0.98	12.1		40	8	1.00(1.36)	1.00		0.25		0.22		0.20
	6	16.6	0.95	39.3			3	0.72	0.83		0.22		0.20		0.18
684A1	1	20.7	0.99	10.7	0.9	38	23	1.00(2.65)	1.00	0.69	0.50	0.62	0.45	0.55	0.40
	2	20.7	0.98	21.3			8	1.00(1.38)	1.00		0.50		0.45		0.40
	6	20.8	0.95	64.5			1	0.38	0.62		0.32		0.29		0.26
685A2	1	18.0	0.99	8.0	0.9	37	19	1.00(2.34)	1.00	0.41	0.25	0.36	0.22	0.31	0.19
	2	18.1	0.98	16.1			13	1.00(1.86)	1.00		0.26		0.23		0.19
	6	18.5	0.95	50.7			3	0.77	0.86		0.23		0.21		0.18
	10	18.8	0.91	67.5			1	0.40	0.63		0.14		0.12		0.11
686A1	1	20.3	0.99	10.3	0.9	42	56	1.00(4.89)	1.00	0.82	0.58	0.72	0.51	0.62	0.44
	2	20.3	0.98	20.5			26	1.00(2.93)	1.00		0.58		0.51		0.44
	6	20.3	0.95	61.5			1	0.33	0.58		0.35		0.31		0.26
	10	20.4	0.91	103.5			1	0.33	0.58		0.37		0.32		0.28
687A1	1	19.7	0.99	9.7	0.9	38	49	1.00(4.22)	1.00	0.58	0.40	0.52	0.36	0.45	0.31
	2	19.7	0.98	19.3			21	1.00(2.50)	1.00		0.40		0.36		0.31
	6	19.9	0.95	60.7			1	0.38	0.62		0.27		0.24		0.21
	10	20.0	0.91	99.5			1	0.38	0.62		0.27		0.24		0.21

(1) Maximum K_o value allowed in analysis =1.0, higher values were assumed to have been caused by disturbance effects.

Table G2. Lowest stress ratios (τ/σ'_{vo}) and ground surface accelerations (a_{max}) necessary to induce liquefaction based on cone penetration test data.

CONE PENETRATION TEST	DEPTH >0.25 m	LOWEST τ/σ'_{vo} M = 5.25	LOWEST a_{max}(g) M = 5.25	LOWEST a_{max}(g) M = 6.75
674 X1	0.25	0.19	0.14	0.11
X2	0.26	0.23	0.17	0.13
670 X1	0.80	0.20	0.14	0.10
X2	0.45	0.21	0.14	0.11
X3	0.49	0.17	0.11	0.09
X4	0.27	0.22	0.15	0.12
668 X2	0.33	0.30	0.23	0.18
X3	0.35	0.30	0.23	0.18
X4	0.39	0.27	0.21	0.16
669 X1	0.27	0.25	0.19	0.15
X2	0.30	0.26	0.20	0.15
671 X1	0.30	0.20	0.16	0.12
X2	0.25	0.19	0.15	0.11
X3	0.29	0.12	0.10	0.07
X4	0.27	0.14	0.11	0.08
X5	0.40	0.13	0.10	0.08
X6	0.31	0.13	0.10	0.08
X7	0.35	0.12	0.10	0.07
X8	0.39	0.16	0.13	0.10
675 X1	1.05	0.18	0.15	0.11
X2	0.56	0.16	0.13	0.10
X3	0.28	0.15	0.12	0.09
X4	0.28	0.18	0.14	0.11
677 X1	0.29	0.32	0.26	0.20
X2	0.25	0.32	0.26	0.20
676 X2	0.60	0.16	0.10	0.07
673 X1	0.35	0.47	0.36	0.28
X2	0.25	0.32	0.24	0.19
X3	0.25	0.18	0.14	0.11
X4	0.28	0.62	0.47	0.37
672 X1	0.28	0.14	0.08	0.06
X2	0.52	0.13	0.07	0.06
679 X1	0.32	0.16	0.13	0.10
678 X2	0.25	0.16	0.13	0.10

Table G3. Estimated wind speeds and wave heights in the northern Bering Sea for different return periods (Arctic Environmental Information and Data Center, 1977).

RETURN PERIOD (YEARS)	MAXIMUM SUSTAINED WIND SPEED (KNOTS)	MAXIMUM SIGNIFICANT WAVE HEIGHT (m)	EXTREME WAVE HEIGHT (m)	AVERAGE WAVE HEIGHT (m) [1]
5	78	13.5	24.5	8.5
10	84	15.5	28.0	9.8
25	94	18.5	33.0	11.7
50	102	20.5	36.0	12.9
100	110	23.0	42.5	14.5[2]

(1) Average wave height = 0.63 x significant wave height (McCormick and Thiruvathukal, 1976).

(2) Waves 14 m high will break in some Norton Sound areas, therefore 13 m high waves were assumed as a maximum value in the analysis. Actually, maximum sustained wave heights in the northern Bering Sea may be less than 13m because the relatively shallow water depths on the wide continental shelf dissipate wave energy.

Table G4. Storm wave induced cyclic stress ratios (τ_c/σ'_{vo}) at different subbottom depths (z) (determined from equation 6).

STATION/ CORE	z (m)	γ_w/γ' (kN/m^3)	d (m)	T (sec)	L (m)	τ_c/σ'_{vo} H = 6m	τ_c/σ'_{vo} H = 7m	τ_c/σ'_{vo} H = 8m	τ_c/σ'_{vo} H = 9m	τ_c/σ'_{vo} H = 10m	τ_c/σ'_{vo} H = 11m	τ_c/σ'_{vo} H = 12m	τ_c/σ'_{vo} H = 13 m
679	0.25	0.94	20	10	122	0.09	0.11	0.12	0.14	0.15	0.17	0.18	0.20
	0.5	0.94				0.09	0.10	0.12	0.13	0.15	0.16	0.18	0.19
	1.0	0.94				0.09	0.10	0.12	0.13	0.15	0.16	0.17	0.19
	1.5	0.94				0.09	0.10	0.11	0.13	0.14	0.16	0.17	0.18
	2.0	0.94				0.08	0.10	0.11	0.12	0.14	0.15	0.17	0.18
	2.5	0.94				0.08	0.09	0.11	0.12	0.13	0.15	0.16	0.18
	3.0	0.94				0.08	0.09	0.11	0.12	0.13	0.14	0.16	0.17
	4.0	0.93				0.07	0.09	0.10	0.11	0.12	0.14	0.15	0.16
	5.0	0.93				0.07	0.08	0.09	0.11	0.12	0.13	0.14	0.15
681A2	0.25	0.97	30	10	140	0.06	0.07	0.08	0.09	0.10	0.12	0.13	0.14
	0.5	0.97				0.06	0.07	0.08	0.09	0.10	0.11	0.12	0.13
	1.0	0.97				0.06	0.07	0.08	0.09	0.10	0.11	0.12	0.13
	1.5	0.96				0.06	0.07	0.08	0.09	0.10	0.11	0.12	0.13
	2.0	0.96				0.06	0.07	0.08	0.09	0.10	0.11	0.12	0.12
	2.5	0.96				0.06	0.07	0.08	0.08	0.09	0.10	0.11	0.12
	3.0	0.95				0.06	0.06	0.07	0.08	0.09	0.10	0.11	0.12
	4.0	0.94				0.05	0.06	0.07	0.08	0.09	0.09	0.10	0.11
	5.0	0.93				0.05	0.06	0.07	0.07	0.08	0.09	0.10	0.11
682A1	0.25	1.69	20	10	122	0.16	0.19	0.22	0.24	0.27	0.30	0.33	0.35
	0.5	1.69				0.16	0.19	0.21	0.24	0.27	0.30	0.32	0.35
	1.0	1.68				0.16	0.18	0.21	0.23	0.26	0.29	0.31	0.34
	1.5	1.67				0.15	0.18	0.20	0.23	0.25	0.28	0.30	0.33
	2.0	1.66				0.15	0.17	0.20	0.22	0.24	0.27	0.29	0.32
	2.5	1.63				0.14	0.16	0.19	0.21	0.23	0.26	0.28	0.30
	3.0	1.60				0.13	0.16	0.18	0.20	0.22	0.25	0.27	0.29
	4.0	1.58				0.13	0.15	0.17	0.19	0.21	0.23	0.25	0.27
	5.0	1.55				0.12	0.14	0.16	0.18	0.20	0.21	0.23	0.25
683A1	0.25	1.01	20	10	122	0.10	0.11	0.13	0.15	0.16	0.18	0.20	0.21
	0.5	1.01				0.10	0.11	0.13	0.14	0.16	0.18	0.19	0.21
	1.0	1.01				0.09	0.11	0.13	0.14	0.16	0.17	0.19	0.20
	1.5	1.01				0.09	0.11	0.12	0.14	0.15	0.17	0.18	0.20
	2.0	1.01				0.09	0.10	0.12	0.13	0.15	0.16	0.18	0.19
	2.5	1.01				0.09	0.10	0.12	0.13	0.14	0.16	0.17	0.19
	3.0	1.01				0.08	0.10	0.11	0.13	0.14	0.16	0.17	0.18
	4.0	1.01				0.08	0.09	0.11	0.12	0.13	0.15	0.16	0.17
	5.0	1.01				0.08	0.09	0.10	0.11	0.13	0.14	0.15	0.17
684A1	0.25	0.94	20	10	122	0.09	0.11	0.12	0.14	0.15	0.17	0.18	0.20
	0.5	0.94				0.09	0.10	0.12	0.13	0.15	0.16	0.18	0.19
	1.0	0.94				0.09	0.10	0.12	0.13	0.15	0.16	0.17	0.19
	1.5	0.94				0.09	0.10	0.11	0.13	0.14	0.16	0.17	0.18
	2.0	0.94				0.08	0.10	0.11	0.12	0.14	0.15	0.17	0.18
	2.5	0.94				0.08	0.09	0.11	0.12	0.13	0.15	0.16	0.18
	3.0	0.94				0.08	0.09	0.11	0.12	0.13	0.14	0.16	0.17
	4.0	0.93				0.07	0.09	0.10	0.11	0.12	0.14	0.15	0.16
	5.0	0.93				0.07	0.08	0.09	0.11	0.12	0.13	0.14	0.15
685A2	0.25	1.26	18	10	120	0.13	0.15	0.18	0.20	0.22	0.24	0.26	0.29
	0.5	1.26				0.13	0.15	0.17	0.20	0.22	0.24	0.26	0.28
	1.0	1.26				0.13	0.15	0.17	0.19	0.21	0.23	0.25	0.28
	1.5	1.25				0.12	0.14	0.16	0.18	0.20	0.23	0.25	0.27
	2.0	1.25				0.12	0.14	0.16	0.18	0.20	0.22	0.24	0.27
	2.5	1.24				0.12	0.13	0.15	0.17	0.19	0.21	0.23	0.25
	3.0	1.23				0.11	0.13	0.15	0.17	0.19	0.20	0.22	0.24
	4.0	1.21				0.10	0.12	0.14	0.16	0.17	0.19	0.21	0.23
	5.0	1.20				0.10	0.11	0.13	0.15	0.16	0.18	0.20	0.21
686A1	0.25	0.98	18	10	120	0.10	0.12	0.14	0.15	0.17	0.19	0.21	0.22
	0.5	0.98				0.10	0.12	0.14	0.15	0.17	0.19	0.20	0.22
	1.0	0.98				0.10	0.12	0.13	0.15	0.16	0.18	0.20	0.21
	1.5	0.98				0.10	0.11	0.13	0.14	0.16	0.18	0.19	0.21
	2.0	0.98				0.09	0.11	0.13	0.14	0.16	0.17	0.19	0.20
	2.5	0.98				0.09	0.11	0.12	0.14	0.15	0.17	0.18	0.20
	3.0	0.98				0.09	0.10	0.12	0.13	0.15	0.16	0.18	0.19
	4.0	0.98				0.08	0.10	0.11	0.13	0.14	0.15	0.17	0.18
	5.0	0.98				0.08	0.09	0.11	0.12	0.13	0.15	0.16	0.17
687A1	0.25	1.04	18	10	120	0.11	0.13	0.15	0.16	0.18	0.20	0.22	0.24
	0.5	1.04				0.11	0.13	0.14	0.16	0.18	0.20	0.22	0.23
	1.0	1.04				0.10	0.12	0.14	0.16	0.17	0.19	0.21	0.23
	1.5	1.04				0.10	0.12	0.14	0.15	0.17	0.19	0.20	0.22
	2.0	1.04				0.10	0.12	0.13	0.15	0.17	0.18	0.20	0.22
	2.5	1.04				0.10	0.11	0.13	0.15	0.16	0.18	0.19	0.21
	3.0	1.04				0.09	0.11	0.13	0.14	0.16	0.17	0.19	0.20
	4.0	1.03				0.09	0.10	0.12	0.13	0.15	0.16	0.18	0.19
	5.0	1.03				0.08	0.10	0.11	0.13	0.14	0.15	0.17	0.18

Table G5. Resistance to liquefaction at different subbottom depths expressed as a field stress ratio (τ_h/σ'_{vo}) (determined from cyclic triaxial test data ($\tau_{cyc\ ave\ max}/\sigma'_c$) corrected for laboratory conditions using equation 2).

CORE	DEPTH (m)	c_m	ϕ' degrees	OCR	K_o (1)	C_r	$\frac{\tau_{cyc\ ave\ max}}{\sigma'_c}$ (2) (triaxial)	$\frac{\tau_h}{\sigma'_{vo}}$ (field)	$\frac{\tau_{cyc\ ave\ max}}{\sigma'_c}$ (2) (triaxial) OCR = 6	$\frac{\tau_h}{\sigma'_{vo}}$ (field)
681A2	0.25	1.0	37	42	1.0(3.78)	1.0	0.22	0.22		
	0.5			39	1.0(3.61)	1.0		0.22		
	1.0			32	1.0(3.21)	1.0		0.22		
	1.5			27	1.0(2.89)	1.0		0.22		
	2.0			22	1.0(2.56)	1.0		0.22		
	2.5			17	1.0(2.19)	1.0		0.22		
	3.0			15	1.0(2.03)	1.0		0.22		
	4.0			11	1.0(1.69)	1.0		0.22		
	5.0			8	1.0(1.39)	1.0		0.22		
682A1	0.25	1.0	35	13	1.0(1.86)	1.0	0.23	0.23	0.91	0.91
	0.5			12	1.0(1.77)	1.0		0.23		0.91
	1.0			11	1.0(1.69)	1.0		0.23		0.91
	1.5			9	1.0(1.50)	1.0		0.23		0.91
	2.0		40	8	1.0(1.36)	1.0		0.23		0.91
	2.5			7	1.0(1.25)	1.0		0.23		0.91
	3.0			7	1.0(1.25)	1.0		0.23		0.91
	4.0			5	1.0(1.01)	1.0		0.23		0.91
	5.0			4	0.87	0.92		0.21		0.84
684A1	0.25	1.0	38	50	1.0(4.27)	1.0	0.33	0.33		
	0.5			39	1.0(3.67)	1.0		0.33		
	1.0			23	1.0(2.65)	1.0		0.33		
	1.5			14	1.0(1.95)	1.0		0.33		
	2.0			8	1.0(1.38)	1.0		0.33		
	2.5			5	1.0(1.04)	1.0		0.33		
	3.0			3	0.76	0.85		0.28		
	4.0			1	0.38	0.61		0.20		
	5.0			1	0.38	0.61		0.20		
685A2	0.25	1.0	37	25	1.0(2.76)	1.0	0.20	0.20	0.77	0.77
	0.5			23	1.0(2.63)	1.0		0.20		0.77
	1.0			19	1.0(2.34)	1.0		0.20		0.77
	1.5			16	1.0(2.11)	1.0		0.20		0.77
	2.0			13	1.0(1.86)	1.0		0.20		0.77
	2.5			11	1.0(1.69)	1.0		0.20		0.77
	3.0			9	1.0(1.49)	1.0		0.20		0.77
	4.0			6	1.0(1.17)	1.0		0.20		0.77
	5.0			4	0.92	0.95		0.19		0.73
686A1	0.25	1.0	42	>100	1.0(7.21)	1.0	0.35	0.35	0.57	0.57
	0.5			90	1.0(6.72)	1.0		0.35		0.57
	1.0			56	1.0(4.89)	1.0		0.35		0.57
	1.5			38	1.0(3.77)	1.0		0.35		0.57
	2.0			26	1.0(2.93)	1.0		0.35		0.57
	2.5			17	1.0(2.20)	1.0		0.35		0.57
	3.0			12	1.0(1.74)	1.0		0.35		0.57
	4.0			5	0.97	0.98		0.34		0.56
	5.0			2	0.53	0.71		0.25		0.40
687A1	0.25	1.0	38	94	1.0(6.30)	1.0	0.26	0.26		
	0.5			75	1.0(5.48)	1.0		0.26		
	1.0			49	1.0(4.22)	1.0		0.26		
	1.5			32	1.0(3.25)	1.0		0.26		
	2.0			21	1.0(2.50)	1.0		0.26		
	2.5			14	1.0(1.95)	1.0		0.26		
	3.0			9	1.0(1.49)	1.0		0.26		
	4.0			4	0.90	0.94		0.24		
	5.0			2	0.59	0.74		0.19		

(1) Maximum allowed $K_o = 1.0$.
(2) Stress ratio required to induce 5% strain in cyclic triaxial test samples after 360 loading cycles (storm wave period = 10 sec for 1 hour duration).

Table G6. Sustained storm wave heights (H) necessary to induce liquefaction in sediment from different stations (determined from a comparison of wave induced stresses in Table G4 with the corrected cyclic sediment resistance in Table G5).

CORE	H	D_L	H	D_L	H	D_L	H	D_L	(1) H OCR = 6
681A2	>13	0							
682A1	9	1.5	10	2.5	11	5.0	12	>5.0	>13
684A1	>13	0							
685A2	9	0.5	10	2.0	11	3.0	12	>5.0	>13
686A1	>13	0							>13
687A1	>13	0							

H = Wave height necessary to cause liquefaction.

D_L = Subbottom depth to which liquefaction may occur.

(1) = Wave heights necessary to liquefy sediment based on overconsolidated triaxial test samples.

LIST OF APPENDIX G FIGURES.

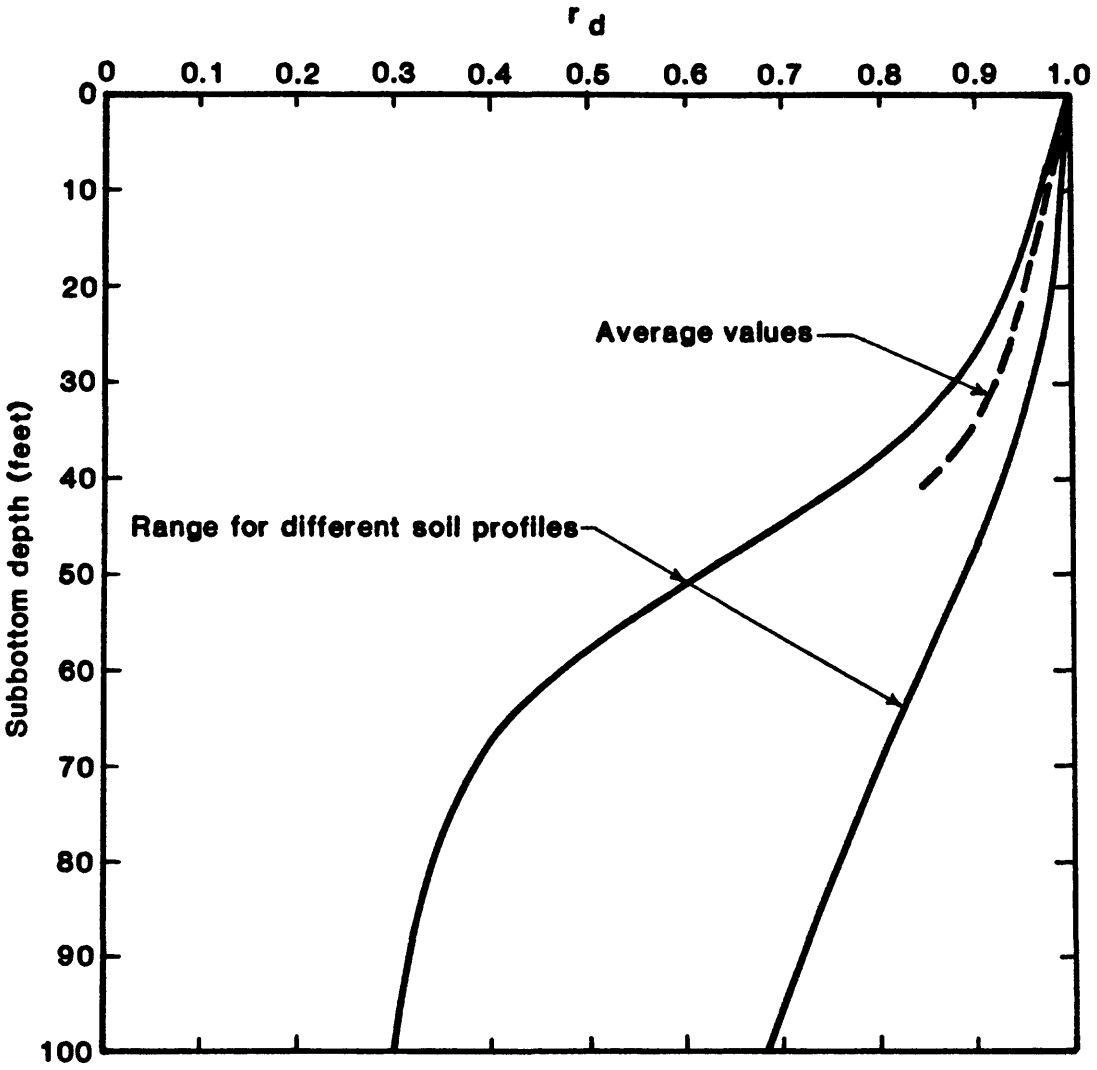

Fig. G1. Range of r_d values vs subbottom depth for different soil profiles (from Seed and Idriss, 1971).

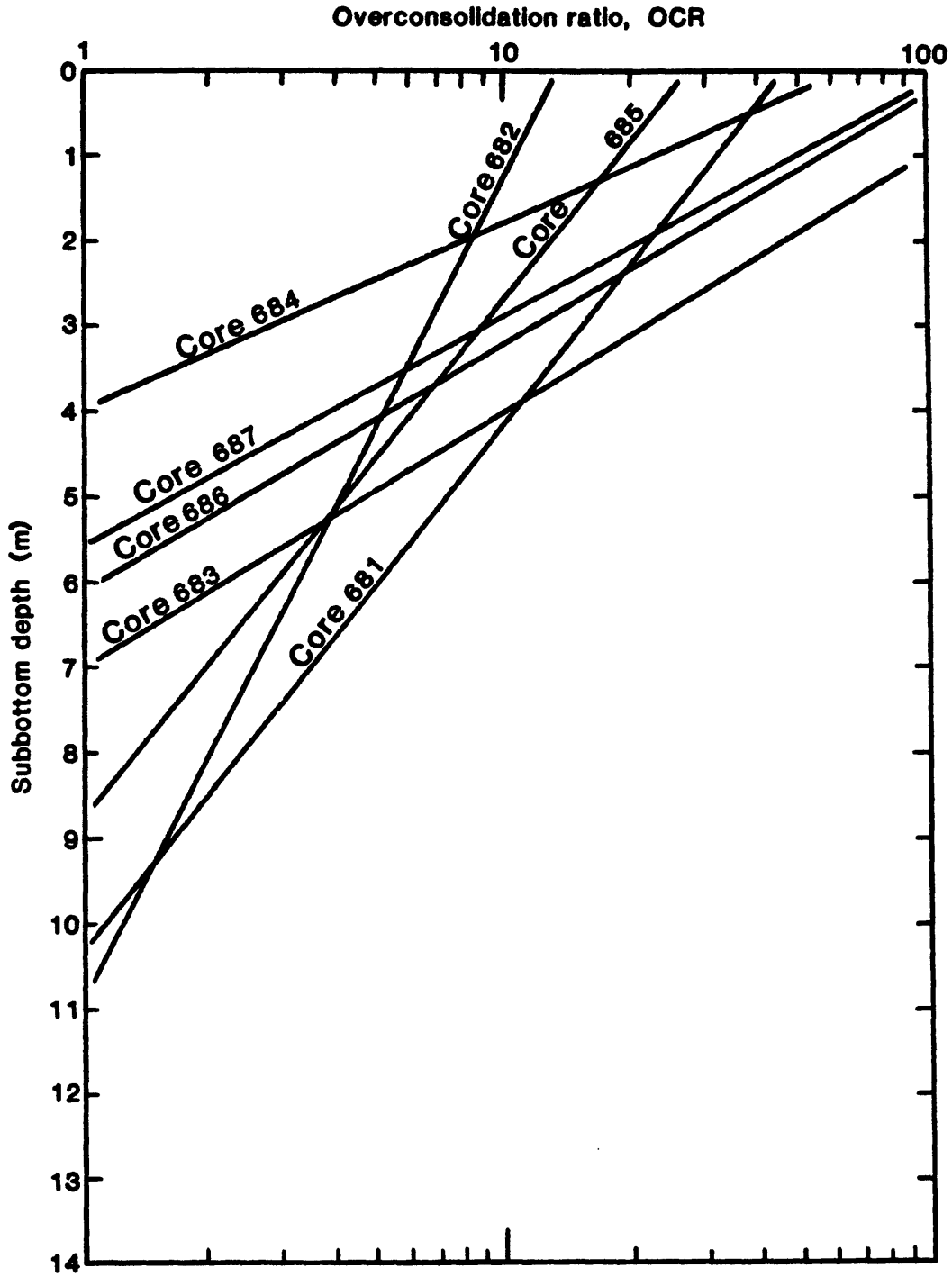

Fig. G2. Overconsolidation ratio determined from consolidation tests versus subbottom depth.

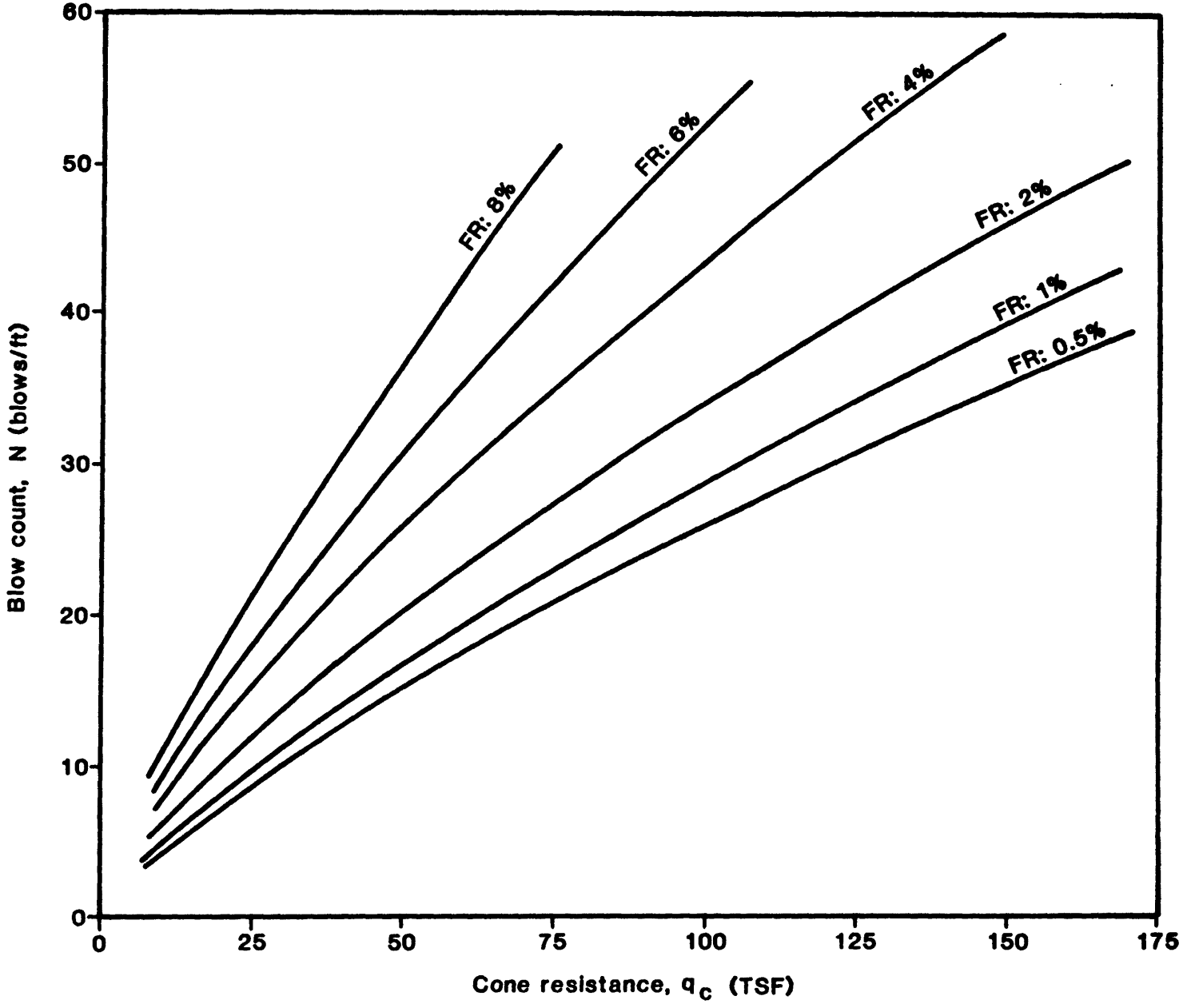

Fig. G3. Correlation of cone resistance (q_c) and friction ratio (FR) obtained from cone penetration tests with standard penetration test blow count (N) (Schmertmann, 1976, cited in Martin and Douglas, 1981).

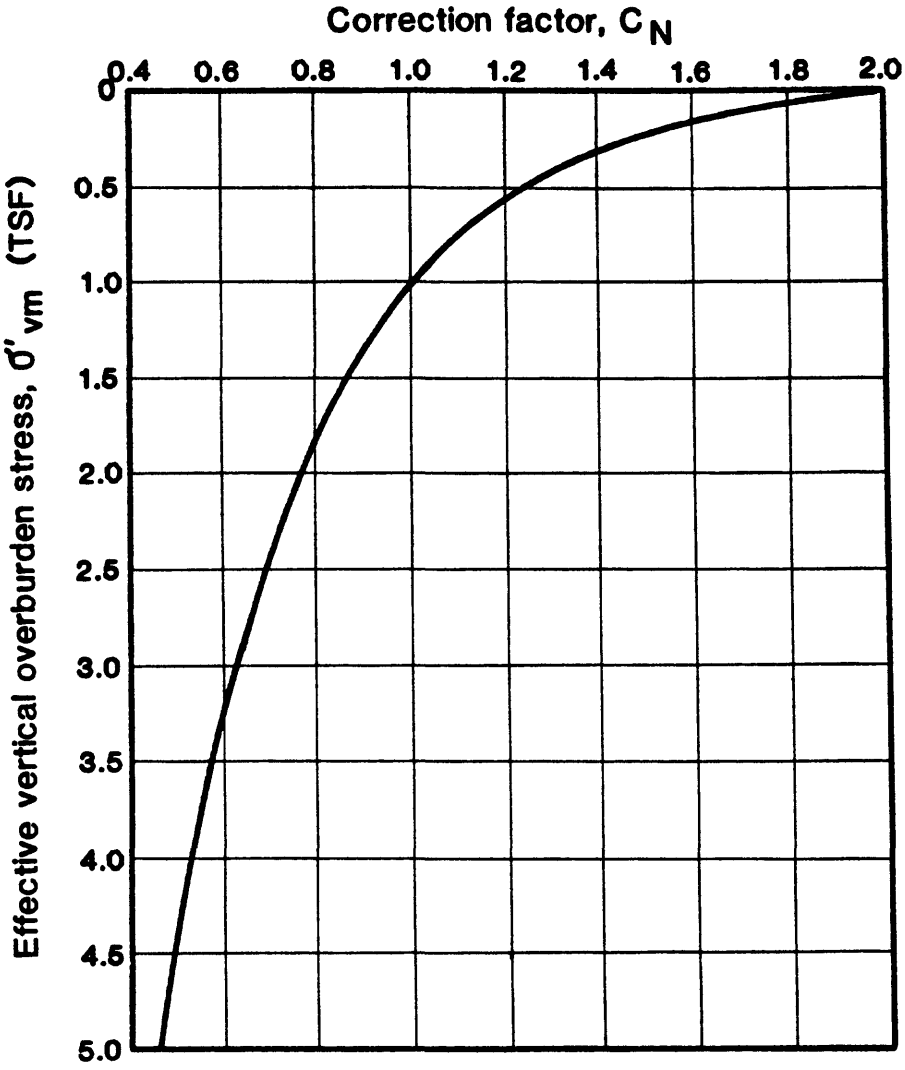

Fig. G4. Chart for correction of N-values in sand for influence of overburden pressure (reference value of effective overburden pressure is 1 ton/sq ft) (from Peck and others, 1974).

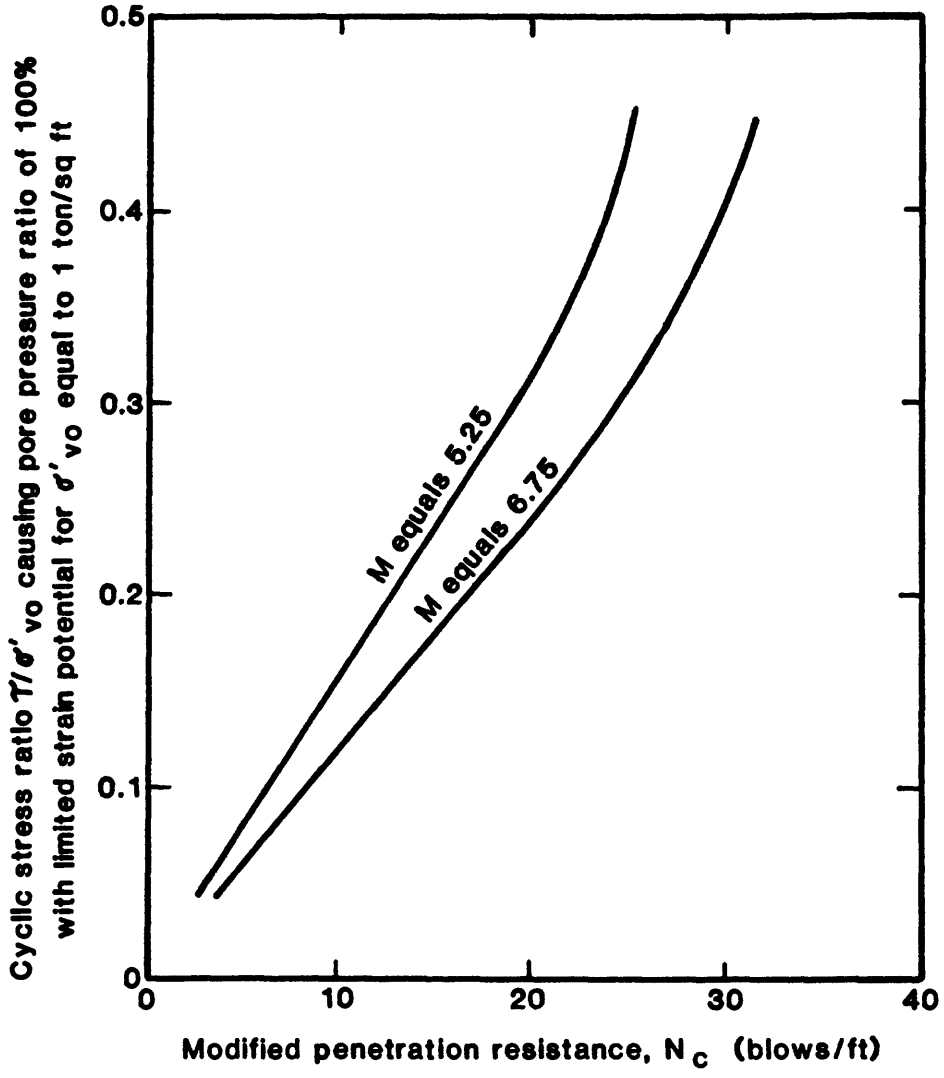

Fig. G5. Liquefaction resistance (τ/σ'_{vo}) versus modified penetration resistance (N_c) for different earthquake magnitudes (from Seed and Idriss, in press).

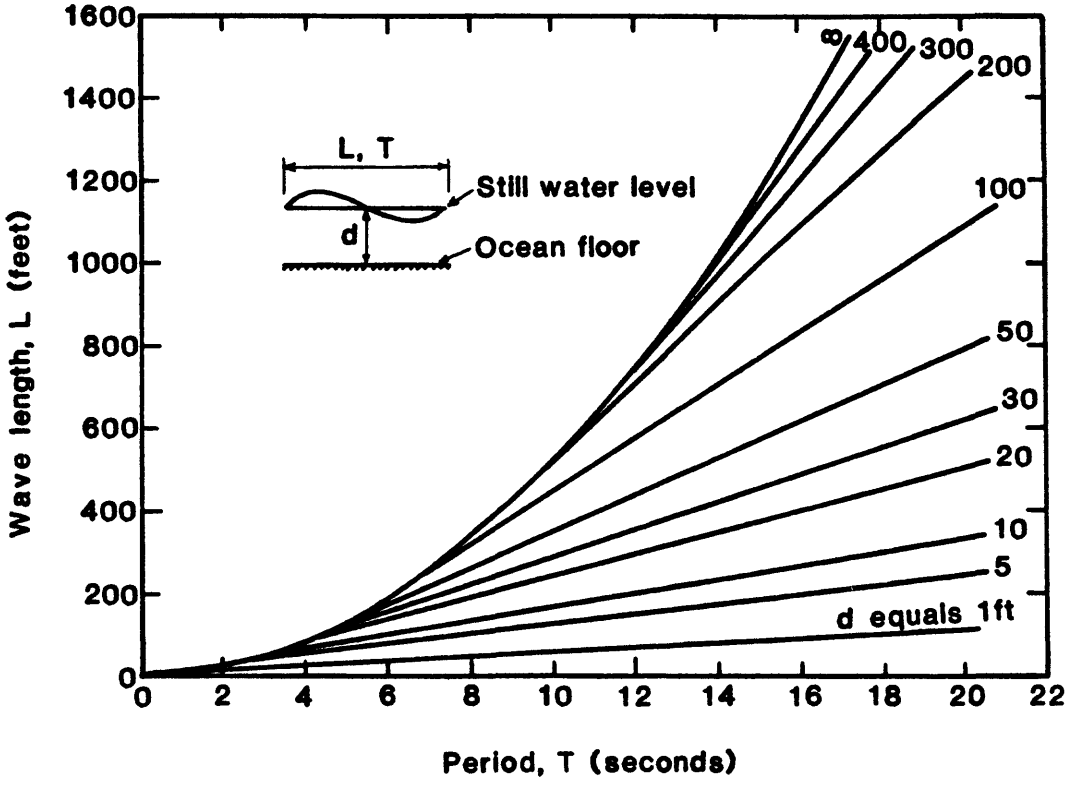

Fig. G6. Relationship between wave period, wavelength, and water depth (Wiegel, 1964, cited in Seed and Rahman, 1978).